United States
Nuclear Regulatory Commission

Passive Nondestructive Assay of Nuclear Materials

Doug Reilly, Norbert Ensslin, Hastings Smith, Jr.,
and Sarah Kreiner

A11

NUREG/CR-5550
LA-UR-90-732

Passive Nondestructive Assay of Nuclear Materials

Date Published: March 1991

Edited by: Doug Reilly, Norbert Ensslin, and Hastings Smith, Jr.
Technical Editor: Sarah Kreiner

Contractor:
Los Alamos National Laboratory
Post Office Box 1663, MS E540
Los Alamos, NM 87545

Prepared for:
Office of Nuclear Regulatory Research
U.S. Nuclear Regulatory Commission
Washington, DC 20555

NRC FIN A7241

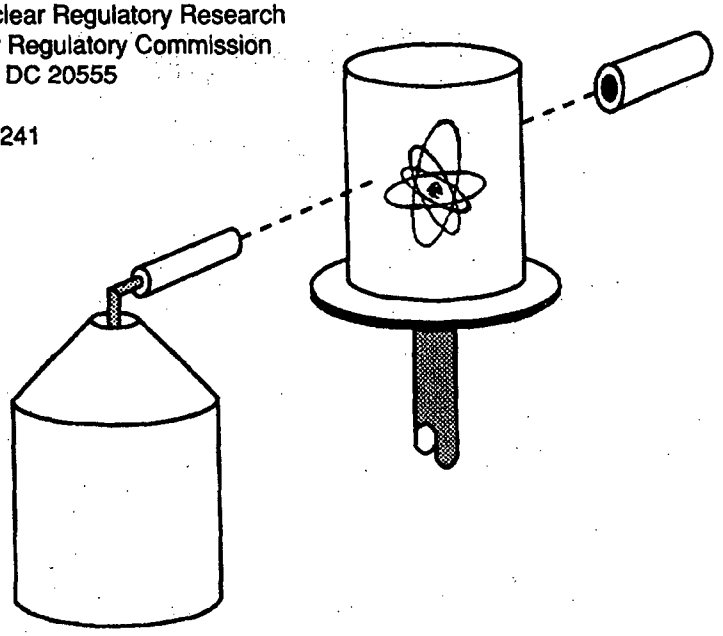

Available as NUREG/CR-5550 from
The Superintendent of Documents
U.S. Government Printing Office
P.O. Box 37082
Washington, DC 20013-7082

National Technical Information Service
5285 Port Royal Road
Springfield, VA 22161

ISBN 0-16-032724-5

PREFACE

This book is a general reference on the theory and application of passive nondestructive assay (NDA) techniques, or PANDA. It is part of a four-volume set on nuclear material measurement and accountability sponsored by the US Nuclear Regulatory Commission (NRC). Although we discuss a few active NDA techniques, they have been treated in detail in another book in the NRC series authored by T. Gozani.

The book's intended audience ranges from NDA neophytes to experienced practitioners. While the major motivation to write this book was provided by the NRC, there has long been a desire at Los Alamos to prepare a text of this kind. Many of the techniques and instruments described herein were developed at Los Alamos, and we welcome the opportunity to describe the techniques more completely than is possible in reports or papers.

We hope that you will find this text a useful and lasting reference to the interesting subject of passive NDA.

Doug Reilly, Norbert Ensslin, and Hastings Smith, Jr.

ACKNOWLEDGMENTS

The writing and preparation of this book was funded by the Office of Nuclear Regulatory Research, U. S. Nuclear Regulatory Commission, and we would like to gratefully acknowledge their support. We would especially like to thank Dr. Sandra Frattali of the Division of Safeguards for her patience and help in guiding and nurturing this project over many years. We would also like to acknowledge the ongoing support of the U.S. Department of Energy, Office of Safeguards and Security, under which the techniques and instrumentation described in this book were developed.

Many people have been involved in the production of this book. It was truly a team effort in which every participant played a vital role. The majority of the participants belong to the Safeguards Assay Group at Los Alamos National Laboratory; however, significant contributions were also made by members of the Advanced Nuclear Technology Group of the Laboratory, the University of Arizona, and Fort Lewis College. The contributing authors are listed at the beginning of the book and on the individual chapters. We would like to acknowledge the help of William B. Wilson (Applied Nuclear Science Group) on Chapter 11 and Stanley Simmonds on Chapter 14. Walt Strohm of Mound Laboratory and Ron Perry of Argonne National Laboratory provided essential information to Chapters 21 and 22 on calorimetry.

This book has benefited greatly from the peer reviewers who provided the contributing authors with corrections and suggestions for improvement. We would like to thank the following reviewers: James Cadieux (Westinghouse Savannah River Corp.), Paul Cloessner (WSRC), Raymond Dewberry (WSRC), John Fleissner (Rocky Flats Plant), Willy Higinbotham (Brookhaven National Laboratory), William Laing (Oak Ridge National Laboratory), and Samuel Untermeyer (Private Consultant).

Douglas Reilly, Norbert Ensslin, and Hastings Smith served as project leaders and principal technical reviewers as well as writers of several chapters. Sarah Kreiner was the technical editor throughout the long course of producing the volume. Much of the credit for the readability of the text goes to Sarah's careful and meticulous editing. Any volume of this size demands a great deal of work from word processors. We were ably served by Sophia Howard and Celina Ortiz who graciously put up with the many changes to the text. The photocomposition and final editing were done by Joyce A. Martinez of the Systems Technology Support Group and Martha Lee DeLanoy of the Writing and Editing Group at Los Alamos.

To all of these people we wish to express our heartfelt thanks.

CONTRIBUTING AUTHORS

Unless otherwise noted, the authors are affiliated with the Los Alamos National Laboratory.

Michael P. Baker (Chapter 13)

Thomas W. Crane (Chapter 13)

Norbert Ensslin (Chapters 11, 16, 20, 23)

Paul E. Fehlau (Chapter 19)

Robert N. Likes, Fort Lewis College, Durango, Colorado (Chapters 21, 22)

Marcia C. Lucas (Chapter 3)

Howard O. Menlove (Chapter 17)

Michael C. Miller (Chapter 10)

George W. Nelson, University of Arizona, Tucson, Arizona (Chapter 2)

Jack L. Parker (Chapters 4, 5, 6)

John R. Phillips (Chapter 18)

T. Douglas Reilly (Chapters 1, 2, 23)

Phil M. Rinard (Chapter 12)

Phyllis A. Russo (Chapter 9)

Thomas E. Sampson (Chapter 8)

Hastings A. Smith, Jr. (Chapters 3, 7, 9, 20, 23)

James K. Sprinkle (Chapter 15)

James E. Stewart (Chapter 14)

Introduction

The term nondestructive assay (NDA) is applied to a series of measurement techniques for nuclear fuel materials. The techniques measure radiation induced or emitted spontaneously from the nuclear material; the measurements are nondestructive in that they do not alter the physical or chemical state of the nuclear material. In some cases, the emitted radiation is unique to the isotope(s) of interest and the radiation intensity can often be related to the mass of the isotopes. Other techniques to measure nuclear material involve sampling the material and analyzing the sample with destructive chemical procedures. NDA obviates the need for sampling, reduces operator exposure, and is much faster than chemical assay; unfortunately NDA is usually less accurate than chemical assay. The development of NDA reflects a trend toward automation and workforce reduction that is occurring throughout our society. NDA measurements are applied in all fuel-cycle facilities for material accounting, process control, criticality control, and perimeter monitoring.

The original impetus for NDA development was the need for increased nuclear material safeguards. As safeguards agencies throughout the world needed more nuclear material measurements, it became clear that rapid measurement methods were required that would not alter the state of nuclear material items. Development efforts to address these needs were supported by the US Nuclear Regulatory Commission, the Department of Energy, and the International Atomic Energy Agency. Rapid nondestructive measurement techniques are required by the safeguards inspectors who must verify the inventories of nuclear material held throughout the world.

NDA techniques are characterized as passive or active depending on whether they measure radiation from the spontaneous decay of the nuclear material or radiation induced by an external source. This book emphasizes passive NDA techniques, although certain active techniques like gamma-ray absorption densitometry and x-ray fluorescence are discussed here because of their intimate relation to passive assay techniques.

The principal NDA techniques are classified as gamma-ray assay, neutron assay, and calorimetry. Gamma-ray assay techniques are treated in Chapters 1–10. Chapters 1–6 deal with basic subjects including the origin of gamma rays, gamma-ray interactions, detectors, instrumentation, and general measurement principles. Chapters 7–10 cover applications to uranium enrichment, plutonium isotopic composition, absorption densitometry, and x-ray fluorescence.

Neutron assay techniques are the subject of Chapters 11–17. Chapters 11–13 cover the origin of neutrons, neutron interactions, and neutron detectors. Chapters 14–17 cover the theory and applications of total and coincidence neutron counting.

Chapter 18 deals with the assay of irradiated nuclear fuel, which uses both gamma-ray and neutron assay techniques. Chapter 19 covers perimeter monitoring, which uses gamma-ray and neutron detectors of high sensitivity to check that no unauthorized nuclear material crosses a facility boundary. The subject of Chapter 20 is attribute and semiquantitative measurements. The goal of these measurements is a rapid verification of the contents of nuclear material containers to assist physical inventory verifications. Waste and holdup measurements are also treated in this chapter. Chapters 21 and 22 cover calorimetry theory and application, and Chapter 23 is a brief application guide to illustrate which techniques can be used to solve certain measurement problems. Appendices A–C contain information on statistical treatment of assay data, radiation safety, and on criticality safety.

TABLE OF CONTENTS

Chapter 10: X-Ray Fluorescence

Chapter 11: Origin of Neutron Radiation

Chapter 12: Neutron Interactions with Matter

Chapter 13: Neutron Detectors

Chapter 14: Principles of Total Neutron Counting

Chapter 15: Total Neutron Counting Instruments and Applications

1

The Origin of Gamma Rays

Douglas Reilly

1.1 GAMMA RAYS AND THE ELECTROMAGNETIC SPECTRUM

Gamma rays are high-energy electromagnetic radiation emitted in the deexcitation of the atomic nucleus. Electromagnetic radiation includes such diverse phenomena as radio, television, microwaves, infrared radiation, light, ultraviolet radiation, x rays, and gamma rays. These radiations all propagate through vacuum with the speed of light. They can be described as wave phenomena involving electric and magnetic field oscillations analogous to mechanical oscillations such as water waves or sound. They differ from each other only in the frequency of oscillation. Although given different names, electromagnetic radiation actually forms a continuous spectrum, from low-frequency radio waves at a few cycles per second to gamma rays at 10^{18} Hz and above (see Figure 1.1). The parameters used to describe an electromagnetic wave—frequency, wavelength, and energy—are related and may be used interchangeably. It is common practice to use frequency or wavelength for radio waves, color or wavelength for light waves (including infrared and ultraviolet), and energy for x rays and gamma rays.

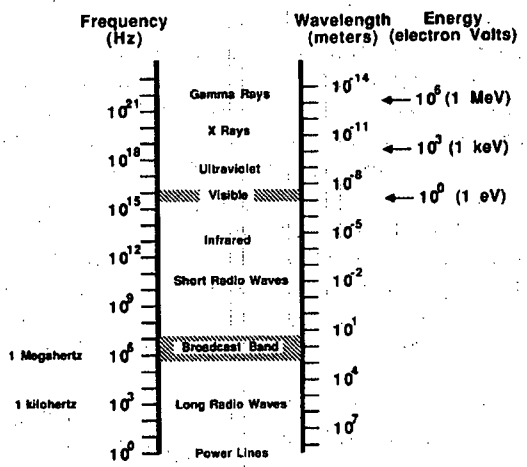

Fig. 1.1 The electromagnetic spectrum showing the relationship between gamma rays, x rays, light waves, and radio waves.

Visible light is emitted during changes in the chemical state of elements and compounds. These changes usually involve the outermost and least tightly bound atomic electrons. The colors of the emitted light are characteristic of the radiating elements and compounds and typically have energies of about 1 eV.* X rays and gamma rays are very high energy light with overlapping energy ranges of 10 keV and above. X rays are emitted during changes in the state of inner or more tightly bound electrons, whereas gamma rays are emitted during changes in the state of nuclei. The energies of the emitted radiations are characteristic of the radiating elements and nuclides.

Knowledge of these high-energy electromagnetic radiations began in Germany in 1895 with the discovery of x rays by Wilhelm Roentgen. After observing that a zinc sulfide screen glowed when it was placed near a cathode-ray discharge tube, Roentgen found that the radiation that caused the glow was dependent on the electrode materials and the tube voltage, that it was not bent by electric or magnetic fields, and that it could readily penetrate dense matter. Natural radioactivity was discovered the following year in France by Henri Becquerel, who observed that uranium salts gave off a natural radiation that could expose or blacken a photographic plate. While studying these phenomena, Marie and Pierre Curie isolated and identified the radioactive elements polonium and radium. They determined that the phenomena were characteristic of the element, not its chemical form.

These "radioactive rays" were intensely studied in many laboratories. In 1899 in England, Ernest Rutherford discovered that 95% of the radiation was effectively stopped by 0.02 mm of aluminum and 50% of the remaining radiation was stopped by 5 mm of aluminum or 1.5 mm of copper. Rutherford named the first component "alpha" and the second, more penetrating radiation, "beta." Both of these radiations were deflected by electric and magnetic fields, though in opposite directions; this fact indicated that the radiations carried electrical charge. In 1900 Paul Villard and Henri Becquerel noted that a photographic plate was affected by radioactive materials even when the plate was shielded by 20 cm of iron or 2 to 3 cm of lead. They also noted that this penetrating radiation showed no magnetic deflection. In 1903 Rutherford named this component "gamma" and stated that "gamma rays are probably like Roentgen rays." Thus the three major radiations were identified and named for the first three letters of the Greek alphabet: α, β and γ.

As indicated by the brief description of their discovery, gamma rays often accompany the spontaneous alpha or beta decay of unstable nuclei. X rays are identical to gamma rays except that they are emitted during rearrangement of the atomic electron structure rather than changes in nuclear structure. X-ray energies are unique to each element but the same for different isotopes of one element. They frequently accompany nuclear decay processes, which disrupt the atomic electron shell.

---

* The electron volt (eV) is a unit of energy equal to the kinetic energy gained by an electron accelerated through a potential difference of 1 V; 1 eV equals 1.602×10^{-19} J. This small unit and the multiple units keV (10^3 eV) and MeV (10^6 eV) are useful for describing atomic and molecular phenomena.

Gamma rays from spontaneous nuclear decay are emitted with a rate and energy (color) spectrum that is unique to the nuclear species that is decaying. This uniqueness provides the basis for most gamma-ray assay techniques: by counting the number of gamma rays emitted with a specific energy, it is possible to determine the number of nuclei that emit that characteristic radiation.

1.2 CHARACTERISTICS OF NUCLEAR DECAY

1.2.1 Nuclear Decay Processes: General

The atomic nucleus is assumed to be a bound configuration of protons and neutrons. Protons and neutrons have nearly the same mass and differ principally in charge: protons have a positive charge of 1 and neutrons are electrically neutral. Different elements have nuclei with different numbers of neutrons and protons. The number of protons in the nucleus is called the atomic number and given the symbol Z. In the neutral atom, the number of protons is equal to the number of electrons. The number of neutrons in the nucleus is given the symbol N. The total number of nucleons (protons and neutrons) in the nucleus is called the atomic mass number and given the symbol A (A = Z + N).

For all nuclear decay processes, the number of unstable nuclei of a given species is found to diminish exponentially with time:

$$n = n_0 \, e^{-\lambda t} \tag{1-1}$$

where n = number of nuclei of a given species at time t
n_0 = number of nuclei at t = 0
λ = decay constant, the parameter characterizing the exponential.

Each nuclear species has a characteristic decay constant. Radioactive decay is most commonly discussed in terms of the nuclear half-life, $T_{1/2}$, which is related to the decay constant by

$$T_{1/2} = (\ell n \, 2)/\lambda \, . \tag{1-2}$$

The half-life is the time necessary for the number of unstable nuclei of one species to diminish by one-half. (Half-lives are commonly tabulated in nuclear data tables). The decay rate or specific activity can be represented in terms of the half-life as follows:

$$R = \frac{1.32 \times 10^{16}}{A \, T_{1/2}} \tag{1-3}$$

where R = rate in decays per second per gram
A = atomic weight
$T_{1/2}$ = half-life in years.

Equation 1–3 is often used to estimate the activity per gram of a sample.

An alpha or beta decay of a given nuclear species is not always accompanied by gamma-ray emission. The fraction of decays that is accompanied by the emission of a specific energy gamma ray is called the branching intensity. For example, the most intense gamma ray emitted by ^{235}U has an energy of 185.7 keV and a branching intensity of 54%. Uranium-235 decays by alpha-particle emission with a half-life of 7.038×10^8 yr. Equation 1-3 thus implies an alpha emission rate of 7.98×10^4/g-s. Only 54% of the alpha particles are accompanied by a 185.7-keV gamma ray; therefore, the specific activity of this gamma ray is 4.3×10^4/g-s.

Of the natural decay radiations only the gamma ray is of interest for nondestructive assay of bulk nuclear materials because the alpha- and beta-particle ranges are very short in condensed matter. Consider the following ranges in copper metal:

5-MeV α: 0.01 mm or 0.008 g/cm^2
1-MeV β: 0.7 mm or 0.6 g/cm^2
0.4-MeV γ: 12 mm or 10.9 g/cm^2(mean free path).

1.2.2 Alpha Decay

The alpha particle is a doubly ionized (bare) $^4He_2$ nucleus. It is a very stable, tightly bound nuclear configuration. When a nucleus decays by alpha emission, the resulting daughter nucleus has a charge that is two units less than the parent nucleus and an atomic mass that is four units less. This generic reaction can be represented as follows:

$$^{A}X_{Z} \rightarrow {}^{A-4}X_{Z-2} + {}^{4}He_2 \ . \qquad (1\text{-}4)$$

The decay can occur only if the mass of the neutral parent atom is greater than the sum of the masses of the daughter and the neutral ^4He atom. The mass difference between the parent and the decay products is called the Q-value and is equal to the kinetic energy of the decay products:

$$Q = (M_p - M_d - M_{He})c^2 \qquad (1\text{-}5)$$

where $M_{p,d,He}$ = neutral atomic mass of the parent, daughter, and ^4He atom
c = velocity of light.

When the parent nucleus decays, most of the energy Q goes to the alpha particle because of its lower mass:

$$E_\alpha = Q(A - 4)/A \ . \qquad (1\text{-}6)$$

The remainder of the available energy goes into the recoil of the daughter nucleus.

Most of the approximately 160 known alpha emitters are heavy nuclei with atomic numbers greater than 82. The energy of the emitted alpha particle ranges from 4 to 10 MeV and the half-lives vary from 10^{-6} s to 10^{10} yr. The short-lived nuclei emit high-energy alpha particles when they decay.

Immediately after the decay of the parent nucleus, the daughter nucleus can be either in the ground state or in an excited state. In the latter case the nucleus can relax by either of two mechanisms: gamma-ray emission or internal conversion. The radiative relaxation leads to emission of one or more gamma rays (typically, 10^{-14} s after the alpha emission) with discreet energies whose sum equals the original excitation energy. During internal conversion the nucleus transfers the excitation energy directly to one of the most tightly bound atomic electrons, usually a K electron. The electron leaves the atom with an energy equal to the difference of the transition energy and the electron binding energy. The resulting vacancy leads to the emission of x rays or electrons (called Auger electrons) with the characteristic energy spectrum of the daughter element. The probability of internal conversion increases strongly with atomic number (Z) and with decreasing excitation energy.

In some cases the alpha decay leads to an excited state that lives much longer than 10^{-14} s. If the lifetime of this state is longer than approximately 10^{-6} s, it is called an isomer of the ground-state nucleus. An example of an isomer is the alpha decay of ^{239}Pu that leads to ^{235}U:

$$^{239}\text{Pu} \rightarrow {}^{235m}\text{U (26 min 99.96\%)} \rightarrow {}^{235}\text{U}$$
$$^{239}\text{Pu} \rightarrow {}^{235}\text{U(0.04\%)} . \qquad (1\text{-}7)$$

The common decay mode of ^{239}Pu leads first to the isomer ^{235m}U, which has a half-life of 26 min. The direct decay to ^{235}U occurs only 0.04% of the time. One of the longest lived isomers is $^{91m}\text{Nb}_{41}$, with a half-life of 60 days.

All the alpha particles, gamma rays, and internal conversion electrons emitted during the decay process have discreet, characteristic energies. The observation of these characteristic spectra showed that nuclei have discreet allowed states or energy levels analogous to the allowed states of atomic electrons. The various spectroscopic observations have provided information for developing the nuclear level schemes presented in handbooks such as the *Table of Isotopes* (Ref. 1). An example appears in Figure 1.2 showing the lower energy levels of ^{235}U populated during the alpha decay of ^{239}Pu. These levels give rise to the characteristic gamma-ray spectrum of ^{239}Pu. Note that the characteristic gamma-ray spectrum is commonly associated with the parent or decaying nucleus even though the energies are determined by the levels of the daughter nucleus. Although this practice may seem confusing, it is universally followed for gamma rays. The confusion is further aggravated by the common use of x-ray nomenclature that associates the characteristic x rays with the daughter element. Hence the alpha decay of ^{239}Pu leads to ^{235}U and is accompanied by the emission of ^{239}Pu gamma rays and uranium x rays.

1.2.3 Beta Decay

In the beta decay process the atomic number (Z) increases or decreases by one unit and the atomic mass number (A) stays constant. In effect, neutrons and protons change state. The three types of beta decay are β^-, β^+, and electron capture.

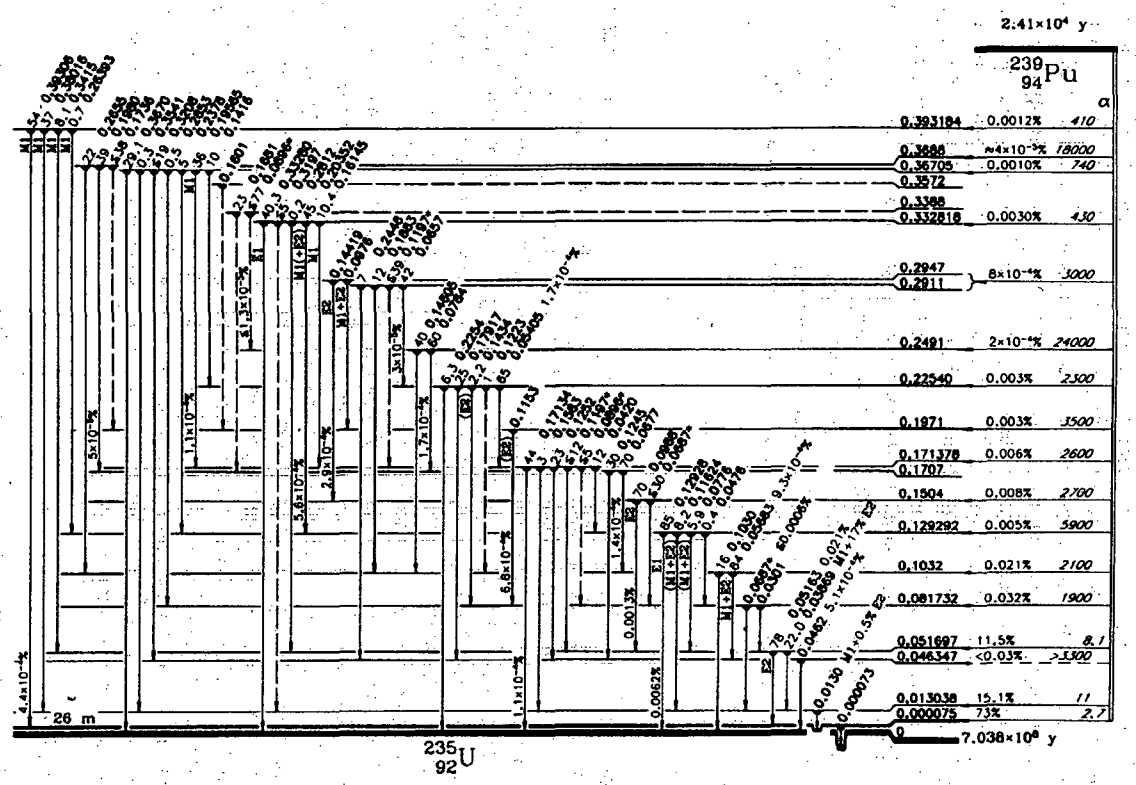

Fig. 1.2 Diagram of some of the nuclear energy levels of ^{235}U. These levels are populated during the decay of ^{239}Pu and give rise to the characteristic gamma-ray spectrum of ^{239}Pu. Figure adapted from Ref. 1.

Beta-minus decay was the first detected process; the β^- particle was found to be a normal electron. During the decay process the nucleus changes state according to the following formula:

$$^{A}X_{Z} \rightarrow {}^{A}X_{Z+1} + e^{-} + \overline{\nu_e} \, . \tag{1-8}$$

The β^- decay process can be thought of as the decay of a neutron into a proton, an electron, and an electron antineutrino. The decay is energetically possible for a free neutron and occurs with a half-life of 12.8 min. This is the common beta-decay process for nuclei with high atomic number and for fission-product nuclei, which usually have significantly more neutrons than protons.

During β^+ decay the nucleus changes state according to the following formula:

$$^{A}X_{Z} \rightarrow {}^{A}X_{Z-1} + e^{+} + \nu_e \, . \tag{1-9}$$

Electron capture competes with the β^+ decay process. The nucleus interacts with an inner atomic electron and, in effect, captures it, changing a proton into a neutron with the emission of a positron and an electron neutrino. The formula for this process is

$$^{A}X_{Z} + e^{-} \rightarrow {}^{A}X_{Z-1} + \nu_e \, . \tag{1-10}$$

All unstable nuclei with atomic number less than 82 decay by at least one of the three processes and sometimes by all three (see Figure 1.3). Beta decay occurs whenever it is energetically possible. It is energetically possible if the following conditions are met for the masses of the neutral parent atoms (p) and the potential daughter atom (d):

β^- decay: $M_p > M_d$

β^+ decay: $M_p > M_d + 2m_e$

Electron capture: $M_p > M_d$. (1-11)

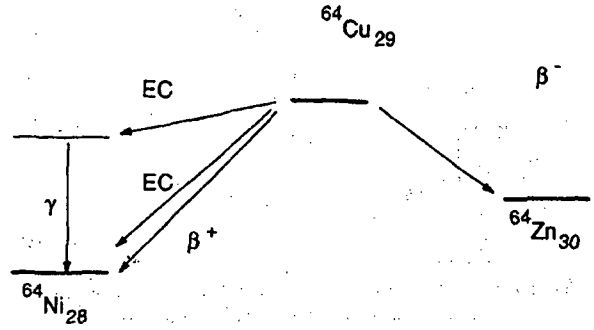

Fig. 1.3 Nuclear decay scheme of ^{64}Cu showing three possible beta decay processes.

Beta decay can be to the ground state or to an excited state in the daughter nucleus. In the latter case the excited state decays by gamma-ray emission or internal conversion.

1.3 X-RAY PRODUCTION

1.3.1 The Bohr Model of the Atom

In the simple Bohr model of the atom, the positive nucleus contains protons and neutrons and has an approximate radius of 1.4×10^{-15} $(A^{1/3})$m and an approximate density of 2×10^{14} g/cm^3. The nucleus is surrounded by a cloud of negative electrons in discrete, well-defined energy levels or orbitals. The radii of these orbitals are in the range 10^{-9} to 10^{-8} m. The original Bohr model had well-localized orbits and led to the familiar planetary diagram of the atom. Although not accepted at present, this concrete model is useful for explaining x-ray production.

The different energy levels are designated K, L_1, L_2, L_3, M_1, ..., M_5, and so forth. (As an example, consider the electron energy levels of uranium illustrated in Figure 1.4.) The electric force between an electron and the positively charged nucleus varies as the inverse square of the separation; therefore, the electrons closer to the nucleus have a higher binding energy B. The binding energy is the energy required to remove the electron from the atom. The K-shell electrons are always the most tightly bound. Quantum mechanics gives a good description of the energies of each level and how the levels fill up for different elements. The chemical properties of the elements are determined by the electron configuration.

In its normal resting configuration the atom is stable and does not radiate. If an electron moves from a higher to a lower energy level, it radiates an x ray.

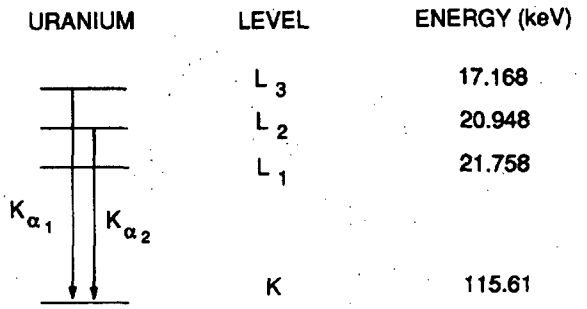

Fig. 1.4 Electron energy levels in uranium. Transitions between the levels shown give rise to the K-series x rays.

1.3.2 X-Ray Production Mechanisms

Various interactions ionize or remove an electron from an atom. All energetic, charged particles interact with electrons as they pass through matter. X-ray and gamma-ray photons also interact with atomic electrons. Nuclear interactions such as internal conversion or electron capture can cause the ionization of atomic electrons.

When an electron leaves an atom, the atom is in an excited state with energy B_i by virtue of the vacancy in the i^{th} electron level. This vacancy may be filled by a more loosely bound electron from an outer orbital, the j^{th} level. The change in energy level is accompanied by the emission of an x ray with energy $B_i - B_j$ or by the emission of an Auger electron with energy $B_i - 2B_j$. In the latter case the atom transfers its excess energy directly to an electron in an outer orbital. The fraction of vacancies in level i that result in x-ray emission is defined as the fluorescence yield W_i. Figure 1.5 shows the variation of the K-shell fluorescence yield with atomic number. X-ray emission is more probable for high-Z elements (for $Z > 70$, $W_K > 95\%$).

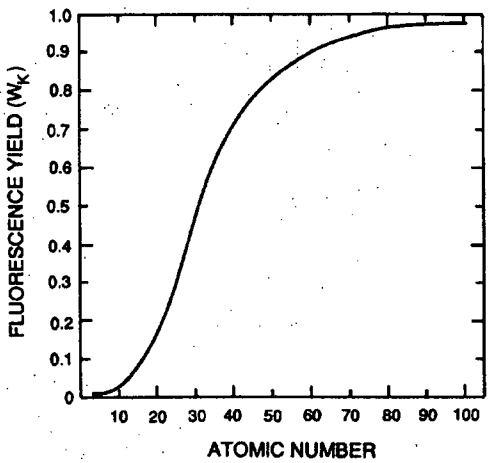

Fig. 1.5 Variation of the K-shell fluorescence yield, W_K, with atomic number.

High-Z materials have high internal conversion coefficients, which means that their normal decay modes lead to vacancies in an inner electron shell (usually K or L) and the production of characteristic x rays. Because these vacancies occur in the daughter atom, the x-ray energies are characteristic of the daughter element. In condensed materials the charged particles (α, β) and gamma rays from the nuclear decay are stopped in the parent material by a series of interactions with atomic electrons; this leads to the production of x rays that are characteristic of the parent atom. Plutonium metal emits uranium x rays by virtue of the internal conversion process that occurs after alpha decay. It also emits plutonium x rays by virtue of alpha-particle-induced x-ray fluorescence.

1.3.3 Characteristic X-Ray Spectra

Each element emits a characteristic x-ray spectrum. All elements have the same x-ray pattern, but the x-ray energies are different. Figure 1.6 shows the characteristic x rays from uranium and lead.

Early investigators developed the system commonly used today for naming x rays. A roman letter indicates the final level to which the electron moves, and a Greek letter plus a number indicates the electron's initial energy level. (The Greek letter was originally related to the x-ray energy and the number to its intensity). Table 1-1 gives the major K x rays of uranium and plutonium. The L and M x rays are of lower energy and are tabulated in the literature.

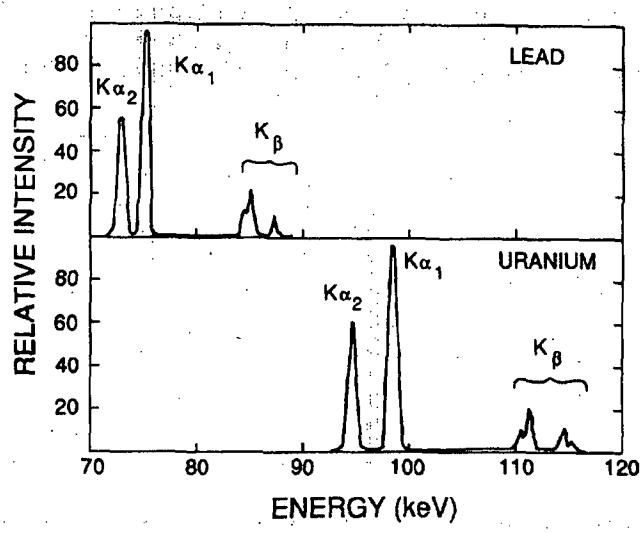

Fig. 1.6 Characteristic x-ray spectra from lead and uranium. Note that the pattern is the same but shifted in energy.

1.4 MAJOR GAMMA RAYS FROM NUCLEAR MATERIAL

1.4.1 Typical Spectra

Figures 1.7 through 1.12 show typical uranium, plutonium, and thorium gamma-ray spectra. The spectra were measured with high-resolution germanium detector systems. Figure 1.7 shows the spectrum of highly enriched uranium from 0 to 3 MeV, with

Table 1-1. Major K x rays of uranium and plutonium[a]

	Levels	Energy (keV)		Intensity[b]	
X Ray	(Final - Initial)	Uranium	Plutonium	Uranium	Plutonium
$K_{\alpha 2}$	K - L_2	94.67	99.55	61.9	62.5
$K_{\alpha 1}$	K - L_3	98.44	103.76	100	100
$K_{\beta 1}$	K - M_3	111.30	117.26	22.0	22.2
$K_{\beta 2}$	K - N_{2-5}	114.5	120.6	12.3	12.5
$K_{\beta 3}$	K - M_2	110.41	116.27	11.6	11.7

[a]Other x rays in the K series are weaker than those listed here. The energies and intensities are from Ref. 1.
[b]Relative intensity, 100 is maximum.

characteristic gamma rays from ^{235}U and the ^{238}U daughter ^{234m}Pa. The intense gamma rays between 140 and 210 keV are often used for the assay of ^{235}U (Figure 1.8 shows this region in more detail). For comparison, Figure 1.9 shows a spectrum of depleted uranium; the spectrum shows the ^{238}U daughter radiations often used for ^{238}U assay. Figures 1.10 and 1.11 are gamma-ray spectra of plutonium with approximate ^{240}Pu concentrations of 14% and 6%, respectively. Note the differences in relative peak heights between the two spectra; these differences are used to determine the plutonium isotopic composition (see discussion in Chapter 8). Figure 1.12 shows the characteristic gamma-ray spectrum of ^{232}Th; all major thorium gamma rays come from daughter nuclides.

1.4.2 Major Gamma-Ray Signatures for Nuclear Material Assay

In principle, any of the gamma rays from nuclear material can be used to determine the mass of the isotope that produces them. In practice, certain gamma rays are used more frequently than others because of their intensity, penetrability, and freedom from interference. The ideal signature would be an intense ($>10^4$ γ/g-s) gamma ray with an energy of several million electron volts. The mass attenuation coefficients of all materials show a broad minimum between 1 to 5 MeV and there are very few natural gamma rays above 1 MeV that can cause interference. Unfortunately, such gamma rays do not exist for uranium or plutonium.

Table 1-2 lists the gamma rays most commonly used for the nondestructive analysis of the major uranium and plutonium isotopes.

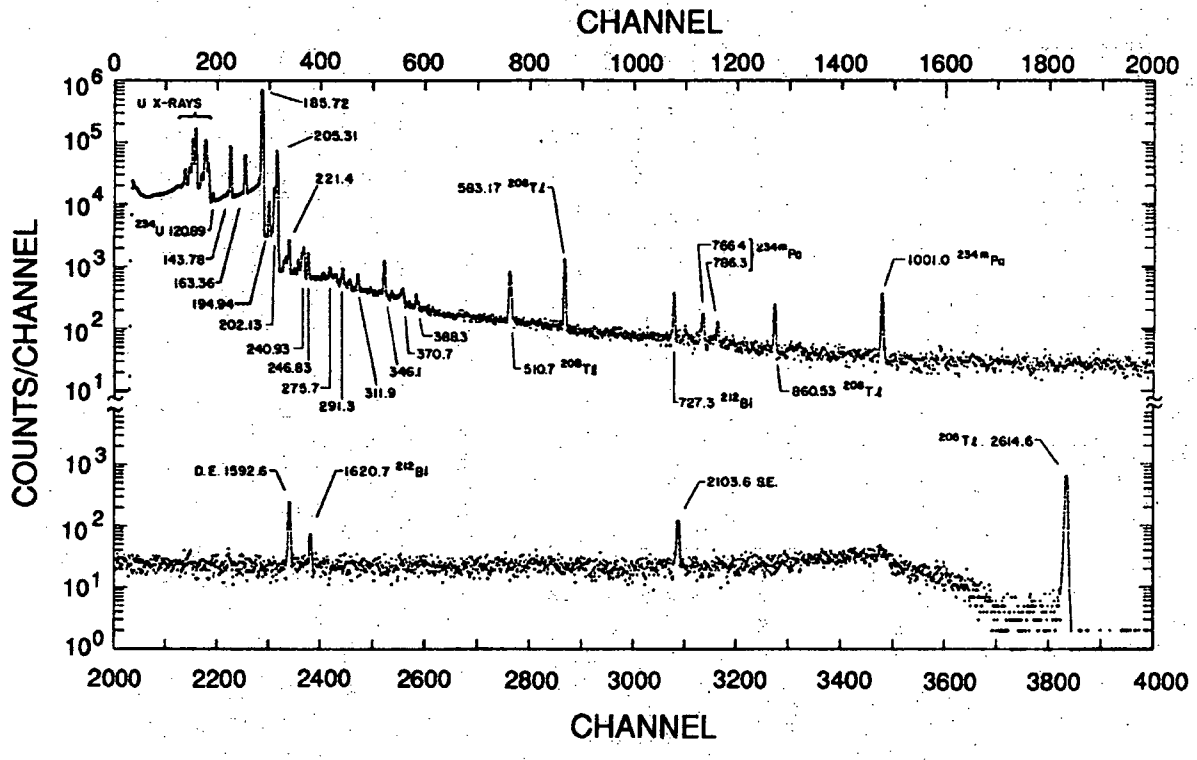

Fig. 1.7 High-resolution gamma-ray spectrum of highly enriched uranium (93% ^{235}U). Energies are given in kiloelectron volts. (S.E. and D.E. are the single- and double-escape peaks of the 2614-keV gamma ray.)

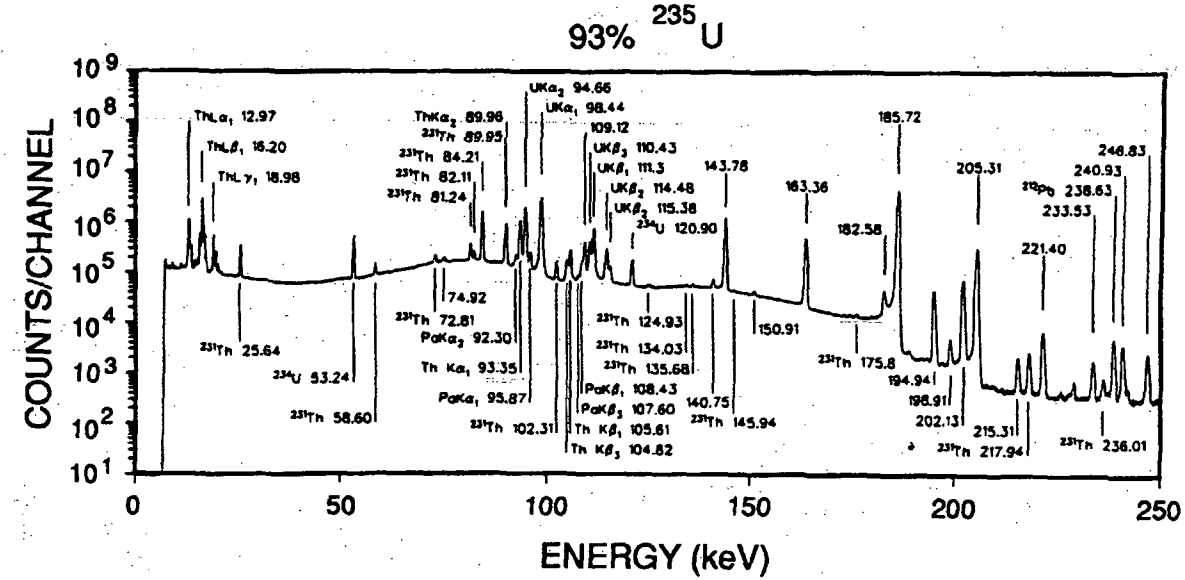

Fig. 1.8 Gamma-ray spectrum of highly enriched uranium showing the intense gamma rays often used for assay of ^{235}U.

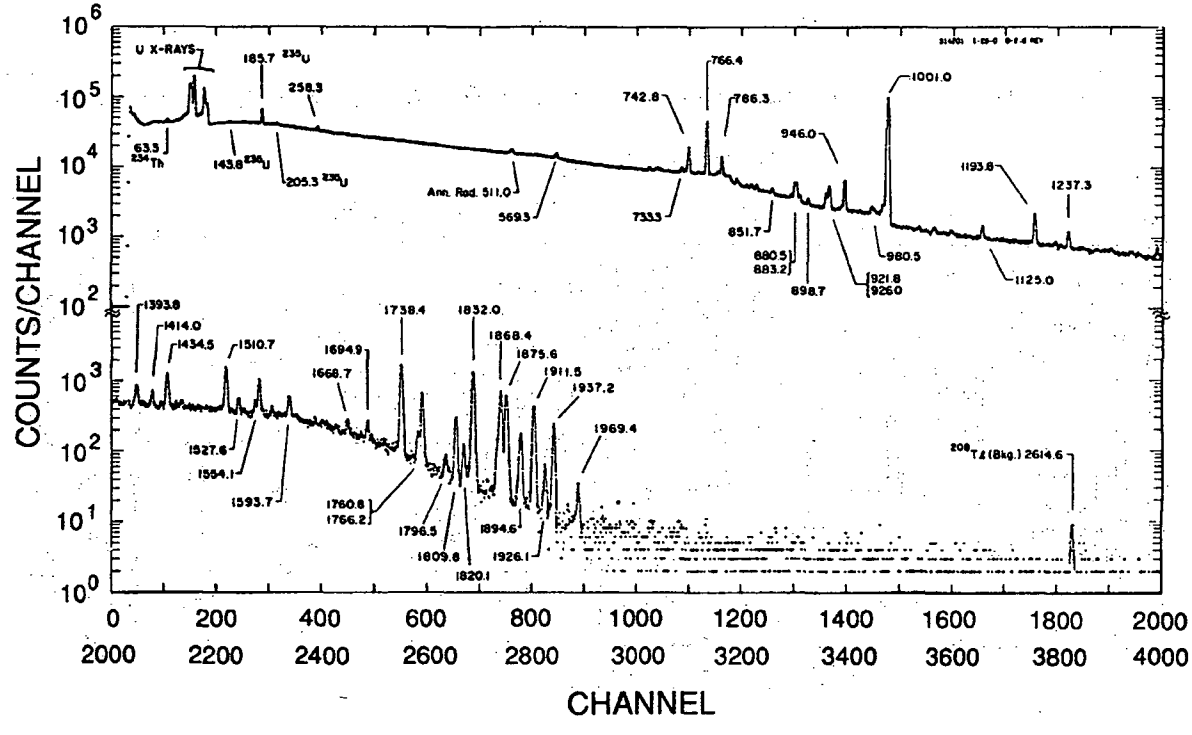

Fig. 1.9 Gamma-ray spectrum of depleted uranium (0.2% ^{235}U). The intense gamma rays at 766 and 1001 keV are from the ^{238}U daughter ^{234m}Pa, and are often used for the assay of ^{238}U. Most of the weak gamma rays above 1001 keV also come from ^{234m}Pa. (Ann. Rad. is annihilation radiation; the small peak at 511 keV is due to positron annihilation.)

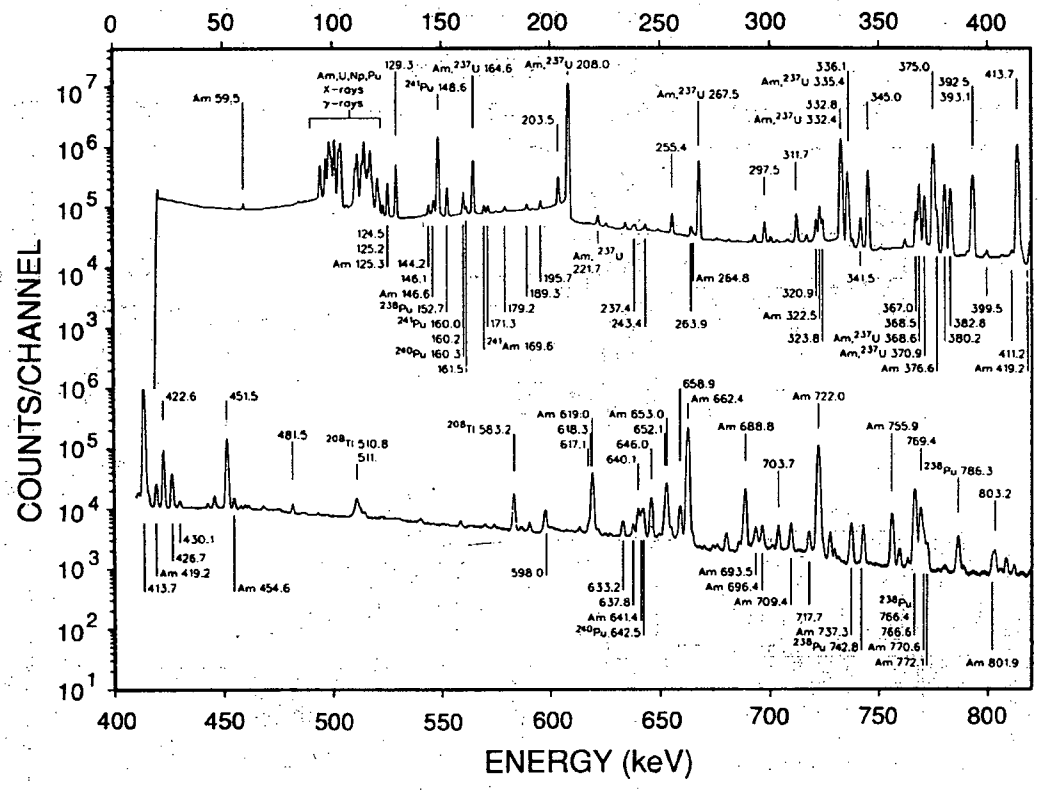

Fig. 1.10 *Gamma-ray spectrum of plutonium with 14% ^{240}Pu and 1.2% ^{241}Am. Compare this spectrum with that of Figure 1.11, noting the difference in relative intensities. Compare the intensities of the gamma rays at 203.5 keV (^{239}Pu) and 208.0 keV (^{237}U, daughter of ^{241}Pu).*

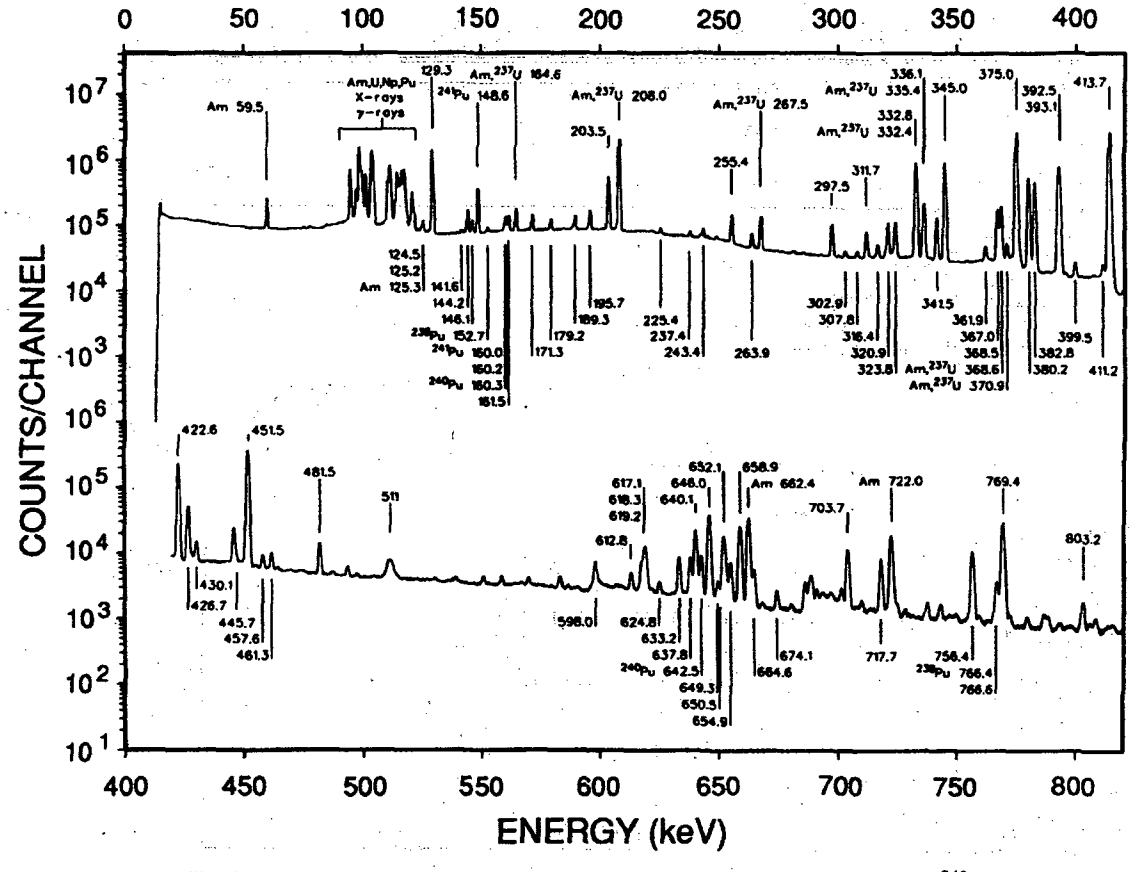

Fig. 1.11 Gamma-ray spectrum of low-burnup plutonium with approximately 6% ^{240}Pu.

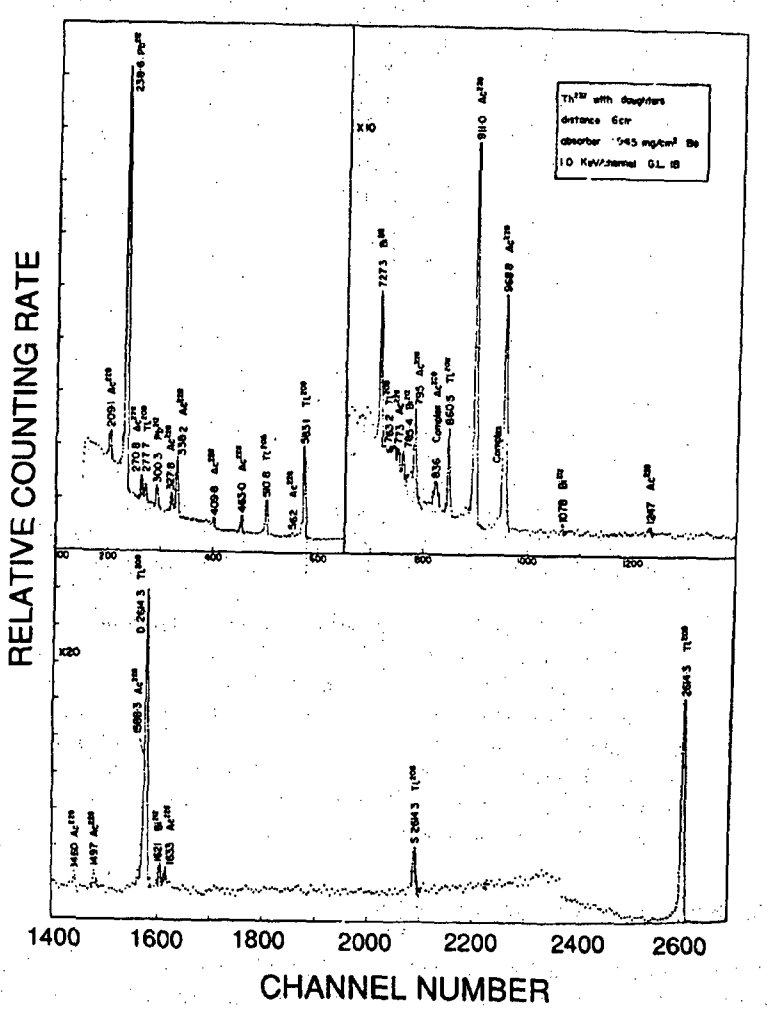

Fig. 1.12 Gamma-ray spectrum of ^{232}Th and its daughter products. Thorium-232 emits no significant gamma rays of its own. The daughter nuclides grow into equilibrium with the ^{232}Th parent over a period of approximately 35 yr. [Figure adapted from F. Adams and R. Dams, Applied Gamma-Ray Spectroscopy, *3rd ed. (Pergamon Press, Oxford, 1970).]*

Table 1-2. Major NDA gamma-ray signatures

Isotope	Energy[a] (keV)	Activity[a] (γ/g-s)	Mean Free Path[b](mm) (High-Z, ρ)	(Low-Z, ρ)
^{234}U	120.9	9.35×10^4	0.23	69
^{235}U	143.8	8.40×10^3	0.36	73
	185.7	4.32×10^4	0.69	80
^{238}U	766.4[c]	2.57×10^1	10.0	139
	1001.0[c]	7.34×10^1	13.3	159
^{238}Pu	152.7	5.90×10^6	0.40	75
	766.4	1.387×10^5	9.5	139
^{239}Pu	129.3	1.436×10^5	0.27	71
	413.7	3.416×10^4	3.7	106
^{240}Pu	45.2	3.80×10^6	0.07	25
	160.3	3.37×10^4	0.45	76
	642.5	1.044×10^3	7.4	127
^{241}Pu	148.6	7.15×10^6	0.37	74
	208.0[d]	2.041×10^7	0.86	83
^{241}Am	59.5	4.54×10^{10}	0.14	38
	125.3	5.16×10^6	0.26	70

[a]Data for uranium isotopes are from Ref. 1; data for plutonium isotopes are from Ref. 2 (energy and branching ratio) and Ref. 3 (half-life).
[b]The mean free path is the absorber thickness that reduces the gamma-ray intensity to 1/e. The mean free path in uranium or plutonium oxide (ρ = 10 g/cm^3) is given for the high-density, high-atomic-number case (high-Z, ρ). The mean free path in aluminum oxide (ρ = 1 g/cm^3) is given for the low-density, low-atomic-number case (low-Z, ρ). Attenuation data are from Ref. 4.
[c]From the ^{238}U daughter ^{234m}Pa. Equilibrium assumed.
[d]From the ^{241}Pu daughter ^{237}U. Equilibrium assumed.

1.4.3 Fission-Product Gamma Rays

Considerable interest has been shown in the measurement of irradiated fuel from nuclear reactors. The irradiated fuel has a high monetary value and a high safeguards value because of the plutonium produced during reactor operation. Gamma rays from the spontaneous decay of uranium and plutonium cannot be used for measurement of irradiated fuel because they are overwhelmed by the very intense gamma rays emitted by fission products that build up in the fuel during irradiation. The total gamma-ray intensity of the fission products from light-water-reactor fuel irradiated to 33 000 MWd/tU (megawatt days per ton of uranium) is approximately 2×10^{10} γ/g-s (g = gram of uranium) one year after removal of the fuel from the reactor, whereas

the major uranium and plutonium gamma rays have intensities in the range 10^3 to 10^4 γ/g-s. In some instances the intensity of one or more fission products can be measured and related to the mass of the contained nuclear material.

Certain high-Z nuclei can fission or split into two or three medium-Z daughter nuclei. The fission process can occur spontaneously or it can be induced when the parent nucleus absorbs a neutron. Spontaneous fission is more probable in nuclei with even atomic mass numbers (A). Induced fission can occur after absorption of either thermal or fast neutrons in nuclei with odd mass numbers; it only occurs after absorption of fast neutrons in even-numbered nuclei. The fission process was first discovered in 1939 by Otto Hahn and Freidrich Strassman and correctly interpreted in the same year by Lise Meitner and Otto Frisch.

The fission of a nucleus is a cataclysmic event when compared with the alpha- and beta-decay processes described in Sections 1.2.2 and 1.2.3. The energy released in fission is approximately 200 MeV. Most of this energy is carried as kinetic energy by the two (rarely three) daughter nuclei (called fission products or fission fragments). The fissioning nucleus also emits an average of two prompt neutrons and six prompt gamma rays at the instant it splits. A typical fission reaction is illustrated by the formula

$$n + {}^{235}U_{92} \rightarrow {}^{137}Cs_{55} + {}^{97}Rb_{37} + 2n \, . \qquad (1\text{-}12)$$

This formula illustrates only one of the many possible fission reactions. The fission-product nuclei themselves are unstable. They have an excess of neutrons and decay by neutron emission or β^- decay (frequently accompanied by gamma-ray emission); the radiations from these reactions are called delayed neutrons and gamma rays. The fission products have half-lives ranging from seconds to years. The gamma rays from fission products can be used to measure irradiated fuel materials.

Typical spectra from irradiated fuel are shown in Figures 1.13 and 1.14. Figure 1.13 shows a spectrum from highly enriched uranium fuel used in a materials test reactor. Figure 1.14 shows an irradiated light-water-reactor fuel spectrum. The most commonly measured fission-product gamma ray is from ^{137}Cs at 661.6 keV. This fission product has a high yield and a sufficiently long half-life (30.2 yr) so that its concentration is proportional to the total number of fissions that have occurred in the fuel. (See Chapter 18 for a more complete discussion of the fission reaction and the measurement of irradiated fuel.)

1.4.4 Background Radiation

All gamma-ray detectors will give some response even in the absence of a measurement sample. This response is due to the ambient background in the location of the detector. The ambient background consists of radiation from nuclear material in nearby storage areas, cosmic-ray interactions, and natural radioactivity in the local environment.

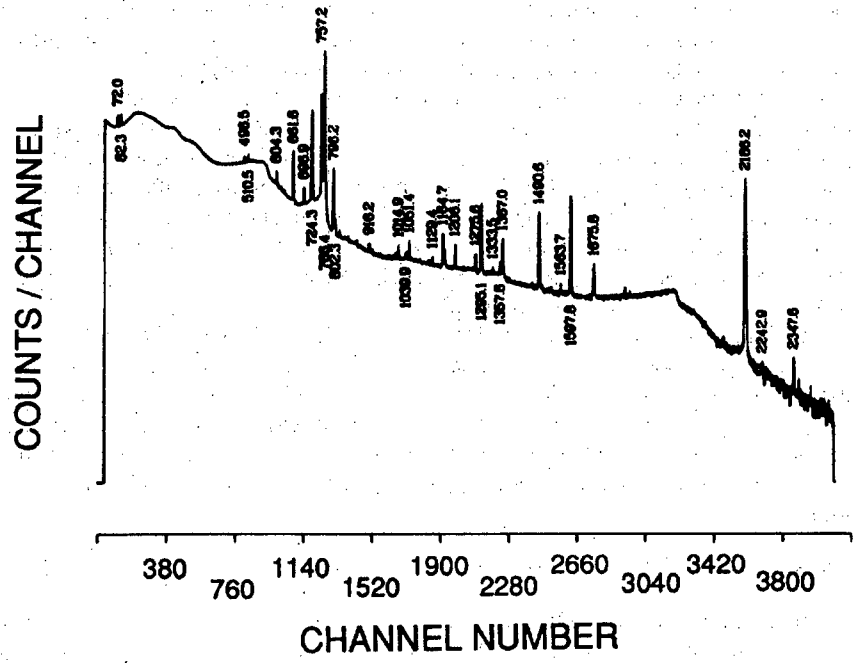

Fig. 1.13 Gamma-ray spectrum of highly enriched uranium fuel irradiated in a materials test reactor. The sample had an average burnup of 36.9% and a cooling time of 1.59 yr.

The radiation from the nuclear material stored nearby is of the same nature as the radiation from the samples to be measured. This background spectrum is similar to the spectra shown in Figures 1.7 through 1.12. It often has a high Compton continuum resulting from degradation and scattering in the materials that separate the detector from the storage area. Background radiation from nuclear material can be minimized with a judicious choice of detector location and shielding.

At the earth's surface, cosmic rays consist primarily of high-energy gamma rays and charged particles. Although a neutron component exists, it has little effect on gamma-ray detectors. The charged particles are mostly muons but also include electrons and protons. The muon flux at sea level is approximately 0.038/cm^2-s; at an altitude of 2000 m, the muon flux increases to approximately 0.055/cm^2-s. The muon interacts with matter as though it were a heavy electron and its rate of energy loss when passing through typical solid or liquid detector materials is approximately 8.6 MeV/cm. A typical penetrating muon deposits approximately 34 MeV in a 40-mm-thick detector. Because this is much more energy than can be deposited by gamma rays from uranium or plutonium, muon interactions often overload or saturate the detector electronics.

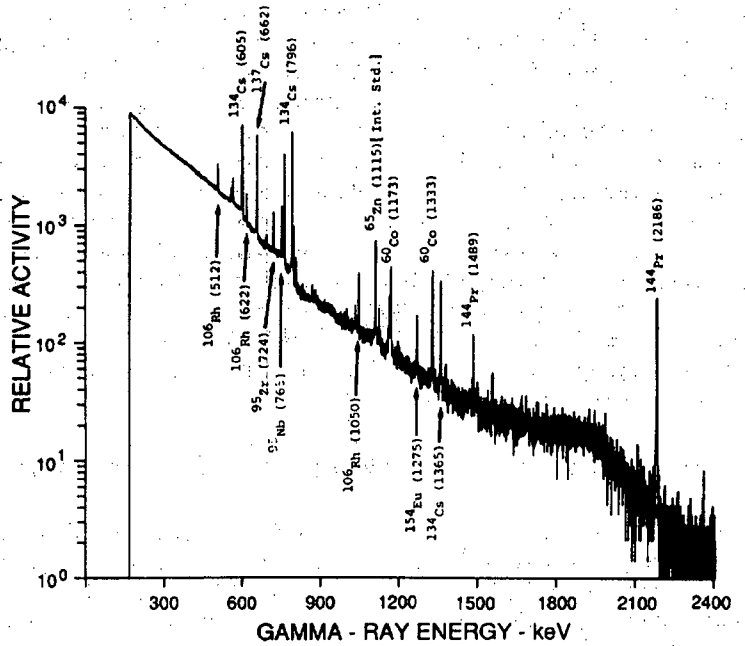

Fig. 1.14 *Gamma-ray spectrum of irradiated pressurized-water-reactor fuel having a burnup of 32 000 MWd/tU (megawatt days per ton of uranium) and a cooling time of 9 months.*

For a detector with a front surface area of 20 cm^2, the typical muon interaction rate at sea level is approximately 0.75/s.

All materials have varying degrees of natural radioactivity. For example: the human body and even gamma-ray detectors have some measurable natural radioactivity; building materials such as concrete can be especially active. The major radioactive species in natural materials are ^{40}K, ^{232}Th and its daughters, and ^{235}U and ^{238}U and their daughters. Potassium-40 has a natural abundance of 0.0117% and decays by electron capture (10.67%) and β^- decay (89.33%) with a half-life of 1.277×10^9 yr. The electron capture is accompanied by the emission of a 1.461-MeV gamma ray that is evident in almost all background gamma-ray spectra. Potassium is present in most organic matter, with ^{40}K being the major source of radioactivity.

Thorium is a common trace element in many terrestial rocks. Thorium-232 is the natural parent to the thorium decay series, which goes through 10 generations before reaching the stable nuclide ^{208}Pb. The half-life of ^{232}Th is 1.41×10^{10} yr. Its major gamma-ray activity comes from ^{208}Tl, ^{212}Bi, and ^{228}Ac.

Uranium is also found as a trace element in many rocks, although it is less common than thorium. The gamma-ray spectrum of unprocessed uranium ore is much different from that of uranium seen in the nuclear fuel cycle. Because of the long half-life of the daughter ^{230}Th (8×10^4 yr), later generations take a long time to grow back into equilibrium after any chemical treatment that separates uranium daughters from the natural ore. Figure 1.15 shows a typical spectrum of uranium ore (compare with Figure 1.9). Natural chemical processes in different rocks can often leach out some of the daughter nuclides and cause different ores to have different gamma-ray emissions.

The natural sources discussed above are common and contribute to the background gamma-ray spectrum in most locations. Other sources of background are occasionally encountered, such as materials contaminated by radioactive tracers. Slag from steel furnaces, which can have measurable levels of ^{60}Co, and uranium tailings are used as a concrete aggregate in some areas. The use of such materials in buildings can contribute to background radiation levels.

1.5 ADDITIONAL GAMMA-RAY PRODUCTION REACTIONS

The discussion in Section 1.4 has been limited to gamma rays that come from the natural decay reactions of radioactive nuclides; these gamma rays provide the bulk of the signatures useful for nondestructive assay. This section discusses gamma rays produced in other nuclear reactions. Some of these radiations can interfere with nondestructive analysis.

1.5.1 Bremsstrahlung (Braking Radiation)

Charged particles continuously decelerate as they move through condensed materials. As they decelerate, they emit photons with a continuous energy spectrum known as bremsstrahlung; these photons are of interest because their energies are often similar to those used for nondestructive assay.

Beta particles from nuclear decay often emit bremsstrahlung photons while stopping. Although beta particles have a very short range in condensed matter and rarely escape from the host material, the bremsstrahlung photons often escape and are detected along with the gamma rays of interest for nondestructive assay. Internal conversion electrons can also contribute to the production of bremsstrahlung radiation. The discrete gamma rays emitted by a decaying nucleus may be superimposed on a continuous bremsstrahlung background. The electron linac (linear accelerator) uses the bremsstrahlung reaction to produce high-energy photons for nuclear research, nuclear medicine, and active nondestructive assay of nuclear materials (Ref. 5).

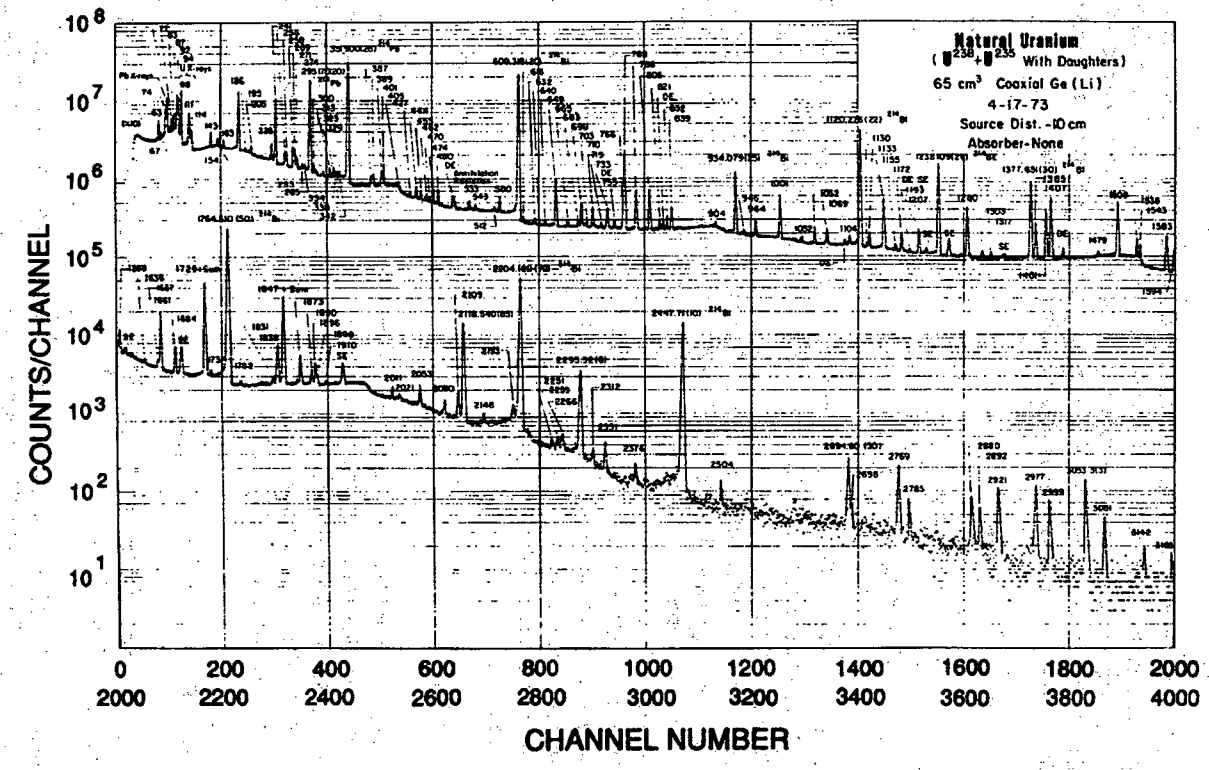

Fig. 1.15 Gamma-ray spectrum of uranium ore. Major radiations are from ^{214}Pb and ^{214}Bi. Compare the spectrum of processed uranium fuel in Figure 1.9; most daughter products are removed during processing. Figure adapted from R. L. Heath, "Gamma-Ray Spectrum Catalogue," Aerojet Nuclear Corporation report ANCR-1000-2 (March 1974).

1.5.2 Particle Reactions

When nuclei interact with other particles, charged or neutral, they often emit gamma rays as products of the interaction. The neutron capture reaction (n,γ) is a classic example. Usually the new nucleus is radioactive and is created in an excited state from which it can decay by gamma-ray emission. The following formulas illustrate the neutron-capture reaction that breeds plutonium in a fission reactor:

$$n + {}^{238}U \rightarrow \gamma + {}^{239}U \text{ (23 min)}$$

$${}^{239}U \rightarrow e^- + \bar{\nu} + {}^{239}Np \text{ (2.3 days)}$$

$${}^{239}Np \rightarrow e^- + \bar{\nu} + {}^{239}Pu \text{ (24 119 yr)}$$

Gamma rays from the capture reaction have discreet energies that are characteristic of the levels of the daughter nucleus. Their energies are typically 8 to 9 MeV for high-atomic-number nuclei.

Inelastic scattering of neutrons (n,n'γ) is usually accompanied by gamma-ray emission. The gamma rays have discrete energies that are characteristic of the levels in the target nucleus. Gamma rays produced by this reaction are usually not of interest for nondestructive assay.

A major source of neutrons from plutonium compounds and UF_6 is the interaction of alpha particles from nuclear decay with low-atomic-number nuclei in the compound or surrounding matrix material. The (α,n) reaction is frequently accompanied by gamma-ray emission from the excited product nucleus. The fluorine reaction can be written as follows:

$${}^{19}F(\alpha,n)\,{}^{22}Na\,.$$

The fluorine reaction usually proceeds to the ground state of ^{22}Na and does not result in gamma-ray emission. However, the subsequent β^+ decay of ^{22}Na leads to gamma rays with energies of 511 and 1275 keV. These radiations are evident in samples of PuF_4 and $^{238}PuO_2$ with trace fluorine impurities. They are not useful as assay signatures, but may be a source of interference.

REFERENCES

1. C. M. Lederer and V. S. Shirley, Eds., *Table of Isotopes*, 7th ed. (John Wiley & Sons, Inc., New York, 1978).

2. R. Gunnink, J. E. Evans, and A. L. Prindle, "A Reevaluation of the Gamma-Ray Energies and Absolute Branching Intensities of ^{237}U, $^{238, 239, 240, 241}Pu$, and ^{241}Am," Lawrence Livermore Laboratory report UCRL-52139 (1976).

3. "Calibration Techniques for the Calorimetric Assay of Plutonium-Bearing Solids Applied to Nuclear Materials Control," ANSI N15.22-1975 (American National Standards Institute, Inc., New York, 1975) and 1986 revision.

4. J. H. Hubbell, "Photon Cross Sections, Attenuation Coefficients, and Energy Absorption Coefficients from 10 keV to 100 GeV," National Bureau of Standards report NSRDS-NBS 29 (August 1969).

5. T. Gozani, *Active Nondestructive Assay of Nuclear Material, Principles and Applications*, NUREG/CR-0602 (US Nuclear Regulatory Commission, Washington, DC, 1981).

2

Gamma-Ray Interactions with Matter

G. Nelson and D. Reilly

2.1 INTRODUCTION

A knowledge of gamma-ray interactions is important to the nondestructive assayist in order to understand gamma-ray detection and attenuation. A gamma ray must interact with a detector in order to be "seen." Although the major isotopes of uranium and plutonium emit gamma rays at fixed energies and rates, the gamma-ray intensity measured outside a sample is always attenuated because of gamma-ray interactions with the sample. This attenuation must be carefully considered when using gamma-ray NDA instruments.

This chapter discusses the exponential attenuation of gamma rays in bulk materials and describes the major gamma-ray interactions, gamma-ray shielding, filtering, and collimation. The treatment given here is necessarily brief. For a more detailed discussion, see Refs. 1 and 2.

2.2 EXPONENTIAL ATTENUATION

Gamma rays were first identified in 1900 by Becquerel and Villard as a component of the radiation from uranium and radium that had much higher penetrability than alpha and beta particles. In 1909, Soddy and Russell found that gamma-ray attenuation followed an exponential law and that the ratio of the attenuation coefficient to the density of the attenuating material was nearly constant for all materials.

2.2.1 The Fundamental Law of Gamma-Ray Attenuation

Figure 2.1 illustrates a simple attenuation experiment. When gamma radiation of intensity I_0 is incident on an absorber of thickness L, the emerging intensity (I) transmitted by the absorber is given by the exponential expression

$$I = I_0 \, e^{-\mu_\ell L} \qquad (2\text{-}1)$$

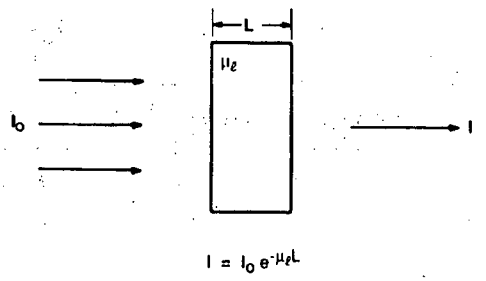

Fig. 2.1 The fundamental law of gamma-ray attenuation. The transmitted gamma-ray intensity I is a function of gamma-ray energy, absorber composition, and absorber thickness.

where μ_ℓ is the attenuation coefficient (expressed in cm^{-1}). The ratio I/I_0 is called the gamma-ray transmission. Figure 2.2 illustrates exponential attenuation for three different gamma-ray energies and shows that the transmission increases with increasing gamma-ray energy and decreases with increasing absorber thickness. Measurements with different sources and absorbers show that the attenuation coefficient μ_ℓ depends on the gamma-ray energy and the atomic number (Z) and density (ρ) of the absorber. For example, lead has a high density and atomic number and transmits

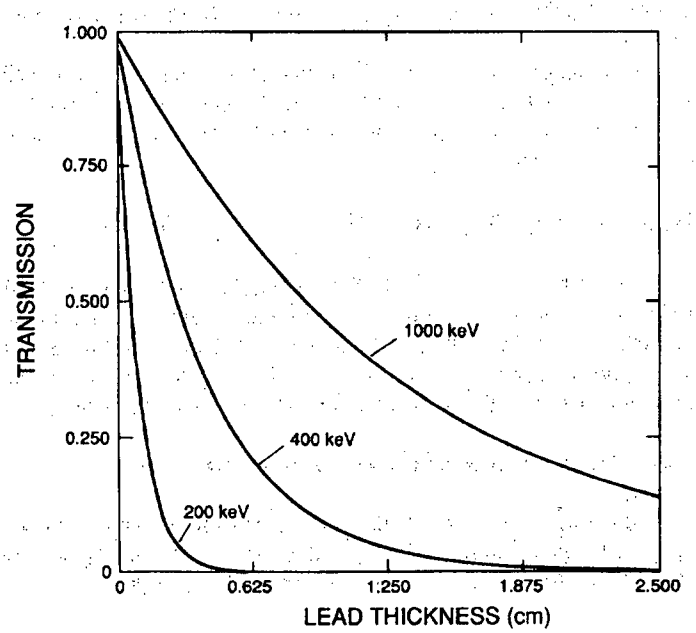

Fig. 2.2 Transmission of gamma rays through lead absorbers.

a much lower fraction of incident gamma radiation than does a similar thickness of aluminum or steel. The attenuation coefficient in Equation 2-1 is called the linear attenuation coefficient. Figure 2.3 shows the linear attenuation of solid sodium iodide, a common material used in gamma-ray detectors.

Alpha and beta particles have a well-defined range or stopping distance; however, as Figure 2.2 shows, gamma rays do not have a unique range. The reciprocal of the attenuation coefficient $1/\mu_\ell$ has units of length and is often called the mean free path. The mean free path is the average distance a gamma ray travels in the absorber before interacting; it is also the absorber thickness that produces a transmission of 1/e, or 0.37.

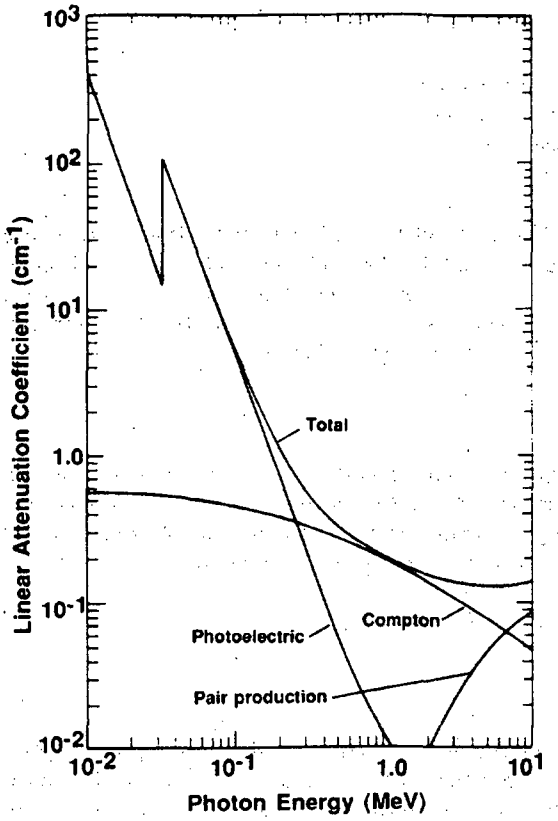

Fig. 2.3 Linear attenuation coefficient of NaI showing contributions from photoelectric absorption, Compton scattering, and pair production.

2.2.2 Mass Attenuation Coefficient

The linear attenuation coefficient is the simplest absorption coefficient to measure experimentally, but it is not usually tabulated because of its dependence on the density of the absorbing material. For example, at a given energy, the linear attenuation coefficients of water, ice, and steam are all different, even though the same material is involved.

Gamma rays interact primarily with atomic electrons; therefore, the attenuation coefficient must be proportional to the electron density P, which is proportional to the bulk density of the absorbing material. However, for a given material the ratio of the electron density to the bulk density is a constant, Z/A, independent of bulk density. The ratio Z/A is nearly constant for all except the heaviest elements and hydrogen.

$$P = Z\,\rho/A \tag{2-2}$$

where P = electron density
Z = atomic number
ρ = mass density
A = atomic mass.

The ratio of the linear attenuation coefficient to the density (μ_ℓ/ρ) is called the mass attenuation coefficient μ and has the dimensions of area per unit mass (cm^2/g). The units of this coefficient hint that one may think of it as the effective cross-sectional area of electrons per unit mass of absorber. The mass attenuation coefficient can be written in terms of a reaction cross section, $\sigma(cm^2)$:

$$\mu = \frac{N_0\sigma}{A} \tag{2-3}$$

where N_0 is Avagadro's number (6.02×10^{23}) and A is the atomic weight of the absorber. The cross section is the probability of a gamma ray interacting with a single atom. Chapter 12 gives a more complete definition of the cross-section concept. Using the mass attenuation coefficient, Equation 2-1 can be rewritten as

$$I = I_0\, e^{-\mu\rho L} = I_0\, e^{-\mu x} \tag{2-4}$$

where $x = \rho L$.

The mass attenuation coefficient is independent of density; for the example mentioned above, water, ice, and steam all have the same value of μ. This coefficient is more commonly tabulated than the linear attenuation coefficient because it quantifies the gamma-ray interaction probability of an individual element. References 3 and 4 are widely used tabulations of the mass attenuation coefficients of the elements. Equation 2-5 is used to calculate the mass attenuation coefficient for compound materials:

$$\mu = \sum \mu_i w_i \tag{2-5}$$

where μ_i = mass attenuation coefficient of i^{th} element
w_i = weight fraction of i^{th} element.

The use of Equation 2-5 is illustrated below for solid uranium hexafluoride (UF_6) at 200 keV:

μ_u = mass attenuation coefficient of U at 200 keV = 1.23 cm^2/g
μ_f = mass attenuation coefficient of F at 200 keV = 0.123 cm^2/g
w_u = weight fraction of U in UF_6 = 0.68
w_f = weight fraction of F in UF_6 = 0.32
ρ = density of solid UF_6 = 5.1 g/cm^3

$\mu = \mu_u w_u + \mu_f w_f = 1.23 \times 0.68 + 0.123 \times 0.32 = 0.88\ cm^2/g$

$\mu_\ell = \mu\rho = 0.88 \times 5.1 = 4.5\ cm^{-1}$.

2.3 INTERACTION PROCESSES

The gamma rays of interest to NDA applications fall in the range 10 to 2000 keV and interact with detectors and absorbers by three major processes: photoelectric absorption, Compton scattering, and pair production. In the photoelectric absorption process, the gamma ray loses all of its energy in one interaction. The probability for this process depends very strongly on gamma-ray energy Eγ and atomic number Z. In Compton scattering, the gamma ray loses only part of its energy in one interaction. The probability for this process is weakly dependent on E and Z. The gamma ray can lose all of its energy in one pair-production interaction. However, this process is relatively unimportant for fissile material assay since it has a threshold above 1 MeV. Reference 3 is recommended for more detailed physical descriptions of the interaction processes.

2.3.1 Photoelectric Absorption

A gamma ray may interact with a bound atomic electron in such a way that it loses all of its energy and ceases to exist as a gamma ray (see Figure 2.4). Some of the gamma-ray energy is used to overcome the electron binding energy, and most of the remainder is transferred to the freed electron as kinetic energy. A very small amount of recoil energy remains with the atom to conserve momentum. This is called photoelectric absorption because it is the gamma-ray analog of the process discovered by Hertz in 1887 whereby photons of visible light liberate electrons from a metal surface. Photoelectric absorption is important for gamma-ray detection because the gamma ray gives up all its energy, and the resulting pulse falls in the full-energy peak.

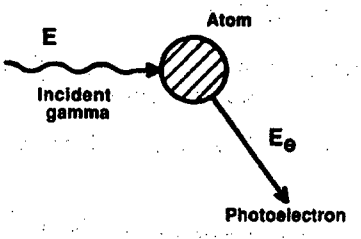

Fig. 2.4 A schematic representation of the photoelectric absorption process.

The probability of photoelectric absorption depends on the gamma-ray energy, the electron binding energy, and the atomic number of the atom. The probability is greater the more tightly bound the electron; therefore, K electrons are most affected (over 80% of the interactions involve K electrons), provided the gamma-ray energy exceeds the K-electron binding energy. The probability is given approximately by Equation 2-6, which shows that the interaction is more important for heavy atoms like lead and uranium and low-energy gamma rays:

$$\tau \propto Z^4/E^3 \tag{2-6}$$

where τ = photoelectric mass attenuation coefficient.

This proportionality is only approximate because the exponent of Z varies in the range 4.0 to 4.8. As the gamma-ray energy decreases, the probability of photoelectric absorption increases rapidly (see Figure 2.3). Photoelectric absorption is the predominant interaction for low-energy gamma rays, x rays, and bremsstrahlung.

The energy of the photoelectron E_e released by the interaction is the difference between the gamma-ray energy $E\gamma$ and the electron binding energy E_b:

$$E_e = E\gamma - E_b. \tag{2-7}$$

In most detectors, the photoelectron is stopped quickly in the active volume of the detector, which emits a small output pulse whose amplitude is proportional to the energy deposited by the photoelectron. The electron binding energy is not lost but appears as characteristic x rays emitted in coincidence with the photoelectron. In most cases, these x rays are absorbed in the detector in coincidence with the photoelectron and the resulting output pulse is proportional to the total energy of the incident gamma ray. For low-energy gamma rays in very small detectors, a sufficient number of K x rays can escape from the detector to cause escape peaks in the observed spectrum; the peaks appear below the full-energy peak by an amount equal to the energy of the x ray.

Figure 2.5 shows the photoelectric mass attenuation coefficient of lead. The interaction probability increases rapidly as energy decreases, but then becomes much

smaller at a gamma-ray energy just below the binding energy of the K electron. This discontinuity is called the K edge; below this energy the gamma ray does not have sufficient energy to dislodge a K electron. Below the K edge the interaction probability increases again until the energy drops below the binding energies of the L electrons; these discontinuities are called the L_I, L_{II}, and L_{III} edges. The presence of these absorption edges is important for densitometry and x-ray fluorescence measurements (see Chapters 9 and 10).

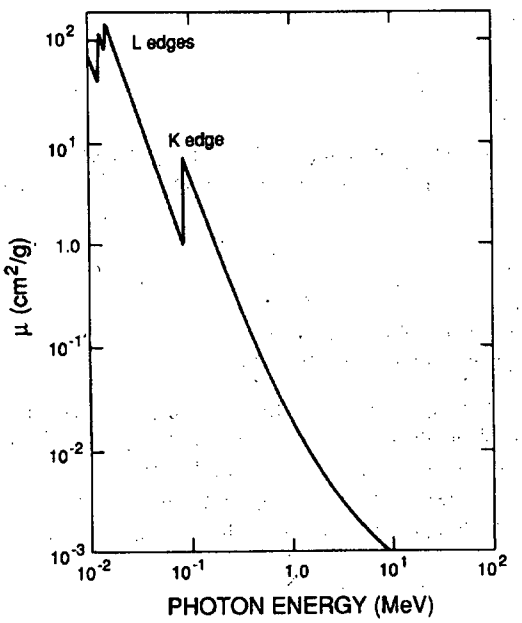

***Fig. 2.5** Photoelectric mass attenuation coefficient of lead.*

2.3.2 Compton Scattering

Compton scattering is the process whereby a gamma ray interacts with a free or weakly bound electron ($E_\gamma \gg E_b$) and transfers part of its energy to the electron (see Figure 2.6). Conservation of energy and momentum allows only a partial energy transfer when the electron is not bound tightly enough for the atom to absorb recoil energy. This interaction involves the outer, least tightly bound electrons in the scattering atom. The electron becomes a free electron with kinetic energy equal to the difference of the energy lost by the gamma ray and the electron binding energy. Because the electron

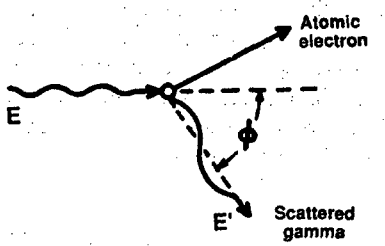

Fig. 2.6 A schematic representation of Compton scattering.

binding energy is very small compared to the gamma-ray energy, the kinetic energy of the electron is very nearly equal to the energy lost by the gamma ray:

$$E_e = E_\gamma - E' \tag{2-8}$$

where E_e = energy of scattered electron
E_γ = energy of incident gamma ray
E' = energy of scattered gamma ray.

Two particles leave the interaction site: the freed electron and the scattered gamma ray. The directions of the electron and the scattered gamma ray depend on the amount of energy transferred to the electron during the interaction. Equation 2-9 gives the energy of the scattered gamma ray, and Figure 2.7 shows the energy of the scattered electron as a function of scattering angle and incident gamma-ray energy.

$$E' = m_0c^2/(1 - \cos\phi + m_0c^2/E) \tag{2-9}$$

where m_0c^2 = rest energy of electron = 511 keV
ϕ = angle between incident and scattered gamma rays (see Figure 2.6).

This energy is minimum for a head-on collision where the gamma ray is scattered 180°and the electron moves forward in the direction of the incident gamma ray. For this case the energy of the scattered gamma ray is given by Equation 2-10 and the energy of the scattered electron is given by Equation 2-11:

$$E'(\text{min}) = m_0c^2/(2 + m_0c^2/E) \simeq m_0c^2/2 = 256 \text{ keV; if } E \gg m_0c^2/2 \,. \tag{2-10}$$

$$E_e(\text{max}) = E/[1 + m_0c^2/(2E)] \simeq E - m_0c^2/2 = E - 256 \text{ keV; if } E \gg m_0c^2/2 \,. \tag{2-11}$$

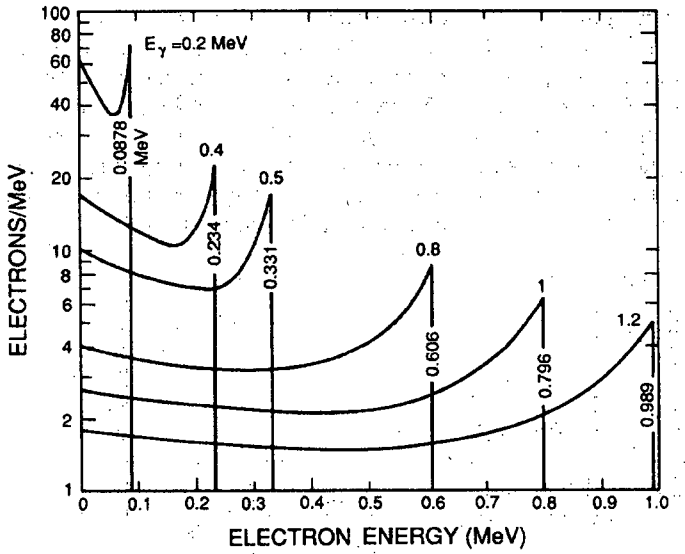

Fig. 2.7 Energy of Compton-scattered electrons as a function of scattering angle and incident gamma-ray energy (Eγ). The sharp discontinuity corresponds to the maximum energy that can be transferred in a single scattering.

For very small angle scatterings ($\phi \simeq 0°$), the energy of the scattered gamma ray is only slightly less than the energy of the incident gamma ray and the scattered electron takes very little energy away from the interaction. The energy given to the scattered electron ranges from near zero to the maximum given by Equation 2-11.

When a Compton scattering occurs in a detector, the scattered electron is usually stopped in the detection medium and the detector produces an output pulse that is proportional to the energy lost by the incident gamma ray. Compton scattering in a detector produces a spectrum of output pulses from zero up to the maximum energy given by Equation 2-11. It is difficult to relate the Compton-scattering spectrum to the energy of the incident gamma ray. Figure 2.8 shows the measured gamma-ray spectrum from a monoenergetic gamma-ray source (^{137}Cs). The full-energy peak at 662 keV is formed by interactions where the gamma ray loses all of its energy in the detector either by a single photoelectric absorption or by a series of Compton scatterings followed by photoelectric absorption. The spectrum of events below the full-energy peak is formed by Compton scatterings where the gamma ray loses only part of its energy in the detector. The step near 470 keV corresponds to the maximum energy that can be transferred to an electron by a 662-keV gamma ray in a single Compton scattering. This step is called a Compton edge; the energy of the Compton edge is given by Equation 2-11 and plotted in Figure 2.9. The small peak at 188 keV in Figure 2.8 is called a backscatter peak. The backscatter peak is formed when the

gamma ray undergoes a large-angle scattering (≃180°) in the material surrounding the detector and then is absorbed in the detector. The energy of the backscatter peak is given by Equation 2-10, which shows that the maximum energy is 256 keV. The sum of the energy of the backscatter peak and the Compton edge equals the energy of the incident gamma ray. Both features are the result of large-angle Compton scattering of the incident gamma ray. The event contributes to the backscatter peak when only the scattered gamma ray deposits its energy in the detector; it contributes to the Compton edge when only the scattered electron deposits its energy in the detector.

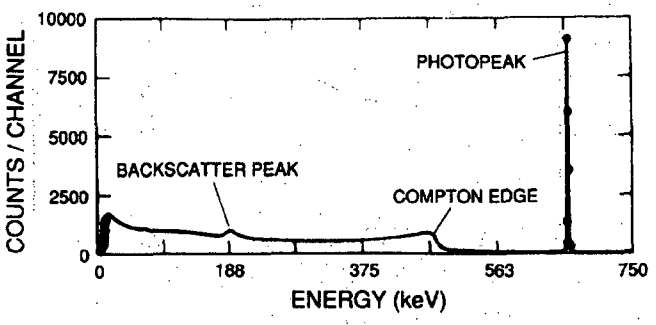

Fig. 2.8 High-resolution spectrum of ^{137}Cs showing full-energy photopeak, Compton edge, and backscatter peak from the 662-keV gamma ray. Events below the photopeak are caused by Compton scattering in the detector and surrounding materials.

Because Compton scattering involves the least tightly bound electrons, the nucleus has only a minor influence and the probability for interaction is nearly independent of atomic number. The interaction probability depends on the electron density, which is proportional to Z/A and nearly constant for all materials. The Compton-scattering probability is a slowly varying function of gamma-ray energy (see Figure 2.3).

2.3.3 Pair Production

A gamma ray with an energy of at least 1.022 MeV can create an electron-positron pair when it is under the influence of the strong electromagnetic field in the vicinity of a nucleus (see Figure 2.10). In this interaction the nucleus receives a very small amount of recoil energy to conserve momentum, but the nucleus is otherwise unchanged and the gamma ray disappears. This interaction has a threshold of 1.022 MeV because that is the minimum energy required to create the electron and positron. If the gamma-ray energy exceeds 1.022 MeV, the excess energy is shared between the electron and positron as kinetic energy. This interaction process is relatively unimportant for nuclear material assay because most important gamma-ray signatures are below 1.022 MeV.

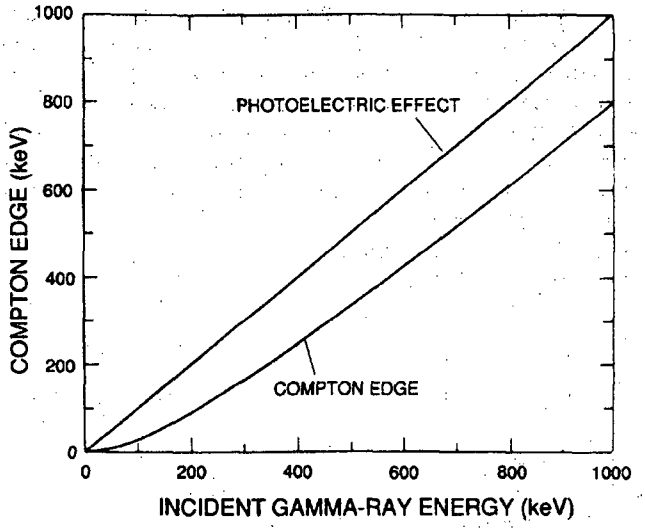

***Fig. 2.9** Energy of the Compton edge versus the energy of the incident gamma ray.*

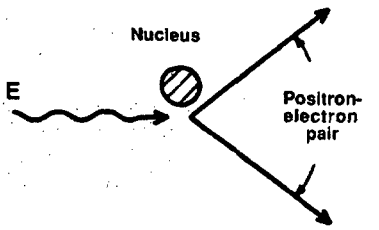

***Fig. 2.10** A schematic representation of pair production.*

The electron and positron from pair production are rapidly slowed down in the absorber. After losing its kinetic energy, the positron combines with an electron in an annihilation process, which releases two gamma rays with energies of 0.511 MeV. These lower energy gamma rays may interact further with the absorbing material or may escape. In a gamma-ray detector, this interaction often gives three peaks for a high-energy gamma ray (see Figure 2.11). The kinetic energy of the electron and positron is absorbed in the detector. One or both of the annihilation gamma rays may escape from the detector or they may both be absorbed. If both annihilation gamma rays are absorbed in the detector, the interaction contributes to the full-energy peak in the measured spectrum; if one of the annihilation gamma rays escapes from

the detector, the interaction contributes to the single-escape peak located 0.511 MeV below the full-energy peak; if both gamma rays escape, the interaction contributes to the double-escape peak located 1.022 MeV below the full-energy peak. The relative heights of the three peaks depend on the energy of the incident gamma ray and the size of the detector. These escape peaks may arise when samples of irradiated fuel, thorium, and ^{232}U are measured because these materials have important gamma rays above the pair-production threshold. Irradiated fuel is sometimes measured using the 2186-keV gamma ray from the fission-product ^{144}Pr. The gamma-ray spectrum of ^{144}Pr in Figure 2.11 shows the single- and double-escape peaks that arise from pair-production interactions of the 2186-keV gamma ray in a germanium detector.

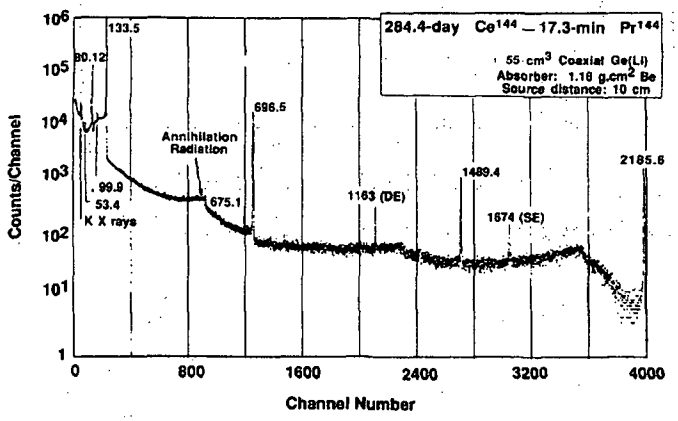

Fig. 2.11 Gamma-ray spectrum of the fission-product ^{144}Pr showing single-escape (SE) and double-escape (DE) peaks (1674 and 1163) that arise from pair-production interactions of 2186-keV gamma rays in a germanium detector.

Pair production is impossible for gamma rays with energy less than 1.022 MeV. Above this threshold, the probability of the interaction increases rapidly with energy (see Figure 2.3). The probability of pair production varies approximately as the square of the atomic number Z and is significant in high-Z elements such as lead or uranium. In lead, approximately 20% of the interactions of 1.5-MeV gamma rays are through the pair-production process, and the fraction increases to 50% at 2.0 MeV. For carbon, the corresponding interaction fractions are 2% and 4%.

2.3.4 Total Mass Attenuation Coefficient

The three interaction processes described above all contribute to the total mass attenuation coefficient. The relative importance of the three interactions depends on

gamma-ray energy and the atomic number of the absorber. Figure 2.12 shows a composite of mass attenuation curves covering a wide range of energy and atomic number. It shows dramatically the interplay of the three processes. All elements except hydrogen show a sharp, low-energy rise that indicates where photoelectric absorption is the dominant interaction. The position of the rise is very dependent on atomic number. Above the low-energy rise, the value of the mass attenuation coefficient decreases gradually, indicating the region where Compton scattering is the dominant interaction. The mass attenuation coefficients for all elements with atomic number less than 25 (iron) are nearly identical in the energy range 200 to 2000 keV. The attenuation curves converge for all elements in the range 1 to 2 MeV. The shape of the mass attenuation curve of hydrogen shows that it interacts with gamma rays with energy greater than 10 keV almost exclusively by Compton scattering. Above

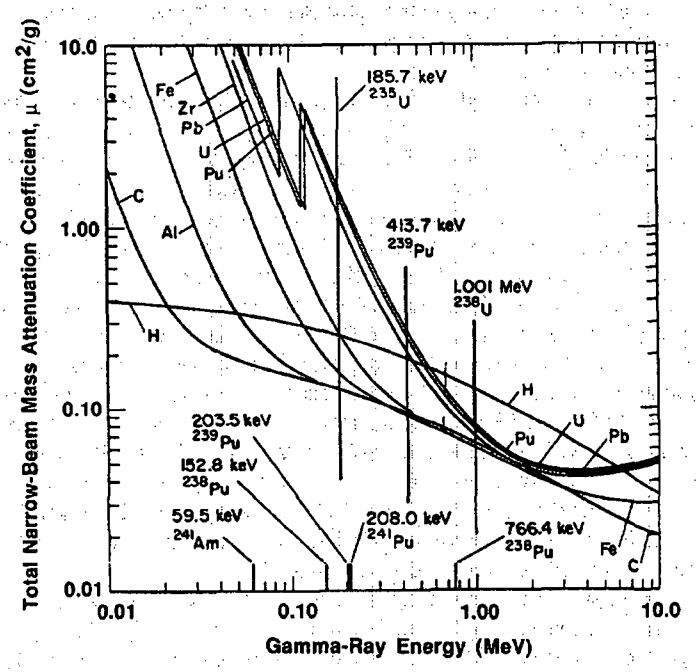

Fig. 2.12 Mass attenuation coefficients of selected elements. Also indicated are gamma-ray energies commonly encountered in NDA of uranium and plutonium.

2 MeV, the pair-production interaction becomes important for high-Z elements and the mass attenuation coefficient begins to rise again. An understanding of the major features of Figure 2.12 is very helpful to the understanding of NDA techniques.

2.4 FILTERS

In many assay applications, the gamma rays of interest can be measured more easily if lower energy gamma rays can be absorbed before they reach the detector. The lower energy gamma rays can cause significant count-rate-related losses in the detector and spectral distortion if they are not removed. The removal process is often called filtering. A perfect filter material would have a transmission of zero below the energy of interest and a transmission of unity above that energy, but as Figure 2.12 shows, such a material does not exist. However, useful filters can be obtained by selecting absorbers of appropriate atomic number such that the sharp rise in photoelectric cross section is near the energy of the gamma rays that must be attenuated but well below the energy of the assay gamma rays.

Filtering is usually employed in the measurement of plutonium gamma-ray spectra. Except immediately after chemical separation of americium, all plutonium samples have significant levels of ^{241}Am, which emits a very intense gamma ray at 60 keV. In most samples, this gamma ray is the most intense gamma ray in the spectrum and must be attenuated so that the plutonium gamma rays can be accurately measured. A thin sheet of cadmium is commonly used to attenuate the ^{241}Am activity. Table 2-1 shows the effect of a cadmium filter on the spectrum from a 2-g disk of plutonium metal. In the absence of the filter, the 60-keV gamma ray dominates the spectrum and may even paralyze the detector. A 1- to 2-mm cadmium filter drastically attenuates the 60-keV activity but only slightly attenuates the higher energy plutonium lines. The plutonium spectrum below 250 keV is usually measured with a cadmium filter. When only the ^{239}Pu 414-keV gamma ray is of interest, lead may be used as the filter material because it will attenuate gamma rays in the 100- to 200-keV region and will stop most of the 60-keV gamma rays. It is interesting to note that at 60 keV the mass attenuation coefficients of lead and cadmium are essentially equal, in spite of the higher Z of lead (82) relative to cadmium (48). This is because the K edge of lead appears at 88 keV, as discussed in Section 2.3.1.

A cadmium filter is often used when measuring ^{235}U because it attenuates gamma rays and x rays in the 90- to 120-keV region and does not significantly affect the 186-keV gamma ray from ^{235}U. Filters may also be used for certain irradiated fuel measurements. The 2186-keV gamma ray from the fission products ^{144}Ce-^{144}Pr is measured in some applications as an indicator of the residual fuel material in leached hulls produced at a reprocessing plant (see Chapter 18). The major fission-product gamma-ray activity is in the 500- to 900-keV region and can be selectively reduced relative to the 2186-keV gamma ray using a 10- to 15-cm-thick lead filter.

Table 2-1. Effect of cadmium filter on plutonium spectrum

	Plutonium Signal (counts/s)[a]			
Absorber (cm)	60 keV	129 keV	208 keV	414 keV
0	3.57×10^6	1.29×10^4	8.50×10^4	2.02×10^4
0.1	2.40×10^4	0.67×10^4	6.76×10^4	1.85×10^4
0.2	1.86×10^2	0.34×10^4	5.37×10^4	1.69×10^4

[a] ^{241}Am = 0.135%; ^{239}Pu = 81.9%; ^{241}Pu = 1.3%. Signal from 2-g disk of plutonium metal, 1 cm diam × 0.13 cm thick.

Graded filters with two or more materials are sometimes used to attenuate the characteristic x rays from the primary filter material before they interact in the detector. When gamma rays are absorbed in the primary filter material, the interaction produces copious amounts of x rays. For example, when the 60-keV gamma rays from ^{241}Am are absorbed in a thin cadmium filter, a significant flux of 23-keV x rays can be produced. If these x rays create a problem in the detector, they can be easily attenuated with a very thin sheet of copper. Because the K x rays of copper at 8 keV are usually of sufficiently low energy, they do not interfere with the measurement. If the primary filter material is lead, cadmium is used to absorb the characteristic K x rays of lead at 73 and 75 keV, and copper is used to absorb the characteristic K x rays of cadmium at 23 keV. In graded filters, the lowest Z material is always placed next to the detector.

2.5 SHIELDING

In NDA instruments, shields and collimators are required to limit the detector response to background gamma rays and to shield the operator and detector from transmission and activation sources. Gamma-ray shielding materials should be of high density and high atomic number so that they have a high total linear attenuation coefficient and a high photoelectric absorption probability. The most common shielding material is lead because it is readily available, has a density of 11.35 g/cm^3 and an atomic number of 82, and is relatively inexpensive. Lead can be molded into many shapes; however, because of its high ductility it cannot be machined easily or hold a given shape unless supported by a rigid material.

In some applications, an alloy of tungsten (atomic number 74) is used in place of lead because it has significantly higher density (17 g/cm^3), can be machined easily, and holds a shape well. Table 2-2 shows some of the attenuation properties of the two materials. The tungsten is alloyed with nickel and copper to improve its machinability.

Table 2-2 shows that at energies above 500 keV the tungsten alloy has a significantly higher linear attenuation coefficient than lead because of its higher density. Thus, the same shielding effect can be achieved with a thinner shield. At energies below 500 keV, the difference between the attenuation properties of the two materials is less significant; the higher density of the tungsten alloy is offset by the lower atomic number. The tungsten alloy is used where space is severely limited or where machinability and mechanical strength are important. However, the tungsten material is over thirty times more expensive than lead; therefore, it is used sparingly and is almost never used for massive shields. The alloy is often used to hold intense gamma-ray transmission sources or to collimate gamma-ray detectors.

Table 2-2. Attenuation properties of lead and tungsten

	Attenuation Coefficient (cm^{-1})		Thickness (cm)[a]	
Energy (keV)	Lead	Tungsten[b]	Lead	Tungsten[b]
1000	0.77	1.08	2.98	2.14
500	1.70	2.14	1.35	1.08
200	10.6	11.5	0.22	0.20
100	60.4	64.8	0.038	0.036

[a]Thickness of absorber with 10% transmission.
[b]Alloy: 90% tungsten, 6% nickel, 4% copper.

REFERENCES

1. R. D. Evans, *The Atomic Nucleus* (McGraw-Hill Book Co., New York, 1955).

2. G. F. Knoll, *Radiation Detection and Measurement* (John Wiley & Sons, New York, 1979).

3. E. Storm and H. Israel, "Photon Cross Sections from 0.001 to 100 MeV for Elements 1 through 100," Los Alamos Scientific Laboratory report LA-3753 (1967).

4. J. H. Hubbel, "Photon Cross Sections, Attenuation Coefficients, and Energy Absorption Coefficients from 10 keV to 100 GeV," National Bureau of Standards report NSRDS-NSB 29 (August 1969).

3

Gamma-Ray Detectors

Hastings A. Smith, Jr., and Marcia Lucas

3.1 INTRODUCTION

In order for a gamma ray to be detected, it must interact with matter; that interaction must be recorded. Fortunately, the electromagnetic nature of gamma-ray photons allows them to interact strongly with the charged electrons in the atoms of all matter. The key process by which a gamma ray is detected is ionization, where it gives up part or all of its energy to an electron. The ionized electrons collide with other atoms and liberate many more electrons. The liberated charge is collected, either directly (as with a proportional counter or a solid-state semiconductor detector) or indirectly (as with a scintillation detector), in order to register the presence of the gamma ray and measure its energy. The final result is an electrical pulse whose voltage is proportional to the energy deposited in the detecting medium.

In this chapter, we will present some general information on types of gamma-ray detectors that are used in nondestructive assay (NDA) of nuclear materials. The electronic instrumentation associated with gamma-ray detection is discussed in Chapter 4. More in-depth treatments of the design and operation of gamma-ray detectors can be found in Refs. 1 and 2.

3.2 TYPES OF DETECTORS

Many different detectors have been used to register the gamma ray and its energy. In NDA, it is usually necessary to measure not only the amount of radiation emanating from a sample but also its energy spectrum. Thus, the detectors of most use in NDA applications are those whose signal outputs are proportional to the energy deposited by the gamma ray in the sensitive volume of the detector.

3.2.1 Gas-Filled Detectors

Gas counters consist of a sensitive volume of gas between two electrodes. (See Figure 3.1.) In most designs the outer electrode is the cylindrical wall of the gas pressure vessel, and the inner (positive) electrode is a thin wire positioned at the center of the cylinder. In some designs (especially of ionization chambers) both electrodes can be positioned in the gas separate from the gas pressure vessel.

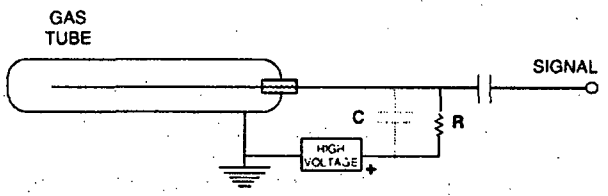

Fig. 3.1 The equivalent circuit for a gas-filled detector. The gas constitutes the sensitive (detecting) volume. The potential difference between the tube housing and the center wire produces a strong electric field in the gas volume. The electrons from ionizations in the gas travel to the center wire under the influence of the electric field, producing a charge surge on the wire for each detection event.

An *ionization chamber* is a gas-filled counter for which the voltage between the electrodes is low enough that only the primary ionization charge is collected. The electrical output signal is proportional to the energy deposited in the gas volume.

If the voltage between the electrodes is increased, the ionized electrons attain enough kinetic energy to cause further ionizations. One then has a *proportional counter* that can be tailored for specific applications by varying the gas pressure and/or the operating voltage. The output signal is still proportional to the energy deposited in the gas by the incident gamma-ray photon, and the energy resolution is intermediate between NaI scintillation counters and germanium (Ge) solid-state detectors. Proportional counters have been used for spectroscopy of gamma rays and x rays whose energies are low enough (a few tens of keV) to interact with reasonable efficiency in the counter gas.

If the operating voltage is increased further, charge multiplication in the gas volume increases (avalanches) until the space charge produced by the residual ions inhibits further ionization. As a result, the amount of ionization saturates and becomes independent of the initial energy deposited in the gas. This type of detector is known as the *Geiger-Mueller (GM) detector*. A GM tube gas counter does not differentiate among the kinds of particles it detects or their energies; it counts only the number of particles entering the detector. This type of detector is the heart of the conventional β-γ dosimeter used in health physics.

Gas counters do not have much use in gamma-ray NDA of nuclear materials. The scintillation and solid-state detectors are much more desirable for obtaining the spectroscopic detail needed in the energy range typical of uranium and plutonium radiation (approximately 100-1000 keV). Gas counters are described in more detail in Chapter 13, since they are more widely used for neutron detection.

3.2.2 Scintillation Detectors

The sensitive volume of a scintillation detector is a luminescent material (a solid, liquid, or gas) that is viewed by a device that detects the gamma-ray-induced light emissions [usually a photomultiplier tube (PMT)]. The scintillation material may be organic or inorganic; the latter is more common. Examples of organic scintillators are anthracene, plastics, and liquids. The latter two are less efficient than anthracene (the standard against which other scintillators are compared). Some common inorganic scintillation materials are sodium iodide (NaI), cesium iodide (CsI), zinc sulfide (ZnS), and lithium iodide (LiI). The most common scintillation detectors are solid, and the most popular are the inorganic crystals NaI and CsI. A new scintillation material, bismuth germanate ($Bi_4Ge_3O_{12}$), commonly referred to as BGO, has become popular in applications where its high gamma counting efficiency and/or its lower neutron sensitivity outweigh considerations of energy resolution (Refs. 3 and 4). A comprehensive discussion of scintillation detectors may be found in Refs. 1, 2, and 5.

When gamma rays interact in scintillator material, ionized (excited) atoms in the scintillator material "relax" to a lower-energy state and emit photons of light. In a pure inorganic scintillator crystal, the return of the atom to lower-energy states with the emission of a photon is an inefficient process. Furthermore, the emitted photons are usually too high in energy to lie in the range of wavelengths to which the PMT is sensitive. Small amounts of impurities (called activators) are added to all scintillators to enhance the emission of visible photons. Crystal de-excitations channeled through these impurities give rise to photons that can activate the PMT. One important consequence of luminescence through activator impurities is that the bulk scintillator crystal is transparent to the scintillation light. A common example of scintillator activation encountered in gamma-ray measurements is thallium-doped sodium iodide [NaI(Tl)].

The scintillation light is emitted isotropically; so the scintillator is typically surrounded with reflective material (such as MgO) to minimize the loss of light and then is optically coupled to the photocathode of a PMT. (See Figure 3.2.) Scintillation photons incident on the photocathode liberate electrons through the photoelectric effect, and these photoelectrons are then accelerated by a strong electric field in the PMT. As these photoelectrons are accelerated, they collide with electrodes in the tube (known as dynodes) releasing additional electrons. This increased electron flux is then further accelerated to collide with succeeding electrodes, causing a large multiplication (by a factor of 10^4 or more) of the electron flux from its initial value at the photocathode surface. Finally, the amplified charge burst arrives at the output electrode (the anode) of the tube. The magnitude of this charge surge is proportional to the initial amount of charge liberated at the photocathode of the PMT; the constant of proportionality is the gain of the PMT. Furthermore, by virtue of the physics of the photoelectric effect, the initial number of photoelectrons liberated at the photocathode is proportional to the amount of light incident on the phototube, which, in turn, is proportional to the amount of energy deposited in the scintillator by the gamma ray (assuming no light

loss from the scintillator volume). Thus, an output signal is produced that is proportional to the energy deposited by the gamma ray in the scintillation medium. As discussed above, however, the spectrum of deposited energies (even for a monoenergetic photon flux) is quite varied, because of the occurrence of the photoelectric effect, Compton effect, and various scattering phenomena in the scintillation medium and statistical fluctuations associated with all of these processes. This is discussed in more detail in Section 3.3.

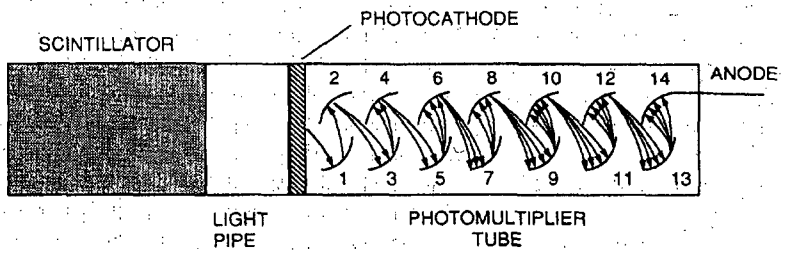

Fig. 3.2 Typical arrangement of components in a scintillation detector. The scintillator and photomultiplier tube are often optically linked by a light pipe. The dynodes (1-13 in the figure) are arranged to allow successive electron cascades through the tube volume. The final charge burst is collected by the anode and is usually passed to a preamplifier for conversion to a voltage pulse.

3.2.3 Solid-State Detectors

In solid-state detectors, the charge produced by the photon interactions is collected directly. The gamma-ray energy resolution of these detectors is dramatically better than that of scintillation detectors; so greater spectral detail can be measured and used for SNM evaluations. A generic representation of the solid-state detector is shown in Figure 3.3. The sensitive volume is an electronically conditioned region (known as the *depleted region*) in a semiconductor material in which liberated electrons and holes move freely. Germanium possesses the most ideal electronic characteristics in this regard and is the most widely used semiconductor material in solid-state detectors. As Figure 3.3 suggests, the detector functions as a solid-state proportional counter, with the ionization charge swept directly to the electrodes by the high electric field in the semiconductor, produced by the bias voltage. The collected charge is converted to a voltage pulse by a preamplifier. The most popular early designs used lithium-drifted germanium [Ge(Li)] as the detection medium. The lithium served to inhibit trapping of charge at impurity sites in the crystal lattice during the charge collection process. In recent years, manufacturers have produced hyperpure germanium (HPGe) crystals, essentially eliminating the need for the lithium doping and simplifying operation of the detector.

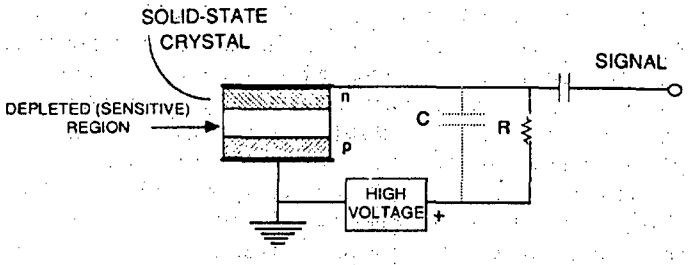

Fig. 3.3 *Typical arrangement of components in a solid-state detector. The crystal is a reverse-biased p-n junction that conducts charge when ionization is produced in the sensitive region. The signal is usually fed to a charge-sensitive preamplifier for conversion to a voltage pulse (see Chapter 4).*

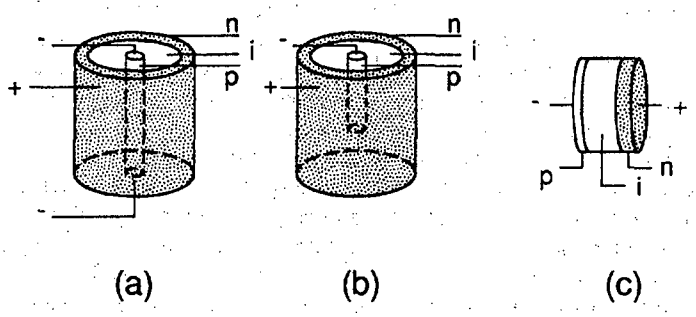

Fig. 3.4 *Illustration of various solid-state detector crystal configurations: (a) open-ended cylindrical or true coaxial, (b) closed-ended cylindrical, and (c) planar. The p-type and n-type semiconductor materials are labeled accordingly. The regions labeled i are the depleted regions that serve as the detector sensitive volumes. In the context of semiconductor diode junctions, this region is referred to as the intrinsic region or a p-i-n junction.*

Solid-state detectors are produced mainly in two configurations: planar and coaxial. These terms refer to the detector crystal shape and the manner in which it is wired into the detector circuit. The most commonly encountered detector configurations are illustrated in Figure 3.4. *Coaxial detectors* are produced either with open-ended (the so-called true coaxial) or closed-ended crystals [Figure 3.4 (a-b)]. In both cases

the electric field for charge collection is primarily radial, with some axial component present in the closed-ended configuration. Coaxial detectors can be produced with large sensitive volumes and therefore with large detection efficiencies at high gamma-ray energies. In addition, the radial electric field geometry makes the coaxial (especially the open-ended coaxial) solid-state detectors best for fast timing applications. The *planar detector* consists of a crystal of either rectangular or circular cross section and a sensitive thickness of 1-20 mm [for example, Figure 3.4 (c)]. The electric field is perpendicular to the cross-sectional area of the crystal. The crystal thickness is selected on the basis of the gamma-ray energy region relevant to the application of interest, with the small thicknesses optimum for low-energy measurements (for example in the L-x-ray region for special nuclear material). Planar detectors usually achieve the best energy resolution, because of their low capacitance; they are preferred for detailed spectroscopy, such as the analysis of the complex low-energy gamma-ray and x-ray spectra of uranium and plutonium.

Because of their high resolution, semiconductor detectors are relatively sensitive to performance degradation from radiation damage. The amount of damage produced in the detector crystal per unit of incident flux is greatest for neutron radiation. Thus, in environments where neutron levels are high (such as accelerators, reactors, or instruments with intense neutron sources), the most significant radiation damage effects will be observed. Furthermore, radiation damage effects can be of concern in NDA applications where large amounts of nuclear material are continuously measured with high-resolution gamma-ray spectroscopy equipment—for example, in measurements of plutonium isotopics in a high-throughput mode.

The primary effect of radiation damage is the creation of dislocation sites in the detector crystal. This increases the amount of charge trapping, reduces the amplitudes of some full-energy pulses, and produces low-energy tails in the spectrum photopeaks. In effect, the resolution is degraded, and spectral detail is lost. An example of this type of effect is shown in Figure 3.5 (Ref. 6). It has been generally observed that significant performance degradation begins with a neutron fluence of approximately 10^9 n/cm^2, and detectors become unusable at a fluence of approximately 10^{10} n/cm^2 (Ref. 7). However, the new n-type HPGe crystals are demonstrably less vulnerable to neutron damage. Procedures have been described in which the effects of the radiation damage can be reversed through warming (annealing) the detector crystal (Ref. 8).

Further details on the design and use of solid-state detectors for gamma-ray spectroscopy may be found in Refs. 1, 2, and 9.

In the quiescent state, the reverse-bias-diode configuration of a germanium solid-state detector results in very low currents in the detector (usually in the pico- to nanoampere range). This leakage current can be further reduced from its room-temperature value by cryogenic cooling of solid-state medium, typically to liquid nitrogen temperature (77 K). This cooling reduces the natural, thermally generated electrical noise in the crystal but constitutes the main disadvantage of such detectors: the detector package must include capacity for cooling, and this usually involves a dewar for containing the liquid coolant. In recent years, attempts have been made

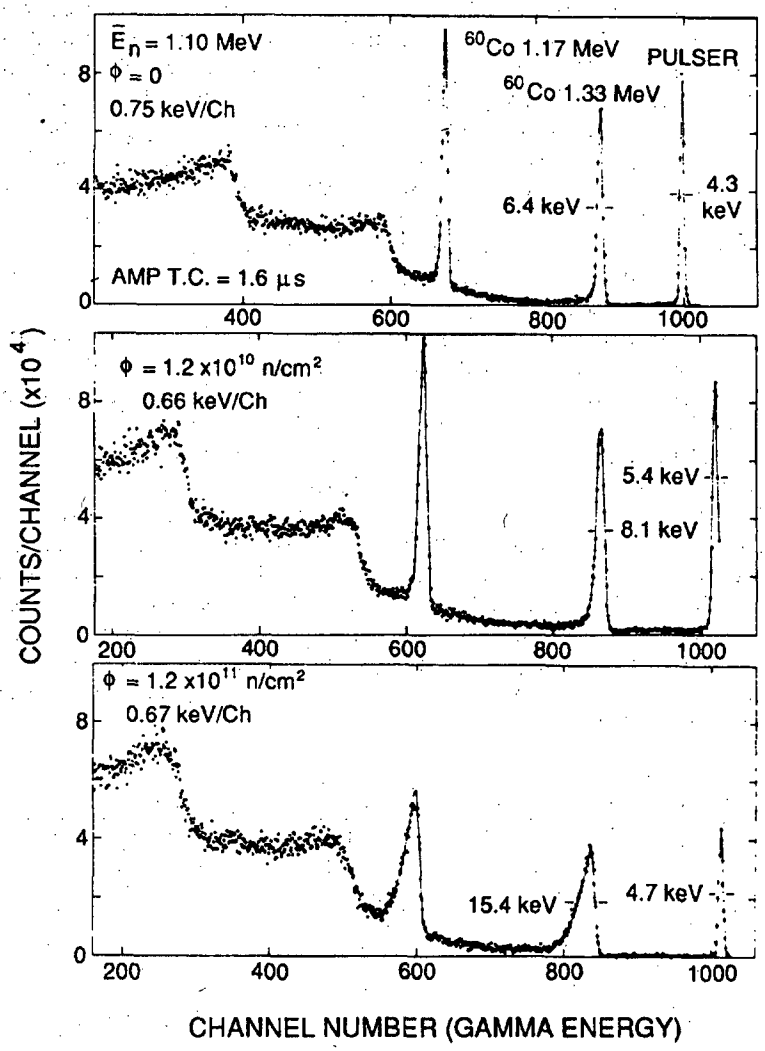

Fig. 3.5 The deterioration of a high-resolution solid-state detector gamma spectrum with increasing neutron fluence (φ). The width of the 1.33-MeV ^{60}Co photopeak is indicated in each spectrum. Only the high-energy portion of the spectrum is shown. Also noted is the width of an electronic pulser peak. (Adapted from Ref. 6.)

to cool the detector material electronically (Ref. 10), but these efforts are still in the experimental stages, and the capability is just beginning to be available commercially.

Another popular solid-state detector material for photon spectroscopy is lithium-drifted silicon [Si(Li)]. The lower atomic number of silicon compared to germanium reduces the photoelectric efficiency by a factor of about 50 (see Chapter 2), but this type of detector has been widely used in the measurement of x-ray spectra in the 1- to 50-keV energy range and finds some application in x-ray fluorescence (XRF) measurements (see Chapter 10). The low photoelectric efficiency of silicon above 50 keV is an advantage when measuring low-energy x rays and gamma rays, because it means that sensitivity to high-energy gamma rays is greatly reduced. Silicon detectors are most heavily used in charged-particle spectroscopy and are also used for Compton-recoil spectroscopy of high-energy gamma rays.

Other solid-state detection media besides germanium and silicon have been applied to gamma-ray spectroscopy. In NDA measurements, as well as many other applications of gamma-ray spectroscopy, it would be advantageous to have high-resolution detectors operating at room temperature, thereby eliminating the cumbersome apparatus necessary for cooling the detector crystal. Operation of room-temperature semiconductor materials such as CdTe, HgI_2, and GaAs has been extensively researched (Ref. 11). Their higher average atomic numbers provide greater photoelectric efficiency per unit volume of material. Some of their performance characteristics are summarized in Table 3-1. However, these detector materials have enjoyed limited application to NDA problems to date, largely because it has not been possible to produce crystals sufficiently large for the total detection efficiencies needed in NDA applications. As crystal-growth technology improves, these detectors may become more attractive as convenient, high-resolution room-temperature detectors for gamma-ray spectroscopy of nuclear materials.

Table 3-1. Comparison of several semiconductor detector materials

Material	Atomic Numbers	Energy per e-h Pair (δ)[a] (eV)	Best γ-Ray Energy Resolution at 122 keV[b] (keV)
Ge (77 K)	32	2.96	0.46
CdTe (300 K)	48, 52	4.43	3.80
HgI_2 (300 K)	80, 53	6.50	3.50
GaAs (300 K)	31, 33	4.2	2.60
NaI (300 K)[c]	11, 53		14.2

[a]This quantity determines the number of charge carriers produced in an interaction. (See Section 3.3.3.)
[b]Representative resolution data, as tabulated in Ref. 12. Energy resolution is discussed further in Section 3.3.3 and in Chapter 5.
[c]While not a semiconductor material, NaI is included in the table for convenient comparison.

3.3 CHARACTERISTICS OF DETECTED SPECTRA

In gamma-ray spectroscopy applications, the detectors produce output pulses whose magnitudes are proportional to the energy deposited in the detecting medium by the incident photons. The measurement system includes some method of sorting all of the generated pulses and displaying their relative numbers. The basic tool for accomplishing this task is the multichannel analyzer (MCA), whose operation is discussed in Chapter 4. The end result of multichannel analysis is a histogram (spectrum) of the detected output pulses, sorted by magnitude. The pulse-height spectrum is a direct representation of the energy spectrum of the gamma-ray interactions in the detection medium and constitutes the spectroscopic information used in gamma-ray NDA.

3.3.1 Generic Detector Response

Regardless of the type of detector used, the measured spectra have many features in common. Consider the spectrum of a monoenergetic gamma-ray source of energy E_0. The gamma-ray spectrum produced by the decaying nuclei is illustrated in Figure 3.6(a). The gamma-ray photons originate from nuclear transitions that involve specific energy changes. There is a very small fluctuation in these energy values because of two effects: (1) the quantum uncertainties in the energies of the transitions (the so-called Heisenberg Uncertainty), and (2) recoil effects as the gamma-ray photons are emitted. These uncertainties are finite, but negligible compared with the other energy-broadening effects discussed below and so are not shown on the figure. Thus, the "ideal" monoenergetic gamma-ray spectrum from free decaying nuclei is essentially a sharp line at the energy E_0.

Since detected gamma-ray photons do not usually come from free nuclei but are emitted in material media, some of them undergo scattering before they emerge from the radioactive sample. This scattering leaves the affected photons with slightly less energy than E_0, and the energy spectrum of photons emitted from a material sample is slightly broadened into energies below E_0 as shown in Figure 3.6(b). The magnitude of this broadening is also quite small with respect to other effects discussed below and is exaggerated in Figure 3.6(b) to call attention to its existence. It should also be noted that some gamma rays, after leaving the sample, will be scattered by external materials before entering the detector, and this effect can show up in the final energy spectrum (see below).

When the gamma ray enters the detection medium, it transfers part or all of its energy to an atomic electron, freeing the electron from its atomic bond. This freed electron then usually transfers its kinetic energy, in a series of collisions, to other atomic electrons in the detector medium.

The amount of energy required to produce electron-ion pairs in the detecting medium determines the amount of charge that will be produced from a detection event involving a given amount of deposited energy (see Table 3-1). A photoelectric interaction transfers all of the incident photon's energy to a photoelectron; this electron subsequently causes multiple ionizations until its energy is depleted. The amount of

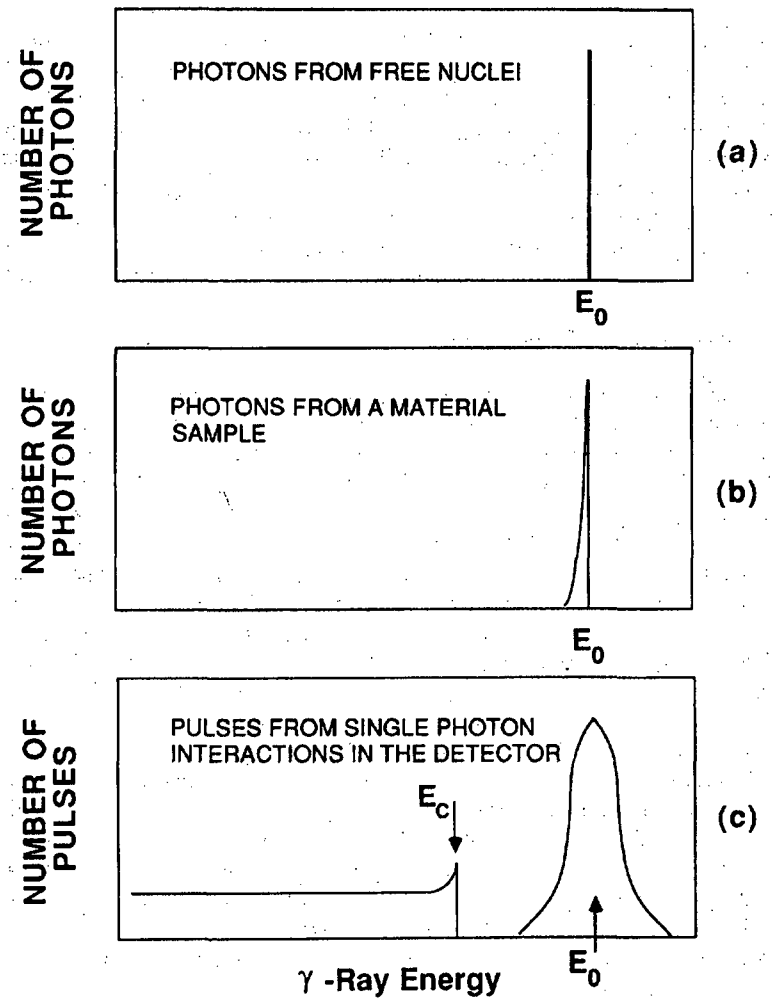

Fig. 3.6 An idealization of the photon spectrum (a) produced by free nuclei, (b) emerging from a material sample, and (c) displayed from interactions in a detecting medium.

charge produced from this type of event is therefore proportional to the actual photon energy. A Compton scattering interaction transfers only part of the incident photon's energy to an ionized electron; and that electron subsequently causes ionizations until its energy is depleted. The amount of charge produced from this type of event is proportional to the partial energy originally lost by the incident photon but conveys no useful information about the actual photon energy. Multiple Compton scattering events for a single photon can produce amounts of charge closer to the value representing the full energy of the original photon; however, Compton-produced signals generally represent one scattering interaction and are lower in magnitude than the full-energy signals. The idealized detector response to the photoelectric and Compton interactions in the detection medium is shown in Figure 3.6(c). The maximum energy that can be deposited in the detection medium from a Compton scattering event comes from an event where the photon is scattered by 180°. The Compton-generated detector pulses are therefore distributed below this maximum energy [E_c in Figure 3.6(c)] and constitute a source of "background" pulses that carry no useful energy information.

The full-energy peak in Figure 3.6(c) is significantly broadened by the statistical fluctuation in the number of electron-ion pairs produced by the photoelectron. This effect is the primary contributor to the width of the full-energy peak and is therefore the dominant factor in the detector energy resolution (see Section 3.3.3).

3.3.2 Spectral Features

A more realistic representation of a detector-generated gamma-ray spectrum from a monoenergetic gamma-ray flux is shown in Figure 3.7. The spectral features labeled A-G are explained below.

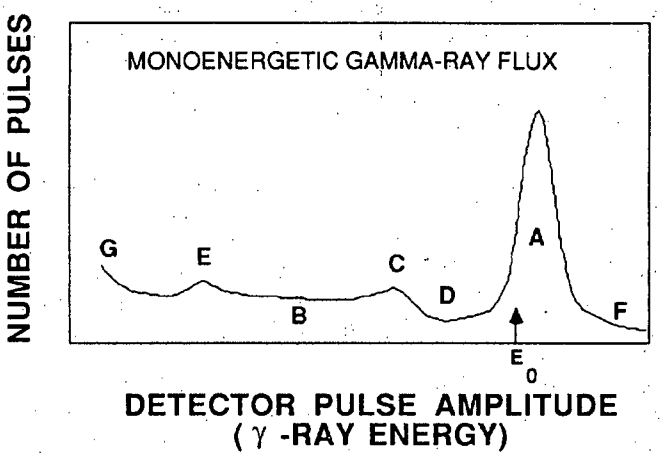

Fig. 3.7 A realistic representation of the gamma detector spectrum from a monoenergetic gamma source. The labeled spectral features are explained in the text.

A. The Full-Energy Photopeak. This peak represents the pulses that arise from the full-energy, photoelectric interactions in the detection medium. Some counts also arise from single or multiple Compton interactions that are followed by a photoelectric interaction. Its width is determined primarily by the statistical fluctuations in the charge produced from the interactions plus a contribution from the pulse-processing electronics (see Section 3.3.3 and Chapter 4). Its centroid represents the photon energy E_0. Its net area above background represents the total number of full-energy interactions in the detector and is usually proportional to the mass of the emitting isotope.

B. Compton Background Continuum. These pulses, distributed smoothly up to a maximum energy E_c (see Figure 3.6), come from interactions involving only partial photon energy loss in the detecting medium. Compton events are the primary source of background counts under the full-energy peaks in more complex spectra.

C. The Compton Edge. This is the region of the spectrum that represents the maximum energy loss by the incident photon through Compton scattering. It is a broad asymmetric peak corresponding to the maximum energy (E_c) that a gamma-ray photon of energy E_0 can transfer to a free electron in a *single* scattering event. This corresponds to a "head-on" collision between the photon and the electron, where the electron moves forward and the gamma-ray scatters backward through 180° (see Section 2.3.2). The energy of the Compton edge is given by Equation 2-11.

D. The "Compton Valley." For a monoenergetic source, pulses in this region arise from either multiple Compton scattering events or from full-energy interactions by photons that have undergone small-angle scattering (in either the source materials or intervening materials) before entering the detector. Unscattered photons from a monoenergetic source cannot produce pulses in this region from a *single* interaction in the detector. In more complex spectra, this region can contain Compton-generated pulses from higher-energy photons.

E. Backscatter Peak. This peak is caused by gamma rays that have interacted by Compton scattering in one of the materials surrounding the detector. Gamma rays scattered by more than 110°-120° will emerge with nearly identical energies in the 200- to 250-keV range. Therefore, a monoenergetic source will give rise to many scattered gamma rays whose energies are near this minimum value (see Ref. 1 and Section 2.3.2). The energy of the backscatter peak is given by Equation 2-10.

F. Excess-Energy Region. With a monoenergetic source, events in this region are from high-energy gamma rays and cosmic-ray muons in the natural background and from pulse-pileup events if the count rate is high enough (see Chapter 4). In a more complex spectrum, counts above a given photopeak are primarily Compton events from the higher-energy gamma rays.

G. Low-Energy Rise. This feature of the spectrum, very near the "zero-pulse-height-amplitude" region, arises typically from low-amplitude electronic noise in the detection system that is processed like low-amplitude detector pulses are. This noise tends to be at rather high frequency and so appears as a high-count-rate phenomenon. Electronic noise is usually filtered out of the analysis electronically (see Chapter 4), so this effect does not usually dominate the displayed spectrum. In more complex gamma-ray spectra, containing many different photon energies, the Compton-edge and backscatter peak features tend to "wash out," leaving primarily full-energy peaks on a relatively smooth Compton background.

3.3.3 Detector Resolution

The resolution of a detector is a measure of its ability to resolve two peaks that are close together in energy. The parameter used to specify the detector resolution is the Full Width of the (full-energy) photopeak at Half its Maximum height (FWHM). If a standard Gaussian shape is assumed for the photopeak, the FWHM is given by

$$\text{FWHM} = 2\sigma\sqrt{\ln 2} \tag{3-1}$$

where σ is the width parameter for the Gaussian. High resolution (small FWHM) not only makes individual definition of close-lying peaks easier but also makes the subtraction of the Compton continuum less uncertain because it is a smaller fraction of the total activity in the peak region. The more complex a gamma-ray spectrum is, the more desirable it is to have the best energy resolution possible.

There are both natural and technological limits to how precisely the energy of a gamma-ray detection event can be registered by the detection system. The natural limit on the energy precision arises primarily from the statistical fluctuations associated with the charge production processes in the detector medium. The voltage integrity of the full-energy pulses can also be disturbed by electronic effects, such as noise, pulse pileup, improper pole-zero settings, etc. These electronic effects have become less important as technology has improved, but their potential effects on the resolution must be considered in the setup of a counting system. The electronic and environmental effects on detector resolution are discussed in more detail in Chapter 4.

The two types of detectors most widely used in gamma-ray NDA applications are the NaI(Tl) scintillation detector and the germanium solid-state detector. The NaI detector generates full-energy peaks that are much wider than their counterparts from the germanium detector. This is illustrated in Figure 3.8, where the wealth of detail evident in the germanium spectrum of plutonium gamma rays is all but lost in the corresponding NaI spectrum.

By considering the statistical limit on the energy precision, it is possible to understand the origin of the difference in the energy resolution achievable with various

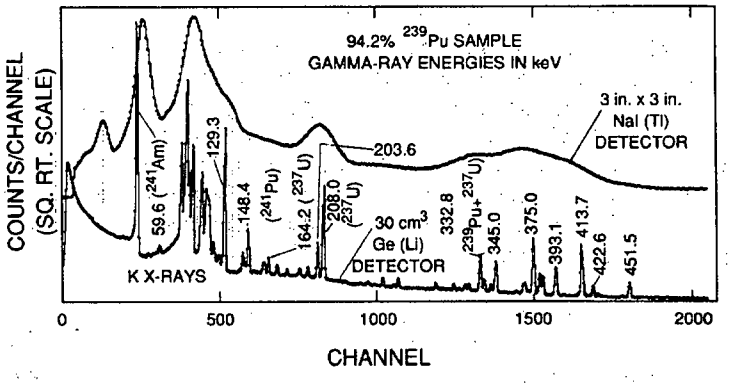

Fig. 3.8 *Gamma-ray spectrum from a plutonium sample with 94.2% ^{239}Pu, taken with a high-resolution solid-state detector [Ge(Li)] and with a NaI scintillation counter. Gamma-ray energies are given in keV.*

types of detectors. Ideally, the number of electron charges (n) produced by the primary detection event depends upon the total energy deposited (E) and the average amount of energy required to produce an electron-ion pair (δ):

$$n = E/\delta \ . \tag{3-2}$$

The random statistical variance in n is the primary source of fluctuation in the full-energy pulse amplitude. However, for some detector types, this statistical variance is observed to be less than (that is, better than) the theoretical value by a factor known as the Fano factor (Ref. 13):

$$\sigma^2(n) = Fn = FE/\delta \ . \tag{3-3}$$

This effect comes from the fact that part of the energy lost by the incident photon goes into the formation of ion pairs and part goes into heating the lattice crystal structure (thermal energy). The division of energy between heating and ionization is essentially statistical. Without the competing process of heating, all of the incident energy would result in ion-pair production, and there would be no statistical fluctuation in n (F = 0). By contrast, if the probability of ion pair production is small, then the statistical fluctuations would dominate (F ≅ 1). For scintillators, the factor F is approximately unity; for germanium, silicon, and gases, it is approximately 0.15 (Refs. 1 and 2). Since the number of charge carriers (n) is proportional to the deposited photon energy (Equation 3-2), the *statistical portion* of the relative energy resolution is given by

$$\Delta E_{stat}/E = 2.35\sigma(n)/n = 2.35[F\delta/E]^{1/2} \ . \tag{3-4}$$

The statistical limits on detector resolution are compared in Table 3-2 for several types of detectors. The electronic contribution to the energy fluctuations (ΔE_{elect}) is essentially independent of photon energy and determined largely by the detector capacitance and the preamplifier. Thus, the total energy resolution can be expressed as the combination of the electronic and statistical effects:

$$\Delta^2 E_{tot} = \Delta^2 E_{elect} + \Delta^2 E_{stat} = \alpha + \beta E \, . \tag{3-5}$$

In Figure 3.9 (Ref. 14) the energy resolutions of scintillation, gas, and solid-state detectors are compared in the low-energy x-ray region. Techniques for measuring resolution are described in Section 5.2.

The argument presented here assumes that the scintillation efficiency is the main factor influencing the number of electrons produced at the photocathode of a scintillation detector. Other factors, such as scintillator transparency, play important roles. To work effectively as a detector, a scintillating material must have a high transparency to its own scintillation light. In a similar vein, factors such as charge carrier mobility

Table 3-2. Theoretical statistical energy resolution at 300 keV for different types of gamma-ray detectors

Detecting Medium	δ (eV)[a]	No. of Electrons, n, for 300 keV[b]	Relative Error in n[c]	Energy Resolution[d] (keV)	High-Energy Resolution[e] (keV)
Ge	2.96	1.0×10^5	0.0032	0.86	1.60
Gas	30.	1.0×10^4	0.010	2.73	- -
NaI	- -[f]	1.0×10^3	0.032	22.6	30.0
BGO	- -[f]	8.0×10^1	0.11	77.6	100.0

[a]Average energy (in eV) required to produce one electron-ion pair in the detecting medium.
[b]The ratio E/δ for E = 300 keV (Equation 3-2).
[c]The quantity $\sigma(n)/n$, or $(1/n)^{1/2}$, without the incorporation of the Fano factor.
[d]The statistical portion of the energy resolution, ΔE_{stat}, from Equation 3-4. Fano factors used were 0.15 for germanium and gas, and 1.0 for the scintillators. These are average values for purposes of illustration.
[e]Resolution at 1332 keV (^{60}Co), calculated the same way as in the previous column, but using the higher energy. Values for gas detectors are not shown, since these detectors are ineffective for spectroscopy at such high energies.
[f]Since the measured charge is collected indirectly in scintillation detectors, this quantity is not relevant; a typical number of electrons produced at a photomultiplier photocathode per keV for NaI is taken from Ref. 1, and the numbers for BGO are based on the fact that its scintillation efficiency is approximately 8% of that for NaI (Ref. 1).

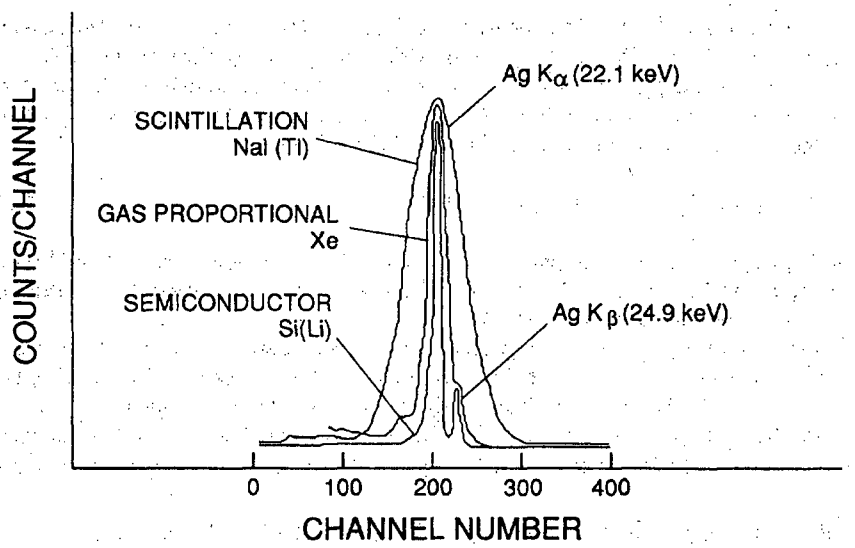

Fig. 3.9 Resolution comparison among NaI scintillation, gas proportional, and Si(Li) semiconductor detectors for the primary x rays of silver. (Adapted from Ref. 14.)

play an important role in determining the resolution of a solid state detector. This discussion is simplified of necessity, but it illustrates the primary reason why germanium detectors resolve so much better than scintillation detectors. See Ref. 1 for a more complete discussion of detector resolution.

3.3.4 Detector Efficiency

The basic definition of absolute photon detection efficiency is

$$\varepsilon_{tot} = \frac{\text{total number of detected photons in the full-energy peak}}{\text{total number of photons emitted by the source}} \tag{3-6}$$

For the discussion to follow, we will be concerned with only full-energy events and thus with the full-energy detection efficiency. This total efficiency can be expressed as the product of four factors:

$$\varepsilon_{tot} = \varepsilon_{geom}\varepsilon_{absp}\varepsilon_{sample}\varepsilon_{int}. \tag{3-7}$$

The *geometric efficiency* ε_{geom} is the fraction of emitted photons that are intercepted by the detector. For a point source this is given by

$$\varepsilon_{geom} = A/(4\pi r^2) \tag{3-8}$$

where A is the cross-sectional area of the detector and r is the source-to-detector distance (described in Section 5.5). This factor is essentially independent of photon energy. It manifests the well-known inverse-square law for counting rates as a function of source-to-detector distance.

The *absorption efficiency* ε_{absp} takes into account the effects of intervening materials (such as the detector housing, special absorbers, etc.) that absorb some of the incoming radiation before it interacts with the detector volume. This term is especially important (it should be $\ll 1$) for low-energy photons for which absorption effects are most pronounced. It has the mathematical form

$$\varepsilon_{absp} = \exp\left[-\sum \mu_i(E_\gamma)\rho_i x_i\right] \tag{3-9}$$

where μ_i, ρ_i, and x_i are the mass absorption coefficient, density, and thickness of the ith intervening material, and the summation is over all types of intervening materials.

The *sample efficiency* ε_{sample} is the reciprocal of the sample self-absorption correction (CF_{atten}) discussed in Chapter 6. This quantity is the fraction of emitted gamma rays that actually emerge from the sample material. For example, in a slab of thickness x and transmission T equal to $\exp[-(\mu\rho x)_s]$, the sample efficiency is

$$\varepsilon_{sample} = \frac{1 - \exp[-(\mu\rho x)_s]}{(\mu\rho x)_s} = \frac{T - 1}{\ln T}. \tag{3-10}$$

This factor clearly depends on the composition of each sample.

The *intrinsic efficiency* ε_{int} is the probability that a gamma ray that enters the detector will interact and give a pulse in the full-energy peak. In simplest terms, this efficiency comes from the standard absorption formula

$$\varepsilon_{int} = 1 - \exp(-\mu\rho x) \tag{3-11}$$

where μ is the photoelectric mass attenuation coefficient, and ρ and x are the density and thickness of the sensitive detector material. This simple expression underestimates the true intrinsic efficiency because the full-energy peak can also contain events from multiple Compton scattering interactions. In general, ε_{int} is also a weak function of r because of the detection of off-axis incident gamma rays. Empirically, ε_{int} can usually be approximated by a power law of the form

$$\varepsilon_{int} \propto a E_\gamma^{-b}. \tag{3-12}$$

Another important term is *relative efficiency*, which has two connotations:

- *Relative to NaI*: It is common practice to specify the efficiency of a germanium detector at 1332 keV (^{60}Co) as a percent of the efficiency of a 3 in. by 3 in. NaI detector at 25-cm source-to-detector distance and the same gamma-ray energy:

$$\varepsilon_{rel\ to\ NaI}(\text{Ge}) = 100\ \varepsilon_{tot}(\text{Ge, 1332 keV})/\varepsilon_{tot}\ (\text{NaI, 1332 keV}) \ . \tag{3-13}$$

The theoretical value of ε_{tot} (NaI, 1332 keV) at 25 cm is 1.2×10^{-3}. Thus, for example, a 30% (relative) germanium detector has a theoretical absolute efficiency at 1332 keV at 25 cm of 3.6×10^{-4}.

- *Relative Efficiency Curve*: (Also called the intrinsic efficiency calibration.) This is a composite curve of the energy dependence of the ratio of the detected count rate to the emitted count rate:

$$\varepsilon_{rel} = N\varepsilon_{absp}\varepsilon_{sample}\varepsilon_{int} \tag{3-14}$$

The factor N emphasizes that, for most assay applications, the absolute value of this total efficiency is not as important as the relative values at different energies. This efficiency also includes the energy-dependent effect of the sample self-absorption ε_{sample} (see Chapter 6 and Equation 3-10), and so must be determined for each sample measured.

The total relative efficiency may be calculated semi-theoretically, or (as is more prudent) it can be measured using many different gamma rays from one isotope. Aspects of this relative efficiency and its measurement are dealt with in greater detail in Chapter 8, and an example of a measured relative efficiency curve, including the sample self-absorption, is shown in Figure 8.14.

Detector efficiencies are usually measured and quoted as absolute photopeak efficiencies for detection of gamma rays from unattenuating point sources. Therefore, their energy dependence is dominated by ε_{int} at the higher energies and by ε_{absp} at the lower energies; the geometrical factor ε_{geom} establishes the overall magnitude of the efficiency. The intrinsic and absorption efficiencies are strongly dependent on the incident photon energy, as illustrated in Figures 3.10 and 3.11 (Ref. 15), where the typical energy dependence of detector efficiency is shown for a planar and a coaxial Ge(Li) detector, respectively.

These figures make three general points:

1. The strong energy dependence of the total detection efficiency causes the recorded photon intensities to be significantly different from the emitted intensities. To perform quantitative assays involving comparison of the intensities of different gamma rays, one must take into account this energy-dependent efficiency correction.
2. When low-energy gamma-ray assays are performed, thin detector volumes should be used. This optimizes the detection efficiency in the low-energy region and reduces the detection efficiency for the unwanted high-energy gamma rays.
3. When high-energy gamma-ray assays are performed, thick detector volumes should be used to provide adequate efficiency for the more penetrating radiation. In addition, selected absorbers at the detector entrance can reduce contributions to the counting rate from unwanted low-energy radiation.

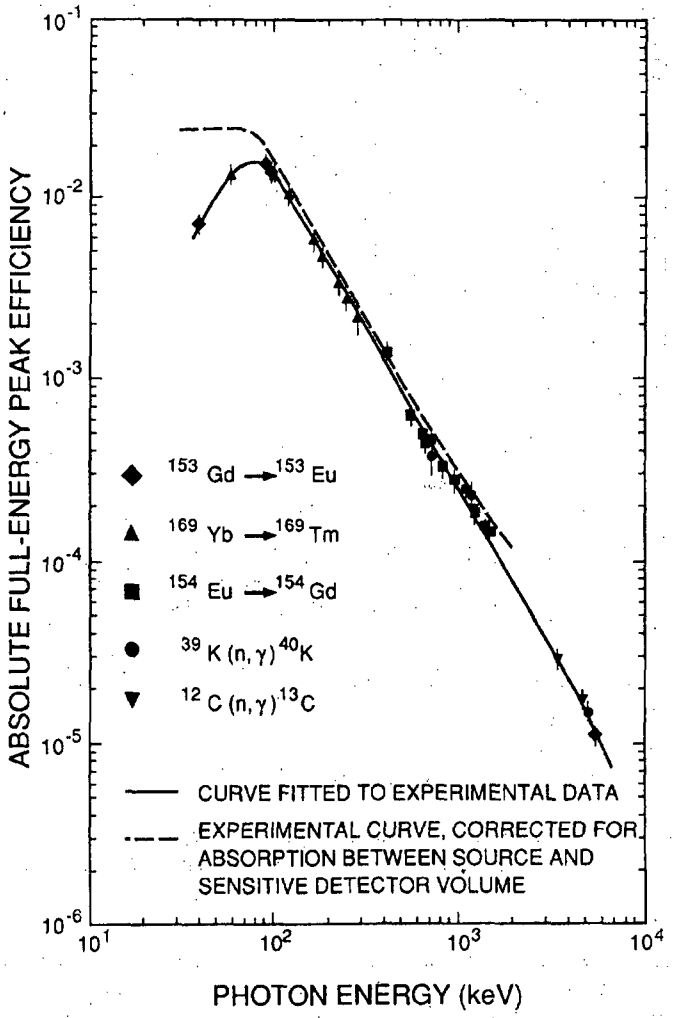

Fig. 3.10 *Absolute full-energy peak efficiency for a point source 54 mm from the face of a 33-mm-diam by 6.8-mm-thick planar Ge(Li) detector (adapted from Ref. 15). The measured data points are from known spontaneous and induced gamma decay processes. The low-energy decrease in efficiency illustrates the increased absorption of the low-energy incident radiation by the detector container and absorbers (ε_{absp}); the decrease in efficiency at high energy illustrates the decreased interaction rate in the detector crystal for higher-energy gamma rays (ε_{int}).*

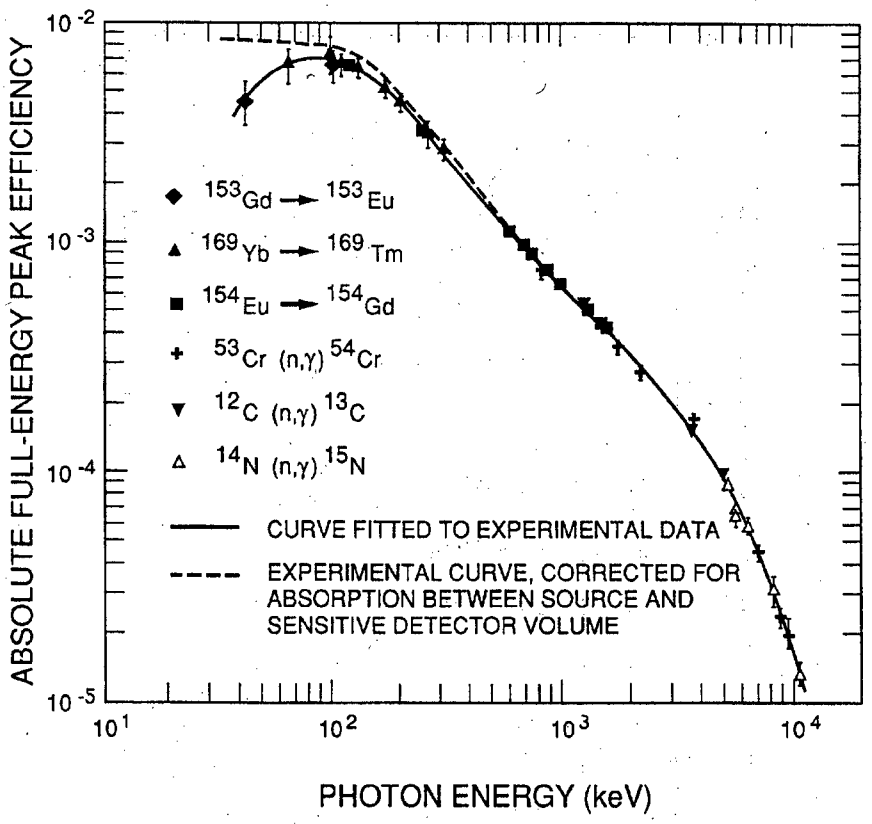

Fig. 3.11 *Same as Figure 3.10, except for a point source 83 mm from the face of a 38-cm^3 true coaxial Ge(Li) detector (adapted from Ref. 15).*

Even though Figures 3.10 and 3.11 illustrate these points for solid-state detectors, these same conclusions apply to NaI detectors as well. For example, uranium enrichment measurements at 186 keV are typically performed with a 2 in. by 1/2 in. scintillation crystal, while plutonium assays at 414 keV are usually done with axially thicker 2 in. by 2 in. scintillators.

3.4 DETECTOR SELECTION

Gamma-ray assay applications have varied objectives that can dictate the use of a variety of detectors. Discussion of the choice of detectors from the standpoint of energy resolution is given in Chapter 4. An additional consideration is the gamma-

ray (or x-ray) energy range of interest in a particular application. In general, the photon energies of major interest in the NDA of nuclear material range from below the x-ray region (85-100 keV) to approximately 400 keV. Exceptions are L_{III}-edge densitometry in the 15- to 30-keV energy range (see Chapter 9), plutonium isotopic measurements in the 400- to 1000-keV range (see Chapter 8), and occasional measurements of ^{238}U daughter activity in the 600- to 1000-keV range. (The major gamma-ray signatures for nuclear material are listed in Table 1-2.) As was illustrated in the discussion above, detectors that are thick in the axial dimension are more efficient for the high-energy applications, and for low-energy gamma- and x-ray measurements, axially thin detectors are better suited because of their optimum detection efficiency at low to medium energies and relative insensitivity to higher-energy radiation. Other factors, such as cost and portability may dictate the use of less expensive and more portable NaI (scintillation) detectors, with the attendant sacrifice of good energy resolution. In recent years, high-resolution detectors have become available with small liquid-nitrogen dewars that render the detector assembly every bit as portable as a NaI detector. However, cost considerations still favor the scintillation detector over the high-resolution detector.

REFERENCES

1. G. F. Knoll, *Radiation Detection and Measurement* (John Wiley & Sons, Inc., New York, 1979).

2. F. Adams and R. Dams, *Applied Gamma-Ray Spectrometry* (Pergamon Press, New York, 1975).

3. C. E. Moss, E. J. Dowdy, and M. C. Lucas, "Bismuth Germanate Scintillators: Applications in Nuclear Safeguards and Health Physics," *Nuclear Instruments and Methods* A242, 480 (1986).

4. P. E. Koehler, S. A. Wender, and J. S. Kapustinsky, "Improvements in the Energy Resolution and High-Count-Rate Performance of Bismuth Germanate," *Nuclear Instruments and Methods* A242, 369 (1986).

5. J. B. Birks, *The Theory and Practice of Scintillation Counting* (Pergamon Press, Oxford, 1964).

6. H. W. Cramer, C. Chasman, and K. W. Jones, "Effects Produced by Fast Neutron Bombardment of Ge(Li) Gamma-Ray Detectors," *Nuclear Instruments and Methods* 62, 173 (1968).

7. P. H. Stelson, J. K. Dickens, S. Raman, and R. C. Trammell, "Deterioration of Large Ge(Li) Diodes Caused by Fast Neutrons," *Nuclear Instruments and Methods* 98, 481 (1972).

8. R. Baader, W. Patzner, and H. Wohlfarth, "Regeneration of Neutron-Damaged Ge(Li) Detectors Inside the Cryostat," *Nuclear Instruments and Methods* 117, 609 (1974).

9. R. H. Pehl, "Germanium Gamma-Ray Detectors," *Physics Today* 30, 50 (Nov., 1977).

10. J. M. Marler and V. L. Gelezunas, "Operational Characteristics of High-Purity Germanium Photon Spectrometers Cooled by a Closed-Cycle Cryogenic Refrigerator," *IEEE Transactions on Nuclear Science* NS 20, 522 (1973).

11. E. Sakai, "Present Status of Room-Temperature Semiconductor Detectors," *Nuclear Instruments and Methods* 196, 121 (1982).

12. P. Siffert et al., "Cadmium Telluride Nuclear Radiation Detectors," *IEEE Transactions on Nuclear Science* NS 22, 211 (1975).

13. U. Fano, "On the Theory of Ionization Yield of Radiation in Different Substances," *Physics Review* 70, 44 (1946); "Ionization Yield of Radiation II: The Fluctuations in the Number of Ions," *Physics Review* 72, 26 (1947).

14. A. F. Muggleton, "Semiconductor X-Ray Spectrometers," *Nuclear Instruments and Methods* 101, 113 (1972).

15. H. Seyfarth, A. M. Hassan, B. Hrastnik, P. Goettel, and W. Delang, "Efficiency Determination for some Standard Type Ge(Li) Detectors for Gamma Rays in the Energy Range from 0.04 to 11 MeV," *Nuclear Instruments and Methods* 105, 301 (1972).

4

Instrumentation for Gamma-Ray Spectroscopy

Jack L. Parker

4.1 INTRODUCTION

The subject of this chapter is the function and operation of the components of a gamma-ray spectroscopy system. In Chapter 3 it was shown that the output pulse amplitude from most gamma-ray detectors is proportional to the energy deposited by the gamma ray. The pulse-height spectrum from such a detector contains a series of full-energy peaks superimposed on a continuous Compton background. Although the spectrum can be quite complicated (for example, see Figure 1.10 of Chapter 1) and thereby difficult to analyze, it contains much useful information about the energies and relative intensities of the gamma rays emitted by the source. The information that is important for the quantitative nondestructive assay (NDA) of nuclear material is contained in the full-energy peaks. The purpose of the electronic equipment that follows the detector is to acquire an accurate representation of the pulse-height spectrum and to extract the desired energy and intensity information from that spectrum.

This chapter provides a relatively brief introduction to the wide variety of instrumentation used in the gamma-ray spectroscopy of nuclear materials. It emphasizes the function of each component and provides information about important aspects of instrument operation. For a detailed description of instrument operation, the reader should refer to the instruction manuals provided with each instrument. Because of the rapidly advancing state-of-the-art of gamma-ray spectroscopy equipment, the best sources of current information are often the manufacturers and users of the instruments. Although the manufacturers are clearly the best source of information about the electronic capabilities of their equipment, those active in the application of gamma-ray spectroscopy to NDA are usually the best source of information on effective assay procedures and the selection of equipment for a given application. Books and reports on gamma-ray spectroscopy equipment are often out of date soon after they are published.

Gamma-ray spectroscopy systems can be divided into two classes according to whether they use single-channel analyzers (SCAs) or multichannel analyzers (MCAs). Figures 4.1 and 4.2 show block diagrams of the two classes. Both systems begin with a detector, where the gamma-ray interaction produces a weak electrical signal that is proportional to the deposited energy. Section 4.2 discusses the process of

selecting an appropriate detector for different NDA applications. Sections 4.3 through 4.8 discuss the basic components of gamma-ray spectroscopy systems; the discussion of each component is presented in the order in which the electrical signal flows through the system. Section 4.9 presents auxiliary electronic equipment. Usually, components other than those shown in Figures 4.1 or 4.2 must be added to form a useful NDA system. Shields, collimators, sample holders, sample changers, scanning mechanisms, and source shutters are discussed in later chapters that describe specific assay techniques and instruments.

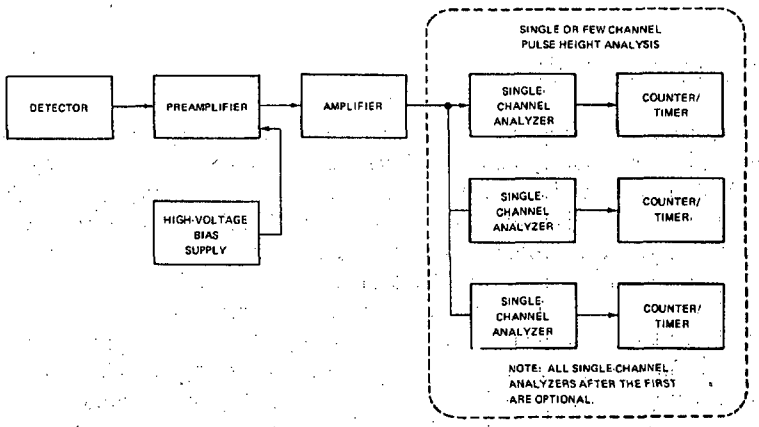

Fig. 4.1 Block diagram of a single-channel-analyzer-based gamma-ray spectroscopy system for simple NDA applications.

4.2 SELECTION OF DETECTOR

Some general guidance is given in this section to the often difficult matter of selecting an appropriate detector for a particular NDA application. There are not only several generic types of detectors but myriad variations of size, shape, packaging configuration, performance, and price. The detector choice must be evaluated in the light of the technical requirements of a proposed application and the nontechnical but often overriding matter of budgetary constraints.

The first and most important detector parameter to consider is resolution. A detector with high resolution usually gives more accurate assays than one with low resolution. The resolution of a germanium detector is typically 0.5 to 2.0 keV in the energy range of interest for NDA applications, whereas the resolution of a NaI detector is 20 to 60 keV. It is easier to determine accurately the area of full-energy peaks in a complex spectrum when the peaks do not overlap, and the probability of overlap is

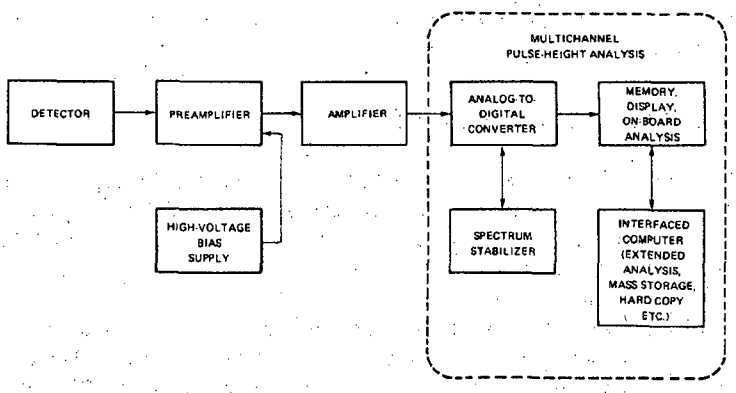

Fig. 4.2 *Block diagram of a multichannel-analyzer-based gamma-ray spectroscopy system for complex NDA applications.*

less with narrower peaks. The background continuum under the full-energy peaks is easier to subtract from a high-resolution spectrum because it is a smaller fraction of the total activity in the peak region. Full-energy-peak areas are easier to evaluate in high-resolution spectra because the interference from small-angle Compton scattering in the sample is reduced. Gamma rays that undergo small-angle scattering lose only a small amount of energy. If these scattered gamma rays still fall in the full-energy-peak region, the calculated full-energy-peak area is likely to be incorrect. This problem is minimized by using a high-resolution detector, which provides narrow, full-energy peaks.

The complexity of the spectrum should influence the detector choice; the more complex the spectrum becomes, the more desirable high resolution becomes. Plutonium has a much more complex gamma-ray spectrum than uranium does, and germanium or silicon detectors are used more often in plutonium assay applications than in uranium assay applications.

The second performance parameter to consider is efficiency, which determines the count rates that can be expected, the time that is required to achieve a given precision, and the sensitivity that can be achieved. Higher efficiency always costs more for a given detector type, but a given efficiency is less expensive to obtain in a low-resolution NaI detector than in a high-resolution germanium detector. There is considerable motivation to use a less-expensive, lower-resolution detector when it can give satisfactory assay results.

Other parameters such as space and cooling requirements and portability must be considered and are sometimes the dominant considerations. The selection of an appropriate detector is often difficult and may involve painful compromises among conflicting requirements. Once the selection is made, considerable care should be taken

to specify all pertinent parameters to prospective vendors to ensure that the desired detector is obtained.

4.3 HIGH-VOLTAGE BIAS SUPPLY

All of the commonly used gamma-ray detectors require a high-voltage bias supply to provide the electric field that collects the charge generated by the gamma-ray interaction in the detector. The bias supply is not a part of the signal path but is required to operate the detector. It is usually the most reliable unit in a spectroscopy system and the easiest to operate.

Germanium and silicon diode detectors require very low currents, typically $<10^{-9}$A. The voltage requirements range from a few hundred volts for a small silicon detector to several thousand volts for a large coaxial germanium detector. Bias supplies for germanium and silicon detectors usually provide up to 5 kV and 100 μA. The voltage-resolution and low-frequency-filtering requirements are modest because there is no charge amplification in the detector. The voltage is usually continuously variable from 0 to 5 kV. In the past, it was necessary to vary the voltage very slowly (<100 V/s) when turning on or changing the detector bias because the field-effect transistor (FET) used in the first stage of the detector preamplifier is easily damaged by sudden voltage surges. However, the protection now provided by the filter included in all high-quality preamplifiers is so good that an FET is rarely destroyed for this reason. Battery packs are sometimes used as bias supplies for germanium and silicon detectors because they are portable and do not generate noise. A charged capacitor can be used as a "power supply" for many hours; in fact, the capacitor in the high-voltage filter located in the preamplifier can often operate a detector for an hour or two.

The bias supply requirements for photomultiplier tubes used with scintillation detectors are more stringent than for solid-state diode detectors. The required voltage is typically a few thousand volts, but the required current is usually 1 to 10 mA. Because the gain of a photomultiplier is a very strong function of the applied voltage, the stability and filtering must be excellent. The 100-μA supplies used with germanium detectors will usually not operate a photomultiplier tube.

Bias supplies come in a variety of packages. The most common is the nuclear instrumentation module (NIM), which plugs into a frame or bin (NIM bin) that supplies the necessary dc voltages to power the module. NIM modules meet internationally accepted standards for dimensions, voltages, wiring, and connectors and are widely used in NDA instrumentation. Other bias supplies fit in NIM bins but take power from the normal ac source. The high-current bias supplies used to power multiple photomultiplier-tube arrays are often mounted in standard 45.7-cm (18-in.)-wide instrumentation racks.

NIM bias supplies frequently use an electronic switching device to generate the required voltage. The switching device generates a high-frequency noise that can find its way into the preamplifier and cause significant degradation of spectral quality. This problem can be minimized by careful grounding and cable positioning. The noise generated by the power supply can also introduce false signals into any pileup rejection circuitry being used. Photomultiplier-tube bias supplies, even those that are not the NIM type, can also be sources of high-frequency noise. As usual, an oscilloscope is a most useful aid in detecting the presence of interfering electrical noise from any source.

Note that detector bias supplies can be lethal. Caution is always required, particularly when working with the high-current supplies that power photomultiplier tubes. Persons who are accustomed to working with low-voltage, low-power, transistorized circuits must be made aware of the danger associated with the use of detector power supplies.

4.4 PREAMPLIFIER

Preamplifiers are required for germanium and silicon detectors and improve the performance of NaI scintillation detectors. The detector output signal is usually a low-amplitude, short-duration current pulse; a typical pulse might be 10 mV high and 200 ns long. The preamplifier converts this current pulse to a voltage pulse whose amplitude is proportional to the energy deposited in the detector during the gamma-ray interaction. To maximize the signal-to-noise ratio of the output pulse and preserve the gamma-ray energy information, the preamplifier must be placed as close to the detector as possible. The closeness of the preamplifier minimizes the capacitance at the preamplifier input, thereby reducing the output noise level. The preamplifier also serves as an impedance-matching device between the high-impedance detector and the low-impedance coaxial cable that transmits the amplified detector signal to the main amplifier. The amplifier and preamplifier may be separated by as much as several hundred meters.

Because the detector and preamplifier must be close, the preamplifier is often in an inconvenient location, surrounded by shielding, and inaccessible during use. Most preamplifiers have no external controls; the gain and pulse-shape adjustments are included in the main amplifier, which is usually in a more convenient location close to the other system electronics. Because it lacks external controls, the preamplifier occupies only a few hundred cubic centimeters. Its small volume is advantageous when the preamplifier must be located inside the detector shielding. The preamplifier is usually housed in a small rectangular box. For single NaI detectors, the preamplifier is often built into the cylindrical housing that holds the photomultiplier-tube socket. In recent years, preamplifiers for germanium and silicon detectors have been packaged in an annular configuration behind the end cap of the detector cryostat. This configuration

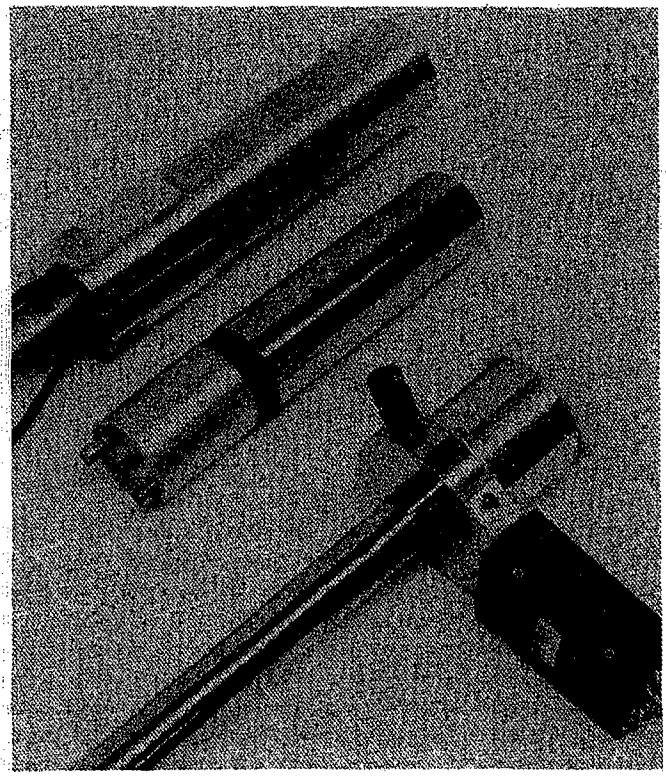

Fig. 4.3 Detectors having annular, cylindrical, and rectangular preamplifiers.

eliminates awkward boxes that stick out at right angles from cryostats and makes the detectors easier to shield. Figure 4.3 shows the basic preamplifier configurations just described.

Although preamplifiers have few controls, they have several connectors. Usually included are one or two output connectors and a test input through which pulses can be routed from an electronic pulser to simulate gamma-ray events for testing the performance of the preamplifier and the other signal-processing instruments in the system. (The simulated gamma-ray peak produced in the acquired spectrum can also give a good estimate of the electronic losses suffered by the system; see Chapter 5.) The detector bias is often applied through a connector mounted on the preamplifier. A multipin connector is usually included to provide the power needed for operating the preamplifier; the power is often supplied by the main amplifier. Certain NaI preamplifiers generate the required low voltage from the detector bias voltage.

The preamplifier output pulse is a fast positive or negative step followed by a very slow decay. The risetime is a few tenths of a microsecond and the decay time is 50 to 100 μs. The amplitude of the fast step is proportional to the charge delivered to the preamplifier input and therefore proportional to the energy deposited in the detector by the gamma ray. The long decay time means that a second pulse often occurs before the tail of the preceding pulse has decayed. This effect is seen in Figure 4.4, which shows the preamplifier output from a large, coaxial germanium detector. The amplitude of the fast-rising step, which contains the important energy information from the gamma-ray interaction, is distorted only if the energy deposition rate becomes so high that the average dc level of the preamplifier rises to where some of the fast-rising steps are beyond the linear range of the amplifier.

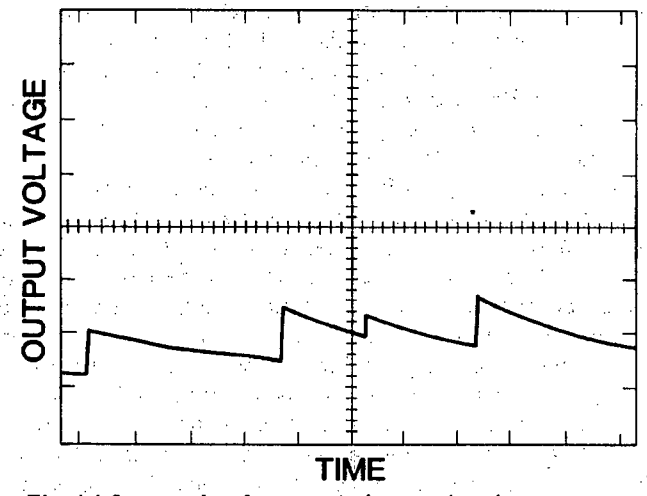

***Fig. 4.4** Output pulses from a typical germanium-detector preamplifier. The important energy information is contained in the amplitude of the fast-rising voltage step (~0.5 μs). The pileup of pulses on the long tails (~50 μs) does not affect the validity of the energy information.*

Most manufacturers offer several preamplifier models that are optimized for different detector types. Parameters such as noise level, sensitivity, risetime, and count-rate capability may be different for different models. The count-rate capability is usually specified as the maximum charge per unit time (C/s) delivered from the detector to the preamplifier input. For germanium and silicon detectors the equivalent energy per unit time (MeV/s) is often specified; when this number is divided by the average gamma-ray energy, the result is the maximum count rate that the preamplifier can handle.

Usually, few choices can be made when selecting a preamplifier for a NaI detector. However, several significantly different options are available for germanium detectors; the selection depends upon the detector and the measurement application. Because germanium detectors are always sold with an integral preamplifier, the selection must be made when the detector is purchased.

Because of its low noise, an FET is always the first amplifying stage in a germanium-detector preamplifier. When germanium detectors were first produced, the FET was always operated at room temperature in the main preamplifier enclosure. However, better resolution can be achieved when the FET is cooled along with the detector crystal. The improvement in resolution is especially significant at gamma-ray energies below 200 keV. Preamplifiers are now available with either room-temperature or cooled FETs. The preamplifier feedback resistor and other associated circuit components may be located inside the cryostat with the FET and the detector crystal. The penalty for the improved performance is that if the FET fails and must be replaced, the cryostat must be opened, usually by the manufacturer at considerable expense to the user. However, preamplifiers that use cooled FETs are now so reliable and so well protected from high-voltage surges that the transistors rarely fail. As a result, this type of preamplifier is now the most commonly used.

Most manufacturers also offer a high- or low-count-rate option. This option is needed because detector resolution cannot be optimized simultaneously for high and low count rates. Most detector-preamplifier units are optimized to operate at low count rates (<10 000 count/s) because this provides the best resolution possible. If the primary application will involve count rates greater than 50 000 count/s, the manufacturer should be asked to optimize the detector for high-count-rate performance.

Germanium detector crystals are fabricated in planar or coaxial geometries; the designation refers to the shape of the crystal and the location of the charge-collecting contacts. Because of their very low electrical capacitance, small planar detectors (<10 cm^3) have lower noise and better resolution than large detectors. To obtain the best possible resolution from small planar detectors, the feedback resistor is sometimes removed from the preamplifier. However, without the feedback resistor, the decay time of the output pulse is very long and the output level increases with each successive pulse. Figure 4.5 shows the output of a preamplifier that does not have a feedback resistor. When the maximum allowable dc level is reached, the preamplifier must be reset using a pulsed-optical or transistorized method. However, the reset pulse can saturate the main amplifier for up to several hundred microseconds, and the data acquisition equipment must be disabled to avoid the analysis of invalid, distorted pulses. Because of this complication, pulsed-optical preamplifiers are chosen only when the small improvement in resolution is absolutely required. Pulsed-optical preamplifiers have a low-count-rate capability, often only 5000 MeV/s rather than the more than 50 000 MeV/s usually available with other types of preamplifiers. For low gamma-ray energies (<100 to 200 keV), the count-rate limitation may not be a problem.

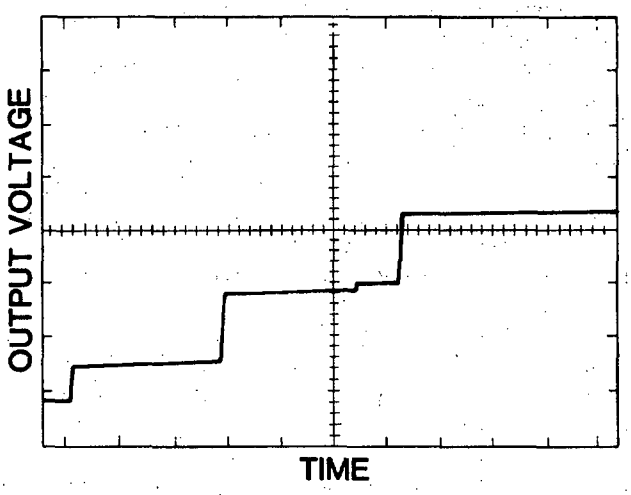

Fig. 4.5 *Output pulses from a pulsed-optical preamplifier on a germanium detector. Because there is no feedback resistor, the noise level is lower than in resistively coupled preamplifiers and the dc output level rises in a stair-step fashion and must be reset when the maximum allowable voltage is reached.*

In recent years, preamplifiers that use variations of the pulsed-optical method have been developed for high-count-rate applications. In one case, the optically coupled reset device is replaced by a transistor network. In another case, the reset is accomplished by optical means but the preamplifier is reset after nearly every event, thereby reducing the amplifier saturation time.

4.5 AMPLIFIER

After leaving the preamplifier, the gamma-ray pulses are amplified and shaped to meet the requirements of the pulse-height-analysis instrumentation that follows the main amplifier. Most spectroscopy-grade amplifiers are single- or double-width NIM modules. Portable multichannel analyzers often have a built-in amplifier, which may be adequate for the intended application.

The main amplifier accepts the low-voltage pulse from the preamplifier and amplifies it into a linear voltage range that is 0 to 10 V for most high-quality amplifiers. Within the linear range all input pulses are accurately amplified by the same factor. The amplification is nonlinear for output pulses that exceed 10 V. The maximum output voltage or saturation voltage of most amplifiers is approximately 12 V. The amplifier gain can be adjusted over a wide range, typically from

10 to 5000. Amplifiers usually have two gain controls (coarse and fine) to allow continuous gain adjustment.

The shaping function of the main amplifier is vital to the production of high-quality spectra. The amplified pulses are shaped to optimize the signal-to-noise ratio and to meet the pulse-shape requirements of the pulse-height-analysis electronics. Because single-channel and multichannel analyzers measure the input pulse amplitude with respect to an internal reference voltage, the amplifier output must return quickly to a stable voltage level, usually zero, between gamma-ray pulses. The stability of the baseline voltage level is extremely important because any baseline fluctuation perturbs the measurement of the gamma-ray pulse amplitude and contributes to the broadening of the full-energy peak.

A narrow pulse shape permits a quick return to baseline. However, the pulse must be wide enough to allow sufficient time to collect all of the charge liberated by the interaction of the gamma ray in the detector. Figure 4.4 shows that 0.25 to 0.5 μs could be sufficient to allow complete charge collection. The pulse shape should also provide a signal-to-noise ratio that minimizes the variation in output pulse amplitude for a given quantity of charge deposited at the preamplifier input. Unfortunately, the pulse width that provides the optimum signal-to-noise ratio is usually wider than that required for a quick return to baseline. At low count rates, the pulse can be wide because the probability is small that a second pulse will arrive before the amplifier output has returned to the baseline level. As the count rate increases, however, the probability that pulses occur on a perturbed baseline also increases, and the spectrum is distorted in spite of the optimum signal-to-noise ratio. A narrower pulse width than required for the optimum signal-to-noise ratio usually gives the best resolution at high count rates; the resolution, however, is not as good as can be obtained at low count rates.

The amplifiers used with high-resolution germanium and silicon detectors employ a combination of electronic differentiation, integration, and active filtering to provide the desired pulse shape. Qualitatively, differentiation removes low frequencies from a signal and integration removes high frequencies. Differentiation and integration are characterized by a time constant, usually having units of microseconds, that defines the degree of attenuation as a function of frequency. The greater the time constant, the greater is the attenuation of low frequencies by differentiation and the attenuation of high frequencies by integration. When both differentiation and integration are used, the low- and high-frequency components are strongly suppressed and a relatively narrow band of middle frequencies is passed and amplified. Because most spectroscopy amplifiers function best when the differentiation and integration time constants are equal, there is usually a single control that selects time constants in the range 0.25 to 12 μs. When the two time constants are equal, the amplifier output pulse is nearly symmetrical (see Figure 4.6). The total pulse width is approximately six times the time constant. At low count rates, large coaxial germanium detectors usually have optimum resolution with time constants of 3 to 4 μs. Small planar germanium detectors

resolve best with time constants of 6 to 8 μs, and small planar silicon detectors usually operate best with values of 8 to 12 μs. The problem of pulse pileup is more severe when long time constants are used to exploit the intrinsically better resolution of the smaller detectors. The time constant used in a given situation depends on the detector, the expected count rate, and whether resolution or data throughput is of greater importance.

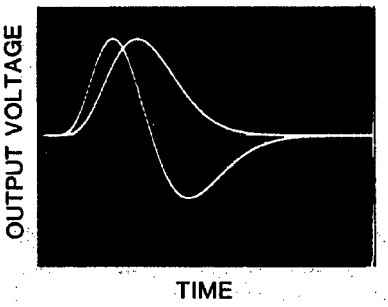

Fig. 4.6 Unipolar and bipolar output signals from a typical spectroscopy amplifier with differentiation/integration pulse shaping.

High-resolution germanium and silicon detectors are relatively slow and require time constants longer than those needed for other types of detectors. NaI scintillation detectors, which have resolutions that are 10 to 20 times worse than those of germanium detectors, operate well with time constants of 0.25 to 1.0 μs. Organic scintillation detectors, which have almost no energy resolution, can operate with time constants of only 0.01 μs; when energy resolution is not required but high-count-rate capability is, they are very useful. Unfortunately, no detector now available combines very high resolution with very high count rate capability.

Spectroscopy amplifiers usually provide two different output pulse shapes: unipolar and bipolar. The bipolar pulse is usually obtained by differentiating the unipolar pulse. Figure 4.6 shows both unipolar and bipolar output signals from a typical spectroscopy amplifier. The unipolar output has a better signal-to-noise ratio and is usually used for energy analysis, whereas the bipolar output has superior timing information and overload recovery. The bipolar pulse shape is usually better for timing applications because the zero crossover point (the point where the bipolar pulse changes sign) is easily detected and is very stable. The crossover point corresponds to the peak of the unipolar output and is nearly independent of output pulse amplitude.

Delay lines can be used in pulse-shaping circuits. Delay-line shaping can provide unipolar or bipolar pulses, depending on whether one or two delay lines are employed. Delay-line amplifiers are economical and provide adequate performance when used with low-resolution detectors; they are rarely used with germanium or silicon detectors because their noise level is higher than that found in amplifiers that use differentiation and integration. The output pulse shape of a delay-line amplifier is distinctly different from that of an amplifier that uses differentiation and integration. Figure 4.7 shows the unipolar and bipolar output signals from a typical delay-line amplifier.

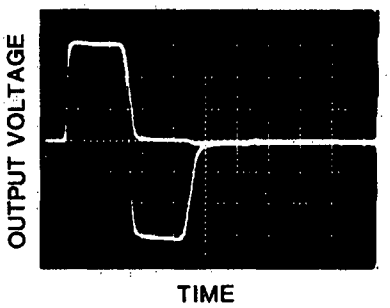

Fig. 4.7 Unipolar and bipolar output signals from an amplifier with delay-line pulse shaping.

4.5.1 Pole-Zero Compensation Circuit

Most amplifiers include a pole-zero compensation circuit to help maintain a stable baseline. The pole-zero circuit was introduced in about 1967 and was the first major improvement in amplifier design after the introduction of transistors. It significantly improves amplifier performance at high count rates. The term "pole zero" arises from the terminology of the Laplace transform methods used to solve the simple differential equation that governs the circuit behavior. The circuit is very simple; it consists of an adjustable resistor in parallel with the amplifier input capacitor. In spite of the simplicity of the circuit, the proper adjustment of the pole-zero control is crucial for correct operation of most modern amplifiers. When the pole-zero control is properly adjusted, the amplifier output returns smoothly to the baseline level in the minimum possible time. When the control is incorrectly adjusted, the following conditions result: the output pulses are followed by a long undershoot or overshoot that perturbs the output baseline and seriously degrades the amplifier performance at high count rates; the full-energy peaks are broader and often have low- or high-energy tails depending on whether an undershoot or overshoot condition exists; accurate determination of the full-energy peak areas is difficult. Figure 4.8 shows the amplifier pulse shapes and full-energy peak shapes that result from correct and incorrect pole-zero adjustment.

Adjustment of the pole-zero circuit is simple and is best accomplished using an oscilloscope to monitor the amplifier output pulse shape and following procedures found in the amplifier manual. The adjustment should be checked whenever the amplifier time constant is changed.

4.5.2 Baseline Restoration Circuit

Baseline restoration (BLR) circuits were added to spectroscopy amplifiers soon after the advent of pole-zero circuits. Like the pole-zero circuit, the BLR helps maintain a stable baseline. The pole-zero circuit is located at the amplifier input and is a very simple circuit; the BLR is located at the amplifier output and is often remarkably complex. The pole-zero circuit prevents undershoot caused by the finite

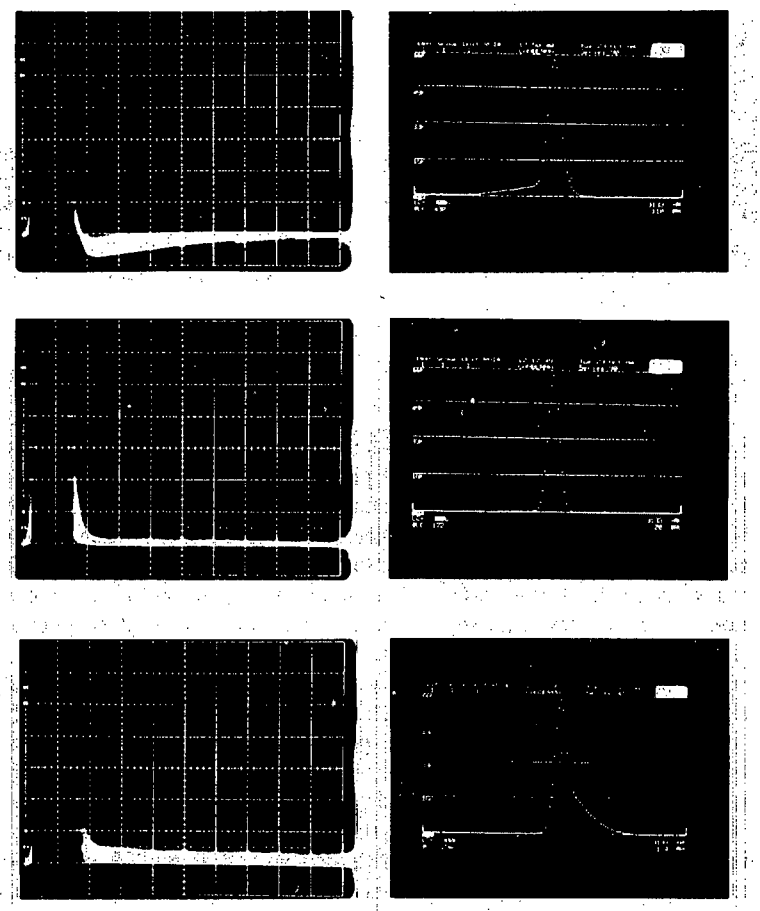

Fig. 4.8 *The effect of pole-zero adjustment on the amplifier output (left) and the full-energy-peak shape (right). The upper frames show pole-zero undercompensation, which causes amplifier undershooting and low-energy tailing on the MCA peak. The middle frames show correct pole-zero compensation. The lower frames show pole-zero overcompensation, which causes amplifier overshooting and high-energy tailing on the MCA peak.*

decay time of the preamplifier output pulse; the BLR suppresses the baseline shifts caused by the ac coupling of the unipolar output pulses. Although operation of the BLR is totally automatic in some amplifiers, other amplifiers have several controls to optimize amplifier performance for different count rates and preamplifier types. The optimum BLR setting is often determined by trial and error.

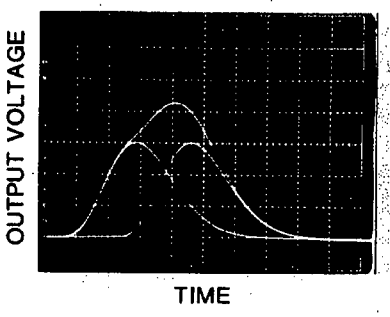

Fig. 4.9 The origin and effect of pulse pileup on the output of a spectroscopy amplifier. When two pulses are separated by less than the amplifier risetime, the amplitude of the resulting sum pulse is not representative of either input pulse.

4.5.3 Pileup Rejection Circuit

Pileup rejection circuits have been added to many top-of-the-line amplifiers to improve performance at high count rates. A pileup rejector uses timing circuitry to detect and reject events where two or more gamma-ray pulses overlap. Such events have a combined pulse amplitude that is not characteristic of any single gamma ray and only increases the height of the background continuum in the acquired spectrum. Figure 4.9 shows how two gamma-ray pulses overlap to produce a pileup pulse. For germanium detectors, the minimum pulse separation that can be resolved by the pileup rejector is approximately 0.5 μs. The pileup rejector usually provides a logic pulse that can be used to prevent analysis of the pileup pulses. In high-count-rate situations, the pileup rejector can provide better resolution and a lower background continuum; as a result, determination of the full-energy-peak areas is simplified. Figure 4.10 shows the improvement in spectral quality that can result from using a pileup rejector. The figure also shows that the pileup rejector can sharpen the appearance of sum peaks such that they may be mistaken for real full-energy peaks.

The considerable benefits of pileup rejection are offset by increased complexity of operation and more stringent requirements for the preamplifier output pulse. The preamplifier output pulse must be free of high-frequency ringing that can cause false pileup signatures in the timing circuits. It must also be free of high-frequency interference from power supplies, scalers, computers, and video display terminals. Such high-frequency pickup is usually filtered out in the main amplifier but can cause false pileup signatures in the pileup rejection circuit and lead to excessive rejection of good gamma-ray pulses and spectral distortions. Considerable care must be used when adjusting pileup rejection circuits.

The proper use of pole-zero, baseline restoration, and pileup rejection circuits can greatly improve the quality of the measured gamma-ray spectrum. Because an oscilloscope is virtually indispensable for adjusting these circuits for optimum performance, a good quality oscilloscope should be readily available to every user of a gamma-ray spectroscopy system. Users should understand the operation of the oscilloscope as

well as they understand the operation of the spectroscopy system. They can detect and/or prevent more difficulty through proper use of the oscilloscope than through the use of any other piece of equipment.

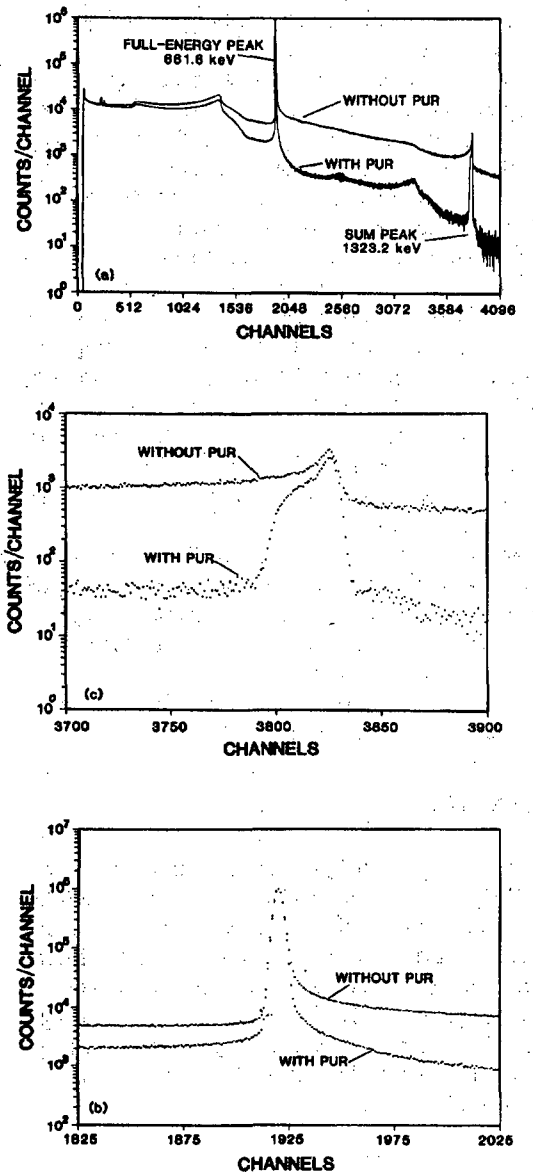

Fig. 4.10 *A high-rate (50 000 count/s) spectrum of ^{137}Cs showing the improved spectral quality obtained with pileup rejection (PUR). Top: the entire spectrum. Middle: the full-energy peak at 661.6 keV. Bottom: the sum peak at 1323.2 keV; pileup rejection reduces the pileup continuum near the sum peak by a factor of 25 but does not significantly reduce the sum-peak amplitude.*

4.5.4 Advanced Concepts in Amplifier Design

Two recent advances in amplifier design improve the ability of gamma-ray spectroscopy systems to operate at high count rates without excessive spectral degradation. Both concepts use a narrow pulse shape to reduce pileup losses while preserving good peak shape, signal-to-noise ratio, and resolution.

In one design, a gated integrator is added to the output of a standard high-quality amplifier. The amplitude of the integrator output pulse is proportional to the integral of the amplifier output pulse. The integrator output is digitized in the normal way by the analog-to-digital converter. For a given gamma-ray interaction, the charge collection time depends on the electric field strength in the detector and the location of the interaction. Charge carriers that are produced far from the collection electrodes or in regions where the electric field is weaker arrive later at the electrodes. Charge that is collected very late may not contribute to the information-carrying part of the preamplifier pulse; such charge is said to cause a ballistic deficit. If the amplifier time constants are comparable to the charge collection time, the integral of the amplifier output pulse is more nearly proportional to the collected charge than is the pulse amplitude. Qualitatively, the integration allows a longer period for charge collection and decreases the ballistic deficit. Shorter time constants can be used with the amplifier-integrator combination than can be used with the amplifier alone. The short time constants reduce pileup losses and increase data throughput. Figure 4.11 shows the amplifier and corresponding integrator output pulse.

The second design uses time-variant filters in place of the normal differentiation-integration filters. The technique requires special preamplifiers and analog-to-digital converters, but it can operate at count rates as high as 10^6 count/s with data throughput rates of 80 000 count/s. Figure 4.12 shows that the output pulse shape from this system is much different from the familiar Gaussian pulse shape.

It should be emphasized that the selection of a detector with excellent charge collection is essential to high-resolution, high-rate spectroscopy.

4.6 SINGLE-CHANNEL ANALYZER

The single-channel analyzer (SCA) is the pulse-height-analysis instrument shown in the simple spectroscopy system of Figure 4.1. Historically, the first pulse-height-analysis instrument was a simple discriminator with a single, adjustable voltage threshold. If the voltage of the amplifier output pulse exceeds the discriminator threshold, the discriminator emits a logic pulse. Logic pulses are used for counting and control functions and have a fixed amplitude and width, usually 5 V and 1 μs in spectroscopy equipment. The threshold voltage is calibrated for its equivalent gamma-ray energy. When the discriminator output is connected to a scaler, the scaler counts all gamma rays that exceed the desired energy threshold.

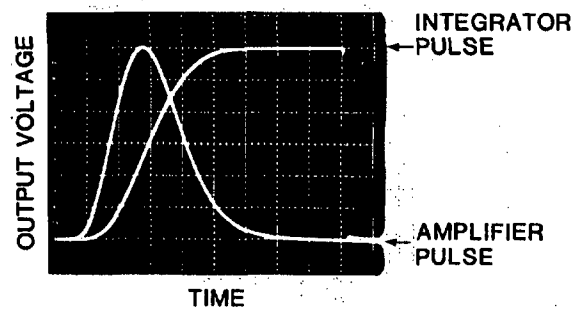

Fig. 4.11 *The regular output and gated-integrator output from an amplifier using gated integration to reduce the ballistic deficit at short time constants. The gated integrator permits good resolution and lower pileup and deadtime losses at high input rates.*

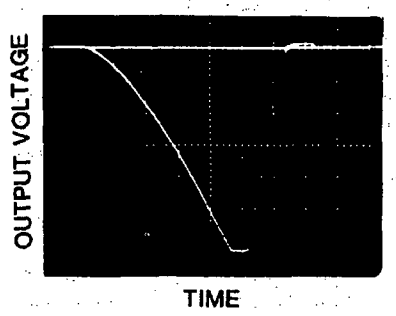

Fig. 4.12 *The output from a pulse processor using time-variant filters to shape preamplifier output pulses.*

An SCA is essentially two discriminators with independent thresholds. If the amplifier pulse amplitude exceeds the lower threshold and is less than the upper threshold, the SCA emits a logic pulse. If the SCA output is connected to a scaler, the scaler will count all gamma rays in a selected energy interval or channel. Figure 4.13 illustrates the function of the SCA.

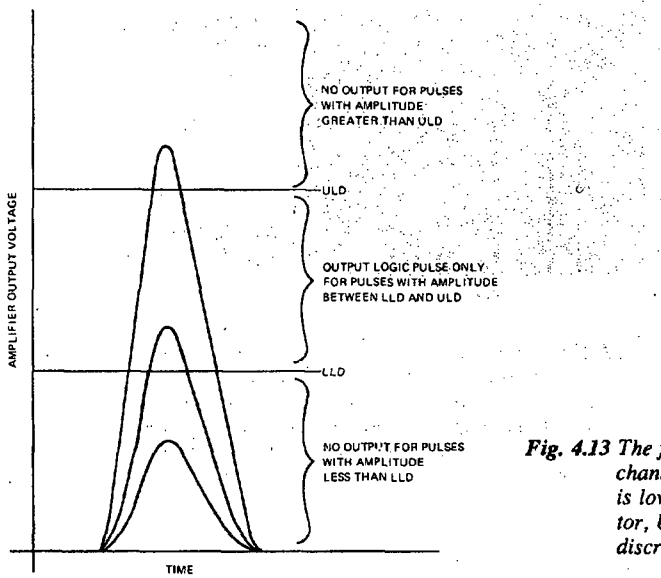

Fig. 4.13 The function of a single-channel analyzer. (LLD is lower-level discriminator, ULD is upper-level discriminator.)

The gamma-ray energy spectrum can be measured by setting a narrow window and taking a series of counts as the window is moved across the energy region of interest as a series of contiguous but nonoverlapping channels. The method is very tedious when the window is narrow and many counts must be taken. Before the advent of multichannel analyzers (MCAs), SCAs were used to measure gamma-ray spectra (see Figure 4.14). The technique was sometimes automated by adding a mechanical drive to the lower threshold control and a recording ratemeter to the SCA output.

The two SCA thresholds may be referenced to the same voltage, usually 0 V. If the upper threshold is referenced to the lower threshold voltage, the count window can be advanced through the spectrum by adjusting only the lower threshold control. Some SCAs can function as two independent discriminators, as an SCA with independent thresholds or as the window SCA just described. Some extract pulse-height information only, and others provide both pulse-height and timing information. Several procedures can be used to set the SCA window to the desired energy interval by gating an oscilloscope or MCA from the SCA output.

4.7 COUNTERS, SCALERS, TIMERS, AND RATEMETERS

The counter/timer shown in Figure 4.1 is the simplest part of the spectroscopy system; its function is to count the SCA output logic pulses.

The terms *counter* and *scaler* are usually used interchangeably. Before the advent of digital electronic displays such as light-emitting diodes and liquid crystal displays,

electromechanical registers were used to indicate the number of pulses counted. The electromechanical registers were very slow and were often preceded by an electronic circuit that emitted a single logic pulse for a fixed number of input logic pulses; the "scaling" factor was often a power of 10. Historically, the term *scaler* was correctly applied to the electronic circuit that preceded an electromechanical register. Although mechanical registers are no longer used, the term scaler is often applied to counting instruments that have no timing or control capability. *Counter* is the preferred and more descriptive term. The term *timer* is usually applied to a separate instrument that measures time and can turn on one or more counters for a selected time interval. In the past, counters and timers were usually separate instruments; now the two functions are often combined in a single instrument, which may be called a *counter/timer* or, simply, a *counter*. A *ratemeter* measures the average pulse rate of the signal applied to its input and may be used in place of, or in conjunction with, a counter.

Modern counters operate at maximum count rates of approximately 2×10^7 count/s and can count two pulses separated by as little as 50 ns. Most counters have a capacity of six decimal digits; however, seven- and eight-digit counters are available. Although counters and timers usually have a visual display of the number of counts or seconds, counters without visual displays are available for applications that only require automatic readout to a computer or printer. Many counters provide an overflow logic pulse to indicate when the count capacity is exceeded. Some counters can be gated (turned on or off) by logic pulses from other control electronics. Other counter options include internal discriminators, printer and computer interfaces, and the ability to count positive or negative input pulses.

Timers are counters that count a fixed frequency oscillator to determine the desired time interval. The reference time signal comes either from the ac line (60 Hz in the United States) or from an internal crystal-controlled oscillator. The line-frequency oscillator is less expensive and is adequate for all but the most demanding applications. If the frequency of the ac power line is averaged over a day, the accuracy of the line-frequency oscillator is very good. If intervals shorter than a day must be measured to better than 0.1%, a crystal-controlled oscillator should be used. Many counter/timer combinations can either count for a preset time or measure the time required to count a preset number of counts; the latter mode allows all measurements to have the same statistical precision.

In the past, all ratemeters were analog instruments that provided a current signal proportional to the average count rate. The rate-related signal was displayed on a meter and was available at an output connector to drive an optional chart recorder. All ratemeters offered a choice of time constants to select how rapidly the instrument responded to count-rate changes. Linear and logarithmic scales were available, and some units gave an audible alarm if the count rate exceeded a preset limit. Modern ratemeters may be either analog or digital instruments. A digital ratemeter is a counter/timer that automatically resets and repeats a count; the count time is often set to 1 s so that the digital display shows the number of counts per second. The visual

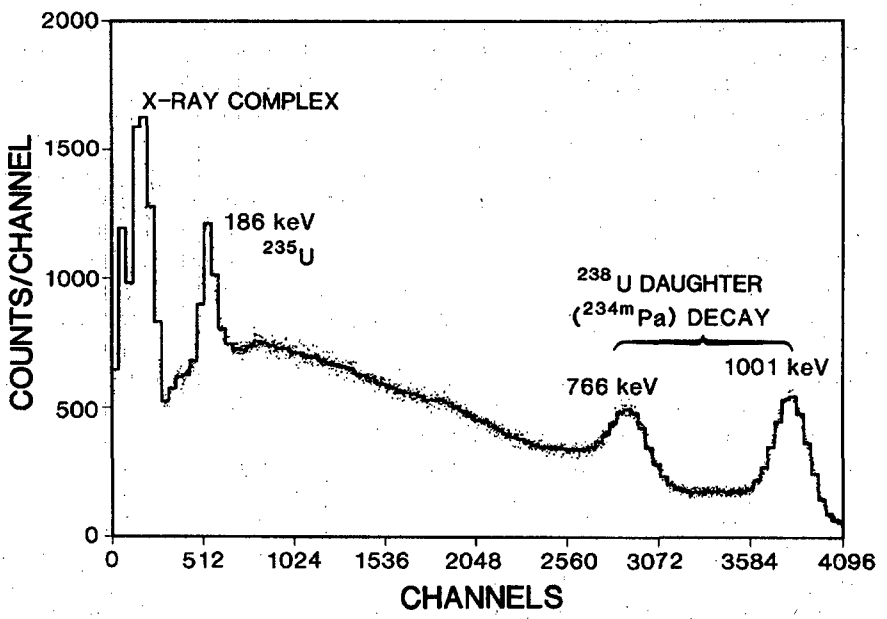

Fig. 4.14 The gamma-ray spectrum of highly enriched uranium measured with a high-quality NaI detector. The points show a 4096-channel MCA spectrum and the histogram shows a 100-channel SCA spectrum. The total number of counts in both spectra is the same; therefore, the precision of an individual point in the 4096-channel spectrum is only about one-sixth that of a corresponding bar in the 100-channel spectrum. The vertical scales of the two spectra have been normalized.

display of a digital ratemeter is far more readable than the meter display of an analog ratemeter. A digital ratemeter is often used to measure the total rate of gamma-ray pulses coming from the system amplifier. Because the total count rate has an important effect on system performance, the count rate is often monitored continuously.

4.8 MULTICHANNEL ANALYZER

The functions listed inside the dashed line in Figure 4.2 are usually performed by a multichannel analyzer (MCA) operating in the pulse-height-analysis mode. The terms multichannel analyzer and pulse-height analyzer (PHA) are often used interchangeably. The MCA can operate in several modes, including pulse-height analysis, voltage sampling, and multichannel scaling. It sorts and collects the gamma-ray pulses coming from the main amplifier to build a digital and visual representation of the pulse-height spectrum produced by the detector.

4.8.1 Analog-to-Digital Converter

The analog-to-digital converter (ADC) performs the fundamental pulse-height analysis and is located at the MCA input. The ADC input is the analog voltage pulse from the main amplifier; its output is a binary number that is proportional to the amplitude of the input pulse. The binary output number is often called an address. Other MCA circuits increment a storage register in the MCA memory that corresponds to the ADC address. The ADC performs a function that is analogous to that of the oscilloscope user saying "five volts" when a 5-V pulse is applied to the oscilloscope input terminals. The ADC accepts pulses in a given voltage range, usually 0 to 8 or 10 V, and sorts them into a large number of contiguous, equal-width voltage bins, or channels. Because of the sorting function, the early MCAs were often called kicksorters, with the amplifier pulse being compared to an electrical kick.

The number of channels into which the voltage range is divided is usually a power of 2 and is called the ADC conversion gain. In the mid 1950s a high-quality ADC could divide 100 V into 256 channels. Now, ADCs routinely divide 10 V into as many as 16 384 channels. This capability is impressive; an individual channel is only 0.6 mV wide. The required conversion gain varies with detector type and with the energy range being examined. Figure 4.15 shows part of an 8192-channel plutonium spectrum measured with a high-resolution germanium detector. The full-energy peaks should contain enough channels to clearly define the structure of the spectrum. As few as five channels may suffice for some situations. When peak fitting is required, 10 or more channels are needed to clearly define peak shape.

The ADC sorts the amplifier output pulses according to voltage; the voltage is proportional to the energy deposited in the detector during the gamma-ray interaction. Like the relationship between voltage and energy, the relationship between channel number and energy is nearly linear. The relationship can be represented by Equation 4-1:

$$E = mX + b \tag{4-1}$$

where E = energy in keV
X = channel number
m = slope in keV/channel
b = zero intercept in keV.

The slope m depends on the conversion gain and the amplifier gain; common values are 0.05 to 1.0 keV/channel. Although it may seem logical to assume that zero energy corresponds to channel zero (b = 0), this is often not the case. The slope and zero intercept can be adjusted to fit the energy range of interest into the desired channel range. For example, plutonium measurements often use gamma rays in the 60- to

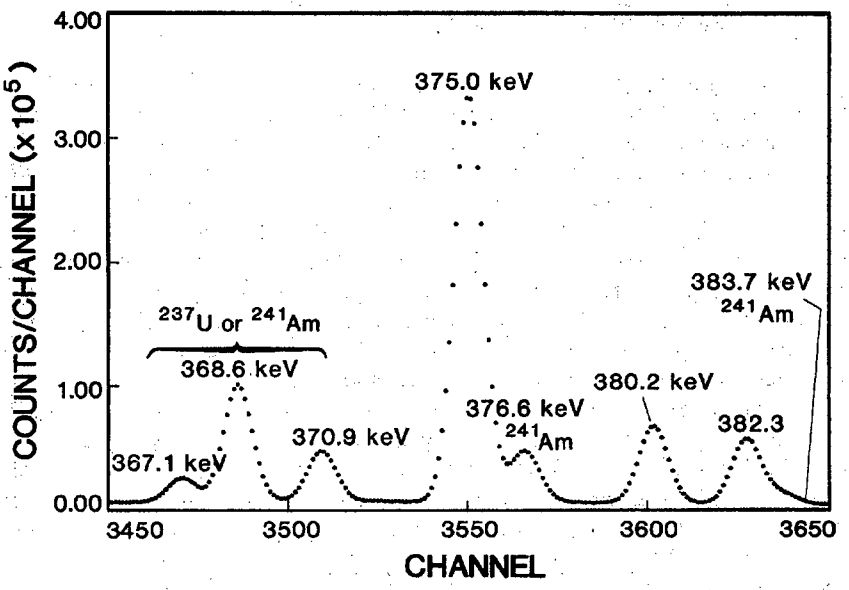

Fig. 4.15 A small portion of an 8192-channel plutonium spectrum taken with a high-quality coaxial germanium detector. The major peak is the 375.0-keV peak from ^{239}Pu decay.

420-keV range. If the gains are adjusted to 0.1 keV/channel and the zero intercept to 20 keV, a 4096-channel spectrum covers the 20- to 429.6-keV energy range and includes the important gamma ray at 413.7 keV. In the example, the channel number can be converted easily to energy. Most ADCs have both analog and digital controls to adjust the zero intercept. The analog control is labeled baseline or zero adjustment, and the digital control is labeled digital offset.

Because preamplifiers, amplifiers, and ADCs are not exactly linear, the relationship shown in Equation 4-1 between energy and channel number is not exact. However, with good equipment, gamma-ray energies can be readily measured to a tenth of a keV by assuming a linear calibration. ADC linearity is usually specified with two numbers: integral and differential linearity. Integral nonlinearity is a slight curvature in the relationship between energy and channel number; differential nonlinearity is a variation in channel width. It is difficult to design an ADC that does not have differential nonlinearity. Often, adjacent channels have measurably different widths, as can be seen when all even-numbered channels have more counts than all odd-numbered channels in a flat region of the spectrum. Such odd-even effects are common and may affect alternate groups of two, four, or even eight channels. A common ADC problem

that can influence assay results is a slow increase of the differential nonlinearity over time. The 1% differential nonlinearity of most ADCs is totally acceptable for most applications.

Two types of ADC are in common use: the Wilkinson and the successive-approximation ADC. A Wilkinson ADC counts pulses from a fast oscillator for a time interval that is proportional to the amplitude of the amplifier pulse. The digitization time determines the channel number assigned to each pulse. A successive-approximation ADC examines the amplifier pulse with a series of analog comparators. The first comparator determines whether the pulse amplitude is in the upper or lower half of the ADC range. Each successive comparator determines whether the pulse amplitude is in the upper or lower half of the voltage interval determined by the previous comparator. Twelve comparators determine the pulse amplitude to one part in 2^{12} (or 4096) channels. The digitization time of a successive-approximation ADC is constant and independent of pulse height. Until recently, Wilkinson ADCs dominated the gamma-ray spectroscopy field because they had superior differential linearity. Now, successive-approximation ADCs have comparable differential linearity and are becoming more popular because they are often faster than Wilkinson ADCs.

ADC speed is an important consideration for high-count-rate spectroscopy. While the ADC is processing one pulse, all other pulses are ignored. The pulse processing time, or deadtime, can be a substantial fraction of the total acquisition time. A deadtime of 25% means that 25% of the information in the amplifier pulse stream is lost. For both ADC types, the deadtime per event is the sum of the digitization time and a fixed processing time (usually 2 to 3 μs). The 450- to 100-MHz oscillators used in Wilkinson ADCs require 12 to 43 μs to digitize and store a gamma-ray event in channel 4000. Successive-approximation ADCs (4096 channels) require 4 to 12 μs to analyze a gamma-ray event. A detailed comparison of ADC speed requires specification of the gamma-ray energy spectrum, the overall system gain, and the ADC range. In general, successive-approximation ADCs are faster than Wilkinson ADCs for spectra with 4096 channels or more. For spectra with few channels, the Wilkinson ADC may be faster. In a spectrum with an average channel number of 512, a 400-MHz Wilkinson ADC has a average deadtime per event of 3 μs.

Several common features appear on most ADCs independent of type or manufacturer. Lower-level discriminators (LLD) and upper-level discriminators (ULD) determine the smallest and largest pulses accepted for digitization. The discriminators can be adjusted to reject uninteresting low- and high-energy events and reduce ADC deadtime. The discriminator adjustment does not affect the overall gamma-ray count rate and cannot be used to reduce pulse pileup losses that occur in the detector, preamplifier, and amplifier. The discriminators form an SCA at the input to the ADC; most ADCs provide an SCA output connector. Most ADCs have coincidence and anticoincidence gates that allow external logic circuits to control the ADC. Pileup rejection circuits frequently provide an inhibit pulse that is fed to the anticoincidence gate to prohibit processing or storage of pileup pulses. The coincidence gate is also used to analyze gamma-ray events that are detected in two separate detectors. Most

ADCs have an adjustable conversion gain and range; the range control determines the maximum channel number to be digitized. There is usually a deadtime indicator that displays fractional deadtime. In computer-based MCAs, the ADC parameters often can be set under program control. Most small MCAs have a built-in ADC; large MCA systems use separate NIM or rack-mounted ADCs.

4.8.2 Spectrum Stabilizers

For germanium and silicon detectors, the relationship of energy and channel number changes with time even though the energy-to-charge-collection factor is constant. The preamplifier, amplifier, and ADC are all subject to small but finite changes in gain and zero level caused by variation in temperature and count rate. Under laboratory conditions, the position of a full-energy peak at channel 4000 may shift only a few channels over a period of many weeks; however, even this small drift may be undesirable. Larger drifts may be encountered in the uncontrolled environment of production facilities. Spectrum stabilizers are electronic modules that fix the position of one or more full-energy peaks by adjusting a gain or dc level in the spectroscopy system to compensate for drift; they are especially recommended for gamma-ray spectroscopy systems that must be operated in uncontrolled environments by unskilled operators (as often required by routine production-plant assay systems). Stabilizers are also recommended whenever channel-summation procedures are used to determine full-energy peak areas.

The spectrum stabilizers used with germanium and silicon detectors are usually digital circuits connected directly to the ADC. The stabilizer examines each gamma-ray-event address generated by the ADC and keeps track of the number of counts in two narrow windows on either side of a selected full-energy-peak channel. The stabilizer generates a feedback signal for the ADC that is proportional to the difference in the number of counts in the two windows. The feedback signal adjusts the ADC gain or zero level so that the average number of counts in each window is the same; the adjustment fixes the position of the selected stabilization peak. Often two peaks are stabilized independently: a peak at the high-energy end of the spectrum is used to adjust ADC gain and another peak at the low-energy end is used to adjust the ADC zero level. With two-point stabilization, the spectroscopy system stability is often so good that no spectral peak shifts position by more than a tenth of a channel over a period of many months. Digital stabilizers can be used to easily establish simple and convenient energy calibrations (for example, $E = 0.1X$).

Stabilization peaks should be free from interference, adequately intense, and present at all times. Often one of the stabilization peaks comes from a gamma-ray source that is attached to the detector to provide a constant signal in the detected spectrum. Usually, such a stabilization source is monoenergetic and provides the low-energy stabilization peak so that its Compton continuum does not interfere with other gamma-ray peaks of interest. In some cases, a very stable pulser may be connected to the

test input of the preamplifier to provide an artificial stabilization peak. Peaks from pulsers or special stabilization sources may also be used to provide corrections for pulse-pileup and deadtime losses (see Chapter 5).

Digital stabilization is not available for all ADCs and it is frequently unavailable for portable MCAs and successive-approximation ADCs. Digital stabilizers are normally single- or double-width NIM modules. All stabilizers have controls to set the desired peak-centroid channel number and the width of the stabilization peak windows; there is often a control to set the stabilizer sensitivity. Digital stabilizers that can be controlled by an external computer are now available; this feature is useful when stabilization peaks must be changed during automatic assay procedures.

Digital stabilizers that have a small correction range are inadequate for use with NaI detectors. In addition, digital stabilizers operate with an ADC and many NaI detector systems use SCAs to acquire the desired spectral information. Because of the relatively greater instability of scintillator/photomultiplier detectors (as large as 1 to 2%/°C), spectrum stabilization is often more necessary for NaI detectors than it is for germanium or silicon detectors.

Scintillation detector stabilizers are similar to digital stabilizers but operate with the amplifier rather than the ADC. The stabilizer compares the count rate on either side of the selected stabilization peak and generates a feedback signal that adjusts the amplifier gain to keep the two count rates equal. NaI stabilizers are packaged as NIM modules and may consist of amplifier/stabilizer combinations or separate stabilizers. When a suitable stabilization peak is not available in the NaI spectrum, a pulser peak cannot be substituted because it can only correct for preamplifier and amplifier instability; the major drift in a NaI system occurs in the photomultiplier tube. Although an external gamma-ray source can provide a stabilization peak, the Compton background from the source can interfere excessively with the gamma rays of interest. An alternative solution is to use a detector with a built-in light pulser. NaI crystals can be grown with a small doping of an alpha-particle-emitting nuclide like ^{241}Am. The alpha-particle interactions in the crystal provide a clean spectral peak with a fixed rate and gamma-ray-equivalent energy. Because the temperature dependences of alpha-particle-induced and gamma-ray-induced scintillation light are not identical, accurate stabilization over a large temperature range may require special temperature compensation circuitry.

4.8.3 Multichannel Analyzer Memory, Display, and Data Analysis

After the ADC converts the amplifier voltage pulse to a binary address, the address must be stored for later observation and analysis. All MCA systems have memory reserved for spectrum storage, and most have a spectral display and some built-in data analysis capability.

Although the most common memory size is 4096 channels, MCAs are available that have other memory sizes such as 1024, 8192, or 16 384 channels. The smaller memory size is adequate for NaI detector applications and for germanium or silicon detector

applications that involve a small energy region. To have sufficient channels in a full-energy peak, an overall system gain of 0.1 keV/channel is often required; however, with this gain, a 1024-channel MCA can only collect data in a 100-keV-wide region. Large MCA systems usually can accept data from several ADCs simultaneously. A 16 384-channel MCA can collect four 4096-channel spectra simultaneously. For multiple ADC applications, MCAs are available with as many as 65 536 channels.

The maximum number of counts that can be stored per channel is often an important consideration because it sets a limit on the precision that can be obtained from a single measurement. Early transistorized MCAs often had a maximum capacity of 65 536 counts per channel. The present standard is typically 10^8 counts per channel, however large MCAs are available with capacities of 1.6×10^7, 2.56×10^8, and even 4×10^9 counts per channel. (The last number quoted is probably more than will ever be required in any anticipated application.) Although the present standard of 10^6 counts per channel is adequate for many low-rate applications, it is a definite limitation for applications involving high-precision measurement of high-activity samples. The limitation is especially apparent when both strong and weak peaks must be measured in a single spectrum, as is the case for many plutonium measurements. The count time must be chosen so that the strongest peak of interest does not overflow the channel capacity; unfortunately this count time may provide unacceptably low precisions for the weaker peak areas, with the result that multiple measurements are required. The intended application must be considered carefully when deciding the MCA memory-size and count-capacity requirements.

A quick and useful way to obtain qualitative and semiquantitative information from a spectrum stored in memory is to look at a plot of channel content versus channel number. Most MCAs have a spectral display and many offer a wide range of display options. All displays offer several vertical and horizontal scale factors and many offer both linear and logarithmic scales. Most displays have one or two cursors (visual markers) that can be moved through the spectrum; the channel number and contents of the cursor locations are displayed numerically on the screen. Most MCAs can intensify selected regions of interest or change the color of the regions of interest to emphasize particular spectral features. A good MCA can display two or more spectra simultaneously and can overlap spectra for careful visual comparison.

Until recently, most MCA displays used cathode-ray tubes with electrostatic deflection. Electrostatic deflection is easily used only for small screen displays, up to approximately 15 by 15 cm. At present, most MCAs use magnetic deflection to allow larger screen size; the display is identical to a television display. Some displays are multicolored, but most are still monochromatic. In either type, each channel is represented by a dot or bar whose vertical height is proportional to the channel contents. Liquid crystal displays are just coming into use, mostly for low-power applications in portable MCAs.

Big-screen, magnetically deflected displays are economical and make an excellent picture but have one annoying drawback. The horizontal oscillator in the magnetic-deflection circuit generates bursts of electromagnetic interference at a frequency of

approximately 16 kHz; the interference is easily picked up on preamplifier signal lines and can cause significant degradation of spectral quality. Great care must be taken in grounding, shielding, and routing signal cables to eliminate or minimize the problem. The video terminals usually used with large MCA/computer systems generate similar interference; all signal cables should be routed well away from the terminals.

Most large MCAs have some built-in data analysis functions. Common analysis functions determine the channel position and width of spectral peaks, the energy calibration, the number of counts in selected regions of interest, and the full-energy peak areas. Other available functions may include smoothing, normalizing, and subtracting (stripping) a background spectrum. The numerical results are usually displayed on the screen or printed on the system terminal. The functions are usually implemented by microprocessors that execute codes from read-only memory.

Large MCAs are frequently interfaced to external computers that can control complete assay systems and execute complex analysis codes. The computer system usually includes one or more mass storage devices such as hard or flexible disks that provide storage for spectral data and analysis programs. The last link in the spectroscopy chain is often a printer that provides hard-copy output of measurement results.

4.9 AUXILIARY ELECTRONIC EQUIPMENT

Figures 4.1 and 4.2 show only the basic components of gamma-ray spectroscopy systems. This section describes other instruments that may be used in addition to the basic components.

The oscilloscope is the most useful auxiliary instrument used with gamma-ray spectroscopy systems. It is virtually indispensable when setting up the spectroscopy system for optimum performance, monitoring system performance, detecting malfunctions or spurious signals, and correcting problems. An expensive oscilloscope is not required; a 50-MHz response, one or two vertical inputs, and an ordinary time base are usually quite adequate. Battery-powered portable oscilloscopes can easily be carried to systems in awkward locations.

Electronic pulsers are used to test system performance and correct for deadtime and pileup losses. Mercury-switch pulsers have excellent pulse amplitude stability but are quite slow and have limited pulse-shape variability. Other electronic pulsers often have high-repetition rate and very flexible pulse shaping but usually have neither great amplitude nor frequency stability. A few pulsers provide random intervals between pulses rather than the more common fixed intervals. Sliding pulsers are used to test ADC linearity; their pulse amplitude is modulated linearly with time.

Cameras are often used to take pictures of MCA and oscilloscope displays. Pictures of waveforms help to document and diagnose problems; pictures of spectra provide a quick and useful way to record information in a notebook. Cameras are available with the necessary adapters to couple them to most oscilloscopes and MCAs. A Polaroid-type film is usually used so that the pictures can be developed quickly.

Many different instruments are available to provide information on gamma-ray pulse timing, usually to establish temporal relationships between two or more detectors. Timing-filter amplifiers sacrifice signal-to-noise performance and overall resolution to preserve timing information. Other instruments examine the preamplifier output, the bipolar output of the main amplifier, or the output of a timing-filter amplifier and they generate a fast logic signal that has a fixed and precise temporal relationship to the gamma-ray events in the detector. The timing is determined using techniques such as fast leading-edge discrimination, constant-fraction discrimination, amplitude/risetime compensation, and zero-crossover pickoff. The timing outputs are either counted or presented to coincidence circuits that determine whether specified time relationships are met by the events in two or more detectors. Depending on the type of detector, the coincidence gates can be as narrow as a few nanoseconds. The logic output of a coincidence circuit is either counted or used as a control signal. When more detailed timing information is required, a time-to-amplitude converter can be used to generate an output pulse whose amplitude is proportional to the time interval between input pulses.

A linear gate can be used as a coincidence or control circuit at the input to an MCA. Linear gates pass analog signals with no change in amplitude or shape if they are gated by control signals that are derived from one of the timing circuits described above. A linear stretcher generates a pulse with the same amplitude as the input pulse but with an adjustable length. A stretcher is occasionally used to condition the amplifier signal before subsequent processing in the ADC. Summing amplifiers, or mixers, produce outputs that are the linear sum of two or more input signals. A mixer can be used in connection with routing signals for collecting spectra from several detectors with a single ADC.

Compton suppression, a common procedure that improves the quality of gamma-ray spectra, uses some of the timing circuits described above. A Compton-suppression spectrometer usually includes a high-resolution detector that is surrounded by a low-resolution, annular detector. The scattered gamma ray from a less-than-full-energy interaction in the high-resolution detector is often detected in the annular detector. A coincidence event between the two detectors inhibits the storage of the high-resolution event in the MCA and reduces the Compton continuum between the full-energy peaks.

4.10 CONCLUDING REMARKS

The instrumentation described in this chapter can be assembled to form different gamma-ray spectroscopy systems for different NDA applications. Many instrument manufacturers can provide integrated spectroscopy systems that include all components from the detector to the output printer. If the user has sufficient expertise, individual components can be procured from different manufacturers. In either case, careful consideration must be given to the requirements of the measurement application before selecting a spectroscopy system from the

nearly endless array of options and configurations. References 1 through 4 provide detailed descriptions of the function and operation of gamma-ray spectroscopy instrumentation. For the user who is not active in gamma-ray spectroscopy, current information is best obtained from research reports, the commercial literature, and the developers and users of state-of-the-art instrumentation.

Gamma-ray assay systems that are dedicated to a particular operation can be very simple to operate. On the other hand, vast versatility and flexibility are provided by combining the appropriate detector, amplifier, MCA, and analysis capability to make a large, modern gamma-ray spectroscopy system. Unfortunately, a complex, versatile instrument can never be truly simple to operate; a labor of several weeks is usually required to master the operation of the typical large system. However, the effort required is usually readily exerted in order to use instruments of truly amazing power. The power of modern gamma-ray spectroscopy systems is perhaps best appreciated by those who remember from personal experience when all spectral measurements were done with a NaI detector, an SCA, and a counter.

Gamma-ray spectroscopy equipment has improved rapidly over the past 25 years as vacuum tubes were replaced by transistors and transistors were replaced by integrated circuits. The microprocessor chip has put greater capability into smaller and smaller volumes. The capability per dollar has increased in spite of inflation. The rate of improvement is still significant, particularly in the capability and flexibility of MCA memory, display, and data analysis. Spectral quality is not progressing as rapidly, although improvement is still occurring in pulse-processing electronics, especially in dealing with very high counts rates (up to 10^6 count/s) from high-resolution germanium detectors. The technology of NaI, germanium, and silicon detectors is quite mature and major improvements are not expected. Still, steady progress in all areas of gamma-ray spectroscopy technology will continue, and unexpected breakthroughs may indeed occur.

REFERENCES

1. G. F. Knoll, *Radiation Detection and Measurement,* second edition (John Wiley & Sons, Inc., New York, 1988).
   This book deals with all types of radiation detectors and associated electronics, including high-resolution gamma-ray spectroscopy systems. The treatment is very broad, with good qualitative explanations and many figures. There are many mathematical formulas and some derivations, but the book is very readable. This is probably the best single reference on gamma-ray spectroscopy equipment.

2. P. W. Nicholson, *Nuclear Electronics* (John Wiley & Sons, Inc., New York, 1974).
   This book is an extensive treatise on the electronics associated with high-resolution detectors. Detailed descriptions are given of detector preamplifiers, pulse shaping, rate-related losses, pulse-height analysis, and spectral resolution.

3. F. Adams and R. Dams, *Applied Gamma-Ray Spectroscopy* (Pergamon Press, Oxford, 1970).
Although older than Reference 1, this work provides a comprehensive coverage of gamma-ray spectroscopy. Information is available on NaI and germanium detectors and the accompanying instrumentation.

4. W. J. Price, *Nuclear Radiation Detection*, 2nd ed. (McGraw-Hill Book Co., New York, 1964).
Although older and of more limited scope than the three preceding references, this book gives useful alternative descriptions of the detection process and the functions of the electronic equipment. It also gives a glance at detectors and analysis methods that are now rarely used and provides an interesting view of spectroscopy equipment at the time when transistors were starting to replace vacuum tubes.

5

General Topics in Passive Gamma-Ray Assay

J. L. Parker

This chapter discusses general topics that apply to the gamma-ray assay techniques discussed in Chapters 7 to 10. All these topics must be understood if optimum results are to be obtained from any assay technique. The topics include

- Energy calibration and determination of peak position
- Energy resolution measurements
- Determination of full-energy-peak area
- Rate-related losses and corrections
- Effects of the inverse-square law
- Detector efficiency measurements.

5.1 ENERGY CALIBRATION AND DETERMINATION OF PEAK POSITION

5.1.1 Introduction

The energy calibration of a gamma-ray spectroscopy system is the relationship between the energy deposited in the detector by a gamma ray and the amplitude of the corresponding amplifier output pulse. The pulse amplitude is measured by the analog-to-digital converter (ADC) of a multichannel analyzer (MCA) or by one or more single-channel analyzers (SCAs). The energy calibration is used to determine the width and location of regions of interest (ROIs), to determine resolution, and to find the energies of any unrecognized gamma rays.

The energy calibration of a good spectroscopy system is nearly linear:

$$E = mx + b \tag{5-1}$$

where E = energy deposited in detector
m = slope
x = amplitude of output pulse
b = intercept.

The assumption of linearity is usually sufficient for nondestructive assay (NDA) techniques. However, no system is exactly linear; each has small but measurable nonlinearities. When a more accurate relationship is necessary, a higher order polynomial is used. Gamma-ray energies can be determined to within 0.01 to 0.05 keV using a nonlinear calibration curve and several standard gamma-ray sources with energies known to better than 0.001 keV.

Low-resolution detectors [for example, NaI(Tl) scintillators] often use Equation 5-1 with a zero intercept (b = 0). The linear approximation is usually good enough for even high-resolution NDA applications. For a good germanium detector, a linear calibration will determine the peak energy to within a tenth of a keV, which is adequate to identify the isotopes present in the measured sample. For most of the isotopes of interest to NDA, the pattern of the gamma-ray spectrum is so distinctive that a visual examination of the MCA display by an experienced person is sufficient to identify the isotopes present. Figure 5.1 shows the characteristic spectrum of low-burnup plutonium, and Figure 5.2 shows the characteristic spectrum of natural uranium (0.7% ^{235}U).

The calibration procedure involves determining the channel location of peaks of known energy and fitting them to the desired calibration function. Often, the gamma rays from the measured nuclear material sample can be used to determine the energy calibration. Figure 5.1 shows that plutonium spectra have interference-free peaks at 59.54, 129.29, 148.57, 164.57, 208.00, 267.54, 345.01, 375.04, and 413.71 keV. Similar internal calibrations are possible for many isotopes (Refs. 1 and 2).

When the measured nuclear material cannot provide an adequate calibration, isotopic standards are used that emit gamma rays of known energies. Table 5-1 lists some of the most frequently used isotopes with the half-lives and energies of their principal emissions (Ref. 3). Most of the isotopes listed emit only a few gamma rays and are useful with both low- and high-resolution detectors. All the isotopes listed in the table are available from commercial vendors. Packaged sources usually contain a single isotope and are produced in a wide variety of geometries. Source strengths between 0.1 and 100 μCi are usually adequate for energy calibration. Convenient sets of six to eight single-isotope sources are available from most vendors. Their use is required for setting up, testing, and checking many performance parameters of spectroscopy systems. The source sets are useful for determining energy calibration, testing detector resolution, measuring detector efficiency, setting the pole-zero adjustment, and correcting for rate-related counting losses.

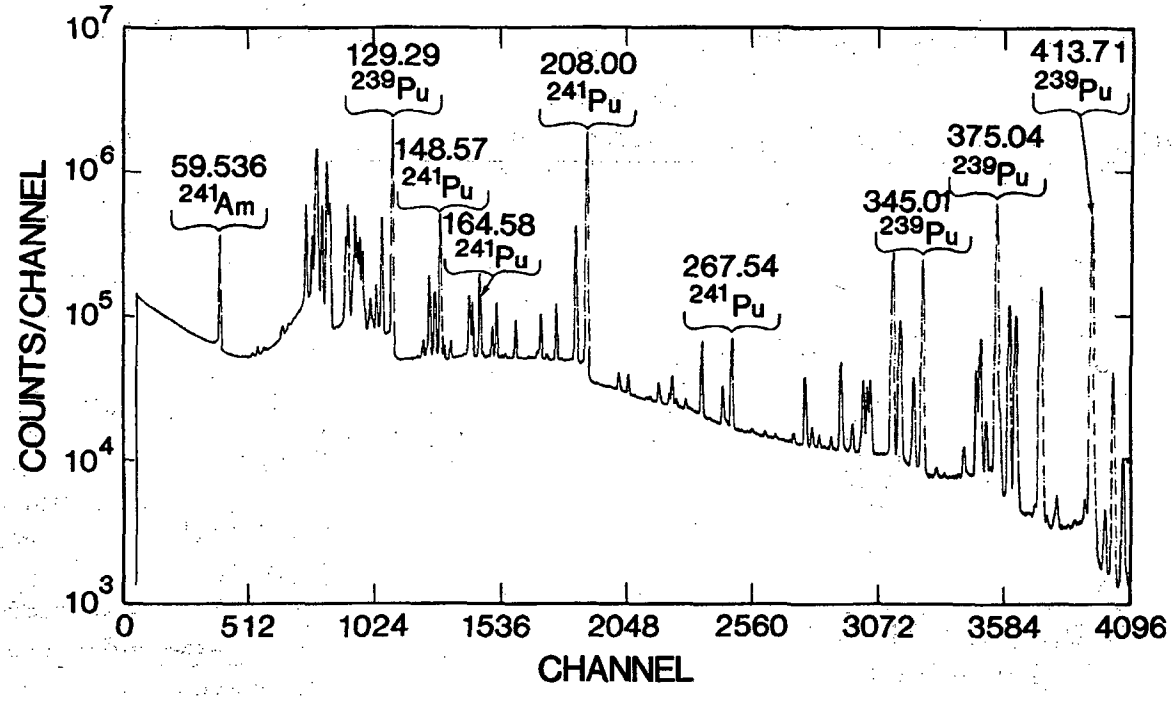

Fig. 5.1 A high-resolution spectrum of low-burnup plutonium. The indicated peaks are useful in the energy calibration of plutonium spectra. The energy in keV is equal to the channel number divided by 10, plus 20.

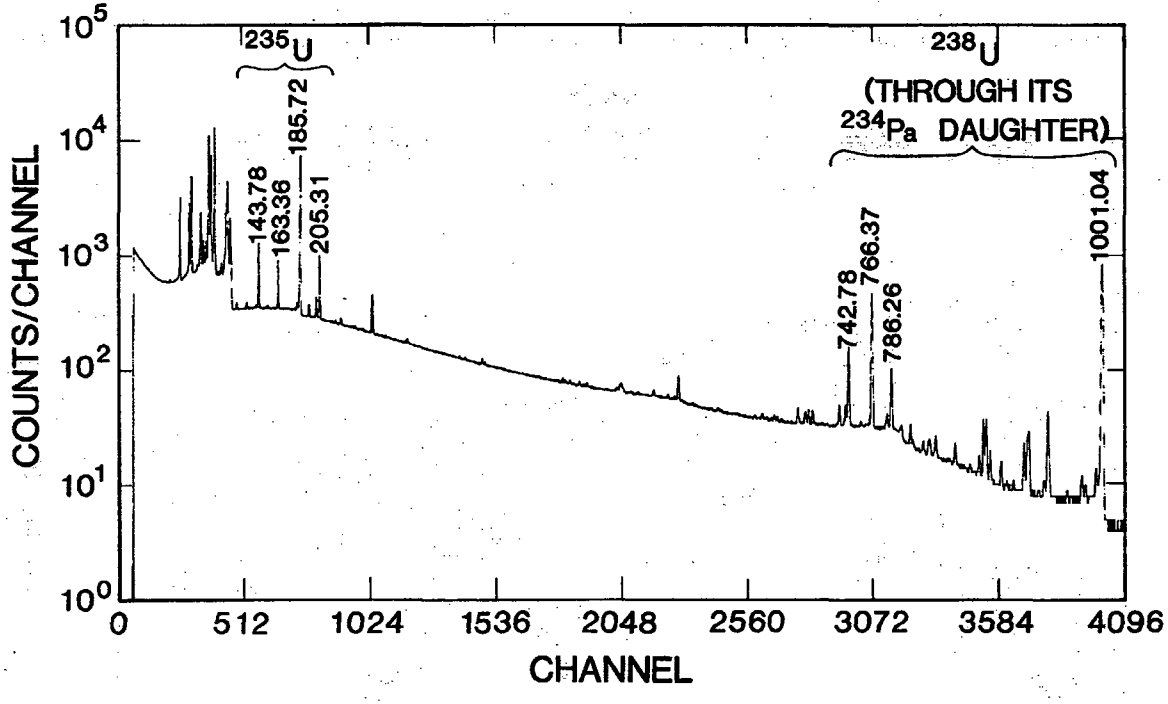

Fig. 5.2 A high-resolution spectrum of natural uranium (0.7% ^{235}U). The energy in keV is equal to the channel number divided by 4.

Table 5-1. Half-lives and energies of major emissions for selected isotopes[a]

Isotopes	Half-Life	Energy (keV)	Remarks
^{241}Am	433 yr	59.54	Many others, but weaker by factors 10^4 or greater
^{137}Cs	29.9 yr	661.64	The only other emission is from Ba K x rays
^{133}Ba	10.9 yr	81.0, 276.40, 302.85, 356.00, 383.85	Several others, but much weaker
^{60}Co	5.3 yr	1173.23, 1332.51	
^{22}Na	2.8 yr	511.01 1274.51	Annihilation radiation
^{55}Fe	2.7 yr	Mn K x rays 5.9, 6.5	Often used for low-energy calibration
^{109}Cd	1.2 yr	88.04	Ag K x rays at 22.16 keV and 24.9 keV
^{54}Mn	312 d	834.8	Monoenergetic source
^{65}Zn	244 d	511.01 1115.5	Annihilation radiation
^{57}Co	271 d	122.06, 136.47	Two others of higher energy, but much weaker
^{75}Se	120 d	121.12, 136.00, 264.65, 279.53, 400.65	Several others, but much weaker

[a]Listed in decreasing order of half-life. All isotopes listed should be useful for at least 1 yr, because the half-lives are greater than 100 days.

Gamma-ray standards are available with several isotopes in one capsule. These multienergy sources are used to define the energy calibration curve and efficiency curve of high-resolution detectors. The National Bureau of Standards (NBS) source SRM-4275 contains ^{125}Sb (2.75-yr half-life), ^{154}Eu (8.49-yr half-life), and ^{155}Eu (4.73-yr half-life) and emits 18 well-resolved gamma rays between 27 and 1275 keV. The emission rates of all 18 certified gamma rays are known to better than 1%.

5.1.2 Linear Energy Calibration

Equation 5-1 describes the assumed functional form for a linear energy calibration. If the positions x_1 and x_2 of two full-energy peaks of energies E_1 and E_2 are known, m and b can be computed from

$$m = \frac{(E_2 - E_1)}{(x_2 - x_1)} \tag{5-2}$$

$$b = \frac{(x_2E_1 - x_1E_2)}{(x_2 - x_1)} . \tag{5-3}$$

For a two-point calibration, the two calibration peaks should be near the low- and high-energy ends of the energy range of interest to avoid long extrapolations beyond the calibrated region.

Often, when an unacceptable degree of nonlinearity exists, several linear calibrations can be used over shorter energy intervals. The high-resolution spectrum of most plutonium samples has nine well-resolved peaks between 59.5 keV and 413.7 keV so that eight linear calibrations can be constructed for the intervals between adjacent peaks; none of the intervals is greater than 78 keV. A series of short linear calibrations can often be as accurate as a single quadratic or higher-order calibration curve.

When more than two peaks span the energy range of interest, least-squares fitting techniques can be used to fit a line to all the peaks. This method can be used to obtain the following expressions for m and b for n peaks:

$$m = \frac{n\sum x_iE_i - \sum x_i \sum E_i}{\Delta} \tag{5-4}$$

$$b = \frac{\sum x_i^2 \sum E_i - \sum x_i \sum x_iE_i}{\Delta} \tag{5-5}$$

where $\Delta = n\sum x_i^2 - \left(\sum x_i\right)^2$.

Most hand calculators can perform a linear least-squares fit. Many MCA systems can determine the x_i and compute m and b for any selected number of peaks. Some systems will also do a quadratic fit.

A linear energy calibration is usually adequate for NDA applications. Table 5-2 gives the results of two-point and nine-point linear calibrations of a high-quality plutonum spectrum. The nominal calibration, E (keV) = 0.1x + 20.0, was established by stabilizing the 59.536-keV gamma ray of ^{241}Am at channel 395.0 and the 413.712-keV gamma ray of ^{239}Pu at channel 3937.0. The second column of Table 5-2 gives the peak positions determined by fitting a Gaussian curve to the upper portion of the peaks. The third and fourth columns give the difference between the accepted energies and those obtained from the two-point and nine-point calibrations. Although there is a measurable curvature to the energy versus channel relation, the maximum error is only ~0.03 keV for the two-point calibration and ~0.017 keV for the nine-point calibration. The consistency of the results in Table 5-2 indicates that the peak positions have been located to within ~0.1 channel (~0.01 keV) and that the accepted energy values are consistent within ~0.01 keV.

Table 5-2. Results of linear energy calibrations of a high-quality plutonium spectrum

Accepted Energies (keV)	Peak Positions (channels)	Energy Difference (keV)[a]	
		Two-Point Calibration	Nine-Point Calibration
59.536	395.00	- - -	− 0.017
129.294	1092.77	0.014	− 0.001
148.567	1285.51	0.014	0.000
164.58	1445.80	0.029	+ 0.015
208.000	1879.96	0.022	+ 0.009
267.54	2475.37	0.019	+ 0.007
345.014	3249.98	0.001	− 0.009
375.042	3550.40	0.013	+ 0.004
413.712	3937.00	- - -	− 0.008

[a]The tabulated numbers are the energies from the calibration minus the accepted energies. For the two-point calibration, m = 0.099993 keV/channel and b = 20.039 keV. For the nine-point calibration, m = 0.099996 keV/channel and b = 20.021 keV.

5.1.3 Determination of Peak Position (Centroid)

Even with high-resolution detectors, full-energy peaks are usually at least several channels wide. The peaks are nearly symmetric, and the peak positions are chosen as the peak centers defined by the axis of symmetry. Full-energy peaks are usually well described by a Gaussian function of the form

$$y(x) = y_0 \exp\left[-(x - x_0)^2 / 2\sigma^2 \right] \tag{5-6}$$

where y(x) = number of counts in channel x
y_0 = peak amplitude
x_0 = peak centroid
σ^2 = variance.

References 4, 5, and 6 provide a detailed explanation of the properties of the Gaussian function. The function is symmetric about x_0, which is the peak centroid used in energy calibration. The parameter y_0 is the maximum value of the function and is nearly equal to the maximum counts per channel in the peak if the background under the peak is negligible. The parameter σ^2 (the variance) is related to the full width at half maximum (FWHM) of the function by

$$\text{FWHM} = 2\sqrt{2 \ln 2}\,\sigma = 2.35482\sigma \,. \tag{5-7}$$

The area under the Gaussian curve is given by

$$\begin{aligned} A &= \sqrt{2\pi}\,\sigma y_0 = 2.507\sigma y_0 \\ &= 1.0645(\text{FWHM})y_0 \,. \end{aligned} \tag{5-8}$$

The constant in the second form of Equation 5-8 is close to 1.0 because the area of a Gaussian is just a little greater than the area of an isosceles triangle with the same height and width at the half-maximum level.

Full-energy peaks are not exactly Gaussian shaped. For high-quality germanium detectors the deviations are hardly visible, but for lower quality detectors the deviations are easily seen as an excess of counts on the low-energy side of the peak (called tailing). At very high rates or with poorly adjusted equipment, high-energy tailing is sometimes visible. The upper one-half to two-thirds of a peak is usually Gaussian, and the centroid determined by fitting a Gaussian to the upper portion of the peak is a well-defined measure of peak position. Figures 5.3(a), (b), and (c) show the 1332.5-keV full-energy peak of ^{60}Co and the fitted Gaussian function. Figure 5.3(a) is from a high-quality germanium detector at low count rate, with properly adjusted electronics. The deviations from the curve are hardly visible except for a very slight low-energy tailing. Figure 5.3(b) is from a detector with poor peak shape. The low-energy tailing is obvious. Figure 5.3(c) is from the same detector as Figure 5.3(a) but at very high rates that cause distinct high-energy tailing and significant deviation from a true Gaussian shape. In all three situations, the Gaussian function fitted to the upper two-thirds of the peak gives a good peak location.

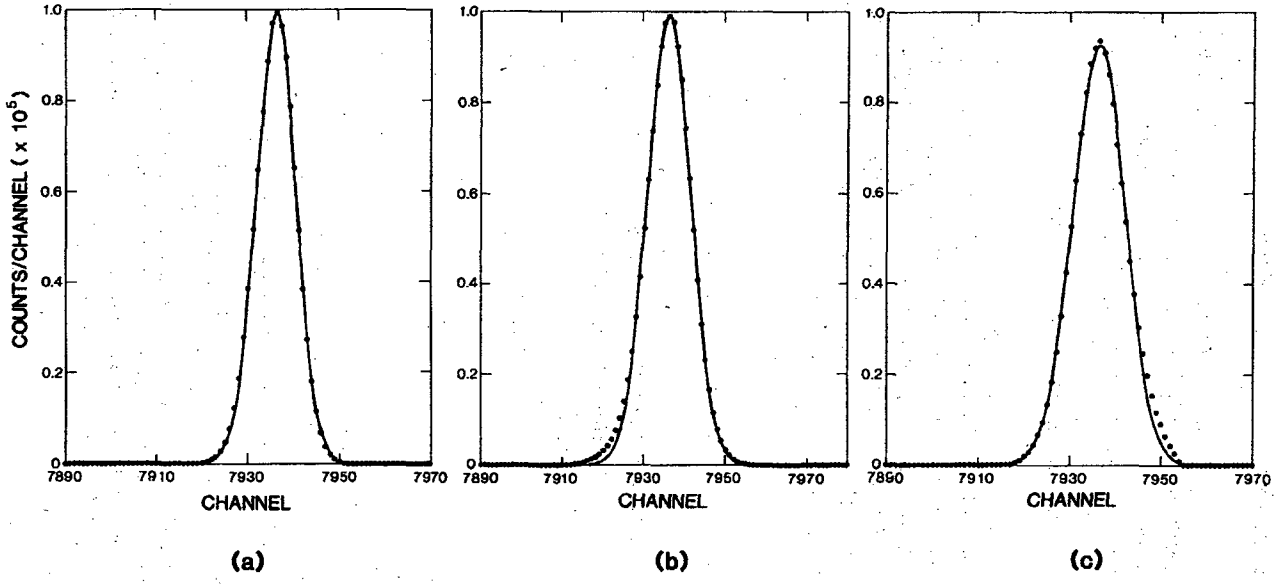

Fig. 5.3 *The 1332.5-keV full-energy peak of ^{60}Co for three combinations of detector and count rate: (a) high-quality germanium detector and low count rate; (b) a germanium detector with poor peak shape; (c) high-quality germanium detector and high count rate. The Gaussian is fitted to the upper two-thirds of the peak.*

5.1.4 Visual Determination of Peak Position

The human eye is very good at bisecting symmetric shapes. When a peak can be spread out sufficiently on the MCA display, estimates of peak positions can often be made to a few tenths of a channel by visual examination. The movable markers (cursors) that are part of most MCA displays help in making visual determinations.

5.1.5 Graphical Determination of Peak Position

Figure 5.4 shows an SCA-acquired spectrum of ^{137}Cs from a high-quality 7.62- by 7.62-cm NaI(Tl) scintillator. It is desirable to plot such spectra as histograms with the width of the bar equal to the window width and the low-energy side of the bar beginning at the threshold voltage setting. Usually the intervals between threshold settings equal the window width. The peak center is determined by drawing a straight line along both sides of the peak through the centers of the bars. The intersection of the two lines is the peak center.

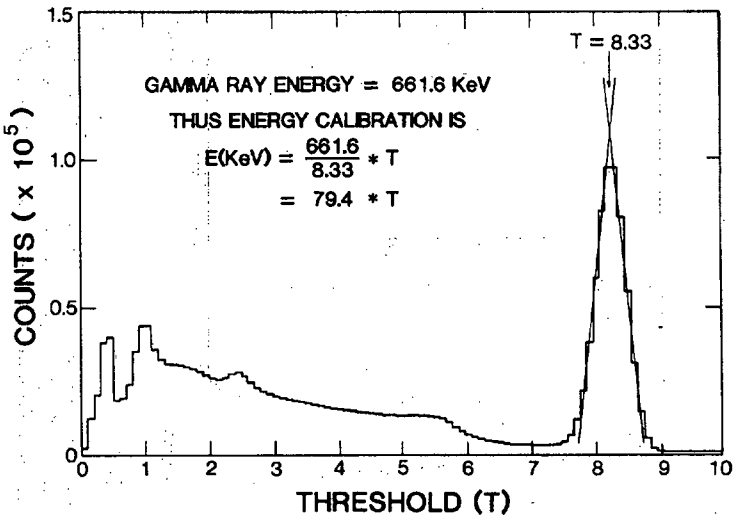

Fig. 5.4 Plot of an SCA-generated spectrum of ^{137}Cs from a 7.62-cm by 7.62-cm NaI(Tl) scintillation detector. The plot shows how visually fitting the intersection of lines along the sides of the peak is a consistent way of estimating the peak center.

5.1.6 Determination of Peak Position by the First-Moment Method

The centroid of a positive function y(x) is given by

$$\bar{x} = \frac{\int_{x_1}^{x_2} x\, y(x)\, dx}{\int_{x_1}^{x_2} y(x)\, dx} \approx \frac{\sum x_i y_i}{\sum y_i} \tag{5-9}$$

where x_1 and x_2 are the bounds of the area considered and y_i is the number of counts in channel x_i. This is called the first-moment method because the numerator of Equation 5-9 is the first moment of y(x). For the Gaussian function (Equation 5-6), $\bar{x} = x_0$. For calculational purposes the integrals are replaced by sums that closely approximate them. The Gaussian function only approaches zero as $x \rightarrow \pm\infty$; however, summing over a region approximately three times FWHM is usually adequate. If the peak is symmetric and if the summed region is symmetric about the peak, good results are obtained even without subtracting the background from under the peak. If a large background continuum lies under the peak and an asymmetrically placed summing region is used, the result will be in error. If the underlying continuum is subtracted, the error in calculated peak location caused by an asymmetric summing region is small. Figure 5.5 shows both a good choice and a poor choice of summing regions. Methods for continuum subtraction are discussed later in this chapter.

The first-moment method is particularly useful for peaks with relatively few counts per channel. It should be used with caution on peaks with distinct asymmetry because the calculated centroid will not coincide with the centroid of the Gaussian portion of the peak that must be determined for the energy calibration. Use of the first-moment procedure does not require that the peak have a Gaussian shape, but only that the peak is symmetric.

5.1.7 Determination of Peak Position by the Five-Channel Method

The five-channel method uses the maximum count channel and two adjacent channels on each side to estimate the peak centroid. The relevant formula is

$$x_0 = x_m + \frac{y_{m+1}(y_m - y_{m-2}) - y_{m-1}(y_m - y_{m+2})}{y_{m+1}(y_m - y_{m-2}) + y_{m-1}(y_m - y_{m+2})} \tag{5-10}$$

where the subscript m refers to the maximum count channel, and y_i refers to the counts in channel x_i.

Equation 5-10 assumes a Gaussian peak shape. Similar formulas can be derived assuming a parabolic shape at the top of the peak. Equation 5-10 works well when there are 6 to 30 channels above the FWHM point and enough counts in the five channels to clearly delineate the shape of the top of the peak. The five-channel method does not work as well as the first-moment method on broad peaks with poor precision. However, the five-channel method is less sensitive than the first-moment method to asymmetric peak tails from a poor detector.

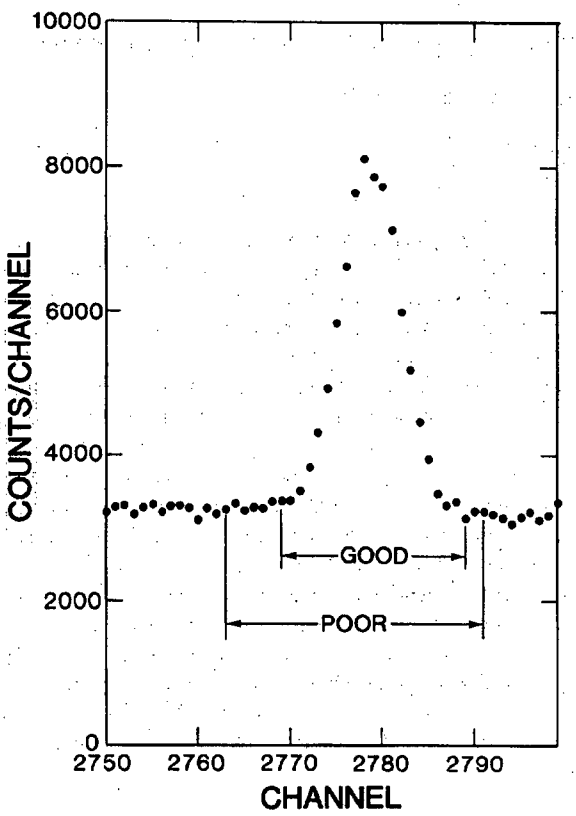

Fig. 5.5 A spectral peak showing good and poor choices of summing regions when determining the peak centroid by the first-moment method.

5.1.8 Determination of Peak Position by a Linearized Gaussian Fit

This procedure transforms the Gaussian-shaped peak into a line and then fits a line to the transformed peak. The slope and intercept of the fitted line are related to x_0 and σ. The background continuum under the peak is first subtracted so that the fit is made only to the Gaussian-shaped peak.

Transformations that linearize the Gaussian function have been applied only recently to determine the parameters of gamma-ray peaks (Ref. 7). The simplest of a class of similar transformations is the function

$$Q(x) = \ln \frac{y(x-1)}{y(x+1)} = \frac{2}{\sigma^2} x - \frac{2x_0}{\sigma^2} \tag{5-11}$$

where y(x) is the number of counts in channel x. The last expression in Equation 5-11 is correct if y(x) is the usual Gaussian function. The linear function Q(x) has a slope m and intercept b given by

$$m = 2/\sigma^2$$

$$b = -2x_0/\sigma^2. \tag{5-12}$$

Solving for σ^2 and x_0 gives

$$\sigma^2 = 2/m$$

$$x_0 = -b/m\ . \tag{5-13}$$

Equation 5-14 gives the expressions for the slope m and the intercept b of the line fit to the set of points [x, Q(x)] by the weighted-least-squares method:

$$b = \frac{1}{\Delta}\left(\sum\frac{x_i^2}{s_i^2}\sum\frac{Q_i}{s_i^2} - \sum\frac{x_i}{s_i^2}\sum\frac{x_iQ_i}{s_i^2}\right)$$

$$m = \frac{1}{\Delta}\left(\sum\frac{1}{s_i^2}\sum\frac{x_iQ_i}{s_i^2} - \sum\frac{x_i}{s_i^2}\sum\frac{Q_i}{s_i^2}\right) \tag{5-14}$$

where

$$\Delta = \sum\frac{1}{s_i^2}\sum\frac{x_i^2}{s_i^2} - \left(\sum\frac{x_i}{s_i^2}\right)^2$$

s_i^2 = estimated variance of Q(x).

The estimated variance of Q(x) is a function only of the uncertainties in y(x):

$$s^2[Q(x)] = s_r^2[y(x-1)] + s_r^2[y(x+1)] \tag{5-15}$$

where $s_r(y) \equiv s(y)/y$.

If the background continuum is small enough to ignore, then

$$s_r^2[y(x)] \approx 1/y(x)\ . \tag{5-16}$$

If the background continuum is subtracted by the straight-line procedure later shown in Section 5.3.3, the expression for $s^2[y(x)]$ is given by

$$s^2[y(x)] = y_t(x) + \frac{1}{4}\left[k^2\frac{B_h}{N_h^2} + (2-k)^2\frac{B_\ell}{N_\ell^2}\right] \tag{5-17}$$

where $k = \dfrac{2(x - x_\ell)}{(x_h - x_\ell)}$.

Also, $y_t(x)$ is the total counts in channel x and the meanings of the other parameters are given in Section 5.3.3.

For a linear fit there are simple expressions for the estimated variance s^2 of m and b:

$$s^2(m) \simeq \frac{1}{\Delta}\sum\frac{1}{s_i^2}$$

$$s^2(b) \simeq \frac{1}{\Delta}\sum\frac{x_i}{s_i^2}\,. \tag{5-18}$$

Although the fitting procedure just described may seem somewhat complex, the fit can be performed by a short computer program in only a few seconds. The Gaussian function should be fit to the top three-fourths to two-thirds of the peak to avoid problems with non-Gaussian tails and imprecise data. The n channels in the peak give $n - 2$ values of Q(x). When at least four or five values of Q(x) are used in the fit, the results are more than adequate to determine the peak centroids needed for the energy calibration. Unfortunately, it is very difficult to estimate the statistical uncertainty in x_0 using this fitting procedure. However, experience indicates that for peaks of reasonable precision, the values of x_0 are good to ~0.1 channel or better.

In automated operations, a test should be made to determine whether a Gaussian function adequately describes the input data. The reduced chi-square statistic χ^2/ν provides such a test. For the linear fit of Q(x) versus x,

$$\chi^2/\nu = \frac{1}{n-2}\left\{\sum\frac{1}{s_i^2}\left[Q_i - (mx_i + b)\right]^2\right\} \tag{5-19}$$

where m and b are computed from Equation 5-14 and n is the number of values of Q(x) in the fit. For good fits, χ^2/ν should be ~1.00. (See Ref. 5 for a very readable discussion of the properties of χ^2/ν.) For low-precision peaks (up to ~10 000 counts/channel), χ^2/ν is really ~1.00 for peaks of qualitatively good shape. As the maximum number of counts per channel increases, χ^2/ν increases even though the

peak shape remains the same. The increase in χ^2/ν does not necessarily mean the fit is inadequate for determining energy calibration or for testing resolution. At low precision, the goodness of fit is dominated by counting statistics; at high precision it is dominated by the inevitable small deviations of the peak shape from a true Gaussian shape, resulting in an increase in the computed value of χ^2/ν. Experience will dictate an acceptable value of χ^2/ν for a given range of peak precision.

Figure 5.6 shows a low-precision spectral peak from a germanium detector (FWHM ~19 channels) with the fitted Gaussian function superimposed upon it. The lower portion of the figure shows the plot of Q(x) versus x for the upper two-thirds of the peak along with the fitted line and the computed peak parameters.

5.1.9 Determination of Peak Position Using a Parabolized Gaussian Fit

The natural logarithm of the Gaussian function is parabolic as is strikingly apparent when full-energy peaks are viewed using the logarithmic display of an MCA. The natural logarithm of the Gaussian (Equation 5-6) gives

$$\ln y = c_2 x^2 + c_1 x + c_0 \tag{5-20}$$

where $c_2 = -1/2\sigma^2$
$c_1 = x_0/\sigma^2$
$c_0 = \ln y_0 - x_0^2/2\sigma^2$.

A fit of Equation 5-20 to the set of points $(x_i, \ln y_i)$ produces values of c_2, c_1, and c_0 that give the parameters of the Gaussian:

$$x_0 = -c_1/2c_2$$

$$\sigma = \sqrt{-1/2c_2}$$

$$\ln y_0 = c_0 - c_1^2/4c_2 \; . \tag{5-21}$$

The fitted curve is a parabola that opens downward and whose axis is parallel to the y-axis. The procedure described here determines y_0 in addition to x_0 and σ, the two parameters obtained from the linear fit to the linearized Gaussian. Therefore, the full-energy-peak area can be determined using Equation 5-8.

Figure 5.7 shows a parabolized Gaussian fit to a high-precision spectral peak from the 122.0-keV gamma ray of ^{57}Co. The same high-quality germanium detector was used in this figure as in Figure 5.3(a). At low energies, charge collection in germanium detectors is more complete than at high energies, with a resultant decrease in

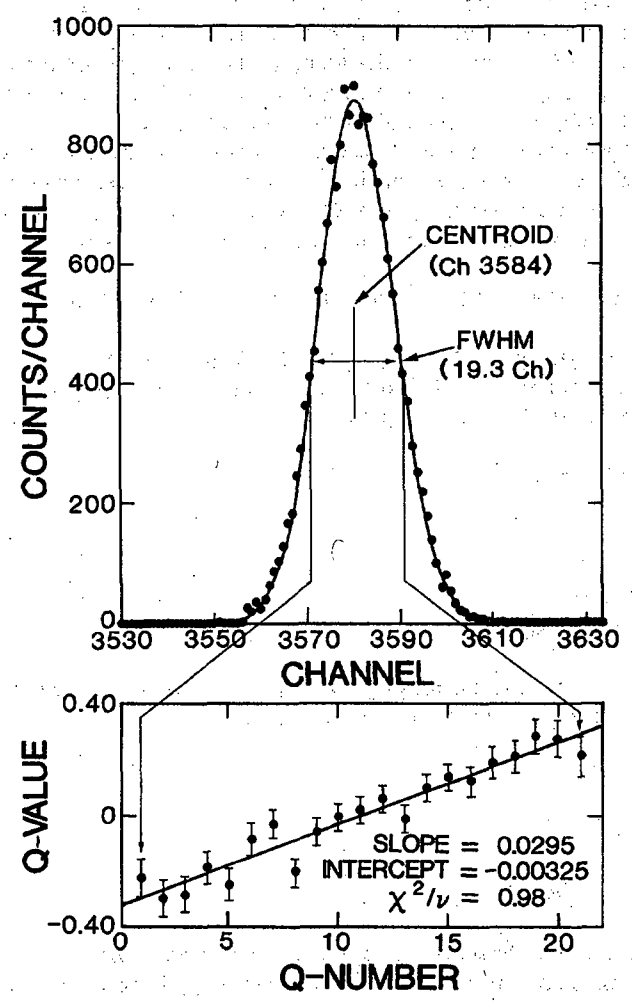

Fig. 5.6 The upper part of the figure shows a low-precision peak from a high-resolution spectrum to which a linearized Gaussian has been fitted. The lower part shows the plot of Q(x) values and the fitted line.

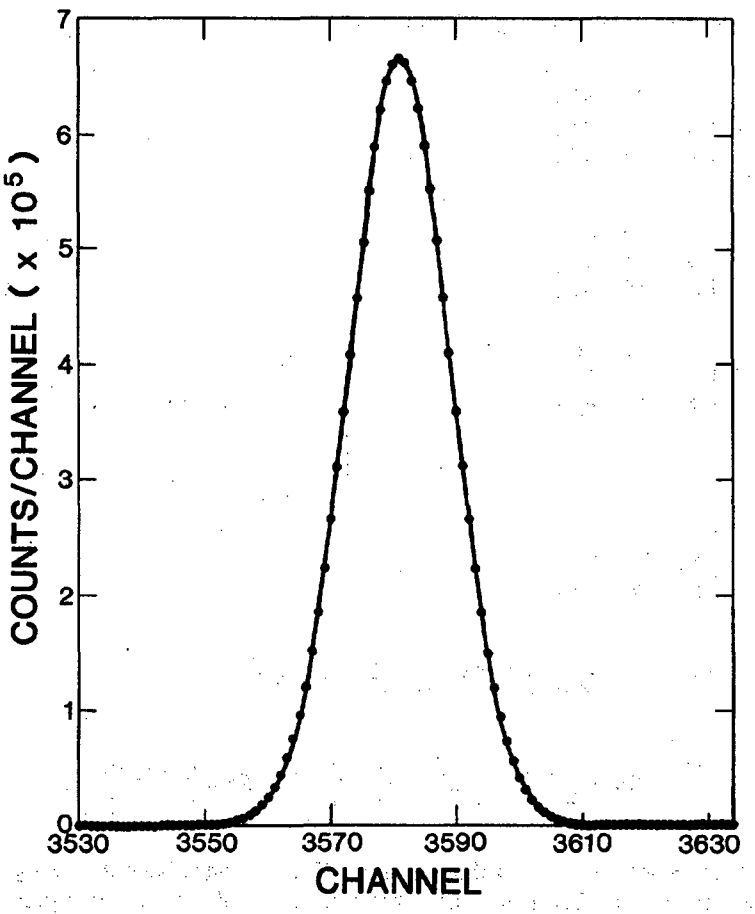

***Fig. 5.7** The 122.0-keV full-energy peak from a ^{57}Co spectrum obtained with a coaxial germanium detector having high resolution and good peak shape. The fitted curve is a "parabolized" Gaussian.*

low-energy tailing. Comparison of Figures 5.3(a) and 5.7 shows that the tailing in the 122-keV peak of Figure 5.7 is even less than the small tailing of the 1332-keV peak in Figure 5.3(a).

The expressions for the weighted quadratic least-squares fit are included for the convenience of possible users. The expressions are given in determinant form and involve eight sums, indicated by S1, S2, ..., S8.

$$c_0 = \frac{1}{\Delta}\begin{vmatrix} S6 & S2 & S3 \\ S7 & S3 & S4 \\ S8 & S4 & S5 \end{vmatrix}$$

$$c_1 = \frac{1}{\Delta}\begin{vmatrix} S1 & S6 & S3 \\ S2 & S7 & S4 \\ S3 & S8 & S5 \end{vmatrix} \qquad (5\text{-}22)$$

$$c_2 = \frac{1}{\Delta}\begin{vmatrix} S1 & S2 & S6 \\ S2 & S3 & S7 \\ S3 & S4 & S8 \end{vmatrix}$$

where

$$\Delta\begin{vmatrix} S1 & S2 & S3 \\ S2 & S3 & S4 \\ S3 & S4 & S5 \end{vmatrix}$$

$$S1 = \sum \frac{1}{s_i^2} \quad S2 = \sum \frac{x_i}{s_i^2} \quad S3 = \sum \frac{x_i^2}{s_i^2} \quad S4 = \sum \frac{x_i^3}{s_i^2}$$

$$S5 = \sum \frac{x_i^4}{s_i^2} \quad S6 = \sum \frac{\ln y_i}{s_i^2} \quad S7 = \sum \frac{x_i \ln y_i}{s_i^2} \quad S8 = \sum \frac{x_i^2 \ln y_i}{s_i^2}.$$

As usual, the sums are over all the points fit. The y_i values have the background continuum subtracted. The remaining expressions required for the fitting procedure are

$$s_i = s(\ln y_i)$$

$$s(\ln y) = \frac{s(y)}{\ln y} \qquad (5\text{-}23)$$

where s(y) is given by Equation 5-17. The expression for χ^2/ν, the goodness-of-fit statistic, is

$$\chi^2/\nu = \frac{1}{n-3}\left\{\sum_i \frac{1}{s_i^2}\left[\ln y_i - \left(c_2 x_i^2 + c_1 x_i + c_0\right)\right]^2\right\} \tag{5-24}$$

where n is the number of points fit and c_2, c_1, and c_0 are the values computed from Equation 5-22.

The remarks made in the previous section about the portion of the peak to be fit and about trends in χ^2/ν values apply equally well here. The quadratic fits put considerable demands on the computer, and occasionally the six significant decimal digits provided by many 16-bit processors running in single precision are insufficient for performing correct quadratic fits on high-precision data.

5.1.10 Determination of Peak Position Using Complex Spectral Fitting Codes

Large fitting codes are used to analyze complex spectra with overlapping peaks. The codes describe the peaks with functions that have a basic Gaussian form, with tailing functions added to describe the peak shape more accurately. An iterative nonlinear least-squares procedure is used to fit the data. The centroid of the Gaussian component of the fitted peak is taken as the peak position for purposes of energy determination.

5.2 DETECTOR RESOLUTION MEASUREMENTS

5.2.1 Introduction

This section is devoted primarily to the measurement of detector resolution. The importance of good resolution and peak shape in obtaining unbiased NDA results cannot be overemphasized. A narrow, Gaussian peak shape simplifies area determination and minimizes the possibility of bias in assay results.

The full width at half maximum (FWHM or FW.5M) is the basic measure of peak resolution. It is usually given in energy units (keV) for high-resolution detectors and expressed as a percentage of the measurement energy for low-resolution detectors. Resolution measured in energy units increases with energy: $FWHM^2 \approx a + bE$. When expressed as a percentage, resolution decreases with energy.

Most detectors give full-energy peaks that are essentially Gaussian above the half-maximum level. The ratio of the full width at heights less than the half maximum to the FWHM has long been used to quantify the quality of the full-energy-peak shape. Manufacturers measure the FWHM and its ratio to the full width at tenth maximum (FW.1M) to describe the peak shape; for many years a value of FW.1M/FW.5M less than 1.9 was regarded as describing a good peak shape. It is now reasonable to specify FW.02M/FW.5M and even FW.01M/FW.5M when the best peak shape is required.

Table 5-3 gives the theoretical ratios for a Gaussian curve and the measured ratios for a high-quality coaxial germanium detector. The table shows that the actual peak shape closely approaches the Gaussian ideal. The ratios at fiftieth and hundredth maximum should be measured after background subtraction.

Table 5-3. Theoretical and measured resolution ratios

	FW.1M / FW.5M	FW.02M / FW.5M	FW.01M / FW.5M
Gaussian	1.823	2.376	2.578
122.0 keV	1.829	2.388	2.599
	(1.003)[a]	(1.005)[a]	(1.008)[a]
1332.5 keV	1.856	2.428	2.640
	(1.018)[a]	(1.022)[a]	(1.024)[a]

[a]The ratio of the measured ratio to the theoretical ratio for a Gaussian.

The pulse spectrum from a detector is continuous, whereas an MCA or SCA groups the pulses in energy intervals. It is assumed that all the events in an interval can be represented by the energy of the center of the interval. When a Gaussian is fitted to the center points of the intervals, the width parameter σ is slightly greater than that of the original continuous distribution. As discussed in Ref. 8, the grouped variance and the actual variance are related by

$$(\sigma^2)_G = (\sigma^2)_A + h^2/12$$
$$(\text{FWHM}^2)_G = (\text{FWHM}^2)_A + 0.462h^2 \qquad (5\text{-}25)$$

where $(\sigma^2)_G$ = grouped variance
$(\sigma^2)_A$ = actual variance
h = group width (MCA channel width or SCA window width).

For MCA spectra, h has units of keV/channel if FWHM is in keV, and h = 1.00 if FWHM is in channels. Table 5-4 gives the ratio $(\text{FWHM})_A/(\text{FWHM})_G$. To measure the actual resolution to 0.1%, the system gain should be adjusted to provide more than 15 channels in $(\text{FWHM})_G$. If $(\text{FWHM})_G$ is 3 channels, the $(\text{FWHM})_A$ is overestimated by ~3%. The correction has no practical bearing on full-energy-peak areas. The Gaussian function fitted to the binned points has the same area (to better than 0.01%) as the continuous distribution because the y_0 parameter is decreased by almost exactly the same factor as the width parameter is increased.

Table 5-4. The ratio of $(FWHM)_A$ to $(FWHM)_G$

$FWHM_G$ (channels)	$\frac{FWHM_A}{FWHM_G}$
3.0	0.9740
5.0	0.9907
10.0	0.9971
15.0	0.9990
20.0	0.9994
25.0	0.9996
30.0	0.9997
35.0	0.9998
40.0	0.9999

5.2.2 Determination of Peak Width by Visual Estimation from MCA Display

Visual estimation works best with MCAs that have horizontal and vertical graticule lines and analog controls for the vertical and horizontal position of the display. Many small MCAs have such features; larger laboratory models usually do not give the user any control over the vertical position of the display.

To determine FWHM to ~1%, the energy gain should be chosen such that FWHM $\geq$ 10 channels. After the spectrum has been accumulated, the display controls are adjusted so that individual channels are resolved and one of the horizontal graticule lines cuts the peak at the half-maximum point. Figure 5.8 shows a peak divided at the half-maximum level. After the peak is bisected, the channels above the horizontal line are counted, estimating to tenths of channels. Because the channels are plotted as points, one really counts the spaces between the points. Usually the continuum on the high-energy side of the peak is regarded as the "bottom" of the peak. The slope of the energy calibration line is used to convert the FWHM value from channels to energy. If the energy calibration is not available, multienergy sources can be used. Large germanium detectors are calibrated with the 122.06- and 136.47-keV gamma rays from ^{57}Co and the 1173.2- and 1332.5-keV gamma rays from ^{60}Co. In either case the energy calibration can be determined from the separation of the peak pair in channels and the known energy difference.* The resolution is then determined by multiplying the FWHM in channels of the 122- or the 1332.5-keV peak and the appropriate energy calibration (keV/channel). With a little practice, values of FWHM (keV) can be determined to within 1%.

*Currently the best value for the energy difference between the two ^{57}Co gamma rays is 14.413 keV; the best value for the energy difference between the two ^{60}Co gamma rays is 159.27 keV.

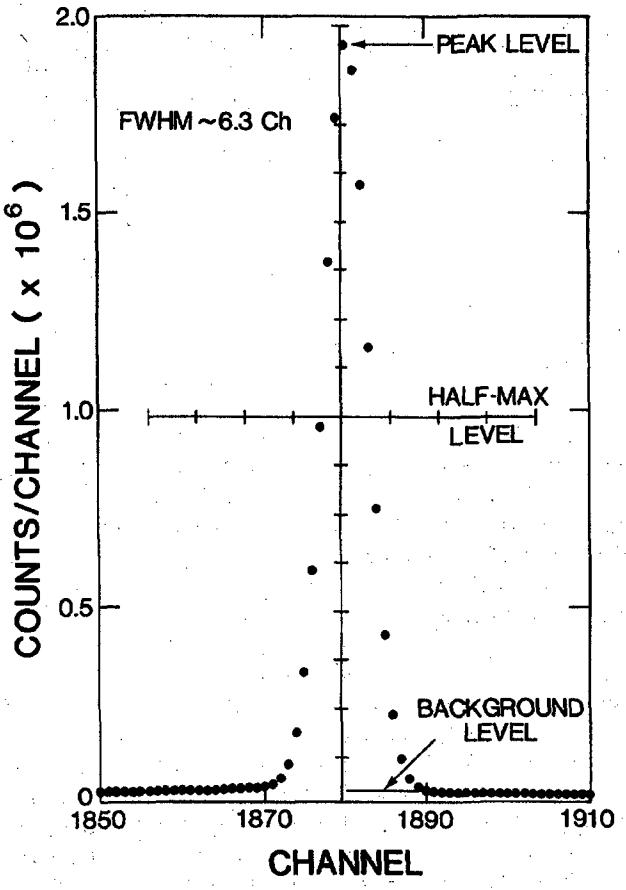

Fig. 5.8 A full-energy peak bisected by the mid-line of an MCA display. The FWHM equals the number of spaces above the half-maximum level.

5.2.3 Graphical Determination of Peak Width

The same type of plot used for energy calibration (Section 5.1.5) may be used for resolution measurement; indeed the two measurements can be combined. The shape of the top of the peak must be sketched to estimate the maximum peak height and the half-maximum line. Figure 5.9 shows the same ^{137}Cs spectrum as shown in Figure 5.4 but indicates the top of the peak, the half-maximum line, and the estimated FWHM.

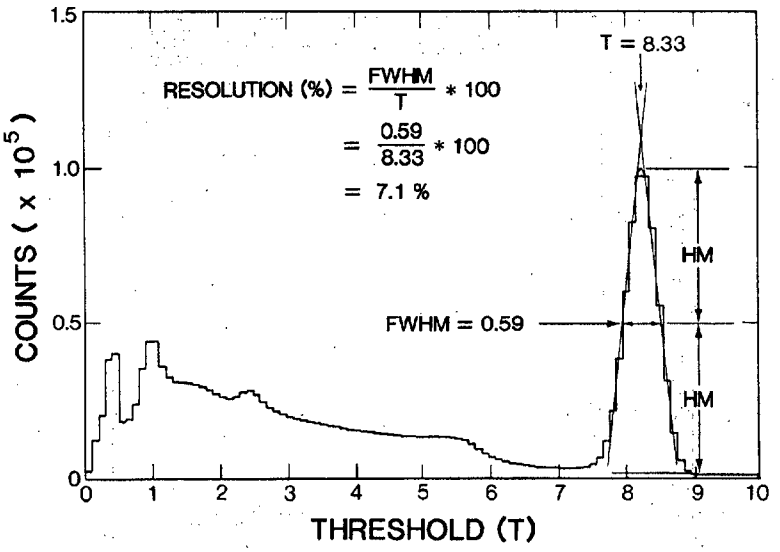

Fig. 5.9 An SCA-generated spectrum of ^{137}Cs from a NaI(Tl) detector. The plot shows how the FWHM and peak centroid are determined.

5.2.4 Determination of Peak Width Using Analytical Interpolation

The procedure described here quantifies the graphical procedure presented in the previous paragraph. Most of the FWHM functions built into modern MCA systems use some variation of this procedure. The interpolation procedure is particularly useful because the full width at any fractional height can be determined easily.

Figure 5.10 shows a full-energy peak with the maximum count channel near the centroid. The line across the peak in the figure indicates the fractional height at which the width is evaluated. The x coordinates of the points where the K * maximum line intersects the peak are

$$x_\ell = \frac{Ky_p - y_1}{y_2 - y_1} + x_1$$

$$x_h = \frac{y_3 - Ky_p}{y_3 - y_4} + x_3 \qquad (5\text{-}26)$$

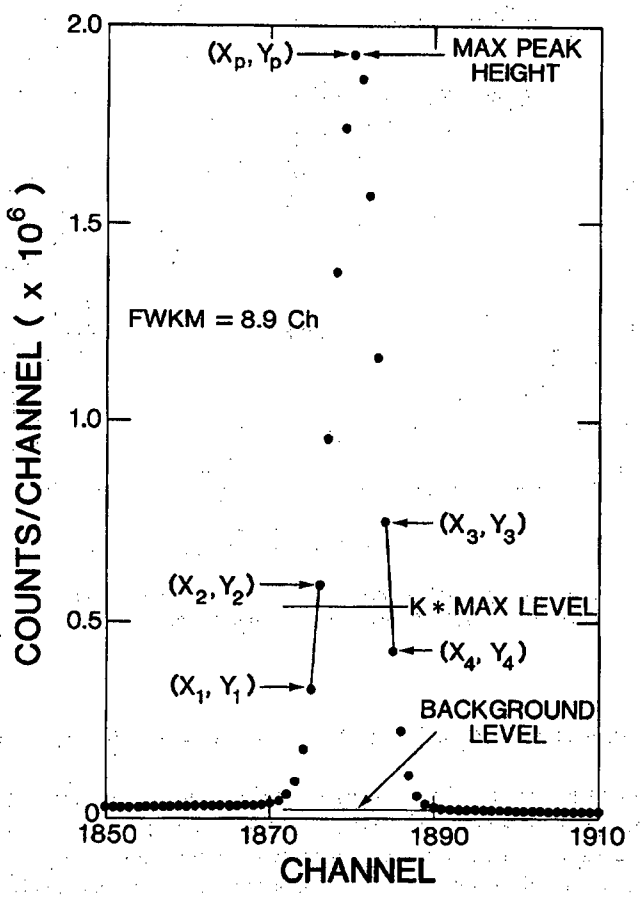

Fig. 5.10 Diagram of the procedure used to determine the FWKM by linear interpolation. The value of K may be between 0.0 and 1.0.

where K = fraction of maximum height at which the width is evaluated
y_x = number of counts in channel x
y_p = number of counts in the channel with maximum counts
x_ℓ = x coordinate of intersection of line K with low-energy side of peak
x_h = x coordinate of intersection of line K with high-energy side of peak
x_1, x_2 = channels below and above x_l
x_3, x_4 = channels below and above x_h.

The full width at the fractional level K (FWKM) is

$$\text{FWKM} = x_h - x_\ell = (x_3 - x_1) + \left[\left(\frac{y_3 - Ky_p}{y_3 - y_4}\right) - \left(\frac{Ky_p - y_1}{y_2 - y_1}\right)\right]. \tag{5-27}$$

To obtain the most accurate results, the value of y_p must be carefully estimated. When two channels with equal counts are at the top of the peak, the maximum value of the peak is clearly higher than the maximum channel value. The maximum channel value underestimates Ky_p and gives a slightly large value for FWKM. The procedure should be applied to peaks that are nearly symmetric about the maximum count channel. The peak maximum y_p can be accurately determined by fitting a Gaussian curve to the upper part of the peak. The peak shape can be accurately determined by using peaks with good statistical precision at all the fractional levels to be measured. For measuring FW.01M, a y_p of $\sim 10^6$ should be used so that the precision at the 0.01 level will still be ~1%. Smoothing might be used to obtain consistent results from a peak with poor precision; however, smoothing always broadens the peak a little.

5.2.5 Determination of Peak Width Using the Second-Moment Method

The second-moment method for determining the width parameter σ is analogous to the first-moment method for determining the centroid. The second moment of the normalized Gaussian function is equal to σ^2, the variance of the function. For the unnormalized function in Equation 5-6, the second moment is

$$\sigma^2 = \frac{\int_{-\infty}^{\infty}(x - x_0)^2\, y(x)\, dx}{\int_{-\infty}^{\infty} y(x)\, dx} \approx \frac{\sum (x_i - x_0)^2\, y_i}{\sum y_i}. \tag{5-28}$$

The parameter σ is related to the FWHM by Equation 5-7.

Any significant background continuum should be subtracted before Equation 5-28 is applied. The sums are calculated over a region equal to or larger than three times the FWHM. The method should not be used on peaks with significant asymmetry or with a non-Gaussian shape.

The procedure is useful for broad Gaussian peaks of poor precision where the linear interpolation method does not work well. The first- and second-moment determinations are usually performed together because the centroid value from the first-moment algorithm is required in the second-moment algorithm.

5.2.6 Determination of Peak Width Using a Linearized Gaussian Fit

Section 5.1.8 shows that Equation 5-11 can be used to linearize a Gaussian curve. The slope and intercept of the fitted line are related to the peak centroid and FWHM (Equations 5-7 and 5-13). The linearized Gaussian procedure is a good test of the energy calibration and detector resolution. Testing both a high-energy peak and a low-

energy peak provides strong assurance that the electronic parts of the NDA system are performing correctly. This test can be an important part of a measurement control program for a high-resolution gamma-ray NDA system.

5.2.7 Determination of Peak Width Using a Parabolized Gaussian Fit

Section 5.1.9 shows that the natural logarithm of the Gaussian function is a quadratic function of x. Fitting this function to the set of points $(x_i, \ln y_i)$ gives the parameters of the Gaussian function x_0, y_0, and σ and provides another way of determining the width of a Gaussian peak.

5.3 DETERMINATION OF FULL-ENERGY-PEAK AREA

5.3.1 Introduction

The gamma-ray pulse-height spectrum contains much useful information about gamma-ray energies and intensities. One of the most important concerns in applying gamma-ray spectroscopy is correct extraction of the desired information. Normally, the most important information is the full-energy-peak areas and their associated uncertainties.

Full-energy peaks in gamma-ray pulse-height spectra rest on a background continuum caused by the Compton scattering of higher energy gamma rays. The most fundamental limitation in obtaining unbiased peak areas is the determination of the background continuum. When the continuum is small with respect to the peak, it can cause only a small fractional error in the peak area. However, when the ratio of the peak area to the continuum area becomes much less than 1.0, the possibility of bias rises rapidly.

For many NDA applications, simple background-subtraction methods are adequate. Under certain circumstances, complex spectral fitting codes with long- and short-term tailing functions must be used. With low-resolution detectors, the problem of including small-angle-scattering events in the peak is severe, but computational corrections can sometimes be applied to resolve the problem (Ref. 9).

5.3.2 Selection of Regions of Interest (ROIs)

The choice of ROI is as important as the choice of algorithms used to evaluate peak areas. Most procedures use two ROIs to define the continuum level on the low- and high-energy sides of a peak or multiplet. The average channel count of an ROI is taken as the continuum level at the center of the ROI. A third ROI defines the peak region.

For a Gaussian function, 99.96% of the area lies within a region centered at x_0 that is three times the FWHM of the function. The amplitude of the Gaussian function at

$x_0 \pm 1.75$ FWHM is only 0.0082% of the maximum value at x_0 so continuum ROIs that begin at this point have minimal contributions from the peak. Thus, a peak ROI of three times the FWHM and continuum ROIs placed symmetrically 3.5 to 4.0 times the FWHM apart should obtain ~99.9% of the peak area.

In principle, the continuum is estimated more precisely if the continuum ROIs are quite wide. However, the possibility of systematic error increases as the energy interval increases. For most NDA applications, continuum ROIs of 0.5 to 1.0 times the FWHM are adequate. With an energy calibration of 0.1 keV/channel, typical background ROIs are three to five channels wide. When the continuum between neighboring peaks is very narrow, ROIs of one or two channels must be used. Peaks whose centers are separated by three times the FWHM can be considered resolved; usually a narrow ROI can be placed between them. It is better to sacrifice statistical precision than to introduce bias by using continuum ROIs that are too wide.

Spectra with significant low- or high-energy tailing may require a wider peak ROI than three times the FWHM. Because peak resolution deteriorates somewhat at high rates, the ROI should be set on a high-rate (low-resolution) spectrum. Usually, better results are obtained if all the ROIs are of equal width; therefore, the ROIs for low-energy peaks and reference pulser peaks are somewhat wider than three times the FWHM.

Computer codes can be written to accurately and consistently choose ROIs. Digital stabilization can be used to keep the desired peaks within a single preselected set of ROIs for long time periods. Sometimes it is desirable to change the spectrum to fit a particular set of ROIs. Codes exist that can reshuffle the contents of a spectrum to give any desired energy calibration with little degradation of spectral quality.

5.3.3 Subtraction of Straight-Line Compton Continuum

It is often adequate to approximate the Compton continuum by a straight line between the high- and low-energy sides of well-resolved peaks or of overlapping peak groups. Figure 5.11 shows how the ROIs are selected and indicates the notation used in the background equations. Note that the continuum ROIs need not be symmetrically placed with respect to the peak ROI nor need they be of equal width. The background is the trapezoidal area beneath the continuum line given by

$$B = [Y(F_p) + Y(L_p)]\,(N_p/2) \tag{5-29}$$

where $Y(F_p) = mF_p + b$

$$Y(L_p) = mL_p + b$$

and where $m = (Y_h - Y_\ell)/(X_h - X_\ell)$

$$b = (X_h Y_\ell - X_\ell Y_h)/(X_h - X_\ell)\,.$$

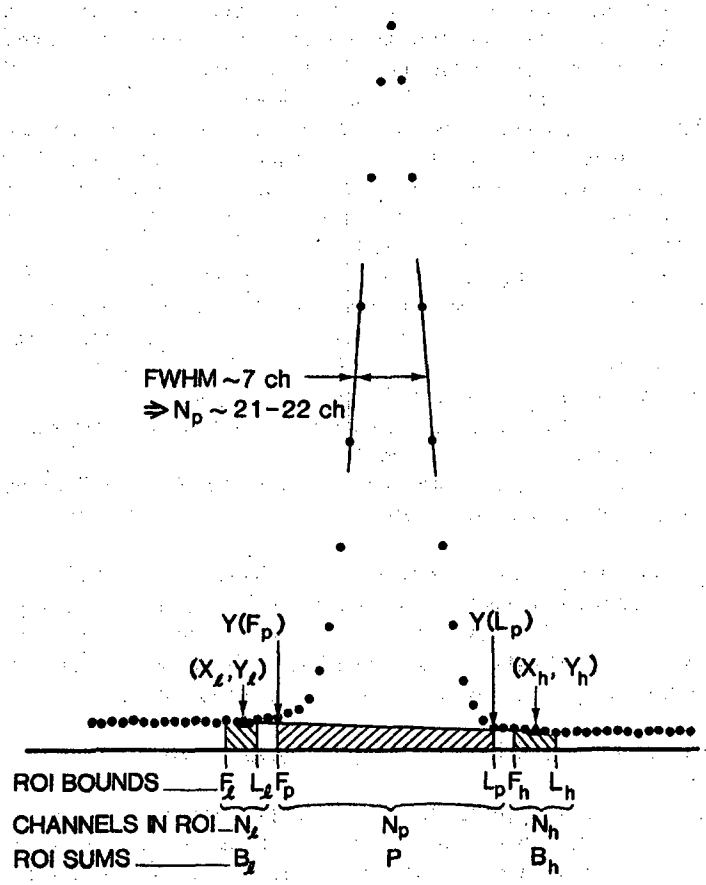

Fig. 5.11 Regions of interest and associated parameters used to compute the net area and the estimated standard deviation of a full-energy peak.

The variance of the background B is

$$S^2(B) = \left(\frac{N_p}{2}\right)^2 \left[K^2 \frac{B_h}{N_h^2} + (2-K)^2 \frac{B_\ell}{N_\ell^2}\right] \tag{5-30}$$

where $K = \dfrac{(F_p + L_p - 2X_\ell)}{(X_h - X_\ell)}$.

Equation 5-30 assumes no uncertainty in the ROI bounds and is a function only of the statistical uncertainties in B_h and B_ℓ, which are estimated by $S^2(B_\ell) = B_\ell$ and $S^2(B_h) = B_h$. Equation 5-30 is correct when the background ROIs are not symmetrically placed relative to the peak ROI. If the continuum ROIs are placed symmetrically relative to the peak ROI, the expressions for both B and $S^2(B)$ are simplified. The symmetry requirement means that $(F_p - X_\ell) = (X_h - L_p)$ and $K = 1$, and so the expressions become

$$B = \left(\frac{Y_\ell + Y_h}{2}\right) N_p = \left(\frac{B_h}{N_h} + \frac{B_\ell}{N_\ell}\right) \frac{N_p}{2} \tag{5-31}$$

and

$$S^2(B) = \left(\frac{N_p}{2}\right)^2 \left(\frac{B_h}{N_h^2} + \frac{B_\ell}{N_\ell{}^2}\right). \tag{5-32}$$

Frequently Equations 5.31 and 5.32 are used even when the symmetry requirement is not met, and if the net peak areas are much greater than the subtracted continuum, little error will result. However, when the peak areas are equal to or less than the subtracted continuum, the error may well be significant. In dealing with complex spectra (the spectra of plutonium are good examples), one is frequently forced to use asymmetrically placed ROIs. When the required computations are performed by interfaced processors, Equations 5-29 and 5-30 should be used because they give the best results that can be obtained with any version of the straight-line procedure.

For computations done with a small calculator, the use of the simplest possible expression is desirable and ROIs should be chosen accordingly. If $N_h = N_\ell \equiv N_c$, Equations 5-31 and 5-32 simplify to

$$B = \frac{N_p}{2N_c}(B_h + B_\ell) \tag{5-33}$$

and

$$S^2(B) = \left(\frac{N_p}{2N_c}\right)^2 (B_h + B_\ell). \tag{5-34}$$

If it is possible to choose $N_c = N_p/2$, the expressions achieve the simplest forms:

$$B = (B_h + B_\ell) \tag{5-35}$$

and

$$S^2(B) = (B_h + B_\ell) = B\,. \tag{5-36}$$

5.3.4 Subtraction of Smoothed-Step Compton Continuum

The Compton continuum beneath a full-energy peak is not a straight line. At a given energy, most of the continuum is caused by large-angle Compton scattering of higher energy gamma rays or by pulse pileup from lower energy interactions. The part of the continuum under a peak that is caused by the gamma ray that generates the peak results from small-angle Compton scattering and full-energy events with incomplete charge collection; this contribution can be described by a smoothed step function.

Gunnink (Ref. 10) devised the original procedure to generate a step-function continuum beneath single peaks or multiplets based on the overlying spectral shape. The procedure provides better results than the straight-line background approximation, especially for overlapping peak multiplets. For clean single peaks, the improvement is often negligible.

Figure 5.12 shows a logarithmic plot of a multiplet and a step-function background. Using the notation of Figure 5.11, the background at channel n is

$$B_n = Y_\ell - D\left[\sum_{i=X_\ell+1}^{i=n} (y_i - Y_h) \Big/ \sum_{i=X_\ell+1}^{i=X_h} (y_i - Y_h)\right] \qquad (5\text{-}37)$$

where y_i = total counts in channel i
$D = Y_\ell - Y_h$
$B(X_\ell) = Y_\ell$
$B(X_h) = Y_h$.

The background Y_h is subtracted from every channel because the Compton events from higher energy gamma rays cannot influence the shape of the smoothed step for lower energy gamma rays. Equation 5-37 is usable when the continuum beneath a peak or multiplet has a slightly negative or zero slope.

A significant complication in using the smoothed-step procedure is that the expression for the precision of the net area becomes exceedingly complicated when derived from Equation 5-37. The precision expression (Equation 5-30) based on the straight-line approximation is much simpler and almost as accurate.

5.3.5 Subtraction of Compton Continuum Using a Single Region of Interest

Estimating the background continuum from a single ROI is sometimes desirable or necessary. For example, a single ROI is often desirable when using a NaI detector and a single-channel analyzer (SCA) to measure ^{235}U enrichment or ^{239}Pu holdup.

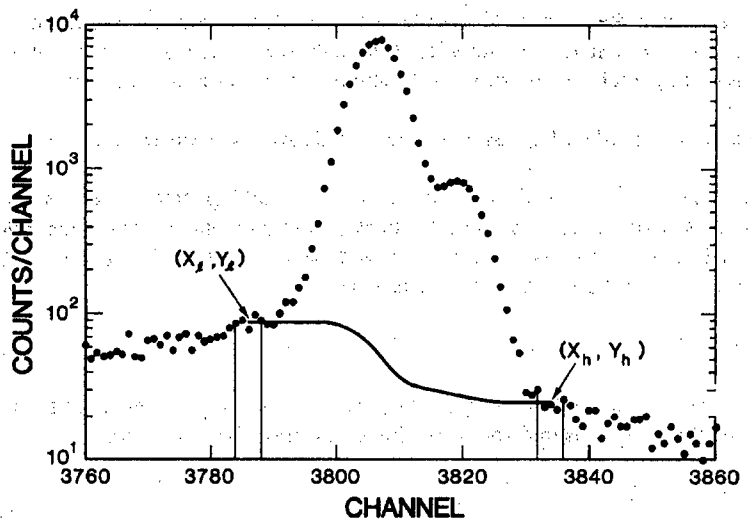

***Fig. 5.12** A peak doublet with the estimated spectral continuum computed by the simple smoothed-step algorithm.*

When the signal-to-background ratio is high, it may be adequate to assume a flat background continuum. Here, the contribution of the continuum to the peak ROI is given by

$$B = \frac{N_p}{N_h} B_h \tag{5-38}$$

$$s(B) \approx \frac{N_p}{N_h}\, s(B_h)\,. \tag{5-39}$$

Although this procedure is most often used with low-resolution scintillators, it is also used with germanium detectors when there is no convenient place for a background ROI on the low-energy side of a peak.

If the background continuum is not flat but can be assumed to have a constant slope over the energy range concerned, Equation 5-38 may be modified to

$$B = KB_h \tag{5-40}$$

where K is a constant factor determined by experiment. If the ambient background radiation is the main contributor to the Compton continuum, a "no sample" spectrum may be used to determine K. If the continuum is strongly dominated by high-energy

gamma rays from the sample, K may be estimated from an MCA spectrum. Often K will change from sample to sample. Although these single-ROI procedures have limited accuracy, their use is preferred to ignoring the continuum problem entirely.

5.3.6 Subtraction of Compton Continuum Using Two-Standard Procedures

Measurement of ^{235}U enrichment using the 185.7-keV gamma ray is a successful application of a single SCA window for background corrections. The assumption of a constant background shape is very good, and the constant K of Equation 5-40 can be determined accurately. The enrichment E is given by

$$E = C(P - KB) \tag{5-41}$$

where C is a constant with units (% ^{235}U/count). For two samples of different and known enrichments measured for equal times, Equation 5-41 becomes

$$\begin{aligned} E_1 &= C(P_1 - KB_1) \\ E_2 &= C(P_2 - KB_2) . \end{aligned} \tag{5-42}$$

The solution to these equations is

$$\begin{aligned} C &= (E_2B_1 - E_1B_2)/(P_2B_1 - P_1B_2) . \\ K &= (E_2P_1 - E_1P_2)/(E_2B_1 - E_1B_2) . \end{aligned} \tag{5-43}$$

Equation 5-41 may be written as

$$E = aP - bB \tag{5-44}$$

where

$$\begin{aligned} a &= \frac{E_2B_1 - E_1B_2}{P_2B_1 - P_1B_2} \\ b &= \frac{P_1E_2 - P_2E_1}{P_2B_1 - P_1B_2} . \end{aligned} \tag{5-45}$$

The two-standard method can be used to measure low-level radioactive contaminations in water or other fluids. See Chapter 7 on uranium enrichment for more details on this procedure.

5.3.7 Using Region-of-Interest Sums to Measure Peak Areas

For well-resolved peaks, the simple summation of counts above the estimated background continuum is probably as good as any other method of finding the peak area. This method avoids any difficulty from imperfections in the peak-shape models of spectral fitting codes. The ROI-summation method is quite tolerant of small variations in peak shape and provides an accurate and straightforward estimate of the precision of the net peak area.

For all ROI-summation procedures, the peak area is given by

$$A = P - B \tag{5-46}$$

where P is the integral of the peak ROI and B is the contribution from the background continuum. The expressions for $S^2(A)$, the estimated variance of the net area, vary according to the procedure used to estimate the background continuum.

When B is estimated by straight-line interpolation from continuum ROIs on either side of the peak ROI, the estimated variance of the peak area is

$$S^2(A) = S^2(P) + S^2(B) = P + S^2(B)\,. \tag{5-47}$$

Equations 5.29 through 5.36 give B and $S^2(B)$ for different conditions on the width and position of the background ROIs relative to the peak ROI. The expressions are summarized in Table 5-5. The simplest expressions are obtained when the background ROIs are symmetrically placed with respect to the peak ROI and have the appropriate widths. When adequate computational capacity is available, the most general form of the expressions should be used so that ROIs can be assigned without constraint.

When the smoothed step function is used to estimate the background continuum, Equations 5-46 and 5-37 combine to give

$$A = P - \sum_{n=F_p}^{L_p} \left\{ Y_\ell - D\left[\sum_{i=X_\ell+1}^{n} (y_i - Y_h) \Big/ \sum_{i=X_\ell+1}^{X_h} (y_i - Y_h) \right] \right\}. \tag{5-48}$$

Because the continuum estimate is a function of the channel counts, the exact expressions for $S^2(A)$ become extremely complex. One of the estimates for $S^2(A)$ given in Table 5-5 should be used.

Table 5-5. Expressions for net full-energy-peak areas and estimated variances[a] (straight-line background assumed)[b]

Conditions on ROIs	Background B	Background Variance $S^2(B)$
Arbitrary position and width of background ROIs	$B = [Y(L_p) + Y(F_p)](N_p/2)$	$S^2(B) = \frac{N_p^2}{2}\left[K^2\frac{B_h}{N_h^2} + (2-K)^2\frac{B_\ell}{N_\ell^2}\right]$
	where	where
	$Y(L_p) = mL_p + b$ and $Y(F_p) = mF_p + b$	$K = \frac{2(X - X_\ell)}{(X_h - X_\ell)} = \frac{(F_p + L_p - 2X_\ell)}{(X_h - X_\ell)}$.
	and where	
	$m = (Y_h - Y_\ell)/(X_h - X_\ell)$ and $B = (X_hY_\ell - X_\ell Y_h)/(X_h - X_\ell)$	
Symmetric placement of background ROIs relative to peak ROI, $(F_p - X_\ell) = (X_h - L_p)$	$B = \frac{N_p}{2}(Y_h + Y_\ell) = \frac{N_p}{2}\left(\frac{B_h}{N_h} + \frac{B_\ell}{N_\ell}\right)$	$S^2(B) = \left(\frac{N_p}{2}\right)^2\left(\frac{B_h}{N_h^2} + \frac{B_\ell}{N_\ell{}^2}\right)$

Table 5-5. (CONT.)

Symmetric placement of background ROIs with $N_\ell = N_h = N_c$	$B = \frac{N_p}{2N_c}(B_h + B_\ell)$	$S^2(B) = \left(\frac{N_p}{2N_c}\right)^2 \left(B_h + B_\ell\right)$
Symmetric placement of background ROIs with $N_\ell = N_h = N_p/2$	$B = (B_h + B_\ell)$	$S^2(B) = (B_h + B_\ell) = B$

[a] $A = P - B$

$S^2(A) = P + S^2(B)$.

[b] Notation summary as in Figure 5.11; LE = low energy; HE = high energy:

F_ℓ, L_ℓ	= first and last channels of LE background ROI
F_p, L_p	= first and last channels of peak ROI
F_h, L_h	= first and last channels of HE background ROI
B_ℓ, P, B_h	= integrals of LE background, peak, and HE background ROIs
N_ℓ, N_p, N_h	= numbers of channels in LE background, peak, and HE background ROIs
$Y_h = B_h/N_h$	= average continuum level in HE background ROI
$Y_\ell = B_\ell/N_\ell$	= average continuum level in LE background ROI
X_h, x_ℓ	= centers of background ROIs
$Y(F_p)$ and $Y(L_p)$	= ordinates of background line at F_p and L_p
m and b	= slope and intercept of background line between (X_ℓ, Y_ℓ) and (X_h, Y_h).

When a single background ROI is used, Equation 5-46 holds for the net peak area, and the expression for $S^2(A)$ is based on Equation 5-47. When the continuum is assumed to be flat (Equation 5-38), the expressions for A and $S^2(A)$ become

$$A = P - \frac{N_p}{N_h} B_h$$

$$S^2(A) = P + \left(\frac{N_p}{N_h}\right)^2 B_h \,. \tag{5-49}$$

If a sloped continuum is assumed (Equation 5-40), the expressions for A and $S^2(A)$ become

$$\begin{aligned} A &= P - KB_h \\ S^2(A) &= P + K^2 B_h \,. \end{aligned} \tag{5-50}$$

Note that although Equations 5-49 and 5-50 may correctly predict the repeatability of measurements, they do not predict any assay bias arising from the approximate nature of the single-ROI background estimate.

5.3.8 Using Simple Gaussian Fits to Measure Peak Areas

As shown in Section 5.1.3, the determination of σ and y_0 by a Gaussian fit also determines the peak area using Equation 5-8. For cleanly resolved peaks, the areas obtained by fitting simple Gaussians are probably no better than those obtained from ROI sums, and may be somewhat worse. This assertion is known to be true for germanium detectors. For NaI scintillators, a Gaussian fit may give more consistent peak areas than ROI methods. The simple Gaussian-fitting procedures do not provide straightforward ways to estimate peak-area precision.

In a few situations, Gaussian fitting is advantageous. When two peaks are not quite resolved such that the desired peak ROIs overlap, a Gaussian can be fitted to one-FWHM-wide ROIs centered on each peak to determine the peak areas. When the centroid location and FWHM are the primary information desired from a Gaussian fit, the area estimate often comes with no extra effort. When a peak has significant low-energy tailing from Compton scattering in the sample or shielding, a simple Gaussian fit to the middle FWHM of the peak can easily obtain the desired area.

When a Gaussian function is transformed to a line that is least-squares fit to obtain the parameters x_0 and σ, the parameter y_0 can also be determined using any of the original data points and Equation 5-6 to solve for y_0. An average of the values of y_0 determined from several points near x_0 gives a satisfactory value for the area equation.

Section 5.1.9 shows that the logarithm of the Gaussian function is parabolic and that a quadratic fit to $\ln(y_i)$ yields all three of the Gaussian parameters x_0, y_0, and σ. The peak area is obtained from Equation 5-8. As with the linearized Gaussian procedure, no simple expressions exist to estimate the precision of the peak areas.

5.3.9 Using Known Shape Parameters to Measure Peak Areas in Multiplets

The previous discussion emphasizes well-resolved single peaks because most applications of gamma-ray spectroscopy to the NDA of nuclear material employ well-resolved peaks. However, to measure isotopic ratios from high-resolution plutonium spectra, it is necessary to analyze unresolved peak multiplets.

If the peak shape is described by an adequate mathematical model in which all the parameters are known except the amplitude, unresolved multiplets can be analyzed quite simply by ordinary noniterative least-squares methods. For some purposes the simple Gaussian function (Equation 5-6) is adequate without any tailing terms. If the position and width parameters x_0 and σ are known, only the amplitude parameter y_0 is unknown. Frequently, the well-resolved peaks in a spectrum can yield sufficient information to determine the x_0 and σ parameters for the unresolved peaks. The gamma-ray energies are accurately known for all fissionable isotopes; therefore, the energy calibration can be determined with sufficient accuracy to calculate the x_0 parameter for all unresolved peaks. The width parameter σ can be determined from the well-resolved peaks and interpolated to the unresolved peaks with the relation $\text{FWHM}^2 = a + bE$, which is quite accurate for germanium detectors above 100 keV. The well-resolved peaks can also yield information needed to determine the parameters of tailing terms in the peak-shape function.

The least-squares fitting procedure for determining the peak amplitudes is most easily described by the following example. The example assumes a three-peak multiplet where all the peaks come from different isotopes. After the Compton continuum is subtracted from beneath the multiplet, the residual spectrum has only the three overlapping peaks and the count in channel i may be written as

$$y_i = A1 \times F1_i + A2 \times F2_i + A3 \times F3_i \tag{5-51}$$

where A1, A2, and A3 are the amplitudes to be determined and F1, F2, and F3 are the functions describing the peak shapes. Assuming that the peaks are well described by a pure Gaussian,

$$\begin{aligned} F1 &= \exp[K1(x_i - x1_0)^2] \\ F2 &= \exp[K2(x_i - x2_0)^2] \\ F3 &= \exp[K3(x_i - x3_0)^2] \end{aligned} \tag{5-52}$$

where $x1_0$, $x2_0$, $x3_0$ = known centroid positions

K1, K2, K3 = $1/2\sigma^2_{1,2,3}$

$\sigma_i = (\text{FWHM})_i / \left(2\sqrt{2 \ln 2}\right)$.

The least-squares fitting procedure determines A1, A2, and A3 to minimize the sum of the squared difference between the actual data points and the chosen function. With derivation the expressions for A1, A2, and A3 are

$$A1 = \frac{1}{D}\begin{vmatrix} \sum yF1 & \sum F1\,F2 & \sum F1\,F3 \\ \sum yF2 & \sum F2^2 & \sum F2\,F3 \\ \sum yF3 & \sum F3\,F2 & \sum F3^2 \end{vmatrix}$$

$$A2 = \frac{1}{D}\begin{vmatrix} \sum F1^2 & \sum yF1 & \sum F1\,F3 \\ \sum F2\,F1 & \sum yF2 & \sum F2\,F3 \\ \sum F3\,F1 & \sum yF3 & \sum F3^2 \end{vmatrix}$$

$$A3 = \frac{1}{D}\begin{vmatrix} \sum F1^2 & \sum F1\,F2 & \sum yF1 \\ \sum F2\,F3 & \sum F2^2 & \sum yF2 \\ \sum F3\,F1 & \sum F3\,F2 & \sum yF3 \end{vmatrix}$$

$$D = \begin{vmatrix} \sum F1^2 & \sum F1\,F2 & \sum F1\,F3 \\ \sum F2\,F1 & \sum F2^2 & \sum F2\,F3 \\ \sum F3\,F1 & \sum F3\,F2 & \sum F3^2 \end{vmatrix} \qquad (5\text{-}53)$$

The pattern of Equation 5-53 can be followed for expanding to additional unknowns. The form of F1, F2, and F3 is not related to the solutions for A1, A2, and A3. The only requirement is that the functions are totally determined except for an amplitude factor. Tailing terms may be added to improve the accuracy of the peak-shape description. When two or more peaks in a multiplet are from the same isotope, the known branching intensities, I_1, I_2 ..., can be used to fit the peaks as a single component. If peaks one and two in the example are from the same isotope, Equation 5-51 becomes

$$y_i = A \times F_i + A3 \times F3_i \qquad (5\text{-}54)$$

where

$$F = \exp[K1(x_i - x1_0)^2] + (I_2/I_1)\exp[K2(x_i - x2_0)^2] .$$

Equation 5-54 has only two unknowns, A and A3. Strictly speaking, the coefficients in F should be $1/E_1$ and $I2/I_1E_2$ where E1 and E2 are the relative efficiencies at the two energies. If available, the efficiencies should be included, but often the related members of the multiplet are so close together in energy that $E1 \approx E2$. When one of the related gamma rays is much more intense than the other, the errors in the intense components caused by assuming E1 = E2 are usually negligible.

5.3.10 Using Complex Fitting Codes to Measure Peak Area

Much time has been invested in the development of computer codes to determine the peak areas from complex, overlapping peak multiplets. A number of successful codes exist, along with many variations for special problems. Helmer and Lee (Ref. 11) review the peak models and background subtraction procedures of most currently used codes.

The complex codes describe full-energy peaks with a basic Gaussian shape plus one or two low-energy tailing terms (long- and short-term tailing) and sometimes a high-energy tailing term. The long-term tail is often not included in the full-energy-peak area because it is ascribed to small-angle Compton scattering within the sample. The long-term tailing function usually is not required for high-resolution spectra. The detailed form of the tailing terms varies from code to code, although the results are often equivalent. The procedures to subtract the Compton continuum also vary; in general, the background subtraction procedures are most in need of improvement.

These fitting codes are often indispensable, but they often require a major learning effort before they can be used intelligently. Learning to use such codes skillfully can be likened to learning to play a large pipe organ; after acquiring some basic skills, one must learn the possibilities and limitations of the many combinations of "stops." The potential user who does not have extensive experience in gamma-ray spectroscopy should consult with knowledgeable users of the code.

Note that all fitting codes perform better on high-quality spectra with good resolution and minimal peak tailing. A fitting code cannot completely compensate for poor-quality detectors and electronics or for sloppy acquisition procedures. It should be said that an ounce of resolution is worth a pound of code. In the past few years, the quality of detectors and electronics has improved in parallel with code development, resulting in the present ability to do measurements that were previously very difficult, if not impossible.

5.4 RATE-RELATED LOSSES AND CORRECTIONS

5.4.1 Introduction

As discussed in Chapter 4, ADC deadtime is defined as the sum of the time intervals during which the ADC is unable to process other events. Deadtime can occur in all NDA system components. The deadtime intervals are either fixed or are a function of system parameters and pulse amplitude.

For MCA-based systems, the deadtime begins when the amplifier output pulse crosses the ADC discriminator threshold. The deadtime includes the pulse risetime, a small fixed time for peak detection and latching, a digitization time, and often the memory storage time. For germanium detector systems using 100-MHz Wilkinson ADCs, the deadtime for an event at channel 4000 is ~55 μs. At rates of only a few thousand counts per second, a significant fraction of information can be lost to system deadtime alone.

For SCA-based systems using NaI(Tl) detectors, the deadtime is much shorter and can often be ignored. The losses in such systems are usually due to pulse pileup.

Pulse pileup is described briefly in Chapter 4. Figure 4.9 shows how two events that occur within an interval less than the amplifier pulse width sum to give a pulse whose amplitude is not proportional to either of the original pulses. Figure 4.10 shows the effect of pileup events on the spectrum. Pileup can occur in the detector, the preamplifier, or the main amplifier, but the overall effect is governed by the slowest component, usually the main amplifier. Pileup always results in a loss of information; the degree of loss depends on the information sought and the gross count rates involved. For example, when counting events above a discriminator threshold, two pileup events are counted as one; if pulse-height analysis is being performed, both events are lost from their respective peaks.

In high-resolution spectroscopy systems, the amplifier pulse width is often comparable to the ADC processing time, and the loss of information caused by pileup may be equal to or greater than the loss caused by deadtime. Although an MCA can operate in a live-time mode and compensate for deadtime losses, it does not fully compensate for pileup losses.

Many texts discuss all counting losses in terms of two limiting cases, both of which are referred to as deadtime [see, for example, Chapter 3 of Knoll (Ref. 12)]. Neither case exactly describes the operation of actual equipment. One case is called nonparalyzable deadtime and is typical of ADC operation; the other is termed paralyzable deadtime and is related to pulse pileup. The terminology is unfortunate because no circuitry is dead during pileup; rather, events are lost from their proper channel because of the pulse distortion. In this book the distinction between deadtime and pileup is preserved because they are two distinctly different loss mechanisms.

The goal of many gamma-ray spectroscopy applications is to compute a corrected rate CR for the gamma ray(s) of interest:

$$CR = RR \times CF(RL) \times CF(AT) \tag{5-55}$$

where RR = raw rate of data acquisition
CF(RL) = rate-related loss correction factor
CF(AT) = attenuation correction factor (See Chapter 6).

When the correction factors are properly defined and computed, CR is the count rate that would be observed if there were no electronic losses and no sample attenuation. The corrected rate CR is often directly proportional to the desired quantity, such as mass of ^{239}Pu or ^{235}U enrichment. All three factors in Equation 5-55 must be determined accurately to obtain accurate assays.

5.4.2 Counting Loss as a Function of Input Rate

In modern spectroscopy systems, counting losses are rarely well described by the simple model of nonparalyzable deadtime; however the model is described here for completeness. In early systems, the deadtime losses were far higher than pileup losses, and the simple nonparalyzable model was quite adequate.

For a fixed deadtime D, CR can be represented as follows:

$$CR = \frac{RR}{1 - RR \times D}. \tag{5-56}$$

Inverting Equation 5-56 gives

$$RR = \frac{CR}{1 + CR \times D} = \frac{1}{1/CR + D}. \tag{5-57}$$

As $CR \rightarrow \infty$, $RR \rightarrow 1/D$ as a limiting value of throughput. The term nonparalyzable arises because RR rises monotonically toward the limit 1/D. For pileup losses, $RR \rightarrow 0$ as $CR \rightarrow \infty$, justifying the term paralyzable.

Although Wilkinson ADCs do not have a fixed deadtime, Equations 5-56 and 5-57 apply if D is set equal to the average deadtime interval. Whether fixed or an average, the deadtime D is rarely determined directly because most users wish to correct for the combined rate-related losses.

Pulse-pileup losses are important in high-resolution spectroscopy for two reasons. First, the relatively long pulse-shaping times required for optimum signal-to-noise ratio yield pulse widths up to 50 μs, which increases the probability of pileup. Second, a small pileup distortion can throw a pulse out of a narrow peak. Because NaI(Tl)

systems operate with time constants of ~3 μs or less, they have lower pileup losses. Furthermore, because the NaI peaks are 10 to 20 times broader than germanium peaks, many events can suffer a slight pileup and still remain within the full-energy peak. However, pileup losses in NaI(Tl) spectra are much harder to correct because of the broader peaks.

Figure 5.13 shows that if an amplifier pulse is preceded or followed by a pulse within approximately half the pulse width, its peak amplitude is distorted. The degree of distortion depends on the amplitude and timing of the interfering pulse relative to the analyzed pulse. Frequently pileup-rejection circuitry is used to detect and prevent analysis of the distorted events. Unfortunately, in rejecting bad pulses almost all systems reject some small fraction of nondistorted pulses.

If no other events occur within the time interval T where pileup is possible, the pulse will be analyzed and stored in its proper location. The fundamental expression from Poisson statistics (Refs. 1 and 3) that applies here is

$$P(N) = \frac{(RT)^N e^{-RT}}{N!} \tag{5-58}$$

where P(N) is the probability of N events occurring within a time interval T if the average rate is R. The probability that an event is not lost to pileup is obtained by setting N = 0 in Equation 5-58:

$$P(0) = e^{-RT} . \tag{5-59}$$

The fraction F of pulses lost to pileup is given by

$$F = 1 - P(0) = 1 - e^{-RT} . \tag{5-60}$$

If RT is much less than 1, Equation 5-60 simplifies to

$$F \approx RT \tag{5-61}$$

which provides a very simple relationship for estimating the pileup losses at lower rates.

If deadtime losses can be ignored, Equation 5-59 describes the throughput of a high-resolution spectroscopy system. The measured raw rate RR is given by

$$RR = Re^{-RT} \tag{5-62}$$

where R is the gross rate of events from the detector. Differentiation of Equation 5-62 shows that RR is maximized at R = 1/T and that the fraction of R stored at that rate is 1/e ≈ 0.37. Thus, at the input rate for maximum throughput, just over a third of the input events are correctly analyzed and stored. The fraction of the input rate that is stored is e^{-RT}, and the stored rate as a fraction of the maximum stored rate 1/(eT) is given by RTe^{1-RT}. Both of these fractions are plotted in Figure 5.14.

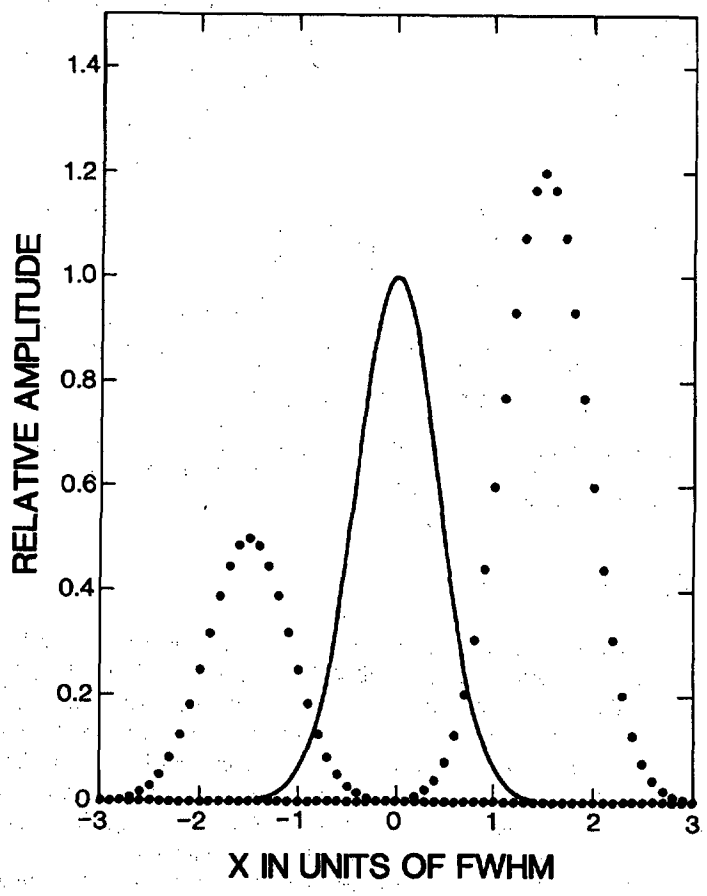

Fig. 5.13 *Three Gaussian curves (amplifier pulses) separated by 1.5 × FWHM. As drawn, there is minimal pileup distortion to any pulse. If the pulse separation is reduced, the distortion will clearly increase.*

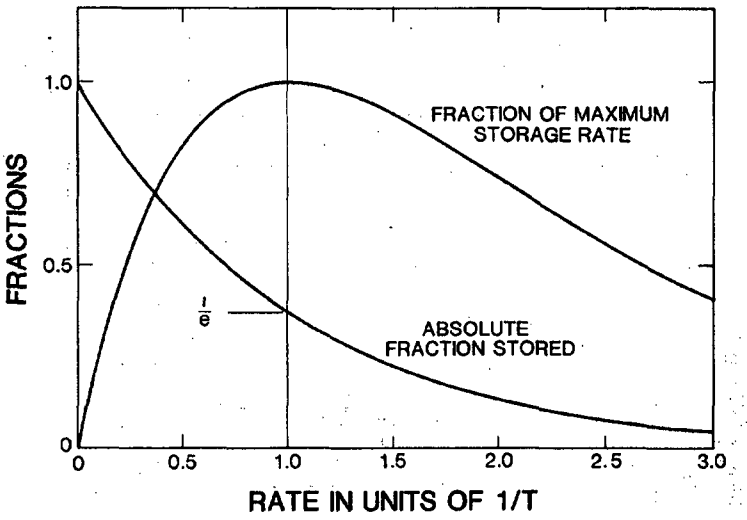

Fig. 5.14 The absolute fraction stored and the fraction of the maximum storage rate for a paralyzable system of deadtime T as a function of input rate in units of 1/T.

5.4.3 Actual Data Throughput

Figure 5.14 shows that the throughput rate peaks at surprisingly low values for ordinary high-resolution gamma-ray spectroscopy systems. For T = 50 μs (a high though common value), 1/T = 20 000 s^{-1} and the maximum throughput is about 7350 s^{-1}. Where long time constants are necessary to produce the desired resolution, throughput must be sacrificed as the price for the highest resolution. In fact, the low-rate side of the throughput curve should be used when possible because it yields better resolution and peak shape. At a rate of 0.6(1/T), the throughput is 90% of maximum; at only 0.5(1/T), the throughput is still 82% of maximum.

Sometimes a spectroscopy system must be operated far beyond the throughput maximum. At a rate of 2/T (40 000 s^{-1} with T = 50 μs), only ~14% of the information is stored, implying a correction for pileup losses of ~7. One important point is evident: to maximize system throughput and minimize the necessary corrections, T must be minimized and some loss of resolution must always be accepted. Fortunately, much progress has been made in recent years to minimize T and still preserve resolution and peak shape (see Chapter 4 and Ref. 13).

If Equations 5-59 through 5-62 are used to estimate throughput rates and loss fractions, R and T must be reasonably well known. The input rate R is usually easy to obtain. Many modern amplifiers include a provision for pileup rejection and have a fast timing channel with a pulse-pair resolution of about 0.5 to 1.0 μs and an output that can be counted with a scaler-timer. Equation 5-56 can be used to refine the value of R when there is significant loss in the fast counting channel. Fast amplifiers and discriminators can be connected to the preamplifier output to measure the gross count rate. The SCA output on the ADC should not be used to measure R because it operates on the much slower amplifier output.

The rejection or loss interval T is more difficult to estimate. If electronic pileup rejection is not used, T can be assumed to be approximately equal to the pulse width (see Figure 5.13). An oscilloscope can be used to measure the width between the 1% or 2% amplitude points of the pulse. For many amplifiers, the pulse width is approximately six times the time constant τ, but this usually underestimates the pileup losses. After a pulse is analyzed, the amplifier output must fall below the ADC lower-level discriminator before another event is accepted. Because the discriminator level is usually low, a pulse preceded by another with less than a full pulse width separation will not be analyzed. To compensate, T might be estimated at about 1.5 times the pulse width for systems without formal pileup rejection.

With electronic pileup rejection, different configurations have somewhat different values of T. One common procedure uses a fast timing circuit to examine the intervals between preamplifier pulses and to generate an inhibit signal if an interval is less than a fixed value. The interval and inhibit signal length are approximately the width of an amplifier pulse. The inhibit signal is applied to the anticoincidence gate of the ADC to prevent analysis of pileup events. The value of T depends on the anticoincidence requirements of the ADC; usually a pulse is rejected if another pulse precedes it within the preset interval or if another pulse follows it before the ADC linear gate closes when digitization begins. Obviously, a good qualitative understanding of the operation of the ADC and pileup rejection circuitry is required to estimate T accurately. Additional losses caused by ADC deadtime can often be ignored. For example, if the pulse width is 35 μs (corresponding to use of ~6-μs time constants) and digitization takes 15 μs or less beginning when the pulse drops to 90% of its maximum value, then the ADC completes digitization and storage before the pileup inhibit signal is released and the ADC contributes no extra loss.

The fraction of good information stored is usually somewhat less than estimated. One reason is that rejection circuitry allows some pileup events to be analyzed, thus causing a loss of good events. Most pileup rejection circuitry has a pulse-pair resolution of 0.5 to 1.0 μs. Pulses separated by less than the resolution time will pile up but are still analyzed, causing sum peaks in the spectrum. When amplifier time constants of $\geq$3 μs are used, the pulse tops are nearly flat for a microsecond, and events within the resolving time of the pileup circuitry sum together almost perfectly, forming sum

peaks that have almost the same shape and width as real peaks. Such peaks are sometimes mistaken for single gamma-ray peaks and have a habit of appearing at embarrassing places in the spectrum.

Another cause of information loss is the generation of long-risetime preamplifier pulses. Usually preamplifier risetimes are a few tenths of a microsecond. However, if the gamma-ray interaction is in a part of the detector where the electric field is weak or where there is an excess of trapping centers, it may take several microseconds to collect the liberated charge. The main amplifier produces a very long, low-amplitude pulse, often two or three times as long as normal. Good events that sum with these long, low-amplitude pulses are lost as useful information. The frequency with which such events are generated depends on detector properties and how the detector is illuminated with gamma rays. Gamma rays falling on the detector edges where fields are often distorted and weak have a much greater chance of not being properly collected. In some applications, a detector performs better at high rates if the gamma rays can be collimated to fall only on its center region. For a relatively poor detector, under fully illuminated conditions, as many as 10% of the detected events can have long risetimes, and this results in a substantial loss of potential information. To achieve high throughput at high rates requires an excellent detector with minimum generation of the poorly collected, slow-rising pulses.

With appropriate sources and equipment, the throughput curve can be determined experimentally. Figure 5.15 shows the throughput curve for a state-of-the-art high-rate system employing time-variant filtering techniques (Chapter 4) to achieve very high throughput with almost constant resolution. A small planar germanium detector is used with a ^{241}Am source. The measured maximum throughput is ~85 000 s^{-1} at an input rate of ~300 000 s^{-1}. However, the paralyzable deadtime model predicts a maximum throughput of 110 000 s^{-1} with an input rate of 300 000 s^{-1}; the simple model is not adequate. The system resolution at 60 keV is almost constant at ~0.63 keV up to an input rate of 100 000 counts/s and then increases smoothly to ~0.72 keV at an input rate of 1 000 000 counts/s. Figure 5.16 shows the throughput curve for ^{241}Am using standard high-quality electronics optimized for high resolution at low count rates with 6-μs shaping constants and a 100-MHz Wilkinson ADC to generate an 8192-channel spectrum. Additional loss comes from resetting the pulsed-optical preamplifier. The maximum throughput of this system is only ~2800 s^{-1}, but the resolution at 60 keV is ~0.34 keV at the lowest rates and is still only ~0.44 keV at 21 500 s^{-1}. The curves of throughput and resolution demonstrate that with the current state-of-the-art one cannot simultaneously obtain high throughput at a high rate and the best resolution. The FWHM increases by a factor of nearly 2 from the system optimized for resolution to that of the system optimized for high throughput. The two experimental curves, though describing very different systems, are similar to one another and to the theoretical curve shown in Figure 5.14 for the purely paralyzable system.

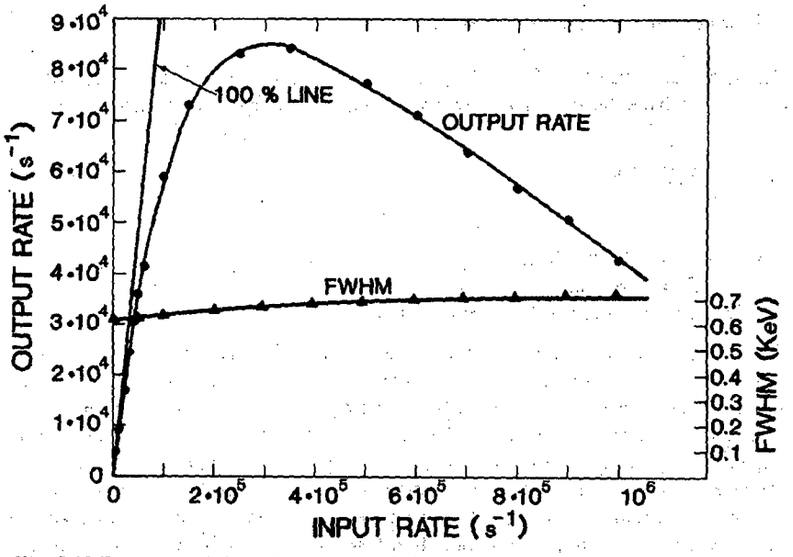

Fig. 5.15 Experimental throughput and resolution curves for a state-of-the-art high-rate gamma-ray spectroscopy system. The straight line indicates 100% throughput.

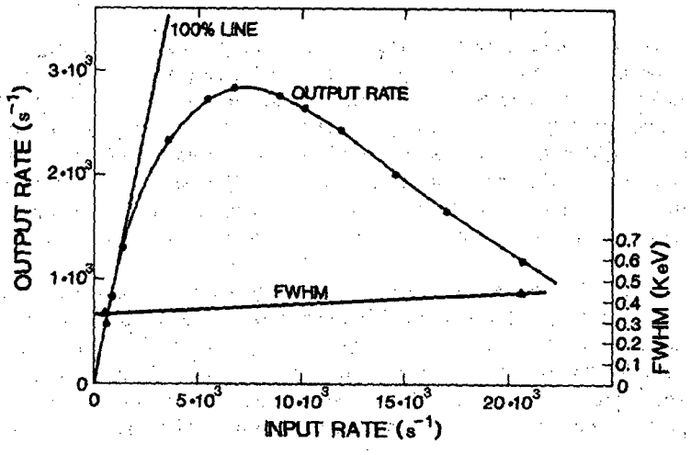

Fig. 5.16 Experimental throughput and resolution curves for a standard gamma-ray spectroscopy system that is optimized for resolution at the expense of throughput. The line indicates 100% throughput.

5.4.4 Correction Methods: General

The determination of the full-energy interaction rates (FEIR) of the gamma rays of interest is fundamental to many NDA procedures. The assayist must determine

$$\text{FEIR} = \frac{A(\gamma)}{TT}\text{CF(RL)} \tag{5-63}$$

where $A(\gamma)$ = full-energy-peak area
TT = true time of acquisition
CF(RL) = rate-related loss correction factor.

Three classes of correction procedures are discussed in this section. For detecting pileup events, the first procedure uses fast-timing electronics to measure the intervals between pulses. Corrections are made by extending the count time or by adding counts to the spectrum during acquisition. The second procedure adds an artificial peak to the spectrum by connecting a pulser to the preamplifier. The third procedure uses a gamma-ray source to generate the correction peak. The second and third procedures both use the variation in the correction-peak area to calculate a correction factor.

All three methods require the assumption that all peaks suffer the same fractional loss from the combined effects of pileup and deadtime; in general, the assumption is good.

5.4.5 Pileup Correction Methods: Electronic

Methods that extend count time employ fast counting circuits that operate directly from the preamplifier output; the time constants involved allow a pulse-pair resolution of 0.5 to 1.0 μs. The time resolution is achieved at the sacrifice of energy resolution so that some small pulses analyzed by the ADC are lost to the timing circuitry. The circuitry can neither detect nor correct for pileup events where the interval is less than the circuit resolving time or where one of the events is below the detection threshold. When two or more pulses are closer together than the chosen pileup rejection interval, the distorted event is not stored and the count time is extended to compensate for the loss.

One method of extending the count time is to generate a deadtime interval that begins when a pileup event is detected and ends when the next good event has been processed and stored; this procedure is approximately correct. The procedure cannot compensate for undetected events; however, with a typical rejection-gate period of 20 μs and a pulse-pair resolving time of $\sim$1 μs, the correction error may be only a few percent. For rates up to several tens of thousands of counts per second, the

total error may be only 1% or less; the necessary circuitry is frequently built into spectroscopy amplifiers. The method requires live-time operation, so the assay period is not known a priori. The method also requires that the count rate and spectral shape are constant during the counting period; this limitation is of no consequence for the assay of long-lived isotopes, but it is important in activation analysis of very short lived isotopes.

In recent years, the activation analysis requirement to handle high count rates and rapidly changing spectral shapes has led to further advancement in deadtime-pileup corrections. Such systems are complex and are just now becoming commercially available. They can handle input rates of hundreds of thousands of counts per second and accurately correct for losses in excess of 90%. The ability to correct for deadtime-pileup losses at high rates can potentially improve the speed of some NDA procedures.

5.4.6 Pulser-Based Corrections For Deadtime and Pileup

The pulser method uses a pulser to insert an artificial peak into the stored spectrum; it has numerous variations depending on the type of pulser used. Most germanium and silicon detector preamplifiers have a TEST input through which appropriately shaped pulses can be injected. These pulses suffer essentially the same deadtime and pileup losses as gamma-ray pulses and form a peak similar to a gamma-ray peak. The pulser peak has better resolution and shape than gamma-ray peaks because it is not broadened by the statistical processes involved in the gamma-ray detection process. The pulser peak area is determined in the same way as a gamma-ray peak area. The number of pulses injected into the preamplifier is easily determined by direct counting or by knowing the pulser rate and the acquisition time.

An advantage of the pulser method is that the artificial peak can usually be placed to avoid interference from gamma-ray peaks. In addition, because all the pulser events are full energy, minimum extra deadtime and pileup are generated. On the other hand, it is difficult to find pulsers with adequate amplitude stability, pulse-shaping capability, and rate flexibility.

Another common problem is the difficulty of injecting pulses through the preamplifier without some undershoot on the output pulse. A long undershoot is objectionable because gamma-ray pulses can pile up on the undershoot like they do on the positive part of the pulse. The amplifier pole zero cannot compensate simultaneously for the different decay constants of the pulser and gamma-ray pulses, and compensation networks are rarely used at the TEST input because of probable deterioration in resolution. The undershoot problem can be minimized by using a long decay time on the pulser pulse (often as long as a millisecond), by using shorter amplifier time constants, and by using high baseline-restorer settings. Some sacrifice of overall resolution is usually required to adequately minimize the undershoot problem.

The simplest approach is to use an ordinary fixed-period pulser, in which the interval between pulses is constant and equal to the reciprocal of the pulse rate. The best amplitude stability comes from the mercury-switch pulser in which a capacitor is charged and discharged through a resistor network by a mercury-wetted mechanical switch. The mechanical switch limits the useful rate of such pulsers to $\leq$100 Hz.

Assuming that the pulser peak and gamma-ray peaks lose the same fraction of events from deadtime and pileup, the appropriate correction factor is

$$CF(RL) = N/A(P) \tag{5-64}$$

where N = number (rate) of pulses injected
A(P) = area (area rate) of pulser peak.

CF(RL) has a minimum value of 1.00 and is the reciprocal of the fraction of events stored in the peaks.

Equation 5-64 is not quite correct because pulser pulses are never lost as a result of their own deadtime, nor do they pileup on one another. Thus the overall losses from gamma-ray peaks are greater than those from the pulser peak although the difference is usually small. At moderate rates, the deadtime and pileup losses are nearly independent and CF(RL) can be corrected with two multiplicative factors to obtain a more accurate result:

$$CF(RL) = \frac{N}{A(P)}(1 + RT_D)(1 + RT) \tag{5-65}$$

where R = pulser rate
T_D = deadtime for pulser pulse
T = pileup interval.

The deadtime T_D can be adequately estimated from the speed of the ADC and, for Wilkinson ADCs, from the position of the pulser peak. The interval T is usually one and one-half to two times the pulse width. If R is $\leq$100 Hz, both factors are usually small. Assuming a typical value of 20 μs for both T_D and T, the value of each additional factor is 1.002 so that the increase in CF(RL) is only ~0.4%. Larger corrections result if greater values of R, T_D, or T are used. If R is increased to 1000 Hz to obtain high precision more quickly, the additional factors make a difference of several percent.

Concern about assay precision brings up a rather curious but useful property of periodic pulsers. The precision of the pulser peak is given by a different relation than that of gamma-ray peaks. The precision of a pulser peak is, in fact, always better than the precision of a gamma-ray peak of the same area because gamma-ray emission

is random and the generation of pulser pulses is not. The precision of gamma-ray peak areas is governed by Poisson statistics whereas the precision of pulser peaks is governed mostly by binomial statistics.

Assuming that the background under the pulser peak is negligible and that the peak area is P, the variance and relative variance of P are given by

$$S^2(P) = P\,(1 - P/N)$$
$$S_r^2(P) = \frac{1}{P}\,(1 - P/N) \tag{5-66}$$

where N is the total number of pulses injected into the spectrum. Assuming again that the Compton continuum is negligible, the variance and relative variance of a gamma-ray peak of area A are given by

$$S^2(A) = A$$
$$S_r^2(A) = 1/A\,. \tag{5-67}$$

Figure 5.17 gives $S_r(P)$ versus P for several choices of P/N and demonstrates that by the time $P/N \approx 0.5$ the improvement in precision is quite negligible.

When the pulser peak rests on a significant continuum, the expressions for S(P) are more complex because of the random nature of the continuum. The pulser peak

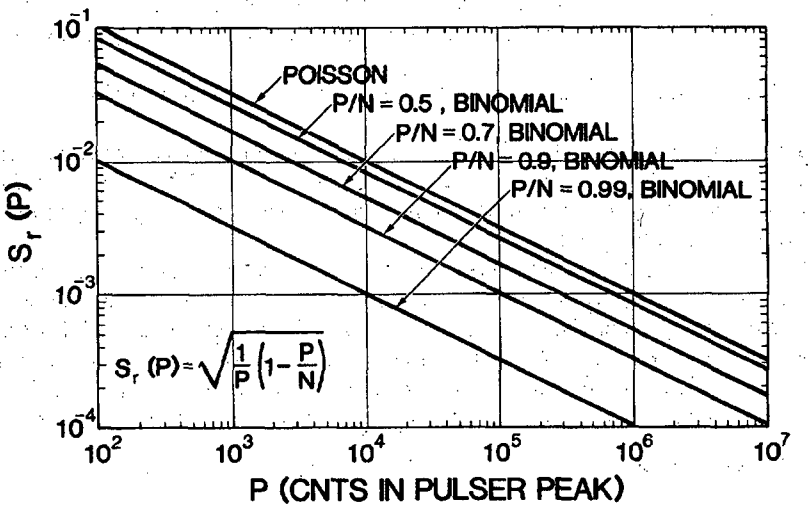

Fig. 5.17 *The relative standard deviation $S_r(P)$ of a pulser peak area P as a function of P for several values of P/N where N is the total number of pulses injected into the spectrum.*

should be placed in a low-continuum (usually high-energy) portion of the spectrum so that the improved precision can be taken advantage of and the simple Equation 5-66 can be used.

The use of a high-energy pulser peak can complicate the minimization of the undershoot. An alternative approach is to use a rectangular pulse that is longer than the amplifier output; then the pole-zero problem disappears and there are no shallow undershoots. Instead, a negative pulse is generated as the pulser output drops. Other events pile up on the negative pulse, but the pulse is cleanly defined and tends to throw pileup events out of their peak. The additional factor for the pileup losses can be written as (1 + 2RT).

If an adequate random pulser were available, CF(RL) would be given simply by Equation 5-64. Unfortunately, although random pulsers have been used successfully in research laboratories, no adequate unit is commercially available. It is difficult to simultaneously achieve the desired amplitude stability, random-interval distribution, and constant average rate required for routine gamma-ray assay applications.

Pulser-based deadtime-pileup corrections are accurate only when both rate and spectral shape are constant throughout the counting period. When the count rate changes during a measurement, proper corrections cannot be made if the pulser operates at a fixed rate. In principle, a correction can be made using a pulser that operates at a rate that is a fixed function of the gross detector rate. Pulsers based on this concept have been built and used successfully (Ref. 14). They are used in activation analysis, half-life studies, accelerator experiments, and anywhere that variable rates with constant spectral shape might be encountered. The use of variable rate pulsers indicates the variety and ingenuity with which the fundamental idea of inserting a synthetic peak into a spectrum has been applied to the problem of deadtime-pileup corrections.

5.4.7 Reference-Source Method for Deadtime-Pileup Corrections

The most accurate method for measuring the deadtime-pileup correction uses a reference source fixed in position relative to the detector. The source provides a constant gamma-ray interaction rate in the detector. The reference peak performs the same function as the pulser peak.

Like the other methods, the reference-source method requires the assumption that all peaks suffer the same fractional loss from deadtime and pileup. Given this assumption, the ratio of any peak area to the reference peak area is independent of such losses. Let $A(\gamma)$ and $FEIR(\gamma)$ represent, as usual, the full-energy-peak area and the full-energy interaction rate of any gamma ray other than the reference gamma ray R. If F is the common fraction stored and TT is the true acquisition time, then the areas are

$$\begin{aligned} A(\gamma) &= F \times FEIR(\gamma) \times TT \\ A(R) &= F \times FEIR(R) \times TT \,. \end{aligned} \tag{5-68}$$

The ratio of the two expressions gives

$$A(\gamma)/A(R) = FEIR(\gamma)/FEIR(R) \tag{5-69}$$

which is independent of both F and TT. Gamma-ray assays often are based directly on the loss-independent ratios $A(\gamma)/A(R)$ without ever explicitly determining CF(RL) or $FEIR(\gamma)$.

For the reference-source gamma ray, the correction factor becomes

$$CF(RL) = FEIR(R) \times TT/A(R) . \tag{5-70}$$

Combining this expression with Equation 5-63 gives

$$FEIR(\gamma) = \frac{A(\gamma)}{A(R)} FEIR(R) \tag{5-71}$$

which is independent of count time. Equation 5-55 for the corrected count rate CR can now be rewritten

$$\begin{aligned} CR(\gamma) &= FEIR(\gamma) \times CF(AT) \\ &= \frac{A(\gamma)}{A(R)} FEIR(R) \times CF(AT) . \end{aligned} \tag{5-72}$$

The magnitude of $CR(\gamma)$ does not depend on the true acquisition time although its precision obviously does.

If assay systems are calibrated with the help of standards, it is unnecessary to know FEIR(R) to obtain accurate assay values. In many assay procedures, the quantity sought, M (isotope or element mass), is proportional to $CR(\gamma)$. In Equation 5-73 through 5-75, K is the calibration constant, the subscript s denotes quantities pertaining to standards, and the subscript u denotes quantities pertaining to unknowns.

$$M_u = \frac{CR(\gamma)_u}{K} = \frac{[A(\gamma)_u/A(R)_u]FEIR(R) \times CF(AT)_u}{K} \tag{5-73}$$

The calibration constant can be determined from a single standard:

$$K = \frac{CR(\gamma)_s}{M_s} = \frac{[A(\gamma)_s/A(R)_s]FEIR(R) \times CF(AT)_u}{M_s} \tag{5-74}$$

Combining Equations 5-73 and 5-74 gives

$$M_u = \frac{[A(\gamma)_u/A(R)_u]CF(AT)_u}{[A(\gamma)_s/A(R)_s]CF(AT)_s} M_s \tag{5-75}$$

which is independent of FEIR(R).

Although an accurate value of FEIR(R) is not needed, it is useful in obtaining approximate values of FEIR(γ), FEIR(R), and CF(RL) so that actual rates of data acquisition are known along with the fraction of information being lost to deadtime and pileup. Having a calibration constant expressed as corrected counts per second per unit mass can be helpful when estimating required assay times.

A reasonably accurate value of FEIR(R) can be obtained by making a live-time count of the reference source alone and estimating a correction for the pileup losses. A more accurate value can be obtained by using a pulser to correct for deadtime-pileup losses.

The reference-source method can be applied to any spectroscopy system without additional electronics. The method avoids problems caused by injecting pulser pulses into a preamplifier and by drift of the reference peak relative to the gamma-ray peaks. It also avoids the extra corrections required by a fixed-period pulser. Additionally, no error occurs because of the finite pulse-pair resolving time, and the reference peak is constantly present for digital stabilization and for checking system performance.

The most significant limitation to the procedure is that a reference source with appropriate half-life and energy is not always available. An additional limitation is that the reference source must have a significant count rate and this causes additional losses and results in poorer overall precision than that achievable using the same count time with other methods. The reference-source method, as well as the simpler pulser method, is only applicable when the count rate and spectral shape are constant.

The reference source should have a long half-life and an intense gamma ray in a clear portion of the spectrum. The energy of the reference gamma ray should be lower than but relatively close to the energy of the assay gamma rays so as not to add to the background beneath the assay peaks. A monoenergetic reference source limits the increase in gross count rate and overall deadtime-pileup losses. Few sources meet all the desired criteria, but several have proven adequate in many applications.

For ^{239}Pu assays based on the 413.7-keV gamma ray, ^{133}Ba is the most useful source. Its 356.0-keV gamma ray does not suffer interference from any plutonium or americium gamma ray and it is within 60 keV of the assay energy. The 10.3-yr half-life is very convenient. Although ^{133}Ba has several other gamma rays, they are all at energies below 414 keV.

For plutonium assays that make use of lower energy gamma rays, ^{109}Cd is a useful reference source. The 88.0-keV gamma ray is its only significant emission except for the ~25-keV ^{109}Ag x rays from electron capture, which are easily eliminated by a thin filter. Its half-life of ~453 days is adequate to give a year or two of use before replacement. Although no interfering gamma rays from plutonium or americium isotopes are present, there is a possible interference from lead x rays fluoresced in the detector shielding. The lead K_{β_2} x ray falls almost directly under the 88.0-keV gamma ray from ^{109}Cd. Interference can be avoided by wrapping the detector in cadmium to absorb the lead x rays, and by using a sufficiently strong ^{109}Cd source that any residual leakage of lead x rays is overwhelmed. If some totally different

shielding material can be used (for example, iron or tungsten alloys), the problem disappears.

For assays of ^{235}U, the 122.0-keV gamma ray from ^{57}Co is used frequently. Its 271-day half-life is adequate, although not as long as might be desired. The 122.0-keV gamma ray is approximately eight times more intense than the 136.5-keV gamma ray, which is the only other gamma ray of significant intensity. Note that in using ^{57}Co for assay of highly enriched uranium samples, the 120.9-keV gamma ray from ^{234}U can be an annoying interference. This problem can be effectively eliminated by using a filter to reduce the intensity of lower energy emissions relative to the 185.7-keV intensity and a sufficiently strong ^{57}Co source to override any residual ^{234}U signal.

Frequently ^{241}Am can be used as a reference source for uranium or other assays. Although the 59.5-keV gamma ray from ^{241}Am is further removed from 186 keV than desirable, it can be used successfully, particularly if steps are taken to reduce the resolution difference. The half-life of 433.6 y is beyond fault. Americium-241 must be absolutely absent from any materials to be assayed. When using ^{169}Yb as a transmission source in densitometry or quantitative ^{235}U assay, ytterbium daughters emit x rays that directly interfere with the 59.5-keV gamma ray, but sufficient filtering combined with adequate source intensity can eliminate any possible difficulty.

The current methods for deadtime-pileup correction assume that all full-energy peaks suffer the same fractional loss. That assumption is not completely true primarily because the width and detailed peak shape are functions of both energy and count rate. In applying the reference-peak method, precautions can be taken to minimize the degree to which the assumption falls short. Four of those precautions, most of which apply to any of the correction methods, are listed below.

- Where possible, apply the procedure only over a narrow energy range.
- Keep the peak width and shape as constant as possible as functions of both energy and count rate, even if that slightly degrades the low-rate and low-energy resolution. Proper adjustment of the amplifier and the pileup rejection can help considerably.
- Avoid a convex or concave Compton continuum beneath important peaks, especially the reference peak. If possible the ratio of the reference peak area to the background area should be ≥ 10.
- Exercise great care in determining peak areas. ROI methods may be less sensitive than some of the spectral fitting codes to small changes in peak shape.

Experimental results indicate that the reference-source method can correct for deadtime and pileup losses with accuracies approaching 0.1% over a wide count-rate range. Such accuracies can also be approached by pulser methods, particularly at lower rates and by some purely electronic methods. However, equipment for the purely electronic methods is very sophisticated.

5.5 EFFECTS OF THE INVERSE-SQUARE LAW

The absolute full-energy detector efficiency varies approximately as the inverse square of the distance between the detector and gamma-ray source. Consider a point source emitting I gamma rays per second. The gamma-ray flux F at a distance R is defined as the number of gamma rays per second passing through a unit area on a sphere of radius R centered at the source. Because the area of the sphere is $4\pi R^2$, the expression for F is

$$F = \frac{I}{4\pi R^2} . \tag{5-76}$$

The detector count rate is proportional to the incident flux, and if the detector face can be approximated by a portion of a spherical surface centered at the source, the count rate has the same $1/R^2$ dependency as the flux. When low-intensity samples are counted, there is a clear motivation to reduce the sample-to-detector distance and increase the count rate. Unfortunately, when the sample-to-detector distance is so small that different parts of the sample have significantly different distances to the detector, the count rates from different parts of the sample vary significantly. This variation can cause an assay error when the distribution of emitting material is nonuniform.

The overall count rate from samples of finite extent does not follow the simple law; usually the variation is less strong than $1/R^2$. Knowledge of a few simple cases can help to estimate overall count rates and response uniformity.

The simplest extended source is a line, which is often an adequate model of a pipe carrying radioactive solutions. Consider an ideal point detector with intrinsic efficiency ε at a distance D from an infinitely long source of intensity I per unit length (Figure 5.18). The count rate from this source can be expressed as

$$CR = 2\int_0^\infty \frac{I\varepsilon \, dr}{r^2 + D^2} = \frac{\pi I \varepsilon}{D} . \tag{5-77}$$

In this ideal case, the count-rate dependence is $1/R$ rather than $1/R^2$; when pipes are counted at distances much smaller than their length, the count-rate variation will be approximately $1/R$.

The count rate from a point detector at a distance R from an infinite plane surface does not depend on R at all. For a detector near a uniformly contaminated glovebox wall, count rates vary little with wall-to-detector distance changes.

When possible the variation of response with position inside a sample should be minimized. The sample-to-detector distance can be increased, but the penalty is a severe loss of count rate. A better strategy is to rotate the sample. Consider the cross section of a cylindrical sample of radius R whose center is at a distance D from a detector (Figure 5.19). Unless D is much greater than R, the count rates for identical sources at positions 1, 2, 3, and 4 vary considerably. The figure shows that if D = 3R, the maximum count-rate ratio is CR(2)/CR(4) = 4. The ratio of the response of a rotating source at radius R to the response at the center (position 1 of Figure 5.19) is

$$\frac{CR(R)}{CR(1)} = \frac{1}{1 + (R/D)^2} . \tag{5-78}$$

The response is the same as that obtained for a uniform nonattenuating circular source of radius R whose center is at a distance D from a detector. Table 5-6 gives the value of this function for several values of R/D compared to CR(2)/CR(1) for the nonrotating source of Figure 5.19. For relatively large values of R/D, rotation improves the uniformity of response. The response variation is even larger when attenuation is considered. Rotation only reduces $1/R^2$ effects; it does not eliminate them completely.

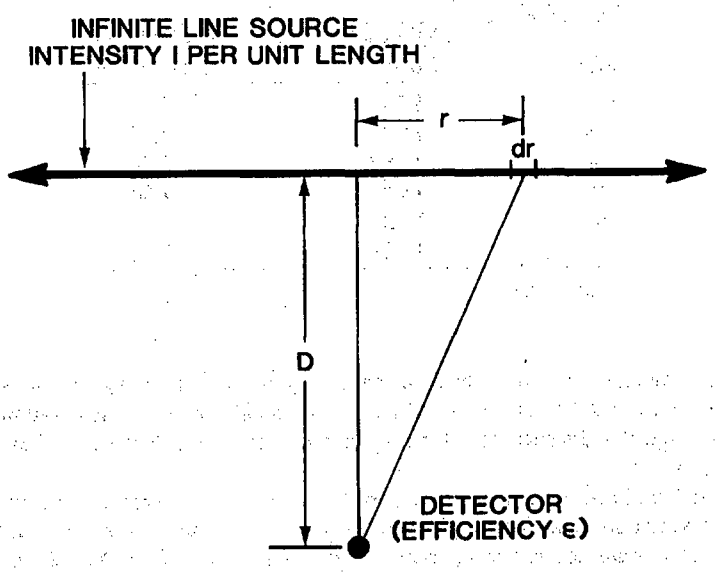

Fig. 5.18 Geometry for computing the response of a point detector to a line source.

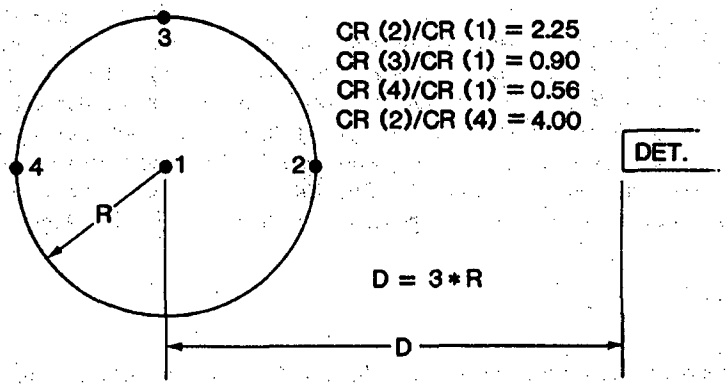

Fig. 5.19 Cross section through a cylindrical sample and a point detector showing how count rate varies with position.

Table 5-6. The effect of sample rotation on count-rate variation

R/D	CR(R)/CR(1) (Rotating)	CR(2)/CR(1) (Nonrotating)
1/2	1.33	4.0
1/3[a]	1.125	2.25
1/4	1.067	1.78
1/5	1.042	1.56
1/6	1.029	1.44
1/7	1.021	1.36

[a]See Figure 5.19.

Rotation reduces response variations caused by radial positioning, but does little to compensate for height variations. If the source height is less than one-third of the sample-to-detector distance, the decrease in response is less than 10% relative to the normal position.

The choice of sample-to-detector distance is a compromise between minimizing the response variations and maintaining an adequate count rate. A useful guideline is that the maximum count-rate variation is less than ±10% if the sample-to-detector distance is equal to three times the larger of the sample radius or the half-height. If a sample cannot be rotated, it helps considerably to count it in two positions 180° apart.

5.6 DETECTOR EFFICIENCY MEASUREMENTS

5.6.1 Absolute Full-Energy-Peak Efficiency

The absolute full-energy-peak efficiency is the fraction of gamma rays emitted by a point source at a particular source-to-detector distance that produces a full-energy interaction in the detector. It is determined as a function of energy by measuring the efficiency at a number of energies and fitting the experimental points with an appropriate function:

$$\varepsilon_A(\gamma) = \text{FEIR}(\gamma)/\text{ER}(\gamma) \tag{5-79}$$

where ε_A = absolute full-energy efficiency
ER(γ) = gamma-ray emission rate.

The determination of FEIR is described in Section 5.4. For high-resolution detectors, care must be taken to correct for pileup and deadtime losses. For low-resolution scintillators, the pileup correction can usually be ignored.

Calibrated sources for absolute calibrations are available from a number of vendors. It is a testimony to the difficulty of measuring accurate emission rates that the quoted accuracies are only between 0.5% and 2.0%. Table 5-1 lists several monoenergetic gamma-ray sources. Multi-isotope, multi-gamma-ray sources, such as the NBS source SRM-4275 (see Section 5.1.1), are convenient when calibrating high-resolution detectors. This source is useful for several years and covers the energy range most often of use in NDA.

Frequently two or more gamma rays are emitted in successive transitions between energy levels of a single excited nucleus. Because the time interval between such cascade gamma rays is very small compared to the charge collection times of germanium, silicon, or NaI(Tl) detectors, the multiple gamma rays are treated as a single interaction. This cascade summing can result in subtractive or additive errors in the measured FEIRs. The problem is significant when the source is so close to the detector that the probability of detecting two or more cascade gamma rays simultaneously is large. If very short source-to-detector distances must be used to enhance sensitivity, cascade-summing problems must be carefully considered. The notes accompanying SRM-4275 contain a good discussion of summing problems as well as other possible difficulties involved in the use of multi-gamma-ray sources.

5.6.2 Intrinsic Full-Energy Efficiency

The intrinsic full-energy efficiency is the probability that a gamma ray loses all of its energy if it enters the detector volume. The absolute full-energy efficiency ε_A and the intrinsic full-energy efficiency ε_I are related by the simple equation

$$\varepsilon_A = \frac{\Omega}{4\pi}\,\varepsilon_I \tag{5-80}$$

where Ω is the solid angle subtended by the detector at the source and $\Omega/4\pi$ is the probability that a gamma ray will enter the detector volume. The intrinsic full-energy efficiency is determined experimentally by measuring the absolute full-energy efficiency and solving Equation 5-80 for ε_I. The values of ε_I computed will depend slightly upon the position of the source with respect to the detector.

Some care is necessary in estimating the solid angle Ω, especially if the detector has an odd shape or is not located on an axis of symmetry. Figure 5.20 shows a point source at a distance D from the face of a cylindrical detector of radius R. The correct expression for the solid angle subtended by the detector at the source is

$$\Omega = 2\pi\left[1 - \left(\frac{D}{\sqrt{D^2 + R^2}}\right)\right] \tag{5-81}$$

where $D/\sqrt{D^2 + R^2} = \text{Cos}\ \Theta$, with Θ being the angle of the solid-angle cone shown in Figure 5.20. However, for a circular detector, an approximate expression is frequently used:

$$\Omega \approx A/D^2 = \pi R^2/D^2 \tag{5-82}$$

where A is the area of the detector face. The first expression in Equation 5-82 can be applied even when the detector is not circular, but is only accurate when A is much less than $4\pi D^2$. Comparing Equations 5-81 and 5-82 shows that as D decreases relative to R, the value for Ω from Equation 5-82 becomes too large. For D/R = 8, Ω is ~1% too large; for D/R = 1, Ω is ~70% too large.

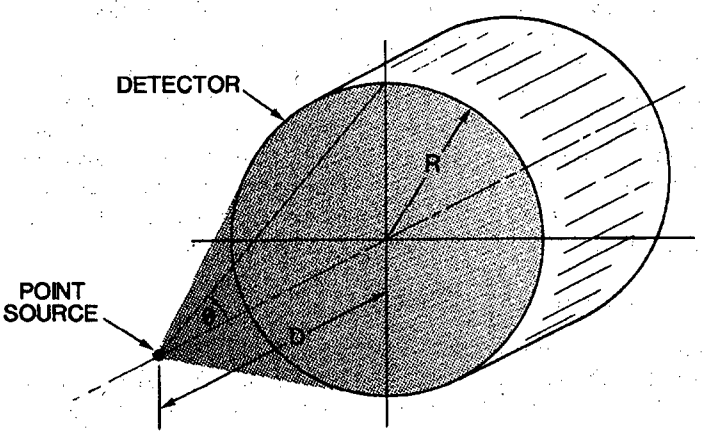

Fig. 5.20 A point source on the axis of a cylindrical detector.

5.6.3 Relative Efficiency

Frequently the actual values of the absolute or intrinsic full-energy-peak efficiency are not needed, and only the ratios of the efficiency at different energies are required. A relative efficiency curve is usually easier to determine than absolute or intrinsic efficiencies. Relative efficiencies differ from absolute or intrinsic efficiencies only by a multiplicative constant that depends upon the procedure used in determining the relative efficiencies. Exact gamma-ray emission rates are not required, only values proportional to the emission rates. When a single multienergy isotope is used, the branching fractions provide the necessary information (Ref. 15). Equation 5-79 can be modified to give relative efficiencies for a single source:

$$\varepsilon_R = A(\gamma)/B(\gamma) \tag{5-83}$$

where $B(\gamma)$ is the branching ratio corresponding to the peak area $A(\gamma)$. Usually relative-efficiency curves are normalized to 1.00 at some convenient energy. A semilog plot of relative efficiency has the same shape as the corresponding absolute-efficiency or intrinsic-efficiency plot. Figure 5.21 shows the relative-efficiency of a coaxial detector as derived from a single spectrum of a thin ^{133}Ba source. Note that sources with negligible self-attenuation must be used when the branching fractions are assumed to be proportional to the rates of gamma rays escaping from the source. This assumption is not true for many steel-encapsulated sources particularly at lower energies.

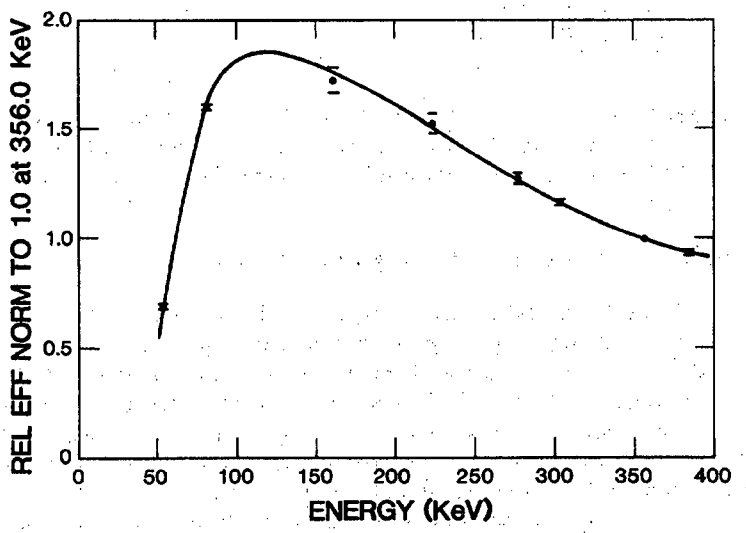

Fig. 5.21 Relative efficiency of a 30%-efficient coaxial germanium detector between ~50 and ~400 keV, as derived from a single spectrum of a thin ^{133}Ba source.

5.6.4 Efficiency Relative to a 7.65-cm by 7.65-cm NaI(Tl) Detector

The manufacturers of germanium detectors usually characterize the efficiency of coaxial detectors by comparing it to the absolute full-energy efficiency of a 7.65-cm by 7.65-cm NaI(Tl) detector. The comparison is always made at 1332.5 keV with a source-to-detector distance of 25.0 cm and the efficiency expressed as a percentage of the NaI(Tl) efficiency. The efficiency of the germanium detector is measured and the absolute full-energy efficiency of the NaI(Tl) detector is assumed to be 0.0012 for the stated energy and distance. The expression for computing the measured germanium-detector efficiency is

$$\varepsilon_{RNaI} = \left[\frac{\text{FEIR}(1332.5)/\text{ER}(1332.5)}{0.0012}\right] 100 \tag{5-84}$$

where FEIR(1332.5) includes corrections for deadtime-pileup losses and ER(1332.5) is the current emission rate. The source-to-detector distance is very difficult to determine accurately because the detector crystal is hidden inside the cryostat end cap. Because the front face of the detector crystal is mounted within 5 mm of the end cap by most manufacturers, the measurement is made at a source-to-end-cap distance of 24.5 cm.

If a 60-Hz pulser is used for the rate-related losses, Equation 5-84 can be rewritten as

$$\varepsilon_{RNaI} = \frac{135.1\ \text{A}(1332.5)}{\text{A(p)}I_0 \exp(-0.1318\text{T})} \tag{5-85}$$

where A(1332.5) and A(p) are the areas of the 1332.5-keV and pulser peaks, and where T is the time in years since the ^{60}Co source had an activity of I_0 microcuries. If the same ^{60}Co source is used consistently, the value of I_0 can be absorbed in the numerical constant.

5.6.5 Efficiency as Function of Energy and Position

Usually NDA calibrations are done using standards that contain known amounts of the isotopes of interest in packages of appropriate shape and size. Because approximate detector efficiencies are used only to estimate expected count rates, there is little need to carefully characterize efficiency as a function of energy and position. A detector so characterized can assay without the use of standards, although generally not with the same ease and accuracy as possible with them. When standards are not available or allowed in an area, verification measurements can be made of items of known geometry and content using the known detector efficiency to predict the FEIRs for a chosen detector-sample configuration. If the measured FEIRs agree within the estimated error with the predicted rates, the item content is regarded as verified.

In constructing appropriate efficiency functions, the absolute efficiency is measured for many energies and positions and then fit to an adequate mathematical model. Cline's method (Ref. 16) combines reasonable accuracy with a straightforward procedure for determining the efficiency parameters. To characterize a detector accurately takes several days or more.

REFERENCES

1. R. Gunnink, J. E. Evans, and A. L. Prindle, "A Reevaluation of the Gamma-Ray Energies and Absolute Branching Intensities of ^{237}U, ^{283,239,240,241}Pu, and ^{241}Am," Lawrence Livermore Laboratory report UCRL-52139 (1976).

2. M. E. Anderson and J. F. Lemming, "Selected Measurement Data for Plutonium and Uranium," Mound Laboratory report MLM-3009 (1982).

3. *Table of Isotopes*, 7th ed., C. M. Lederer and V. S. Shirley, Eds. (John Wiley & Sons, Inc., New York, 1978).

4. R. D. Evans, *The Atomic Nucleus* (McGraw-Hill Book Co., New York, 1955), Chapters 23–25.

5. P. R. Bevington, *Data Reduction and Error Analysis for the Physical Sciences* (McGraw-Hill Book Co., New York, 1969).

6. Y. Beers, *Introduction to the Theory of Error* (Addison-Wesley Publishing Co., Inc., Reading, Massachusetts, 1962).

7. T. Mukoyama, "Fitting of Gaussian to Peaks by Non-Iterative Method," *Nuclear Instrument and Methods* 125, 289–291 (1975).

8. S. L. Meyer, *Data Analysis for Scientists and Engineers* (John Wiley & Sons, Inc., New York, 1975), p. 37.

9. R. B. Walton, E. I. Whitted, and R. A. Forster, "Gamma-Ray Assay of Low-Enriched Uranium Waste," *Nuclear Technology* 24, 81–92 (1974).

10. R. Gunnink, "Computer Techniques for Analysis of Gamma-Ray Spectra," Lawrence Livermore Laboratory report UCRL-80297 (1978).

11. R. G. Helmer and M. A. Lee, "Analytical Functions for Fitting Peaks From Ge Semiconductor Detectors," *Nuclear Instruments and Methods* 178, 499–512 (1980).

12. G. K. Knoll, *Radiation Detection and Measurement* (John Wiley & Sons, Inc., New York, 1979).

13. J. G. Fleissner, C. P. Oertel, and A. G. Garrett, "A High Count Rate Gamma-Ray Spectrometer System for Plutonium Isotopic Measurements," *Journal of the Institute of Nuclear Materials Management* 14, 45–56 (1986).

14. H. H. Bolotin, M. G. Strauss, and D. A. McClure, "Simple Technique for Precise Determination of Counting Losses in Nuclear Pulse Processing Systems," *Nuclear Instruments and Methods* 83 1–12 (1970).

15. R. A. Meyer, "Multigamma-Ray Calibration Sources," Lawrence Livermore Laboratory report M-100 (1978).

16. J. E. Cline, "A Technique of Gamma-Ray Detector Absolute Efficiency Calibration for Extended Sources," Proc. American Nuclear Society Topical Conference on Computers in Activation Analysis and Gamma-Ray Spectroscopy, Mayaguez, Puerto Rico (1978), pp. 185–196 (Conf. 780421).

6

Attenuation Correction Procedures

Jack L. Parker

6.1 INTRODUCTION

The nondestructive assay (NDA) of nuclear material must deal with large sample sizes and high self-absorption. Typical containers range from 2-L bottles to 220-L drums, and even a small sample with a high concentration of nuclear material has significant self-attenuation. Although gamma-ray self-attenuation may frequently be ignored in the filter papers or small vials encountered in radiochemical applications, it usually cannot be ignored in NDA measurements of nuclear material.

Because the size and shape of nuclear material samples vary widely, it is difficult to construct appropriate calibration standards. In principle, calibration standards are not needed if the detector efficiency is accurately known as a function of source position and energy, if the counting geometry and the sample size and shape are accurately known, and if the gamma-ray emission rates are accurately known. However, it is tedious to characterize a detector efficiency with sufficient accuracy, and there are still significant uncertainties in the values of the specific activities for many important gamma rays. The use of calibration standards reduces or eliminates the need to accurately know the detector efficiency, the counting geometry, and the specific activities.

The most authoritative guide for calibrating NDA systems, ANSI N15.20-1975 (Ref. 1), rather firmly insists that a calibration standard is "an item physically and chemically similar to the items to be assayed," a restriction no longer necessary for gamma-ray assay. The guide also insists that calibration standards "must be chosen so that their contained masses of the nuclide(s) of interest span the mass range expected for the items to be assayed." This restriction may be considerably relaxed. Relatively few standards are usually needed to calibrate gamma-ray assay systems for the accurate assay of items covering a wide range of size, shape, chemical composition, and mass.

Sections 6.2 to 6.6 describe the nature and computation of the attenuation correction factor CF(AT). A more detailed discussion of this subject is given in Ref. 2. Section 6.7 discusses calibration standards and Section 6.8 describes assay systems using transmission-corrected procedures.

6.2 PROCEDURES

6.2.1 Preliminary Remarks

The procedures and methods described herein are best applied with high-resolution gamma-ray detectors. The methods and correction factors may be used for assays with low-resolution detectors, but additional care must be exercised to avoid unnecessary error, and the ultimate accuracy will be not be as good.

The most unpleasant and important fact in applying gamma-ray spectroscopy is that the raw count rate for a given gamma ray is not usually proportional to the amount of the nuclide emitting the gamma ray. Two reasons for the lack of proportionality are the rate-related electronic processes of deadtime and pulse pileup and the self-attenuation of the sample. Accurate gamma-ray assays demand accurate corrections for both the electronic losses and the losses caused by sample self-attenuation. Corrections for electronic losses are described in detail in Chapter 5.

6.2.2 General Description of Assay Procedure

If the raw data-acquisition rate is multiplied by appropriate correction factors for both the rate-related electronic losses and the sample self-attenuation, we may write (as in Equation 5-60 of Section 5.4)

$$CR = RR \times CF(RL) \times CF(AT)$$

or

$$CR = FEIR \times CF(AT) \tag{6-1}$$

where CR = total corrected rate
RR = raw rate of data acquisition
CF(RL) = correction factor for rate-related electronic losses
CF(AT) = correction factor for self-attenuation in sample
FEIR = full-energy interaction rate.

If the correction factors are properly defined and computed, CR is the data-acquisition rate that would have been observed if there were no electronic losses and if the sample were changed to a simpler shape (such as a point or line) with no self-attenuation. Thus computed, CR is proportional to the mass of the isotope emitting the gamma ray of interest. We can then write

$$CR = K \times M \tag{6-2}$$

where M is the mass of the isotope being assayed and K is a calibration constant. The calibration constant K is determined by the use of appropriate standards and includes

the effects of detector efficiency, subtended solid angles, and gamma-ray emission rates. The CF(AT) is determined so that the CRs for both unknown and standard are those that would have been observed if they had had the same nonattenuating spatial configuration.

The above, in essence, constitutes a general approach to passive gamma-ray assay. The individual steps of this approach are

(1) Measure the raw data-acquisition rate.
(2) Determine the correction for rate-related electronic losses.
(3) Determine the correction for gamma-ray self-attenuation.
(4) Compute the total corrected rate, which is proportional to the mass of the isotope being assayed.
(5) Determine the constant of proportionality, the calibration constant, by use of appropriate physical standards, making sure that the CR for both standards and unknowns represents the same nonattenuating geometrical shape in the same position with respect to the detector.

Both RR and CF(RL) are relatively easy to determine accurately and are discussed in detail in Chapter 5.

6.2.3 Necessary Assumptions for Determining the Self-Attenuation Correction Factor

In determining CF(AT), the basic question is, what fraction of the gamma rays of interest that are emitted in directions such that they could reach the detector actually do reach the detector? If the sample material can be characterized by a single linear attenuation coefficient μ_ℓ, the fraction of gamma rays that escape unmodified from the sample can, in general, be computed. Determining μ_ℓ is the key to determining CF(AT).

Two assumptions seem adequate to permit accurate gamma-ray assays:

- The mixture of gamma-ray-emitting material and matrix material is reasonably uniform and homogeneous in composition and density.
- The gamma-ray-emitting particles are small enough that the self-attenuation within the individual particles is negligible.

These assumptions guarantee that the linear attenuation coefficient is single-valued on a sufficiently macroscopic scale that it can be used to accurately compute the gamma-ray-escape fraction. There are no restrictions on the chemical composition of the sample. All that is required is that μ_ℓ can be computed or measured. Unknown samples need not have the same or even similar chemical compositions as the calibration standards. There are also no basic assumptions about the size and shape of standards, although there are limitations.

The assumption of "reasonable" uniformity is admittedly vague and difficult to define. What constitutes reasonable uniformity depends on the gamma-ray energy, the chemical composition of the sample, and the accuracy required. Some sample types almost always satisfy the assumptions and some almost never do so.

The mass attenuation coefficients μ (Chapter 2) of the elements impose the fundamental restrictions on the size, shape, composition, and density of samples that can be successfully assayed by gamma-ray methods. Figure 6.1 shows mass attenuation coefficients for selected elements ranging from hydrogen (Z = 1) to plutonium (Z = 94). Qualitatively, the information in the graph defines nearly all the possibilities and limitations of passive gamma-ray NDA. Note that μ for uranium at 185.7 keV is nearly six times larger than that for plutonium at 413.7 keV. This means that the assay of ^{235}U by its 185.7-keV gamma ray is subject to considerably more stringent limitations on sample size, particle size, and uniformity than is the assay of ^{239}Pu

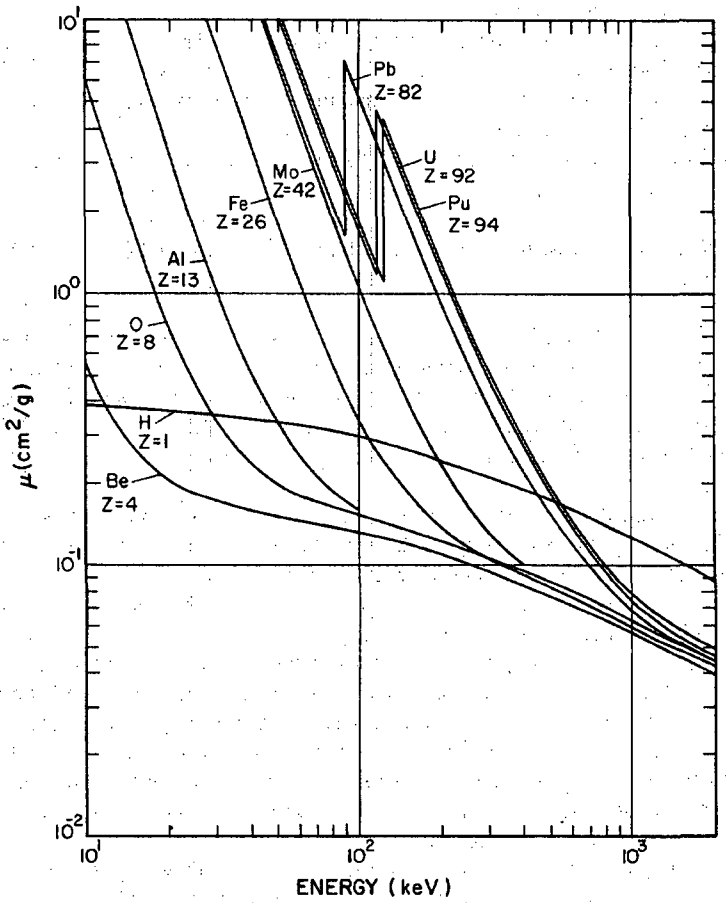

Fig. 6.1 Total mass attenuation coefficients (without coherent scattering contribution) vs energy for nine elements ranging in atomic number Z from 1 to 94 (Ref. 3).

by its 413.7-keV gamma ray. Below ~80 keV, the μ of most elements rises rapidly, making attenuation problems unmanageably severe for all but small samples of very small particle size.

Figure 6.2 is given as an aid in estimating self-attenuation for individual particles.* It gives the fraction of gamma rays escaping unscattered from spherical sources as a function of the product $\mu\rho$D, where D is the diameter of the sphere. As an example, for a 200-μm-diameter, ρ = 10 g/cm^3 particle of UO_2, $\mu\rho D \simeq 0.28$, indicating that ~10% of the 185.7-keV gamma rays emitted are scattered with some energy loss or are completely absorbed within the particle.

Solutions meet the criteria for accurate gamma-ray assay, assuming that there are no contained particulates or precipitates. Pure powders (PuO_2, UO_2, U_3O_8, and so forth) almost always are suitable, as are certain well-mixed scrap materials such as incinerator ash. High-temperature gas reactor (HTGR) coated fuel particles and HTGR-type rods come close to meeting the requirements, but assay results are low by 5 to 10% unless correction is made for the self-attenuation in the particle kernels (Ref. 5). Small quantities of high-Z gamma emitters (<10 g) mixed with low-Z,

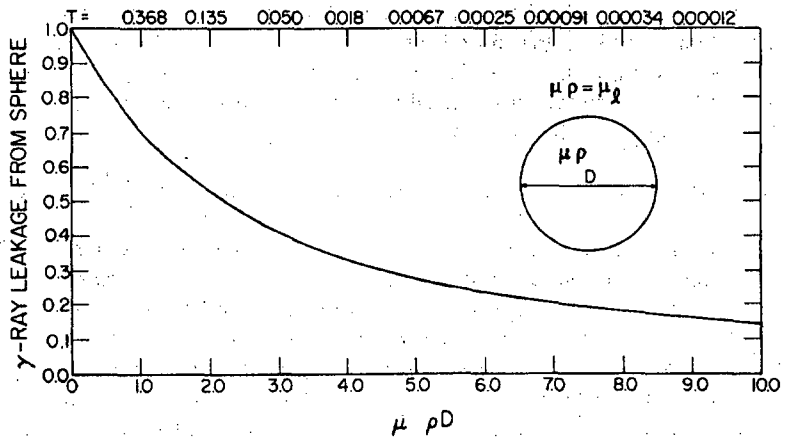

***Fig. 6.2** Fraction of gamma rays escaping unscattered and unabsorbed from spherical sources as a function of $\mu\rho$D. Coherent (elastic) scattering has been neglected.*

* The expression for the fraction of gamma rays escaping unscattered and unabsorbed from a sphere whose attenuation properties are characterized by $X = \mu\rho D$ is given by

$$F = \frac{3}{2X}\left[1 - \frac{2}{X^2} + \exp(-X)\left(\frac{2}{X} + \frac{2}{X^2}\right)\right].$$

For proof of this expression, see Ref. 4.

low-density combustibles may meet the requirement if there are no agglomerations of the powder with significant self-attenuation. Large quantities of high-Z powders (greater than about 100 g) will almost surely create some significantly attenuating agglomerations when mixed with such combustibles. Among the worst cases are metal chips of high-Z, high-density metals or fuel pellets mixed with low-Z, low-density matrices; in these situations assays may well be low by factors of 2 or 3 or even more. This fact causes one to be cautious about using gamma-ray methods to screen heterogeneous materials for possible criticality dangers.

It must be emphasized that the degree to which materials satisfy the two assumptions is the most important factor in determining the potential accuracy of a gamma-ray assay. Experience indicates, for example, that small samples of solution (up to a few tens of cubic centimeters) may be assayed with accuracies of a few tenths of a percent. Samples of uniform, homogeneous powders of volumes up to a few liters have been assayed with accuracies approaching 1% in spite of significant density gradients. Larger containers of waste (for example, 30-gal. drums) rarely satisfy the assumptions well enough to allow errors of $<10\%$, and the error will be much worse for the extremely heterogeneous cases.

Another important general fact about gamma-ray assay is that the results are almost always low when samples that do not satisfy the assumptions are assayed in conjunction with calibration standards that do satisfy the assumptions. The procedures that accurately determine the self-attenuation in acceptable samples underestimate the correction in samples that fail to satisfy the required conditions.

6.2.4 Methods for Determining the Sample Linear Attenuation Coefficient

Four principal methods have been employed to determine the sample μ_ℓ (Ref. 6). The oldest method avoids the issue by using representative standards. In this procedure a set of calibration standards are prepared as nearly identical as possible in size, shape, and composition to the unknowns. The standards are counted in a fixed geometry to prepare a calibration curve, and the assay is accomplished by counting the unknowns in the same geometry and comparing the count directly with the calibration curve. This procedure produces good results only if the unknowns and standards are sufficiently similar that the same concentration of assay material in each gives rise to the same μ_ℓ and, therefore, to the same CF(AT). The representative standard procedure also assumes that the pileup and deadtime losses are equal for equal concentrations of assay isotopes. This method is only applicable when the nature and composition of the assay samples are well known and essentially unvarying.

A second method exploits previous knowledge of the chemical composition, mass, and shape to compute μ_ℓ. Sufficient prior knowledge to compute the sample μ_ℓ does not necessarily mean that the assay result is known in advance. In many cases, μ_ℓ is almost purely dependent on the matrix composition and mass, which is reasonably well known. When only verification measurements are required on well-characterized materials, the approach is useful even when the assay material contributes significantly

to the sample self-attenuation. Computation of the sample μ_ℓ from knowledge of the chemical composition and densities is straightforward. References 3 and 7 tabulate the necessary mass attenuation coefficients.

Another method of determining CF(AT) involves measuring the intensity ratio of gamma rays of two different energies from the same isotope and comparing it with the same ratio from a thin source (negligible self-attenuation) containing the same isotope. This method is of limited use because, in general, μ_ℓ is not uniquely related to the measured intensity ratios. Some prior knowledge of the nature of the sample is also required to obtain the actual correction factors. Furthermore, not all isotopes have a pair of gamma rays of the appropriate energies. Nevertheless, the method has proved useful in specific cases and has the potential for giving warning when the assumptions on uniformity and particle size are grossly violated.

The fourth and most general method of obtaining μ_ℓ involves measuring the transmission through the sample of a beam of gamma rays from an external source. From the fundamental law of gamma-ray attenuation, the transmission is

$$T = \exp(-\mu_\ell x) \tag{6-3}$$

where x is the thickness of the sample. Solving for μ_ℓ, we obtain

$$\mu_\ell = \frac{-\ln(T)}{x}. \tag{6-4}$$

This method requires no knowledge of the chemical composition or density of the sample, just the basic assumptions on uniformity and particle size. In fact, it is often the preferred method even when some knowledge of the sample composition is available, particularly when the best obtainable accuracy is desired. The experimentally measured μ_ℓ includes all the effects of chemical composition and density.

The transmission method can identify those samples for which accurate quantitative assays are impossible because of excessive self-attenuation. As the measured transmission decreases, its precision deteriorates along with the precision of the sample μ_ℓ, thus creating error in the computed value of CF(AT). The precision and accuracy of the measured transmission become unacceptable for transmissions between 0.01 and 0.001. Transmission values $\leq$0.001 (perhaps even negative) almost always indicate an unassayable sample.

6.3 FORMAL DEFINITION OF CORRECTION FOR SELF-ATTENUATION

6.3.1 The General Definition

Expressions for CF(AT) can be formulated in a number of useful ways. The formulation adopted here is a multiplicative correction factor that gives a corrected count rate that is directly proportional to the quantity of isotope being measured. It is useful

to define CF(AT) with respect to a specified geometrical shape, which is often simpler than the actual shape.

$$\mathrm{CF(AT)} = \frac{\mathrm{FEIR}(\mu_\ell = 0;\ \text{Specified Shape})}{\mathrm{FEIR}(\mu_\ell \neq 0;\ \text{Real Shape})} \tag{6-5}$$

where $\mathrm{FEIR}(\mu_\ell = 0, \text{Specified Shape})$ = the FEIR that would have been measured if the sample were totally nonattenuating ($\mu_\ell = 0$) and if it were changed to the specified shape

$\mathrm{FEIR}(\mu_\ell \neq 0, \text{Real Shape})$ = the actual measured FEIR from the sample.

In practice, CF(AT) is not computed from Equation 6-5; it is determined from μ_ℓ, the geometrical configuration, and the position of the sample relative to the detector. Most often the expressions for CF(AT) are not integrable in terms of elementary functions, so numeric methods must be used.

Generally, the detector efficiency need not be known. Usually one can assume a point detector with equal efficiency for all angles of incidence, which considerably simplifies the computations. This assumption is usually good when the distance between sample and detector is at least several times the maximum dimension of either the detector or the sample. If the sample-to-detector distance must be kept small for reasons of efficiency and if the highest obtainable accuracy is required, the actual measured or calculated detector efficiency as a function of energy and position may be used. Cline (Ref. 8) describes a procedure for creating an efficiency function based on measurements of standard sources, which should be adequate for almost all requirements.

6.3.2 Useful Specified Shapes

The most useful specified shapes are

- the actual sample shape
- a point
- a line.

If one has many samples and standards of the same shape and size, then CF(AT) may be computed with respect to a nonattenuating sample of the same shape. When the sample is sufficiently uniform and homogeneous and of reasonable size, let the detector view the whole sample and use the CF(AT) computed with respect to a nonattenuating point. This allows the standards and the unknowns to be of different size, shape, and chemical composition. However, for such assays to be accurate, the entire contents must be reasonably well represented by a single μ_ℓ.

Samples often have vertical composition and density gradients, the natural consequence of filling relatively narrow containers from the top. The material tends to fall into the containers in layers. In such cases, a single μ_ℓ cannot adequately characterize the whole sample, but narrow layers or segments can be adequately characterized by

a single μ_ℓ value. The assay accuracy can be improved by using a segmented scan in which the detector views the sample through a collimator that defines relatively narrow horizontal segments in which μ_ℓ can be assumed constant. For such segmented scans, it is best to compute the CF(AT) with respect to a nonattenuating line along the axis of the containers. In this way, cylindrical samples may be accurately assayed with respect to standards of quite different diameters.

6.4 IMPORTANT PARAMETERS OF THE SELF-ATTENUATION CORRECTION FACTOR

The correction factor for self-attenuation, CF(AT), is a function of many parameters. Those currently recognized as significant are listed below in decreasing order of importance:

- the μ_ℓ of the sample material
- the volume and shape of the sample material
- the μ_ℓ of the sample container
- the size and shape of the sample container
- the position and orientation of the sample relative to the detector
- the size, shape, and efficiency of the detector.

In many situations the dependence of CF(AT) on several of the parameters is mild. For example, when the sample-to-detector distance is at least several times the maximum dimensions of the detector, the dependence of CF(AT) on the size, shape, and efficiency of the detector is often negligible. When the distance between a cylindrically shaped sample and the detector is at least several times the maximum dimension of either sample or detector, CF(AT) is usually a strong function of the sample μ_ℓ, a mild function of the sample dimensions and distance from the detector, and has negligible dependence on the detector size, shape, and efficiency.

The greatest simplifications occur in the far-field case, where the maximum dimensions of both sample and detector are negligible compared with their separation. In the far-field case, dependence on the inverse-square law becomes negligible and all gamma rays reach the detector along essentially parallel paths. There is no dependence on detector size or shape, on small changes in the sample-to-detector distance, or on sample size except for the influence of size on the fraction of gamma rays escaping from the sample. Simple analytic expressions can be derived for several sample shapes. These expressions are often useful approximations for assay situations that are not truly far field. Indeed, the far-field situation is a useful reference case against which to compare near-field cases.

It is usually advantageous to plot CF(AT) vs the parameter of strongest dependence (μ_ℓ) and to plot separate curves for specific values of other parameters. Because μ_ℓ is often found by measuring the gamma-ray transmission T and using the relationship $T = \exp(-\mu_\ell x)$, it is generally more convenient to plot CF(AT) vs ln(T).

Consider the expression for CF(AT) for the far-field assay of a box-shaped sample viewed normal to a side.

$$CF(AT) = \frac{\mu\ell x}{[1 - \exp(-\mu\ell x)]} \tag{6-6}$$

where x is the sample thickness along the normal to the detector. Using $T = \exp(-\mu\ell x)$, we can write the simple expression

$$CF(AT) = \frac{-\ln(T)}{(1 - T)}. \tag{6-7}$$

If $T \ll 1$, $CF(AT) \simeq -\ln(T)$, so a plot of CF(AT) vs ln(T) is nearly linear. Figure 6.3 gives a plot of Equation 6-7. It also shows CF(AT) vs ln(T) for cylindrical and spherical samples where T is measured across the sample diameter. All the cases have the form $CF(AT) \simeq -k \ln(T)$ for $T \ll 1$. This approximate ln(T) dependence exists for most assay geometries and is very useful to keep in mind.

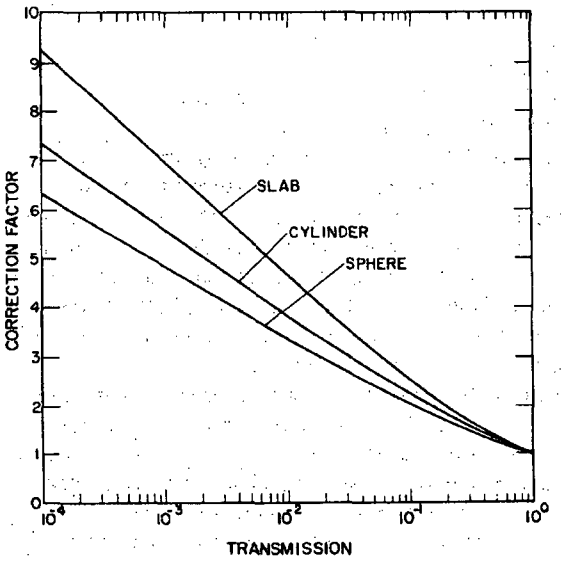

Fig. 6.3 Far-field correction factors for slab, cylindrical, and spherical samples as a function of transmission. The transmission is measured normal to the face of the slab sample and along a diameter of the cylindrical and spherical samples.

6.5 ANALYTIC FAR-FIELD FORMS FOR THE SELF-ATTENUATION CORRECTION FACTOR

In general, the near-field integral expressions for CF(AT) cannot be integrated in terms of elementary functions. However, far-field expressions have been derived for

three simple sample geometries: box shaped (rectangular parallelepipeds), cylindrical, and spherical. Figure 6.3 gives the far-field CF(AT) for all three sample shapes, and Table 6-1 gives numeric values for the three cases.

Table 6-1. Far-field correction factors for slab, cylinder, and sphere as functions of transmission

Transmission	Slab[a]	Cylinder[b]	Sphere[b]
1.0000	1.000	1.000	1.000
0.8000	1.116	1.097	1.086
0.6000	1.277	1.231	1.202
0.4000	1.527	1.434	1.376
0.2000	2.012	1.816	1.701
0.1000	2.558	2.238	2.054
0.0500	3.153	2.692	2.431
0.0200	3.992	3.326	2.956
0.0100	4.652	3.826	3.370
0.0010	6.915	5.552	4.805
0.0001	9.211	7.325	6.288

[a]Transmission normal to surface.
[b]Transmission along a diameter.

6.5.1 Box-Shaped Samples

The box-shaped sample is the only one for which a simple derivation exists. From Equation 6-5, we can write CF(AT) with respect to a nonattenuating sample (specified shape same as real shape) as

$$\mathrm{CF(AT)} = \frac{\int_v \rho \mathrm{I} \varepsilon \, \mathrm{dV}}{\int_v \rho \mathrm{I} \varepsilon \exp(-\mu_\ell \mathrm{r}) \, \mathrm{dV}} \tag{6-8}$$

where ρ = spatial density of the isotope being assayed (g/cm^3)
I = emission rate of the assay gamma ray (γ/g-s)
ε = absolute full-energy detection efficiency
μ_ℓ = linear attenuation coefficient of the sample
r = distance that gamma rays travel within the sample
dV = volume element.

The parameters ρ, I, and μ_ℓ are constant, whereas ε and r are functions of position. It is the exponential term in the denominator that, for most geometrical configurations, cannot be integrated in terms of elementary functions.

Consider the configuration shown in Figure 6.4. The parameter I is a constant for a given isotope, and by virtue of the fundamental assumptions on uniformity, ρ and μ_ℓ are also constant. The far-field assumption is equivalent to assuming that ϵ is also a constant.

Because of the far-field assumption, only the integration in X is significant. After the obvious cancellations,

$$CF(AT) = \frac{\int_0^X dx}{\int_0^X \exp[-\mu_\ell(X - x)]dx} \tag{6-9}$$

This evaluates to

$$CF(AT) = \frac{\mu_\ell X}{1 - \exp(-\mu_\ell X)} \tag{6-10}$$

as in Equation 6-6.

6.5.2 Cylindrical Samples

For a cylindrical sample viewed along a diameter in the far field (Ref. 9),

$$CF(AT) = \frac{1}{2} \quad \frac{\mu_\ell D}{I_1(\mu_\ell D) - L_1(\mu_\ell D)} \tag{6-11}$$

where L_1 = modified Struve function of order 1
I_1 = modified Bessel function of order 1
D = sample diameter
μ_ℓ = linear attenuation coefficient of the sample.

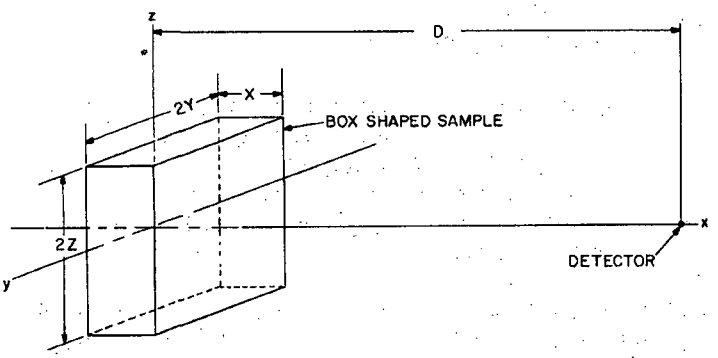

Fig. 6.4 Counting geometry for a slab-shaped sample with coordinates and dimensions for use in deriving the far-field correction factor.

The expression is very compact, but it is inconvenient to use because of the Struve and Bessel functions (Ref. 10). Equation 6-11 was used to generate the curve for a cylinder in Figure 6.3. Note that the CF(AT) for a cylinder is a little less than those for a slab or box-shaped sample. In the cylindrical sample, fewer gamma rays must penetrate the maximum thickness of material; hence, the fraction escaping is greater and the CF(AT) is smaller.

6.5.3 Spherical Samples

For a spherical sample in the far field, the correction factor is (Ref. 4)

$$\mathrm{CF(AT)} = \left(\frac{3/2}{\mu_\ell \mathrm{D}} \left\{ 1 - \frac{2}{(\mu_\ell \mathrm{D})^2} + \exp(-\mu_\ell \mathrm{D}) \left[\frac{2}{\mu_\ell \mathrm{D}} + \frac{2}{(\mu_\ell \mathrm{D})^2} \right] \right\} \right)^{-1} \quad (6\text{-}12)$$

This expression is plotted in Figure 6.3. The CF(AT) for a sphere is smaller than that for either the parallelepiped or cylinder. On the average, gamma rays travel shorter distances to escape from a sphere than from either a cylinder or a cube. Spherical samples are rarely met in practice, but the reciprocal of CF(AT) gives the fraction of gamma rays escaping from spherical particles and is useful in deciding whether a sample meets the required assumption on particle size. Figure 6.2 was generated from Equation 6-12.

6.6 NUMERIC COMPUTATION IN THE NEAR FIELD

6.6.1 General Discussion

For most if not all near-field situations in which the inverse-square dependence must be treated explicitly, the resulting expressions cannot be integrated in terms of elementary functions. As a result, numeric methods must be used, which implies the use of computers. However, even with the power of modern computers, the simplest model should be used to describe the assay situation. It is often possible to simplify the computations by assuming a point or line detector with efficiency independent of angle of incidence. For complicated geometries, Monte Carlo photon transport codes can be used. However, the NDA situations can usually be handled with simplified models and straightforward one-, two-, or three-dimensional numeric integration methods using simple codes and small computers. The accuracy of gamma-ray NDA is usually determined more by the sample uniformity and homogeneity than by the accuracy of the CF(AT) computation.

Approximate analytic forms exist that give adequately accurate values for CF(AT) over reasonable ranges of transmission. A few such forms are described below. The adequacy of a particular expression can be determined by comparison with more accurate numeric computations. Approximate analytic forms often provide the capability to derive analytic expressions for the precision of CF(AT).

6.6.2 A Useful One-Dimensional Model

A common assay geometry is that in which a germanium detector views a bottle of solution from below. Both detector and sample are well approximated by right-circular cylinders. Assume that the axes of symmetry of the bottle and the detector coincide and that the detector radius is r_d, the sample radius is r_s, the sample depth is D, and the distance from sample to detector is d (Figure 6.5). If d is a few times greater than both r_d and r_s, no gamma ray impinges on the detector at angles greater than $\sim 10°$ to the common axis. Inasmuch as $\cos \Theta \geq 0.95$ for angles $< 19°$, it is clear that no gamma ray travels more than a few percent greater distance on its way to the detector than those that travel parallel to the common centerline. Therefore, the assay situation can be described by a one-dimensional model consisting of a point detector and a line sample of "depth" D and linear attenuation coefficient μ_ℓ separated from the detector by a distance d as indicated in Figure 6.6. This model contains the effects of the inverse-square law and gamma-ray attenuation, which are the main influences on the CF(AT).

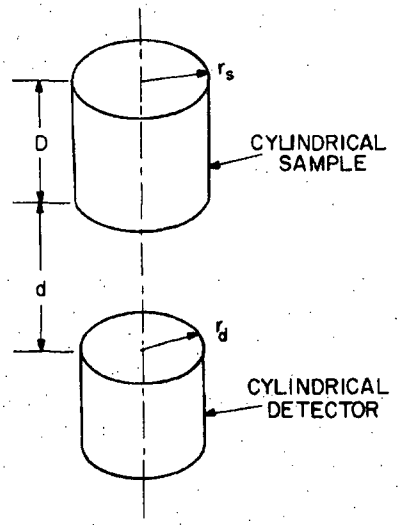

Fig. 6.5 Commonly used vertical assay geometry for which a one-dimensional model is appropriate for computing CF(AT).

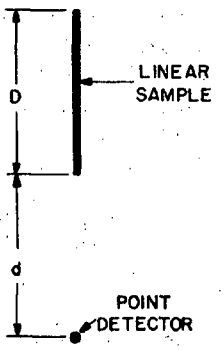

Fig. 6.6 One-dimensional model for computing CF(AT).

Using this model, CF(AT) with respect to a nonattenuating sample is

$$CF(AT) = \left[\int_0^D \frac{dx}{(d+x)^2}\right] \Big/ \int_0^D \frac{[\exp(-\mu_\ell x)]dx}{(d+x)^2} \tag{6-13}$$

where all constants pertaining to the detector efficiency and gamma-ray emission rates have cancelled. The numerator integrates to D/[d(d + D)], but as simple as the denominator appears to be, it cannot be integrated in terms of elementary functions. However, it can be written as a sum in a simple way. The expression for CF(AT) then becomes

$$CF(AT) = \left[\frac{D}{d(d+D)}\right] \Big/ \sum_{I=1}^{N} \frac{\{\exp[-\mu_\ell(I-0.5)\Delta x]\}\Delta x}{[d+(I-0.5)\Delta x]^2} \tag{6-14}$$

where $\Delta x = D/N$ and N is the number of intervals for the numeric integration. Generally, taking $N \simeq 100$ gives the result to <0.1%. The numeric integration could, of course, be done with better accuracy and in fewer steps using Simpson's rule or other more elegant methods. Equation 6–14 shows clearly the functional dependence of CF(AT) on d, D, and μ_ℓ and the equivalence of the integral and the sum. The parameter D is well defined as the sample depth. The parameter d, however, is less well defined because the gamma rays interact throughout the detector and because the average interaction depth is a function of energy. Experience shows that if the nominal value of d is at least a few times D, then with the help of a set of standards covering a wide range of μ_ℓ, the value of d in Equation 6-14 can be adjusted to give CF(AT) such that the corrected rate per unit activity is nearly constant over a wide range of μ_ℓ. The adjustment of d compensates for the imprecisely known sample-to-detector distance and for deviation of the one-dimensional model from the actual three-dimensional assay geometry.

Figure 6.7 shows results of a measurement exercise using the procedure just described. The samples were 25-mL solutions of depleted uranium nitrate in flat-bottomed bottles of 10 cm^2 area (right-circular cylinders 3.57 cm in diameter and 2.5 cm deep). The uranium concentration varied from 5 to 500 g/L, and all the samples were spiked with an equal amount of ^{75}Se; ^{75}Se was the source material, uranium served as an absorber only. The detector crystal was ~4.0 cm in diameter and ~4.0 cm long. For the 136.0-keV gamma ray of ^{75}Se, the corrections for electronic losses, CF(RL), varied by only ~10%, whereas the corrections for gamma-ray attenuation, CF(AT), varied by ~275%.

Because each sample had identical amounts of ^{75}Se, the corrected 136.0-keV rate should have been equal for all samples. The upper part of the figure gives the fractional deviation of the corrected rates from the average of all and indicates the typical precision of the measurements. All the corrected rates are within about ±0.5% of the average. In this case, the actual distance of the sample bottom to the average

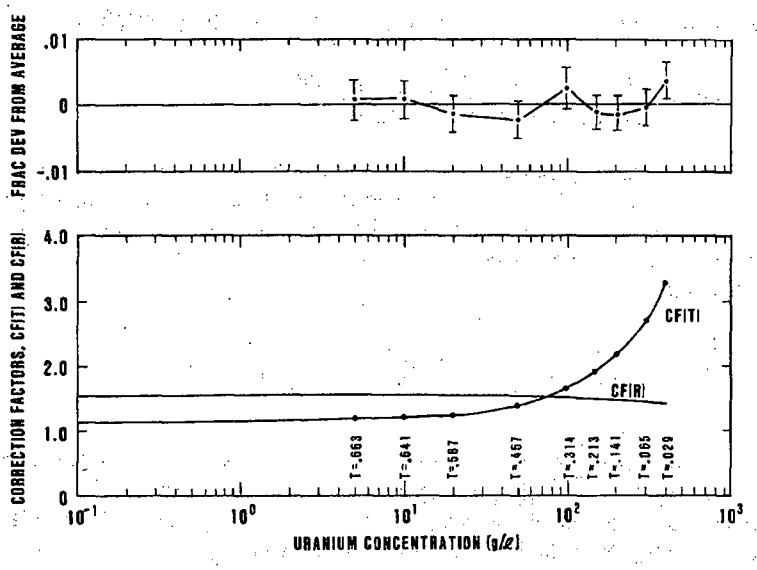

Fig. 6.7 Results of a measurement exercise designed to test the usefulness of a one-dimensional model for computing CF(AT) = CF(T).

interaction depth in the detector was ~8 cm and the adjusted value was 9.0 cm. Qualitatively, the one-dimensional model gives values of CF(AT) that are a little low compared with the correct three-dimensional model because the gamma rays pass through slightly greater thicknesses of solution than in the one-dimensional model. Increasing d increases CF(AT) overall and also increases CF(AT) more for lower values of T. Hence, the value of d used in computations is usually a little higher than the physical value.

If a set of solution samples has variable but determinable depths, one would prefer to compute CF(AT) with respect to a nonattenuating point so that the corrected rates from all the samples can be compared directly. The ratio between CF(AT) with respect to the nonattenuating point and CF(AT) with respect to the nonattenuating sample is (1 + D/d), independent of μ_ℓ. All CF(AT) values, for both standards and unknowns, should be computed with respect to the same nonattenuating shape so that the corrected rates are directly comparable.

6.6.3 A Useful Two-Dimensional Model

In another common assay geometry, a detector views a cylindrical sample from the side (Figure 6.8). If the sample depth is less than the sample diameter and if the distance from the detector to the sample center is at least several times the sample diameter, then a simple two-dimensional model can often be used to compute CF(AT).

The model is a point detector at a distance D from the center of a circular sample of radius R (Figure 6.9). The detector efficiency is essentially constant for gamma rays originating at any point within the sample volume. The correction factor with respect to the nonattenuating sample can be written as

$$CF(AT) \simeq \frac{(\pi/2)\ln[1 - R^2/D^2]}{\sum_{m=1}^{M} \sum_{n=1}^{N} \{\exp[-\mu\varrho t(m,n)]\Delta A(n)/L^2(n,m)\}} \quad (6\text{-}15)$$

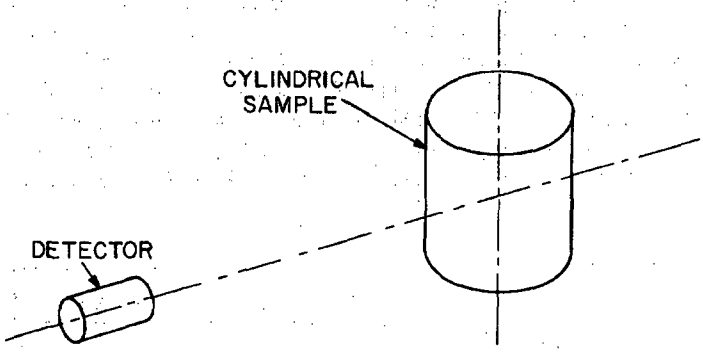

***Fig. 6.8** Typical assay geometry for which a two-dimensional model for computing CF(AT) is usually adequate.*

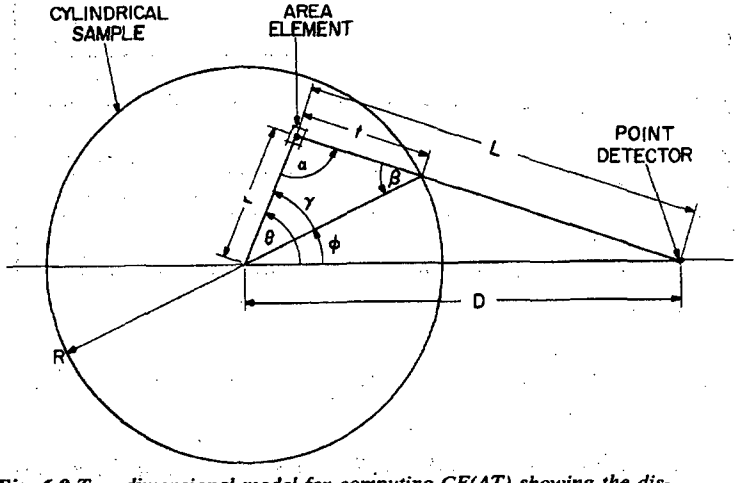

***Fig. 6.9** Two-dimensional model for computing CF(AT) showing the distances that must be determined and the variables in terms of which they must be expressed. Note that $0 \leq \alpha \leq \pi$, $\beta \leq \pi/2$, and $0 \leq \gamma \leq \pi$.*

The derivation of this expression is given in Ref. 2. The ratio of CF(AT) calculated relative to the nonattenuating sample and CF(AT) calculated relative to a nonattenuating point is $-(D^2/R^2)\,\mathrm{Ln}(1 - R^2/D^2)$. For a fixed value of T, CF(AT) is a function only of the ratio D/R. Figure 6.10 gives CF(AT) as a function of D/R for several values of T. The essential point is that CF(AT) decreases slowly as D/R decreases; the larger changes occur for the smaller values of T. This behavior is a consequence of the inverse-square law. For a given value of T, CF(AT) asymptotically approaches a maximum as $D/R \rightarrow \infty$. The deviations from the far-field ($D/R = \infty$) case are plotted in Figure 6.11. For $T > 0.001$ and $D/R > 50$, all deviations are $\leq 1\%$. Therefore, $D/R \geq 50$ can be regarded as the far-field situation for most purposes. The variation of CF(AT) with T is much stronger than the variation with the ratio D/R.

The results presented in Figures 6.10 and 6.11 were obtained with a minicomputer using values of M = 200 and N = 200 for which all the results are within 0.1% of what the actual integrals would give. The total number of area elements computed was 40 000, and the time required was ~2 min per value. The exact time required

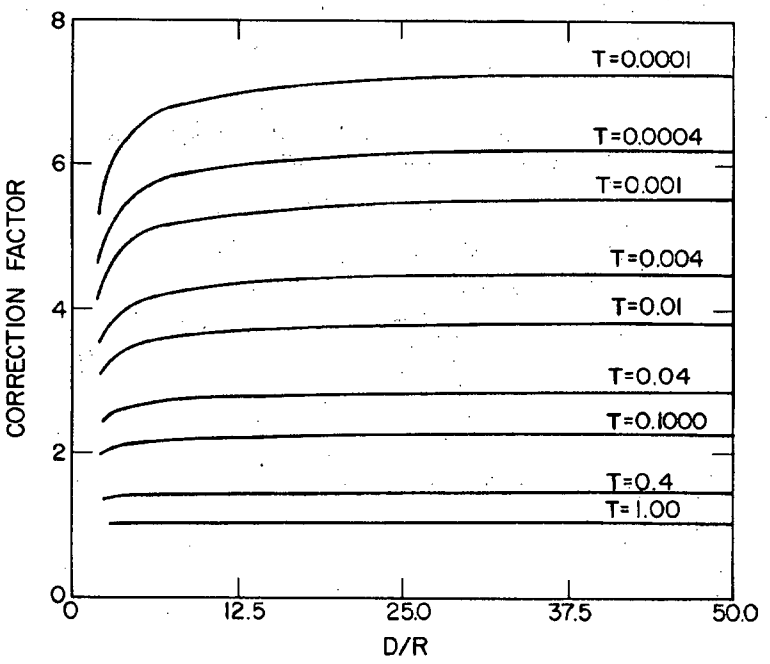

Fig. 6.10 *Correction factors with respect to a nonattenuating sample as computed from the two-dimensional model. They are plotted vs the ratio D/R for various values of the transmission T, where D is the distance from the center of the cylindrical sample to the point detector and R is the radius of the sample.*

depends greatly on the computing equipment and programming language used. For two-dimensional numeric integrations, results of high accuracy can be obtained in about a minute. For a three-dimensional model, a modest extension in derivation and programming, if the third dimension is also given 200 increments, the required execution time increases to hundreds of minutes.

6.6.4 A Three-Dimensional Model

As a final model for an assay geometry, consider the segmented assay of cylindrical samples. In this case (Figure 6.12), a detector views the sample through a horizontal collimator, which defines sample segments that are assayed individually. The sample is usually as close to the collimator as possible. The detector is often a right-circular cylinder of germanium ~5.0 cm in diameter and ~5.0 cm long. The inverse-square-law effects caused by the collimator must be considered explicitly; the two-dimensional model is not adequate.

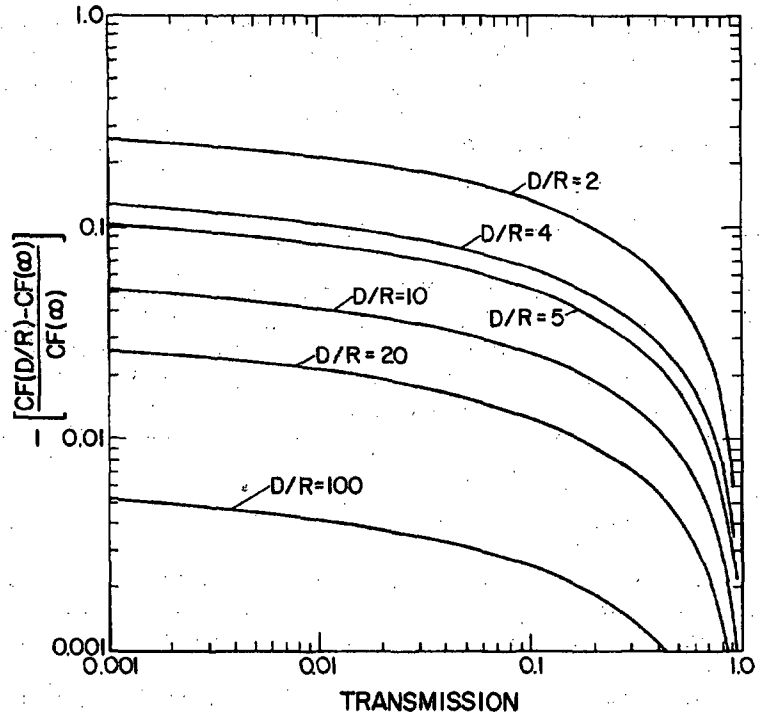

***Fig. 6.11** Deviations of near-field values of CF(AT) from the far-field values as a function of transmission for various values of D/R.*

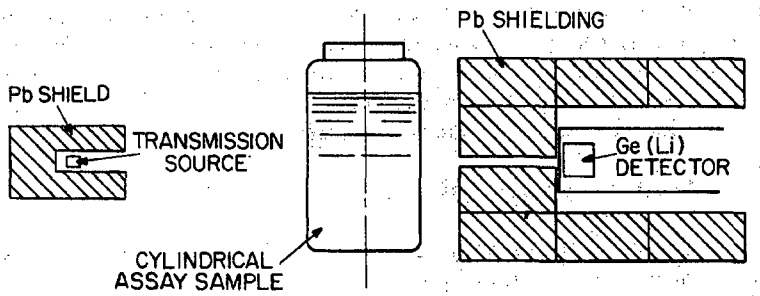

Fig. 6.12 Typical segmented assay situation for which a three-dimensional model for computing CF(AT) is appropriate.

The model consists of a perfect collimator (no leakage) and a vertical line detector centered at the rear of the collimator. The detector efficiency is assumed to be independent of either the position or angle at which the gamma rays strike the line detector. The distance from the emitting element to the detector is increased by a constant that is approximately equal to the average interaction depth in the detector. Inasmuch as materials are often packaged in metal containers that significantly attenuate the emitted gamma rays, the packaging is included in the model. The derivation of the three-dimensional model is outside the scope of this text; it is treated fully in Ref. 2.

6.6.5 Approximate Forms and Interpolation

The most accurate way to compute CF(AT) for reasonable assay geometries is to use a simple mathematical model and numeric integration. However, because of lengthy execution times, it is often desirable to compute CF(AT) for a few values of T (or μ_ℓ) and to use an interpolation scheme to find CF(AT) for intermediate values. The interpolation problem can be approached in several ways.

Since CF(AT) has an approximate log(T) dependence (see Figure 6.3), it is reasonable to use a fitting function of the form

$$CF(AT) = A + B\ \log(T) + C\ [\log(T)]^2. \tag{6-16}$$

The computer need only store the constants A, B, and C for each assay geometry. This scheme works very well over wide ranges of T. In a typical segmented scanning situation, A, B, and C can be determined to give values of CF(AT) correct to $\leq$0.3% for $0.008 \leq T \leq 0.30$.

A particularly simple scheme is based on the far-field form of CF(AT) for a slab: $-\ln(T)/(1 - T)$. Observing that a circle is not very different from a square (see Figure 6.3), one is led to try

$$CF(AT) \simeq \frac{-\ln(T^k)}{(1 - T^k)} \tag{6-17}$$

with $k < 1$ as an approximate function for cylindrical samples, even in the near-field situation. This form also has a ln(T) dependence for $T \ll 1$ and has only one constant to be determined. Figures 6.13 and 6.14 provide a feeling for how accurate the approximate form might be. Figure 6.13 gives the fractional deviation of Equation 6-17 from the correct far-field values for a cylinder (Equation 6-11) as a function of T and k. Figure 6.14 compares the approximate and correct values for a near-field assay of a cylindrical sample where D/R = 5/1. In Figure 6.13, $k = 0.82$ gives CF(AT) correct within ±1% for $0.01 \leq T \leq 1.0$, and in Figure 6.14, $k = 0.75$ gives CF(AT) correct within ±1.5% for $0.01 \leq T \leq 1.0$.

The choice of an interpolation procedure or approximate function for CF(AT) depends on the accuracy desired or possible for the materials to be assayed. For a field measurement of a heterogeneous drum containing ^{235}U, the accuracy is determined far more by the heterogeneity of the sample material than by the function used for CF(AT). When ±25% accuracy is all that can be hoped for, it is wasteful to set up a model and do numeric integrations for CF(AT). On the other hand, if the samples are solutions, where careful modeling and computation can yield accuracies <1%, the effort is fully justified.

6.6.6 The Effects of Absolute and Relative Error in the Self-Attenuation Correction Factor

It is assumed that gamma-ray assay systems are calibrated with suitable physical standards. It is also assumed that CF(AT) is determined for both the unknowns and the standards. Generally, CF(AT) is mainly a function of the measured transmission T with some influence from the geometrical parameters.

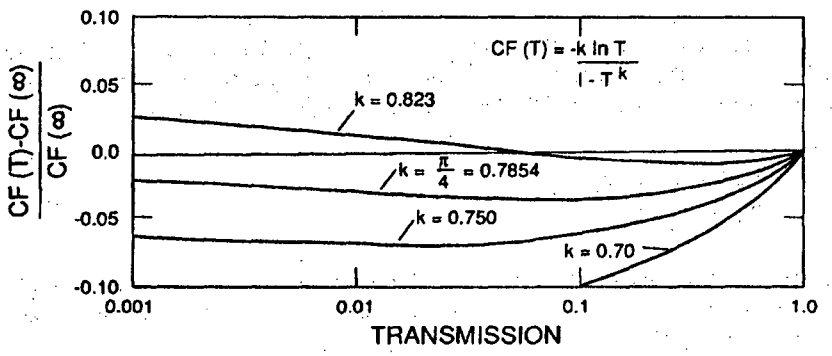

Fig. 6.13 Deviations of the values of CF(AT) computed from the approximate expression $CF(T) = -k \ln T/(1 - T^k)$ from the far-field values for a cylinder for several values of the parameter k.

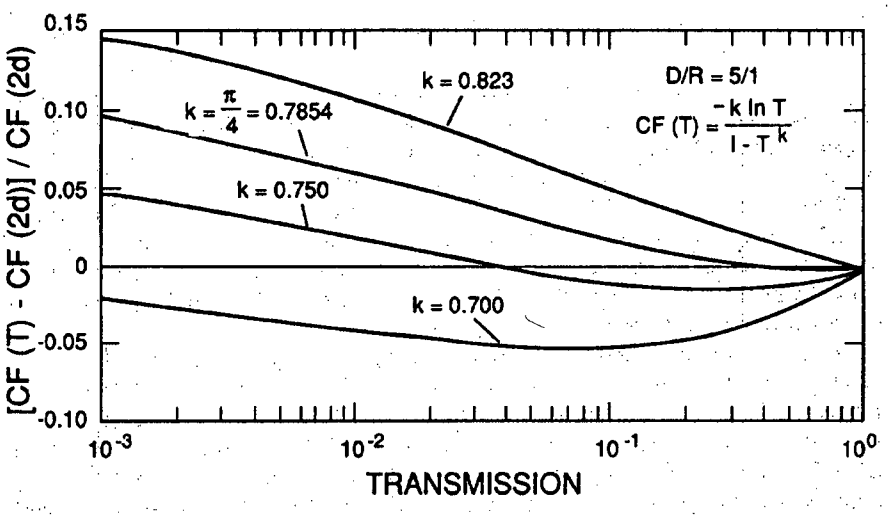

Fig. 6.14 Deviations of the values of CF(AT) computed from the approximate expression $CF(T) = -k \ln T/(1 - T^k)$ *from the values from the two-dimensional model for cylindrical samples for D/R = 5. They are plotted as functions of the transmission T for several values of the parameter k.*

The consequences of using an incorrect function for CF(AT) should be investigated. Figure 6.15 shows a true and a false CF(AT) function. Let the following notation be adopted:

CF(T) = CF(AT) as a function of T
G = mass of assay isotope in unknown.

The superscripts *f* and *t* indicate quantities associated with the false and true functions for CF(AT), and the subscripts *u* and *s* indicate quantities associated with the unknown and the standard. The ratio of the incorrect result to the correct result is

$$\frac{G^f}{G^t} = \frac{CF^f(T_u)/CF^t(T_u)}{CF^f(T_s)/CF^t(T_s)}. \tag{6-18}$$

The ratio does not depend directly on the absolute error in CF(T) but only on a ratio of ratios. If this ratio of ratios is ~1.00, the assays will be correct in spite of any absolute error in CF(AT).

This result demonstrates that it is easier to calibrate an assay system correctly for a narrow range of transmission (which usually implies a narrow range of concentration of the assay isotope) than for a broad range. It also emphasizes that great care must

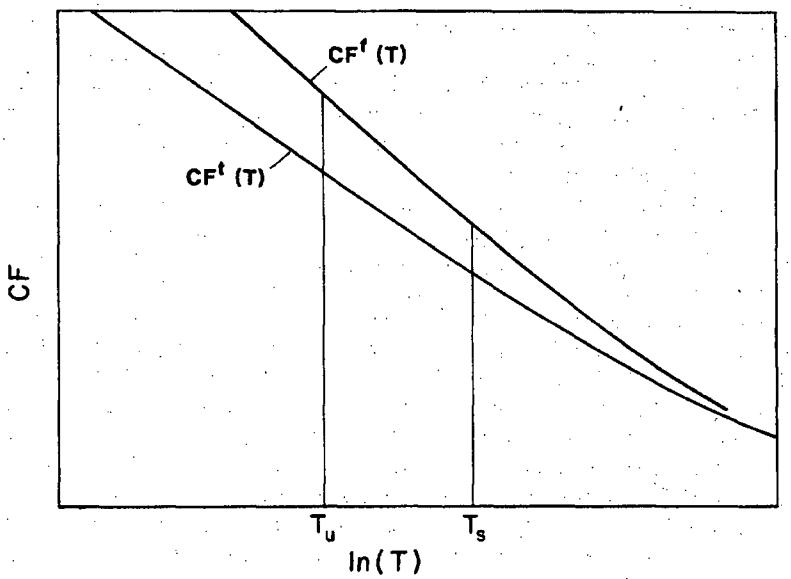

Fig. 6.15 This graph can be used to illustrate the consequences of using an incorrect function for CF(AT). $CF^f(T)$ represents the incorrect or false function for CF(AT) and $CF^t(T)$ represents the correct function. T_u and T_s represent the transmissions of unknown and standard, respectively.

be used in modeling the assay geometry and computing CF(AT) if high accuracy is required over a wide range of concentrations.

Considering the difficulty in computing CF(AT), why not use standards to determine a variable calibration constant as a function of T? Indeed that can be done, but preferably only as a fine tuning of a system calibration. A variable calibration constant or nonlinear calibration curve only sweeps under the rug the things that are not understood about the physics of the assay arrangement.

6.6.7 Precision of Self-Attenuation Correction Factor and Total Corrected Rate

In a properly operating gamma-ray NDA system, the precision is almost totally a function of the random nature of the emission and detection of the gamma rays. The influence of electronic fluctuations and drifts should almost never influence the precision of the results at a level >0.1%. The dominant statistical component of the assay precision can usually be estimated from the full-energy peak areas and their precisions. The overall precision, including any contribution from the equipment, is estimated from replicate assays. The electronic and mechanical stability of the assay system can be evaluated by comparing the overall precision with that estimated from peak areas and their precisions.

Consider the influence of the precision of CF(AT) on the precision of the final assay. The assay is proportional to CR, which is given (see Equation 6-1) as CR = FEIR × CF(AT). The procedures used to derive expressions for σ(CR), σ(FEIR), and σ[CF(AT)] are covered in detail in many sources (two relatively simple sources are Refs. 11 and 12). The intent here is only to emphasize a few points relative to obtaining a reasonable expression for σ(CR).

If CR can be written as an analytic function of the peak areas, then an expression for σ(CR) can be derived. However, when CF(AT) is found by numeric procedures, σ(CR) cannot be computed directly. An approximate function for CF(AT) can be used to derive an expression for σ(CR). The approximate forms for CF(AT) are often not sufficiently accurate to compute CR, but they usually provide an adequate expression for σ(CR). In Section 6.6.2 a one-dimensional model was used to determine CF(AT) for the assay of cylindrical samples. To derive an expression for σ(CR), one could use Equation 6-7 or the modified form Equation 6-17 for CF(AT). The proper value of k would be chosen by comparison with precisions computed from replicate assays. This procedure gives the accuracy provided by numeric integration of a more accurate model for CF(AT) and still provides good estimates of σ(CR).

Although σ(CR) is the assay precision, σ[CF(AT)] alone is sometimes of interest. The expression for σ[CF(AT)] will always be simpler than that for σ(CR). If no peak areas are common to the expressions for FEIR and CF(AT), then

$$\sigma_r(\mathrm{CR}) = \sqrt{\sigma_r^2(\mathrm{FEIR}) + \sigma_r^2[\mathrm{CF(AT)}]} \tag{6-19}$$

where $\sigma_r(x) \equiv \sigma(x)/x$. If there are peak areas common to the expressions for FEIR and CF(AT), Equation 6-19 is not valid, and the expression for CR must be written as an explicit function of the peak areas concerned. Expressions for precision are frequently complex, but considerable simplification can usually be achieved by judicious approximations. The effort to make such simplifications reduces the computation time and provides a better understanding of the main source of imprecision.

6.7 FACTORS GOVERNING THE REQUIRED NUMBER OF STANDARDS

The current insistence that the mass range in NDA standards span the expected range in the unknowns can be considerably relaxed. The evidence for this allegation is implicit in the foregoing sections.

The insistence that the standards span the range of expected masses seems rooted in the expectation that a nonlinear calibration function will be fitted to the measured response data. For gamma-ray NDA systems, those response data might be RR or FEIR. Such plots are quite nonlinear, and extrapolation of a nonlinear function beyond the data points is not particularly safe. However, if the multiplicative correction factors CF(RL) and CF(AT) are properly defined and computed, a total corrected rate is obtained, which is a linear function of mass. If the calibration function is linear

(Equation 6-2), extrapolation is far less hazardous than with the nonlinear calibration functions, and most of the logical force is taken from the requirement that the mass range of the standards span that of the unknowns.

With Equation 6-2, the calibration constant, K can be determined with a single standard. However, it is wise to use several standards, spanning a reasonable mass range, and perhaps varying other parameters such as matrix density and composition or sample size. The use of several standards helps confirm that CF(RL) and CF(AT) are being correctly determined and that Equation 6-2 is valid. If some nonlinearity is detected, the first concern should be to correct the problem(s), whether in equipment or in computation of CF(RL) or CF(AT), rather than to add terms to the calibration equation. Modifying the calibration equation simply disguises the effects of poorly adjusted equipment, incorrect algorithms for CF(RL) and CF(AT), equipment malfunction, or even outright ignorance of proper procedures and methods. After the equipment and the computational algorithms are as good as possible, if there is still some nonlinearity, then consideration can be given to modifying the calibration equation. Because such problems often result from a wide range of count rates, consider first two or more linear, two-parameter calibrations over more restricted mass ranges. Such adjustment of the calibration function should be required infrequently. The accuracy is more often limited by inhomogeneity or excessive particle size, and a single one-parameter linear calibration is nearly always sufficient.

The extent to which one may safely extrapolate a linear calibration beyond its data points depends on whether the extrapolation is toward lower or higher masses. At low concentrations of the assay isotope, the self-attenuation is usually dominated by the matrix, and CF(AT) changes very slowly over a wide range of concentration. Similarly, the count rates are low so that CF(RL) not only changes slowly but is small and accurately determined. As a result, one usually has high confidence when extrapolating down to the lowest detectable levels. As an example, consider the assay of ^{235}U solutions by the 185.7-keV gamma ray. For reasonably sized samples (>25 mL), a concentration of ~10 g/L ^{235}U may well give a precision of ~0.5% in ~1000 s. A sample of 0.1 g/L ^{235}U concentration has nearly the same CF(AT) and gives a precision of ~5% in a 1000-s assay, which might well be acceptable. However, it would take ~100 000 s to count a 0.1-g/L ^{235}U standard to 0.5% precision, which might well be required if it were included in the calibration data. A great deal of time can be wasted counting very low level standards.

The extrapolation to mass values higher than those in the standards must be approached more cautiously, especially if the highest mass standard is at a level where both CF(AT) and CF(RL) are changing rapidly or where the gross count rates are approaching the limits of the electronics to maintain adequate resolution and peak shape. The system performance at the higher masses and count rates should be confirmed with some source material even if no standard exists at the desired mass level. For example, if it has been confirmed that the system is able to accurately measure a transmission of 1% at a count rate of 50 000 s^{-1}, then there is reasonable confidence in assaying an unknown with 1% transmission at 50 000 s^{-1} even if the highest mass

standard has an ~2% transmission and gives a gross rate of ~40 000 s^{-1}. If the entire mass range gives only modest count rates and small and slowly varying values of CF(RL) and CF(AT), it is safer to extrapolate upward.

By way of final comment, the possession of an appropriate set of standards does not compensate for lack of knowledge of how to use them or for maladjusted or malfunctioning equipment, inappropriate assay geometries, incorrect expressions for the correction factors, or assay samples that do not adequately meet the requirements on uniformity and homogeneity. All the items are important factors in achieving accurate gamma-ray assays, and none can be safely neglected. When the pertinent factors are properly addressed, including proper and efficient use of calibration standards, gamma-ray NDA can provide economical, timely, and accurate assays for many materials.

6.8 GAMMA-RAY RATIO METHODS

Gamma-ray ratio methods are of some limited use in determining CF(AT). A detailed treatment of the many ratio techniques is beyond the scope of this book, but a short discussion can give the reader a feeling for some of the possibilities and limitations. The basic idea is to determine μ_ℓ and CF(AT) from the ratio of gamma-ray intensities at different energies. Consider a slab-shaped sample of thickness x containing an isotope that emits gamma rays at energies E_1 and E_2; assume that the unattenuated emission rates are equal. Using Equation 6-6, the peak area (A) ratio is

$$\frac{A_2}{A_1} = \frac{CF(E_1)}{CF(E_2)} = \frac{\mu_\ell(E_1)}{\mu_\ell(E_2)} \text{ for } \mu_\ell x \gg 1. \tag{6-20}$$

If the matrix composition or an "effective Z" is known or assumed, it may be possible to use the measured ratio of attenuation coefficients to determine the individual coefficients and evaluate CF(E). This is the idea behind all ratio methods, namely that different energy gamma rays are attenuated differently and may carry information about the attenuation properties of the material they pass through.

The gamma-ray ratio methods require the assumptions on uniformity and particle size discussed in Section 6.2.3 in order to give accurate results. If the assumptions are not met, the transmission-corrected methods give results that are usually low. Ratio methods give results that are generally greater than those from transmission methods, but may overcompensate depending on the size of the emitting particles.

Gamma-ray ratio methods require some additional knowledge of the sample. The required information varies with the procedure but often includes the sample density and the "effective" atomic number Z. The "effective" atomic number usually implies that the mass attenuation curve of the sample matches the curve for some single element. For multielement mixtures, especially those containing hydrogen, the curve may not closely match that of a single element.

In many cases, ratio methods can give a warning when the assumptions on uniformity and particle size are violated. Unfortunately, though the ratios can give a warning of potentially inaccurate assay situations, there is no way currently known whereby the ratio methods can consistently correct for the problems detected. A combination of transmission and ratio methods gives the most information about a given sample.

It is often assumed that the ratio methods are simpler to apply because they do not require the use of a transmission source. In practice it is doubtful that they are simpler because (a) the ratio methods require either the measurement or computation of the required "no attenuation" value of the ratio, (b) the ratio methods require some knowledge of the matrix composition, (c) in many applications the ratio method requires the net weight and volume of the sample, and (d) the ratio methods frequently require iterative procedures to arrive at the best result. Both transmission and ratio methods, for best results, will usually require a knowledge of the sample dimensions and its position relative to the detector.

6.9 ASSAY EXAMPLES

This chapter concludes with some topics useful to gamma-ray assays and a few actual measurement examples. The NRC-published *Handbook of Nuclear Safeguards Measurement Methods* (Ref. 13) gives the main design features and performance specifications for many gamma-ray assay systems.

6.9.1 Useful Gamma-ray Combinations for Assay, Transmission, and Reference Peaks

A sample of the material being assayed can sometimes be used as the transmission source, thus determining the transmission at exactly the required energy. Frequently, however, it is impossible to obtain such a source with sufficient intensity (uranium and plutonium are excellent at absorbing their own gamma rays). A number of considerations govern the choice of a transmission source for assaying a given isotope: the transmission gamma rays(s) should be close to the assay gamma-ray energy; the transmission energy should be lower than the assay energy so that the Compton continuum of the transmission gamma ray does not fall beneath the assay peak; the transmission gamma ray should not interfere with any gamma ray involved in the assay. Similar considerations apply to the choice of reference source for deadtime/pileup correction. Over the years many useful source combinations have been found and used. Table 6-2 gives some combinations which have been particularly useful.

6.9.2 Interpolation and Extrapolation of Transmission

Interpolating to an assay energy between two transmission peaks is preferable to extrapolating beyond one or more transmission peaks. Table 6-2 shows that the assay

Table 6-2. Useful source combinations

Isotope Assayed	Transmission Source	Correction Source
^{238}Pu	^{137}Cs	^{133}Ba
766.4 keV	661.6 keV	356.3 keV
^{239}Pu	^{75}Se	^{133}Ba
413.7 keV	400.1 keV	356.3 keV
^{235}U	^{169}Yb	^{57}Co
185.7 keV	177.2, 198.0 keV	122.0 keV
^{238}U	^{54}Mn	^{137}Cs
1000.1 keV	834.8 keV	661.6 keV
^{237}Np	^{203}Hg	^{235}U
311.9 keV	279.2 keV	185.7 keV

of ^{235}U by its 185.72-keV gamma ray with measured transmissions at 177.2 keV and 198.0 keV offers this advantageous situation. Assuming a linear relationship between transmission and energy, the transmission at any intermediate energy E is given by

$$T(E) = \left(\frac{E2 - E}{E2 - E1}\right)T1 + \left(\frac{E - E1}{E2 - E1}\right)T2. \tag{6-21}$$

If E = 185.7, E1 = 177.2, and E2 = 198.0, then T(E) = 0.591(T1) + 0.409(T2) .

When the transmission gamma rays are close in energy (21 keV apart in this example), the linear interpolation is usually adequate, but if the transmission peaks are much farther apart, it may not be so. If three or more well-spaced gamma rays are emitted by the transmission source, it may be possible to fit the measured points to give accurate values of transmission for intermediate energies. If the gamma-ray attenuation of a given sample is dominated by a high-Z element (uranium, plutonium, thorium, etc.), the mass attenuation coefficient of the sample is very close to a power law in energy:

$$\mu(E) = K\,E^{-\gamma} \tag{6-22}$$

where K and γ are constants. If this is true, ln(−ln T) vs ln E is linear and interpolation over large energy ranges is feasible.

When only one transmission can be measured, correction to the assay energy is often possible based on approximate knowledge of the chemical composition of the sample. The applicable equation is

$$T_a = T_t^{\alpha} \tag{6-23}$$

where $\alpha = \mu_a/\mu_t$

μ_a, μ_t = mass attenuation coefficients at assay and transmission energies.

As an example, consider the assay of ^{239}Pu (414 keV) contaminated incinerator ash using ^{137}Cs (662 keV) as a transmission source. This mixture can be treated as two components, one having the attenuation properties of oxygen, and the other, those of plutonium. Table 6-3 illustrates the change in $\alpha(\mu_a/\mu_t)$ with the plutonium weight fraction (F_{Pu}). Because most incinerator ash is less than 10% plutonium by weight, $\alpha = 1.27$ might be picked as an average value for the measurements.

Table 6-3. The variation in $\mu(414)/\mu(662)$ with plutonium weight fraction

F_{Pu}	$\alpha = \mu(414)/\mu(662)$
0	1.21
0.1	1.33
0.3	1.54
0.5	1.71
0.7	1.84
0.9	1.95

	Mass Attenuation Coefficients (cm^2/g)	
	414 keV	662 keV
μ_{Pu}	0.26	0.13
μ_O	0.093	0.077

6.9.3 Uranium-235 Assay in Far-Field Geometry

Table 6-4 gives the results of uncollimated, far-field assays for ^{235}U in 13 standards of 4 distinct sample types. The germanium detector was located about 80 cm from the center of the samples. The reference source used for deadtime and pileup correction was ^{241}Am. For standard types 1, 2, and 3, the correction factors for sample self-attenuation (CF_{186}) were computed using μ values derived from the measured gamma-ray transmissions (T_{186}). The computational algorithms were similar to those discussed in Section 6.6.2. For the type 4 standards, which are uranium metal of accurately known mass and size, the correction factors were calculated from the simple far-field expression in Equation 6–6. Table 6-4 shows the corrected interaction rates per gram of ^{235}U (response), which should be the same for all 13 standards. The response is normalized to the average of the three type 2 responses. The average of the 13 results is 0.999, the standard deviation is ~0.5%, and the maximum deviation from the average is ~1.1%. This represents excellent agreement, considering the wide range of size, shape, chemical composition, and uranium content, especially noting that the correction factors range from 1.26 to 3.30.

Table 6-4. Calibration standard intercomparison

Standard	Type 1				Type 2			Type 3			Type 4		
Container	polypropylene bottle							3-dram vial			thin plastic bag		
Size/shape	8.26 cm i.d. × 17 cm high							14.7 mm i.d. × 5 cm high			disk 5.08 cm diam × 0.25 to 0.50 mm thick		
Composition	U_3O_8 & graphite				solution U & HNO_3			solution U &HNO or HCL			U metal		
^{235}U (%)	92.83				10.08			93.12			93.15		
Uranium (g)	200.0	100.0	50.0	10.00	155.8	103.7	52.0	4.246	2.546	0.848	21.49	9.579	9.058
^{235}U (g)	185.7	92.8	46.4	9.28	15.70	10.45	5.24	3.956	2.371	0.790	20.02	8.92	8.44
T_{186}	0.022	0.091	0.184	0.335	0.033	0.064	0.123	0.249	0.377	0.588	0.210	0.499	0.518
CF_{186}	3.30	2.32	1.88	1.54	2.994	2.552	2.132	1.729	1.493	1.263	1.976	1.388	1.365
Response (s-g $^{235}U)^{-1}$	5.104	5.038	5.042	5.096	5.084	5.116	5.090	5.104	5.110	5.104	5.101	5.074	5.074
Normalized response	1.002	0.989	0.989	1.000	0.998	1.004	0.999	1.002	1.003	1.002	1.001	0.996	0.996

The results show that any of the four sets could serve as practical standards for far-field gamma-ray assay of any of the other sets. Some gamma-ray procedures (for example, near-field segmented scanning) are not as insensitive to size and shape as the far-field procedures. Still, a relatively small set of physical standards can usually calibrate most passive gamma-ray assay systems.

6.9.4 Plutonium-239 Solution Assay in Near-Field Geometry

The assay geometry indicated in Figure 6.16 is used for the near-field assay of ^{239}Pu in solution. The sample bottle is a right-circular cylinder with a bottom area of 10 cm^2 and depth of 4.0 cm. The maximum sample volume is 40 mL; however, typical sample volumes are only 25 mL. The sample is only about 5 cm from the detector end cap and the distance to the effective interaction depth is 7 or 8 cm. This is a distinctly near-field situation that creates increased difficulties in correctly

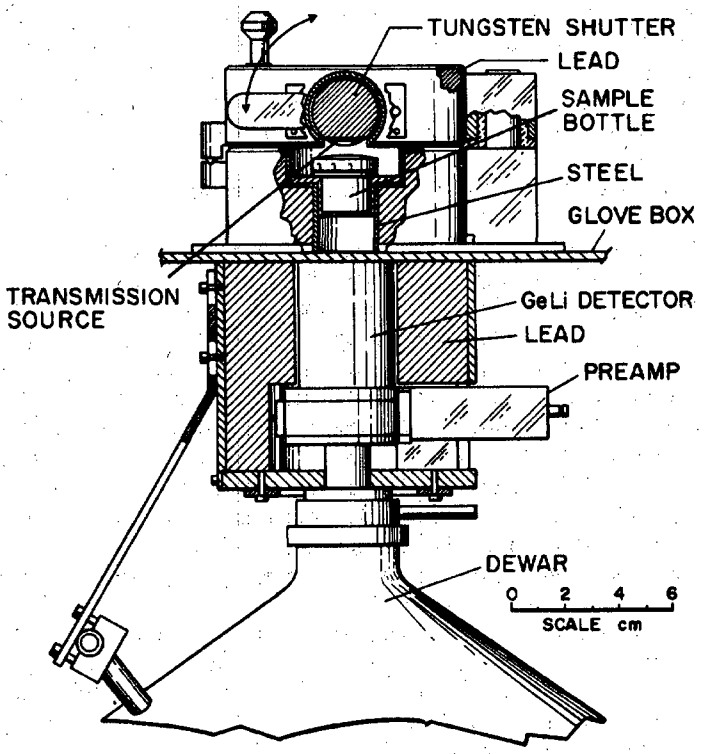

Fig. 6.16 *Cutaway drawing showing arrangement of the detector, sample, and shielding used for the near-field assay of ^{239}Pu in solution.*

computing the CF(AT). In principle, one would like to increase the sample-to-detector distance in order to simplify the computations. Unfortunately, that would reduce the count rates to where the required assay times would be excessively long.

The 88.0-keV gamma ray of ^{109}Cd is used as the reference for deadtime/pileup corrections. The reference source is fastened firmly to the detector end cap. To avoid interpolation or extrapolation, a plutonium metal disk is used as the transmission source so it is necessary to make separate sample-alone and sample-with-source runs and subtract to obtain the transmissions. For lower plutonium concentrations, the more intense 129.3-keV gamma ray gives more precise transmission values and a more precise overall assay than does the 413.7-keV gamma ray. At higher concentrations, the 413.7-keV gamma ray with its higher penetrability has both better signal and transmission and gives a more precise assay than does the 129.3-keV gamma ray. The weighted average of the 129.3- and 413.7-keV-based assays is used for the final assay, giving an overall measurement precision that is quite flat over a wide range of concentration.

This assay system uses the one-dimensional model for CF(AT) described in Section 6.6.2. The sample-to-detector distance is an adjustable parameter to flatten the plot of total corrected rate vs concentration. When properly adjusted and calibrated, this system measures ^{239}Pu in plutonium solutions with a bias of <1% for concentrations from 1 to 400 g Pu/L. Using 1000-s counts for both the sample-only and sample-with-transmission source runs, the precision is <1.0% for all concentrations of >1 g Pu/L.

6.9.5 Transmission-Corrected Segmented Scanning

In Section 6.6.4, segmented scanning was given as an example of an assay procedure in which a relatively simple three-dimensional model could be used to calculate CF(AT). This section concludes with some discussion of the reasons for using such a procedure and of some actual geometrical configurations and source combinations.

In the process of filling scrap and waste containers, vertical variations frequently occur in the volume densities of both source and matrix materials. Radial inhomogeneities are often less pronounced, and their effects can be substantially reduced by sample rotation. The different layers may substantially meet the requirements on homogeneity even though large differences exist between layers. In such cases the container may be assayed as a vertical stack of overlapping segments. The advantages of the segmented scanning procedure are gained at the loss of some degree of sensitivity; hence a system employing segmented scanning would probably not be used on samples containing <1 g of ^{239}Pu or ^{235}U.

Figure 6.17 shows the spatial relationships of detector, collimator, assay sample, transmission source, and reference source for a system tailored to the assay of ^{239}Pu in cylindrical containers <20 cm in diameter. It also gives approximate values for the intensities of the transmission and reference sources. Figure 6.18 shows a photograph of a segmented gamma scanner (SGS).

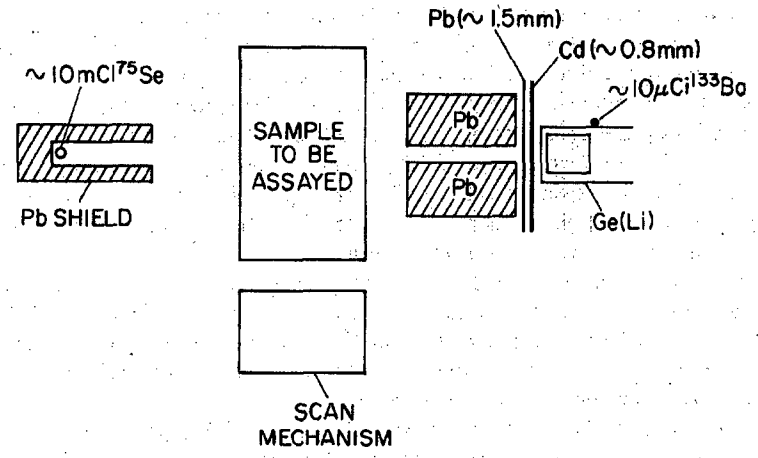

Fig. 6.17 General arrangements for segmented, transmission-corrected, gamma-ray assay. The specific situation shown is tailored to the assay of ^{239}Pu in cylindrical containers.

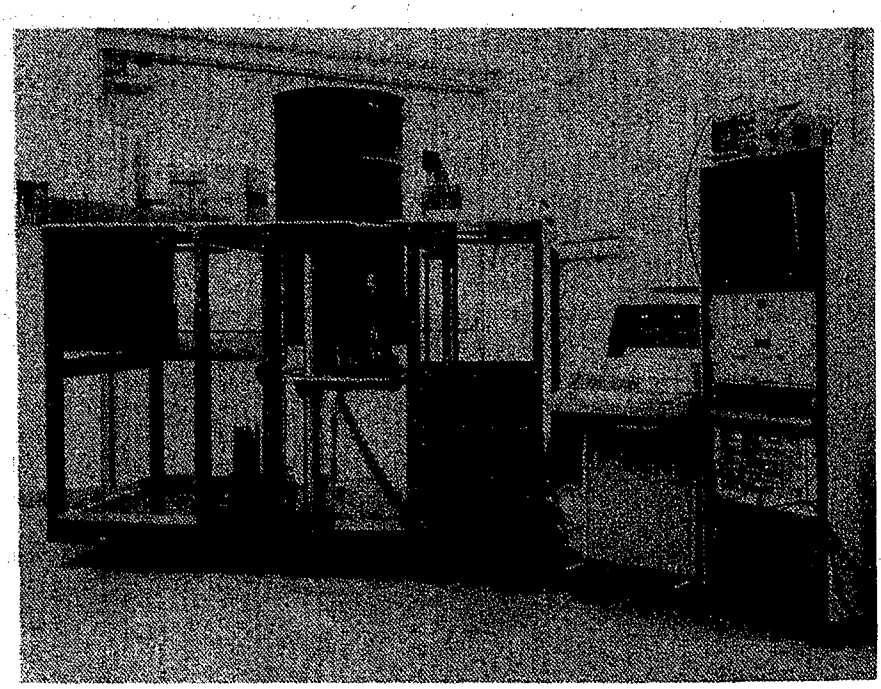

Fig. 6.18 SGS system showing scan table for 55-gal. drums.

The sample container is positioned as close as possible to the collimator to maximize count rates and give the best segment resolution. The segment overlap is determined by the sample size, collimator dimensions, and the relative positions of the segments. In Figure 6.17, a collimator 1.25 cm high and 10 cm deep provides a reasonable trade-off in sensitivity and spatial resolution. For 30- and 55-gal. drums, a collimation 5 cm high and 20 cm deep is a reasonable choice. The spatial resolution cannot be as sharp in the latter case, but it is sufficient to provide useful information on the uniformity of material distribution. The choice of collimator material is usually lead. If space is a consideration, a tungsten alloy may be used.

To maximize count rates, the detector is as close as possible to the collimator. For the plutonium measurement, a filter of lead (~1.5 mm) and cadmium (~0.8 mm) reduces the rate of low-energy events from ^{241}Am and the x rays of both plutonium and lead. For ^{235}U assay, the cadmium alone should suffice, because there is not the 60-keV ^{241}Am flux found in plutonium materials.

For ^{239}Pu assay, ^{75}Se is the transmission source and ^{133}Ba is the reference source. About 10 mCi of ^{75}Se provides usable intensity for at least 1 yr in spite of the relatively short 120-day half-life. Sources of this strength must be encased in a collimator shield to avoid undue personnel exposure. The 356.0-keV gamma ray of ^{133}Ba provides the reference; it can also be used for spectrum stabilization because it is always present in the acquired spectrum. The 10.4-yr half-life is convenient; a single source usually lasts the useful life of a germanium detector. A source of ~10 μCi may be positioned anywhere on the front or side of the detector end cap; however, a slightly better peak shape results when the source is mounted on the front of the end cap along the crystal axis.

Segmented scans may be accomplished in several ways, described as discrete or continuous scans. In a continuous scan, the rotating sample moves past the collimator at a constant speed. The count time is often chosen as the time required for the container to move the height of the collimator. In a discrete scan, the sample is positioned vertically, counted, repositioned, counted again, etc. This mode of operation avoids detector microphonics caused by vibration in the vertical drive system. In practice, a segment spacing equal to one-half of the collimator height works well and might be recommended as a "rule of thumb." The continuous mode probably gives a somewhat better value for the average transmission within a segment. The discrete scan is usually easier to achieve. It also lends itself to two-pass assays in which the container is counted once with the transmission source exposed and once with it shuttered off. The two-pass scheme is useful when the utmost sensitivity and accuracy is desired, and is particularly useful when ^{169}Yb is used as a transmission source in ^{235}U assays. Other variations in the application of the segmented scanning procedure are possible and are described in Refs. 14 and 15.

REFERENCES

1. *American National Standard Guide to Calibrating Nondestructive Assay Systems*, ANSI N15.20-1975 (American National Standards Institute, New York, 1975).

2. J. L. Parker, "The Use of Calibration Standards and Correction for Sample Self-Attenuation in Gamma-Ray Nondestructive Assay," Los Alamos National Laboratory report LA-10045 (August 1984).

3. J. H. Hubbell, "Photon Cross Sections, Attenuation Coefficients, and Energy Absorption Coefficients from 10 keV to 100 GeV," National Bureau of Standards report NSRDS-NBS 29 (August 1969).

4. J. P. Francois, "On the Calculation of the Self-Absorption in Spherical Radioactive Sources," *Nuclear Instruments and Methods* 117, 153-156 (1974).

5. J. L. Parker, "A Correction for Gamma-Ray Self-Attenuation in Regular Heterogeneous Materials," Los Alamos National Laboratory report LA-8987-MS (September 1981).

6. J. L. Parker and T. D. Reilly, "Bulk Sample Self-Attenuation Correction by Transmission Measurement," Proc. ERDA X- and Gamma-Ray Symposium, Ann Arbor, Michigan, May 19-21, 1976 (Conf. 760539).

7. W. H. McMaster, N. Kerr Del Grande, J. H. Mallett, and J. H. Hubbell, "Compilation of X-Ray Cross Sections," Lawrence Radiation Laboratory report UCRL-50174, Sec. II, Rev. 1 (1969).

8. J. E. Cline, "A Technique of Gamma-Ray Detector Absolute Efficiency Calibration for Extended Sources," Proc. American Nuclear Society Topical Conference on Computers in Activation Analysis and Gamma Ray Spectroscopy, Mayaguez, Puerto Rico (1978), pp. 185-196 (Conf. 780421).

9. "Self-Shielding Correction for Photon Irradiation of Slab and Cylindrical Samples," Gulf General Atomic, Inc., Progress Report GA-9614 (July 1, 1968–June 30, 1969).

10. *Handbook of Mathematical Functions With Formulas, Graphs, and Mathematical Tables*, Milton Abramowitz and Irene A. Stegun, Eds., National Bureau of Standards, Applied Mathematics Series 55 (1970).

11. Yardley Beers, *Introduction to the Theory of Error* (Addison-Wesley Publishing Co., Inc., Reading, Massachusetts, 1962).

12. Philip R. Bevington, *Data Reduction and Error Analysis for the Physical Sciences* (McGraw-Hill Book Company, New York, 1969).

13. *Handbook of Nuclear Safeguards Measurement Methods*, Donald R. Rogers, Ed., NUREG/CR-2078, MLM-2855 (US Nuclear Regulatory Commission, Washington, DC, 1983).

14. E. R. Martin, D. F. Jones, and J. L. Parker, "Gamma-Ray Measurements with the Segmented Gamma Scan," Los Alamos Scientific Laboratory report LA-7059-M (December 1977).

15. American Society For Testing and Materials, "Standard Test Method for Nondestructive Assay of Special Nuclear Material in Low-Density Scrap and Waste by Segmented Passive Gamma-Ray Scanning," Vol. 12.01, C853-82, 1989, p. 366, ASTM, Philadelphia.

7

The Measurement of Uranium Enrichment

Hastings A. Smith, Jr.

7.1 INTRODUCTION

Uranium and plutonium samples are present in the nuclear fuel cycle in a wide variety of isotopic compositions; so the isotopic composition of a sample is often the object of measurement (see Chapter 8). In this chapter, we consider a special case of isotopic analysis: the determination, by radiation measurement, of the fractional abundance of a specific isotope of an element. This measurement is most often applied to uranium samples to establish the fraction of fissile ^{235}U, commonly referred to as the *uranium enrichment*. The term "enrichment" is used because the fraction of the sample that is ^{235}U is usually higher than that in naturally occurring uranium.

Three isotopes of uranium are prevalent in nature (their isotopic atom abundances are shown in parentheses): ^{238}U (99.27%), ^{235}U (0.720%), and ^{234}U (0.006%). The ^{234}U comes from the alpha decay of ^{238}U:

$$^{238}U \xrightarrow{\alpha} {}^{234}Th \xrightarrow{\beta(24\ D)} {}^{234m}Pa \xrightarrow{\beta(1.2\ m)} {}^{234}U\ . \tag{7-1}$$

Other isotopes may be present if the sample is reactor-produced; the isotopes include ^{236}U (from neutron capture on ^{235}U) and ^{237}U [from (n,2n) reactions on ^{238}U].

The ^{235}U *atom* fraction for uranium is defined as follows:

$$E_a(\text{at\%}) = \frac{\text{No. of atoms } ^{235}U}{\text{No. of atoms U}} \times 100\ . \tag{7-2}$$

The enrichment can also be expressed as a *weight* fraction:

$$E_w(\text{wt\%}) = \frac{\text{No. of grams } ^{235}U}{\text{No. of grams U}} \times 100\ . \tag{7-3}$$

The two enrichment fractions are related by

$$E_w(\text{at\%}) = \frac{235E_a}{238\ -\ 0.03E_a} \approx \frac{235}{238}E_a\ . \tag{7-4}$$

Uranium enrichments in light-water-reactor (LWR) fuel are typically in the few percent range. CANDU reactors use natural uranium, and materials testing reactors (MTR) use highly enriched uranium (enrichments from 20% to 90%). Determination of uranium enrichment in samples is a key measurement for process or product control in enrichment and fuel fabrication plants, and is very important in international safeguards inspections to verify that uranium stock is being used for peaceful purposes.

Enrichment measurement principles can be used to determine any isotopic fraction if a radiation signature is available and if a few specific measurement conditions are met. The discussion that follows describes various enrichment measurement techniques and their applications.

7.2 RADIATIONS FROM URANIUM SAMPLES

The isotopes of uranium emit alpha, beta, neutron, and gamma radiation. The primary radiation used in passive NDA of uranium samples is gamma radiation, which is usually dominated by emissions from ^{235}U decay. However, in low-enriched uranium samples, the x radiation is the most intense component of the emission spectrum. The 185.7-keV gamma ray is the most frequently used signature to measure ^{235}U enrichment. It is the most prominent single gamma ray from any uranium sample enriched above natural ^{235}U levels. There are no common interferences except in reprocessed fuel where the 236-keV gamma ray from the ^{232}Th daughter, ^{212}Pb, usually swamps the ^{235}U line. Table 7-1 lists the most intense gamma rays from uranium isotopes of interest (see Ref. 1). Data on the alpha and neutron radiations from uranium isotopes can also be found in Ref. 1. Gamma-ray spectra from uranium samples of varying degrees of enrichment are shown in Figures 7.1 (Ref. 1) and 7.2 (Ref. 2) for high- and low-resolution gamma detectors, respectively.

7.3 INFINITE-SAMPLE GAMMA MEASUREMENT TECHNIQUE

The principles of gamma-ray uranium enrichment measurement (Refs. 3 through 5) were first applied to the measurement of UF_6 cylinders (Ref. 6). The basic measurement procedure involves viewing a uranium sample through a collimated channel with a gamma-ray detector (Figure 7.3). The enrichment is deduced from the intensity of the ^{235}U 186-keV gamma ray. If the uranium sample is large enough, the 186-keV gamma rays from only a fraction of the total sample reach the detector because of the strong absorption of typical uranium-bearing materials at this energy. This "visible volume" of the sample is determined by the collimator, the detector geometry, and the mean free path of the 186-keV radiation in the sample material. Its

size (illustrated in Figure 7.3 by the dashed lines) is independent of the enrichment because the different uranium isotopes all have the same attenuation properties. If the depth of the sample along the collimation axis is much larger than the mean free path of 186-keV photons in the sample material, all samples of the same physical composition would present the same visible volume to the detector. This is the so-called "infinite-thickness" criterion. Table 7-2 lists the mean-free-path and infinite-thickness values for the 186-keV gamma ray in commonly encountered uranium compounds. For many common uranium materials, the infinite-thickness criterion is satisfied with quite modest sample sizes. However, because we see no deeper into the sample than certain distances, as indicated in Table 7-2, gamma-ray-based enrichment measurements often sample only the *surface* of the uranium material. Then, for enrichment measurements to be meaningful for the entire sample, the material must be isotopically uniform.

Table 7-1. Gamma radiation from uranium isotopes[a]

Isotope	Gamma-Ray Energy (keV)	Specific Intensity (gamma/s-g of isotope)
^{232}U	129.1	6.5×10^8
	270.5	3.0×10^7
	327.8	2.7×10^7
^{233}U	119.0	3.9×10^4
	120.8	3.2×10^4
	146.4	6.6×10^4
	164.6	6.4×10^4
	245.3	3.8×10^4
	291.3	5.8×10^4
	317.2	8.3×10^4
^{234}U	120.9	5.4×10^5
^{235}U	143.8	7.8×10^3
	163.4	3.7×10^3
	185.7	4.3×10^4
	202.1	8.0×10^2
	205.3	4.0×10^3
^{238}U	742.8	7.1
In equilibrium	766.4	2.6×10^1
with ^{234m}Pa	786.3	4.3
	1001.0	7.5×10^1

[a]Ref. 1.

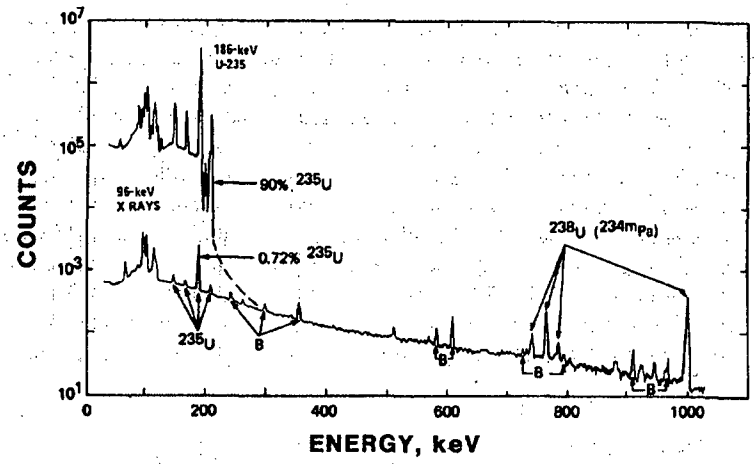

Fig. 7.1 Gamma-ray spectra from natural (0.7% ^{235}U) and 90%-enriched uranium, measured with an unshielded 14%-efficiency Ge(Li) detector. The peaks labeled ^{238}U (^{234m}Pa) are from the decay of ^{234m}Pa. Background peaks are labeled B. Note the dominance in the spectrum of the 186-keV peak from ^{235}U decay. (Figure from Ref. 1.)

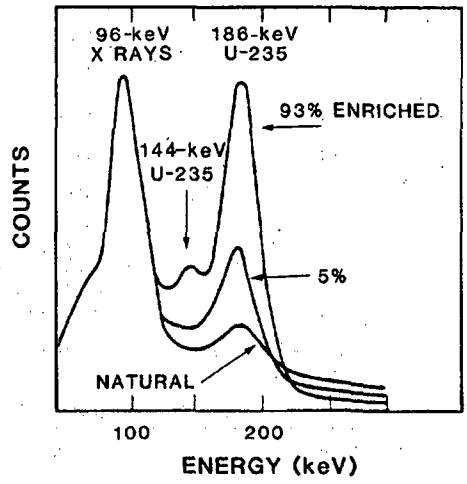

Fig. 7.2 Gamma-ray spectra from natural, 5%-enriched, and 93%-enriched uranium samples, measured with a NaI(Tl) scintillation detector. As the ^{235}U enrichment increases, the 186-keV peak becomes more intense and the background (from the ^{238}U daughters) above the peak energy becomes weaker. (Figure from Ref. 2.)

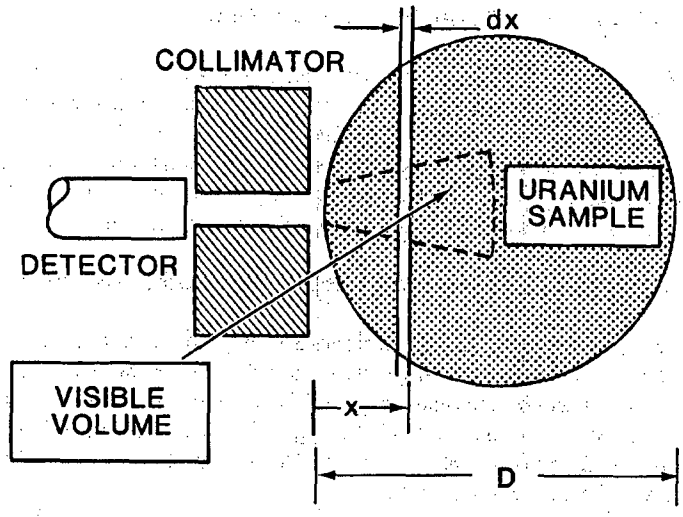

Fig. 7.3 The basic elements of a gamma-ray uranium-enrichment measurement setup. For purposes of illustration, the size of the visible volume compared with the detector and collimator is exaggerated. Normally the depth of the visible volume is much smaller than the source-to-detector distance.

Table 7-2. Mean free paths and infinite thicknesses for 186-keV photons in uranium compounds

Uranium Compound	Density (ρ) (g/cm^3)	Mean Free Path (cm)[a]	"Infinite" Thickness (cm)[b]
Metal	18.7	0.04	0.26
UF_6 (solid)	4.7	0.20	1.43
UO_2 (sintered)	10.9	0.07	0.49
UO_2 (powder)	2.0	0.39	2.75
U_3O_8 (powder)	7.3[c]	0.11	0.74
Uranyl nitrate	2.8	0.43	3.04

[a]Equal to $1/\mu\rho$ at 186 keV for the material in question.
[b]Defined as 7 mean free paths, the distance for which the error in assuming infinite-sample size is less than 0.1% (see Equation 7-8).
[c]Highly packed powder.

7.3.1 One-Component Example (Uranium Metal)

For a given detector/collimator geometry, all samples of pure uranium metal have identical visible volumes, since the mean free path of the 186-keV gamma ray is the same for each sample. As a result, the detector views ^{235}U radiation from the same amount of total uranium, regardless of the size of the metal sample. Since the 186-keV intensity, although heavily absorbed, is still proportional to the number of ^{235}U atoms in the visible volume, it is proportional to the *atom* enrichment of the sample.

7.3.2 Two-Component Example (Uranium and Matrix Material)

The prototypical enrichment sample consists of uranium and a (usually low-Z) matrix material. The measurement geometry is still the same as that shown in Figure 7.3, but the absorption by the matrix material is an added factor in the measurement. Exhaustive summaries of the theory of this type of measurement have been published (Refs. 7 and 8). Given below is a summary of the key mathematical results necessary to analyze enrichment measurements.

Consider a gamma-ray measurement on a two-component sample of thickness D, where the sample-to-detector distance is large compared with the depth of the visible volume. This feature permits the neglect of $1/r^2$ effects during integration over the sample volume. The counting rate from an infinitesimal section of the sample (see Figure 7.3) is given by

$$dR = \varepsilon E_w S\, dm_U \exp(-\mu\rho x) \exp(-\mu_c \rho_c t_c) \tag{7-5}$$

where $dm_U = A\ \rho_U\ dx$,

ε = detection efficiency at the assay energy

E_w = uranium enrichment (*weight* percent, see Equation 7-3)

A = collimator channel area

S = specific activity of the gamma ray (185.7 keV, see Table 7-1)

$\mu_c\rho_c$ = linear photon absorption coefficient of the sample container at the assay energy

t_c = single wall thickness of the sample container.

The quantity $\mu\rho$ represents the linear photon absorption coefficient of the combined uranium (U) and the matrix (m) at the assay energy:

$$\mu\rho = \mu_U \rho_U + \mu_m \rho_m \ . \tag{7-6}$$

Integration of Equation 7-5 over the sample thickness gives the total 186-keV count rate:

$$R = \varepsilon E_w SA\ \rho_U \exp(-\mu_c \rho_c t_c) \int_0^D \exp(-\mu\rho x)\ dx \tag{7-7}$$

which reduces to

$$E_w = \left[\frac{\mu_U}{\varepsilon SA}\right] R \left[\frac{F \exp(\mu_c \rho_c t_c)}{1 - \exp(-\mu\rho D)}\right] \tag{7-8}$$

where

$$F = 1 + (\mu_m \rho_m / \mu_U \rho_U) \, . \tag{7-9}$$

If the sample thickness D is large enough, then the exponential in the denominator of Equation 7-8 is negligible compared to 1, making variations in sample dimensions unimportant. This is the origin of the infinite-thickness criterion. The first bracket in Equation 7-8 contains factors that depend only on the instrument properties (ε and A) and the intrinsic properties of uranium (μ_U and S) and thus constitutes the basic calibration constant of the measurement. If the unknown samples and calibration standards have identical containers, then the factor, $\exp(\mu_c \rho_c t_c)$, can be subsumed into the calibration constant; otherwise the factor must be used to obtain a container correction. (See Section 7.7.)

The factor F in Equation 7-8 reflects the matrix effects. If the calibration standards and the unknown samples have the same matrix properties, then this factor can also be included in the calibration constant. If the sample matrix factor F differs from the calibration matrix factor F_s, then a small correction is also necessary for this difference. Table 7-3 gives values for this multiplicative correction (F/F_s) for various uranium compounds (Ref. 2).

Table 7-3. Material composition correction factors (F/F_s)[a]

Nuclear Material of Calibration Standards (Factor F_s)	Nuclear Material of Items Measured (Factor F)					
	U	UC	UC_2	UO_2	U_3O_8	UF_6
U (100% U)	1.00	1.00	1.00	1.01	1.01	1.04
UC (95% U)	1.00	1.00	1.00	1.01	1.01	1.03
UC_2 (91% U)	0.99	1.00	1.00	1.00	1.01	1.03
UO_2 (88% U)	0.99	0.99	1.00	1.00	1.00	1.03
U_3O_8 (85% U)	0.99	0.99	0.99	1.00	1.00	1.02
UF_6 (68% U)	0.96	0.97	0.97	0.98	0.98	1.00
U nitrate (47% U)	0.92	0.92	0.93	0.93	0.93	0.95

[a]Ref. 2.

7.3.3 Instrumentation and Infinite-Sample Technique: Applications

The basic measurement apparatus is a collimated gamma-ray detector and its associated electronics. An early version of such instrumentation was the SAM-II and a NaI(Tl) scintillation detector (Ref. 6). Gamma-ray pulses were analyzed with a dual single-channel analyzer (SCA), with one window set on the 186-keV energy region (C1 in Figure 7.4) and the second window set on a background region above the assay peak (C2 in Figure 7.4).

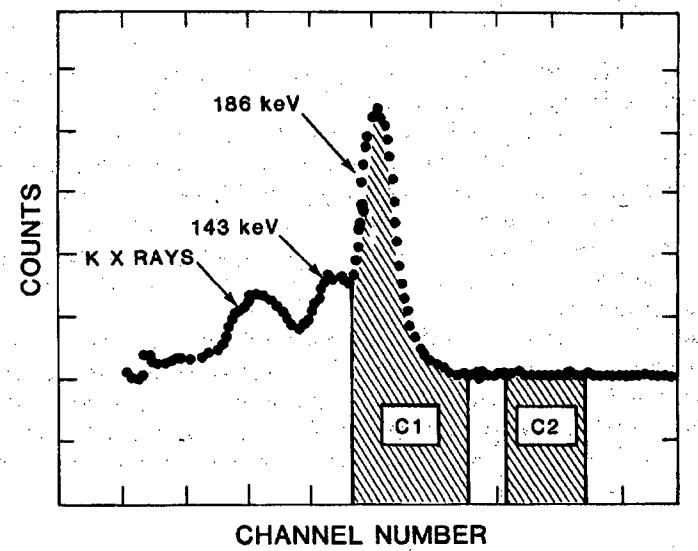

Fig. 7.4 A low-resolution uranium gamma-ray spectrum, showing the two energy regions used in the enrichment measurement.

The uranium enrichment is proportional to the *net* 186-keV count rate (R in Equation 7-8), which is given by

$$R = C1 - f\,C2\ . \qquad (7\text{-}10)$$

This equation represents the subtraction of a background from the gross rate in the chosen 186-keV peak energy region. The major contribution to the background comes from the higher energy gamma rays of ^{238}U daughters that Compton scatter in the detector. Even though C2 is not actually in the assay energy region, it represents the background under the assay region, to within a scale factor (f, to be determined by calibration). Since the enrichment (either atom or weight) is proportional to the net rate R, we have

$$E = a\ R\ F \exp(\mu_c \rho_c t_c) = F \exp(\mu_c \rho_c t_c)(a\ C1 - a\ f\ C2)\ . \quad (7\text{-}11)$$

The calibration constant a contains all of the geometric factors and the intrinsic uranium constants in Equation 7-8. The matrix factor F and the container wall attenuation correction factor $\exp(\mu_c \rho_c t_c)$ have been displayed explicitly to emphasize their roles when standards and unknowns are made of different types of materials or packaged in different containers. If the measurement is performed on materials of the same type packaged in the same container, then $F \exp(\mu_c \rho_c t_c)$ can be included in the calibration constant. The enrichment is then written in terms of the measured data (C1 and C2):

$$E = a\ C1 + b\ C2\ . \quad (7\text{-}12)$$

The calibration constants a and b (= −a f) now include the container attenuation and the matrix factor and are determined by measurement of two standards of known enrichments E_1 and E_2.

With the SAM-II, the calibration constants were applied through digital rate multipliers to the outputs of the two SCAs. An up/down scaler displayed the difference between the scaled C1 and C2 values, thereby displaying the uranium enrichment. An in-line extension of the SAM-II type of measurement has been installed at the Portsmouth Gaseous Diffusion Plant (GDP) (Ref. 9). It has been in operation for more than 12 years and continues to assay the output liquid UF_6 product with a relative accuracy of 0.25% (1σ). The instrument was developed for continuous determination of both the ^{235}U enrichment (by gamma-ray measurement) and the ^{234}U enrichment (by neutron measurement; see Section 7.6 and Chapter 15). A drawing of the gamma-ray portion of the measurement apparatus is shown in Figure 7.5.

More recent instrumentation (Ref. 10) employs a portable, battery-powered, microprocessor-based MCA with the NaI detector (Figure 7.6). The instrument acquires a full uranium spectrum, integrates the counts in selected regions of interest corresponding to the count windows C1 and C2 (for example, as in Figure 7.4), computes the enrichment and its statistical uncertainty, and presents the results on an alphanumeric display. The two-parameter, two-standard calibration procedure is also incorporated into the instrument software. A similar method is used for routine enrichment checks by some plant operators (Ref. 11). These gamma-spectroscopic techniques are used in many in-plant and field applications, including the measurement of UF_6 in storage cylinders. As with earlier measurements, many current applications still use NaI scintillation detectors (Ref. 6). However, high-resolution spectrometry with semiconductor detectors is more effective in avoiding problems of interference from ^{238}U daughters deposited on the inner surfaces of the containers. The high-resolution detector is especially helpful where chemical processes have concentrated ^{238}U daughters in the deposit or in the uranium material itself. Some commercial processes have been observed to produce up to a ten-fold concentration of ^{238}U daughters. The radiation from the daughters produces a high Compton background in the detector, which can complicate the evaluation of the 185.7-keV peak area.

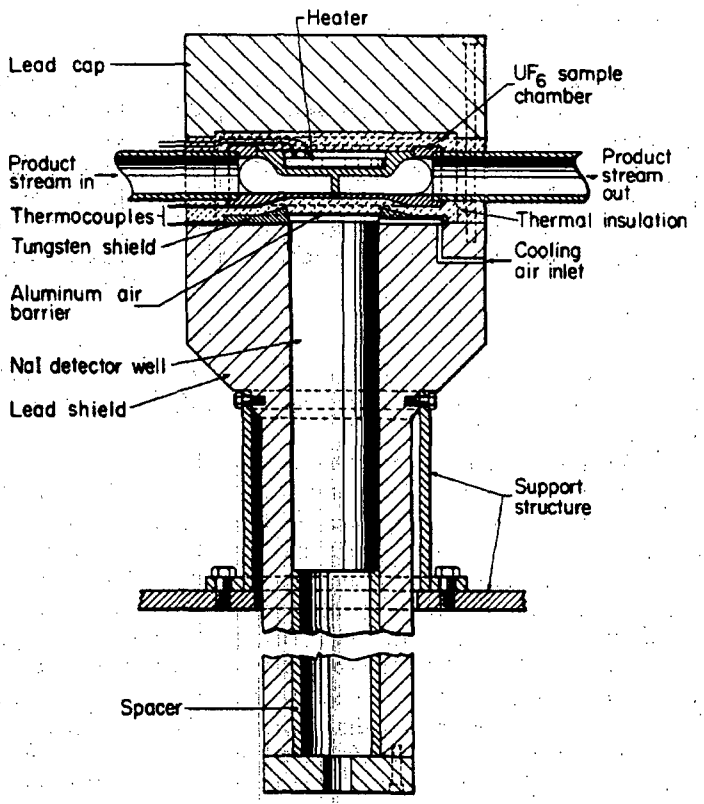

Fig. 7.5 The detector and shield assembly of the gamma-ray enrichment meter at the Portsmouth GDP. The liquid UF_6 product flows through the sample chamber, where the 186-keV gamma-ray intensity is measured to determine the UF_6 enrichment. (Figure from Ref. 9.)

While not strictly an infinite-thickness technique, there is a procedure used in the analytical chemistry laboratories of some fuel processors, such as General Electric in Wilmington, North Carolina, that deserves mention. Small samples of process materials are dissolved and prepared as dilute, aqueous samples of uranyl nitrate in standard ampules. The ^{238}U daughters are removed from the solution before measurement. These samples are inserted in NaI well counters and measured against a carefully prepared range of isotopic standards. The technique can provide a very accurate (0.1–0.2%) assay of uranium enrichment. General Electric measures thousands of samples each year using this technique.

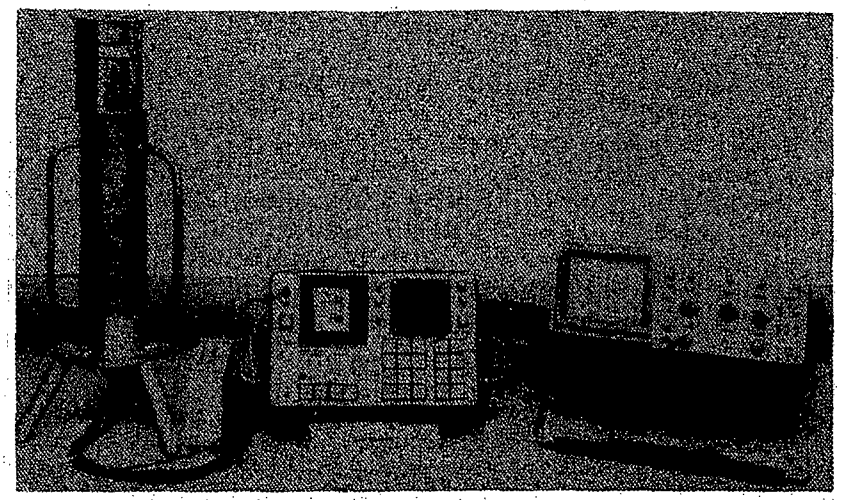

Fig. 7.6 Gamma-ray uranium enrichment measurement equipment, including a portable, microprocessor-based MCA and a NaI(Tl) gamma-ray detector. This instrumentation can be battery powered and is suited for mobile field applications.

7.4 PEAK-RATIO TECHNIQUES

7.4.1 Theory

For arbitrary, noninfinite uranium samples (for example, thin foils, contamination deposits, or dilute solutions), it is difficult to correct the 186-keV gamma intensity for absorption in order to yield enrichment. This difficulty arises because the factor $[1 - \exp(-\mu\rho D)]$ in Equation 7-8 is difficult to estimate. The peak-ratio technique requires the measurement of *ratios* of gamma-ray intensities from the major isotopes and the use of that information to determine the uranium enrichment. The technique is basically identical to the plutonium isotopic analysis procedure described in Chapter 8. In the simplest case of low ^{235}U enrichment, ^{235}U and ^{238}U are essentially the only components. Since the sum of their isotopic fractions (f) is then equal to 1, the ^{235}U atom enrichment is (recall Equation 7-2)

$$E_a = f_{235} = N(235)/[N(235) + N(238)] = (1 + f_{238}/f_{235})^{-1} . \qquad (7\text{-}13)$$

If ^{234}U or ^{236}U is present in the sample in significant amounts, one can measure other gamma peak ratios that involve these isotopes. Then the expression for the ^{235}U atom enrichment will contain these other ratios. (For an example relating to plutonium isotopic analysis, see Chapter 8.)

The main challenge to the peak-ratio technique is the determination of the isotopic ratio f_{238}/f_{235}. The most intense gamma-ray peaks from ^{238}U are those in the 700- to 1000-keV energy range from its ^{234m}Pa daughter (see Table 7-1). The large energy difference between the ^{234m}Pa (^{238}U) gamma rays and the 186-keV ^{235}U gamma ray necessitates a significant correction for the different relative detection efficiencies (including photon absorption through the sample material and container). Establishing this relative efficiency curve as a function of energy requires the measurement of known peak intensities over the energy range of interest. (See Chapter 8 for details relating to plutonium isotopic analysis.) For uranium measurements, one must determine several gamma intensities from the two main isotopes (^{235}U and ^{238}U) and normalize the measurements to a common efficiency curve.

7.4.2 Applications

In one application of this procedure, the normalization factor k between the relative efficiency curves for the ^{235}U gamma intensities and the ^{238}U intensities is determined iteratively (Ref. 12). The atom enrichment in Equation 7-13 then becomes

$$E_\alpha = [1 + k\,(\lambda_{235}/\lambda_{238})]^{-1} \qquad (7\text{-}14)$$

where λ_A is the nuclear decay constant for the uranium isotope of mass A, and k is the iteratively determined ratio of the two activities of the isotopes of interest:

$$k = A(^{238}U)/A(^{235}U)\,. \qquad (7\text{-}15)$$

To determine the relative efficiency curve, a weak ^{234m}Pa gamma ray at 258.3 keV and a ^{234}Th gamma ray at 63.3 keV are included to extend the efficiency data from ^{238}U decay to the energy region where ^{235}U gamma rays are prominent.

A similar philosophy has been applied (Refs. 13 through 16) with the use of high-resolution gamma-ray spectroscopy in the narrow 89- to 99-keV energy range. In one approach (Refs. 13 through 15) the lines used for isotopic measurements were situated in the 92.4- to 93.4-keV range: the intensities of the 92.4- and 92.8-keV lines of ^{234}Th were used as a measure of the ^{238}U concentration of the sample, and the 93.35-keV thorium $K_{\alpha 1}$ line was used as a measure of the ^{235}U concentration. The ^{238}U contribution to the 93.35-keV line was taken into account in the calibration. Uranium K_α x rays were used for the energy and efficiency calibrations. Better than 1% agreement with mass-spectroscopic analyses was achieved in laboratory studies. Another approach (Ref. 16) used the 89.9-keV thorium K x ray from ^{235}U decay and the 92-keV gamma-ray doublet from ^{234}Th; the results agreed with standard values to within 1%.

Both of the low-energy peak-area ratio techniques rely on the equilibrium between the ^{234}Th daughter and the ^{238}U parent. Since the half-life of ^{234}Th is 24 days, equilibrium is usually achieved in 120 to 168 days (97% and 99%, respectively, of

equilibrium activity) after chemical separation. The narrow energy range minimizes uncertainties in the energy-dependent relative photopeak efficiencies, and the empirical determination of these efficiencies for each sample makes this enrichment measurement technique less dependent on knowledge of the matrix materials. However, neither of the low-energy techniques has yet found significant field application.

7.4.3 Summary of Peak-Ratio Techniques

The methods described above have the advantage that peak *ratios* are measured, allowing the uranium enrichment to be determined without the use of enrichment standards or the determination of geometry-dependent calibration constants. In addition, the samples do not need to satisfy the infinite-thickness criterion. Furthermore, the relative efficiency corrections are made for each sample and include not only the absorption by the sample material but also that by the sample container and any external absorbers. The plutonium isotopics measurements described in Chapter 8 have the same advantages. The disadvantages of this technique are related to

- The low intensity of the ^{238}U daughter radiation for the higher-energy method
- The need for secular equilibrium between the ^{238}U and its daughters
- The need for isotopic homogeneity in the sample.

The need for isotopic homogeneity manifests itself in cases where residual sample material from other sources may be in the container with the material currently being measured—for example, in the measurement of UF_6 cylinders in which uranium from previous shipments may have deposited on the walls of the cylinder.

The peak ratio methods of determining uranium enrichment can also, in principle, be applied to "infinite" samples. However, in those cases, the peak-ratio methods are more cumbersome and time-consuming and usually have no advantage over the enrichment-meter technique, which is simpler, faster, and less expensive.

7.5 GAS-PHASE URANIUM ENRICHMENT MEASUREMENT TECHNIQUES

An extreme case of performing enrichment measurements on a noninfinite sample is the measurement on UF_6 in the gaseous phase. In one technique (Refs. 17 through 20) the ^{235}U concentration was determined from a measurement of the 186-keV gamma-ray emission rate R from the decay of ^{235}U, and the total uranium concentration was determined by measuring the transmission (T_{60}) through UF_6 gas of 60-keV gamma rays from an external ^{241}Am source. Figure 7.7 shows the measurement system, with the orientation of the NaI(Tl) detector and the sample chamber and the location of the ^{241}Am transmission source. The (atomic) enrichment E_a was related to the measured count rate R of the 186-keV rays by

$$E_a = R/(C \ln T_{60}) \qquad (7\text{-}16)$$

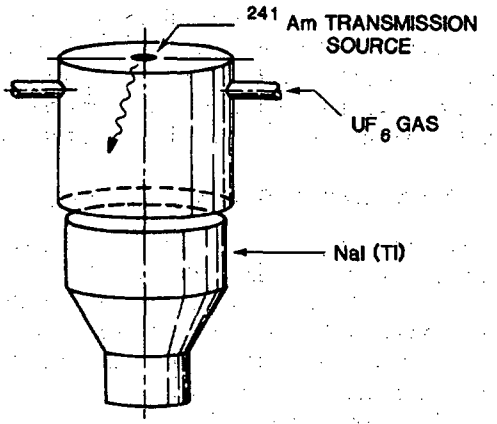

Fig. 7.7 The NaI(Tl)-based gas-phase UF_6 enrichment monitor. The NaI detector views 60-keV gamma rays from the ^{241}Am source (for transmission measurement) and 186-keV gamma rays from the sample chamber (for ^{235}U determination). (Figure from Ref. 18.)

where R was corrected for deadtime losses and attenuation in the gas, C was a calibration constant, and $\ln(T_{60})$ was proportional to the total uranium in the sample. Since the measurement accounted for variations in UF_6 density, the measured assay was independent of the UF_6 pressure. This method produced assay results with measured accuracies better than 1% relative over the range of UF_6 enrichments of 0.72 to 5.4 at%, using a single-point calibration. For 1.0%-enriched UF_6 at 700 torr, a 0.74% relative precision was obtained for a 1000-s counting time (Ref. 19). This technique was applied at relatively high UF_6 pressures; so the data signals were dominated by radiation from the UF_6 gas, making interferences from uranium deposits on the inner surface of the sample chamber unimportant. A NaI(Tl) gamma-ray detector was used during test and evaluation of this instrument in 1982 at the Paducah product feed line of the Oak Ridge Gaseous Diffusion Plant (ORGDP). The instrument was modified for high-resolution gamma-ray detection and tested in 1983. A prototype of the high-resolution instrument (Refs. 20 and 21) for the Portsmouth Gas Centrifuge Enrichment Plant (GCEP) was built and tested at the ORGDP in 1984 (see Figure 7.8).

At lower UF_6 pressures (for example, tens of torr) the density of the UF_6 gas is not great enough for a transmission measurement to have sufficient sensitivity. Furthermore, the radiation from material deposited on the container surfaces becomes a significant fraction of the total signal, and careful corrections for this interference are then required for accurate results. Passive gamma-ray counting and (active) x-ray fluorescence have been combined to verify the approximate enrichment of gaseous UF_6 at low pressures in cascade header pipework (Refs. 22 through 26). The gamma-ray intensities from the decay of ^{235}U (186 keV) and ^{238}U daughter products in the pipework deposits and the UF_6 gas were measured to determine the ^{235}U present in

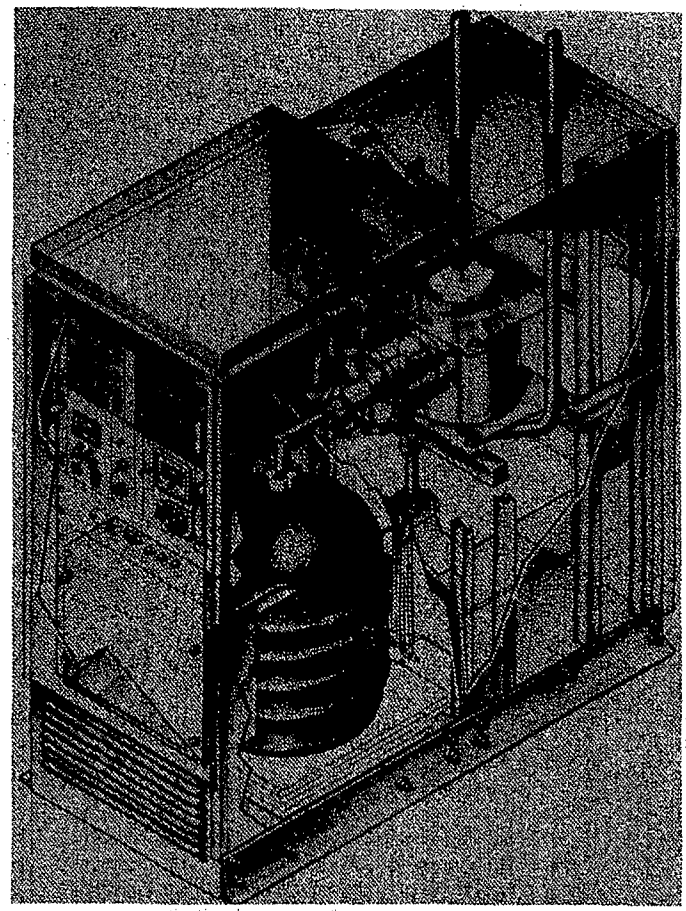

Fig. 7.8 *The UF_6 gas-phase enrichment monitor cabinet for the Portsmouth GCEP. Half of the cabinet houses the detector and electronics, and the other half contains the heated chamber for UF_6 and its associated hardware. (Figure from Ref. 21.)*

the gas. The correction for radiation from the uranium deposited on the inner surface of the pipework was established with gamma rays from ^{234}Th and ^{231}Th decays (Refs. 25 and 26). The total mass of uranium in the gas was measured using x-ray fluorescence with the 122-keV gamma rays from a ^{57}Co excitation source. The ratio of the intensities of the 186-keV gamma rays from the UF_6 gas to the uranium $K_{\alpha 1}$ x rays was calibrated to give a direct measurement of the gas enrichment. A variation

of the correction for uranium deposits (Refs. 24 through 26) determined the correction for the deposited uranium by passive gamma-ray measurements under two different collimation conditions (see Figure 7.9). In both applications, the instruments were capable of providing a "go/no-go" decision on whether the measured enrichment was less than or greater than 20%, thus providing the capability of detection of highly enriched uranium for enrichment plant safeguards.

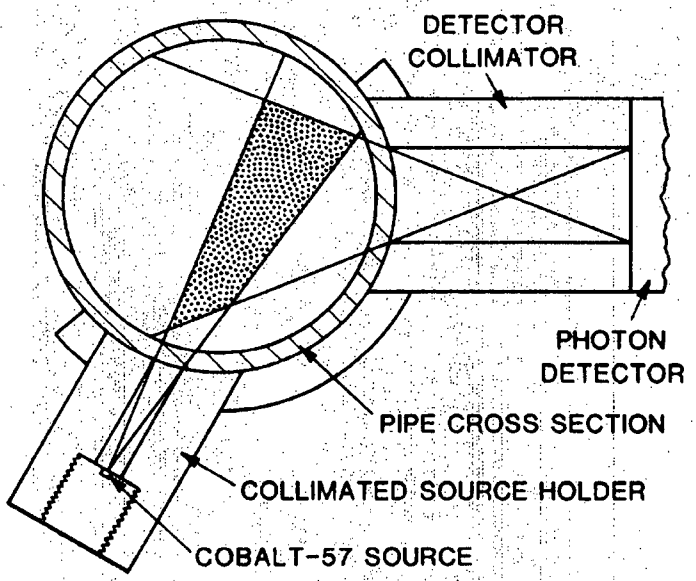

Fig. 7.9 The detector/collimator arrangement for the enrichment measurement of low-pressure UF_6 in pipe work. The assembly consists of a collimated source holder and detector collimator rigidly connected to the pipework. The overlap of the two fields of view isolates a volume of gas in the middle of the pipe from the wall deposits. A tiny ^{57}Co source is used to fluoresce x rays in the gas. (Figure from Ref. 24.)

7.6 NEUTRON-BASED ENRICHMENT MEASUREMENTS

Another passive technique for verification of uranium enrichment of UF_6 is the detection of neutrons emitted from the sample as a result of $^{19}F(\alpha,n)$ reactions (Ref. 27). Uranium-234 is the dominant alpha emitter in enriched uranium and hence, indirectly, the principal source of neutrons in UF_6. Also, because the enrichment of ^{234}U follows

the enrichment of ^{235}U, passive total neutron counting can provide a rough measure of ^{235}U enrichment. The ratio of $^{235}U/^{234}U$ may vary by as much as a factor of 4 over the range of depleted to highly enriched uranium for the gaseous diffusion enrichment process; but for low-enriched uranium (<5%), it is more nearly constant, and verification measurements of limited accuracy may be possible without specific ^{234}U isotopic data (Refs. 6, 9, and 28). Further discussion of this technique is presented in Chapter 15.

7.7 CONTAINER WALL ATTENUATION CORRECTIONS

The standard relationship between the enrichment and the measured data (Equation 7-8) includes the term $\exp(\mu_c\rho_c t_c)$ that corrects for the attenuation of the measured radiation by the walls of the sample container. The attenuation may be included in the calibration if the calibration standards and the unknown samples have the same type of container. In some cases this simplification is not possible, and a container wall attenuation correction must be applied in each measurement. This section considers correction methods for an infinite-thickness enrichment measurement where the sample matrix is constant. If T_x, the transmission of one wall thickness of the unknown sample container, is defined by

$$T_x = \exp[-(\mu_c\rho_c t_c)_x] \tag{7-17}$$

and T_s is similarly defined as the container wall transmission in the calibration measurements, then the unknown enrichment is

$$E = KR(E_A)T_s/T_x \tag{7-18}$$

where K is the calibration constant, and $R(E_A)$ is the net gamma-ray peak count rate from the unknown sample at the assay energy (E_A = 186 keV), measured through the container wall. The discussion that follows presents two methods for determining this container attenuation correction, T_s/T_x. In addition, the verification of UF_6 cylinders is discussed to provide an example of a class of measurements where this correction is especially critical.

7.7.1 Direct Measurement of Wall Thickness

If the container composition and wall thickness at the measurement point are known for both the calibration and sample measurements, then T_s/T_x can be calculated directly from the exponential expression

$$T_s/T_x = \exp[(\mu_c\rho_c t_c)_s - (\mu_c\rho_c t_c)_x] \tag{7-19}$$

where ρ_c represents the density of the container material and μ_c is evaluated at the assay energy. The container wall thickness (t_c) can be measured directly using an ultrasonic thickness gauge (See Figure 7.10). A burst of ultrasound is transmitted by

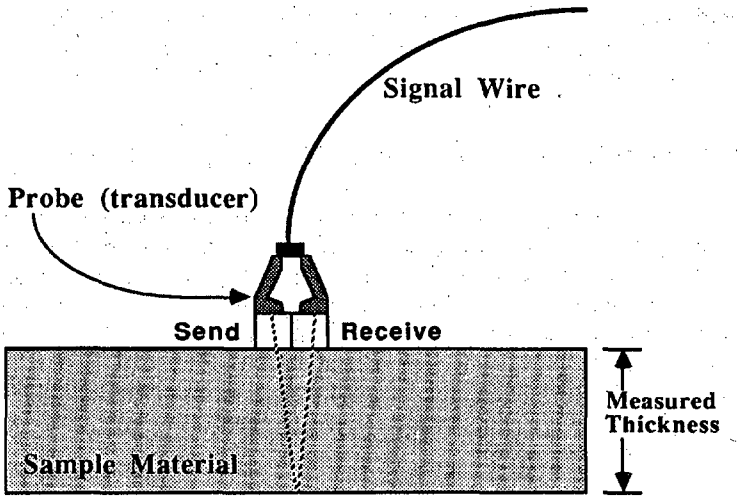

Fig. 7.10 Probe placement in an ultrasonic measurement of thickness. The probe must be acoustically coupled to the outer surface of the material for the ultrasound pulse to enter the material without being severely attenuated. The coupling is accomplished with a liquid compound (usually supplied with the thickness gauge) placed between the probe face and the material surface.

the probe into the container material and travels until it reaches a material of substantially different physical character from the container material. The sound is then reflected back to the probe. The gauge electronics performs a precise measurement of the time needed for the ultrasound pulse to make the round trip in the container material and thereby determines the thickness of the material. Such thickness gauges are available commercially, and thickness results can be read usually to ±0.1 mm. Recent calibration measurements (Ref. 29) showed a fluctuation of ±0.055 mm from repeated measurements on a calibrated steel disc having a thickness of 13.500 mm, which corresponds to a relative standard deviation of 0.4%.

7.7.2 Internal-Line Ratio Technique

The transmission ratio T_s/T_x can also be determined from the ratio of intensities of different-energy gamma rays from one isotope, assuming the sample material

is infinitely thick for the gamma rays measured (see Section 7.3.2). Generally, high-resolution gamma-ray spectroscopy is required to resolve the peaks of interest. For corrections to ^{235}U enrichment measurements, there are several reasonably intense gamma rays near the 186-keV peak energy (see Table 7-1). Consider a case in which the intensities of a peak above and a peak below the 186-keV gamma ray (at energies E_H and E_L, respectively) are measured in addition to the assay peak area. With the transmission as defined in Equation 7-17, we have

$$\frac{T_s(E_A)}{T_x(E_A)} = \left[\frac{T_x(E_H)/T_s(E_H)}{T_x(E_L)/T_s(E_L)}\right]^{\frac{\mu_A}{\mu_L-\mu_H}} \tag{7-20}$$

where the subscripts of the μ's refer to the energies at which the μ's are evaluated. To simplify the calculation of the transmission ratios at E_H and E_L, we recall the definition of transmission from the measurement point of view:

$$T = R/R_0 \, . \tag{7-21}$$

Here, R is the measured peak count rate, attenuated by the container wall, and R_0 is the measured peak count rate from a sample with an infinitesimally thin container (that is, $t_c \rightarrow 0$). In practice, R_0 cannot be measured, but since the expression in Equation 7-20 contains transmission *ratios*, we can re-express these ratios in terms of ratios of *measured peak areas*:

$$\frac{T_s(E_A)}{T_x(E_A)} = \left[\frac{R_x(E_H)/R_s(E_H)}{R_x(E_L)/R_s(E_L)}\right]^{\frac{\mu_A}{\mu_L-\mu_H}} \tag{7-22}$$

where $R(E_{H,L})$ is the peak area at energy $E_{H,L}$. The fractional error in the transmission ratio T_s/T_x is just the exponent $\mu_A/(\mu_L - \mu_H)$ times the fractional error of the measured peak-area ratio expression in the bracket on the right of Equation 7-22. Thus, it is advantageous to make the exponent as small as possible, which means selecting peaks that are not too close in energy. Table 7-4 shows values for the exponent for two commonly encountered container materials and two choices of measurement peaks. Note that one choice includes the ^{235}U assay peak.

Although the internal-line ratio technique is a convenient technique for determining the container attenuation correction, there are no published accounts of its application in enrichment measurements. The major difficulty with using the technique is the time required to obtain adequate statistical precision in the auxiliary gamma-ray peak areas.

Table 7-4. Values of exponent function $\mu_A/(\mu_L - \mu_H)$ for common container materials

E_H/E_L	Iron	Monel	Aluminum	Polyethylene[a]
205 keV/144 keV	2.57	2.17	8.13	8.88
186 keV/144 keV	3.20	2.78	11.09	11.83

[a]Low-density polyethylene, as used in containers.

7.7.3 Measurement of UF_6 Cylinders

One of the most common container types in enrichment measurements is the large cylinder used to ship and store UF_6 in liquid or solid form. These cylinders vary in size and wall thickness. Table 7-5 gives some pertinent parameters for the most common cylinder types (Ref. 30). The large, high-density wall thicknesses of the cylinders means that minor variation in wall thickness can result in significant variation in gamma-ray count rate. The relationship between the relative fluctuation of the enrichment result and the relative fluctuation of the wall thickness is obtained by differentiation of Equation 7-8:

$$dE/E = \mu_c \rho_c (dt_c/t_c) = 1.12(dt_c/t_c) \tag{7-23}$$

where the second result is for steel ($\mu_c = 0.144$ cm^2/g at 186 keV and $\rho_c = 7.8$ g/cm^3). Thus, a 10% variation in cylinder wall thickness (only 0.05 in. for type 30B cylinders) will cause a 12% bias in the corresponding enrichment measurement. Use of a thickness-gauge measurement of the wall thickness reduces the measurement error to a few tenths of one percent, essentially removing the wall thickness from consideration as a source of measurement bias. The UF_6 enrichment measurement apparatus for cylinders can be calibrated by using one or more cylinders as standards, which may then be sampled for analysis. Alternatively, standards of U_3O_8 or UF_4 of known enrichment may be used, with the appropriate corrections for matrix differences (that is, the factor F/F_s in Table 7-3).

Early studies of enrichment measurements on type 30B and 5A cylinders with NaI scintillation detectors (Ref. 6) achieved assay results with relative standard deviations of 5% for type 30B cylinders and <1% for type 5A cylinders. Count times were on the order of a few minutes, and the wall thickness measurement took only a few seconds. Good acoustic coupling between the thickness-gauge probe and the cylinder surface was obtained by sanding the paint off a spot within the area viewed by the gamma-ray detector; the uncertainty in the thickness measurement was estimated at 0.4%. A more recent study of enrichment measurements on type 48 and 30 UF_6 cylinders (Ref. 28) achieved similar results, even with the use of high-resolution gamma-ray detection equipment.

Table 7-5. Physical characteristics of selected UF_6 storage and shipping cylinders[a]

	Cylinder Type			
Characteristic	5A	8A	30B	48X
Nominal diameter (in.)	5	8	30	48
Nominal length (in.)	36	56	81	121
Material of construction	Monel	Monel	steel	steel
Wall thickness (in.)	1/4	3/16	1/2	5/8

[a]Ref. 30.

7.8 EXTENSION OF THE ENRICHMENT METER PRINCIPLE TO OTHER APPLICATIONS

7.8.1 Concentration Meter

Under certain limits of uranium concentration, uranium measurements using the enrichment meter principle become uranium *concentration* measurements (Ref. 5). The same mathematical expressions govern both cases (Equation 7-8); the dependence of the result on the uranium and matrix concentrations is contained in the factor F in Equation 7-9. For matrices with effective $Z \leq 30$, the ratio μ_m/μ_U is less than 0.1. Then for $\rho_m/\rho_U \leq 1$, the value of the correction factor F is very close to 1, and the count rate is almost directly proportional to the enrichment:

$$R = KEF = KE \,. \tag{7-24}$$

The domain in which $\mu_m\rho_m/\mu_U\rho_U \leq 0.1$ is therefore referred to as the "enrichment domain."

At the other end of the spectrum are measurements for which the uranium concentration is very low compared with that of the matrix. In cases where $\mu_m\rho_m/\mu_U\rho_U \geq 10$, the unity term in F can be ignored. Then, if the enrichment and μ values are known, Equation 7-24 becomes

$$R = KEF = K'E(\rho_U/\rho_m) \tag{7-25}$$

with an error of $\leq 10\%$. K' is another calibration constant. The domain for which $\mu_m\rho_m/\mu_U\rho_U \geq 10$ can therefore be called the "concentration meter" domain. The infinite-thickness criterion still must be met in this domain. Examples of samples that would fall into the concentration domain are containers with uranium-contaminated material such as dilute uranium-bearing solutions or uranium holdup in a Raschig-ring tank (Ref. 5).

7.8.2 Mixing (Blend) Ratio in Mixed-Oxide Fuel

The enrichment meter concept may also be used for quality control of different reactor-fuel blends, for example, PuO_2, UO_2, U-C, and Th-C, or in general for the assay of any fissionable material having a suitable low-energy gamma ray so that the sample satisfies the infinite-thickness criterion (Refs. 4 and 31). In the more general case of mixtures of several components, the counting rate from a specific gamma ray from an isotope with enrichment E is given by

$$R = ESA\varepsilon/(\mu_1 F) \tag{7-26}$$

where F is now the more general form of the expression in Equation 7-9:

$$F = 1 + \left[1/(\mu_1\rho_1)\right] \sum_{i=2}^{n} \mu_i\rho_i \ . \tag{7-27}$$

The running index i denotes the relevant elemental constituents in the blend of materials in the sample, and the specific subscript 1 denotes the element whose isotope emits the "signal" gamma ray of interest. For the case of a PuO_2 + UO_2 blend and the detection of a plutonium ("signal") gamma ray (the 129-keV gamma ray meets the infinite-thickness criterion), the above expression reduces to

$$R = \frac{ESA\varepsilon}{\mu_{Pu}K(1+r)} \tag{7-28}$$

where r is the blending ratio, ρ_U/ρ_{Pu}. The constant K reflects the higher-order contributions from the matrix and the SNM mixture and has values near unity. The fraction 1/(1+r) reflects the essential change in attenuation of plutonium gamma rays by the addition of uranium. Since K is quite insensitive to gross changes in the blending ratio (Ref. 4), the response of an infinite-sample enrichment measurement is therefore directly proportional to E/(1+r); that is, it will sense variations in either the isotopic enrichment or the blending ratio. Concurrent measurement of one of the uranium gamma rays in this example could, in principle, permit monitoring of both the plutonium enrichment and the blending ratio independently, provided the uranium isotopic composition were known.

REFERENCES

1. M. E. Anderson and J. F. Lemming, "Selected Measurement Data for Plutonium and Uranium," Mound Laboratory report MLM-3009 (1982).

2. T. R. Canada, *An Introduction to Non-Destructive Assay Instrumentation, A Training Manual for the International Atomic Energy Agency Inspectorate*, (International Atomic Energy Agency, Vienna, 1984).

3. J. T. Russell, "Method and Apparatus for Nondestructive Determination of ^{235}U in Uranium," US Patent No. 3 389 254, June 1968.

4. T. D. Reilly, R. B. Walton, and J. L. Parker, "The Enrichment Meter—A Simple Method for Measuring Isotopic Enrichment," in "Nuclear Safeguards Research and Development Program Status Report, September–December, 1970," G. Robert Keepin, Comp., Los Alamos Scientific Laboratory report LA-4605-MS (1970), p. 19.

5. J. L. Parker and T. D. Reilly, "The Enrichment Meter as a Concentration Meter," in "Nuclear Analysis Research and Development, Program Status Report, September–December 1972," G. Robert Keepin, Comp., Los Alamos Scientific Laboratory report LA-5197-PR (1972), p. 11.

6. R. B. Walton, T. D. Reilly, J. L. Parker, J. H. Menzel, E. D. Marshall, and L. W. Fields, "Measurement of UF_6 Cylinders with Portable Instruments," *Nuclear Technology* 21, 133 (1974).

7. L. A. Kull and R. O. Ginaven, "Guidelines for Gamma-Ray Spectroscopy Measurements of ^{235}U Enrichment," Brookhaven National Laboratory report BNL-50414 (1974).

8. P. Matussek, "Accurate Determination of the ^{235}U Isotope Abundance by Gamma Spectrometry: A User's Manual for the Certified Reference Material EC-NRM-171/NBS-SRM-969," Institut für Kernphysik report KfK 3752, Kernforschungszentrum, Karlsruhe, Federal Republic of Germany (1985).

9. T. D. Reilly, E. R. Martin, J. L. Parker, L. G. Speir, and R. B. Walton, "A Continuous In-Line Monitor for UF_6 Enrichment," *Nuclear Technology* 23, 318 (1974).

10. J. K. Halbig, S. F. Klosterbuer, and R. A. Cameron, "Applications of a Portable Multichannel Analyzer in Nuclear Safeguards," Proc. of the IEEE 1985 Nuclear Science Symposium, San Francisco, California, October 23-25, 1985. Also available as Los Alamos National Laboratory document LA-UR-85-3735 (1985).

11. D. R. Terry, "Development of IAEA Safeguards Measurements for Enrichment Plants," *Transactions of the American Nuclear Society* 50, 176 (1985).

12. R. J. S. Harry, J. K. Aaldijk, and J. P. Braak, "Gamma-Spectroscopic Determination of Isotopic Composition Without Use of Standards," *Proc. IAEA Symposium, "Safeguarding Nuclear Materials,"* Vienna, October 20-24, 1975, Vol. II (1975), p. 235.

13. T. N. Dragnev and B. P. Damyanov, "Methods for Precise, Absolute Gamma-Spectrometric Measurements of Uranium and Plutonium Isotopic Ratios," *Proc. IAEA Symposium on Nuclear Material Safeguards*, Vienna, Austria, October 2-6, 1978, IAEA-SM-231, Vol. I (1978), p. 739.

14. T. N. Dragnev, B. P. Damyanov, and K. S. Karamanova, "Non-Destructive Measurements of Uranium and Thorium Concentrations and Quantities," *Proc. of the IAEA Symposium on Nuclear Material Safeguards*, Vienna, Austria, October 2-6, 1978, IAEA-SM-231, Vol. II (1978), p. 207.

15. T. N. Dragnev, B. P. Damyanov, and G. G. Grozev, "Simplified Procedures and Programs for Determining Uranium and Plutonium Isotopic Ratios," *Proc. IAEA Symposium on Nuclear Material Safeguards*, Vienna, Austria, November 8-12, 1982, IAEA-SM-260, Vol. II (1982), p. 258.

16. R. Hagenauer, "Nondestructive Determination of Uranium Enrichment Using Low-Energy X and Gamma Rays," *Nuclear Materials Management* XI, 216 (1982).

17. J. W. Tape, M. P. Baker, R. Strittmatter, M. Jain, and M. L. Evans, "Selected Nondestructive Assay Instruments for an International Safeguards System at Uranium Enrichment Plants," *Nuclear Materials Management* VIII, 719 (1979).

18. R. B. Strittmatter, J. N. Leavitt, and R. W. Slice, "Conceptual Design for the Field Test and Evaluation of the Gas-Phase UF_6 Enrichment Meter," Los Alamos Scientific Laboratory report LA-8657-MS (1980).

19. R. B. Strittmatter, "A Gas-Phase UF_6 Enrichment Monitor," *Nuclear Technology* 59, 355 (1982).

20. R. B. Strittmatter, L. A. Stovall, and J. K. Sprinkle, Jr., "Development of an Enrichment Monitor for the Portsmouth GCEP," *Proc. Conference on "Safeguards Technology: The Process-Safeguards Interface,"* Hilton Head Island, SC, November 28-December 3, 1983, (Conf. 831106, 1984), p. 63.

21. R. B. Strittmatter, R. R. Pickard, J. K. Sprinkle, Jr., and J. R. Tarrant, "Data Evaluation of a Gas-Phase UF_6 Enrichment Monitor," *Proc. ESARDA/INMM Joint Specialist Meeting on NDA Statistical Problems*, Ispra, Italy, September 12-14, 1984, p. 243.

22. D. A. Close, J. C. Pratt, H. F. Atwater, J. J. Malanify, K. V. Nixon, and L. G. Speir, "The Measurement of Uranium Enrichment for Gaseous Uranium at

Low Pressure," *Proc. of the 7th Annual Symposium on Safeguards and Nuclear Material Management, ESARDA*, Liege, Belgium, May 21-23, 1985, p. 127.

23. D. A. Close, J. C. Pratt, J. J. Malanify, and H. F. Atwater, "X-Ray Fluorescent Determination of Uranium in the Gaseous Phase," *Nuclear Instruments and Methods A* 234, 556 (1985).

24. D. A. Close, J. C. Pratt, and H. F. Atwater, "Development of an Enrichment Measurement Technique and its Application to Enrichment Verification of Gaseous UF_6," *Nuclear Instruments and Methods A* 240, 398 (1985).

25. T. W. Packer and E. W. Lees, "Measurement of the Enrichment of Uranium in the Pipework of a Gas Centrifuge Plant," *Proc. 6th Annual Symposium on Safeguards and Nuclear Material Management, ESARDA*, Venice, Italy, May 14-18, 1984, p. 243.

26. T. W. Packer and E. W. Lees, "Measurement of the Enrichment of UF_6 Gas in the Pipework of a Gas Centrifuge Plant," *Proc. 7th Annual Symposium on Safeguards and Nuclear Material Management, ESARDA*, Liege, Belgium, May 21-23, 1985, p. 299.

27. T. D. Reilly, J. L. Parker, A. L. Evans, and R. B. Walton, "Uranium Enrichment Measurements on UF_6 Product Cylinders," in "Nuclear Safeguards Research and Development, Progress Status Report, May–August 1971," G. Robert Keepin, Comp., Los Alamos Scientific Laboratory report LA-4794-MS (1971), p. 16.

28. J. L. Weiman, "Practical Uncertainty Limits in Gamma-Ray Enrichment Measurements on Low-Enriched Uranium Hexafluoride," *Proc. ESARDA/INMM Joint Specialist Meeting on NDA Statistical Problems*, Ispra, Italy, September 12-14, 1984, p. 101.

29. L. R. Stieff, R. B. Walton, T. D. Reilly, L. W. Fields, R. L. Walker, W. T. Mullins, and J. I. Thoms, "Neutron Measurements of ^{234}U Isotopic Abundances in UF_6 Samples," *Nuclear Materials Management* IV, 179 (1975).

30. "Uranium Hexafluoride: Handling Procedures and Container Criteria," Oak Ridge Operations Office report ORO-651, Revision 4 (1977).

31. G. W. Nelson, S. -T. Hsue, T. E. Sampson, and R. G. Gutmacher, "Measurement of Uranium/Plutonium Blending Ratio," in "Safeguards and Security Progress Report, January–December 1984," Darryl B. Smith, Comp., Los Alamos National Laboratory report LA-10529-PR (1986), p. 19.

8

Plutonium Isotopic Composition by Gamma-Ray Spectroscopy

T. E. Sampson

8.1 INTRODUCTION

An accurate measurement of plutonium isotopic composition is usually required to interpret the results of neutron coincidence or calorimetry measurements. Several methods have been developed for determining plutonium isotopic composition by gamma-ray spectroscopy; some of the early approaches are described in Refs. 1 through 5. An American Society for Testing and Materials standard test method has been written for plutonium isotopic analysis using gamma-ray spectroscopy (Ref. 6). Different methods have been developed for different sample types.

This chapter introduces the characteristics of plutonium spectra that influence isotopic measurements, describes useful spectral regions, and presents the principles of spectral analysis important to isotopic measurement. It includes descriptions of typical data collection hardware, details of data analysis methods, and descriptions of several implemented systems with examples of their accuracy and precision.

8.2 BACKGROUND

8.2.1 Decay Characteristics of Plutonium Isotopes

Most plutonium samples contain the isotopes ^{238}Pu, ^{239}Pu, ^{240}Pu, ^{241}Pu, and ^{242}Pu. Americium-241 and ^{237}U are always present as decay products of ^{241}Pu. Table 8-1 lists some of the decay characteristics of these important isotopes.

8.2.2 Decay Characteristics of ^{241}Pu

The decay of ^{241}Pu is shown in Figure 8.1. Because of the long half-life of ^{241}Am, the concentration of the ^{241}Am daughter continues to increase for up to 75 yr. Aged plutonium samples often have very high ^{241}Am content, especially if the initial ^{241}Pu concentration was high.

Table 8-1. Decay characteristics for isotopes useful in plutonium isotopic measurements

Isotope	Half-Life (yr)	Activity (dis/s-g)	Specific Power (MW/g Isotope)
^{238}Pu	87.74 ± 0.04	6.3330×10^{11}	567.57 ± 0.026
^{239}Pu	24 119 ± 26	2.2942×10^{9}	1.9288 ± 0.0003
^{240}Pu	6564 ± 11	8.3971×10^{9}	7.0824 ± 0.0020
^{241}Pu	14.348 ± 0.022	3.8244×10^{12}	3.412 ± 0.002
^{242}Pu	376 300 ± 900	1.4522×10^{8}	0.1159 ± 0.0003
^{241}Am	433.6 ± 1.4	1.2655×10^{11}	114.20 ± 0.50
^{237}U	(6.75 days)	9.4080×10^{7} [a]	- - -

[a] Uranium-237 activity computed assuming ^{241}Pu-^{237}U equilibrium (see Figure 8.1). Alpha branching ratio of ^{241}Pu assumed to be 2.46×10^{-5}.

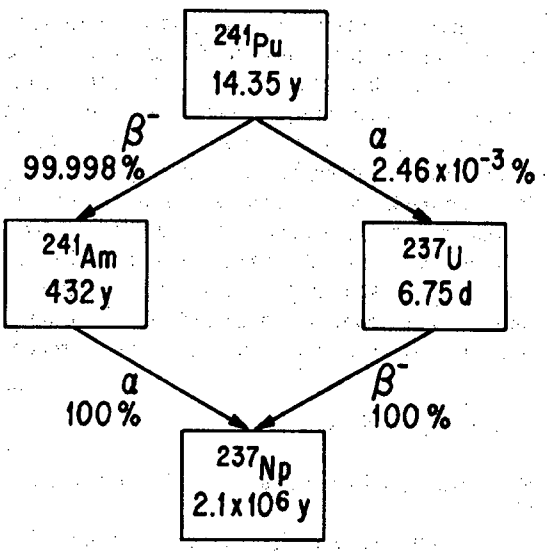

Fig. 8.1 Decay scheme of ^{241}Pu and its daughters.

Because of its short half-life, the ^{237}U daughter rapidly comes into secular equilibrium (Ref. 7) with its ^{241}Pu parent. After approximately 47 days (7 half-lives), gamma rays from the decay of ^{237}U can be used as a measure of ^{241}Pu. Because ^{237}U has several strong gamma rays, it is especially useful for plutonium isotopic measurements. In this chapter the terms ^{241}Pu-^{237}U equilibrium or aged refer to

samples where ^{237}U is in secular equilibrium with ^{241}Pu. Samples in which ^{241}Pu-^{237}U equilibrium does not exist are called freshly separated. For those samples, ^{237}U cannot be used as a measure of ^{241}Pu.

Figure 8.1 shows that both ^{241}Am and ^{237}U decay to the same isotope, ^{237}Np. Both isotopes can populate the same excited states in ^{237}Np and give rise to identical gamma rays. Thus, most of the useful ^{237}U gamma-ray peaks have a contribution from ^{241}Am. The amount of this contribution depends upon the particular gamma ray and the time since americium was last separated from the sample. Figure 8.2 shows the relative contributions for important ^{237}U gamma rays. A correction should be made to ^{241}Pu-^{237}U peaks for their ^{241}Am content.

8.2.3 Determination of ^{242}Pu Concentration

Plutonium-242 has only a few gamma rays, similar in energy and branching ratio to those from ^{240}Pu. However, the long half-life of ^{242}Pu and its low abundance in most plutonium make its detection by gamma-ray measurement impossible. Instead, empirical isotopic correlations (Ref. 8) are used to predict the ^{242}Pu content from the other isotopic fractions. Such predictions generally produce acceptable results for the concentration of ^{242}Pu (typically 0.03 to 5%) found in most plutonium, if process batches have not been mixed and ^{241}Am has neither been added nor removed.

8.2.4 Spectral Interferences

Many regions of the gamma-ray spectrum can contain interfering gamma rays from other isotopes in the sample. For example: very high burnup samples often contain ^{243}Am and its ^{239}Np daughter; aged samples may contain ^{237}Np and its daughter ^{233}Pa; and samples from reprocessed fuel may contain fission products. All the possible interferences cannot be listed here; however, by knowing the history of a sample, the spectroscopist can anticipate possible spectral interferences.

8.2.5 Applications of Plutonium Isotopic Measurements

The principal application of plutonium isotopic measurements is to support other nondestructive assay (NDA) methods in providing the total plutonium content of a sample. Two methods that use plutonium isotopic results are calorimetry and neutron coincidence counting.

Calorimetry uses the isotopic information to calculate the specific power P (W/g Pu) of a sample from the measured isotopic fractions and the known specific power for each isotope (see Chapters 21 and 22).

The response of neutron coincidence counters is a complicated function of all the plutonium isotopes and ^{241}Am. A measurement of isotopic composition is required to convert the coincidence counter response to plutonium mass (see Chapter 16).

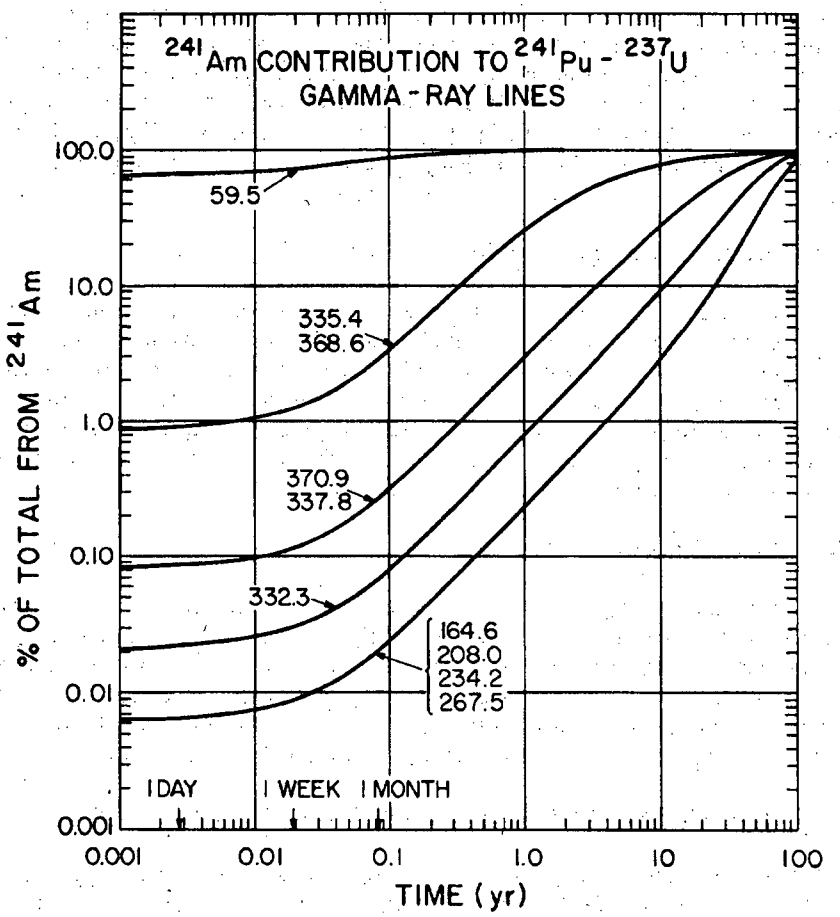

Fig. 8.2 Americium-241 contribution to ^{237}U gamma-ray peaks (energy in keV) as a function of time since separation. Uranium and americium concentrations are zero at t = 0.

8.3 SPECTRAL REGIONS USEFUL FOR ISOTOPIC MEASUREMENTS

This section describes the spectral features that are important for the measurement of plutonium isotopic composition. The descriptions follow the practice used in works of Gunnink et al. (Ref. 9) and Lemming and Rakel (Ref. 10) in which the spectrum is divided into several different regions. The gamma-ray spectrum of plutonium varies greatly with isotopic composition and ^{241}Am concentration. Two sample spectra are shown in Figures 8.3 and 8.4. Figure 8.3 represents low burnup and low ^{241}Am; Figure 8.4 represents intermediate burnup and relatively high ^{241}Am. Similar examples are given for each of the spectral regions to illustrate the variability that may be encountered.

Table 8-2 lists most of the gamma rays that are useful for plutonium isotopic measurements. The list shows that the lower energy gamma rays are more intense than those at higher energies. The lower energy gamma rays should be used whenever possible, however, it is often impossible to use them.

8.3.1 The 40-keV Region

The 40-keV region has been used mainly for analysis of freshly separated solutions from which ^{241}Am and ^{237}U have been removed. If too much ^{241}Am is present, its 60-keV gamma ray overwhelms all other peaks in the region. Usually, the 40-keV region is useful for 15 to 30 days after a separation of americium and uranium. A typical spectrum from a high-burnup reprocessing plant solution (Ref. 11) is shown in Figure 8.5; Table 8-3 lists the peak energies and intensities. When the gamma rays can be measured, the 40-keV region is the most useful region for measuring ^{238}Pu, ^{239}Pu, and ^{240}Pu. The region does not have a measurable ^{241}Pu gamma ray; ^{241}Pu concentration is usually measured from its 148.6-keV gamma ray. Small contributions from ^{241}Pu and ^{237}U interfere with the ^{238}Pu peak at 43.5 keV, the ^{240}Pu peak at 45.2 keV, and the ^{239}Pu peak at 51.6 keV.

Several experimenters have used this region for solution measurements: Gunnink (Ref. 12) and Russo (Ref. 11) have measured freshly separated solutions from a reprocessing plant; Umezawa (Ref. 13) and Bubernak (Ref. 14) have applied these measurements to samples prepared in an analytical laboratory; and Li (Ref. 15) has measured submilligram-sized solid samples with modest ^{241}Am content. Gunnink uses absolute counting techniques and calibrates with known solution standards; Umezawa uses absolute counting with a calibrated detector; Bubernak calibrates with samples of known isotopic composition; and Russo and Li measure isotopic ratios that are independent of calibration standards as discussed in Section 8.4.

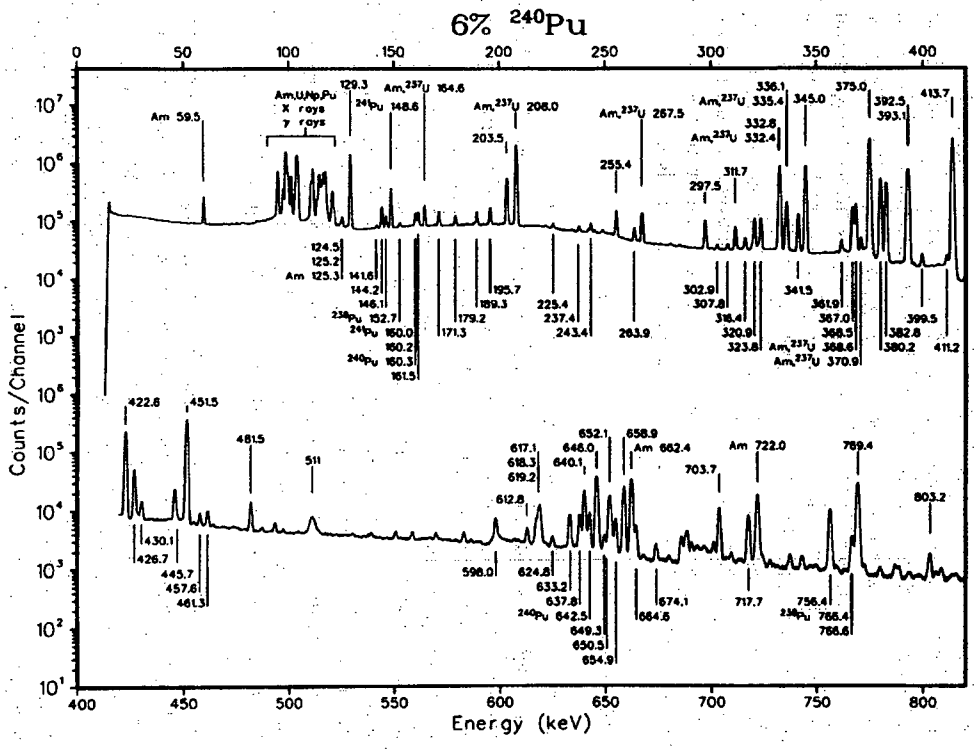

Fig. 8.3 *Gamma-ray spectrum from 500 g of plutonium metal measured with a coaxial germanium detector (at 1332 keV: relative efficiency = 11.7%, FWHM = 1.75 keV). Isotopic composition (wt%): 238, 0.012%; 239, 93.82%; 240, 5.90%; 241, 0.240%; 242, 0.02%; ^{241}Am, 630 μg/g plutonium. Peaks not labeled with a specific isotope are from ^{239}Pu.*

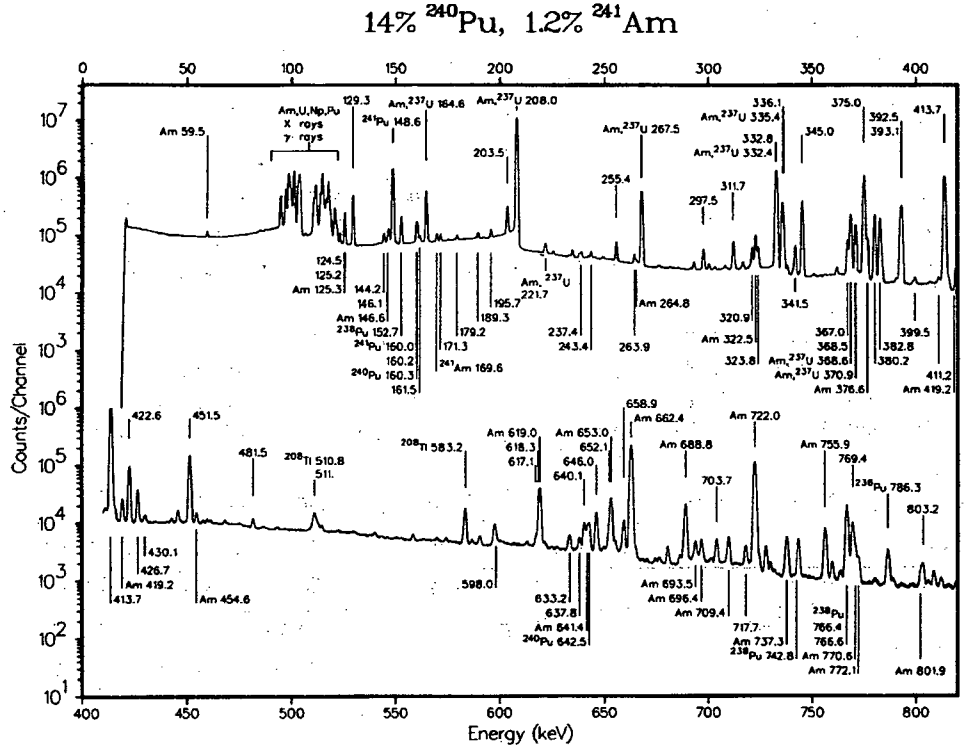

Fig. 8.4 *Gamma-ray spectrum from 530 g of plutonium as PuO_2 measured with a coaxial germanium detector (at 1332 keV: relative efficiency = 10.2%, FWHM = 1.65 keV). Isotopic composition (wt%): 238, 0.202%; 239, 82.49%; 240, 13.75%; 241, 2.69%; 242, 0.76%; ^{241}Am, 11 800 μg/g plutonium. Peaks not labeled with a specific isotope are from ^{239}Pu.*

Table 8-2. Useful gamma rays in various energy regions

Region	^{238}Pu		^{239}Pu		^{240}Pu		^{241}Pu		^{241}Am	
(keV)	(keV)	(γ/s-g)	(keV)	(γ/s-g)	(keV)	(γ/s-g)	(keV)	(γ/s-g)	(keV)	(γ/s-g)
40-60	43.48	2.49×10^{8}	51.63	6.19×10^{5}	45.23	3.80×10^{6}	- - -		59.54	4.54×10^{10}
90-105	99.86	4.59×10^{7}	98.78	2.80×10^{4}	104.24	5.86×10^{5}	103.68	3.86×10^{6}	98.95	2.57×10^{7}
									102.97	2.47×10^{7}
120-450	152.68	6.05×10^{6}	129.29	1.44×10^{5}	160.28	3.38×10^{4}	148.57	7.15×10^{6}	125.29	5.16×10^{6}
			203.54	1.28×10^{4}			164.58[a]	1.73×10^{6}	335.40	6.28×10^{5}
			345.01	1.28×10^{4}			208.00[a]	2.04×10^{7}		
			375.04	3.60×10^{4}			332.35[a]	1.14×10^{6}		
			413.71	3.42×10^{4}			370.93[a]	1.04×10^{5}		
450-800	766.41	1.39×10^{5}	645.97	3.42×10^{2}	642.48	1.05×10^{3}	- - -		662.42	4.61×10^{5}
			717.72	6.29×10^{1}					721.99	2.48×10^{5}

[a]Uranium-237 daughter of ^{241}Pu with ^{241}Pu-^{237}U equilibrium.

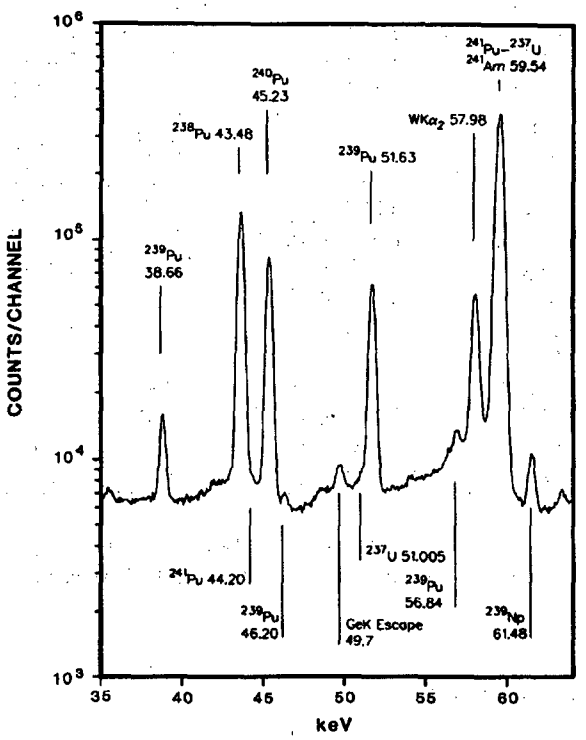

Fig. 8.5 Gamma-ray spectrum in the 40-keV region from a freshly separated 185-g/L solution of plutonium in nitric acid. Isotopic composition (wt%): 238, 0.649%; 239, 67.01%; 240, 21.80%; 241, 8.11%; 242, 2.44%. The W $K_{\alpha 2}$ x ray arises from the shielding around the detector (Ref. 11).

Table 8-3. Peak energies and intensities in 40-keV region[a]

Isotope	Energy (keV)	Branching Ratio (photons/dis)	Error (%)	Activity (photons/s-g)
^{239}Pu	38.664	1.050×10^{-4}	1.00	2.4089×10^{5}
^{239}Pu	40.410	1.620×10^{-6}	10.00	3.7165×10^{3}
^{239}Pu	42.060	1.650×10^{-6}	3.00	3.7854×10^{3}
^{237}U	43.430	5.904×10^{-9}	7.00	2.2579×10^{4} [b]
^{238}Pu	43.477	3.930×10^{-4}	0.30	2.4889×10^{8}
^{241}Pu	44.200	4.180×10^{-8}		1.5986×10^{5}
^{241}Pu	44.860	8.360×10^{-9}		3.1972×10^{4}
^{240}Pu	45.232	4.530×10^{-4}	0.20	3.8039×10^{6}
^{239}Pu	46.210	7.370×10^{-6}	10.00	1.6908×10^{4}
^{239}Pu	46.690	5.800×10^{-7}	6.00	1.3306×10^{3}
^{237}U	51.005	8.364×10^{-8}	2.00	3.1987×10^{5} [b]
^{239}Pu	51.629	2.700×10^{-4}	0.20	6.1942×10^{5}
^{239}Pu	54.040	2.000×10^{-6}	1.40	4.5883×10^{3}
^{241}Pu	56.320	2.500×10^{-8}		9.5610×10^{4}
^{239}Pu	56.760	9.750×10^{-9}		3.7288×10^{4}
^{239}Pu	56.838	1.130×10^{-5}	1.00	2.5924×10^{4}
^{237}U	59.536	8.487×10^{-6}	0.20	3.2458×10^{7} [b]
^{241}Am	59.536	3.590×10^{-1}		4.5432×10^{10}
^{237}U	64.832	3.198×10^{-7}	0.50	1.2230×10^{6} [b]

[a]Ref. 9.

[b]Uranium-237 activity computed assuming ^{241}Pu-^{237}U equilibrium. Uranium-237 branching ratio includes 2.46×10^{-5} ^{241}Pu alpha branch to ^{237}U.

8.3.2 The 100-keV Region

The 100-keV region is the most complex region of the gamma-ray spectrum of plutonium. Table 8-4 lists 14 gamma rays and x rays in this region. The uranium x rays arise from plutonium decay and can be used to measure the plutonium isotopes. The neptunium x rays arise from the decay of ^{241}Am and ^{237}U, and the plutonium x rays appear in larger or more concentrated samples from gamma-ray and alpha-particle-induced x-ray fluorescence. The 100-keV region is the only region in which gamma rays from all isotopes are present.

Table 8-4. Peak energies and intensities in 100-keV region[a]

Isotope	Energy (keV)	Branching Ratio (photons/dis)	Error (%)	Activity (photons/s-g)	X Ray
^{238}Pu	94.658	1.050×10^{-6}	1.40	6.6497×10^{5}	U $K_{\alpha 2}$
^{239}Pu	94.658	4.220×10^{-5}	0.25	9.6813×10^{4}	U $K_{\alpha 2}$
^{240}Pu	94.658	6.360×10^{-7}	5.00	5.3406×10^{3}	U $K_{\alpha 2}$
^{241}Pu	94.658	3.030×10^{-6}	0.50	1.1588×10^{7}	U $K_{\alpha 2}$
^{239}Pu	96.130	2.230×10^{-7}	20.00	5.1160×10^{2}	
^{237}U	97.071	3.887×10^{-6}	0.40	1.4865×10^{7}	Np $K_{\alpha 2}$[b]
^{241}Am	97.072	1.180×10^{-5}	2.00	1.4933×10^{6}	Np $K_{\alpha 2}$
^{238}Pu	98.441	1.690×10^{-6}	1.00	1.0703×10^{6}	U $K_{\alpha 1}$
^{239}Pu	98.441	6.760×10^{-5}	0.30	1.5508×10^{5}	U $K_{\alpha 1}$
^{240}Pu	98.441	1.020×10^{-6}	5.00	8.5651×10^{3}	U $K_{\alpha 1}$
^{241}Pu	98.441	4.850×10^{-6}	0.50	1.8548×10^{7}	U $K_{\alpha 1}$
^{239}Pu	98.780	1.220×10^{-5}	3.00	2.7989×10^{4}	
^{241}Am	98.951	2.030×10^{-4}	0.50	2.5690×10^{7}	
Pu[c]	99.530				Pu $K_{\alpha 2}$
^{238}Pu	99.864	7.240×10^{-5}	0.20	4.5851×10^{7}	
^{237}U	101.066	6.199×10^{-6}	0.30	2.3708×10^{7}	Np $K_{\alpha 1}$[b]
^{241}Am	101.066	1.900×10^{-5}	1.40	2.4045×10^{6}	Np $K_{\alpha 1}$
^{241}Am	102.966	1.950×10^{-4}	0.50	2.4677×10^{7}	
^{239}Pu	103.020	2.170×10^{-6}	1.60	4.9783×10^{3}	
^{241}Pu	103.680	1.010×10^{-6}	0.50	3.8627×10^{6}	
Pu[c]	103.748				Pu $K_{\alpha 1}$
^{240}Pu	104.244	6.980×10^{-5}	0.40	5.8612×10^{5}	

[a]Ref. 9.

[b]Uranium-237 activity computed assuming ^{241}Pu-^{237}U equilibrium. Uranium-237 branching ratio includes 2.46×10^{-5} ^{241}Pu alpha branch to ^{237}U.

[c]Plutonium x rays are produced in high-mass or high-concentration samples by gamma-ray- and alpha-particle-induced x-ray fluorescence.

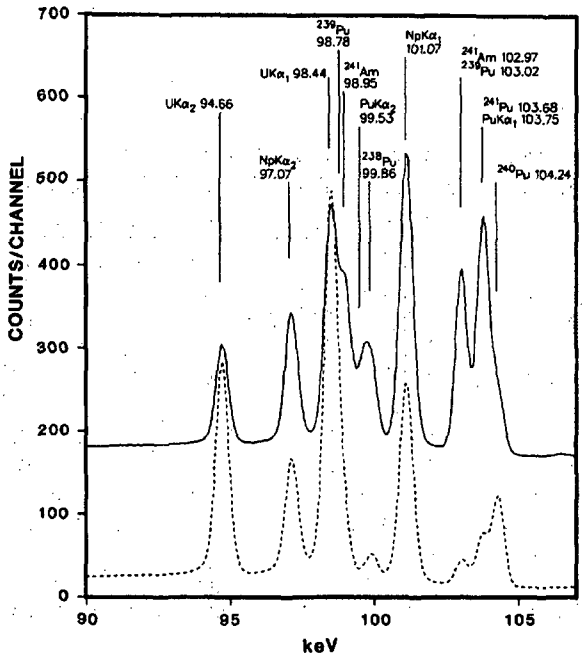

Fig. 8.6 Gamma-ray spectrum in the 100-keV region measured with a HPGe detector with resolution of 490 eV at 122 keV. Solid line: 530 g of plutonium as PuO_2. Isotopic composition (wt%): 238, 0.302%; 239, 82.49%; 240, 13.75%; 241, 2.69%; 242, 0.76%; ^{241}Am, 11 800 μg/g plutonium. Dashed line: 10 mL of 20-g/L solution of plutonium in 1M HNO_3. Isotopic composition (wt%): 238, 0.027%; 239, 91.65%; 240, 7.68%; 241, 0.532%; 242; 0.12%; ^{241}Am, 315 μg/g plutonium.

The strong, overlapping, interfering nature of the spectrum in the 100-keV region is shown in Figure 8.6. The entire isotopic distribution may be determined from this region for low-burnup solution samples (Ref. 4); a spectrum from such a sample is shown at the bottom of Figure 8.6. The complexity of the region requires peak-fitting or response-function (Refs. 4 and 16) analysis. Low-burnup PuO_2 has also been analyzed using response-function methods. High-burnup solutions have been analyzed using response-function methods in this region (Ref. 12), but such analysis is difficult. The increased alpha and gamma-ray activity of high-burnup and high-concentration solutions fluoresces plutonium x rays at 99.53 and 103.75 keV. These

x rays interfere with the gamma-ray peaks at 99.86 keV from ^{238}Pu and 104.24 keV from ^{240}Pu. The intrinsic line shape of x rays is different from that of gamma rays; this difference must be considered in the analysis of this region by response-function methods.

8.3.3 The 125-keV Region

The 125-keV region is used to measure ^{241}Am and ^{239}Pu from gamma rays at 125.29 and 129.29 keV. There are strong interferences to the 125.29-keV ^{241}Am gamma ray from ^{239}Pu lines at 125.21 and 124.51 keV. The ^{241}Am peak area is difficult to measure for ^{241}Am concentrations below a few hundred micrograms per gram of plutonium. For an americium concentration of 500 μg/g Pu, the ^{239}Pu interference contributes over 50% of the 125.3-keV peak area; for an americium concentration of 5000 μg/g Pu, over 90% of the peak area is from ^{241}Am. The ^{239}Pu interference can be removed by peak fitting (Ref. 17) or stripping (Ref. 18). Many measurements use absorbers or filters (see Section 8.5.3) to reduce the count rate of lower energy gamma rays. These absorbers affect the count rate in the 125-keV region. A 0.15-cm-thick cadmium filter transmits only 35% of the incident gamma rays at 125.3 keV.

Table 8-5 lists the gamma-ray energies and intensities in the 125-keV region. Figure 8.7 shows this spectral region; the plutonium K_β x rays at 116.3, 117.3, and 120.6 keV (omitted from Table 8-5) complicate the analysis of this region by making it difficult to find an interference-free background region below 124.5 keV. High-burnup material (solid line, Figure 8.7) generally gives a stronger ^{241}Am peak but a weaker ^{239}Pu peak than low-burnup material does. For high-burnup material, the precision of the ^{239}Pu peak at 129.29 keV is worse because there is less ^{239}Pu in the sample and because the background continuum under the peak is usually higher as a result of the intense ^{241}Pu and ^{237}U gamma rays at higher energies.

Table 8-5. Peak energies and intensities in 125-keV region[a]

Isotope	Energy (keV)	Branching Ratio (photons/dis)	Error (%)	Activity (photons/s-g)
^{239}Pu	119.708	3.000×10^{-7}	2.00	6.8825×10^{2}
^{241}Pu	121.200	6.850×10^{-9}		2.6197×10^{4}
^{241}Am	122.994	1.000×10^{-5}	0.80	1.2655×10^{6}
^{239}Pu	123.620	1.970×10^{-7}	6.00	4.5195×10^{2}
^{239}Pu	124.510	6.130×10^{-7}	3.00	1.4063×10^{3}
^{239}Pu	125.210	7.110×10^{-7}	2.00	1.6311×10^{3}
^{241}Am	125.292	4.080×10^{-5}	0.50	5.1633×10^{6}
^{239}Pu	129.294	6.260×10^{-5}	0.20	1.4361×10^{5}

[a]Ref. 9.

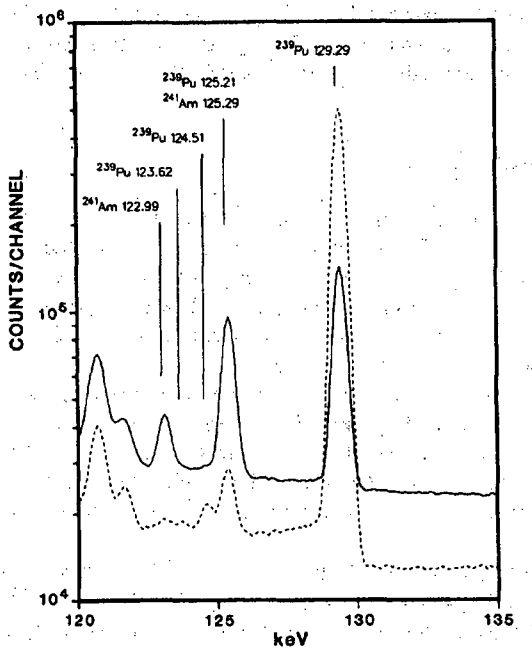

Fig. 8.7 Gamma-ray spectrum of PuO_2 in the 125-keV region measured with a HPGe detector with resolution of 490 eV at 122 keV. Isotopic compositions (wt%): (solid line) 238, 0.378%; 239, 78.89%; 240, 15.28%; 241, 4.42%; 242, 1.04%; ^{241}Am, 14 300 μg/g plutonium; and (dashed line) 238, 0.016%; 239, 93.51%; 240, 6.15%, 241, 0.28%; 242, 0.039%; ^{241}Am, 480 μg/g plutonium.

8.3.4 The 148-keV Region

The two most important peaks in the 148-keV region are the 148.57-keV ^{241}Pu peak and the 152.68-keV ^{238}Pu peak. The 148.57-keV peak is the only useful gamma ray outside of the complex 100-keV region that comes directly from ^{241}Pu. The 152.68-keV peak, although weak, is often the only useful gamma ray from ^{238}Pu above 100 keV. (In some high-burnup samples, the 766.4-keV peak can be used for ^{238}Pu measurement.) The 144.21- and 143.35-keV ^{239}Pu lines are often used in isotopic composition measurements; however, in mixed-oxide samples the ^{235}U gamma ray at 143.76 keV can be an interference. Americium-241 peaks at 146.56 and 150.11 keV complicate window settings and background determination for methods that use simple channel summation procedures to determine peak areas. An additional interference

can arise in systems that use a ^{109}Cd reference source (Refs. 11 and 12). Here, the 88.04-keV ^{109}Cd gamma ray can sum with the 59.54-keV ^{241}Am gamma ray to produce a pileup peak at 147.6 keV. Other sum peaks can interfere with the 152.68-keV ^{238}Pu peak (U $K_{\alpha 2}$ at 94.66 keV plus ^{241}Am at 59.54 keV equals 154.2 keV).

The weak 153-keV ^{238}Pu peak is usually on a high background continuum and yields a poor precision for low-burnup (0.01 wt% ^{238}Pu) material. The precision can be as poor as 10% for typical measurements. It is widely recognized that the branching ratio of the 153-keV gamma ray is approximately 2.5% lower than the value cited in Table 8-6. Branching ratio biases are discussed in Ref. 19. Figure 8.8 shows a plot of the peaks in this region from high- and low-burnup material.

Table 8-6. Peak energies and intensities in 148-keV region[a]

Isotope	Energy (keV)	Branching Ratio (photons/dis)	Error (%)	Activity (photons/s-g)
^{239}Pu	141.657	3.200×10^{-7}	2.00	7.3413×10^{2}
^{239}Pu	143.350	1.730×10^{-7}	4.00	3.9689×10^{2}
^{239}Pu	144.211	2.830×10^{-6}	0.60	6.4925×10^{3}
^{239}Pu	146.077	1.190×10^{-6}	0.60	2.7300×10^{3}
^{241}Am	146.557	4.610×10^{-6}	1.00	5.8340×10^{5}
^{241}Pu	148.567	1.870×10^{-6}	0.30	7.1516×10^{6}
^{241}Am	150.110	7.400×10^{-7}	2.00	9.3648×10^{4}
^{238}Pu	152.680	9.560×10^{-6}	0.50	6.0544×10^{6}

[a]Ref. 9.

8.3.5 The 160-keV Region

For a single detector system not using the 40- or 100-keV region, the 160-keV complex is the only one that can be used for measuring ^{240}Pu. Table 8-7 lists the energies and intensities of the major gamma rays in the 160-keV region. The ^{240}Pu gamma ray at 160.28 keV has strong interferences from ^{241}Pu at 159.95 keV and ^{239}Pu at 160.19 keV. This three-peak complex (Figure 8.9) is only partially resolved from the 161.45-keV ^{239}Pu line. Peak-fitting, peak-stripping, or response-function methods must be used to isolate the ^{240}Pu intensity. The statistical precision of the ^{240}Pu component is seldom measured to better than ~2%.

The intensity of the entire complex increases with increasing burnup, but the fractional contribution from ^{240}Pu decreases. Table 8-8 illustrates how the relative fraction of ^{240}Pu in the 160-keV complex decreases from almost 70% for material with 6% ^{240}Pu to 25% for material with 20% ^{240}Pu. This decrease occurs because ^{241}Pu increases more rapidly than ^{240}Pu as burnup increases.

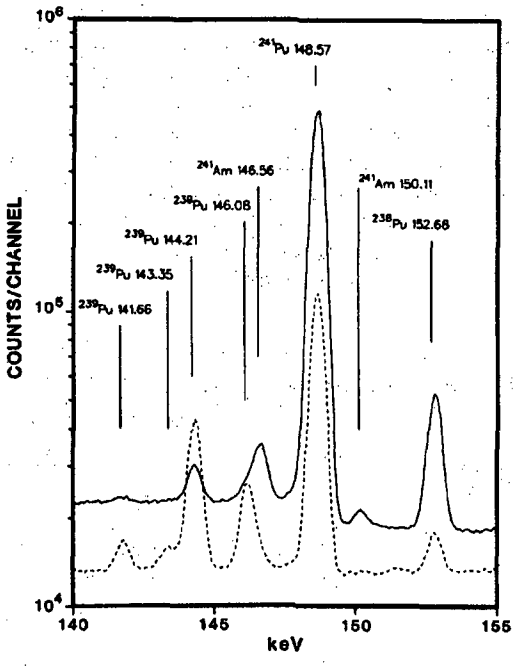

Fig. 8.8 Gamma-ray spectrum of PuO_2 in the 148-keV region measured with a HPGe detector with resolution of 490 eV at 122 keV. Isotopic compositions (wt%): (solid line) 238, 0.378%; 239, 78.89%; 240, 15.28%; 241, 4.42%; 242, 1.04%; ^{241}Am, 14 300 μg/g plutonium; and (dashed line) 238, 0.016%; 239, 93.51%; 240, 6.15%; 241, 0.28%; 242, 0.039%; ^{241}Am, 480 μg/g plutonium.

Table 8-7. Peak energies and intensities in 160-keV region[a]

Isotope	Energy (keV)	Branching Ratio (photons/dis)	Error (%)	Activity (photons/s-g)
^{239}Pu	158.100	1.000×10^{-8}	10.00	2.2942×10^{1}
^{241}Pu	159.955	6.740×10^{-8}		2.5776×10^{5}
^{239}Pu	160.190	6.200×10^{-8}	20.00	1.4224×10^{2}
^{240}Pu	160.280	4.020×10^{-6}	0.70	3.3756×10^{4}
^{239}Pu	161.450	1.200×10^{-6}	0.40	2.7530×10^{3}
^{237}U	164.580	4.526×10^{-7}	0.50	1.7311×10^{6} [b]
^{241}Am	164.580	6.670×10^{-7}	3.00	8.4410×10^{4}
^{241}Am	165.930	2.320×10^{-7}	4.00	2.9360×10^{4}

[a]Ref. 9.

[b]Uranium-237 activity computed assuming ^{241}Pu-^{237}U equilibrium. Uranium-237 branching ratio includes 2.46×10^{-5} ^{241}Pu alpha branch to ^{237}U.

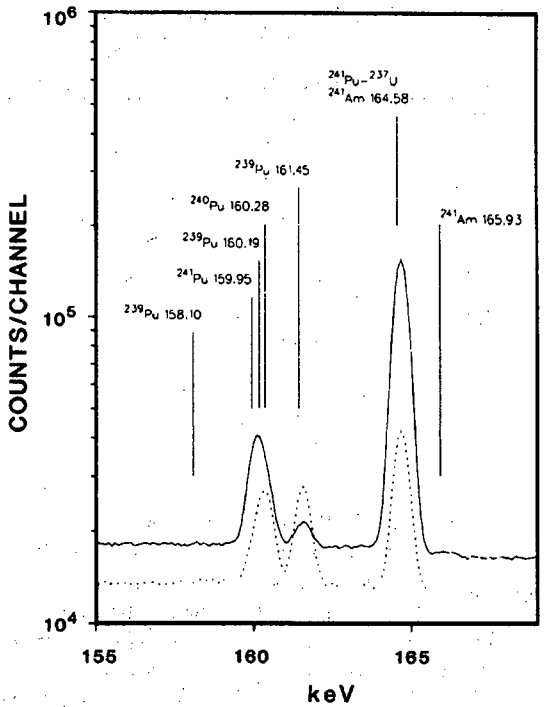

Fig. 8.9 *Gamma-ray spectrum of PuO_2 in the 160-keV region measured with a HPGe detector with resolution of 490 eV at 122 keV. Isotopic compositions (wt%): (solid line) 238, 0.378%; 239, 78.89%; 240, 15.28%; 241, 4.42%; 242, 1.04%; ^{241}Am, 14 300 μg/g plutonium; and (dashed line) 238, 0.016%; 239, 93.51%; 240, 6.15%; 241, 0.28%; 242, 0.039%; ^{241}Am 480 μg/g plutonium.*

Because the 164.58-keV peak comes from the ^{237}U daughter of ^{241}Pu, it can be used for ^{241}Pu only after equilibrium has been attained. A correction is often made for the ^{241}Am contribution to the 164.58-keV peak. The summing of x rays and gamma rays from the 100-keV region with the 59.5-keV ^{241}Am gamma ray can interfere with the 160-keV complex. These sum peaks can be eliminated by using a filter to selectively absorb gamma rays and x rays from the 60- and 100-keV regions before they interact with the detector (Ref. 20). In mixed-oxide samples, the ^{235}U gamma ray at 163.35 keV can interfere with the 164.58-keV peak if the ratio of ^{235}U to ^{241}Pu is greater than approximately 1.5.

Table 8-8. Components of 160-keV complex

Isotope	Weight Percent	Percentage of 160 Complex from Indicated Isotope
239	93.5	4.5
240	6.0	69.1
241	0.3	26.4
239	86.0	1.5
240	12.0	50.4
241	1.5	48.1
239	67.0	0.3
240	20.0	24.6
241	8.0	75.1

8.3.6 The 208-keV Region

The strong ^{241}Pu-^{237}U peak at 208.00 keV dominates the 208-keV region. Usually it is the most intense peak in the spectrum. It has a contribution from ^{241}Am that becomes approximately 1% (relative) after 4 yr. Because this gamma-ray comes from ^{237}U, it can be used only for aged samples. Its strength and freedom from interference make it suitable for shape and energy calibrations for analysis methods using peak fitting or response functions. For mixed oxides, ^{235}U peaks at 202.1 and 205.3 keV can interfere with the 203.54-keV ^{239}Pu line. The ^{239}Pu/^{241}Pu ratio formed with the 203.54/208.00 line pair gives best results for low-burnup material. For high-burnup material, the precision of the 203.54-keV ^{239}Pu peak becomes worse because of the Compton background and the long tail from the very strong 208.00-keV ^{237}U peak. High ^{241}Am (~1%) can cause a few tenths of a percent interference with the 203.5-keV peak; however, the effects of this interference can be removed easily. Table 8-9 and Figure 8.10 list and display the parameters and spectral features of the 208-keV region.

8.3.7 The 332-keV Region

The 332-keV region has contributions from ^{241}Pu-^{237}U, ^{241}Am, and ^{239}Pu as shown in Table 8-10 and Figure 8.11. For high-burnup aged material the ratio of the 345.01-keV ^{239}Pu peak to the 332.35-keV ^{241}Pu-^{237}U peak is useful for measuring the ^{239}Pu/^{241}Pu ratio. Both the 332.35- and 335.40-keV peaks from ^{241}Pu-^{237}U contain very close interferences from ^{239}Pu peaks. In Figure 8.11, the plot of a very low-burnup sample (98% ^{239}Pu) illustrates how close these two interferences are. Table 8-11 gives the relative magnitudes of these ^{239}Pu interferences for different isotopic compositions. After the ^{239}Pu interferences are removed, the two peak complexes are

left with both ^{241}Pu-^{237}U and ^{241}Am components that can be used to measure the ^{241}Pu/^{241}Am ratio (Ref. 3). Peak fitting, peak stripping, or response functions are required to analyze this region.

Table 8-9. Peak energies and intensities in 208-keV region[a]

Isotope	Energy (keV)	Branching Ratio (photons/dis)	Error (%)	Activity (photons/s-g)
^{239}Pu	203.537	5.600×10^{-6}	0.20	1.2847×10^{4}
^{241}Am	203.870	2.900×10^{-8}	6.00	3.6700×10^{3}
^{237}U	208.000	5.338×10^{-6}	0.20	2.0415×10^{7} [b]
^{241}Am	208.000	7.910×10^{-6}	0.50	1.0010×10^{6}

[a]Ref. 9.

[b]Uranium-237 activity computed assuming ^{241}Pu-^{237}U equilibrium. Uranium-237 branching ratio includes 2.46×10^{-5} ^{241}Pu alpha branch to ^{237}U.

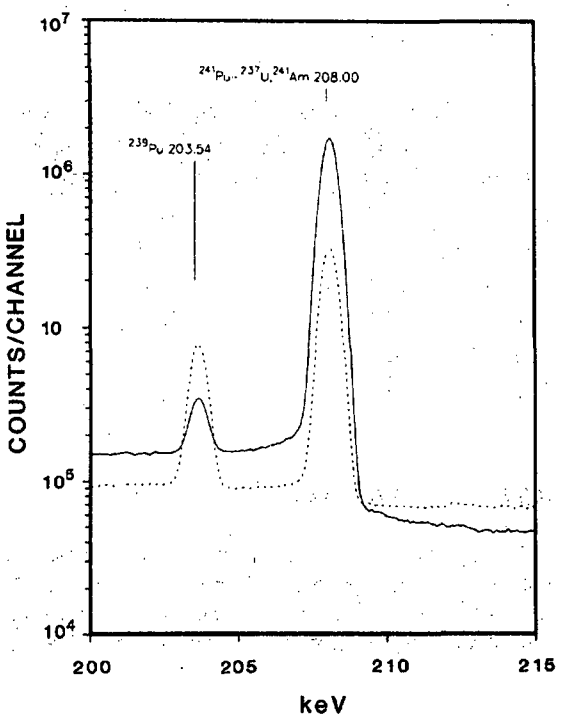

Fig. 8.10 *Gamma-ray spectrum of PuO_2 in the 208-keV region measured with a HPGe detector with resolution of 490 eV at 122 keV. Isotopic compositions (wt%): (solid line) 238, 0.378%; 239, 78.89%; 240, 15.28%; 241, 4.42%; 242, 1.04%; ^{241}Am, 14 300 μg/g plutonium; and (dashed line) 238, 0.016%; 239, 93.51%; 240, 6.15%; 241, 0.28%; 242, 0.039%; ^{241}Am, 480 μg/g plutonium.*

Table 8-10. Peak energies and intensities in 332-keV region[a]

Isotope	Energy (keV)	Branching Ratio (photons/dis)	Error (%)	Activity (photons/s-g)
^{237}U	332.354	2.977×10^{-7}	0.30	1.1384×10^{6} [b]
^{241}Am	332.354	1.490×10^{-6}	0.30	1.8856×10^{5}
^{239}Pu	332.838	5.060×10^{-6}	0.20	1.1608×10^{4}
^{237}U	335.405	2.386×10^{-8}	1.00	9.1258×10^{4} [b]
^{241}Am	335.405	4.960×10^{-6}	0.30	6.2769×10^{5}
^{239}Pu	336.107	1.134×10^{-6}	0.30	2.6016×10^{3}
^{241}Am	337.720	4.290×10^{-8}	5.00	5.4290×10^{3}
^{237}U	337.720	2.189×10^{-9}	5.00	8.3732×10^{3} [b]
^{237}U	340.450	4.059×10^{-10}	20.00	1.5523×10^{3} [b]
^{239}Pu	341.510	6.620×10^{-7}	0.40	1.5187×10^{3}
^{239}Pu	345.014	5.592×10^{-6}	0.20	1.2829×10^{4}

[a]Ref. 9.

[b]Uranium-237 activity computed assuming ^{241}Pu-^{237}U equilibrium. Uranium-237 branching ratio includes 2.46×10^{-5} ^{241}Pu alpha branch to ^{237}U.

Table 8-11. Components of 332 and 336 complexes (^{241}Am neglected)

Isotope	Weight Percent	Percentage of 332 Complex from Indicated Isotope	Percentage of 336 Complex from Indicated Isotope
239	93.5	76.1	89.9
241	0.3	23.9	10.1
239	86.0	36.9	62
241	1.5	63.1	38
239	67.0	7.9	19.3
241	8.0	92.1	80.7

8.3.8 The 375-keV Region

The 375-keV region, shown in Figure 8.12 and Table 8-12, has components from the same isotopes as the 332-keV region: ^{241}Pu-^{237}U, ^{241}Am, and ^{239}Pu. For all isotopes except ^{239}Pu, the branching ratios are lower than in the 332-keV region, so the isotopic information will be less precise. The strong 375.04-keV ^{239}Pu peak is

often used for relative efficiency determination. The ^{241}Am interference at 376.59 keV becomes bothersome above concentrations of a few thousand micrograms per gram of plutonium.

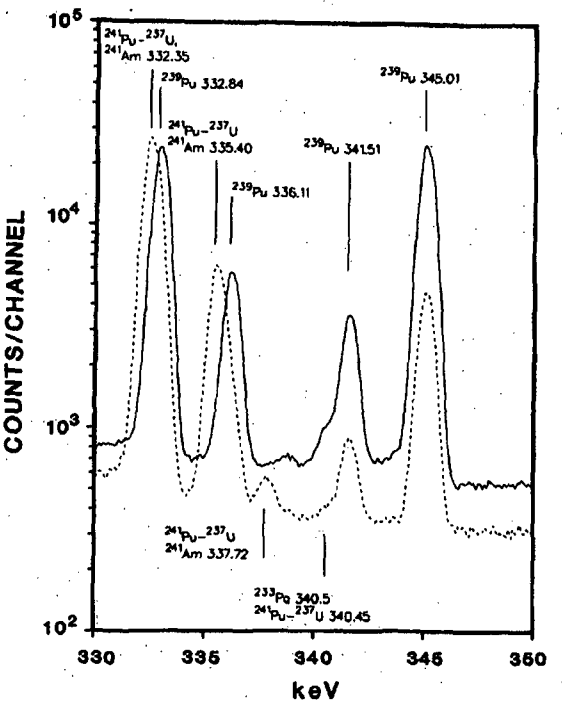

Fig. 8.11 Gamma-ray spectrum of PuO_2 in the 332-keV region measured with a HPGe detector with resolution of 490 eV at 122 keV. Isotopic compositions (wt%): (solid line) 238, 0.0024%; 239, 97.96%; 240, 2.01%; 241, 0.020%; 242, 0.0030%; ^{241}Am, 11 μg/g plutonium; and (dashed line) 238, 0.378%; 239, 78.89%; 240, 15.28%; 241, 4.42%; 242, 1.04%; ^{241}Am, 14 300 μg/g plutonium.

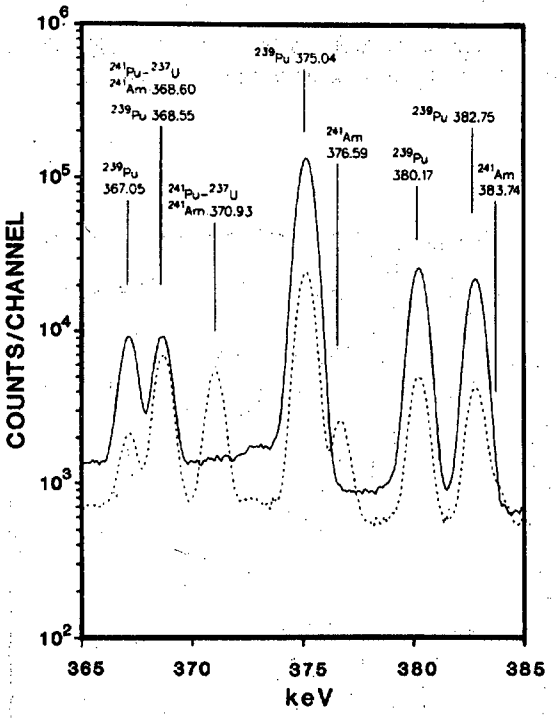

Fig. 8.12 Gamma-ray spectrum of PuO_2 in the 375-keV region measured with a HPGe detector with resolution of 490 eV at 122 keV. Isotopic compositions (wt%): (solid line) 238, 0.0024%; 239, 97.96%; 240, 2.01%; 241, 0.020%; 242, 0.0030%; ^{241}Am, 11 μg/g plutonium; and (dashed line) 238, 0.378%; 239, 78.89%; 240, 15.28%; 241, 4.42%; 242, 1.04%; ^{241}Am, 14 300 μg/g plutonium.

8.3.9 The 640-keV Region

Figure 8.13 and Table 8-13 show the characteristics of the 640-keV region. This is the only region above 160 keV that can be used for measuring ^{240}Pu. The region is useful only for large samples because of the low intensity of the 642.48-keV ^{240}Pu gamma ray. Nearby peaks from ^{239}Pu and ^{241}Am complicate the region. The 645.97- and 662.42-keV peaks are useful for measuring ^{239}Pu and ^{241}Am. The other gamma rays in the region are not generally used but must be considered for peak-fitting or response-function analysis.

Table 8-12. Peak energies and intensities in 375-keV region[a]

Isotope	Energy (keV)	Branching Ratio (photons/dis)	Error (%)	Activity (photons/s-g)
^{239}Pu	367.050	8.650×10^{-7}	0.30	1.9844×10^{3}
^{239}Pu	368.550	9.030×10^{-7}	0.30	2.0716×10^{3}
^{237}U	368.605	1.055×10^{-8}	2.00	4.0360×10^{4} [b]
^{241}Am	368.605	2.170×10^{-6}	0.30	2.7462×10^{5}
^{237}U	370.934	2.713×10^{-8}	1.40	1.0377×10^{5} [b]
^{241}Am	370.934	5.230×10^{-7}	0.80	6.6186×10^{4}
^{239}Pu	375.042	1.570×10^{-5}	0.10	3.6018×10^{4}
^{241}Am	376.595	1.383×10^{-6}	0.70	1.7502×10^{5}
^{239}Pu	380.166	3.051×10^{-6}	0.20	6.9995×10^{3}
^{239}Pu	382.751	2.587×10^{-6}	0.20	5.9350×10^{3}
^{241}Am	383.740	2.820×10^{-7}	1.50	3.5687×10^{4}

[a]Ref. 9.
[b]Uranium-237 activity computed assuming ^{241}Pu-^{237}U equilibrium. Uranium-237 branching ratio includes 2.46×10^{-5} ^{241}Pu alpha branch to ^{237}U.

A large-volume coaxial detector (10% relative efficiency or greater) should be used in the 640-keV region; analysis schemes that also analyze data from the 100 to 400-keV region should use two detectors (Ref. 20).

If fission products such as ^{95}Zr-^{95}Nb and ^{137}Cs are present in the sample, their gamma rays will complicate the analysis of the 640-keV region. A fission product concentration as low as 10 μCi/g Pu can make the analysis of this region impossible.

8.4 MEASUREMENT PRINCIPLES

8.4.1 Measurement of Isotopic Ratios

The photopeak area for any single gamma ray can be written as

$$C(E_j^i) = \lambda^i N^i BR_j^i \varepsilon(E_j) \tag{8-1}$$

where $C(E_j^i)$ = photopeak area of gamma ray j with energy E_j emitted from isotope i
λ^i = decay constant of isotope i ($\lambda^i = \ln 2/T_{1/2}^i$, where $T_{1/2}^i$ is the half-life of isotope i)
N^i = number of atoms of isotope i

BR_j^i = branching ratio (gamma rays/disintegration) of gamma ray j from isotope i

$\varepsilon(E_j)$ = total efficiency for photopeak detection of gamma ray with energy E_j. Includes detector efficiency, geometry, sample self-absorption, and attenuation in materials between the sample and detector.

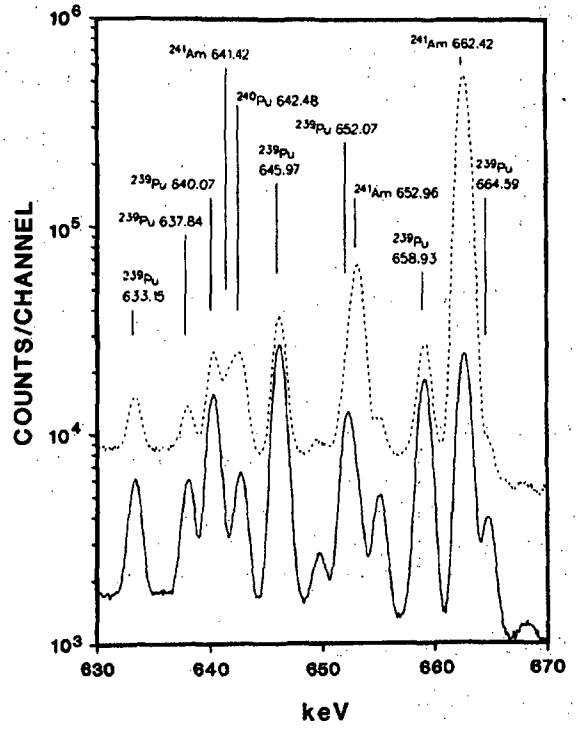

Fig. 8.13 Gamma-ray spectrum in the 640-keV region. Dashed line: 530 g of plutonium as PuO_2 measured with a coaxial HPGe detector (at 1332 keV: efficiency = 10.2%, FWHM = 1.65 keV). Isotopic composition (wt%): 238, 0.302%; 239, 82.49%; 240, 13.75%; 241, 2.69%; 242, 0.76%; ^{241}Am, 11 800 μg/g plutonium. Solid line: 500 g of plutonium metal measured with a coaxial HPGe detector (at 1332 keV: efficiency = 11.7%, FWHM = 1.75 keV). Isotopic composition (wt%): 238, 0.012%; 239, 93.82%; 240, 5.90%; 241, 0.240%; 242, 0.028%; ^{241}Am, 630 μg/g plutonium.

The photopeak area can be written also in terms of the mass of the isotope as

$$C(E_j^i) = \gamma_j^i \, M_i \, \varepsilon(E_j) \tag{8-2}$$

where γ_j^i = photon emission rate of gamma ray j from isotope i in γ/s-g
M_i = mass of isotope i (g) .

Table 8-13. Peak energies and intensities in 640-keV region[a]

Isotope	Energy (keV)	Branching Ratio (photons/dis)	Error (%)	Activity (photons/s-g)
^{241}Am	633.000	1.260×10^{-8}	15.00	1.5945×10^{3}
^{239}Pu	633.150	2.530×10^{-8}	1.20	5.8042×10^{1}
^{239}Pu	637.837	2.560×10^{-8}	1.20	5.8730×10^{1}
^{239}Pu	640.075	8.200×10^{-8}	0.60	1.8812×10^{2}
^{241}Am	641.420	7.100×10^{-8}	4.00	8.9851×10^{3}
^{240}Pu	642.480	1.245×10^{-7}	1.00	1.0454×10^{3}
^{239}Pu	645.969	1.489×10^{-7}	0.40	3.4160×10^{2}
^{239}Pu	649.321	7.120×10^{-9}	7.00	1.6334×10^{1}
^{239}Pu	650.529	2.700×10^{-9}	15.00	6.1942×10^{0}
^{239}Pu	652.074	6.550×10^{-8}	0.60	1.5027×10^{2}
^{241}Am	652.960	3.770×10^{-7}	2.00	4.7710×10^{4}
^{239}Pu	654.880	2.250×10^{-8}	1.20	5.1618×10^{1}
^{239}Pu	658.929	9.690×10^{-8}	0.70	2.2230×10^{2}
^{241}Am	662.420	3.640×10^{-6}	0.30	4.6065×10^{5}
^{239}Pu	664.587	1.657×10^{-8}	1.60	3.8014×10^{1}
^{239}Pu	668.200	3.930×10^{-10}	30.00	9.0160×10^{-1}

[a]Ref. 9.

These two equations may be rearranged to give expressions for the atom and mass ratios of two isotopes. The atom ratio is given by

$$\frac{N^i}{N^k} = \frac{C(E_j^i)}{C(E_m^k)} \times \frac{T_{1/2}^i}{T_{1/2}^k} \times \frac{BR_m^k}{BR_j^i} \times \frac{RE(E_m)}{RE(E_j)} . \tag{8-3}$$

The similar expression for the mass ratio is

$$\frac{M^i}{M^k} = \frac{C(E_j^i)}{C(E_m^k)} \times \frac{\gamma_m^k}{\gamma_j^i} \times \frac{RE(E_m)}{RE(E_j)} . \tag{8-4}$$

In Equations 8-3 and 8-4, the photopeak areas C(E) are measured and the half-lives $T_{1/2}$, branching ratios BR, and photon emission rates γ are either known or can be calculated from nuclear data. The total efficiency has been expressed in terms of

the relative efficiency RE. Geometry factors cancel and the relative efficiency ratio includes only sample self-absorption, attenuation in materials between the sample and detector, and detector efficiency. The use of an efficiency ratio removes the need for reproducible geometry and makes the isotopic ratio method applicable to samples of arbitrary size, shape, and composition.

A relative efficiency curve can be determined from the measured spectrum of every sample. Equations 8-1 and 8-2 give the following proportionality for gamma rays from a single isotope *i*:

$$\varepsilon(E_j) \propto RE(E_j) \propto \frac{C(E_j^i)}{BR_j^i} \propto \frac{C(E_j^i)}{\gamma_j^i}. \tag{8-5}$$

Because efficiency ratios are used in Equations 8-3 and 8-4, only the shape of the relative efficiency curve is important; either of the ratios given in Equation 8-5 can be used. The peak areas C(E) of strong, interference-free gamma rays from a single isotope are used to define the relative efficiency curve. Curve-fitting (Ref. 17) or interpolation techniques are used to define the relative efficiency at energies between the measured points. To better define the shape of the relative efficiency curve, points from more than one isotope can be used by normalizing one isotope to another (Refs. 17 and 18). Gamma rays from ^{239}Pu and ^{241}Pu-^{237}U are most often used to define the relative efficiency curve in the range from 130 to 450 keV. Figure 8.14 shows two examples of measured relative efficiency curves.

It is advantageous to use closely spaced gamma rays to measure isotopic ratios because the relevant relative efficiency ratios will be near unity. However, the relative efficiency correction must be applied even for closely spaced lines in the 120- to 200-keV region. A typical correction for the 152.7-keV/148.6-keV ratio (^{238}Pu/^{241}Pu) can be 10%.

After appropriate isotopic ratios are measured, it is usually desirable to calculate absolute isotopic fractions. The sum of all isotopic fractions must equal unity. Neglecting ^{242}Pu, this implies that

$$1 = f_{238} + f_{239} + f_{240} + f_{241} \tag{8-6}$$

where f_i is the isotopic fraction of isotope *i*.

Dividing Equation 8-6 by f_{241} gives

$$\frac{1}{f_{241}} = \frac{f_{238}}{f_{241}} + \frac{f_{239}}{f_{241}} + \frac{f_{240}}{f_{241}} + 1 . \tag{8-7}$$

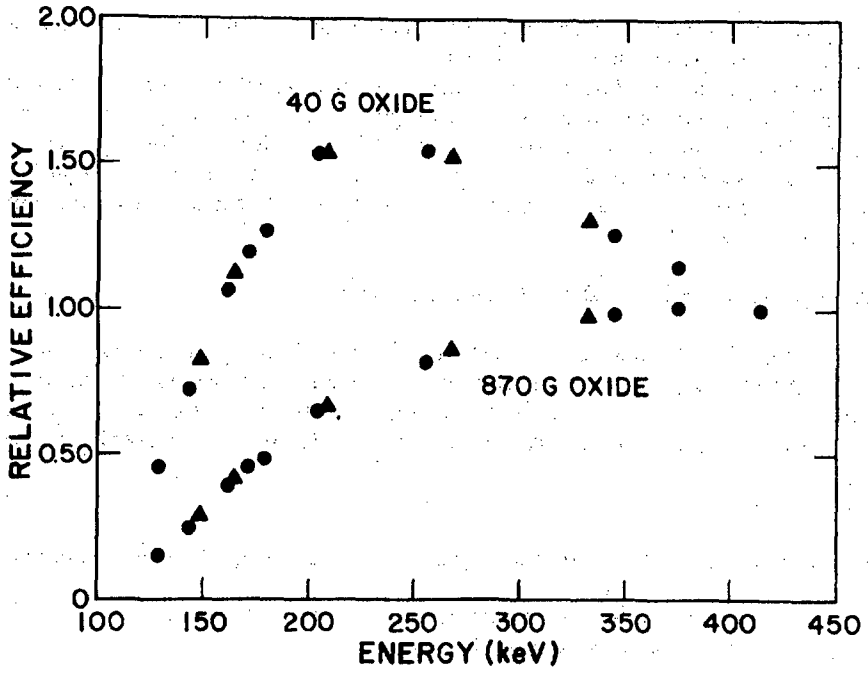

Fig. 8.14 Typical relative efficiency curves for a 200-mm² by 10-mm-deep planar HPGe detector (^{239}Pu peaks are indicated with solid circles and ^{241}Pu-^{237}U peaks with solid triangles). Both curves are normalized to 1.00 at 414 keV. The curve obtained for the 870-g PuO_2 sample shows the effect of higher attenuation.

Equation 8-7 expresses the isotopic fraction of ^{241}Pu (f_{241}) in terms of the three measured ratios f_{238}/f_{241}, f_{239}/f_{241}, and f_{240}/f_{241}. The remainder of the isotopic fractions are obtained from

$$f_i = f_{241} \times \left[\frac{f_i}{f_{241}}\right] \quad i = 238, 239, 240 . \tag{8-8}$$

Section 8.5.3 discusses the incorporation of ^{242}Pu into this analysis. If the ratio of ^{241}Am to any of the plutonium isotopes (usually ^{239}Pu) has been measured, then the absolute fraction of ^{241}Am can be calculated from

$$f_{Am} = f_i \times \frac{f_{Am}}{f_i} . \tag{8-9}$$

Note that this formula gives the weight or atom fraction of ^{241}Am in the sample with respect to total plutonium, not total sample.

The isotopic ratio method may be applied to samples of arbitrary size, shape, and composition. The method works as long as the plutonium isotopic composition and the Am/Pu ratio are uniform throughout the sample. The plutonium may be nonuniformly distributed as long as the above uniformity is present. A method was developed at Mound Laboratory to measure electrorefining salt residues that have a nonuniform Am/Pu ratio (Ref. 21).

8.4.2 Measurement of Absolute Isotopic Mass

Although the ratio method discussed in Section 8.4.1 can be applied to arbitrary samples, a more specialized method can be used to measure samples with reproducible geometries. The absolute measurement of isotope mass has been used by Gunnink and coworkers (Refs. 4, 12, and 16) for solution samples. This method uses the equation

$$C(E_j^i) = K_j^i m^i \tag{8-10}$$

where $C(E_j^i)$ = photopeak area of gamma ray j with energy E_j emitted from isotope i

K_j^i = calibration constant for gamma ray j from isotope i

m^i = mass of isotope i in sample.

Reference standards that have the same geometry as the unknown samples are used to determine the calibration constants. Self-attenuation corrections may be needed to account for differences between calibration standards and unknowns. The size and shape of the samples are carefully chosen to minimize (but not eliminate) self-absorption corrections. Given the mass of each isotope in the sample, the isotopic fractions are obtained from

$$f_i = \frac{m^i}{\sum_{i=238}^{241} m^i} . \tag{8-11}$$

8.4.3 The ^{242}Pu Isotopic Correlation

Plutonium-242 cannot be measured directly because of its low activity, low abundance, and weak gamma rays. Instead, isotopic correlation techniques (Ref. 8) are used to predict the ^{242}Pu abundance from knowledge of the other isotopic fractions. It is well known that correlations exist among the plutonium isotopic abundances because of the nature of the neutron capture reactions that produce the plutonium

isotopes in nuclear reactors. Because these correlations depend upon the reactor type and details of the irradiation history, it is difficult, if not impossible, to find a single correlation that is optimum for all material. Gunnink (Ref. 8) suggests that the correlation

$$242 = \frac{K(240)(241)}{(239)^2} \quad (\text{where } 242 = f_{242}) \tag{8-12}$$

is linear and relatively independent of reactor type. When the isotopic fractions are given in weight percent, the constant K equals 52. One disadvantage to this correlation is that it depends on ^{241}Pu, which decreases in absolute abundance by about 5% per year. The correlation works best if the ^{241}Pu abundance can be corrected to the time of fuel discharge from the reactor. When the discharge time is not known, a partial correction can be made by adding the quantities of ^{241}Am to the ^{241}Pu before computing the correlation. The total gives the ^{241}Pu content at the time of the last chemical separation.

A correlation not involving ^{241}Pu has been suggested (Refs. 8 and 22):

$$242 = \frac{K(240)^3}{(239)^2} . \tag{8-13}$$

This correlation is linear for a given reactor type, but the slope K depends on reactor type.

After the isotopic fraction of ^{242}Pu has been determined using a suitable correlation, known value, or stream average, the other isotopic fractions should be corrected using

$$f_i^c = f_i(1 - f_{242}) \tag{8-14}$$

where f_i^c are the normalized isotopic fractions including ^{242}Pu. This correction renormalizes the fractions so that the sum over all the plutonium isotopes equals unity.

8.5 DATA ACQUISITION

8.5.1 Electronics

A detailed discussion of the instrumentation used for gamma-ray spectroscopy is presented in Chapter 4. Plutonium isotopic measurement systems use conventional, high-quality, nuclear instrumentation modules (NIM). Digital gain and zero-point stabilization are required for methods using channel-summation or response-function methods to evaluate peak areas. A multichannel analyzer (MCA) with a 4096-channel memory is used for most applications. Systems that use two detectors require two analog-to-digital converters and an 8192-channel memory.

The extensive data analysis requirements dictate that the MCA be interfaced to a computer. A 16-bit minicomputer with a 32-kword memory is adequate. A disk is needed for program and data file storage. Simple analysis can be done with programmable calculators after peak areas are obtained.

8.5.2 Detectors

All data analysis methods benefit from the use of a detector that gives the best possible resolution and peak shape. These parameters are most important when selecting a detector for a plutonium isotopic system. A planar, high-purity-germanium detector is used in most applications. A detector with a front surface area of 200 mm^2 and a thickness of 10 to 13 mm gives a good trade-off between resolution and efficiency. Such detectors are available commercially with a resolution (full width at half maximum) better than 500 eV at 122 keV. A peak-shape specification of 2.55 or better for the ratio of full width at one-fiftieth maximum to full width at half maximum at 122 keV helps ensure good peak shape. Good detectors give values of 2.5 or below for this parameter. The low efficiency of planar detectors restricts their use to regions below 400 keV. High-quality coaxial detectors can be used in the 100- to 400-keV region, but their lower resolution complicates the analysis of partially resolved peaks using channel-summation methods.

A coaxial detector with a relative efficiency of 10% or higher is required for measurements in the 600-keV region. Again, resolution is important. The very best resolution may negate the need to peak fit the entire 600-keV region (Ref. 17). Resolutions of 1.7 keV or better at 1332 keV are available.

8.5.3 Filters

Filters must be used in nearly all situations to reduce the count rate from the 59.54-keV ^{241}Am gamma ray that dominates the unfiltered spectrum from any aged sample. If the detector is unfiltered, the americium peak will cause unnecessary deadtime and will sum with x rays and gamma rays in the 100-keV region to produce interferences in the 150- to 165-keV region. Typical filters use 0.15 to 0.30 cm of cadmium and 0.025 cm of copper to selectively absorb the 59.54-keV gamma ray. A reasonable rule of thumb is to design the filter to reduce the 60-keV peak height to just less than the peak heights in the 100-keV region. A thicker filter will unnecessarily reduce the intensity of the important plutonium peaks in the 120- to 200-keV area (see Section 8.3.3). A further test for an adequate filter is to check that the region between 153 and 160 keV is flat and contains no sum peaks (Ref. 20). A more complete discussion of filter design is given in Chapter 2.

Little, if any, filtering is needed for freshly separated samples (no ^{241}Am or ^{237}U) when using the 100-keV region or the 40-keV region. If the detector is shielded with lead, the shield is often lined with approximately 0.25 cm of cadmium to suppress lead x rays (72 to 87 keV) that would otherwise appear in the spectrum.

8.5.4 Count Rate and Sample/Detector Geometry

The sample-to-detector distance or detector collimation is varied to achieve the desired count rate. The count rate is usually kept below 20 000 counts/s to maximize resolution. Developments in high-count-rate spectroscopy (Refs. 23 and 24) may soon allow the use of a much higher count rate. Count rates as high as 60 000 counts/s have been documented for plutonium isotopic measurements (Ref. 25).

Solution measurements use a fixed sample geometry and a disposable vial or a refillable cell. The sample thickness is chosen to optimize the measurement with respect to concentration and energy considerations.

If small samples are placed too close to the detector, gamma rays emitted in cascade may cause coincidence sum peaks in the spectrum because of the large solid angle subtended by the detector (Ref. 19). An example of this effect is the coincidence summing of the 129- and 203-keV gamma rays from ^{239}Pu; the sum peaks can interfere with the 332-keV complex from ^{241}Pu-^{237}U. An effect of 1.6% has been noted in the 332-keV region using a planar detector and a sample-to-detector distance of 3 to 4 cm. Large samples are generally placed at a greater distance from the detector, making this effect less important.

Large plutonium samples have high neutron emission rates; 1 kg of plutonium emits 1 to 2 $\times$ 10^5 n/s. High neutron exposure is known to damage germanium detectors and degrade detector resolution. It is difficult to minimize this effect, because, as the sample-to-detector distance is increased, the count time must be increased and the neutron dose remains essentially constant.

8.5.5 Count Time

The count time required to produce the desired precision is a function of the spectral region studied. In the 40- and 100-keV regions, count times of 1000 s to 1 h are usually satisfactory. Count times of 1 or 2 h or longer are often necessary when using gamma rays above 120 keV to measure high-mass samples, although in some situations samples as small as 10 g can be measured to better than 1% in less than 30 min. Small samples (1 to 2 g or less) may require overnight measurement times. For large samples, simple verification of the ^{239}Pu/^{241}Pu ratio may take only a few minutes. Some specific examples are discussed in Section 8.7.

8.6 SPECTRAL ANALYSIS

This section discusses spectral analysis techniques used for the measurement of plutonium isotopic composition. A general and more complete discussion of the methods used to determine photopeak areas is given in Section 5.3.

8.6.1 Region-of-Interest Summation

Region-of-interest (ROI)-summation or channel-summation techniques are often used to determine photopeak areas for plutonium isotopic composition measurements because they are easy to implement, understand, and use. Both linear and smoothed-step-function backgrounds are used. ROI-summation techniques work well to determine the areas of single isolated gamma-ray peaks but are less satisfactory for the analysis of overlapping peaks such as those found in the 125-, 160-, 332-, and 375-keV regions of the plutonium spectrum. When ROI summation is used to obtain the total area of a multiplet, the individual components can be isolated by an integral stripping method using neighboring peaks and known relative efficiency differences. This analysis generally leads to a loss of precision.

Electronic spectrum stabilizers are often included in systems that use ROI-summation techniques. The background windows must be chosen carefully so that they do not include any of the numerous weak plutonium or ^{241}Am gamma-ray peaks. This is particularly critical when measuring materials with high americium concentration.

8.6.2 Peak Fitting

A detailed description of peak-fitting techniques is given in Section 5.3. The techniques developed by Gunnink and coworkers at Livermore (Ref. 26) are widely used for both plutonium isotopic measurements and general gamma-ray spectroscopy. The GRPANL program (Refs. 27 and 28) was developed by Gunnink specifically to analyze the multiple peaks of the plutonium spectrum; it also forms the basis for the area determination routines of the GRPAUT program (Ref. 17) used at Mound Laboratory.

Both GRPANL and GRPAUT use a smoothed-step-function background and a Gaussian function with an exponential tail to describe the photopeak. The equation for the photopeak function is

$$Y_i = Y_0\{\exp[\alpha (X_i - X_0)^2] + T(X_i)\} \tag{8-15}$$

where Y_i = net counts in channel X_i for a single peak
Y_0 = peak amplitude
α = $-4 \ln 2/(\text{FWHM})^2 = 1/2\sigma^2$ where σ is the standard deviation of the Gaussian function
X_0 = peak centroid
$T(X_i)$ = tailing function at channel X_i.

The tailing function is given by

$$T(X_i) = \{A \exp[B(X_i - X_0)] + C \exp[D(X_i - X_0)]\} \times \{1 - \exp[0.4\alpha(X_i - X_0)^2]\}\delta \tag{8-16}$$

where A and C = short- and long-term tailing amplitude
B and D = short- and long-term tailing slope
δ = 1 for $X_i < X_0$
δ = 0 for $X_i \geq X_0$.

The second term brings the tailing function smoothly to zero at X_0 as shown in Figure 8.15. For many applications the long-term tail can be neglected (C = 0); for large multiplets with strong peaks, it should be included.

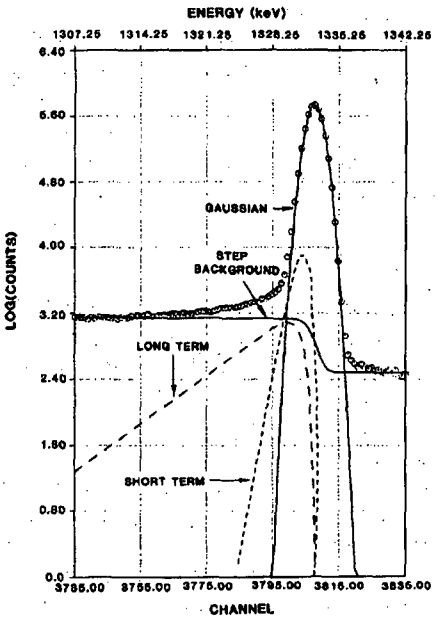

Fig. 8.15 *Gamma-ray photopeak obtained with Ge(Li) detector showing (1) Gaussian, (2) short-term tailing, (3) long-term tailing, and (4) smoothed-step background contributions to spectral peak shape (Ref. 28).*

When all seven parameters in Equations 8-15 and 8-16 are treated as free parameters, the peak-fitting process is usually slow, although today's computers often permit a sufficiently fast analysis. Fortunately, many of the parameters can be predetermined (see Section 5.3). The peak positions X_0 and width parameters α can be determined from two strong, isolated, reference peaks such as the 148- and 208-keV peaks from ^{241}Pu and ^{237}U. Because the gamma-ray branching ratios are well known, the relative intensities of peaks from the same isotope can be fixed.

Experience (Ref. 26) shows that the short-term tailing slope B is constant for a given detector system and should be measured for a high-energy peak where tailing is large. The short-term tailing amplitude A is given by

$$\ln A = k_1 + k_2 E \,. \qquad (8\text{-}17)$$

After B has been fixed, A can be determined from the two peaks that were used to determine the peak positions and width parameters.

If the long-term tailing is zero, the only free parameters are the peak amplitudes Y_0, and the fitting procedure is relatively fast. GRPANL allows other parameters to be free, but this increases the analysis time. The step-function background is determined first and subtracted from the acquired spectrum. GRPANL uses an iterative, nonlinear least-squares technique (Refs. 26 and 27) to fit the residual photopeak activity. Because the method is iterative, the analysis time depends on the number of peaks, the number of free parameters, and the type of computer system. Typically, analysis of a plutonium spectrum containing over 50 peaks in 15 groups in the 120- to 450-keV range takes about 10 min on a Digital Equipment Corporation PDP-11/23 computer or 3 to 4 min on a PDP-11/73. The analysis time is usually much shorter than the data accumulation time.

GRPANL can fit x-ray peaks that have a different intrinsic line shape (Lorentzian) than gamma rays (Ref. 29). This feature is necessary to fit peaks in the 100-keV region.

8.6.3 Response-Function Analysis

Response-function analysis uses the principles discussed in Section 8.6.2 to calculate the shape of the detector response to a particular isotope in a particular energy region. The peak-fitting procedure assigns a separate term with the form of Equation 8-15 to each photopeak in the analysis region and allows some or all of the shape parameters to be free. The response-function analysis uses the same equation but fixes all shape parameters and the relative amplitudes Y_0 of all the peaks from the same isotope; the only free parameters in the fitting procedure are the amplitudes of the isotopes that contribute peaks to the analysis region. The fitting procedure is reduced to a linear least-squares analysis that can be quickly solved.

The peak-shape characteristics of the detector must be known or determined from the spectrum of the sample under study. If the parameters are determined directly from each spectrum, variations that are due to different count rates or instrumental changes are automatically registered. (The procedure used to determine peak positions and shape parameters is discussed in Sections 5.3 and 8.6.2.) Given the shape parameters and positions for all gamma-ray peaks, it is easy to compute the response profile of each isotope in the analysis region. Response-function analysis has been used to fit the complex 100-keV region (Refs. 4, 12, and 16) and the many regions between 120 and 370 keV (Refs. 30 and 31). The formalism of Ref. 29 should be used to compute x-ray line shapes when analyzing the 100-keV region.

8.7 IMPLEMENTED SYSTEMS

This section discusses the characteristics and performance of four plutonium isotopic measurement systems that are in routine use in the United States.

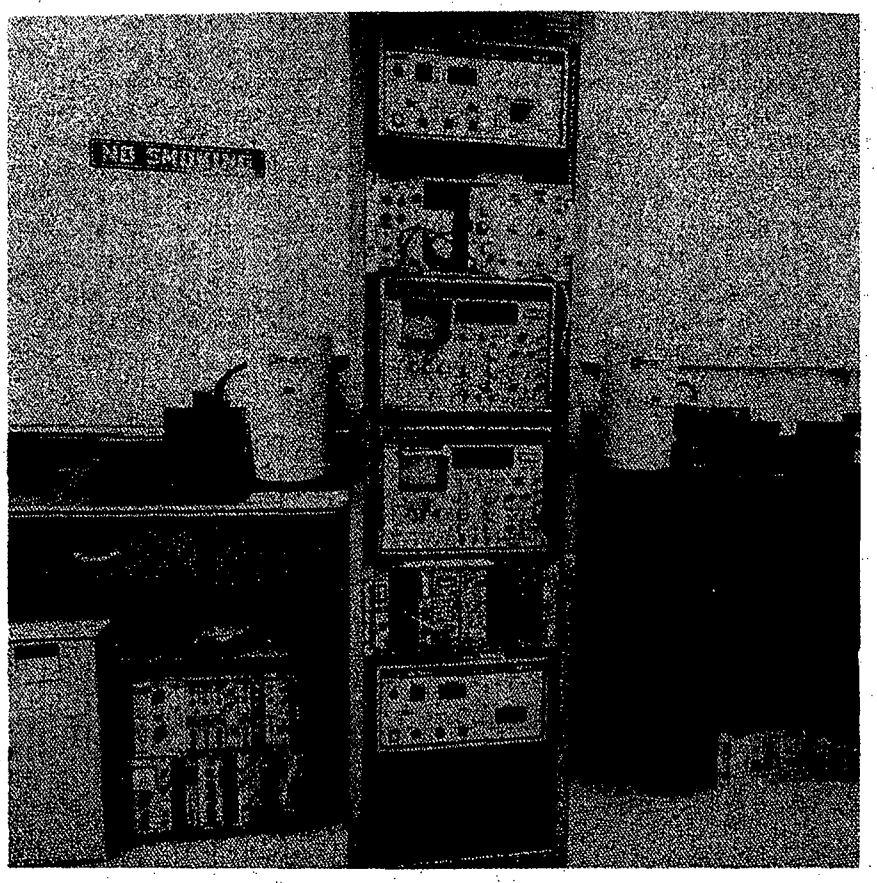

Fig. 8.16 *Plutonium isotopic system implemented at Rockwell-Hanford. (Photo courtesy of R. A. Hamilton, Rockwell-Hanford.)*

8.7.1 Rockwell-Hanford Company

The Rockwell-Hanford Company uses a plutonium isotopic measurement system in conjunction with a calorimeter to measure the plutonium content of solid samples of plutonium oxide, metal, mixed oxide, impure oxide, and scrap (Ref. 32). The system described here was used until 1984; the GRPAUT program, developed at Mound, is now used. The system, shown in Figure 8.16, uses four 300-mm^2 by 7-mm-deep planar HPGe detectors. The sample-to-detector distance is adjusted to give a count rate of 3000 counts/s; samples are counted for 10 000 s. No sample rotation is used. Spectra acquired in the MCA are analyzed in an off-line computer. Selected peaks

in the 120- to 400-keV range are analyzed using the isotope ratio method outlined in Ref. 3. Only the fundamental branching ratios and half-lives are used in the isotope ratio expressions. Bias corrections are not made and ^{242}Pu is not calculated.

Table 8-14 shows part of the large volume of performance data obtained during measurement of 14 standards that span the range from 2 to 24% ^{240}Pu. In Table 8-14 the measured isotope fractions have been used to calculate the rate of heat production in each sample; the definition of specific power and its importance to calorimetry are given in Chapter 21. The measurement precision for the specific power is 0.5 to 1.0% and the bias is of the same order. When applied to determining the specific power, plutonium isotopic measurement by gamma-ray spectroscopy is somewhat forgiving. Biases in one isotope fraction are partially cancelled by the normalization condition that all isotopes must sum to unity.

Table 8-14. Performance of Rockwell-Hanford isotopic system for specific power

	Isotope Fraction (wt%)						
Isotope	1(oxide)	2(metal)	3(oxide)	4(oxide)	5(oxide)	6(metal)	7(metal)
^{238}Pu	0.0003	0.0008	0.028	0.14	0.064	0.069	0.089
^{239}Pu	97.56	93.73	91.64	87.87	86.50	80.77	73.81
^{240}Pu	2.40	6.03	7.65	10.23	11.78	17.10	22.83
^{241}Pu	0.038	0.21	0.569	1.49	1.42	1.66	2.26
^{241}Am	0.059	0.138	0.447	1.26	0.088	1.12	2.13
No. of measurements							
	102	103	102	109	98	103	101
Precision of specific power (% RSD) calculated from measurement reproducibility							
	1.02%	0.72%	0.65%	0.55%	0.84%	0.62%	0.53%
Bias: Specific power from NDA divided by specific power from mass spectrometry values							
	0.9914	0.9921	1.003	1.008	1.016	1.002	1.028

8.7.2 Los Alamos National Laboratory

The Plutonium Processing Facility at Los Alamos has an isotopic composition measurement system that uses an isotopic ratio technique (Refs. 3, 18, and 33). Spectra are acquired with 200-mm^2 by 10-mm-deep planar HPGe detectors. The sample-to-detector distance is adjusted to give the desired count rate that may be as high as 20 000 counts/s. Digital gain stabilization is used so that ROI-summation techniques can be used to evaluate peak areas. The spectral regions between 120 and 400 keV are analyzed to determine isotopic ratios. All isotopic ratios are measured relative to ^{241}Pu. Different gamma-ray ratios are used for aged and freshly separated material; Table 8-15 lists the ratios used in the analysis. Equation 8-12 is used to

estimate ^{242}Pu; a correlation constant of 90 is used for materials with a wide range of reactor histories. The required relative efficiency ratios are determined from a set of strong, clean ^{239}Pu and ^{241}Pu-^{237}U lines that are normalized to each other. Simple linear and quadratic interpolation and extrapolation are used to obtain needed ratios. On-line analysis has been applied to material with 2 to 18% ^{240}Pu and up to 2.0% ^{241}Am. The system components are shown in Figure 8.17; the two detectors can acquire data from two samples simultaneously. The existing analysis program can handle up to four detectors.

Table 8-15. Ratios used in Los Alamos plutonium isotopic system

Isotopic	Gamma-Ray Energy of Samples (keV)	
Ratio	Aged	Freshly Separated
238/241	152.7/148.6	152.7/148.6
239/241[a]	345.0/332.4	129.3/148.6
	203.5/208.0	
240/241	160.3/164.6	160.3/148.6
Am/239[a]	125.3/129.3	125.3/129.3[b]
	169.6/171.3	

[a]A weighted average of the two ratios is used.
[b]The ^{241}Am is usually too low to measure.

Because ROI-summation techniques cannot separate overlapping peaks, clean neighboring peaks are used to subtract interferences. Table 8-16 lists the gamma-ray peaks used for this subtraction. The ^{241}Pu/^{241}Am ratio is determined from the 332-keV region; this ratio is used to subtract the ^{241}Am contribution from the ^{241}Pu-^{237}U peaks at 164.6, 208.0, 267.5, and 332.4 keV.

The fundamental constants in each isotopic ratio equation are adjusted slightly by measuring standard reference materials. This procedure compensates for possible biases in the measured peak areas as might be expected using channel-summation methods where there are close interferences in the 125-, 160-, and 332-keV regions. The calibration standards included a wide variety of plutonium oxide and metal samples with masses ranging from less than 0.5 g to approximately 1 kg.

Figure 8.18 shows the average accuracy of the Los Alamos system; ^{239}Pu, ^{240}Pu, and ^{241}Pu are measured to better than 0.2% and ^{238}Pu and ^{241}Am are measured to a few percent. These values are limited by the accuracy of the standards. The precision of the measurement is shown in Figure 8.19 as a function of count time. Figure 8.20 shows the precision of the specific power measurement, which is used in conjunction with a calorimetry measurement to give total plutonium mass. The specific power can be determined to better than 1% with a 30-min measurement and to about 0.5% with a 2-h measurement.

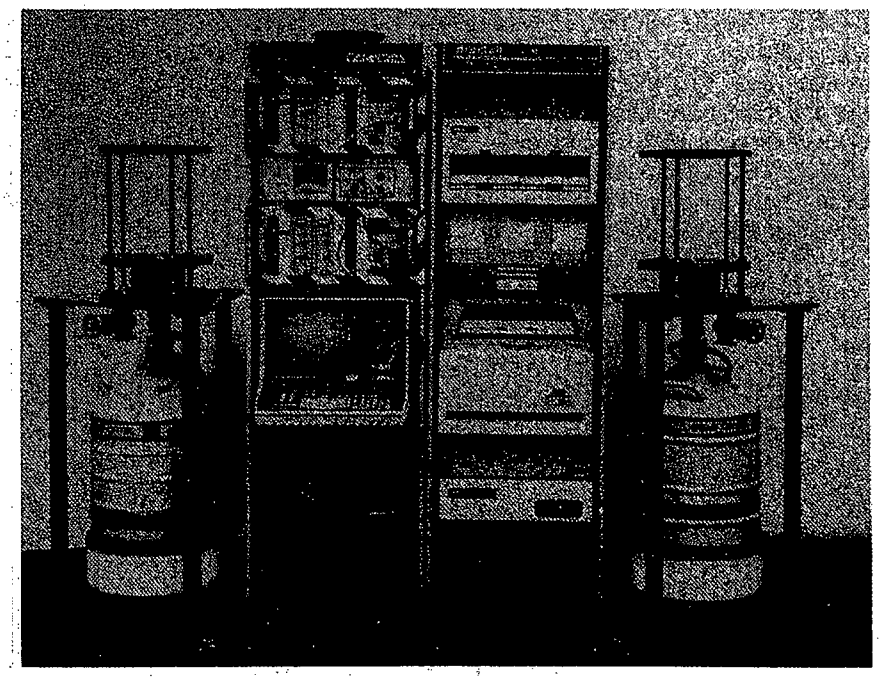

Fig. 8.17 Los Alamos multiple-detector plutonium isotopic system.

Table 8-16. Peaks used for interference subtraction

Region (keV)	Interfering Isotope	Peak Used for Subtraction (keV)
125	^{239}Pu	129.3
160	^{239}Pu	161.5
160	^{241}Pu	164.6[a]
332	^{239}Pu	345.0

[a]For aged material only.

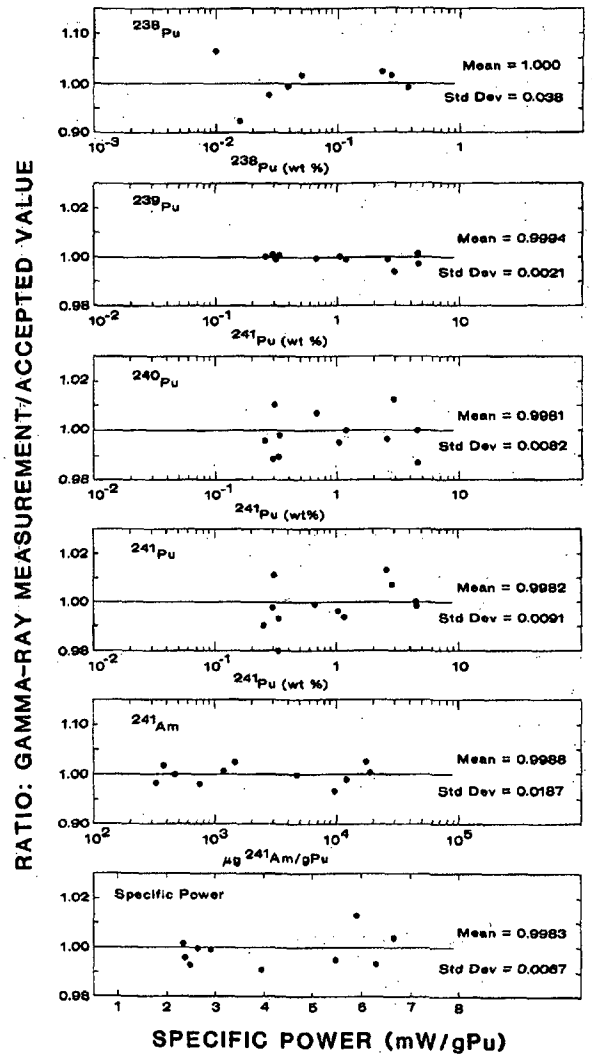

Fig. 8.18 Accuracy of the Los Alamos plutonium isotopic system for a wide range of material types and isotopic composition.

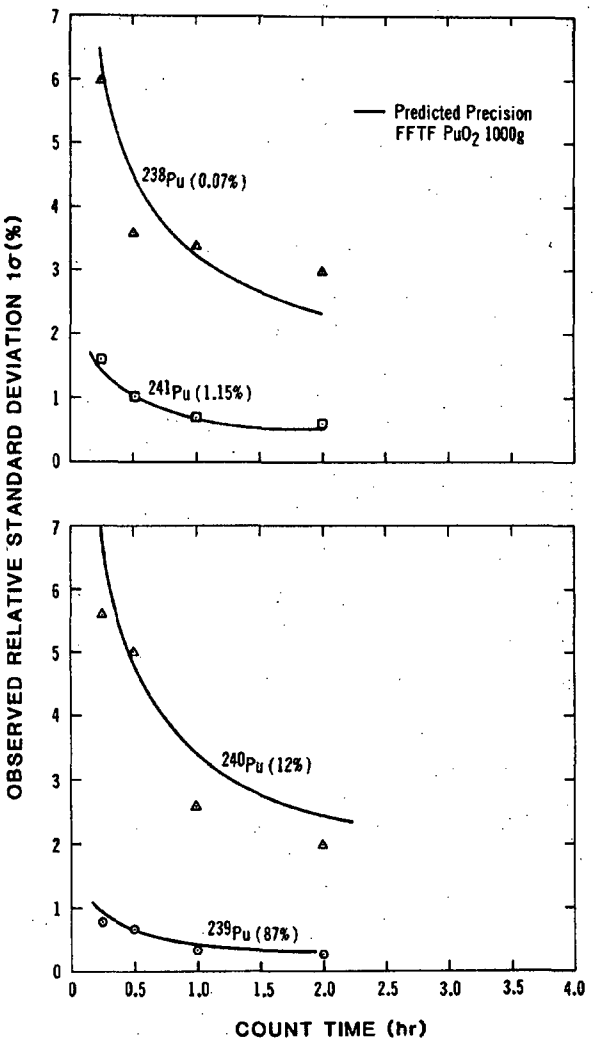

Fig. 8.19 Precision of the Los Alamos plutonium isotopic system as determined from 30 measurements of a 1-kg sample of PuO_2 (12% ^{240}Pu). The solid line is the precision predicted from counting statistics.

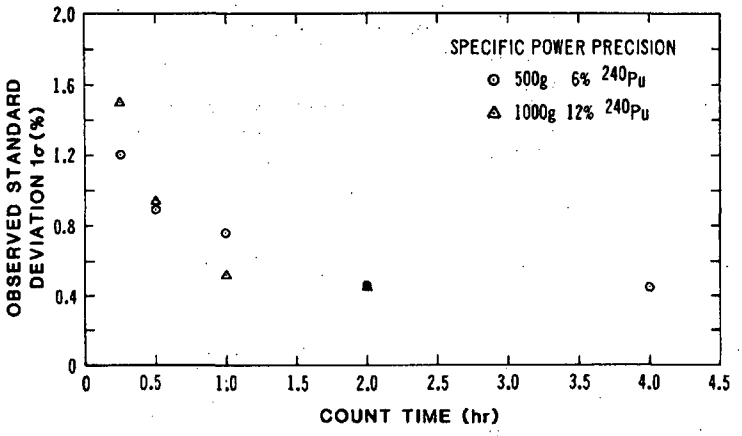

Fig. 8.20 Precision of the Los Alamos plutonium isotopic system for the determination of specific power as used to interpret calorimeter measurements. Precision calculated from 30 measurements (circles indicate a 500-g sample of plutonium metal with 6% ^{240}Pu, triangles indicate a 1-kg sample of PuO_2 with 12% ^{240}Pu).

8.7.3 Mound Facility

Investigators at the Mound Facility have carried out plutonium isotopic measurements in support of their calorimetry effort for some time. They use the peak-fitting programs GRPANL and GRPAUT described in Section 8.6.2. Long-term tailing is not used. The slope of the short-term tail B is fixed during initial detector characterization. The peak amplitudes Y_0 and widths α are free parameters; in some cases the short-term-tail amplitude is a free parameter. Over 50 peaks are fit in the region from 120 to 450 keV; the 640-keV region is also analyzed. Table 8-17 lists the ratios used in the GRPAUT program. A relative efficiency curve is determined from ^{239}Pu, ^{241}Pu-^{237}U, and ^{241}Am peaks; weighted least-squares techniques are used to fit the measured points to a smooth curve (see Equation 8.18). Equation 8-13 is used to estimate ^{242}Pu.

$$\ln \varepsilon_i = A_0 + \sum_{j=1}^{2} A_j / E_i^j + \sum_{j=1}^{3} A_{j+2} (\ln E_i)^j + A_6 \delta_6 + A_7 \delta_7 \qquad (8\text{-}18)$$

where ε_i = relative efficiency
E_i = gamma-ray energy
A_6, A_7 = constants to normalize ^{241}Pu-^{237}U and ^{241}Am points to ^{239}Pu
δ_6, δ_7 = 1 for ^{241}Pu and ^{241}Am, and 0 otherwise.

Table 8-17. Peak ratios calculated in GRPAUT

Ratio	Energy(keV)
241/239	208/203[a]
241/239	148/144
241/239	165/161
241/239	148/129[a]
238/239	153/144
238/241	153/148[a]
240/239	160/161
240/241	160/165
240/241	160/148[a]
Am/239	125/129
Am/239	335/345[a]
Am/239	369/375[a]
Am/239	662/646
Am/239	772/718

[a]Ratios used to calculate isotopic fractions. Weighted averages are used where appropriate.

The GRPAUT program has been used in several applications. Reference 20 describes a two-detector method that uses a planar detector in the 120- to 300-keV region and a coaxial detector in the 300- to 700-keV region. The coaxial detector is used to measure the 642.48-keV ^{240}Pu and 662.42-keV ^{241}Am gamma rays; the detector is heavily filtered to absorb gamma rays with energy below 100 keV. The precision for a 50 000-s count time is ~2% for both the 160/148 ^{240}Pu/^{241}Pu ratio and for the 642/646 ^{240}Pu/^{239}Pu ratio. For large samples, the 662/646 ^{241}Am/^{239}Pu ratio is significantly more precise than the 125/129 ^{241}Am/^{239}Pu ratio.

Figure 8.21 shows a system developed at Mound for the simultaneous calorimetric and gamma-ray spectroscopic assay of plutonium (Refs. 34 and 35). This system reduces operator radiation exposure through less sample handling and also reduces data transcription errors. Table 8-18 summarizes the measurement results obtained using the transportable assay system at three nuclear facilities. The measured samples contained from a few hundred grams to 2 kg of plutonium oxide and metal; most samples had a nominal ^{240}Pu concentration of 6%. Count times were generally 10 000 to 50 000 s. The total plutonium mass was measured with an accuracy of better than 1% and a precision of 1 to 3%.

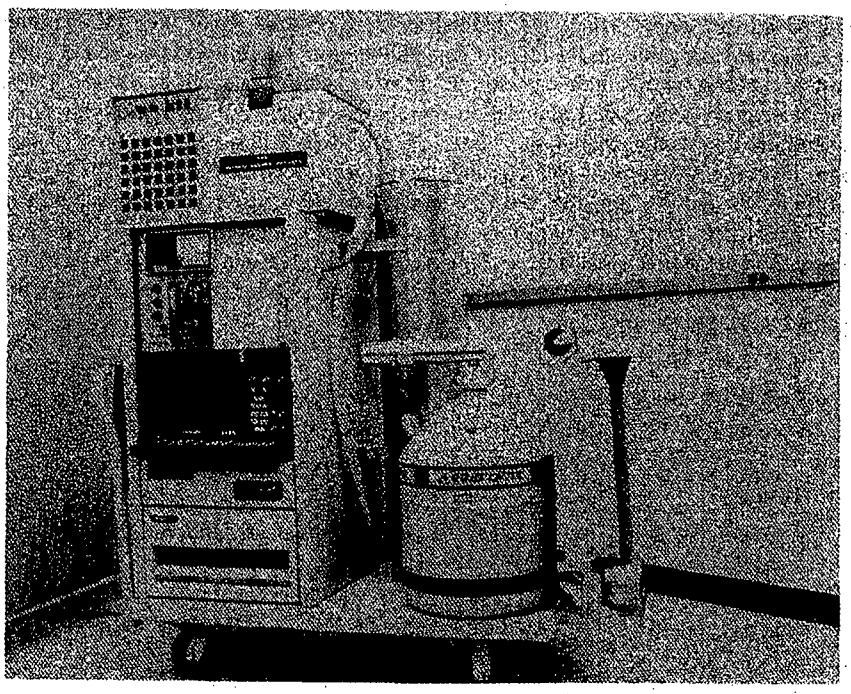

Fig. 8.21 Transportable calorimeter with simultaneous calorimetry/gamma-ray spectroscopy capability. (Photo courtesy of J. G. Fleissner, Mound Facility.)

Table 8-18. Simultaneous assay with transportable calorimeter and gamma-ray spectroscopy system[a]

Site	No. of Samples	Total Plutonium Assay Average Ratio Measured/Accepted	Precision of Ratio (%)
1	18	0.997	1.7
2	20	1.007	0.7
3	13	1.00	3.0

[a]Ref. 35.

8.7.4 Lawrence Livermore National Laboratory

The response-function analysis method has been used extensively by Gunnink and coworkers at Lawrence Livermore National Laboratory. In the early 1970s, they

installed an instrument using this method at the Savannah River Plant to measure low-concentration solutions of low-burnup plutonium. The instrument used a high-resolution planar germanium detector to measure a 10-mL solution sample. The samples required only small attenuation corrections because of their low plutonium concentration and small thickness (1 cm). Because americium had been freshly separated from the solutions, it was possible to analyze the 40-keV region. The system analyzed both the 40- and the 100-keV regions; these regions yield measurements with significantly better precision than that obtainable using regions above 120 keV. The measurement precision with a count time of only 10 min is within a factor of 2 of that customarily assigned to mass spectrometry. Table 8-19 lists some results obtained with this system.

Table 8-19. Performance of the plutonium isotopic assay system at the Savannah River Plant (response-function method)[a]

Isotope	Abundance (%)	Av Bias (%)	Precision (%)
1. Freshly separated solutions, 10-min count time, 3 g/L plutonium:			
238	0.008	5.6	4.7
239	93.46	0.048	0.049
240	5.88	0.75	0.72
241	0.65	0.96	1.9
2. Aged solutions, 60-min count time, 4 g/L plutonium:			
238	0.018	7.6	5.7
239	90.92	0.14	0.09
240	8.40	1.6	0.94
241	0.661	0.64	0.61
Am	- - -	0.08	0.26
Total Pu	5.4 g/L	0.46	0.35

[a]Ref. 4.

Gunnink developed a similar instrument to measure high-burnup (~20% ^{240}Pu), high-concentration (~250-g Pu/L) reprocessing plant solutions (Ref. 12). The instrument is installed at the reprocessing plant in Tokai-Mura, Japan. The 40-keV region is analyzed when measuring freshly separated solutions. In addition, the 148-keV peak and the 94-keV U $K_{\alpha 2}$ x-ray peak (which has contributions from all the plutonium isotopes) are used to measure ^{241}Pu, and the 129-keV gamma-ray peak is used to measure ^{239}Pu. Peak areas are determined using simple ROI-summation techniques; interfering peaks are stripped out channel by channel before summing. For aged solutions, response-function methods are applied to the 100-keV region. The 208- and

59-keV peaks are used to determine the energy calibration and the peak-shape parameters. Numerous interferences are stripped out of the 100-keV complex before fitting the response functions. The instrument is calibrated with known solution standards to measure the absolute concentration of each isotope. Equation 8-12 is used to estimate ^{242}Pu.

The very thin sample cell (~1 mm thick) shown in Figure 8.22 allows a 0.25-mL sample to be viewed by the detector. The cell is mounted on the detector face as shown in Figure 8.23, and the plutonium solution to be measured is pumped into the sample cell from a glovebox. Fresh solutions are counted for 15 to 30 min; aged solutions for 30 min to 1 h. Table 8-20 summarizes the performance of the Tokai system when measuring both freshly separated and aged process solutions.

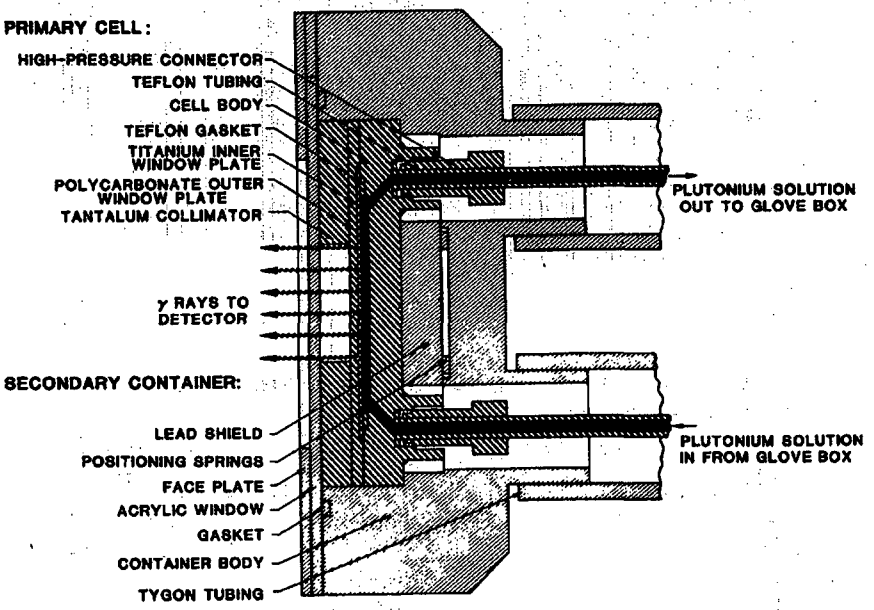

Fig. 8.22 *Sample cell used with the plutonium isotopic assay system installed at the Tokai-Mura reprocessing plant in Japan (Ref. 12). The cell fits over the front of a HPGe detector; plutonium solutions are pumped to the cell from a glovebox in the analytical laboratory. (Photo courtesy of R. Gunnink, Lawrence Livermore National Laboratory.)*

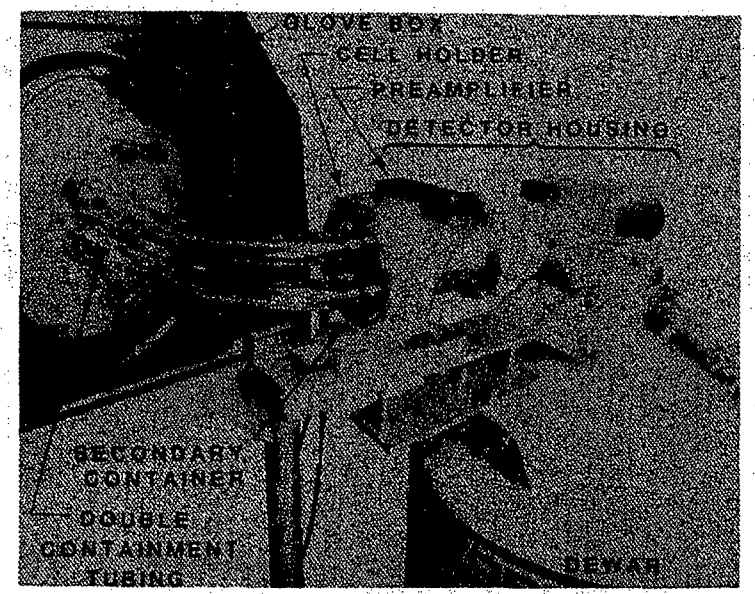

Fig. 8.23 HPGe detector and sample cell used with plutonium isotopic assay system installed at the Tokai-Mura reprocessing plant in Japan (Ref. 12). (Photo courtesy of R. Gunnink, Lawrence Livermore National Laboratory.)

Table 8-20. Performance of Tokai isotopic assay system; 94 samples, 130– to 270-g/L plutonium[a]

Isotope	Abundance (%)	Bias (%)	Precision (%)
238	0.5 – 1.0	0.1 – 0.8	0.4 – 0.7
239	60 – 75	0.01 – 0.3	0.08 – 0.4
240	17 – 23	0.02 – 0.4	0.2 – 1.3
241	5 – 11	0.02 – 0.8	0.2 – 0.8

[a]Ref. 12.

Response-function techniques have also been applied by Ruhter and Camp (Refs. 30 and 31) to solid samples using gamma rays in the 120- to 450-keV region. They developed a portable instrument for the use of safeguards inspectors at the International Atomic Energy Agency.

Another system is described by Gunnink in Ref. 36; it makes use of all the data available in the spectrum, accommodates two detectors (high and low energy), and analyzes data with both response functions and ROI peak integration. This system can obtain better precision than other systems can when measuring arbitrary samples because of its response-function analysis of the 100-keV region.

8.7.5 Summary of Measurement Precision

For all techniques discussed, the measurement precision is influenced most by the spectral region analyzed; a higher precision is obtained when measuring the lower energy regions that have higher gamma-ray emission rates. Table 8-21 summarizes the measurement precision attainable for different energy regions. Measurement accuracy is usually commensurate with precision.

Table 8-21. Typical measurement precision (%)

Region (keV)	Count Time	238	239	240	241	Am	Specific Power
40	10-30 min	0.3-5	0.05-0.5	0.2-1.0	0.2-1.0	- - -	- - -
100	30-60 min	0.3-5	0.05-0.5	0.2-1.0	0.2-0.8	0.1-1.0	0.1-1.0
>120	1-4 h[a]	>1-10	0.1-0.5	1-5	0.3-0.8	0.2-10	0.3-2

[a]With high-count-rate systems these precisions can be realized in less than 30 min.

REFERENCES

1. Francis X. Haas and Walter Strohm, "Gamma-Ray Spectrometry for Calorimetric Assay of Plutonium Fuels," *IEEE Transactions on Nuclear Science* NS-22, 734 (1975).

2. T. Dragnev and K. Scharf, "Nondestructive Gamma Spectrometry Measurement of $^{239}Pu/^{240}Pu$ and $Pu/^{240}Pu$ Ratios," *International Journal of Applied Radiation and Isotopes* 26, 125 (1975).

3. J. L. Parker and T. D. Reilly, "Plutonium Isotopic Determination by Gamma-Ray Spectroscopy," in "Nuclear Analysis Research and Development Program Status Report, January–April 1974," G. Robert Keepin, Ed., Los Alamos Scientific Laboratory report LA-5675-PR (1974).

4. R. Gunnink, J. B. Niday, and P. D. Siemens, "A System for Plutonium Analysis by Gamma-Ray Spectrometry. Part 1: Techniques for Analysis of Solutions," Lawrence Livermore Laboratory report UCRL-51577, Part 1 (April 1974).

5. R. Gunnink, "A Simulation Study of Plutonium Gamma-Ray Groupings for Isotopic Ratio Determinations," Lawrence Livermore Laboratory report UCRL-51605 (June 1974).

6. "Determination of Plutonium Isotopic Composition by Gamma-Ray Spectrometry," ASTM Standard Test Method C1030-84, in *1985 Annual Book of ASTM Standards* (American Society for Testing and Materials, Philadelphia, 1985), Section 12, pp. 788–796.

7. R. D. Evans, *The Atomic Nucleus* (McGraw Hill, New York, 1955), p. 484.

8. R. Gunnink, "Use of Isotope Correlation Techniques to Determine ^{242}Pu Abundance," *Nuclear Materials Management* 9 (2), 83–93 (1980).

9. R. Gunnink, J. E. Evans, and A. L. Prindle, "A Reevaluation of the Gamma-Ray Energies and Absolute Branching Intensities of ^{237}U, $^{238, 239, 240, 241}$Pu, and ^{241}Am," Lawrence Livermore Laboratory report UCRL-52139 (October 1976).

10. J. F. Lemming and D. A. Rakel, "Guide to Plutonium Isotopic Measurements Using Gamma-Ray Spectrometry," Mound Facility report MLM-2981 (August 1982).

11. P. A. Russo, S.-T. Hsue, J. K. Sprinkle, Jr., S. S. Johnson, Y. Asakura, I. Kando, J. Masui, and K. Shoji, "In-Plant Measurements of Gamma-Ray Transmissions for Precise K-Edge and Passive Assay of Plutonium Concentration and Isotopic Fractions in Product Solutions," Los Alamos National Laboratory report LA-9440-MS (PNCT 841-82-10) (1982).

12. R. Gunnink, A. L. Prindle, Y. Asakura, J. Masui, N. Ishiguro, A. Kawasaki, and S. Kataoka, "Evaluation of TASTEX Task H: Measurement of Plutonium Isotopic Abundances by Gamma-Ray Spectrometry," Lawrence Livermore National Laboratory report UCRL-52950 (October 1981).

13. H. Umezawa, T. Suzuki, and S. Ichikawa, "Gamma-Ray Spectrometric Determination of Isotopic Ratios of Plutonium," *Journal of Nuclear Science and Technology* 13, 327–332 (1976).

14. J. Bubernak, "Calibration and Use of a High-Resolution Low-Energy Photon Detector for Measuring Plutonium Isotopic Abundances," *Analytica Chimica Acta* 96, 279–284 (1978).

15. T. K. Li, T. E. Sampson, and S. Johnson, "Plutonium Isotopic Measurement for Small Product Samples," Proceedings of Fifth Annual ESARDA Symposium on Safeguards and Nuclear Material Management, Versailles, France, April 19–21, 1983, paper 4.23.

16. R. Gunnink, "Gamma Spectrometric Methods for Measuring Plutonium," Proceedings of the American Nuclear Society National Topical Meeting on Analytical Methods for Safeguards and Accountability Measurements of Special Nuclear Material, Williamsburg, Virginia, May 15–17, 1978.

17. J. G. Fleissner, "GRPAUT: A Program for Pu Isotopic Analysis (A User's Guide)," Mound Facility report MLM-2799 (January 1981).

18. T. E. Sampson, S. Hsue, J. L. Parker, S. S. Johnson, and D. F. Bowersox, "The Determination of Plutonium Isotopic Composition by Gamma-Ray Spectroscopy," *Nuclear Instruments and Methods* 193, 177–183 (1982).

19. H. Ottmar, "Results from an Interlaboratory Exercise on the Determination of Plutonium Isotopic Ratios by Gamma Spectrometry," Kernforschungszentrum Karlsruhe report KfK 3149 (ESARDA 1/81) (July 1981).

20. J. G. Fleissner, J. F. Lemming, and J. Y. Jarvis, "Study of a Two-Detector Method for Measuring Plutonium Isotopics," in *Measurement Technology for Safeguards and Materials Control* Proceedings of American Nuclear Society Topical Meeting, Kiawah Island, South Carolina, November 26–30, 1979, pp. 555–567.

21. J. G. Fleissner, "Nondestructive Assay of Plutonium in Isotopically Heterogeneous Salt Residues," Proceedings of Conference on Safeguards Technology, Hilton Head Island, Department of Energy publication CONF-831106 (1983).

22. H. Umezawa, H. Okashita, and S. Matsurra, "Studies on Correlation Among Heavy Isotopes in Irradiated Nuclear Fuels," Symposium on Isotopic Correlation and Its Application to the Nuclear Fuel Cycle held by ESARDA, Stresa, Italy, May 1978.

23. K. Kandiah and G. White, "Status at Harwell of Opto-Electronic and Time Variant Signal Processing for High Performance Nuclear Spectrometry with Semi-Conductor Detectors," *IEEE Transactions on Nuclear Science* NS-28 (1), 1–8 (1981).

24. F. J. G. Rogers, "The Use of a Microcomputer with In-Field Nondestructive Assay Instruments," International Symposium on Recent Advances in Nuclear Materials Safeguards, International Atomic Energy Agency, Vienna, Austria, November 8-12, 1982.

25. J. G. Fleissner, "A High Count Rate Gamma-Ray Spectrometer for Pu Isotopic Measurements," Proceedings of Institute of Nuclear Materials Management 26th Annual Meeting, Albuquerque, New Mexico (1985).

26. R. Gunnink and J. B. Niday, "Computerized Quantitative Analysis by Gamma-Ray Spectrometry. Vol. 1. Description of the GAMANAL Program," Lawrence Livermore Laboratory report UCRL-51061, Vol. 1 (March 1972).

27. R. Gunnink and W. D. Ruhter, "GRPANL: A Program for Fitting Complex Peak Groupings for Gamma and X-Ray Energies and Intensities," Lawrence Livermore Laboratory report UCRL-52917 (January 1980).

28. J. G. Fleissner and R. Gunnink, "GRPNL2: An Automated Program for Fitting Gamma and X-Ray Peak Multiplets," Monsanto Research Corporation Mound Facility report MLM-2807 (March 1981).

29. R. Gunnink, "An Algorithm for Fitting Lorentzian-Broadened K-Series X-Ray Peaks of the Heavy Elements," *Nuclear Instruments and Methods* 143, 145 (1977).

30. W. D. Ruhter and D. C. Camp, "A Portable Computer to Reduce Gamma-Ray Spectra for Plutonium Isotopic Ratios," Lawrence Livermore Laboratory report UCRL-53145 (May 1981).

31. W. D. Ruhter, "A Portable Microcomputer for the Analysis of Plutonium Gamma-Ray Spectra," Lawrence Livermore National Laboratory report UCRL-53506, Vols. I and II (May 1984).

32. R. A. Hamilton, Rockwell-Hanford letter R83-0763, to T. E. Sampson (February 24, 1983).

33. S. -T. Hsue, T. E. Sampson, J. L. Parker, S. S. Johnson, and D. F. Bowersox, "Plutonium Isotopic Composition by Gamma-Ray Spectroscopy," Los Alamos Scientific Laboratory report LA-8603-MS (November 1980).

34. D. A. Rakel, "Gamma-Ray Measurements for Simultaneous Calorimetric Assay," *Nuclear Material Management* X, 467 (1981).

35. D. A. Rakel, J. F. Lemming, W. W. Rodenburg, M. F. Duff, and J. Y. Jarvis, "Results of Field Tests of a Transportable Calorimeter Assay System," 3rd Annual ESARDA Symposium on Safeguards and Nuclear Materials Management, Karlsruhe, Federal Republic of Germany, May 6-8, 1981, p. 73.

36. R. Gunnink, "Plutonium Isotopic Analysis of Nondescript Samples by Gamma-Ray Spectrometry," Conf. on Analytical Chemistry in Energy Technology, Gatlinburg, Tennessee, October 6-8, 1981.

9

Densitometry

Hastings A. Smith, Jr., and Phyllis A. Russo

9.1 INTRODUCTION

The term "densitometry" refers to measurement of the density of a material by determining the degree to which that material attenuates electromagnetic radiation of a given energy. Chapter 2 details the interaction of electromagnetic radiation (specifically x rays and gamma rays) with matter. Because electromagnetic radiation interacts with atomic electrons, densitometry measurements are element-specific, not isotope-specific. Two phenomena occur during a densitometry measurement: first, part of the incident radiation energy is absorbed; and second, the ionized atoms emit characteristic x rays as they return to their stable atomic ground states. This latter process, known as x-ray fluorescence (XRF), is a powerful method for element-specific assays. (See Chapter 10 for details of the XRF technique.) In some cases, gamma-ray transmission measurements can provide information not only on the bulk density of a sample but also on its composition. Because the absorption of low-energy photons (primarily by the photoelectric effect) is a strong function of the atomic numbers (Z) of the elements in the sample, a measurable signature is provided on which an assay can be based.

This chapter describes various densitometry techniques involving measurement of photon absorption at a single energy and at multiple energies and measurement of differential photon attenuation across absorption edges. Applications using these techniques are discussed, and measurement procedures with typical performance results are described.

All densitometry measurements discussed in this chapter are based on determination of the transmission of electromagnetic radiation of a given energy by the sample material. The mathematical basis for the measurement is the exponential absorption relationship between the intensity (I_0) of photon radiation of energy (E) incident on a material and the intensity (I) that is transmitted by a thickness (x) of the material:

$$I = I_0 \exp(-\mu\rho x) \tag{9-1}$$

where ρ is the mass density of the material and μ is the mass attenuation coefficient, which is evaluated at the photon energy E. The incident and transmitted intensities are the measured quantities. Their ratio (I/I_0) is called the transmission (T) of the material at the photon energy of interest. If any two of the three quantities in the exponent expression are known from other data, the third quantity can be determined by the transmission measurement. A strong advantage of a procedure that measures photon transmissions is that the data are handled as a ratio of two similarly measured quantities, thereby removing many bothersome systematic effects that often complicate the measurement of absolute photon intensity.

The measured electromagnetic radiation can originate from an artificial x-ray source (which emits photons with a continuous energy spectrum) or from a natural gamma-ray source (which emits gamma rays with discrete energies). The sample material is placed between a photon source and a photon detector (see Figure 9.1). The transmission of the sample is determined by measuring the photon intensity of the source both with (I) and without (I_0) the sample material present.

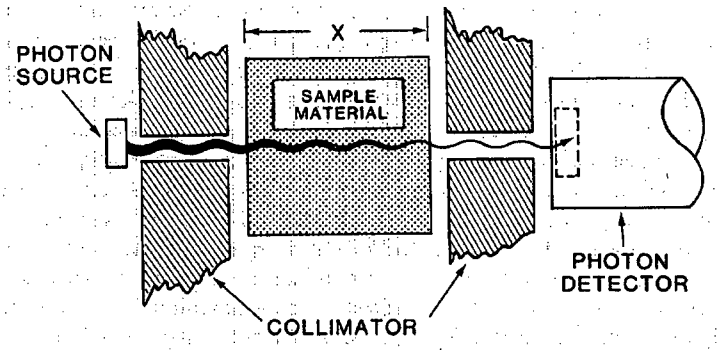

Fig. 9.1 Key components of a densitometry measurement.

9.2 SINGLE-LINE DENSITOMETRY

9.2.1 Concentration and Thickness Gauges

If a sample is composed of one type of material—or of a mixture of materials whose composition is tightly controlled except for one component—then the sample transmission at one gamma-ray energy can be used as a measure of the concentration (density ρ) of the varying component. Normally, discrete-energy gamma-ray sources are used. For example, consider a two-component system, such as a solution of uranium and nitric acid, whose components have respective densities ρ and ρ_0 and mass attenuation coefficients μ and μ_0 at a given gamma-ray energy. The natural logarithm of the photon transmission at that energy is given by

$$\ln T = -(\mu\rho + \mu_0\rho_0)x \ . \tag{9-2}$$

With ρ as the unknown concentration,

$$\rho = -\left(\frac{1}{\mu x}\right)\ln T - \frac{\mu_0\rho_0}{\mu} \ . \tag{9-3}$$

Equation 9-3 may be applied as a gauge for the concentration of an unknown amount of substance (ρ) in a known, carefully controlled solvent concentration (ρ_0).

In applying the concentration gauge to special nuclear material (SNM) solutions (uranium and plutonium), it is critical both that the mass attenuation coefficients be well characterized for the solvent (μ_0) and the SNM (μ) and that the solvent composition (ρ_0) be well known and constant from sample to sample. The sample solutions should not be vulnerable to contamination because contamination would cause variations in the effective values of ρ_0 and μ_0.

Single-line measurement can also be applied as a thickness gauge for materials of known and tightly controlled composition. On-line measurement of the transmitted photon intensity at one energy through metals and other solids in a constant measurement geometry is a direct measure of the thickness (x) of those materials. Such information is useful for timely control of some commercial production processes.

9.2.2 Measurement Precision

Consider the case of a single-line concentration measurement in which no significant fluctuations are present in the solvent composition. The measurement precision of the unknown quantity (ρ) is determined by the statistical variance of the transmission (T). The relative precision of the density measurement is obtained by differentiating Equation 9-3:

$$\frac{\sigma(\rho)}{\rho} = \left(\frac{1}{\ln T}\right)\left[\frac{\sigma(T)}{T}\right] \ . \tag{9-4}$$

This expression shows that there is a range of transmission values over which the relative precision of the density measurement is smaller than that of the transmission (the favorable precision regime, $|\ln T| > 1$ or $T < 0.37$. For larger transmission values, the relative precision of the density is larger than that of the transmission and the measurement suffers accordingly. Note that when T approaches 1, the expression for the relative precision diverges because of the factor 1/(ln T). Because the sample material is absorbing none of the incident radiation, there is no assay signal.

The range of useful transmission values can also be related to a characteristic concentration, $\rho_c = 1/\mu x$. When $\ln T > 1$, then $\rho > \rho_c$ and the measurement is in the favorable precision regime; but when $\rho < \rho_c$, the assay signal is too small and the precision is unfavorable. By determining the favorable operating range from

the point of view of this characteristic concentration, one can choose a reasonable sample thickness (x), given the intrinsic properties of the sample material to be measured (μ) and the expected range of sample concentrations.

Because of the symmetry in ρ and x in Equations 9-1 through 9-3, Equation 9-4 also expresses the relative precision of a thickness measurement. For a thickness measurement, the precision can be enhanced by a judicious choice of photon energy.

There are limits both on how high and on how low the sample transmission should be for optimum measurement precision. Because $T = I/I_0$ and the intensities are statistically varying quantities, Equation 9-4 can be rewritten as

$$\frac{\sigma(\rho)}{\rho} = \frac{1}{\ln T}\left(\frac{T+1}{I_0\,T}\right)^{1/2} \qquad (9\text{-}5)$$

A plot of this relationship in Figure 9.2 shows the deterioration of the measurement precision at the high- and low-concentration extremes. The optimum range of T is below the point where $\ln T = 1$, in keeping with the definition of ρ_c. The range of T over which the quantity $\sigma(\rho)/\rho$ is near a minimum determines the instrument design features (sample thickness, measurable concentration range, and photon energy). These features are also important in the more complex densitometry measurements described in Sections 9.3 and 9.4.

Note that the above discussion deals with the measurement precision determined by counting statistics alone. Generally, other factors can cause added fluctuations in the measurement results; they include variations in the matrix material (solvent) and possible instrumental fluctuations. As a result, the precision of an assay instrument should be determined by making replicate measurements of known standards representing the full range of sample and solvent properties.

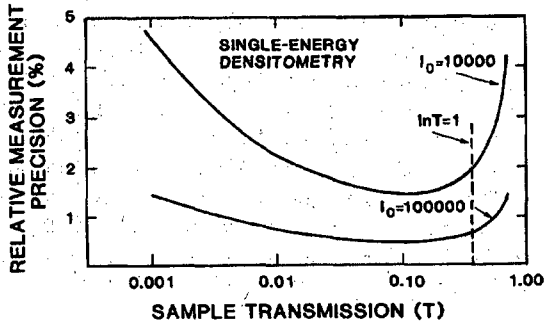

Fig. 9.2 *Precision of single-energy densitometry as a function of sample transmission for two values of incident photon total counts (from Equation 9-5). The optimum transmission is that which gives the smallest relative measurement precision. This corresponds to a concentration that is greater than the characteristic concentration, ρ_c, where $\ln T = 1$. (Note the logarithmic scale on the horizontal axis.)*

9.3 MULTIPLE-ENERGY DENSITOMETRY

Measurement of photon transmission at one energy allows for the assay of only one substance or of only one component of a mixture; the concentration of the other components must be kept constant. Measurement of photon transmission at two energies allows for the assay of two components of a mixture. Such a compound measurement stands the greatest chance for success the more the attenuation coefficients of the two components differ from one another. Analysis of the concentration of a high-Z element in a low-Z solvent is an excellent example of a two-energy densitometry measurement.

9.3.1 Analysis of Two-Energy Case

Consider a mixture of two components with (unknown) concentrations ρ_1 and ρ_2. Let the mass attenuation coefficient of component i measured at energy j be given by

$$\mu_i^j = \mu_i(E_j) \tag{9-6}$$

and define the transmission at energy j as

$$T_j = \exp\left[-\left(\mu_1^j\rho_1 + \mu_2^j\rho_2\right)x\right] . \tag{9-7}$$

The measurement of two transmissions gives two equations for the two unknown concentrations:

$$\begin{aligned}(-\ln T_1)/x = M_1 &= \mu_1^1\rho_1 + \mu_2^1\rho_2 \\ (-\ln T_2)/x = M_2 &= \mu_1^2\rho_1 + \mu_2^2\rho_2 .\end{aligned} \tag{9-8}$$

By attributing the measured absorption to the two sample components, we are actually defining the incident radiation to be the intensity transmitted by an empty sample container. The solution to the above equations is

$$\begin{aligned}\rho_1 &= (M_1\mu_2^2 - M_2\mu_2^1)/D \\ \rho_2 &= (M_2\mu_1^1 - M_1\mu_1^2)/D \\ D &= \mu_1^1\mu_2^2 - \mu_2^1\mu_1^2 .\end{aligned} \tag{9-9}$$

For Equation 9-8 to have a solution, the determinant of the coefficients, D, must be nonzero. This condition is virtually assured if the mass attenuation coefficients for the two components have significantly different energy dependences. Physically, this has the meaning that the assay is feasible if the components can be distinguished from one another by their absorption properties. This criterion further suggests two possible choices of photon energies. First, if two widely differing energies are used, the differ-

ent slopes of μ vs E for the high-Z and the low-Z components suffice to differentiate between them. Second, by choosing photon energies near and on either side of an absorption edge for the heavier (higher-Z) component, the energy dependence for the mass attenuation coefficient of the higher-Z material will appear to have the opposite slope to that of the low-Z component, making the two components easily distinguishable. This approach is especially promising in assays of SNM in low-density matrices or in assays of two SNM components.

9.3.2 Measurement Precision

The primary source of random measurement uncertainty is the statistical variance of the transmission measurements. The expression for the relative precision of each component's concentration is given by

$$\frac{\sigma(\rho_1)}{\rho_1} = \frac{1}{\mu_2^1 \ln T_2 - \mu_2^2 \ln T_1} \left\{ \left[\mu_2^2 \frac{\sigma(T_1)}{T_1}\right]^2 + \left[\mu_2^1 \frac{\sigma(T_2)}{T_2}\right]^2 \right\}^{1/2}$$

$$\frac{\sigma(\rho_2)}{\rho_2} = \frac{1}{\mu_1^2 \ln T_1 - \mu_1^1 \ln T_2} \left\{ \left[\mu_1^2 \frac{\sigma(T_1)}{T_1}\right]^2 + \left[\mu_1^1 \frac{\sigma(T_2)}{T_2}\right]^2 \right\}^{1/2} \quad (9\text{-}10)$$

Note that because the assay result varies inversely with the sample thickness (see Equation 9-8), the sample thickness (x) must be very well known or held constant within close tolerance.

9.3.3 Extension to More Energies

In principle, the multiple-energy densitometry technique can be extended to three or more energies to measure three or more sample components. In practice, such a broadening of the technique undermines the sensitivity of the measurement for some sample components, because it is extremely difficult to select gamma-ray energies that can sample different energy dependences of the absorption of each of the components. Accordingly, multiple-energy densitometry is rarely extended beyond the two-energy case.

9.4 ABSORPTION-EDGE DENSITOMETRY

Absorption-edge densitometry is a special application of two-energy densitometry. The photon energies at which the transmissions are measured are selected to be as near as possible to, and on opposite sides of, the absorption-edge discontinuity in the energy dependence of the mass attenuation coefficient for the unknown material (Ref. 1). Both the K and the L_{III} absorption edges have been used in nondestructive

assay of special nuclear material (see Section 9.7 for specific applications). Figure 9.3 shows the attenuation coefficients for plutonium, uranium, and selected low-Z materials and includes the K and L edges for the heavy elements.

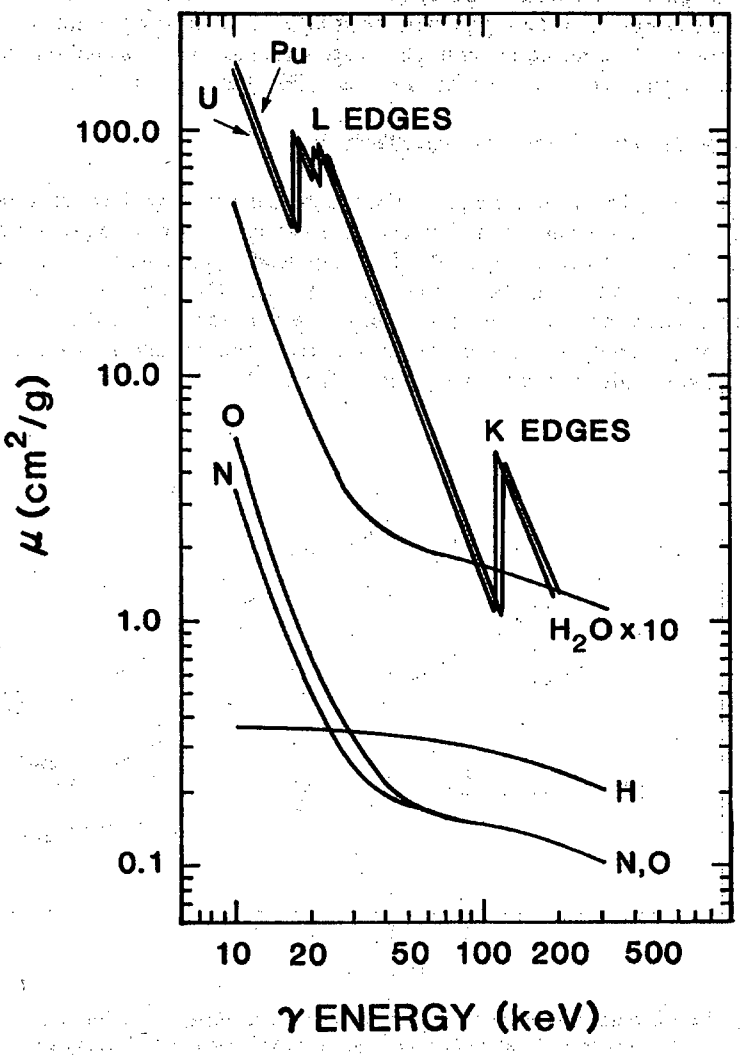

***Fig. 9.3** Energy dependence of the photon mass attenuation coefficients for uranium, plutonium, and selected low-Z materials. Note the absorption-edge discontinuities for uranium and plutonium in the 17- to 20-keV (L edge) and 115- to 122-keV (K edge) energy regions.*

Absorption-edge densitometry involves the measurement of the transmission of a tightly collimated photon beam through the sample material. The collimation defines the measurement geometry and also reduces interference from radiation emitted by the sample material. Because the collimation selects only a small fraction of the sample volume, the sample must be highly uniform for the assay to be representative of all of the material. As a result, the absorption-edge technique is best suited for solution assays, although it has been used for assays of solids (Refs. 2 through 4).

9.4.1 Description of Measurement Technique

Consider the typical case of a high-Z (SNM) component in a low-Z (solvent) matrix. Figure 9.4 depicts the attenuation coefficients and measurement energies above (U) and below (L) an absorption edge. (The discussion emphasizes K-edge measurements, but the analysis is similar in the L-edge region as well.) The subscript s refers to the measured element, and the subscripts M and m refer to the high- and low-Z matrix elements, respectively. The magnitudes of the attenuation coefficient discontinuities and the edge energies of interest are given in Table 9-1.

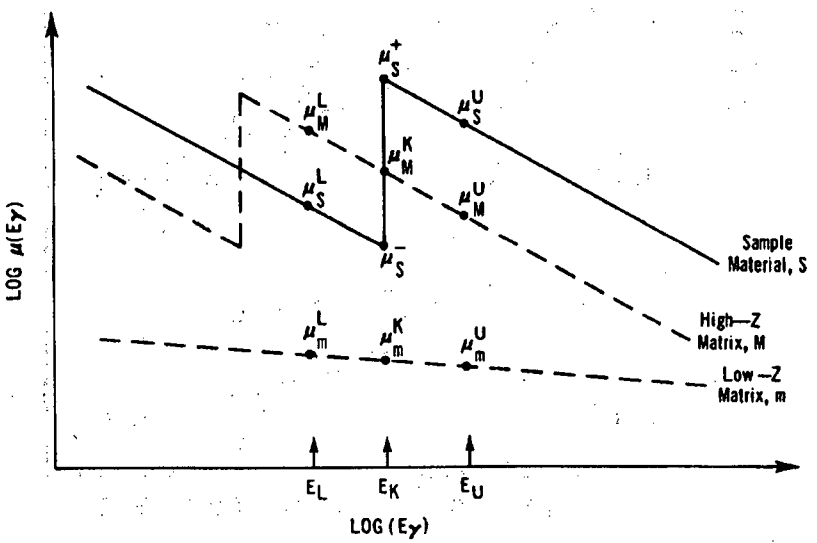

Fig. 9.4 Expanded schematic of the mass attenuation coefficient as a function of photon energy. Curves are shown for a sample material (s), assumed to be a heavy element, a heavy-element matrix component (M), and a light-element matrix component (m).

Table 9-1. Absorption-edge energies and discontinuities for selected SNM components

Property	Uranium	Plutonium
E(K)	115.6 keV	121.8 keV
$E(L_{III})$	17.2 keV	18.0 keV
$\Delta\mu$(K)	3.7 cm^2/g	3.4 cm^2/g
$\Delta\mu(L_{III})$	55.0 cm^2g	52.0 cm^2/g

Equation 9-11 gives the transmission of photons through the solution at the two measurement energies E_U and E_L.

$$\ln T_L = -(\mu_s^L \rho_s + \mu_m^L \rho_m)x$$
$$\ln T_U = -(\mu_s^U \rho_s + \mu_m^U \rho_m)x \; . \tag{9-11}$$

To solve for the measured element concentration,

$$\rho_s = \frac{1}{\Delta\mu x}\ln\left(\frac{T_L}{T_U}\right) + \rho_m\left(\frac{\Delta\mu_m}{\Delta\mu}\right) \tag{9-12}$$

where

$$\Delta\mu = \mu_s^U - \mu_s^L > 0$$
$$\Delta\mu_m = \mu_m^L - \mu_m^U > 0 \; . \tag{9-13}$$

The second term in Equation 9-12 expresses the contribution from the solvent matrix. Because the transmissions are measured relative to an empty sample container, the transmission of the sample container does not influence Equation 9-12. Note the similarity of Equation 9-12 to the single-line case (Equation 9-3), with μ's replaced by $\Delta\mu$'s.

Because the matrix term in Equation 9-12 is independent of SNM concentration and sample cell geometry, it can be applied to any absorption-edge densitometry measurement for which the solution transmissions are measured relative to an empty sample container. Ideally, if $E_L = E_U = E_K$, then $\Delta\mu_m = 0$, and the measurement is completely insensitive to any effects from the matrix. In practice, however, the two measurement energies differ by a finite amount, so some residual matrix correction may be necessary. In cases where the matrix contribution may be significant, it can be determined empirically by assaying a solution that contains only the matrix material or its effect can be deduced analytically. For further discussion of matrix corrections for absorption-edge densitometry, see Section 9.4.4.

The ratio of the two transmissions at the two measurement energies ($R = T_L/T_U$) is the measured quantity, and $\Delta\mu$ and x are constants that can be evaluated from

transmission measurements with calibrated standards of well-defined concentrations. With judiciously chosen photon energies, this technique will provide very reliable, nearly matrix-independent assays of specific elements whose absorption edges lie between the transmission source energies.

9.4.2 Measurement Precision

Differentiation of Equation 9-12 gives the relative precision of a densitometry measurement:

$$\frac{\sigma(\rho_s)}{\rho_s} = \left(\frac{1}{\Delta\mu\rho_s x}\right)\left[\frac{\sigma(R)}{R}\right] = \left(\frac{1}{\ln R}\right)\left[\frac{\sigma(R)}{R}\right] . \qquad (9\text{-}14)$$

The fractional error in R is determined by the counting statistics of the transmission measurements. In analogy with the discussion of Equation 9-4, the choice of measurement parameters can be guided by reference to a characteristic concentration, $\rho_c = 1/\Delta\mu x$. When $\rho > \rho_c$, the measurement is in the favorable precision regime, where $\sigma(\rho)/\rho < \sigma(R)/R$. But if the SNM concentration is too far above ρ_c, the excessive absorption deteriorates the measurement precision, primarily because of the enhanced absorption of the transmission gamma rays above the absorption edge. The statistical fluctuations of the very small transmitted intensity at E_U is then overpowered by the statistical fluctuations of the background in that energy region.

Table 9-2 shows the values of these characteristic concentrations for a 1-cm transmission path length (x = 1 cm). The table implies, for example, that for a 1-cm sample cell thickness, K-edge assays of plutonium concentrations greater than 300 g/L would be in the favorable precision regime. For assays of 30-g/L solutions, the sample cell thickness should be greater than 0.5 cm for L_{III}-edge assays and greater than 9 cm for K-edge assays.

Table 9-2. Characteristic concentrations for uranium and plutonium

Characteristic Concentration	Uranium (g/L)	Plutonium (g/L)
$\rho_c(K)$	270	294
$\rho_c(L_{III})$	18	19

A more analytical approach can be used to optimize measurement parameters. Figure 9.5 shows the calculated statistical measurement precision (Equation 9-14) as a function of transmission path length (x) for a variety of SNM concentrations. The figure shows, for example, that a densitometer designed for 30-g/L SNM solution assays should have a sample cell thickness of 7 to 10 cm.

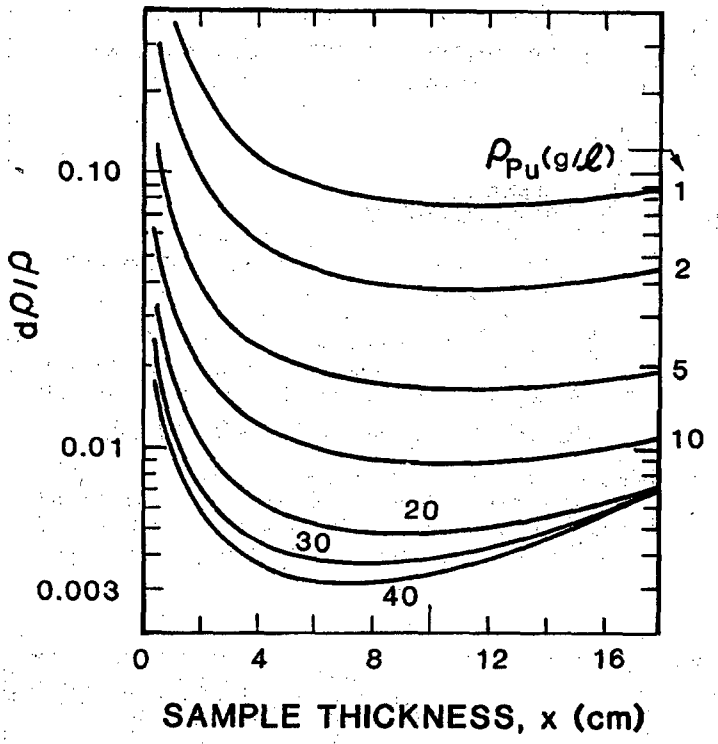

***Fig. 9.5** Calculated relative statistical uncertainty in plutonium concentration by K-edge densitometry as a function of sample cell thickness (transmission path length). The empty cell transmission counts below the K edge (I_{0L}) were taken to be 2 × 10^6 in the 121.1-keV photopeak.*

The final test in evaluating the design of a densitometer is empirical determination of the assay precision. Figure 9.6 shows the precision of a series of measurements on a K-edge densitometer designed for low- to medium-concentration plutonium solution assays with a 7-cm-thick sample cell (Ref. 5). Figure 9.6 agrees well with the theoretical curve shown in Figure 9.5.

Calculations of measurement precision are helpful in determining design parameters for optimum instrument performance. Figure 9.7 shows the results of such calculations for both K- and L_{III}-edge densitometers (Ref. 6). The ranges of plutonium concentrations over which the relative measurement precision is better than 1% are shown for different sample thicknesses (x).

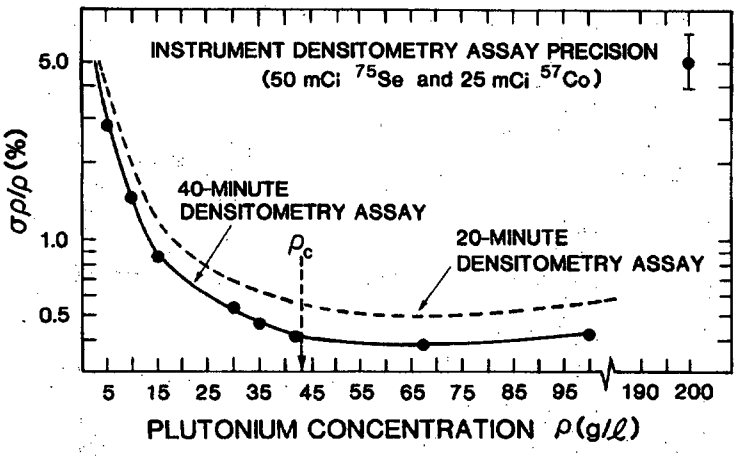

Fig. 9.6 Relative statistical precision achieved in a plutonium concentration measurement by K-edge densitometry as a function of sample concentration, for a sample cell thickness of 7 cm. Note the broken scale above 100 g/L. Curves are shown for two count times (Ref. 5).

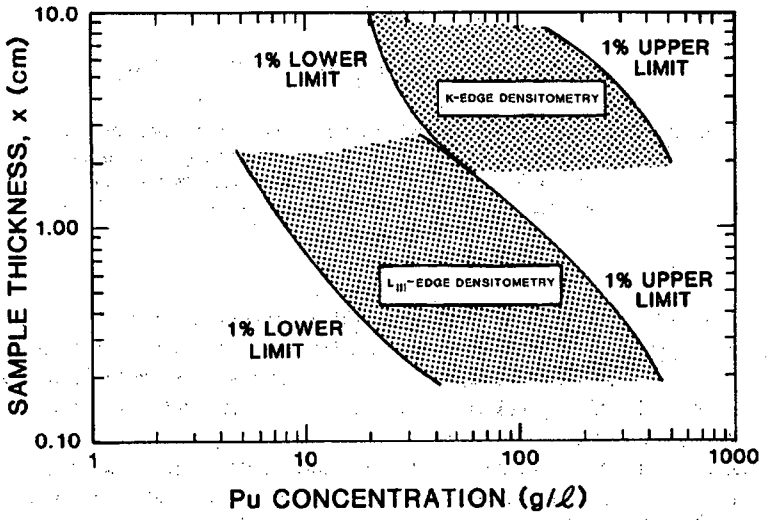

Fig. 9.7 Indications of sample transmission thicknesses (x) over which plutonium concentration assays can be performed by absorption-edge densitometry to better than 1% statistical precision. Shaded regions for the K- and L_{III}-edge techniques show plutonium concentration ranges over which this precision is achievable.

9.4.3 Measurement Sensitivity

A useful parameter in the specification of a nondestructive assay instrument is its "minimum detectable limit," which is that quantity of nuclear material that produces an assay signal significantly above background in a reasonable count time (Refs. 7 and 8). For nuclear waste measurements, where the minimum detectable limit is an important instrument specification, an assay signal that is three standard deviations (99% confidence level) (Ref. 9) above background is considered to be significant. This limit can also be regarded as a measurement sensitivity, in that it characterizes a lower limit of SNM that can be detected with some level of confidence.

Because absorption-edge densitometers are usually built for specific assay applications in well-defined SNM solution concentration ranges, the minimum detectable limit is not particularly important. However, the measurement sensitivity can serve as a convenient quantity for comparing design approaches and other factors that influence instrument performance.

To obtain an expression for the measurement sensitivity of an absorption-edge densitometer, the assay background must be defined so that the minimum detectable assay signal can be determined. The statistical uncertainty in the measured density is given in Equation 9-14. The ratio R of the two transmissions above and below the absorption edge is composed of raw gamma-ray (or x-ray) photon intensities that vary according to the usual statistical prescriptions. When the SNM concentration is zero, the solution is entirely matrix material (typically acid) and

$$T_U \approx T_L = T = \exp(-\mu_m \rho_m x) \, . \tag{9-15}$$

When the the SNM concentration is zero, R = 1. Then the definition of T gives

$$\sigma(\rho) = \frac{1}{\Delta\mu x}\left(\frac{1}{I_{0U}} + \frac{1}{I_{0L}} + \frac{1}{TI_{0U}} + \frac{1}{TI_{0L}}\right)^{1/2} . \tag{9-16}$$

Equation 9-16 expresses the uncertainty in the background. The three-sigma criterion provides an expression for the minimum detectable limit (or sensitivity, s) for an absorption-edge densitometer:

$$s = \frac{3}{\Delta\mu x}\left[\left(\frac{1}{I_{0U}} + \frac{1}{I_{0L}}\right)\left(\frac{T+1}{T}\right)\right]^{1/2} \quad (g/L) \tag{9-17}$$

where the units of $\Delta\mu x$ are cm^3/g.

Equation 9-17 shows that the measurement sensitivity is affected by several measurement parameters:

- The sensitivity suffers in low-transmission samples.
- Long counts of the unattenuated photon intensities (I_0) improve measurement sensitivity.

- L-edge measurements (with their larger $\Delta\mu$ are more sensitive than K-edge measurements (if all other measurement parameters remain the same).
- An increase in sample cell thickness may improve the measurement sensitivity, but the accompanying decrease in T will compete with that improvement.

9.4.4 Matrix Effects

The absorption-edge technique is insensitive to the effects of matrix materials if both transmissions are measured at the absorption edge. However, with a finite energy separation of the transmission gamma rays, the matrix contribution is nonzero and is represented by the second term in Equation 9-12. This term can become significant for low SNM concentrations, ρ_s, or when the spacing between the assay energies, E_L and E_U, becomes large; either condition threatens the validity of the inequality $\Delta\mu_m\rho_m \ll \Delta\mu\rho_s$.

The natural width of the absorption edge (less than 130 eV) and the energy resolution of the detection system (typically 500 eV or more) are intrinsic limitations to the design of an instrument that attempts to minimize the effects of matrix attenuation by using closely spaced assay energies. The limited availability of useful, naturally occurring radioisotopes also leads to compromises in the choice of transmission sources.

One very useful technique for reducing the matrix effect is an extrapolation procedure applied to the measured transmission data (Refs. 2 and 5). The procedure attempts to extrapolate the measured transmissions to the energy of the absorption edge. This extrapolation is possible because the energy dependence of the mass attenuation coefficients over narrow energy ranges is known to be a power law:

$$\log \mu(E) = k \log E + B \,. \tag{9-18}$$

The slope parameter (k) is essentially the same for elements with $Z > 50$, with an average value of approximately -2.55 near the uranium and plutonium K edges (Ref. 2). Table 9-3 gives the extracted values for the slopes and intercepts of several substances of interest to SNM assay (Ref. 10).

As an example of a general assay case, consider a solution of SNM in a low-Z solvent, with possible additional heavy-element ($Z > 50$) matrix contaminants. Equation 9-12 generalizes to

$$\rho_s = \left(\frac{1}{\Delta\mu x}\right)\ln\left(\frac{T_L}{T_U}\right) + \rho_M\left(\frac{\Delta\mu_M}{\Delta\mu}\right) + \rho_m\left(\frac{\Delta\mu_m}{\Delta\mu}\right) . \tag{9-19}$$

The subscript M refers to the high-Z matrix contaminant, and the subscript m represents the low-Z matrix (solvent); and in analogy with Equation 9-13, $\Delta\mu_M = \mu_M^L - \mu_M^U$ (see Figure 9.4). The measured transmissions are then extrapolated to the SNM K edge using the energy dependence of $\mu(E)$ for the heavy elements. Because the slope parameters (k) for $Z > 50$ are all essentially the same, the SNM and high-Z

Table 9-3. Slopes (k) and intercepts (B) for the linear dependence of log μ(E) vs log E for various materials of interest in the 100- to 150-keV energy region (log to base 10)[a]

Solution Component	k	B
Plutonium (above K edge)	−2.48	5.83
(below K edge)	−2.56	5.42
Uranium (above K edge)	−2.49	5.82
(below K edge)	−2.71	5.65
Tungsten	−2.50	5.65
Tin	−2.45	5.12
Iron	−1.57	2.70
Aluminum	−0.500	0.227
Water	−0.306	−0.153
Nitric Acid	−0.314	−0.171

[a]Ref. 10.

matrix absorption coefficients can be transformed with the same k (for example, the average value, −2.55). As a result, the transformed $\Delta\mu_M$ vanishes and the assay result becomes

$$\rho_s = \left(\frac{1}{\Delta\mu_{\pm}\mathrm{x}}\right)\ln\left(\frac{\mathrm{T}_L^a}{\mathrm{T}_U^b}\right) + \left(\frac{\mathrm{c}\mu_m^K\rho_m}{\Delta\mu_{\pm}}\right) \tag{9-20}$$

where $\Delta\mu_{\pm}$ (which equals $\mu_s^+ - \mu_s^-$, see Figure 9.4) is now defined across the absorption edge (in this case, the K edge) rather than between the energies E_L and E_U. The constants a, b, and c are defined as

$$\mathrm{a} = (\mathrm{E}_K/\mathrm{E}_L)^k$$

$$\mathrm{b} = (\mathrm{E}_K/\mathrm{E}_U)^k$$

$$\mathrm{c} = (\mathrm{E}_K/\mathrm{E}_L)^{k-k'} - (\mathrm{E}_K/\mathrm{E}_U)^{k-k'} \tag{9-21}$$

where k = −2.55 and k′ = −0.33 (the average value of k for elements with atomic numbers less than 10). This procedure renders the assay essentially independent of the heavy-element matrix but still leaves a residual correction for the light-element matrix. It is not possible to remove the effects of both the light- and heavy-element matrix materials because $k \neq k'$. The transmissions must be corrected for the acid matrix contributions because the transmissions are measured relative to an empty sample cell. If the reference spectra (the I_0 intensities) were taken with the cell full of a representative acid solution, no acid matrix correction would be necessary. However,

any fluctuation in acid molarity would bias the measurement of an actual sample. The density of nitric acid (ρ_m) and the acid molarity (M) are related (Ref. 11) by

$$\rho_m = 1 + 0.03\ \mathrm{M}\ . \tag{9-22}$$

For plutonium K-edge assays in which the K edge is closely bracketed by ^{57}Co and ^{75}Se gamma rays (see Section 9.4.6), this low-Z matrix correction is small but may be important at low plutonium concentrations. For example, the correction term in Equation 9-20 for 3 M nitric acid is equivalent to approximately 0.87 g Pu/L (Ref. 5). Equation 9-22 shows that fluctuations in acid molarity cause fluctuations in the acid matrix correction that are only 3% as large; so careful control of the acid molarity is important only at very low SNM concentrations.

For uranium K-edge assays with a ^{169}Yb transmission source (E_L = 109.8 keV, E_U = 130.5 keV), the extrapolation procedure greatly improves the quality of the assay results. This is demonstrated graphically in Ref. 2, where assays of uranium solutions with varying tin concentrations were shown to be matrix-independent with the extrapolation correction. Several other matrix effects studies are described in Ref. 12.

9.4.5 Choice of Measurement Technique

Because of differences in the $\Delta\mu$ values at the K edge versus the L_{III} edge, the measurement sensitivity (defined in Equation 9-17) is more than an order of magnitude larger at the L_{III} edge than at the K edge, other parameters being equal (see also Table 9-1). However, because of the higher penetrability of photons at the K-edge energies, thicker samples can be used for the K-edge measurements, thereby enhancing K-edge sensitivity.

If significant quantities of lower-Z elements (such as yttrium and zirconium) are present in a sample, the K edges of these elements cause discrete interferences that bias the L_{III} assays of uranium and plutonium (Ref. 12). Furthermore, detector resolution at L_{III} energies limits the ability to perform L_{III}-edge assays in the presence of significant amounts of neighboring elements (uranium with protactinium or neptunium; plutonium with neptunium or americium). The K-edge measurements are not subject to such interferences. In addition, the higher photon energies required for the K-edge transmission measurements permit the use of thicker or higher-Z materials for sample-cell windows, an important practical consideration for in-plant operation. Finally, more flexibility exists in the availability of discrete-gamma-ray transmission sources for K-edge measurements.

9.4.6 Transmission Sources

The most versatile transmission source is the bremsstrahlung continuum produced by an x-ray generator. The intensity of this source can be varied to optimize the count rate for a variety of sample geometries, concentrations, and thicknesses.

The x-ray generator voltage (which determines the assay energy range) can be adjusted and the spectrum tailored appropriately for the assay of specific elements. Furthermore, matrix effects can be minimized by extrapolation of the measured transmissions to the absorption edge. Commercial units are available with power supplies that are highly stable and x-ray tubes that are long-lived for long-term reliable operation in either the K- or the L_{III}-edge energy regions.

The use of discrete gamma-ray lines that bracket the absorption edge, the alternative to the continuum transmission sources, has been demonstrated successfully in several instruments. This technique is appropriate for K-edge assays. Discrete gamma rays are not available as primary emissions in the L_{III}-edge energy region. This approach depends on the availability of relatively slowly decaying radioisotopes that emit gamma rays of appropriate energies and sufficient intensities. For example, a convenient combination for the K-edge assay of plutonium (E_K = 121.8 keV) is the 121.1-keV gamma ray from ^{75}Se (half-life = 120 days) and the 122.1-keV gamma ray from ^{57}Co (half-life = 270 days). The proximity of both energies to the plutonium absorption edge minimizes the effects of the matrix and enhances the sensitivity of the assay (Ref. 1). Because of the different half-lives, accurate decay corrections or frequent measurements of the unattenuated intensities (I_0) are required. The use of ^{169}Yb (half-life = 32 days) for uranium assay at the K edge (Refs. 2 and 3) has the advantage of requiring no decay correction because both gamma rays come from the same source. However, the larger energy separation (E_L = 109.8 keV, E_K = 115.6 keV, E_U = 130.5 keV) introduces a larger matrix sensitivity (larger $\Delta\mu_m$) and a smaller assay sensitivity (smaller $\Delta\mu$). Furthermore, to maintain acceptable counting statistics, the source must be replaced frequently because of the short half-life of ^{169}Yb. The extrapolation technique discussed in Section 9.4.4 is especially effective in reducing the matrix sensitivity. A detailed discussion of convenient radioisotopic sources for absorption-edge densitometry appears in Ref. 1. Several variations on these two basic transmission source configurations are discussed in Ref. 12.

9.5 SINGLE-LINE DENSITOMETERS

The measurement of photon transmission at a single energy has been applied using low-resolution detectors for assay of SNM in solution and in reactor fuel elements. These instruments use low-energy gamma-ray transmission sources to minimize the ratio μ_0/μ (see Equation 9-3) and thus reduce the sensitivity to variations in the low-Z matrix.

One instrument uses an ^{241}Am transmission source mounted in the center of an annular cell containing SNM solution (Refs. 13 and 14). The cell is surrounded by a 4π plastic scintillator. The instrument separates the transmitted 60-keV gamma ray from the background sample radiation by modulating the source with a rotating, slotted tungsten shield. Designed to assay high concentrations (>200 g/L) of SNM, the instrument is sensitive to 1% changes in SNM concentration at the 95% confidence level.

A single-line densitometer has been used to determine the density of SNM in pelleted and compacted ceramic fuel elements (Ref. 15). The 67- and 76-keV gamma rays of ^{171}Tm and the 84-keV gamma ray of ^{170}Tm are detected by a 1-in.-diam NaI(Tl) detector. The gross detector signals are counted in the multichannel scaling mode as the fuel elements are scanned to give the SNM density profile. The sensitivity of the instrument to SNM is 0.2 g/cm^3 at the 95% confidence level.

9.6 DUAL-LINE DENSITOMETERS

Dual-line densitometry has application to solids (fuel elements) and to solutions. Low- and high-resolution gamma spectrometers have been used and have been applied to the assay of a low- and high-Z component, as well as to the assay of two high-Z components.

A dual-line densitometer has been used to determine the densities of the low-Z (silicon and carbon) and high-Z (thorium and uranium) components in high-temperature gas-cooled reactor (HTGR) fuel pellets (Refs. 16 and 17). The transmission source provides two widely differing gamma-ray energies (122 keV from ^{57}Co and 1173 and 1332 keV from ^{60}Co), so that the sensitivity to the two components is based on the different slopes of μ vs E at low and high Z's. Equation 9-9 applies in this case. Fuel pellet cakes containing 92 to 95% thorium and 5 to 8% ^{238}U with a low-Z to heavy-Z weight ratio of 1.6 to 2.4 were assayed in 2-min measurement periods. The sensitivity to changes in the weight of either component was 3% or better at the 95% confidence level.

Dual-line solution densitometry has also been applied to the assay of two SNM components by measuring transmissions at two low gamma-ray energies (Refs. 18 and 19). The transmission energies were chosen to bracket the L-absorption edges of the higher-Z component (element 2) in such a way that, in Equation 9-8, $\mu_2^1 = \mu_2^2$ and $\mu_1^1 > \mu_1^2$. Thus, Equation 9-8 can be solved to give the concentration of element 1, independent of element 2:

$$\rho_1 = \left(\frac{1}{\Delta\mu_1 x}\right)\ln\left(\frac{T_1}{T_2}\right) \tag{9-23}$$

where $\Delta\mu_1 = \mu_1^2 - \mu_1^1$. The measured T_2 and ρ_1 are then used to obtain the concentration of element 2:

$$\rho_2 = \left(\frac{\ln T_2}{\mu_2^2}\right) - \frac{\rho_1\mu_1^2}{\mu_2^2} \tag{9-24}$$

Dual-line densitometry has been applied to thorium and uranium assay using secondary sources of niobium and iodine K_α x rays (at 16.6 and 28.5 keV, respectively) fluoresced by a 100-mCi ^{241}Am source. These x-rays bracket the L edges of uranium.

However, 16.6 keV is just above the L_{III} absorption edge of thorium (at 16.3 keV). Measurements were performed using low-resolution (Ref. 18) and high-resolution (Ref. 19) gamma-ray spectroscopy. The high-resolution experiments used reference solutions containing mixtures of thorium and uranium with total SNM concentrations between 35 and 70 g/L. In the range $0.25 \leq \rho_{Th}/\rho_U \leq 4.0$, the precision of the thorium and uranium concentration assay was 1% or better for 4000-s count periods.

9.7 ABSORPTION-EDGE DENSITOMETERS

Assay of uranium and plutonium solutions by the absorption-edge densitometry technique has been demonstrated in field tests of several instruments that perform K-edge or L_{III}-edge measurements. The instruments were designed for solution scrap recovery or reprocessing applications. Each instrument uses a high-resolution gamma-ray spectrometer (typically HPGe for K-edge assays and Si(Li) for L_{III}-edge assays) and a computer-based multichannel analyzer. The measurement precision achieved in each case approaches the statistical prediction, which is typically 0.5% or better for short ($\leq$30-min) count periods.

The transmission sources used by the K-edge instruments are discrete gamma-ray sources or bremsstrahlung continuum (x-ray) sources. The 109.8- and 130.5-keV gamma rays of ^{169}Yb are used for discrete K-edge assays of uranium, and the 121.1- and 122.1-keV gamma rays of ^{75}Se and ^{57}Co are used for discrete K-edge assays of plutonium. Only x-ray generators have been used in the L_{III}-edge instruments.

The absorption-edge assay relies on Equation 9-12. The assay precision (Equation 9-14) depends on several variables, including $\Delta\mu$, x, solution concentration, count time, and incident beam intensity. It is therefore convenient in comparing various instruments to use the characteristic concentration parameter $[\rho_c = (1/\Delta\mu x)]$ for each instrument. The instrument relative precision is defined as the precision measured at the optimum concentration for a fixed count period. This optimum concentration is that for which the relative precision $[\sigma(\rho)/\rho]$ is a minimum (see Figures 9.5 and 9.6).

Tables 9-4 and 9-5 list the K-edge and L_{III}-edge densitometers that have undergone field testing. The characteristic concentration (ρ_c) and the empirically determined optimum concentration (shown in parentheses beneath ρ_c) are given for each instrument. The tables specify the solutions used to obtain the data and quote the measured precisions at the optimum concentrations in specified count periods. Detailed discussions of the instruments listed in Tables 9-4 and 9-5 are given in Sections 9.7.1 and 9.7.2.

9.7.1 K-Absorption-Edge Densitometers

Given below are descriptions of several K-edge densitometers that have been tested and evaluated under actual or simulated in-plant environments. Table 9-4 summarizes the performance data for the instruments.

Table 9-4. K-absorption-edge densitometers.

Instrument Test Location	ρ_c $\rho_{optimum}$ (g/L)	SNM	Solution Type	Precision 1σ (%)	Live Time (s)	References
1. Los Alamos	135 (300)	U	HEU SR[a], misc.	0.5	1000	12,20,21
2. Oak Ridge Y-12	55 (100)	U	HEU SR, misc.	0.5	600	22,23
3. Barnwell AGNS	80 (200)	Pu	prepared (fresh, aged)	0.2	1200	12,24,25
4. Tokai (Japan) PNC	150 (300)	Pu	RP[b] product (fresh, aged)	0.2	2000	12,26,27,28
5. Savannah River SRP	40 (60)	Pu	RP product (fresh)	0.2	2000	5,12,29
6. Seibersdorf (Austria) IAEA (portable)	150 (300)	Pu	prepared	0.3	500	30
7. Karlsruhe (FRG) KfK (continuum source)	150 (300)	U	prepared	0.2	1000	12,31,32
		Pu	RP product	0.2	1000	33
		U(+Pu)	[RP feed U:Pu::3:1]	0.2	1000	
		Pu(+U)		1.0	1000	

[a]SR = Scrap Recovery.
[b]RP = Reprocessing Plant.

Table 9-5. L_{III}-absorption-edge densitometers.

Instrument Test Location	ρ_c optimum (g/L)	SNM	Solution Type	Precision 1σ (%)	Live Time (s)	References
1. Savannah River SRL	16 (50)	U or Pu U (+Pu) Pu (+U)	RP[a] product [RP product U:Pu::2:1]	0.3 0.2 1.0	1000 2000 2000	12,21,34
2. Argonne NBL	16 (50)	U or Pu U (+Pu) Pu (+U)	prepared [prepared U:Pu::2:1]	0.3 0.2 0.9	1000 2000 2000	35
3. Barnwell AGNS	19 (55)	U	U, natural enrichment (flowing)	0.7	250	36
4. Los Alamos (Compact)	16 (60)	U	U, natural enrichment	0.2	1000	37

[a]RP = Reprocessing Plant.

1. Los Alamos National Laboratory (Refs. 12, 20, and 21). The Los Alamos uranium solution assay system (USAS) is a hybrid assay instrument used off-line at the Los Alamos high-enriched uranium (HEU) scrap recovery facility. The USAS measurement head is shown in Figures 9.8 and 9.9.

The USAS applies three distinct gamma-ray methods to assay uranium concentration in 20- or 50-mL uranium solution samples (in disposable plastic sample vials) in three concentration ranges. Waste solutions with uranium concentrations in the range 0.001 to 0.5 g/L are counted for 2000 s with no transmission correction. Process solutions with concentrations in the range 1 to 50 g/L are measured using a ^{169}Yb transmission source. The highest range, 50 to 400 g/L, corresponding to product solutions, is assayed by the K-edge method using a ^{169}Yb transmission source. Accuracies of 0.7-1.5% can be achieved in measurement times of 400-2000 s.

The assay results are used for process control and nuclear material accounting. The instrument was in routine use in the scrap recovery facility from January 1976 until August 1984 when the facility was closed.

2. Oak Ridge Y-12 Plant (Refs. 22 and 23). The HEU scrap recovery facility at the Oak Ridge Y-12 Plant uses a solution assay system (SAS) that is analogous to the USAS. The K-edge method is used to assay 50-mL uranium solution samples in the concentration range 50 to 200 g/L. The samples include but are not limited to the product. The SAS uses a ^{169}Yb transmission source and disposable plastic sample vials.

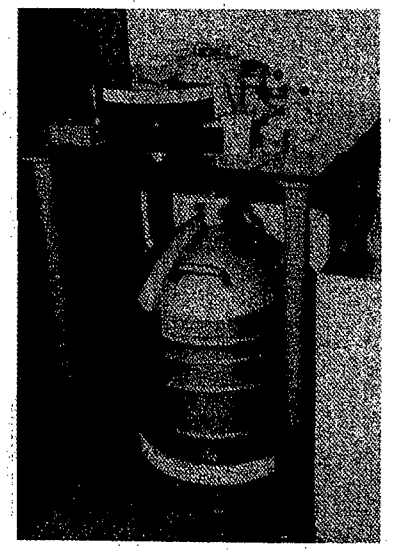

Fig. 9.8 The USAS measurement head.

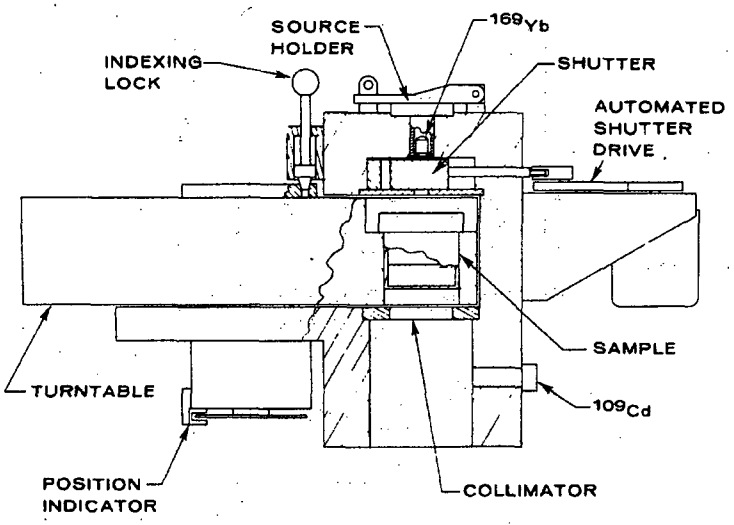

Fig. 9.9 Scale line drawing of the USAS measurement head. The solution thickness in the transmission path is 2 cm.

The system was put into routine use at Y-12 in October 1981 for process control and materials accounting.

3. Allied General Nuclear Services (AGNS) (Refs. 12, 24, and 25). A discrete-source K-edge densitometer was evaluated for plutonium assay at the Allied General Nuclear Services facility in Barnwell, South Carolina, during 1977-78. The hybrid instrument performed passive and K-edge measurements on prepared 10-mL solution samples of typical light-water-reactor plutonium in a fixed quartz sample cell. The transmission source was a combination of ^{75}Se and ^{57}Co. The results were reported for cells of different transmission path lengths.

4. Power Reactor and Nuclear Fuel Development Corporation (PNC) (Refs. 12 and 26 through 28). A discrete-source K-edge densitometer operates in the Tokai-Mura Reprocessing Plant analytical laboratory of the Power Reactor and Nuclear Fuel Development Corporation in Japan. Freshly separated and aged plutonium solution samples of the products of boiling-water-reactor and pressurized-water-reactor fuel reprocessing are assayed by the K-edge method in a two-cycle assay (first with a ^{75}Se transmission source, then with ^{57}Co). Figure 9.10 shows the location of the measurement station under the glove box at the Tokai-Mura plant laboratory. Figure 9.11 is a scale line drawing of the measurement head, which includes a well extending down from the glove-box floor. The instrument performs an isotopics assay on the fresh solutions in a third cycle. The solution samples are assayed in a well that is an

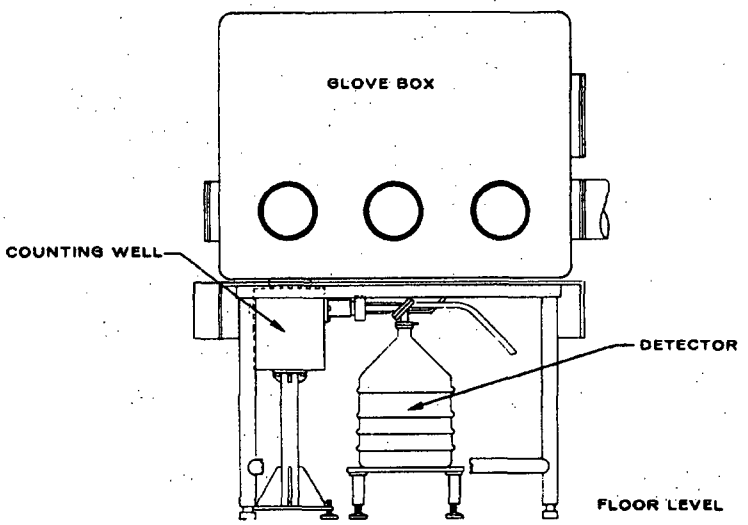

Fig. 9.10 The Tokai K-edge densitometer measurement station beneath the laboratory glove box.

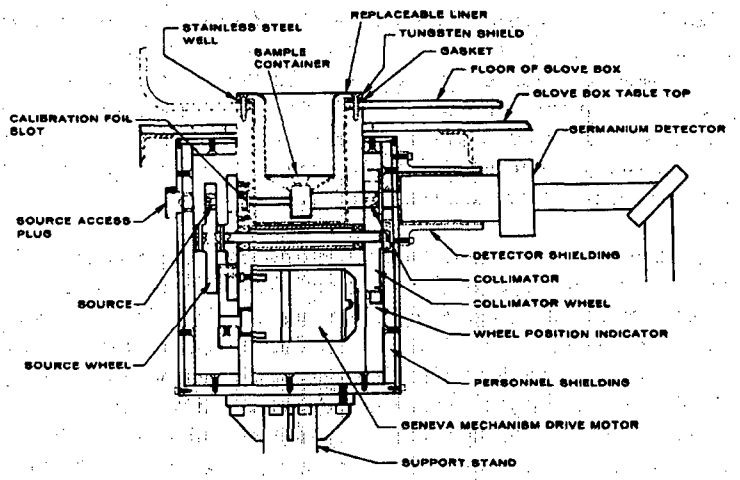

Fig. 9.11 Scale line drawing of the Tokai K-edge densitometer measurement head. The solution thickness in the transmission path is 2 cm.

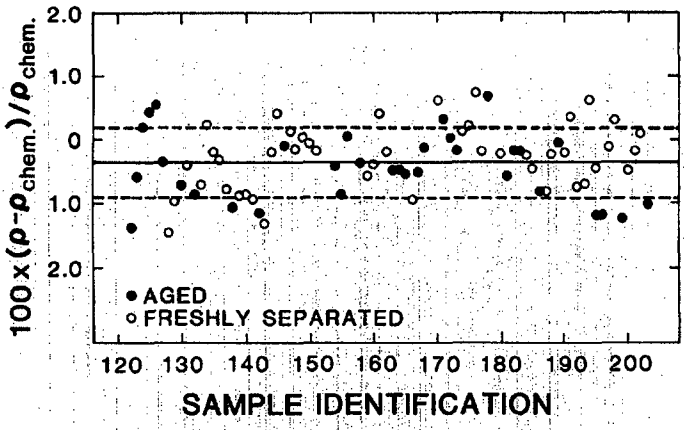

Fig. 9.12 Percent difference between 600-s K-edge and destructive assays for plutonium concentration, plotted as a function of sample identification number. The solid line is the average relative result of −0.36%. This apparent bias is the result of calibration (in 1979) using only a small number of reference samples (see Ref. 27).

extension of a glove box. The gamma-ray detector and the transmission sources are external to the glove box. The sample cells are disposable plastic vials that require approximately 10 mL of solution.

The Tokai instrument was installed in November 1979 and was operated through 1980 in an evaluation mode. The instrument has been in routine use in the facility since early 1981. Figure 9.12 is a plot of the percent difference between K-edge assay results and the reference values (from destructive analysis) obtained throughout 1981 during routine facility use of the instrument (Ref. 28). The densitometer has been available for facility use by IAEA inspectors since 1982.

5. Savannah River Plant (SRP) (Refs. 5, 12, and 29). A discrete-source K-edge plutonium solution densitometer was designed for in-line testing at the Savannah River Plant. A flow-through stainless steel sample cell was plumbed into a bypass loop on process solution storage tanks and resided in a protrusion of the process containment cabinet. The detector and transmission sources were located outside the containment cabinet on either side of the protrusion for measurement of the gamma-ray transmissions through the solution-filled cell. Figure 9.13 is a detailed illustration of the measurement station for this densitometer. Figure 9.14 illustrates the installation of the instrument in the process plumbing. The measurements were performed on

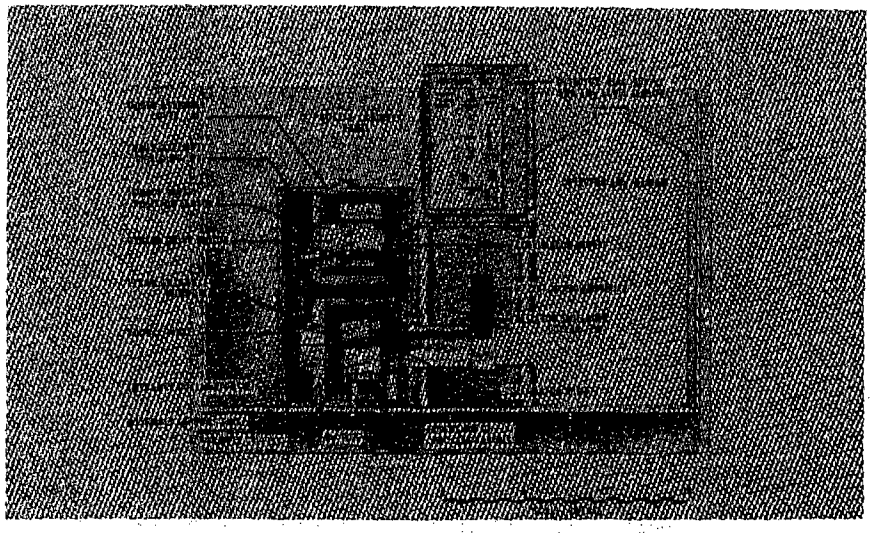

Fig. 9.13 The measurement station for the SRP in-line plutonium solution densitometer. The source positioning mechanism and collimator wheels (shown at the left) straddle the process cabinet extension so that the sample cell (inside the process cabinet containment) is between the transmission sources and the detector, in a standard transmission-measurement geometry. The sample cell thickness is 7 cm.

approximately 100 mL of static solution, after circulation of the tank solution through the bypass loop. (The freshly separated plutonium in the solutions is produced during reprocessing of low-burnup fuel.) The K-edge transmission measurements were performed in two cycles, as with the Tokai instrument, and a third cycle determined the plutonium isotopic composition. The instrument was also used to investigate the measurement of plutonium concentration in the presence of uranium admixtures. The extrapolation procedure described in Section 9.4.4 was used on solutions with uranium-to-plutonium ratios greater than 2:1 (see Ref. 5). The off-line testing of the instrument took place at the plant from April 1980 until December 1981. Figure 9.6 (see Section 9.4.2) is a plot of the measurement precision versus concentration (over the range 5 to 200 g/L) obtained in this testing phase (Ref. 5). The in-line testing began in December 1982 and ended in June 1983.

Fig. 9.14 *In-line installation of the SRP plutonium solution densitometer. A by-pass plumbing loop brings plutonium-bearing solution from one of the holding tanks to the measurement cell. Provision is made for draining the cell into an intermediate reservoir so that samples of material just assayed can be removed for off-line verification by destructive analysis.*

6. International Atomic Energy Agency (IAEA) Safeguards Analytical Laboratory (Ref. 30). A portable K-edge densitometer has been designed for testing as an inspection tool to authenticate the concentrations of plutonium samples inside glove boxes. The densitometer consists of hardware to hold and shield the detector and transmission sources and a portable multichannel analyzer equipped with electronics for the analog signal processing. The hardware slides inside the glove of the glove box so that a plutonium solution sample in a disposable plastic vial can be mounted and clamped in a holder between the detector and transmission source for the two-cycle K-edge assay. Figures 9.15 and 9.16 show the measurement head of the portable K-edge instrument inserted in a glove-box glove.

The portable densitometer has been tested at the IAEA's Safeguards Analytical Laboratory in Seibersdorf, Austria, since November 1983. A second unit is scheduled for field testing by IAEA inspectors in Japan.

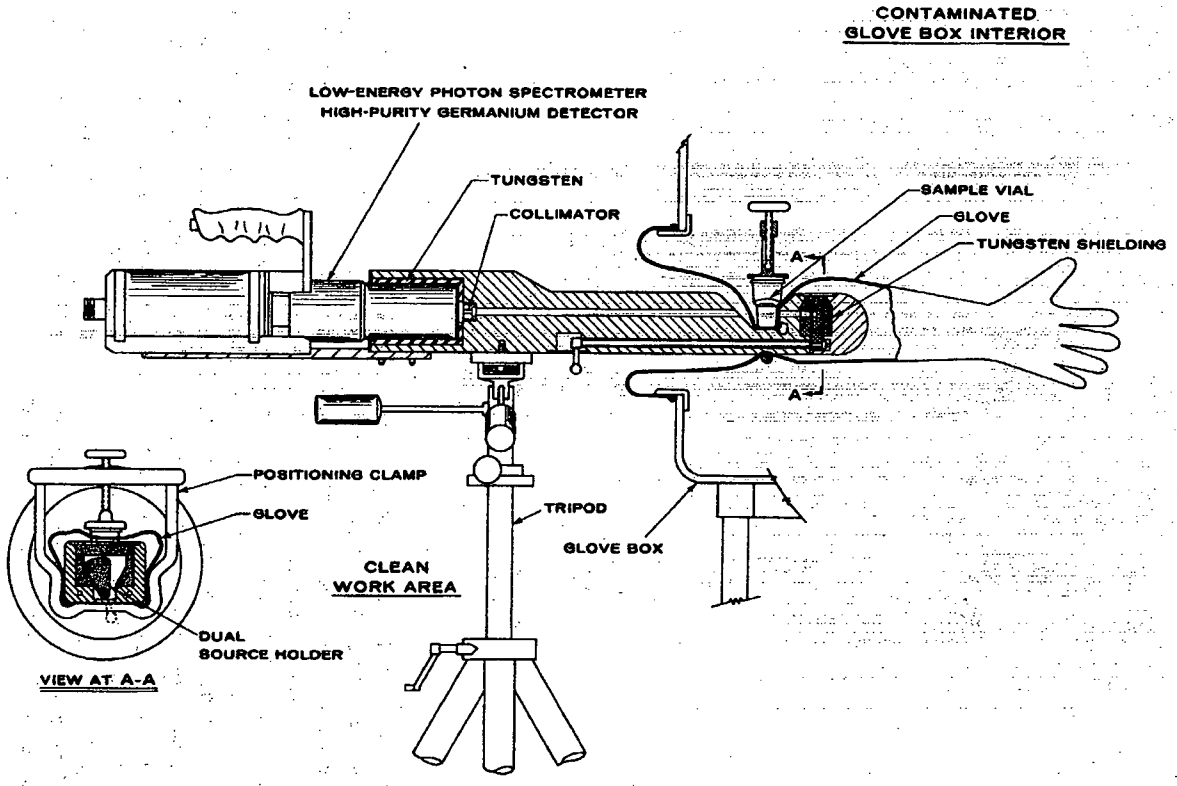

Fig. 9.15 Scale line drawing of the measurement head of the portable K-edge densitometer inserted in a glove-box glove. The sample cell thickness in the transmission path is 2 cm.

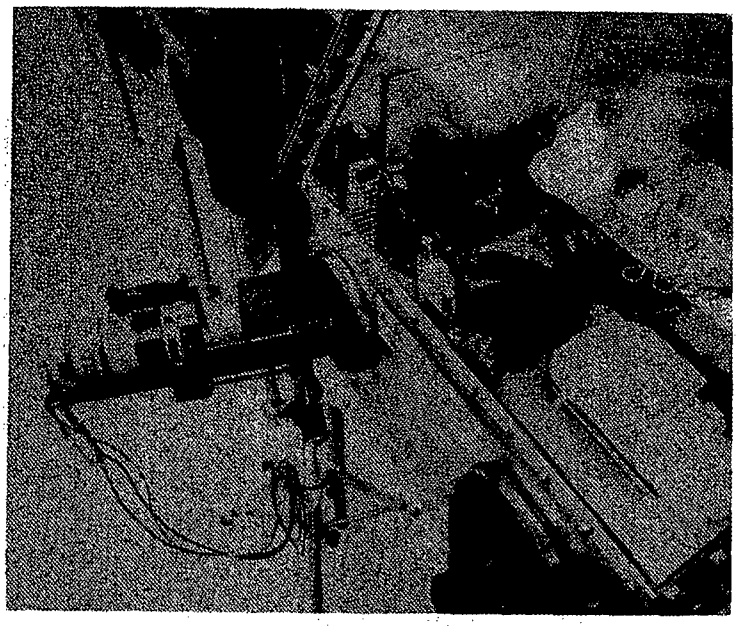

***Fig. 9.16** The portable K-edge densitometer, positioned for measurement.*

7. Kernforschungszentrum Karlsruhe (KfK) (Refs. 12 and 31 through 33). A continuum-source K-edge densitometer has been tested at Kernforschungszentrum Karlsruhe in Karlsruhe, Federal Republic of Germany (FRG), since 1978. The detector and x-ray head reside outside a glove box, and the samples and collimators are inside the glove box. The instrument has been used to assay reprocessing product solutions and fast-breeder-reactor reprocessing feed solutions for concentrations of both uranium and plutonium. A hybrid version of this instrument was used for assaying light-water-reactor feed solutions in which the plutonium content is approximately 1% of the uranium content. The continuum source served both as a transmission source for K-edge assay of uranium and as a fluorescing source for x-ray fluorescence (XRF) assay of the plutonium/uranium concentration ratio. The intensity of the continuum source allows the highly restrictive sample collimation required for K-edge and XRF assays while greatly reducing the passive count rate from the samples, which contain high levels of fission products.

Figure 9.17 is a line drawing of the measurement head for the hybrid instrument. Figure 9.18 shows the K-edge densitometer at Karlsruhe.

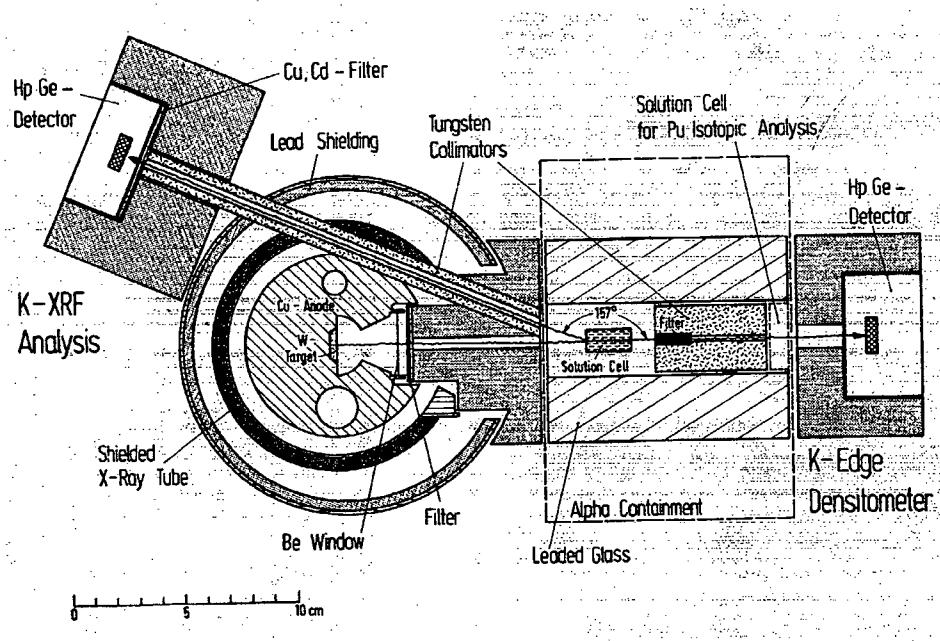

***Fig. 9.17** Cross-sectional view of the KfK combined K-edge/XRF system. The size of the alpha containment, a standard glove box, is not shown to scale. The sample cell thickness in the transmission path is 2 cm.*

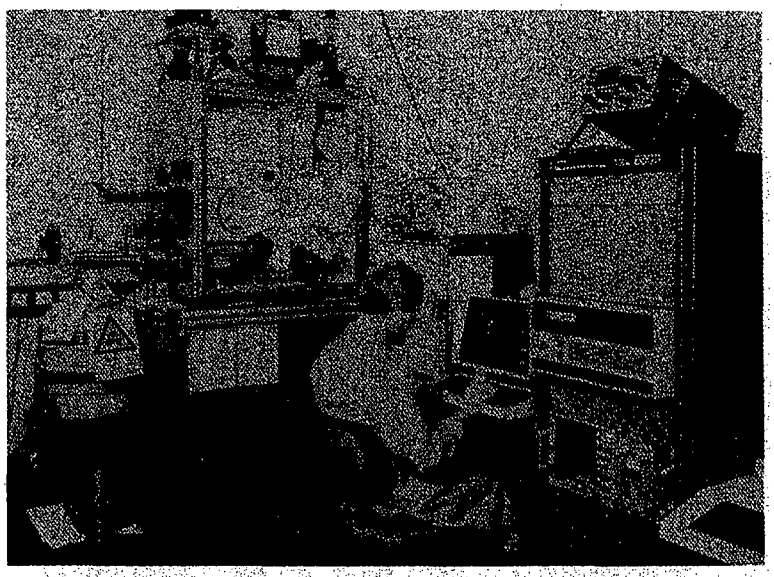

***Fig. 9.18** The KfK K-edge densitometer evaluated under the FRG support program to the IAEA.*

9.7.2 L_{III}-Absorption-Edge Densitometers

Given below are descriptions of several L_{III}-edge densitometers that have been tested and evaluated under actual or simulated in-plant environments. The first three L_{III}-edge densitometers described were designed to be equivalent, mechanically and electronically. Figure 9.19, a photograph of the AGNS instrument, represents all three instruments; Figure 9.20 is a line drawing of the measurement head for all three instruments. Table 9-5 summarizes the performance data for the instruments.

1. Savannah River Laboratory (SRL) (Refs. 12, 21, and 34). The L_{III}-edge densitometer at the Savannah River Laboratory was tested in conjunction with a solution coprocessing demonstration facility. The stainless steel flow-through solution sample cell (fitted with plastic windows) was plumbed into the glove box that housed the coprocessing setup, so that solution from various points in the process could be introduced into the cell for L_{III}-edge assay of either uranium or plutonium or both. The instrument measured 15-mL static solutions in the cell; before each assay, the instrument was flushed several times with the solution. The assay precisions obtained for pure uranium or plutonium solutions are plotted versus concentration in Figure 9.21. The instrument operated at Savannah River from 1978 until 1980.

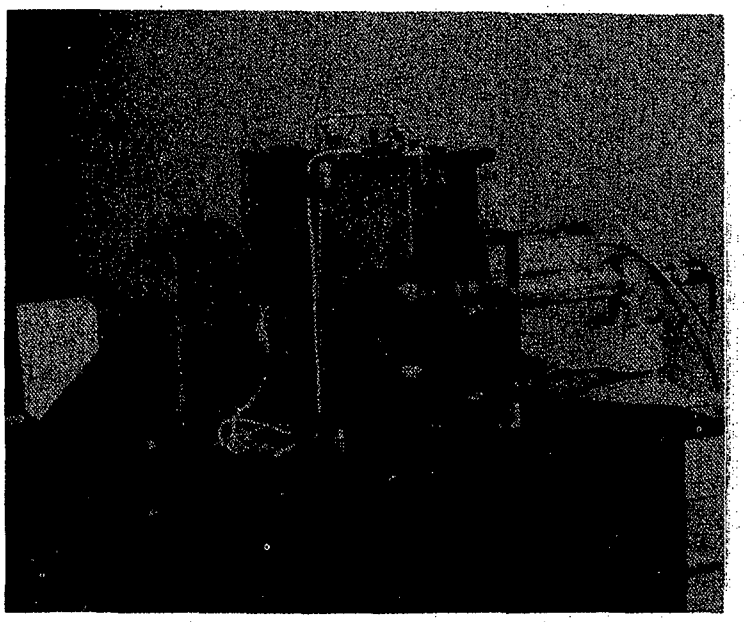

Fig. 9.19 The AGNS L_{III}-edge densitometer. Shown (left to right) are the electronics inside an environmental enclosure, the measurement station, and the hard-copy terminal.

2. New Brunswick Laboratory (NBL) (Ref. 35). The L_{III}-edge densitometer at the US Department of Energy New Brunswick Laboratory at Argonne was designed to reproduce the measurement geometry and assay method of the Savannah River Laboratory instrument. Prepared reference solutions of uranium, plutonium, and mixed solutions were used in a carefully controlled evaluation of the precision and accuracy of this instrument. The NBL assay results are compared with reference values for pure uranium solutions in Figure 9.22. The sensitivity to matrix contaminants with low-, intermediate-, and high-Z elements was examined for contamination levels up to 10% (of SNM) by weight. This evaluation took place from 1980 to 1981.

3. Allied General Nuclear Services (AGNS) (Ref. 36). An L_{III}-edge densitometer designed to perform continuous assays of uranium concentration in flowing process streams was tested in 1981 at the AGNS Barnwell facility. The stainless steel flow-through cell was plumbed into a line that continuously sampled the product stream of a solvent extraction column. The instrument operated for seven days without interruption, providing uranium concentration results every 5 min, analyzing flowing solutions

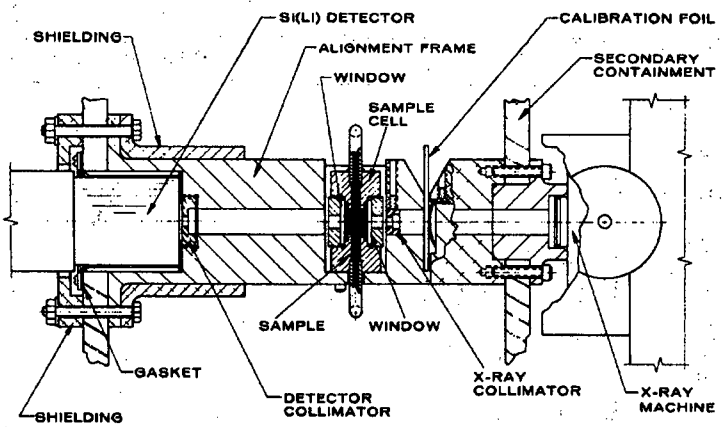

Fig. 9.20 Scale line drawing of the L_{III}-edge densitometer measurement head for the SRL, NBL, and AGNS instruments. The flow-through sample cell is shown cut off at the inlet and outlet tubes. The darkened area indicates the solution in the cell (1-cm transmission path length). The materials for secondary containment, shielding, frame, sample cell, and collimator are polycarbonate (Lexan™), stainless steel, aluminum, stainless steel (with Kel-F™ windows), and brass, respectively.

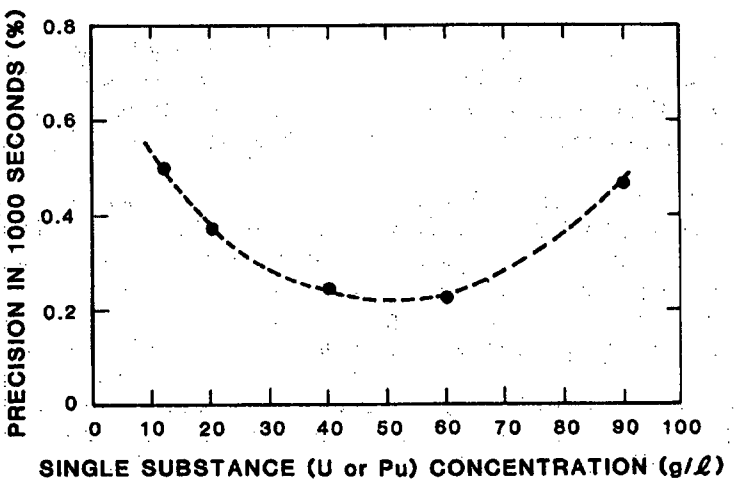

Fig. 9.21 Precision (1σ) measured at SRL for 1000-s L_{III}-edge assays of uranium or plutonium plotted versus concentration. The dashed line is the calculated standard deviation, based on counting statistics, using Equation 9-14.

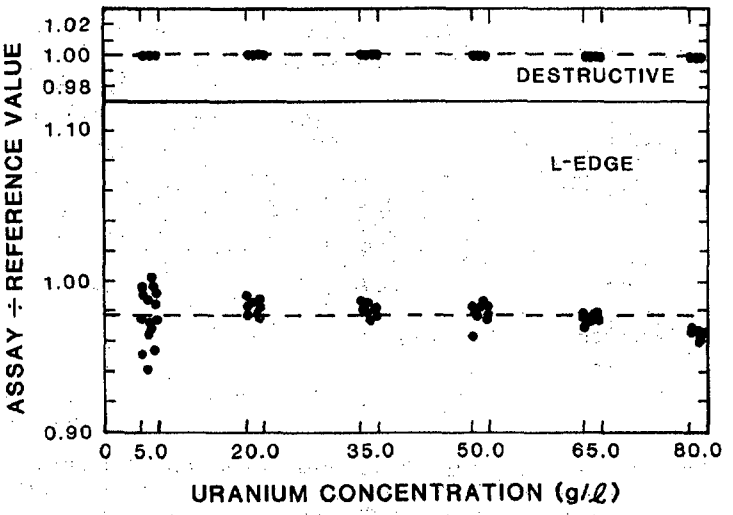

Fig. 9.22 Comparison of single 1000-s L_{III}-edge assays and destructive analysis of solution samples introduced into the sample cell of the NBL instrument. Groups of three data points plotted vertically represent repeated assays of the same sample. These data were used to establish the calibration of the NBL instrument.

from startup (essentially zero uranium concentration) to steady-state levels of approximately 40 g/L. The instrument provided a hard copy of the near-real-time results automatically to a materials control and accounting computer programmed to draw near-real-time material balances using readouts from process monitoring equipment.

4. Los Alamos National Laboratory (Ref. 37). A compact L_{III}-edge densitometer was tested in 1984 at Los Alamos in the Group Q-1 Safeguards Laboratory. This instrument used a commercial x-ray generator designed for portable applications. Figure 9.23 shows the measurement head. Although a standard rack of electronics was employed for analog signal processing and for data acquisition and analysis, the portable multichannel analyzer used in the compact K-edge densitometer at Seibersdorf (see Section 9.7.1) could have been employed in the L-edge densitometer at Los Alamos, allowing portable applications to be considered for L_{III}-edge measurements. The performance of the compact densitometer with prepared reference solutions of uranium was equal to that of the L_{III}-edge instruments tested previously.

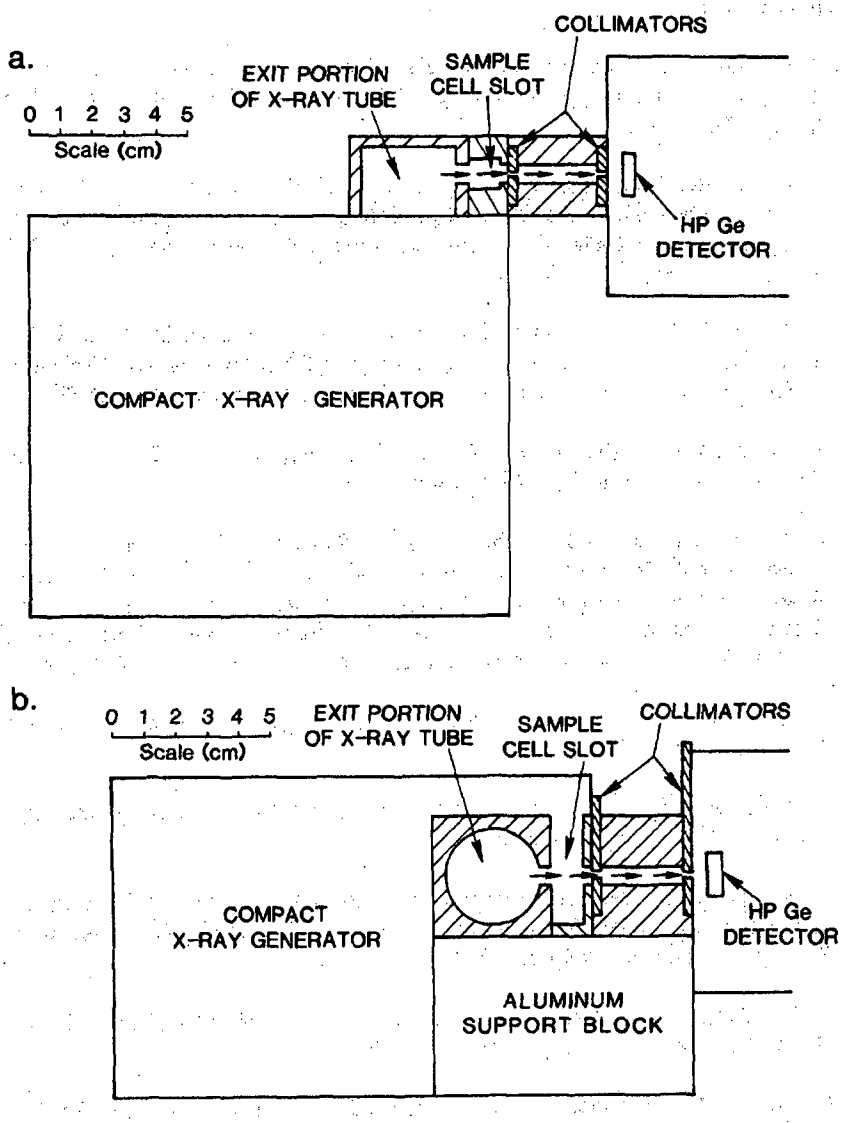

Fig. 9.23 *Scale line drawings of the compact L_{III}-edge densitometer measurement head: (a) view from above in the horizontal plane of the x-ray transmission path; (b) side view. The solution thickness in the trasmission path is 1 cm.*

REFERENCES

1. T. R. Canada, J. L. Parker, and T. D. Reilly, "Total Plutonium and Uranium Determination by Gamma-Ray Densitometry," *Transactions of the American Nuclear Society* 22, 140 (1975).

2. T. R. Canada, D. G. Langner, and J. W. Tape, "Nuclear Safeguards Applications of Energy-Dispersive Absorption-Edge Densitometry," in *Nuclear Safeguards Analysis*, E. A. Hakkila, Ed. (American Chemical Society, Washington, DC, 1978), Series No. 79, p. 96.

3. T. R. Canada, S. -T. Hsue, D. G. Langner, D. R. Martin, J. L. Parker, T. D. Reilly, and J. W. Tape, "Applications of the Absorption-Edge Densitometry Technique to Solutions and Solids," *Nuclear Materials Management* 6 (3), 702 (1977).

4. R. L. Bramblett, "Passive and Active Measurements of SNM in 55-Gallon Drums," *Nuclear Materials Management* 4, 137 (1975).

5. H. A. Smith, Jr., T. Marks, S. S. Johnson, L. R. Cowder, J. K. Sprinkle, Jr., C. O. Shonrock, R. W. Slice, D. L. Garcia, K. W. MacMurdo, R. L. Pollard, L. B. Baker, P. Christie, and J. P. Clark, "Test and Evaluation of the In-Line Plutonium Solution K-Absorption-Edge Densitometer at the Savannah River Plant: Phase I, Off-Line Testing," Los Alamos National Laboratory report LA-9124-MS (1982).

6. S. -T. Hsue to R. B. Walton, "Densitometry Design," Los Alamos document Q-1-80-243 (May 1980).

7. L. A. Currie, "Limits for Quantitative Detection and Quantitative Determination," *Analytical Chemistry* 40, 586 (1968).

8. C. E. Crouthamel et al., "A Compilation of Gamma-Ray Spectra (NaI Detector)," in *Applied Gamma-Ray Spectrometry*, F. Adams and R. Dams, Eds. (Pergamon Press, Braunschweig, Hungary, 1970).

9. T. W. Crane, "Detectability Limits and Precision for Shufflers," Los Alamos National Laboratory report LA-10158-MS (1984).

10. E. Storm and H. I. Israel, "Photon Cross Sections from 0.001 to 100 MeV for Elements 1 through 100," Los Alamos Scientific Laboratory report LA-3753 (1967).

11. *Handbook of Chemistry and Physics*, 55th ed., R. C. Weast, Ed. (Chemical Rubber Company Press, Cleveland, Ohio, 1975).

12. P. A. Russo, S. -T. Hsue, D. G. Langner, and J. K. Sprinkle, Jr., "Nuclear Safeguards Applications of Energy-Dispersive Absorption-Edge Densitometry," *Nuclear Materials Management* 9, 730 (1981).

13. F. Brown, D. R. Terry, J. B. Hornsby, R. G. Monk, F. Morgan, J. Herrington, P. T. Good, K. C. Steed, and V. M. Sinclair, "Application of Instrumental Methods to the Determination of Nuclear Fuel Materials for Safeguards," in *Safeguards Techniques*, Proc. IAEA Karlsruhe Symp. (IAEA, Vienna, Austria, July 1970), Vol. II, p. 125.

14. D. R. Terry and A. P. Dixon, "A Portable Gamma Absorptiometer for Safeguards Use in Nuclear Fuel Reprocessing Plants," Atomic Weapons Research Establishment report AWRE/44/88/28 Cos 28, Aldermaston, England (1975).

15. J. E. Ayer and D. R. Schmitt, "A Gamma-Ray Absorptiometer for Nuclear Fuel Evaluation," *Nuclear Technology* 27, 442 (1975).

16. T. Gozani, H. Weber, and Y. Segal, "A Gamma-Ray Transmission Gauge for Determination of Heavy and Light Metal Loading of Fuel Elements," *Nuclear Materials Management* 2 (3), 139 (1973).

17. T. Gozani, *Active Nondestructive Assay of Nuclear Materials, Principles and Applications*, NUREG/CR-0602, (US Nuclear Regulatory Commission, Washington DC, 1981), p. 118.

18. G. Bardone, M. Aparo, and F. V. Frazzoli, "Dual-Energy X-Ray Absorptiometry for the Assay of Mixed Special Nuclear Material in Solution," in *Proc. Second Annual Symposium on Safeguards and Nuclear Materials Management*, Edinburgh, Scotland, March 26-28, 1980 (European Safeguards Research and Development Association, Brussels, Belguim, 1980), p. 270.

19. M. Aparo, B. Mattia, F. V. Frazzoli, and P. Zeppa, "Dual-Energy X-Ray Absorptiometer for Nondestructive Assay of Mixed Special Nuclear Material in Solution," in *Proc. Fifth Annual Symposium on Safeguards and Nuclear Materials Management*, Versailles, France, April 19-21, 1983 (European Safeguards Research and Development Association, Brussels, Belgium, 1983), p. 271.

20. J. K. Sprinkle, Jr., H. R. Baxman, D. G. Langner, T. R. Canada, and T. E. Sampson, "The In-Plant Evaluation of a Uranium NDA System," in *Proc. American Nuclear Society Topical Conference on Measurement Technology for Safeguards and Materials Control*, Kiawah Island, South Carolina, November 26-28, 1979 (National Bureau of Standards, Washington, DC, 1980), p. 324.

21. T. R. Canada, J. L. Parker, and P. A. Russo, "Computer-Based In-Plant Nondestructive Assay Instrumentation for the Measurement of Special Nuclear Materials," in *Proc. American Nuclear Society Topical Conference on Computers in Activation Analysis in Gamma-Ray Spectroscopy*, Mayaguez, Puerto Rico. April 30-May 4, 1978 (US DOE Technical Information Center), p. 746.

22. H. H. Hogue and S. E. Smith, "Off-Line Nondestructive Analysis at a Uranium Recovery Facility," in *Safeguards Technology: The Process-Safeguards Interface*, Proc. American Nuclear Society-INMM Topical Conference, Hilton Head Island, South Carolina, November 28-December 2, 1983 (Conf. 831106, 1984).

23. H. H. Hogue and S. E. Smith, "Nondestructive Analysis at the Oak Ridge Y-12 Plant," Oak Ridge Y-12 Plant report Y-2297 (1984).

24. K. J. Hofstetter, G. A. Huff, R. Gunnink, J. E. Evans, and A. L. Prindle, "On-Line Measurement of Total and Isotopic Plutonium Concentrations by Gamma-Ray Spectrometry," in *Analytical Chemistry in Nuclear Fuel Reprocessing*, W. S. Lyon, Ed. (Science Press, Princeton, New Jersey, 1978), p. 266, and University of California report UCRL-52220 (1977).

25. K. J. Hofstetter and G. A. Huff, "On-Line Isotopic Concentration Monitor," Allied General Nuclear Services report AGNS-1040-2.3-52 (1978).

26. L. R. Cowder, S. -T. Hsue, S. S. Johnson, J. L. Parker, P. A. Russo, J. K. Sprinkle, Jr., Y. Asakura, T. Fukuda, and I. Kondo, "An Instrument for the Measurement of Pu Concentration and Isotopics of Product Solutions at Tokai-Mura," in *Proc. Second Annual Symposium on Safeguards and Nuclear Materials Management*, Edinburgh, Scotland, March 26-28, 1980 (European Safeguards Research and Development Association, Brussels, Belgium, 1980), p. 119.

27. P. A. Russo, S. -T. Hsue, J. K. Sprinkle, Jr., S. S. Johnson, Y. Asakura, I. Kondo, J. Masui, and K. Shoji, "In-Plant Measurements of Gamma-Ray Transmissions for Precise K-Edge and Passive Assay of Plutonium Concentration and Isotopic Fractions in Product Solutions," Los Alamos National Laboratory report LA-9440-MS (1982).

28. Y. Asakura, I. Kondo, J. Masui, K. Shoji, P. A. Russo, S. -T. Hsue, J. K. Sprinkle, Jr., and S. S. Johnson, "In-Plant Measurements of Gamma-Ray Transmissions for Precise K-Edge and Passive Assay of Plutonium Concentration and Isotopic Abundances in Product Solutions at the Tokai Reprocessing Plant," *Nuclear Materials Management* 11, 221 (1982).

29. H. A. Smith, Jr., T. Marks, L. R. Cowder, C. O. Shonrock, S. S. Johnson, R. W. Slice, J. K. Sprinkle, Jr., K. W. MacMurdo, R. L. Pollard, and L. B. Baker, "Development of In-Line Plutonium Solution NDA Instrumentation at the Savannah River Plant," in *Proc. Second Annual Symposium on Safeguards and Nuclear Materials Management*, Edinburgh, Scotland, March 26-28, 1980 (European Safeguards Research and Development Association, Brussels, Belgium, 1980), p. 123.

30. L. R. Cowder, S. F. Klosterbuer, R. H. Augustson, A. Esmailpour, R. Hawkins, and E. Kuhn, "A Compact K-Edge Densitometer," in *Proc. Sixth Annual Symposium on Safeguards and Nuclear Materials Management*, Venice, Italy, May 14-18, 1984 (European Safeguards Research and Development Association, Brussels, Belgium, 1984), p. 261.

31. H. Eberle, P. Matussek, H. Ottmar, I. Michel-Piper, M. R. Iyer, and P. P. Chakraborty, "Nondestructive Elemental and Isotopic Assay of Plutonium and Uranium in Nuclear Materials," Nuclear Safeguards Technology 1978 (International Atomic Energy Agency, Vienna, Austria, 1979), Vol. II, p. 27.

32. H. Eberle, P. Matussek, I. Michel-Piper, and H. Ottmar, "Assay of Uranium and Plutonium in Solution by K-Edge Photon Absorptiometry Using a Continuous X-Ray Beam," in *Proc. Second Annual Symposium on Safeguards and Nuclear Materials Management*, Edinburgh, Scotland, March 26-28, 1980 (European Safeguards Research and Development Association, Brussels, Belgium, 1980), p. 372.

33. H. Eberle, P. Matussek, I. Michel-Piper, and H. Ottmar, "Operational Experience with K-Edge Photon Absorptiometry for Reprocessing Feed and Product Solution Analysis," in *Proc. Third Annual Symposium on Safeguards and Nuclear Materials Management*, Karlsruhe, Fed. Rep. Germany, May 6-8, 1981 (European Safeguards Research and Development Association, Brussels, Belgium, 1981), p. 109.

34. P. A. Russo, T. R. Canada, D. G. Langner, J. W. Tape, S. -T. Hsue, L. R. Cowder, W. C. Moseley, L. W. Reynolds, and M. C. Thompson, "An X-Ray L_{III}-Edge Densitometer for Assay of Mixed SNM Solutions," in *Proc. First Annual Symposium on Safeguards and Nuclear Materials Management*, Brussels, Belgium, April 25-27, 1979 (European Safeguards Research and Development Association, Brussels, Belgium, 1979), p. 235.

35. W. J. McGonnagle, M. K. Holland, C. S. Reynolds, N. M. Trahey, and A. C. Zook, "Evaluation and Calibration of a Los Alamos National Laboratory L_{III}-Edge Densitometer," US Department of Energy New Brunswick Laboratory report NBL-307 (1983).

36. P. A. Russo, T. Marks, M. M. Stephens, A. L. Baker, and D. D. Cobb, "Automated On-Line L-Edge Measurement of SNM Concentration for Near-Real-Time Accounting," Los Alamos National Laboratory report LA-9480-MS (1982).

37. M. L. Brooks, P. A. Russo, and J. K. Sprinkle, Jr., "A Compact L-Edge Densitometer for Uranium Concentration Assay," Los Alamos National Laboratory report LA-10306-MS (1985).

10

X-Ray Fluorescence

M. C. Miller

10.1 INTRODUCTION

The potential use of x rays for qualitative and quantitative elemental assay was appreciated soon after x rays were discovered. The early applications used Geiger-Mueller tubes and elaborate absorber arrays or crystal diffraction gratings to measure x rays. Later, advances in semiconductor detectors and associated electronics opened up the field of energy-dispersive x-ray fluorescence (XRF) analysis for general elemental assay.

XRF analysis is based on the fact that the x rays emitted from an ionized atom have energies that are characteristic of the element involved. The x-ray intensity is proportional to both the elemental concentration and the strength of the ionizing source. Photon ionization, which is achieved using either an x-ray tube or radioisotope, is most applicable to the nondestructive assay of nuclear material. Other methods of ionization are generally prohibitive because of the physical size and complexity of the ionization source.

XRF analysis is a complementary technique to densitometry (Chapter 9). Densitometry measures photons that are transmitted through the sample without interaction, whereas XRF measures the radiation produced by photons that interact within the sample. As indicated by Figure 10.1, densitometry is usually better suited for measuring samples with high concentrations of the element of interest, whereas XRF is the more useful technique for measuring samples with lower concentrations.

The literature on XRF analysis includes several general references (Refs. 1 through 4) that provide a thorough discussion of the method, with extensive bibliographies and information on attenuation correction procedures and both energy- and wavelength-dispersive XRF.

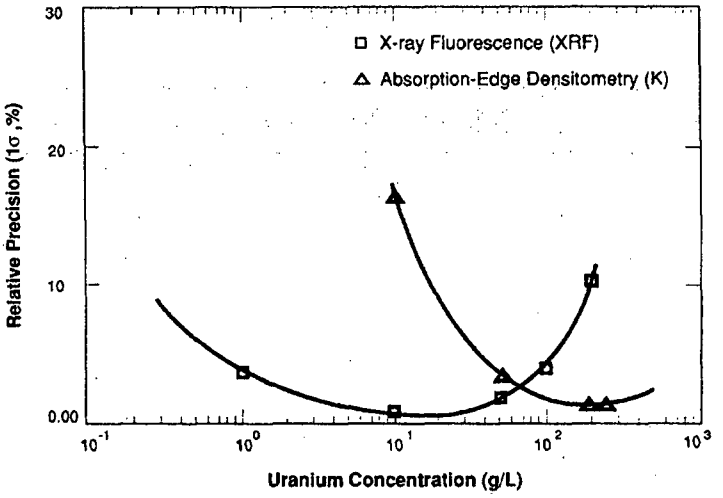

Fig. 10.1 Solution assay precision vs uranium concentration for typical XRF measurements (squares) and absorption-edge densitometry measurements (triangles).

10.2 THEORY

10.2.1 X-Ray Production

Section 1.3 of Chapter 1 contains a brief discussion of x-ray production. X rays originate from atomic electron transitions and are element-specific. In the stable atom, electrons occupy discrete energy levels that are designated (in order of decreasing binding energy) K, L_1, L_2, L_3, M_1, ..., M_5, N_1, ..., N_7, and so forth. The binding energy is the energy that must be expended to remove an electron from a given orbit. The vacancy thus created is filled by an electron from an outer orbit. The resultant loss in potential energy may appear as an x ray whose energy is equal to the difference in the binding energies of the two electron states. For example, if a uranium K electron is removed from the atom and an electron from the L_3 level falls into its place, the energy of the emitted x ray is 98.428 keV (115.591 keV minus 17.163 keV). The x ray produced by this transition is designated $K_{\alpha 1}$. The K-series x rays are produced by outer electrons filling a K-shell vacancy. Each x-ray transition has a specific probability or intensity. The K-to-L_3 transition is the most probable, and other intensities are usually expressed relative to $K_{\alpha 1}$. Figure 10.2 depicts the transitions involved in the production of the most abundant K and L x rays. Table 10-1 presents the major K and L lines of uranium and plutonium, along with their relative intensities. Figures 10.3 and 10.4 show the K and L x-ray spectra of uranium.

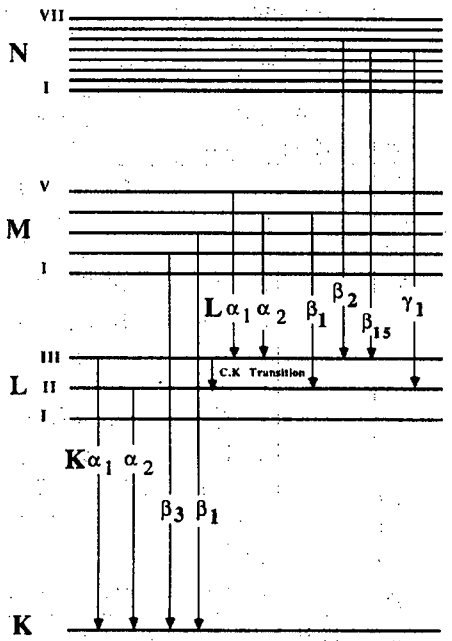

Fig. 10.2 Diagram of energy levels showing the atomic transitions that produce the major K and L x rays. (C.K. = Coster Krönig)

10.2.2 Fluorescence Yield

All ionizations do not result in x-ray emission. The Auger effect is a competing mechanism of atomic relaxation. In this process, the atom regains energy stability by emitting an outer shell electron. The ratio of the number of emitted x rays to the total number of ionizations is called the fluorescence yield ω_i, where i designates the shell involved. Fluorescence yield increases with atomic number and is greater than 95% for K x rays of elements with $Z > 78$ (see Figure 10.5). For a given element, the fluorescence yield decreases from the K series to the L and M series. The fluorescence yield can be approximated by (Ref. 1)

$$\omega_i = Z^4/(A_i + Z^4) \tag{10-1}$$

where A_i is approximately 10^6 for the K shell and 10^8 for the L shell.

10.2.3 Photon Transmission

For a photon to eject an electron, the photon energy must be greater than or equal to the electron binding energy. For example, to ionize K electrons of plutonium, the energy of the excitation photon must be at least 121.82 keV.

Table 10-1. Energies and relative intensities of the major K and L x rays of uranium and plutonium

Line	Transition (Final - Initial)	Energies in keV[a] Uranium (%)[b]	Plutonium (%)
$K_{\alpha 1}$	K - L_3	98.44 (100)	103.76 (100)
$K_{\alpha 2}$	K - L_2	94.66 (61.9)	99.55 (62.5)
$K_{\beta 1}$	K - M_3	111.31 (22.0)	117.26 (22.2)
$K_{\beta 3}$	K - M_2	110.43 (11.6)	116.27 (11.7)
$K_{\beta 2}$	K - $N_{2,3}$	114.34, 114.57 (12.3)	120.44, 120.70 (12.5)
$L_{\alpha 1}$	L_3 - M_5	13.62 (100)[c]	14.28 (100)
$L_{\alpha 2}$	L_3 - M_4	13.44 (10)	14.08 (10)
$L_{\beta 2}$	L_3 - N_5	16.43 (20)	17.26 (20)
L_ι	L_3 - M_1	11.62 (1-3)	12.12 (1-3)
$L_{\beta 1}$	L_2 - M_4	17.22 (50)	18.29 (50)
$L_{\gamma 1}$	L_2 - N_4	20.17 (1-10)	21.42 (1-10)
$L_{\beta 3}$	L_1 - M_3	17.45 (1-6)	18.54 (1-6)
$L_{\beta 4}$	L_1 - M_2	16.58 (3-5)	17.56 (3-5)

[a]Calculated from *Table of Isotopes*, Appendix III (L lines) (C. M. Lederer and V. S. Shirley, Eds., 7th ed. [John Wiley & Sons, Inc., New York, 1978]).
[b]Intensities relative to either $K_{\alpha 1}$ or $L_{\alpha 1}$ in percent.
[c]Approximate only (from Ref. 4).

The fraction of photons, F, that interact with the atomic electrons of a particular material is given by

$$F = 1 - \exp(-\mu\rho x) \tag{10-2}$$

where μ = mass attenuation coefficient
ρ = density of sample
x = thickness of sample.

If one plots the mass attenuation coefficient vs photon energy for a given element, sharp discontinuities (known as "absorption edges") are observed. Figure 10.6 shows the mass attenuation coefficient for uranium and plutonium. The edges indicate the sudden decrease in the photoelectric cross section for incident photon energies just below the binding energy of that particular electron state. The photoelectric interaction is the dominant process involved in photon-excited x-ray excitation.

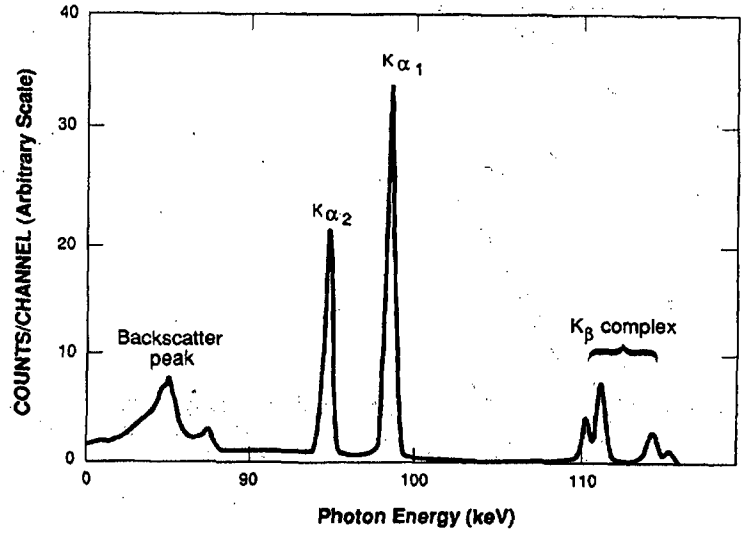

Fig. 10.3 K x-ray spectrum of uranium. The excitation source is ^{57}Co.

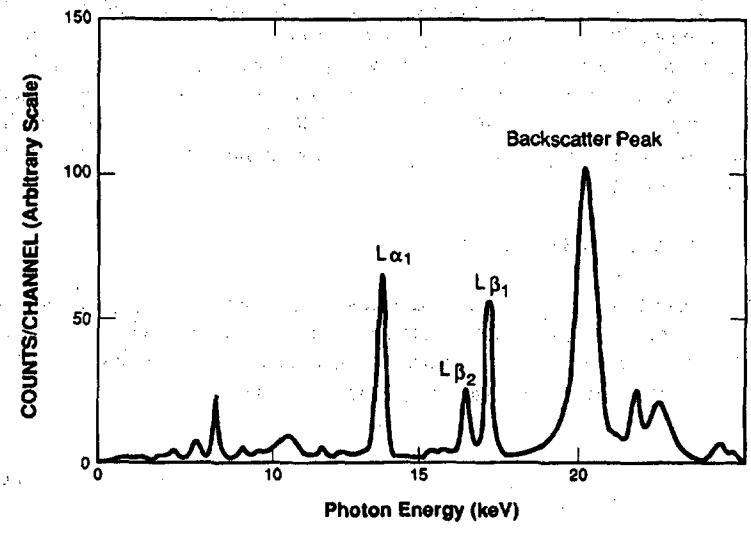

Fig. 10.4 L x-ray spectrum of uranium. The excitation source is ^{109}Cd.

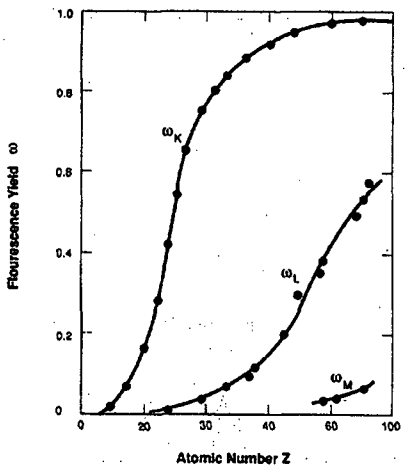

Fig. 10.5 Fluorescence yield for K, L, and M x rays as a function of atomic number.

Attenuation limits the sample size that can be analyzed by x-ray transmission techniques. Figure 10.7 shows the mean free path of 400-, 100-, and 20-keV photons in water and in a 50-g/L uranium solution. In general, transmission techniques are applicable for samples whose transmission path lengths are less than four or five mean free paths.

Equation 10-2 is useful when comparing K XRF and L XRF. For L XRF, μ is larger and more of the excitation flux interacts with the sample. For K XRF, μ is smaller and both the excitation photons and x rays are attenuated less (relative to L XRF). This attenuation difference implies that L XRF is more sensitive (more x rays produced per unit excitation flux and cross-sectional area) than K XRF. On the other hand, K XRF allows greater flexibility with respect to the choice of sample container and intervening absorbers.

10.2.4 Measurement Geometry

The choice of geometry is very important in an XRF system. Although photoelectric interactions of the excitation photons with analyte atoms are of primary interest, other interactions, particularly Compton backscatter interactions, must be considered. The energy of a Compton-scattered gamma ray is (see Section 2.3.2 of Chapter 2 and Ref. 5)

$$E' = \frac{511}{(1 - \cos\phi + 511/E)} \tag{10-3}$$

where E', E = scattered, incident photon energy in keV
ϕ = angle between incident and scattered photons.

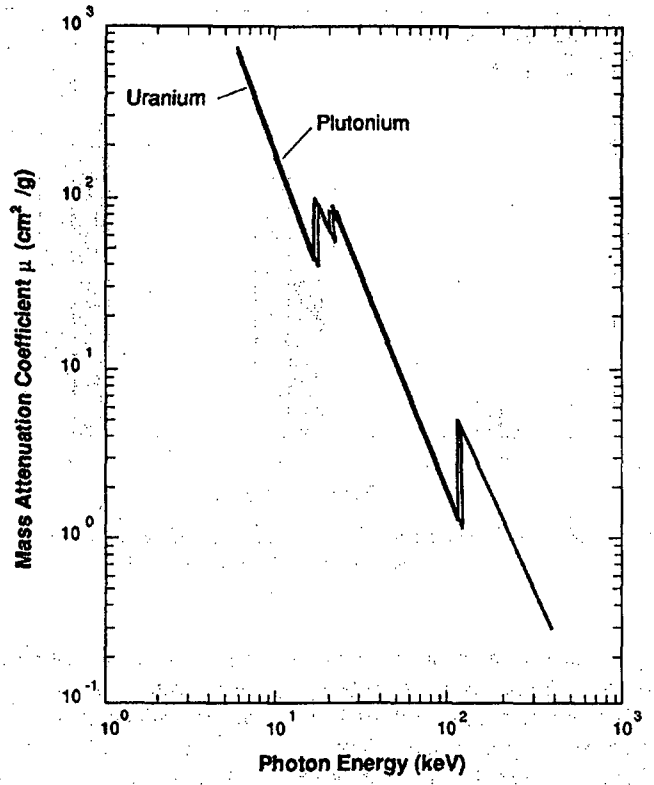

Fig. 10.6 *Mass attenuation coefficient vs energy for uranium and plutonium.*

The energy E′ is a minimum when $\phi = 180°$, and photons that have scattered at or near this angle can produce a backscatter peak in the measured spectrum. For 122-keV photons from ^{57}Co (a suitable source for K XRF of uranium or plutonium), the backscatter peak is at 82.6 keV. If the scattering angle ϕ is 90°, E′ is 98.5 keV, which is in the middle of the K x-ray spectrum from uranium and plutonium. If ^{57}Co is used as an excitation source, the measurement geometry should be arranged such that ϕ is close to 180° for most of the scattered gamma rays that reach the detector. This arrangement puts the backscatter peak and the Compton continuum of scattered photons below the characteristic x rays and minimizes the background under the x-ray photopeaks (see Figure 10.3). The annular source described later in the chapter provides this favorable geometry. For L x rays, the geometry is not as critical because E′(180°) is 20.3 keV for 22-keV silver x rays from ^{109}Cd (a good L XRF source for uranium), and the backscatter peak is above the x-ray region of interest. Scattering

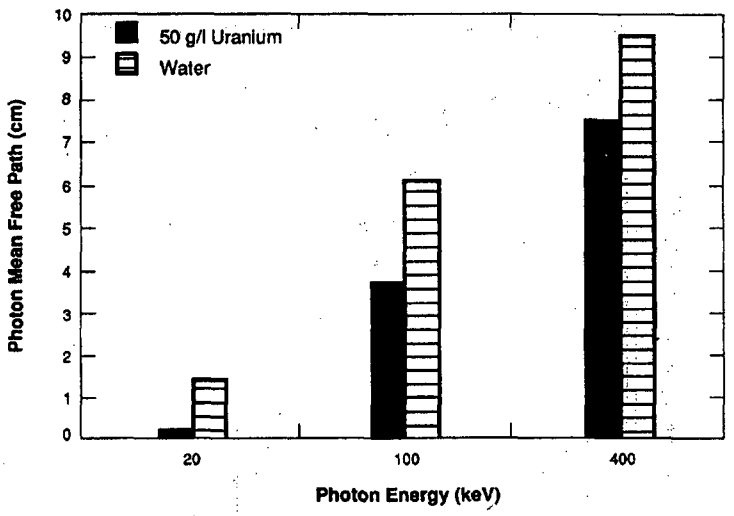

Fig. 10.7 Mean free path of 400-, 100-, and 20-keV photons in water (ρ = 1 g/cm^3) and in a 50-g/L uranium solution.

materials near the detector must be carefully controlled to minimize the magnitude of the backscatter peak. Some investigators (Ref. 6) use excitation sources with energies much higher than the binding energy of interest, thereby minimizing the scattering effects in the spectral region of the induced x rays. This approach requires higher-intensity excitation sources (by an order of magnitude or more) in order to produce sufficient x-ray activity.

The detector must be shielded from the excitation source and other background radiation to reduce deadtime and pileup losses. Detector collimation is usually necessary to limit the interference from unwanted sources. To stabilize the x-ray response, the relative positions of the source, sample, and detector must be fixed; often these components are physically connected. Figure 10.8 shows a possible geometry for a transmission-corrected XRF analysis.

10.3 TYPES OF SOURCES

Two types of sources are commonly used: discrete gamma-ray or x-ray sources and continuous sources such as x-ray generators. Each has advantages and disadvantages. The selection of a suitable source involves consideration of type, energy, and strength. It is most efficient to choose a source whose energy is above but as close as possible to the absorption edge of interest. As shown by the graph of μ vs photon energy

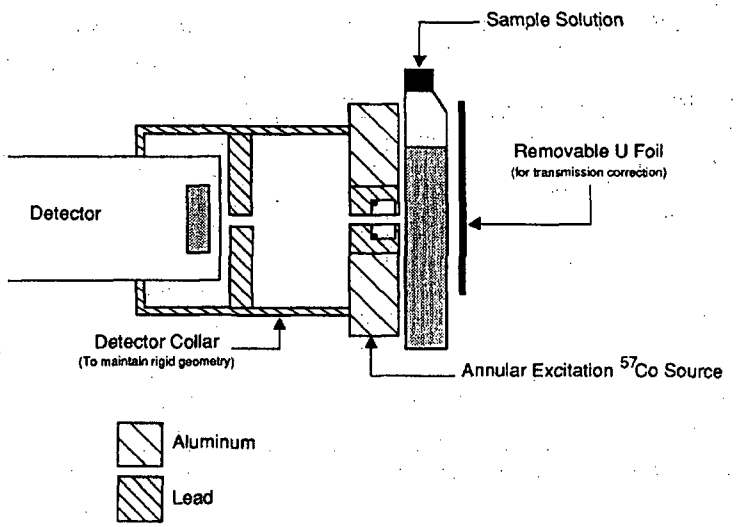

Fig. 10.8 *Cross-sectional view of geometry for a transmission-corrected assay using an annular excitation source.*

in Figure 10.6, the value of the mass attenuation coefficient is greatest just above an absorption edge.

Cobalt-57 emits a gamma ray at 122 keV, an efficient energy for K-shell ionization of either uranium or plutonium. X-ray generators are available for K XRF of uranium and plutonium, but they are too bulky for portable applications. A good discrete source for L XRF of uranium and plutonium is ^{109}Cd, which emits silver K x rays ($K_{\alpha 1}$ energy = 22 keV). X-ray generators are available that are small enough for portable applications that require photons in the 25-keV energy range.

Discrete line sources are small, extremely stable, and operationally simple, making them attractive for many XRF applications. Their major disadvantage is that they decay with time and require periodic replacement. (Two commonly used sources, ^{57}Co and ^{109}Cd, have half-lives of 272 days and 453 days, respectively.) Another disadvantage is that discrete sources cannot be turned off, causing transportation and handling difficulties. Because the source strength is often 1 mCi or greater, both personnel and detector must be carefully shielded. Table 10-2 lists some radioisotopes that can be used for XRF analysis of uranium and plutonium. The geometry of the annular source shown in Figure 10.9 is commonly used because it shields the detector from the excitation source and minimizes backscatter interference.

Table 10-2. Excitation sources suitable for uranium and plutonium assay

Radionuclide	Half-Life	Decay Mode	Useful Emissions	
			Type	Energy (keV)
^{57}Co	270 d	electron capture	gamma rays	122
			gamma rays	136
^{109}Cd	453 d	electron capture	Ag K x rays	22
^{75}Se	120 d	electron capture	gamma rays	121
			gamma rays	136
^{144}Ce	285 d	beta decay	Pr K x rays	36
			gamma rays	134
^{125}I	60 d	electron capture	Te K x rays	27
			gamma rays	35
^{147}Pm-Al	2.6 y	beta decay	continuum	12-45[a]

[a]End point of bremsstrahlung spectrum.

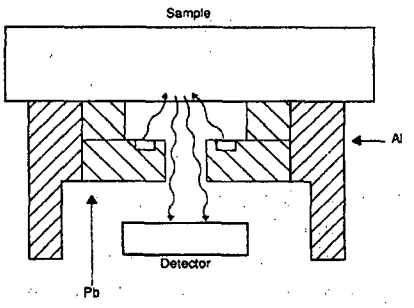

Fig. 10.9 Annular excitation source.

X-ray generators produce bremsstrahlung by boiling electrons off a filament and accelerating them into a target. Because they require a high-voltage supply and a means of dissipating the heat produced in the target, x-ray generators can be bulky, especially for higher operating potentials. Small generators are available that operate below 70 keV, and portable generators, with power ratings up to 50 W, are available that do not require elaborate cooling systems. For a given power rating, higher maximum operating voltage is achieved at the expense of lower available current.

The spectrum from an x-ray generator spans the energy range from the accelerating potential of the generator to the transmission cutoff of the x-ray window. The shape I(E) and total intensity (I) of this distribution is given by (Ref. 4)

$$I(E) \propto iZ(V - E)E$$
$$I \propto iZV^2 \qquad (10\text{-}4)$$

where i = tube current
V = operating voltage
Z = atomic number of target.

Figure 10.10 shows the output spectrum from an x-ray generator. In addition to the continuous spectrum, the characteristic x rays of the target material are produced. These x rays may cause an interference, which can be removed with filters. The filter chosen should have an absorption edge just below the energy to be attenuated.

X-ray generators can be switched on and off, and their energy distribution and intensity can be varied as desired. They typically provide a more intense source of photons than radioisotopic sources ($\sim 10^{12}$ photons/s or greater). However, their flexibility is possible only at the expense of simplicity and compactness. Because an x-ray generator is an electrical device, system failures and maintenance problems are possible concerns. The assay precision is dictated by the stability of the x-ray tube. Modern generators exhibit less than 0.1% fluctuation for short-term stability and 0.2 to 0.3% for long-term stability. Figure 10.11 shows two different portable x-ray generators.

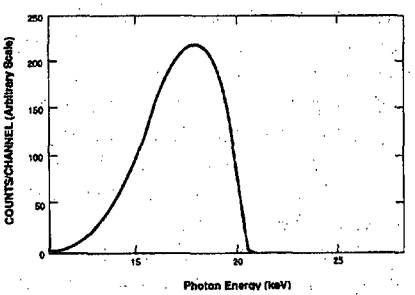

Fig. 10.10 *Typical x-ray generator spectrum. The generator target is tungsten and the operating potential is 20.4 kV.*

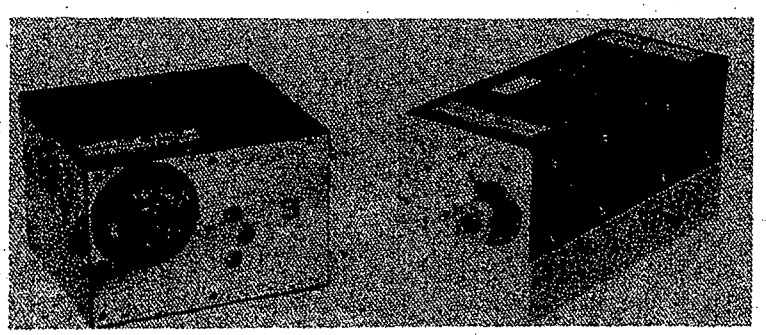

Fig. 10.11 *Portable x-ray generators.*

Other sources may be used for XRF. A secondary fluorescent source uses a primary photon source to excite the characteristic x rays of a target, and the target x rays are used to excite the sample to be analyzed. The primary excitation source can be discrete or continuous. This scheme can produce a great variety of monoenergetic excitation photons, depending on the target material. The major drawback is the need for a high-intensity primary source. If the primary source is a radioisotope, radiation safety may be an important concern. It is possible to make a bremsstrahlung source using a radioisotope rather than an x-ray generator. Such a source consists of a beta-decaying isotope mixed with a target material (for example, ^{147}Pm-Al, with aluminum being the target material).

10.4 CORRECTION FOR SAMPLE ATTENUATION

10.4.1 Effects of Sample Attenuation

As in passive gamma-ray assays, sample attenuation is a fundamental limitation to the accuracy of XRF analysis. Attenuation corrections are required for the x rays leaving the sample and also for the gamma rays or x rays from the excitation source. X-ray fluorescence analysis is unsuitable for large, solid samples, because the attenuation is too large to be accurately treated with any correction procedure. For example, the mean free path of 122-keV gamma rays in uranium metal is approximately 0.013 cm. The low penetrability of this radiation means that XRF can be accurately used only if the sample is smooth and homogeneous. This limitation is even more true for L XRF using 22-keV photons. X-ray fluorescence can be used to accurately assay dilute uranium solutions because the mean free path of photons in water is approximately 6.4 cm at 122 keV and 1.7 cm at 22 keV. Because the excitation source energy is above the absorption edge and the energies of the characteristic x rays are just below the absorption edge, the attenuation of the excitation radiation is higher and determines the range of sample thickness that can be accurately assayed. Figure 10.12 plots the mean free path of 122-keV gamma rays as a function of uranium concentration (uranyl nitrate in 4-M nitric acid).

Attenuation considerations also affect the choice of sample containers. Because the K x rays of uranium and plutonium are in the 100-keV range, metal containers can be tolerated, and K XRF can be applied to in-line measurements. L x rays, however, are severely attenuated by even thin metal containers and can only be measured in low-Z containers, such as plastic or glass.

10.4.2 General Assay Equation

For quantitative analysis, the x-ray emission rate must be related to the element concentration. The desired relation, as presented in Section 5.4.1 of Chapter 5, is

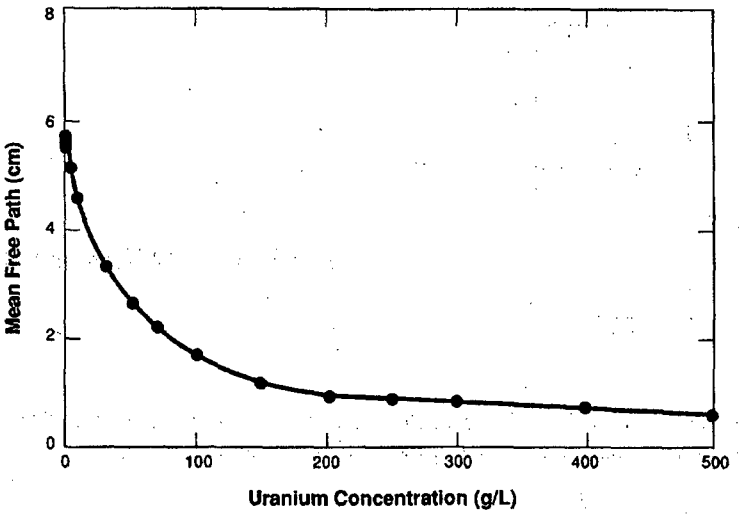

Fig. 10.12 *The 122-keV photon mean free path vs uranium concentration (uranyl nitrate in 4-M nitric acid).*

$$\rho = \frac{RR \times CF(RL) \times CF(AT)}{K} \tag{10-5}$$

where ρ = element concentration
RR = raw rate of x-ray detection
CF(RL) = correction factor for rate-related losses
CF(AT) = correction factor for attenuation
K = calibration constant.

CF(RL) can be determined using either pulser or radioisotope normalization (see Section 5.4 of Chapter 5). The attenuation correction has two parts, one for excitation radiation and one for fluoresced x rays.

Consider a far-field measurement geometry where the sample is approximated by a slab and the excitation source is monoenergetic (see Figure 10.13). The flux F_γ of excitation photons at a depth x in the sample is given by

$$F_\gamma = I_\gamma \exp(-\mu^\gamma X/\cos\phi) \; . \tag{10-6}$$

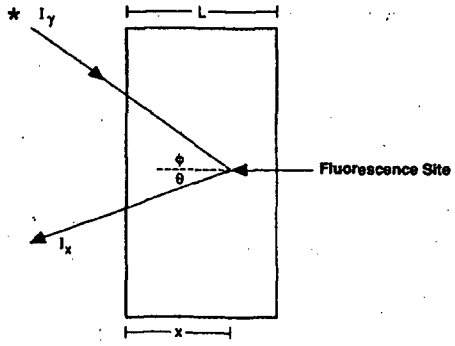

Fig. 10.13 General XRF slab geometry.

The variables in Equation 10-6 through 10-10 are defined in Table 10-3. The number of excitation photons that interact in the volume dx and create a $K_{\alpha 1}$ x ray is

$$F_x\, dx = F_\gamma \tau \rho \omega B \frac{dx}{\cos\phi} \,. \tag{10-7}$$

The fluoresced x rays are attenuated in the sample according to

$$F_x(\text{out}) = F_x \exp(-\mu^x X/\cos\theta) \,. \tag{10-8}$$

Combining and integrating Equations 10-6 through 10-8 yields the following expression for the x-ray rate at the detector surface:

$$I_x = \frac{I_\gamma \tau \rho \omega B \Omega}{4\pi[(\cos\theta/\cos\phi)\mu^\gamma + \mu^x]} \left\{1 - \exp\left[-\left(\frac{\mu^\gamma}{\cos\phi} + \frac{\mu^x}{\cos\theta}\right) L\right]\right\}. \tag{10-9}$$

The factor $(\Omega/4\pi)\cos\phi/\cos\theta$ has been added for normalization. If an x-ray generator is used as the excitation source, Equation 10-9 must be integrated from the absorption edge to the maximum energy of the generator.

When the sample is infinitely thick for the radiation of interest, Equation 10-9 becomes

$$I_x = \frac{I_\gamma \tau \rho \omega B \Omega}{4\pi[(\cos\theta/\cos\phi)\mu^\gamma + \mu^x]} \,. \tag{10-10}$$

This equation is similar to that of the enrichment meter (see Chapter 7). The result is very important for XRF analysis because it implies that the x-ray rate is directly proportional to the concentration of the fluoresced element.

In plutonium and highly enriched uranium materials, the self-excitation of x rays by the passive gamma rays can complicate the assay. For mixed uranium/plutonium materials, the dominant signals are passive x rays from the alpha decay of plutonium. When the excitation source can fluoresce both plutonium and uranium (as can ^{57}Co and ^{109}Cd), additional uranium fluorescence is caused by the plutonium x rays. A separate passive count is usually required to correct for this interference.

Table 10-3. Variables in Equations 10-6 through 10-10

I_0	excitation flux at sample surface
τ	photoelectric cross section, K shell, γ energy
ρ	concentration of element s
ω	K fluorescence yield
B	branching ratio for $K_{\alpha 1}$
Ω	detector solid angle
$\mu^{\gamma} = \sum \mu_i^{\gamma} \rho_i$	linear attenuation coefficient, γ energy, element i
$\mu^{x} = \sum \mu_i^{x} \rho_i$	linear attenuation coefficient, x energy, element i
ϕ	incident angle of excitation
Θ	exiting angle of x ray
L	slab thickness

10.4.3 Attenuation Correction Methods

The most effective XRF methods account for sample attenuation. The simplest approach uses calibration curves derived from chemically similar standards. The method is effective only if the standards are well characterized, match the samples chemically, and span the concentration range to be assayed in sufficient numbers to define the calibration curve. Changes in matrix composition may require recalibration with new standards.

A procedure that is less sensitive to matrix variation is the transmission-corrected assay (Refs. 7 through 9) in which a transmission measurement is made for each sample to correct for attenuation. Consider the attenuation correction factor for the situation shown in Figure 10.13 (assume that $\Theta = 0$). The expression for CF(AT) has the functional form for a slab that was discussed in Chapter 6:

$$CF(AT) = \frac{-\ln \alpha}{1 - \alpha} \tag{10-11}$$

where

$$\alpha = \exp\left[-\left(\frac{\mu^{\gamma}}{\cos\phi} + \mu^{x} \right) L \right] .$$

A measurement of the transmissions of the excitation and the fluoresced x rays can be used to determine α. For this method, a foil of the element being measured is placed behind the sample and the induced x-ray signal is measured with and without the sample. An additional measurement (see Figure 10.14) is made with the sample only (no foil), and α is computed from

$$\alpha = \frac{I_T - I_S}{I_0} \tag{10-12}$$

where I_T = fluoresced x-ray intensity with foil plus sample
I_S = fluoresced x-ray intensity with sample only
I_0 = fluoresced x-ray intensity with foil only.

This measurement includes the attenuation of the excitation source and of the induced x-ray signal. Although there are advantages to using the same element in the transmission foil as that being assayed, other elements can be used if their characteristic x rays are sufficiently close to those of the assay element. For example, thorium metal has been used successfully for the measurement of uranium solutions.

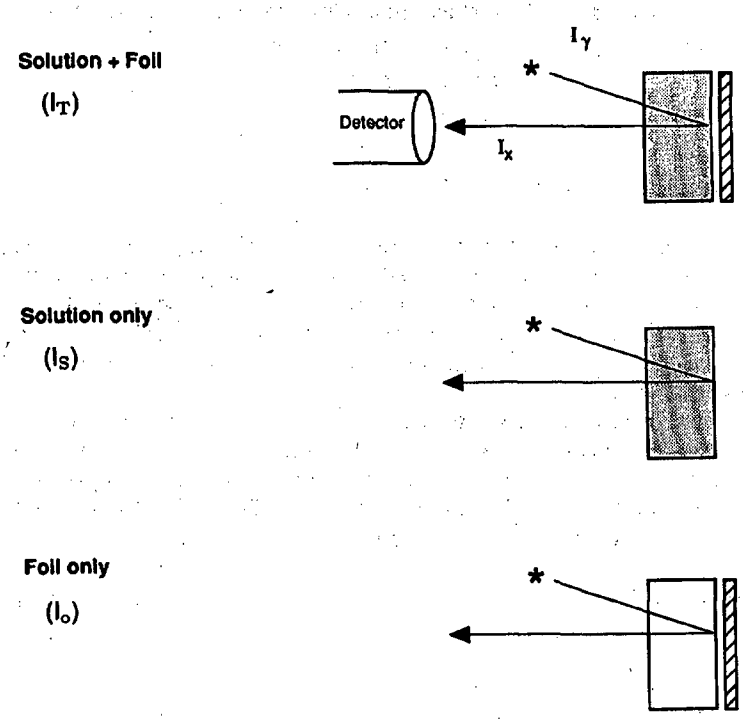

Fig. 10.14 Explanation of the three measurements required to determine the transmission for XRF assay of uranium solutions.

A suitable number of standards is needed to evaluate the calibration constant K in Equation 10-5. Equations 10-11 and 10-12 are exact only for a far-field geometry, and most XRF measurements are made in a near-field geometry. Therefore, even with rate and sample attenuation corrections, it is important to use several standards to evaluate the calibration constant K.

10.5 APPLICATIONS AND INSTRUMENTATION

Instrumentation used in XRF analysis is similar to that of other gamma-ray assay systems: detector, associated electronics, multichannel analyzer, and excitation source. This instrumentation is discussed in detail in Chapter 4.

XRF analysis has been used in analytical chemistry laboratories for many years. In most cases, an x-ray generator is used rather than a radioisotope as an excitation source. Low- to intermediate-Z elements are measured, and sample preparation is a key factor in the analysis. Many techniques require that the sample be homogenized and pressed prior to analysis. When the sample can be modified to optimize the assay, XRF analysis is very sensitive. Short count times (<1000 s) can yield accurate and precise data, with sensitivities in the nanogram range (Ref. 1). Complete XRF systems are available commercially.

Several XRF measurement techniques are used for materials containing uranium or plutonium. John et al. (Ref. 10) used a ^{57}Co source to excite uranium x rays in solutions and simultaneously observed the 185.7-keV gamma ray from ^{235}U as a measure of enrichment. The ratio of the fluoresced x-ray emission to the 185.7-keV gamma-ray intensity was found to be independent of uranium concentration in the 8- to 20-g/L range for enrichments of 0.4 to 4.5% ^{235}U. Accuracies of better than 1% were reported.

Rowson and Hontzeas (Ref. 11) proposed a Compton-scattering-based correction for sample attenuation to measure uranium ores. An annular 50-mCi ^{241}Am source was used to excite characteristic x rays from a molybdenum foil (~17.4 keV), which can only excite the L_{III} subshell in uranium. This considerably simplifies the L x-ray spectrum. Matrix corrections were determined from the ratio of the molybdenum K_α backscatter to the uranium L_α x rays. Canada and Hsue (Ref. 12) give a good theoretical description of this method and suggest an improvement that involves additional ratios using the K_β or L_β lines to further minimize matrix effects.

Baba and Muto (Ref. 13) used an x-ray generator to excite the L x-ray spectrum of uranium- and plutonium-bearing solutions. An internal standard was used to determine the matrix attenuation correction. A known and constant amount of lead nitrate was added to all solutions and the uranium or plutonium L_α x-ray activity was normalized to the rate of the lead L_α x ray. A linear calibration (to within 1% for uranium and 2% for plutonium) was obtained for 200-s measurements. The solution concentrations ranged from 0.1 to 200 g/L of uranium and up to 50 g/L of plutonium. Mixed uranium/plutonium solutions were also measured.

Karamanova (Ref. 14) investigated the use of beta-particle-induced XRF in addition to gamma-ray excitation for K XRF analysis of uranium and mixed uranium/thorium oxides. A ^{57}Co source was used for gamma-ray excitation, and a ^{90}Sr-^{90}Y source was used for beta-particle-induced fluorescence. Since the attenuation cross sections of the matrix and the heavy element are similar for beta-particle excitation, the volume of sample is essentially constant and the net x-ray signal is proportional to the concentration of the element being assayed. Samples with uranium concentrations of 0.5 to 88% were measured with precisions of 0.1%.

Several investigators have measured reprocessing plant solutions. These solutions can contain fission products and have high U/Pu ratios, making them very difficult to assay by passive techniques. They require either extensive chemical separations or a sensitive technique such as XRF. Pickles and Cate (Ref. 15) employed XRF using an x-ray generator. Samples with U/Pu ratios of up to 400 and fission product activities of 2 Ci/g were analyzed with a precision of 1% and an accuracy of 2% in the mass range of 1 to 58 μg using a 10-min count. The samples were evaporated onto a thin polycarbonate film to minimize sample attenuation. Figure 10.15 shows the instrumental configuration. The sample chamber contained titanium sheets on either side of the sample mount. X rays from the titanium provided a rate-loss correction. A magnetic beta-particle trap and a lead collimator were employed to reduce the passive signal at the detector.

Camp et al. (Refs. 16 and 17) use a ^{57}Co excitation source to fluoresce K x rays from uranium and plutonium in product streams at reprocessing plants. Total heavy element concentrations of 1 to 200 g/L are assayed using a nonlinear polynomial calibration. The self-attenuation correction uses the incoherently scattered 122-keV gamma rays from ^{57}Co (Ref. 16) or an actual transmission measurement using the 122-keV gamma ray (Ref. 17). In samples containing both uranium and plutonium, a passive count is made to correct for passive x-ray emission.

Andrew et al. (Ref. 18) investigated the feasibility of measuring uranium and uranium/thorium solutions with uranium concentrations of 10 to 540 g/L. For solutions containing both uranium and thorium, errors in the U/Th ratio were 0.4%. Uncertainties in concentration measurements were 0.5% for single element solutions and 1% for mixed solutions. This work was extended to uranium/plutonium solutions from reprocessing plants (Refs. 19 and 20). Uranium and plutonium solutions in the range of 1 to 10 g/L with a fission product activity of 100 μCi/mL were measured by tube-excited K XRF. The data analysis was similar to that used for uranium/thorium solutions, and the authors suggested combining K XRF and K-edge densitometry to obtain absolute element concentrations.

Ottmar et al. (Refs. 21 and 22) investigated the combination of K XRF and K-edge densitometry using an x-ray generator. The two techniques are complementary and produce a measurement system with a wide dynamic range. Light-water-reactor dissolver solutions with activities of $\sim$100 Ci/L and U/Pu ratios of $\sim$100 have been accurately measured with this system. The major component, uranium ($\sim$200 g/L), is determined using absorption-edge densitometry, whereas the U/Pu ratio is determined

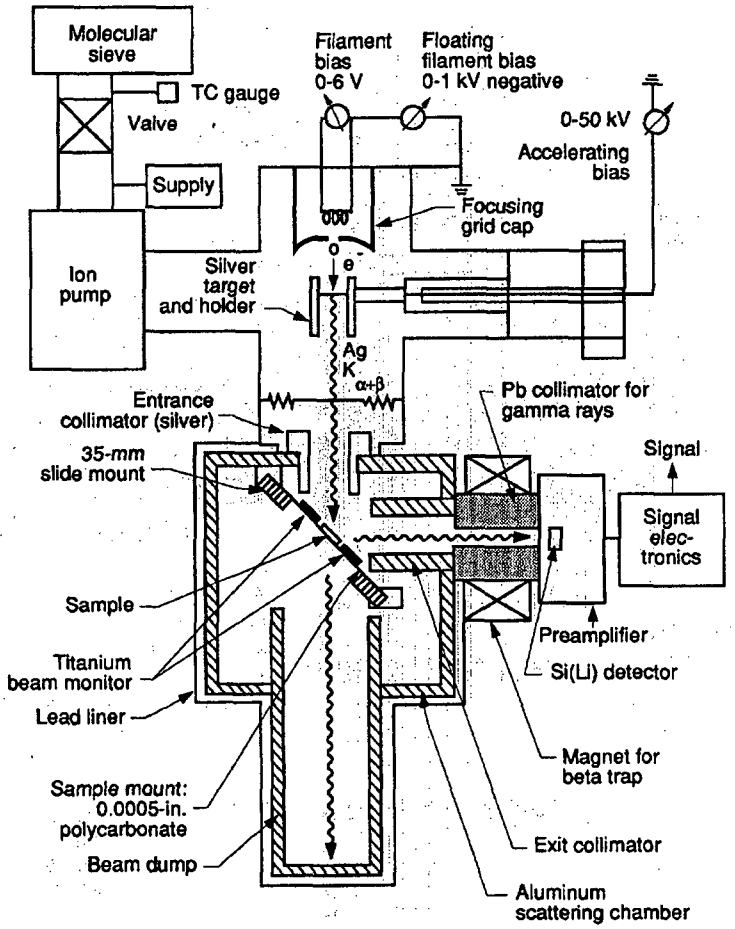

Fig. 10.15 *Schematic drawing of system used by Pickles and Cate (Ref. 15).*

by XRF. Precisions of 0.25% for the uranium concentration and 1% for the U/Pu ratio are obtained in 1000-s count times. Two sample cells are employed: a 2-cm glass cuvette (whose dimensions are known to ± 2 μm) for the densitometry measurement, and a 1-cm-diam polyethylene vial for the XRF measurement. The XRF measurement is made at a back angle of $\sim 157°$ in order to maximize the signal-to-background ratio. Figure 10.16 shows this hybrid system.

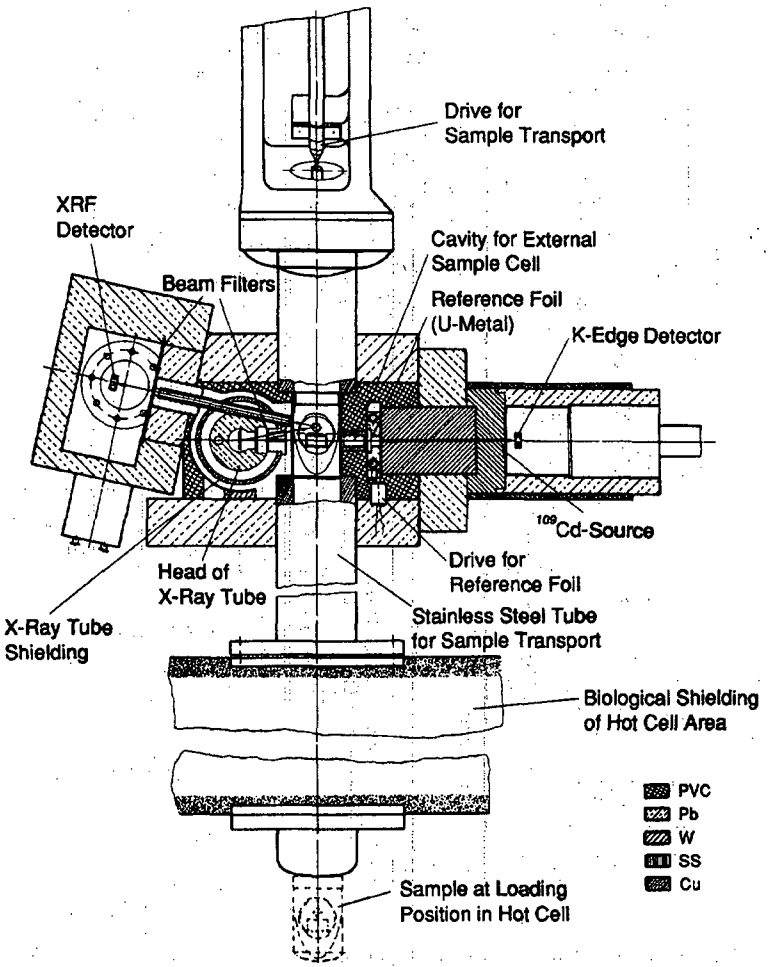

***Fig. 10.16** Schematic drawing of hybrid K-edge/K XRF system (Ref. 21). (Courtesy of H. Ottmar).*

Lambert et al. (Ref. 23) employed secondary-excitation L XRF to measure the U/Pu ratio in mixed-oxide fuel pellets. A pellet with 25% PuO_2 and 75% UO_2 gave a precision of about 0.5% in a 3-min count time. The desired x rays were excited using selectable secondary target foils (rhodium). The method requires good sample homogeneity because the portion of sample analyzed ($\sim$30-μm depth of analysis) is relatively small.

REFERENCES

1. E. P. Bertin, *Principles and Practice of X-Ray Spectrometric Analysis* (Plenum Press, New York, 1975).

2. R. Jenkins, R. W. Gould, and D. Gedcke, *Quantitative X-Ray Spectrometry* (Marcel Dekker, Inc., New York, 1981).

3. R. Tertian and F. Claisse, *Principles of Quantitative X-Ray Fluorescence Analysis* (Heyden & Son, Inc., Philadelphia, Pennsylvania, 1982).

4. R. Woldseth, *All You Ever Wanted to Know About XES* (Kevex Corp., Burlingame, California, 1973).

5. G. F. Knoll, *Radiation Detection and Measurement* (John Wiley & Sons, Inc., New York, 1979), p. 310.

6. P. Martinelli, "Possibilities of Plutonium Analysis by Means of X-Ray Fluorescence with an Iridium-192 Radioactive Source," *Analysis* 8 (10), 499–504 (1980).

7. R. Strittmatter, M. Baker, and P. Russo, "Uranium Solution Assay by Transmission-Corrected X-Ray Fluorescence," in "Nuclear Safeguards Research and Development Program Status Report, May–August 1978," Los Alamos Scientific Laboratory report LA-7616-PR (1979), pp. 23–24.

8. T. R. Canada, D. C. Camp, and W. D. Ruhter, "Single-Energy Transmission-Corrected Energy-Dispersive XRF for SNM-Bearing Solutions," Los Alamos National Laboratory document LA-UR-82-557.

9. P. Russo, M. P. Baker, and T. R. Canada, "Uranium-Plutonium Solution Assay by Transmission-Corrected X-Ray Fluorescence," in "Nuclear Safeguards Research and Development Program Status Report, September–December, 1977," Los Alamos Scientific Laboratory report LA-7211-PR (1978), pp. 22–28.

10. J. John, F. Sebesta, and J. Sedlacek, "Determination of Uranium Isotopic Composition in Aqueous Solutions by Combined Gamma Spectrometry and X-Ray Fluorescence," *Journal of Radioanalytical Chemistry* 78 (2), 367–374 (1983).

11. J. W. Rowson and S. A. Hontzeas, "Radioisotopic X-Ray Analysis of Uranium Ores Using Compton Scattering for Matrix Correction," *Canadian Journal of Spectroscopy* 22 (1), 24–30 (1977).

12. T. R. Canada and S.-T. Hsue, "A Note on the Assay of Special Nuclear Materials in Solution by X-Ray Fluorescence," *Nuclear Materials Management* XI (2), 91 (1982).

13. Y. Baba and H. Muto, "Determination of Uranium and Plutonium in Solution by Energy-Dispersive X-Ray Fluorescence Analysis," *Bunseki Kagaku* 32, T99–T104 (1983).

14. J. Karamanova, "Development of an Express NDA Technique (using radioisotopic sources) for the Concentration Measurements of Nuclear Materials, 1 November 1974-30 June 1977," International Atomic Energy Agency report IAEA-R-1557R (1977).

15. W. L. Pickles and J. L. Cate, Jr., "Quantitative Nondispersive X-Ray Fluorescence Analysis of Highly Radioactive Samples for Uranium and Plutonium Concentrations," Lawrence Livermore Laboratory report UCRL-7417 (1973).

16. D. C. Camp and W. D. Ruhter, "Nondestructive, Energy-Dispersive X-Ray Fluorescence Analysis of Product Stream Concentrations from Reprocessed Nuclear Fuels," in *Proc. American Nuclear Society Topical Conference on Measurement Technology for Safeguards and Materials Control*, Kiawah Island, South Carolina, November 26–28, 1979 (National Bureau of Standards, Washington, DC, 1980), p. 584.

17. D. C. Camp, W. D. Ruhter, and K. W. MacMurdo, "Determination of Actinide Process- and Product-Stream Concentrations Off-line or At-line by Energy-Dispersive X-Ray Fluorescence Analysis," in *Proc. Third Annual Symposium on Safeguards and Nuclear Materials Management*, Karlsruhe, Federal Republic of Germany, May 6-8, 1981 (European Safeguards Research and Development Association, Brussels, Belgium, 1981), p. 155.

18. G. Andrew, B. L. Taylor, and B. Metcalfe, "Estimation of Special Nuclear Materials in Solution by K X-ray Fluorescence and Absorption Edge Densitometry," United Kingdom Atomic Energy Authority report AERE-R9707 (1980).

19. G. Andrew and B. L. Taylor, "The Measurement of Pu and U in Reprocessing Plant Solutions by Tube-Excited K X-Ray Fluorescence," United Kingdom Atomic Energy Authority report AERE-R9864 (1980).

20. G. Andrew and B. L. Taylor, "The Feasibility of Using K-XRF for the On-line Measurement of Pu/U Ratios of Highly Active Dissolver Solutions," United Kingdom Atomic Energy Authority report AERE-M3134 (1980).

21. H. Ottmar, H. Eberle, P. Matussek, and I. Michel-Piper, "Qualification of K-Absorption Edge Densitometry for Applications in International Safeguards," International Atomic Energy report IAEA-SM-260/34 (1982).

22. H. Ottmar, H. Eberle, P. Matussek, and I. Michel-Piper, "How to Simplify the Analytics for Input-Output Accountabilty Measurements in a Reprocessing Plant," Kernforschungszentrum Karlsruhe report KfK 4012 (1986).

23. M. C. Lambert, M. W. Goheen, M. W. Urie, and N. Wynhoff, "An Automated X-Ray Spectrometer for Mixed-Oxide Pellets," Hanford Engineering Development Laboratory report HEDL-SA1492 (1978).

11

The Origin of Neutron Radiation

N. Ensslin

11.1 INTRODUCTION

The nuclear materials that are accounted for in the nuclear fuel cycle emit neutrons as well as gamma rays. For most isotopes the neutron emission rate is very low compared to the gamma-ray emission rate. For other isotopes the neutron emission rate is high enough to provide an easily measurable signal. If the sample of interest is too dense to permit the escape of gamma rays from its interior, then assay by passive neutron detection may be the preferred technique.

Neutrons are emitted from nuclear materials with a wide spectrum of energies. As they travel through matter, they interact and change their energy in a complex manner (see Chapter 12). However, neutron detectors (see Chapter 13) do not usually preserve information about the energy of the detected neutrons. Consequently, neutron assay consists of counting the number of emitted neutrons without knowing their specific energy. (This is in sharp contrast to gamma-ray assay, where gamma rays of discrete energy are emitted by specific radioactive isotopes.) How then can the assayist obtain a neutron signal that is proportional to the quantity of the isotope to be measured?

This chapter describes the production of neutrons by spontaneous fission, by neutron-induced fission, and by reactions with alpha particles or photons. In many cases these processes yield neutrons with unusually low or high emission rates, distinctive time distributions, or markedly different energy spectra. This information can be used to obtain quantitative assays of a particular isotope *if* the sample's isotopic composition is known and only a few isotopes are present.

The discussion of neutron radiation in this chapter emphasizes features that can be exploited by the assayist. Chapters 14 and 15 focus on total neutron counting techniques that exploit high emission rates or unusual energy spectra. Chapters 16 and 17 describe coincidence counting techniques based on neutron time distributions.

11.2 SPONTANEOUS AND INDUCED NUCLEAR FISSION

The spontaneous fission of uranium, plutonium, or other heavy elements is an important source of neutrons. An understanding of this complex process can be aided by visualizing the nucleus as a liquid drop (Figure 11.1). The strong, short-range nuclear forces act like a surface tension to hold the drop together against the electrostatic repulsion of the protons. In the heaviest elements the repulsive forces are so strong that the liquid drop is barely held together. There is a small but finite probability that the drop will deform into two droplets connected by a narrow neck (saddle point). The two

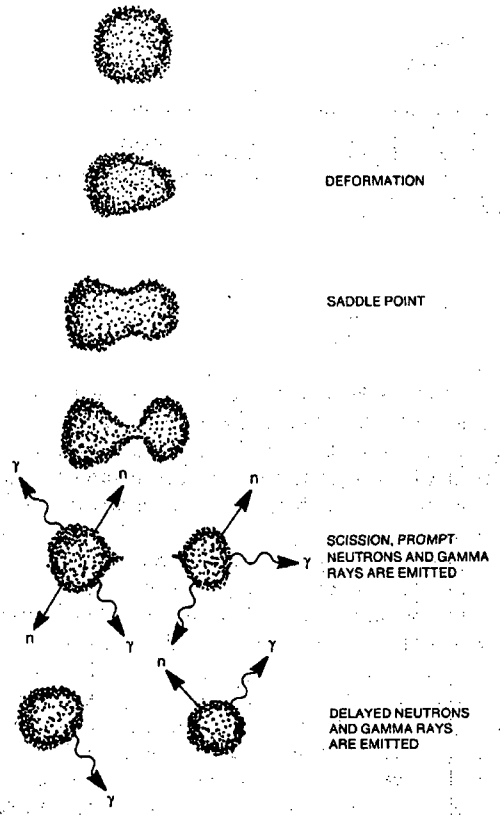

Fig. 11.1 Spontaneous fission of a nucleus represented as the breakup of a liquid drop.

droplets may spontaneously separate (scission) into two fragments. Within 10^{-13} s of scission, each of the two fragments emits a number of prompt neutrons and gamma rays. The fragments are usually unequal in size, with mass distributions centered near atomic numbers 100 and 140 (see Figure 18.2 in Chapter 18). These fission fragments carry away the majority of the energy released in fission (typically 170 MeV) in the form of kinetic energy. Also, within milliseconds or seconds, many of the fragments decay by beta-particle emission into other isotopes that may emit delayed neutrons or gamma rays.

Spontaneous fission is a quantum mechanical process involving penetration of a potential barrier. The height of the barrier, and hence the fission rate, is a very sensitive function of atomic number Z and atomic mass A. The fission yields of some heavy isotopes are summarized in Table 11-1 (Refs. 1 through 6). For thorium, uranium, and plutonium, the fission rate is low compared to the rate of decay by alpha-particle emission, which dominates the total half-life. For californium and even heavier elements, the fission rate can approach the alpha decay rate. The fission yield of ^{240}Pu, 1020 n/s-g (Refs. 4 and 5), is the most important single yield for passive neutron assay because ^{240}Pu is usually the major neutron-emitting plutonium isotope present.

Table 11-1. Spontaneous fission neutron yields

Isotope A	Number of Protons Z	Number of Neutrons N	Total Half-Life[a]	Spontaneous Fission Half-Life[b] (yr)	Spontaneous Fission Yield[b] (n/s-g)	Spontaneous Fission Multiplicity[b,c] ν	Induced Thermal Fission Multiplicity[c] ν
^{232}Th	90	142	1.41×10^{10} yr	$>1 \times 10^{21}$	$>6 \times 10^{-8}$	2.14	1.9
^{232}U	92	140	71.7 yr	8×10^{13}	1.3	1.71	3.13
^{233}U	92	141	1.59×10^{5} yr	1.2×10^{17}	8.6×10^{-4}	1.76	2.4
^{234}U	92	142	2.45×10^{5} yr	2.1×10^{16}	5.02×10^{-3}	1.81	2.4
^{235}U	92	143	7.04×10^{8} yr	3.5×10^{17}	2.99×10^{-4}	1.86	2.41
^{236}U	92	144	2.34×10^{7} yr	1.95×10^{16}	5.49×10^{-3}	1.91	2.2
^{238}U	92	146	4.47×10^{9} yr	8.20×10^{15}	1.36×10^{-2}	2.01	2.3
^{237}Np	93	144	2.14×10^{6} yr	1.0×10^{18}	1.14×10^{-4}	2.05	2.70
^{238}Pu	94	144	87.74 yr	4.77×10^{10}	2.59×10^{3}	2.21	2.9
^{239}Pu	94	145	2.41×10^{4} yr	5.48×10^{15}	2.18×10^{-2}	2.16	2.88
^{240}Pu	94	146	6.56×10^{3} yr	1.16×10^{11}	1.02×10^{3}	2.16	2.8
^{241}Pu	94	147	14.35 yr	(2.5×10^{15})	(5×10^{-2})	2.25	2.8
^{242}Pu	94	148	3.76×10^{5} yr	6.84×10^{10}	1.72×10^{3}	2.15	2.81
^{241}Am	95	146	433.6 yr	1.05×10^{14}	1.18	3.22	3.09
^{242}Cm	96	146	163 days	6.56×10^{6}	2.10×10^{7}	2.54	3.44
^{244}Cm	96	148	18.1 yr	1.35×10^{7}	1.08×10^{7}	2.72	3.46
^{249}Bk	97	152	320 days	1.90×10^{9}	1.0×10^{5}	3.40	3.7
^{252}Cf	98	154	2.646 yr	85.5	2.34×10^{12}	3.757	4.06

[a]Ref. 1.
[b]Ref. 2. Values in parentheses are from Ref. 3 and have estimated accuracies of two orders of magnitude. Pu-240 fission rate is taken from Refs. 4 and 5.
[c]Ref. 6.

The strong dependence of spontaneous fission rates on the number of protons and neutrons is important for assay considerations. The fission rate for odd-even isotopes is typically 10^3 lower than the rate for even-even isotopes, and the fission rate for odd-odd isotopes is typically 10^5 lower. These large differences are due to nuclear spin effects (Ref. 7). As the fissioning nucleus begins to deform, the total ground-state nuclear spin must be conserved. However, the quantized angular momentum orbits of the individual neutrons or protons have different energies with increasing deformation. The lowest energy orbit of the undeformed nucleus may not be the lowest energy orbit in the deformed nucleus. In the case of heavy even-even nuclei, whose total ground-state spin is zero, the outermost pairs of neutrons and protons can simultaneously couple their spins to zero while shifting to the lowest energy orbits. In the case of odd nuclei, a single neutron or proton must occupy the orbit that conserves total nuclear spin even though extra energy is required (Refs. 8 and 9). This effect raises the fission barrier and makes odd-even and odd-odd isotopes more rigid against spontaneous fission than even-even isotopes.

Among the even-even isotopes with high spontaneous fission yields are ^{238}U, ^{238}Pu, ^{240}Pu, ^{242}Pu, ^{242}Cm, ^{244}Cm, and ^{252}Cf. Isotopes with odd neutron numbers or odd proton numbers do not have high spontaneous fission yields, as described above. However, isotopes with odd neutron numbers can easily be induced to fission if bombarded with low-energy neutrons; absorption of an extra neutron yields an unbounded neutron pair whose pairing energy is now available to excite the compound nucleus to an energy near the fission barrier. Among the even-odd isotopes that can be fissioned by neutrons of zero energy but have low spontaneous fission yields are ^{233}U, ^{235}U, and ^{239}Pu. These isotopes are called "fissile." Even-even isotopes, such as ^{238}U and ^{240}Pu, that are not easily fissioned by low-energy neutrons are called "fertile." This term comes from reactor theory and refers to the fact that through neutron capture these isotopes are fertile sources of fissile isotopes. Examples of induced fission cross sections for fertile and fissile isotopes are given in Chapter 12.

11.3 NEUTRONS AND GAMMA RAYS FROM FISSION

Prompt neutrons and gamma rays emitted at the time of scission are the most useful for passive assay because of their intensity and penetrability. Many passive assay instruments, such as coincidence counters, are designed to detect prompt fission neutrons and are often also sensitive to gamma rays. For this reason this section describes both neutron and gamma-ray emissions.

Figure 11.2 shows an energy spectrum of the neutrons emitted during the spontaneous fission of ^{252}Cf (Refs. 10 and 11). The mean energy is 2.14 MeV. The spectrum depends on many variables such as fission fragment excitation energy and average total fission energy release, but can be approximated by a Maxwellian distribution N(E) where N(E) varies as $\sqrt{E}\exp(-E/1.43\ \text{MeV})$. This spectrum is proportional to $\sqrt{E}$ at low energies; it then falls exponentially at high energies. The neutron spectra for spontaneous fission of ^{240}Pu and thermal-neutron induced fission of ^{233}U, ^{235}U, and ^{239}Pu can also be approximated by Maxwellian distributions, with spectrum parameters 1.32, 1.31, 1.29, and 1.33 MeV, respectively (Refs. 12 and 13).

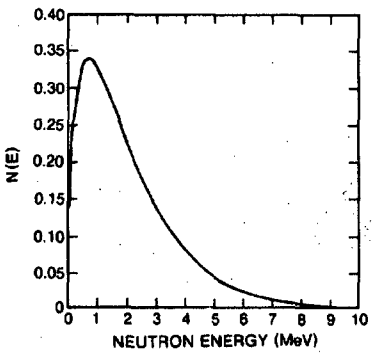

Fig. 11.2 *Prompt neutron spectrum from the spontaneous fission of ^{252}Cf, as calculated from a Maxwellian distribution with "temperature" T = 1.43 MeV.*

The number of neutrons emitted in spontaneous or induced fission is called the neutron multiplicity. Average neutron multiplicities $\bar{\nu}$ are included in the last two columns of Table 11-1. For neutron-induced fission the multiplicity increases slowly and linearly with the energy of the incoming neutron (Ref. 14). The multiplicities given in the last column of Table 11-1 are approximately correct for thermal- or low-energy incident neutrons.

From one fission to another the neutron multiplicity may vary from 0 to 6 or more, depending on the distribution of excitation energy among the fission fragments. Table 11-2 (Refs. 15, 16, and 17) lists the measured prompt neutron multiplicity distributions P(ν) of some important isotopes for spontaneous or thermal-neutron-induced fission. Uncertainties on the individual probabilities vary from 1 to 5% near the maxima to 30 to 50% near the end points. Terrell (Ref. 18) has shown that the multiplicity distributions for both spontaneous and thermal-neutron-induced fission can be approximated by a Gaussian distribution centered at $\bar{\nu}$, the mean multiplicity:

$$P(\nu) = \frac{1}{\sqrt{2\pi\sigma^2}} e^{-(\nu-\bar{\nu})^2/2\sigma^2} \tag{11-1}$$

A distribution width σ of 1.08 can be used as an approximation for all isotopes except ^{252}Cf, where 1.21 should be used.

Information about the neutron multiplicity distribution in fission is used in the analysis of coincidence counting (see Chapter 16). One question that has arisen in this regard is whether the neutron multiplicity and the mean neutron energy are correlated. In other words, if the number of neutrons emitted in a fission is above average, will the mean neutron energy be below average? The available experimental evidence indicates that the mean neutron emission energy is approximately constant and that the number of neutrons emitted increases with the amount of available energy (Ref. 19). Thus the mean energy may be approximately independent of the multiplicity.

After a nucleus undergoes fission, prompt neutrons are evaporated from the fission fragments until the remaining excitation energy is less than the neutron binding energy. At this point, prompt gamma rays carry away the remaining energy and angular momentum. On the average, 7 to 10 prompt gamma rays are emitted, with a total energy of 7 to 9 MeV (Ref. 7). Figure 11.3 shows the prompt gamma-ray spectrum accompanying spontaneous fission of ^{252}Cf, as recorded by a sodium iodide detector (Ref. 20). A

Table 11-2. Measured prompt fission multiplicity distributions

Probability Distribution	^{235}U Induced Fission[a]	^{238}Pu Spontaneous Fission[b,c]	^{239}Pu Induced Fission[a]	^{240}Pu Spontaneous Fission[a]	^{242}Pu Spontaneous Fission[a]	^{252}Cf Spontaneous Fission[a]
P(0)	0.033	0.054	0.011	0.066	0.068	0.002
P(1)	0.174	0.205	0.101	0.232	0.230	0.026
P(2)	0.335	0.380	0.275	0.329	0.334	0.127
P(3)	0.303	0.225	0.324	0.251	0.247	0.273
P(4)	0.123	0.108	0.199	0.102	0.099	0.304
P(5)	0.028	0.028	0.083	0.018	0.018	0.185
P(6)	0.003		0.008	0.002	0.003	0.066
P(7)						0.015
P(8)						0.002
$\bar{\nu}$	2.406	2.21	2.879	2.156	2.145	3.757
$\overline{\nu(\nu-1)}$	4.626	3.957	6.773	3.825	3.794	11.962
$\overline{\nu(\nu-1)(\nu-2)}$	6.862	5.596	12.630	5.336	5.317	31.812

[a]Ref. 15.
[b]Ref. 16.
[c]Ref. 17.

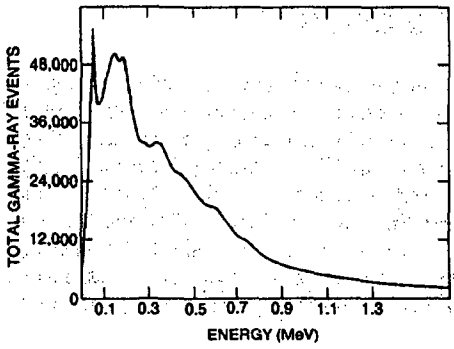

Fig. 11.3 Prompt gamma-ray spectrum accompanying spontaneous fission of ^{252}Cf, as recorded by a sodium iodide detector (Ref. 20).

spectrum obtained with a high-resolution detector might reveal many discrete transitions, although the transitions would be Doppler-broadened by the recoil of the fission fragments. Prompt gamma rays from fission are of much lower intensity than the gamma rays that follow alpha decay (see Chapter 1). Thus they are not useful for passive assay, despite their relatively high energy. However, prompt gamma rays from fission are useful for coincidence counting, where their high multiplicity can lead to a strong signal.

This section includes brief descriptions of the delayed neutrons and gamma rays emitted after fission. In passive assay systems the delayed neutrons and gamma rays are usually masked by the stronger prompt emissions. The time delay, however, is often used by active assay systems to discriminate between the interrogation source and the induced fission signal. For additional details on these delayed signals, see Ref. 21.

Delayed neutrons originate from some of the isotopes produced during beta decay of fission fragments. They are emitted by highly excited isotopes as soon as the isotopes are created by the beta decay of their precursors. Thus, delayed neutrons appear with half-lives characteristic of their precursors. Although there are many such isotopes, delayed neutrons can be categorized into six groups with decay half-lives ranging from 200 ms to 55 s (Ref. 22). The neutron yield of each group is different for each uranium or plutonium isotope. In principle, active assay systems can use this variation as an indication of the isotopic composition of the irradiated sample (Ref. 21), but in practice this use is difficult to implement. Delayed neutron energy spectra are highly structured, as opposed to the smooth Maxwellian distributions of prompt neutrons. Also, the average energy of delayed neutrons is only 300 to 600 keV, as opposed to the 2-MeV average of prompt neutrons. Most important, the number of delayed neutrons is typically only 1% of the number of prompt neutrons. Thus, delayed neutrons contribute to passive neutron measurements, but their effect is not large.

Delayed gamma rays from fission have a higher intensity and slower emission rate than delayed neutrons. Their average multiplicity and energy is comparable to that of prompt gamma rays: 6 to 8 gamma rays, each with an average energy close to 1 MeV. There is no clear-cut distinction between the emission time of prompt and delayed gamma rays as there is for prompt and delayed neutrons. Gozani (Ref. 21) has used a time of 10^{-9} s after fission as a convenient demarcation. The delayed gamma rays so defined are then emitted over times of several seconds or minutes. The intensity of these gamma rays is two orders of magnitude above the intensity of delayed neutrons.

11.4 NEUTRONS FROM (α,n) REACTIONS

Nuclei can decay spontaneously by alpha- or beta-ray emission as well as by fission. Alpha particles are helium nuclei with two protons and two neutrons, and beta particles are energetic free electrons. In principle, all nuclei of atomic mass greater than 150 are unstable towards alpha decay. However, alpha decay is a quantum mechanical barrier penetration process like spontaneous fission, and the Coulomb barrier is high enough to make alpha decay unlikely for all but the heaviest elements. Table 11-3 (Refs. 1, 2, and 23 through 25) lists the alpha decay rates of some heavy elements. The total half-lives of the isotopes listed in the table are almost the same as the alpha decay half-lives, except for ^{241}Pu and ^{249}Bk, where beta decay dominates, and ^{252}Cf, where the spontaneous fission rate is about 3% of the alpha decay rate.

The alpha decay process leads to the emission of gamma rays from unstable daughters (see Chapter 1). Also, the alpha particles can produce neutrons through (α,n) reactions with certain elements. This source of neutrons can be comparable in intensity to spontaneous fission if isotopes with high alpha decay rates such as ^{233}U, ^{234}U, ^{238}Pu, or ^{241}Am are present. This section describes the production of neutrons by (α,n) reactions and provides some guidelines for calculating the expected neutron yield.

Following are two examples of (α,n) reactions that occur in many nuclear fuel cycle materials:

$$\alpha + {}^{18}\mathrm{O} \rightarrow {}^{21}\mathrm{Ne} + \mathrm{n}$$

$$\alpha + {}^{19}\mathrm{F} \rightarrow {}^{22}\mathrm{Na} + \mathrm{n}$$

The alpha particle is emitted from uranium or plutonium with energies in the range of 4 to 6 MeV. Because ^{234}U is the dominant alpha emitter in enriched uranium, the average energy for alpha particles emitted from uranium is 4.7 MeV (see Table 11-3). For plutonium, an average energy of 5.2 MeV is typical. In air, the range of alpha particles from uranium is 3.2 cm and the range of alpha particles from plutonium is 3.7 cm. The range in other materials can be estimated from the Bragg-Kleeman rule (Ref. 26):

$$\text{range} = 0.00032 \frac{\sqrt{A}}{\text{density (g/cm}^3\text{)}} \times \text{range in air} \qquad (11\text{-}2)$$

where A is the atomic weight of the material. The range in uranium and plutonium oxide is roughly 0.006 cm and 0.007 cm, respectively. Thus the alpha particles lose energy very rapidly when traveling through matter. In many cases this short range means that the alpha particle can never reach nearby materials in which (α,n) reactions could take place. If, however, elements such as oxygen or fluorine are intimately mixed with the alpha-emitting nuclear material, an (α,n) reaction may take place because the alpha particle can reach these elements before it loses all its energy.

When the alpha particle arrives at another nucleus, the probability of a reaction depends on the Q-value, the threshold energy, and the height of the Coulomb barrier. The Q-value is the difference in binding energies between the two initial nuclei and the two final reaction products. A positive Q-value means that the reaction will release energy. A negative Q-value means that the alpha particle must have at least that much

Table 11-3. (Alpha,n) reaction neutron yields

Isotope A	Total Half-Life[a]	Alpha Decay Half-Life[a]	Alpha Yield[a] (α/s-g)	Average Alpha Energy[a] (MeV)	(α,n) Yield in Oxide[b] (n/s-g)	(α,n) Yield in UF_6/PuF_4[c] (n/s-g)
^{232}Th	1.41×10^{10} yr	1.41×10^{10} yr	4.1×10^{3}	4.00	2.2×10^{-5}	
^{232}U	71.7 yr	71.7 yr	8.0×10^{11}	5.30	1.49×10^{4}	2.6×10^{6}
^{233}U	1.59×10^{5} yr	1.59×10^{5} yr	3.5×10^{8}	4.82	4.8	7.0×10^{2}
^{234}U	2.45×10^{5} yr	2.45×10^{5} yr	2.3×10^{8}	4.76	3.0	5.8×10^{2}
^{235}U	7.04×10^{8} yr	7.04×10^{8} yr	7.9×10^{4}	4.40	7.1×10^{-4}	0.08
^{236}U	2.34×10^{7} yr	2.34×10^{7} yr	2.3×10^{6}	4.48	2.4×10^{-2}	2.9
^{238}U	4.47×10^{9} yr	4.47×10^{9} yr	1.2×10^{4}	4.19	8.3×10^{-5}	0.028
^{237}Np	2.14×10^{6} yr	2.14×10^{6} yr	2.6×10^{7}	4.77	3.4×10^{-1}	
^{238}Pu	87.74 yr	87.74 yr	6.4×10^{11}	5.49	1.34×10^{4}	2.2×10^{6}
^{239}Pu	2.41×10^{4} yr	2.41×10^{4} yr	2.3×10^{9}	5.15	3.81×10^{1}	5.6×10^{3}
^{240}Pu	6.56×10^{3} yr	6.56×10^{3} yr	8.4×10^{9}	5.15	1.41×10^{2}	2.1×10^{4}
^{241}Pu	14.35 yr	5.90×10^{5} yr	9.4×10^{7}	4.89	1.3	1.7×10^{2}
^{242}Pu	3.76×10^{5} yr	3.76×10^{5} yr	1.4×10^{8}	4.90	2.0	2.7×10^{2}
^{241}Am	433.6 yr	433.6 yr	1.3×10^{11}	5.48	2.69×10^{3}	
^{242}Cm	163 days	163 days	1.2×10^{14}	6.10	3.76×10^{6}	
^{244}Cm	18.1 yr	18.1 yr	3.0×10^{12}	5.80	7.73×10^{4}	
^{249}Bk	320 days	6.1×10^{4} yr	8.8×10^{8}	5.40	1.8×10^{1}	
^{252}Cf	2.646 yr	2.731 yr	1.9×10^{13}	6.11	6.0×10^{5}	

[a]Ref. 1.
[b]Ref. 2.
[c]UF_6, Refs. 23 and 24; PuF_4, Ref. 25.

energy in the center-of-mass reference frame before the reaction can proceed. If this minimum energy requirement is transformed to the laboratory reference frame, it is called the threshold energy:

$$\text{Threshold energy} = -Q(1 + 4/A) \text{ if Q is negative}$$
$$\text{Threshold energy} = 0 \text{ if Q is positive.} \quad (11\text{-}3)$$

The Coulomb barrier is the strength of the electrostatic repulsion that the alpha particle must overcome to enter the target nucleus and react.

$$\text{Coulomb barrier (MeV)} = \frac{Z_1 Z_2 e^2}{r_0 (A_1^{1/3} + A_2^{1/3})} \quad (11\text{-}4)$$

where $Z_1 = 2$, $A_1 = 4$, $e^2 = 1.44$ MeV-fm, $r_0 = 1.2$ fm, and Z_2 and A_2 refer to the target nucleus (Ref. 27). Thus, an (α,n) reaction is energetically allowed only if the alpha particle has enough energy to (1) overcome or penetrate the Coulomb barrier and (2) exceed the threshold energy. (Note that the two energy requirements are not additive.) Table 11-4 (Refs. 26 and 28) summarizes these properties for a series of low-mass isotopes.

Table 11-4 shows that (α,n) reactions with 5.2-MeV alpha particles are possible in 11 low-Z elements. In all elements with atomic number greater than that of chlorine, the reaction is energetically not allowed. The observed yield of neutrons from (α,n) reactions is given in Table 11-5 (Refs. 29 through 33) for thick targets. A thick target is a material that is much thicker than the range of the alpha particle and one in which the alpha particles lose energy only in the target element. From Equation 11-2, the range of alpha particles in solids is on the order of 0.01 cm.

(Alpha,n) reactions can occur in compounds of uranium or plutonium such as oxides or fluorides and in elements such as magnesium or beryllium that may be present as impurities. The neutron yield per gram of source nuclide in pure oxides and fluorides is given in the last two columns of Table 11-3. In other materials the yield will depend very sensitively on the alpha activity of the nuclear isotopes, the alpha particle energy, the reaction Q-values, the impurity concentrations, and the degree of mixing (because of the short range of the alpha particle).

Equations 11-5 through 11-7 give a prescription for estimating the (α,n) yield in uranium or plutonium oxides with impurities (perfect mixing is assumed). First, the yield in oxide is

$$Y_{oxide} = \sum_i M_i Y_i \quad (11\text{-}5)$$

where M_i is the mass in grams of the ith isotope and Y_i is the neutron yield per gram of each alpha-emitting isotope as given in Table 11-3. The summation over i should include ^{241}Am, which is a strong alpha emitter. The yields for compounds can also be estimated by multiplying the thick target yields in Table 11-5 by the reduction factor K (Refs. 34 and 35):

$$K = \frac{S_t N_t}{S_t N_t + S_\alpha N_\alpha} \quad (11\text{-}6)$$

Table 11-4. (Alpha,n) Q-values, threshold energies, and Coulomb barriers

Nucleus	Natural Abundance (%)	Q-Value[a] (MeV)	Threshold Energy[a] (MeV)	Coulomb Barrier (MeV)	Maximum Neutron Energy for 5.2-MeV Alpha[b]
^{4}He	100	−18.99	38.0	1.5	
^{6}Li	7.5	−3.70	6.32	2.1	
^{7}Li	92.5	−2.79	4.38	2.1	1.2
^{9}Be	100	+5.70	0	2.6	10.8
^{10}B	19.8	+1.06	0	3.2	5.9
^{11}B	80.2	+0.16	0	3.2	5.0
^{12}C	98.9	−8.51	11.34	3.7	
^{13}C	1.11	+2.22	0	3.7	7.2
^{14}N	99.6	−4.73	6.09	4.1	
^{15}N	0.4	−6.42	8.13	4.1	
^{16}O	99.8	−12.14	15.2	4.7	
^{17}O	0.04	+0.59	0	4.6	5.5
^{18}O	0.2	−0.70	0.85	4.6	4.2
^{19}F	100	−1.95	2.36	5.1	2.9
^{20}Ne	90.9	−7.22	8.66	5.6	
^{21}Ne	0.3	+2.55	0	5.5	7.6
^{22}Ne	8.8	−0.48	0.57	5.5	4.5
^{23}Na	100	−2.96	3.49	6.0	1.8
^{24}Mg	79.0	−7.19	8.39	6.4	
^{25}Mg	10.0	+2.65	0	6.4	7.7
^{26}Mg	11.0	+0.03	0	6.3	5.0
^{27}Al	100	−2.64	3.03	6.8	2.2
^{29}Si	4.7	−1.53	1.74	7.2	3.4
^{30}Si	3.1	−3.49	3.96	7.2	1.4
^{37}Cl	24.2	−3.87	4.29	8.3	1.0

[a]Ref. 28.
[b]Ref. 26.

where S_t and S_α are the rates at which the alpha particle loses energy in the target material and in the alpha-emitting isotope and N_t and N_α are the atom densities. Some values of the ratio S_α/S_t are given in Ref. 34.

The yield from elements that exist as impurities in the oxide can be estimated by computing the impurity element (α,n) yield relative to the oxide (α,n) yield. The approximation in Equation 11-7 ignores differences in alpha energy between isotopes and differences in target densities that result from the presence of impurities:

$$Y_{impurity} \approx Y_{oxide} \sum_j \frac{P_j A_O I_j S_j}{P_O A_j I_O S_i} \qquad (11\text{-}7)$$

where P_j is the (α,n) neutron yield in the impurity element, from Table 11-5. P_O is the yield in oxygen: 0.059 n/10^6 plutonium alpha particles or 0.040 n/10^6 uranium alpha particles. A_j is the atomic weight of the impurity element, and A_O = 16 for oxygen. I_j is

Table 11-5. Thick-target yields from (α,n) reactions (error bars estimated from scatter between references)

Element (Natural Isotopic Composition)	Neutron Yield per 10^6 Alphas of Energy 4.7 MeV (^{234}U)	Neutron Yield per 10^6 Alphas of Energy 5.2 MeV (av. Pu)	References	Av. Neutron Energy (MeV) for 5.2 MeV Alphas (Ref. 29)
Li	0.16 ± 0.04	1.13 ± 0.25	30	0.3
Be	44 ± 4	65 ± 5	31	4.2
B	12.4 ± 0.6	17.5 ± 0.4	29, 30, 33	2.9
C	0.051 ± 0.002	0.078 ± 0.004	29, 30, 31	4.4
O	0.040 ± 0.001	0.059 ± 0.002	29, 30, 31	1.9
F	3.1 ± 0.3	5.9 ± 0.6	29, 30, 33	1.2
Na	0.5 ± 0.5	1.1 ± 0.5	32	
Mg	0.42 ± 0.03	0.89 ± 0.02	29, 30, 31	2.7
Al	0.13 ± 0.01	0.41 ± 0.01	29, 30, 31	1.0
Si	0.028 ± 0.002	0.076 ± 0.003	29, 30, 31	1.2
Cl	0.01 ± 0.01	0.07 ± 0.04	32	

the impurity concentration expressed in parts per million (by weight) of oxide. I_O is the concentration of oxygen expressed in the same way, such as 118 000 ppm for PuO_2 or 154 000 ppm for high-enriched U_3O_8. The total yield from (α,n) reactions is then the sum of Equations 11-5 and 11-7.

The (α,n) yields in Table 11-5 are accurate to 5 to 10% for the best-measured elements. The oxide (α,n) yields in Table 11-3 are known to 10% or better. Thus, the neutron yield calculations are accurate to 10% at best, even with perfect mixing. In moist compounds, liquids, or gases, the estimates given are not valid.

The energy of the neutron emitted in an (α,n) reaction depends on the energy that the alpha particle has at the time of the reaction and on the Q-value of the reaction in the isotope. Average thick-target neutron energies are given in Table 11-5. Maximum neutron energies are given in the last column of Table 11-4. Several spectra are given in Figures 11.4 and 11.5 below.

Another important characteristic of neutrons from (α,n) reactions is that only one neutron is emitted in each reaction. These events constitute a neutron source that is random in time with a multiplicity of 1. This characteristic is exploited by neutron coincidence counters (Chapters 16 and 17), which can distinguish between spontaneous fission neutrons and neutrons from (α,n) reactions.

Note that both (α,n) and (α,p) reactions may leave the nucleus in an excited state, from which the nucleus decays to the ground state by emitting one or more gamma rays. For example:

$$^{19}F(\alpha,n)\,^{22}Na^* \xrightarrow{\gamma} {}^{22}Na \xrightarrow[2.6\ yr]{\beta^+} {}^{22}Ne^* \xrightarrow{\gamma\,(1275\ keV)} {}^{22}Ne$$

$$^{19}F(\alpha,p)\,^{22}Ne^* \xrightarrow{\gamma} {}^{22}Ne^* \xrightarrow{\gamma\,(1275\ keV)} {}^{22}Ne\ .$$

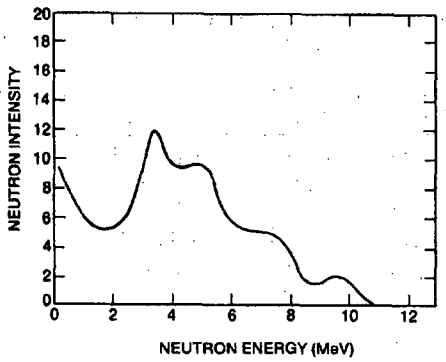

Fig. 11.4 *Typical neutron spectrum of an AmBe source.*

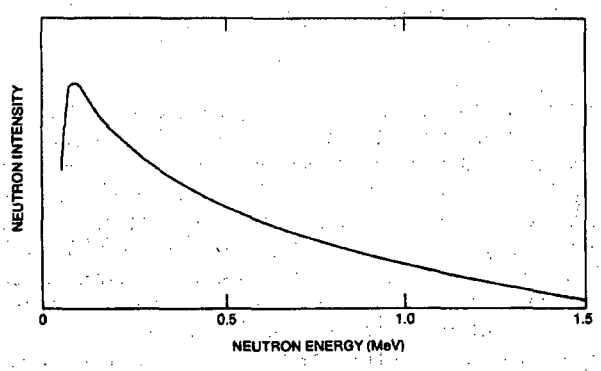

Fig. 11.5 *Typical neutron energy spectrum of an AmLi source.*

Here the asterisk refers to a nucleus in an excited state. Because many of the gamma rays from these reactions are of high energy and are often emitted nearly simultaneously with the neutron, they can affect the response of total neutron counters or neutron coincidence counters containing detectors that are sensitive to gamma rays.

11.5 NEUTRONS FROM OTHER NUCLEAR REACTIONS

Spontaneous fission, induced fission, and (α,n) reactions are the primary sources of neutrons observed in passive measurements. However, other reactions such as (γ,n), (n,n′), and (n,2n) may take place in the sample or detector assembly and contribute slightly to the observed count rate. This section describes these reactions briefly; examples are given in Table 11-6. These reactions are more important in active nondestructive assay measurements; details can be found in Ref. 21.

Table 11-6. Other nuclear reactions that may affect passive neutron counting

Radiation Source	Threshold Energy[a] (MeV)	Target Material	Reaction	Outgoing Radiation	Outgoing Energy[a]
Gamma	1.665	beryllium	(γ,n)	neutron	8(Eγ−1.665)/9 MeV
Gamma	2.224	deuterium	(γ,n)	neutron	(Eγ−2.224)/2 MeV
Neutron	0	hydrogen	(n,γ)	gamma	2.224 MeV
Proton	1.880	lithium-7	(p,n)	neutron	≥30 keV
Proton	1.019	tritium	(p,n)	neutron	≥0 keV
Neutron	0.1-1.0	lead	(n,n′)	neutron	
Neutron	0.1-1.0	tungsten	(n,n′)	neutron	
Neutron	0.1-1.0	uranium	(n,n′)	neutron	
Neutron	1.851	beryllium	(n,2n)	neutrons	
Neutron	3.338	deuterium	(n,2n)	neutrons	
Neutron	5.340	tungsten	(n,2n)	neutrons	

[a]Ref. 28.

The (γ,n) reaction can produce neutrons in any element if the gamma-ray energy is high enough. The typical minimum threshold energy (~8 MeV) is much higher than the energies of gamma rays emitted from radioactive nuclides. However, the (γ,n) threshold energies for beryllium (1.66 MeV) and deuterium (2.22 MeV) are anomalously low. Thus, it is possible to create a photoneutron source by surrounding relatively intense, long-lived, high-energy gamma-ray sources such as ^{124}Sb or ^{226}Ra with a mantle of beryllium or D_2O. A detailed list of photoneutron sources is given in Table 4.3 of Ref. 21. For passive assay applications it is only necessary to keep in mind that prompt fission gamma rays or gamma rays from some (α,n) reactions can produce extra neutrons if the detector assembly contains beryllium or deuterium. Or, conversely, neutrons can be captured in hydrogen to produce deuterium and 2.22-MeV gamma rays. These possibilities are included in Table 11-6.

Inelastic neutron scattering (n,n′) can occur in heavy nuclei with neutron energies of roughly 0.1 to 1.0 MeV or higher. This reaction is possible if the target nucleus has energy levels low enough to be excited by the neutron. The probability of this reaction is not high, and the number of neutrons present is not altered. However, the average energy of neutrons in the material will decline somewhat faster than would be expected from elastic scattering alone.

The (n,2n) reaction can increase the number of neutrons present, but the threshold energy in most elements is in the range of 10 MeV. For deuterium, beryllium, and tungsten the thresholds are lower, but the number of extra neutrons produced is likely to be small. The possibility of (n,2n) reactions should be considered only when the neutrons are known to have high energy, when deuterium, beryllium, or tungsten are present, and when the coincidence count rates to be measured are very low. In such cases the observed response may be enhanced.

11.6 ISOTOPIC NEUTRON SOURCES

Compact, portable neutron sources are useful for laboratory work, for verifying the proper operation of assay instruments, or for irradiating samples to obtain other induced signals. For accountability or safety purposes it is often important to have sources that contain little or no plutonium or uranium. Such sources can be manufactured by using other isotopes that emit neutrons by spontaneous fission or by taking advantage of (α,n) reactions between strong alpha-particle-emitting isotopes and low-Z materials.

Californium-252 is the most commonly used spontaneous fission neutron source; it can be fabricated in very small sizes and still provide a strong source for a practical period of time. Table 11-7 summarizes some of the properties of ^{252}Cf; Figures 11.2 and 11.3 give the prompt neutron and gamma-ray spectra. For some applications it is important to remember that ^{252}Cf neutrons are emitted with an average multiplicity of 3.757. Thus they are strongly correlated in time and will generate coincidence events.

Sources that emit random, uncorrelated neutrons can be manufactured by mixing alpha emitters such as ^{238}Pu or ^{241}Am with beryllium, lithium, fluorine, or other elements in which (α,n) reactions are possible. Table 11-8 (Refs. 1, 26, and 36) summarizes the characteristics of some common (α,n) sources. One important feature for practical applications is the half-life of the heavy element that emits the alpha particles. The sources listed in Table 11-8 all have long half-lives, with the exception of $^{210}PoBe$. Another important feature is the neutron energy spectrum obtained from the source. In some cases it is important to have a high-energy, highly penetrating neutron source. In other cases it may be important to avoid neutron energies high enough to fission plutonium or uranium isotopes (that is, the source must provide subthreshold interrogation) or high enough to excite (n,2n) reactions.

Table 11-7. Characteristics of ^{252}Cf

Total half-life	2.646 yr
Alpha half-life	2.731 yr
Spontaneous fission half-life	85.5 yr
Neutron yield	2.34×10^{12} n/s-g
Gamma-ray yield	1.3×10^{13} γ/s-g
Alpha-particle yield	1.9×10^{13} α/s-g
Average neutron energy	2.14 MeV
Average gamma-ray energy	1 MeV
Average alpha-particle energy	6.11 MeV
Neutron activity	4.4×10^{9} n/s-Ci
Neutron dose rate	2300 rem/h-g at 1 m
Gamma dose rate	140 rem/h-g at 1 m
Conversion	558 Ci/g
Decay heat	38.5 W/g
Avg. spontaneous fission neutron multiplicity	3.757
Avg. spontaneous fission gamma multiplicity	8

Table 11-8. Characteristics of some isotopic (α,n) sources

Source	Half-Life[a] (yr)	Average Alpha Energy[a] (MeV)	Average Neutron Energy[a] (MeV)	Maximum Neutron Energy[b] (MeV)	Gamma Dose in mrem/h at 1 m/(10^6 n/s)[c]	Curies per Gram[d]	Yield in 10^6 n/s-Ci[c]
^{210}PoBe	0.38	5.3	4.2	10.9	0.01	4490	2-3
^{226}RaBe	1600	4.8	4.3	10.4	60	1	0-17
^{238}PuBe	87.74	5.49	4.5	11.0	0.006	17	2-4
^{238}PuLi	87.74	5.49	0.7	1.5	~1	17	0.07
$^{238}PuF_4$	87.74	5.49	1.3	3.2	~1	17	0.4
$^{238}PuO_2$	87.74	5.49	2.0	5.8	~1	17	0.003
^{239}PuBe	24 120.	5.15	4.5	10.7	6	0.06	1-2
$^{239}PuF_4$	24 120.	5.15	1.4	2.8	~1	0.06	0.2
^{241}AmBe	433.6	5.48	5.0	11.0	6	3.5	2-3
^{241}AmLi	433.6	5.48	0.3	1.5	2.5	3.5	0.06
^{241}AmB	433.6	5.48	2.8	5.0		3.5	
^{241}AmF	433.6	5.48	1.3	2.5		3.5	

[a]Ref. 1.
[b]Ref. 26.
[c]Ref. 36.
[d](Alpha yield/s-g)/(3.7×10^{10} dps/Ci).

Two common (α,n) sources in use today are ^{241}AmBe and ^{241}AmLi. Typical neutron energy spectra for these two sources are given in Figures 11.4 and 11.5. The energy spectra can vary somewhat because of impurity elements or imperfect mixing. [Also, (α,n) spectra can change their shape somewhat in time, depending on the source construction and the particular isotopes involved.] Note that AmLi sources are usually fabricated by mixing $^{241}AmO_2$ with lithium oxide and that (α,n) reactions in the oxide contribute a high-energy tail to the spectrum.

The ^{241}AmBe sources are compact and relatively inexpensive and do not require much gamma-ray shielding. However, the high-energy spectrum permits (n,2n) reactions that will produce coincidence counts. The ^{241}AmLi sources are less compact and more expensive and require tungsten shields. Because of their low-energy neutron spectra, they are the most widely used sources for subthreshold interrogation in active assay and for random-neutron check sources in passive coincidence counting. For the latter application it is important to be aware of the possibility of plutonium contamination in the americium, which can yield spurious coincidence counts from spontaneous fission.

(Alpha,n) sources also emit gamma and beta radiation, and in many cases the dose observed outside the container is dominated by gamma radiation. (For comparison, the dose from 10^6 n/s is about 1 mrem/h at 1 m.) The neutron yield of an (α,n) source relative to its total radiation output in curies may thus be an important selection criterion. This ratio is given in the last column of Table 11-8. Because of their high gamma-ray output, some (α,n) sources should be encapsulated in shielding material. For example, ^{241}AmLi sources are enclosed in 1/4- to 3/8-in.-thick tungsten to shield against the intense 60-keV gamma rays from americium decay.

11.7 CONCLUSIONS

What properties of neutron radiation can be used by the assayist to measure the quantity of specific isotopes? Several important features are summarized below:

1. The odd-even effect in spontaneous fission means that only fertile isotopes like ^{238}U, ^{238}Pu, ^{240}Pu, and ^{242}Pu are strong emitters of high-energy (2-MeV average) neutrons. For metallic samples of plutonium the total neutron emission rate is usually directly related to the masses of the even isotopes that are present. This is also true for metallic uranium, although kilogram quantities are required for practical assays because of the lower neutron emission rate.
2. The prompt neutron multiplicity (ν = 2 to 3) means that coincidence counting techniques can provide a nearly unique signature for the presence of the even isotopes. However, the multiplicity does not vary enough from one isotope to another to permit discrimination between them.
3. The detection of prompt fission gamma rays along with the neutrons can greatly enhance instrument sensitivity. However, the different behavior of neutrons and gamma rays in the sample matrix and in the detector increases the difficulty of relating the measured response to the sample mass. Therefore, this approach is not recommended for most applications. The use of prompt gamma rays alone is an almost untouched field, but relating measured response to sample mass is again likely to be a difficult problem.

4. Delayed neutron yields are too low for passive assay. Delayed gamma rays are usually not detected by neutron detectors, but they contribute to the response of scintillators. Both delayed neutrons and delayed gamma rays are very important for active assay but not for passive assay.
5. Fissile isotopes like ^{235}U and ^{239}Pu are assayed either by active techniques or indirectly by passive assay of adjacent fertile isotopes if the isotopic composition of the sample is known.
6. (Alpha,n) reactions allow good passive assays of compounds such as $^{238}PuO_2$ and $^{234}UF_6$. Again, the quantity of other isotopes can be inferred from the known isotopic composition. (Alpha,n) reactions can also yield unwanted passive emissions that complicate the assay. Neutron coincidence counting is often used to discriminate against (α,n) reactions.

The principles and applications of these techniques are described in Chapters 14 through 17.

REFERENCES

1. C. M. Lederer and V. S. Shirley, Eds., *Table of Isotopes*, 7th ed. (John Wiley & Sons, Inc., New York, 1978).

2. R. T. Perry and W. B. Wilson, "Neutron Production from (α,n) Reactions and Spontaneous Fission in ThO_2, UO_2, and $(U,PU)O_2$ Fuels," Los Alamos National Laboratory report LA-8869-MS (June 1981).

3. D. L. Johnson, "Evaluation of Neutron Yields from Spontaneous Fission of Transuranic Isotopes," *Transactions of the American Nuclear Society* 22, 673 (1975).

4. P. Fieldhouse, D. S. Mather, and E. R. Culliford, "The Spontaneous Fission Half-Life of ^{240}Pu," *Journal of Nuclear Energy* 21, 749 (1967).

5. C. Budtz-Jorgensen and H. H. Knitter, "Neutron-Induced Fission Cross Section of Plutonium-240 in the Energy Range from 10 keV to 10 MeV," *Nuclear Science and Engineering* 79, 380 (1981).

6. Evaluated Nuclear Data File ENDF/B-V (available from and maintained by the National Nuclear Data Center at Brookhaven National Laboratory).

7. E. K. Hyde, *The Nuclear Properties of the Heavy Elements, III, Fission Phenomena* (Dover Publications, New York, 1971).

8. J. O. Newton, "Nuclear Properties of the Very Heavy Elements," *Progress in Nuclear Physics* 4, 234 (1955).

9. J. A. Wheeler, in *Niels Bohr and the Development of Physics* (Pergamon Press, London, 1955), p. 166.

10. J. W. Boldeman, D. Culley, and R. Cawley, "The Fission Neutron Spectrum from the Spontaneous Fission of ^{252}Cf," *Transactions of the American Nuclear Society* 32, 733 (1979).

11. W. P. Poenitz and T. Tamura, "Investigation of the Prompt Neutron Spectrum for Spontaneously-Fissioning ^{252}Cf," Proc. Int. Conf. Nucl. Data Sci. Technol., Antwerp, Belgium, Sept. 1982, p. 465.

12. D. G. Madland and J. R. Nix, "New Calculation of Prompt Fission Neutron Spectra and Average Prompt Neutron Multiplicities," *Nuclear Science and Engineering* 81, 213 (1982).

13. J. Terrell, "Neutron Yields from Individual Fission Fragments," *Physical Review* 127, 880 (1962).

14. W. G. Davey, "An Evaluation of the Number of Neutrons Per Fission for the Principal Plutonium, Uranium, and Thorium Isotopes," *Nuclear Science and Engineering* 44, 345 (1971).

15. J. W. Boldeman and M. G. Hines, "Prompt Neutron Emission Probabilities Following Spontaneous and Thermal Neutron Fission," *Nuclear Science and Engineering*, 91, 114 (1985).

16. D. A. Hicks, J. Ise, and R. Pyle, *Physical Review* 101, 1016 (1956).

17. M. S. Zucker and N. Holden, "Parameters for Several Plutonium Nuclides and ^{252}Cf of Safeguards Interest," Proc. Sixth Annual Symp. ESARDA, Venice, 1984, p. 341.

18. J. Terrell, "Distribution of Fission Neutron Numbers," *Physical Review* 108, 783 (1957).

19. A. Gavron and Z. Fraenkel, "Neutron Correlations in Spontaneous Fission of ^{252}Cf," *Physical Review C* 9, 623 (1974).

20. H. R. Bowman, S. G. Thompson, and J. O. Rasmussen, "Gamma-Ray Spectra from Spontaneous Fission of ^{252}Cf," *Physical Review Letters* 12 (8), 195 (1964).

21. T. Gozani, *Active Nondestructive Assay of Nuclear Materials, Principles and Applications*, NUREG/CR-0602 (US Nuclear Regulatory Commission, Washington, DC, 1981).

22. G. R. Keepin, *Physics of Nuclear Kinetics* (Addison-Wesley Publishing Co., Inc., Reading, Massachusetts, 1965).

23. T. E. Sampson, "Neutron Yields from Uranium Isotopes in Uranium Hexafluoride," *Nuclear Science and Engineering* 54, 470 (1974).

24. W. B. Wilson, J. E. Stewart, and R. T. Perry, "Neutron Production in UF_6 from the Decay of Uranium Nuclides," *Transactions of the American Nuclear Society* 38, 176 (1981).

25. W. B. Wilson, Los Alamos National Laboratory memorandum T-2-M-1432, to N. Ensslin (1983).

26. R. D. Evans, *The Atomic Nucleus* (McGraw-Hill Book Co., New York, 1955).

27. J. B. Marion and F. C. Young, *Nuclear Reaction Analysis* (John Wiley & Sons, Inc., New York, 1968), p. 108.

28. R. J. Howerton, "Thresholds and Q-Values of Nuclear Reactions Induced by Neutrons, Protons, Deuterons, Tritons, ^{3}He Ions, Alpha Particles, and Photons," Lawrence Livermore National Laboratory report UCRL-50400, V24 (1981).

29. G. J. H. Jacobs and H. Liskien, "Energy Spectra of Neutrons Produced by Alpha Particles in Thick Targets of Light Elements," *Annals of Nuclear Energy* 10, 541 (1983).

30. J. K. Bair and J. Gomez del Campo, "Neutron Yields from Alpha-Particle Bombardment," *Nuclear Science and Engineering* 71, 18 (1979).

31. D. West and A. C. Sherwood, "Measurements of Thick-Target (α,n) Yields from Light Elements," *Annals of Nuclear Energy* 9, 551 (1982).

32. J. Roberts, "Neutron Yields of Several Light Elements Bombarded with Polonium Alpha Particles," U.S. AEC report MDDC-731 (1947).

33. W. B. Wilson and R. T. Perry, "Thick-Target Neutron Yields in Boron and Fluorine," Los Alamos National Laboratory memorandum T-2-M-1835 to N. Ensslin (1987).

34. M. E. Anderson and J. F. Lemming, "Selected Measurement Data for Plutonium and Uranium," Mound Laboratory report MLM-3009 (1982).

35. D. West, "The Calculation of Neutron Yields in Mixtures and Compounds from the Thick Target (α,n) Yields in the Separate Constituents," *Annals of Nuclear Energy* 6, 549 (1979).

36. Joint Publication Research Center, *Neutron Sources*, JPRS-48421 (Washington, DC, July 1969).

12

Neutron Interactions with Matter

P. Rinard

12.1 INTRODUCTION

How neutrons interact with matter affects the ways in which assays can be performed with neutrons. Neutron interactions with the assay material affect the interpretation of neutron measurements and limit the amount of fissile material the assay instrument can contain safely. A neutron detector is based on some neutron interaction with the material in the detector. Also, neutron interactions with shielding materials are necessary to protect radiation workers.

This chapter provides fundamental information about neutron interactions that are important to nuclear material measurements. The first section describes the interactions on the microscopic level where individual neutrons interact with other particles and nuclei. The concepts are then extended to macroscopic interactions with bulk compound materials.

12.2 MICROSCOPIC INTERACTIONS

12.2.1 The Cross-Section Concept

The probability of a particular event occurring between a neutron and a nucleus is expressed through the concept of the cross section. If a large number of neutrons of the same energy are directed into a thin layer of material, some may pass through with no interaction, others may have interactions that change their directions and energies, and still others may fail to emerge from the sample. There is a probability for each of these events. For example, the probability of a neutron not emerging from a sample (that is, of being absorbed or captured) is the ratio of the number of neutrons that do not emerge to the number originally incident on the layer. The cross section for being absorbed is the probability of neutrons being absorbed divided by the areal atom density (the number of target atoms per unit area of the layer). The cross section thus has the dimensions of area; it must be a small fraction of a square centimeter because of the large number of atoms involved. Because this type of cross section describes the probability of neutron interaction with a single nucleus, it is called the microscopic cross section and is given the symbol σ. (A macroscopic cross section for use with bulk matter is defined in Section 12.3.)

Another approach to understanding the concept of the microscopic cross section is to consider the probability of a single neutron attempting to pass through a thin layer of

material that has an area A and contains N target nuclei, each of cross-sectional area s. The sum of all the areas of the nuclei is Ns. The probability of a single neutron hitting one of these nuclei is roughly the ratio of the total target area Ns to the area of the layer A. In other words, the probability of a single neutron having a collision with a nucleus is Ns/A or (N/A)s, the areal target density times s. On the atomic level, however, cross sections for neutron interactions are not simply the geometrical cross-sectional area of the target. By replacing this s by the σ of the preceding paragraph, σ might be thought of as an effective cross-sectional area for the interaction. The cross section for the interaction retains the dimensions of area that s had.

The physical cross-sectional area s of a heavy nucleus is about 2×10^{-24} cm^2. Interaction cross sections for most nuclei are typically between 10^{-27} and 10^{-21} cm^2. To avoid the inconvenience of working with such small numbers, a different unit of area is used: the barn, denoted by the symbol b. It is defined to be 10^{-24} cm^2, so that the physical cross-sectional area of a heavy nucleus is about 2 b. Many neutron interaction cross sections range between 0.001 and 1000 b.

Each type of event has its own probability and cross section. The probability of each type of event is independent of the probabilities of the others, so the total probability of any event occurring is the sum of the individual probabilities. Similarly, the sum of all the individual cross sections is the total cross section.

12.2.2 The Energy-Velocity Relationship for Neutrons

Cross-section magnitudes are strong functions of neutron energy, as discussed in Section 12.2.4. As a preliminary to that discussion, this section describes the relationship between neutron energy and velocity. This connection is important not only for understanding cross sections but also for estimating the time that neutrons are present in regions such as those found in assay instruments.

The classical expression for kinetic energy, $E = mv^2/2$, is sufficiently accurate because even a kinetic energy of 100 MeV is still only about one-tenth of the rest-mass energy of a neutron (939.55 MeV). For velocity v in meters per second and kinetic energy E in MeV,

$$E = 5.227 \times 10^{-15} v^2 \tag{12-1}$$

and

$$v = 1.383 \times 10^7 E^{1/2}. \tag{12-2}$$

Figure 12.1 shows a graph of these equations for ready use. The graph shows, for example, that a 1-MeV neutron has a speed of 1.383×10^7 m/s and therefore will cross a 15-cm sample region in a typical assay instrument in about 11 ns. A thermal neutron with an energy of 0.025 eV (see Section 12.2.3) has a speed of 2187 m/s and will cross the same 15-cm region in about 70 μs.

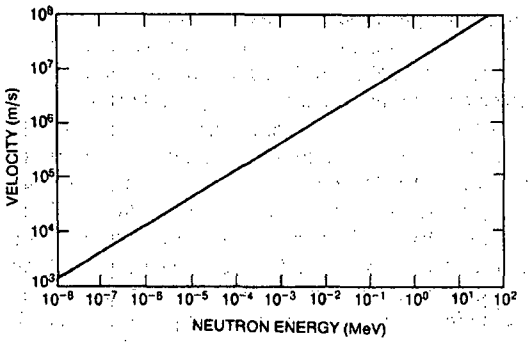

Fig. 12.1 *Graph showing the relationship between a neutron's speed and its kinetic energy.*

12.2.3 Types of Interactions

A neutron can have many types of interactions with a nucleus. Figure 12.2 shows the types of interactions and their cross sections. Each category of interaction in the figure consists of all those linked below it. The total cross section σ_t expresses the probability of any interaction taking place.

A simple notation can be used to give a concise indication of an interaction of interest. If a neutron n impinges on a target nucleus T, forming a resultant nucleus R and the release of an outgoing particle g, this interaction is shown as T(n,g)R. The heavy nuclei are shown outside the parentheses. To denote a type of interaction without regard for the nuclei involved, only the portion in parentheses is shown. An example of an (n,p) reaction is $^{5}B(n,p)^{5}Be$.

An interaction may be one of two major types: scattering or absorption. When a neutron is scattered by a nucleus, its speed and direction change but the nucleus is left with the same number of protons and neutrons it had before the interaction. The nucleus will have some recoil velocity and it may be left in an excited state that will lead to the eventual release of radiation. When a neutron is absorbed by a nucleus, a wide range of radiations can be emitted or fission can be induced.

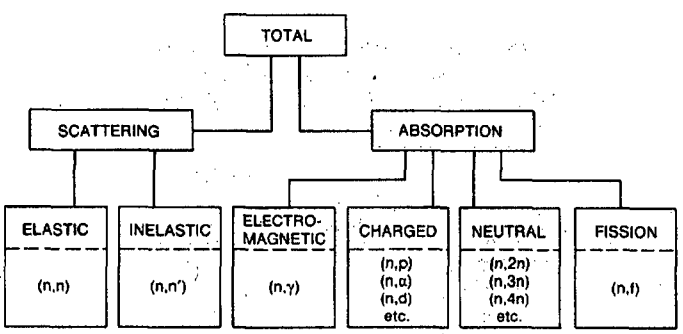

Fig. 12.2 *Various categories of neutron interactions. The letters separated by commas in the parentheses show the incoming and outgoing particles.*

Scattering events can be subdivided into elastic and inelastic scattering. In elastic scattering, the total kinetic energy of the neutron and nucleus is unchanged by the interaction. During the interaction, a fraction of the neutron's kinetic energy is transferred to the nucleus. For a neutron of kinetic energy E encountering a nucleus of atomic weight A, the average energy loss is $2EA/(A+1)^2$. This expression shows that in order to reduce the speed of neutrons (that is, to moderate them) with the fewest number of elastic collisions, target nuclei with small A should be used. By using hydrogen, with A = 1, the average energy loss has its largest value of E/2. A neutron with 2 MeV of kinetic energy will (on the average) have 1 MeV left after one elastic collision with a hydrogen nucleus, 0.5 MeV after a second such collision, and so on. To achieve a kinetic energy of only 0.025 eV would take a total of about 27 such collisions. (A neutron of energy 0.025 eV is roughly in thermal equilibrium with its surrounding medium and is considered a "thermal neutron." From the relation E = kT where k is Boltzmann's constant, an energy E of 0.025 eV corresponds to a temperature T of 20°C.) In general, after n elastic collisions, the neutron's energy is expected to change from E_0 to $E_n = E_0[(A^2+1)/(A+1)^2]^n$. To reach E_n from E_0 thus requires $n = \log(E_n/E_0)/\log[(A^2+1)/(A+1)^2]$ collisions, on the average. Table 12-1 gives examples of the number of collisions required to "thermalize" a 2-MeV neutron in some materials.

Inelastic scattering is similar to elastic scattering except that the nucleus undergoes an internal rearrangement into an excited state from which it eventually releases radiation. The total kinetic energy of the outgoing neutron and nucleus is less than the kinetic energy of the incoming neutron; part of the original kinetic energy is used to place the nucleus into the excited state. It is no longer easy to write an expression for the average energy loss because it depends on the energy levels within the nucleus. But the net effect on the neutron is again to reduce its speed and change its direction. If all the excited states of the nucleus are too high in energy to be reached with the energy available from the incoming neutron, inelastic scattering is impossible. In particular, the hydrogen nucleus does not have excited states, so only elastic scattering can occur in that case. In general, scattering moderates or reduces the energy of neutrons and provides the basis for some neutron detectors (for example, proton recoil detectors).

Table 12-1. Average number of collisions required to reduce a neutron's energy from 2 MeV to 0.025 eV by elastic scattering

Element	Atomic Weight	Number of Collisions
Hydrogen	1	27
Deuterium	2	31
Helium	4	48
Beryllium	9	92
Carbon	12	119
Uranium	238	2175

Instead of being scattered by a nucleus, the neutron may be absorbed or captured. A variety of emissions may follow, as shown in Figure 12.2. The nucleus may rearrange its internal structure and release one or more gamma rays. Charged particles may also be emitted; the more common ones are protons, deuterons, and alpha particles. The nucleus may also rid itself of excess neutrons. The emission of only one neutron is indistinguishable from a scattering event. If more than one neutron is emitted, the number of neutrons now moving through the material is larger than the number present before the interaction; the number is said to have been multiplied. Finally, there may be a fission event, leading to two or more fission fragments (nuclei of intermediate atomic weight) and more neutrons (see Chapter 11).

Many safeguards instruments have neutron detectors that use an absorption reaction as the basis of the detection technique. The lack of an electric charge on the neutron makes direct detection difficult, so the neutron is first absorbed by a nucleus, which then emits a charged particle (such as a proton or deuteron). Helium-3, uranium-235 and boron-10 are commonly used in detectors because they have large absorption cross sections for the production of charged particles with low-speed neutrons.

When moderation alone is desired, absorption should be avoided. For example, hydrogen is a better moderator than deuterium (that is, it requires fewer collisions to achieve a particular low speed), but it also has a larger absorption cross section for neutrons. The net effect is that deuterium will yield more thermal neutrons than hydrogen and may be the preferred moderating material.

The cross sections associated with the various interactions described above can be designated by the following notation:

σ_t = total cross section ($\sigma_s + \sigma_a$)
σ_s = total scattering cross section ($\sigma_{el} + \sigma_i$)
σ_{el} or $\sigma_{n,n}$ = elastic scattering cross section
σ_i or $\sigma_{n,n'}$ = inelastic scattering cross section
σ_a or σ_c = absorption or capture cross section
σ_{ne} = nonelastic cross section, $\sigma_t - \sigma_{el}$
$\sigma_{n,\gamma}$ = radiative capture cross section
σ_f or $\sigma_{n,f}$ = fission cross section
$\sigma_{n,p}$ = (n,p) reaction cross section.

12.2.4 Energy Dependence of Cross Sections

All of the cross sections described above vary with neutron energy and with the target nucleus, sometimes in a dramatic way. This section gives some generalizations about the energy dependence of cross sections and shows data (Ref. 1) for a few important nuclei.

Figure 12.3 is the total cross section for ^{239}Pu for incident neutrons of 0.001-eV to 10-MeV energy. Note that as a general rule the cross section decreases with increasing energy. At low energies, below 1 MeV, the elastic cross section is nearly constant, whereas the inelastic scattering cross section and absorption cross sections are proportional to the reciprocal of the neutron's speed (that is, 1/v). So at low energies the total cross section can be nearly constant or decreasing with energy, depending on which type of event dominates. For example, in ^{239}Pu the inelastic cross section dominates and the total cross section decreases as 1/v. Similar behavior is observed for most light and

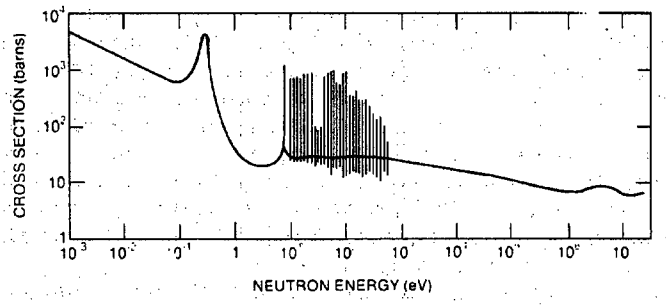

Fig. 12.3 Total neutron cross section of ^{239}Pu.

intermediate weight nuclei as well. Figures 12.4 and 12.5 illustrate the low-energy total cross-section behavior of boron and cadmium. The unusually high absorption cross sections of these two materials make them useful as thermal-neutron poisons.

At higher energies the cross section may have large peaks superimposed on the 1/v trend. These peaks are called resonances and occur at neutron energies where reactions with nuclei are enhanced. For example, a resonance will occur if the target nucleus and the captured neutron form a "compound" nucleus, and the energy contributed by the neutron is close to that of an excited state of the compound nucleus.

In heavy nuclei, large and narrow resonances appear for neutron energies in the eV range. For energies in the keV region the resonances can be too close together to resolve. In the MeV region the resonances are more sparse and very broad, and the cross sections become smooth and rolling. For light nuclei, resonances appear only in the MeV region and are broad and relatively small. For nuclei with intermediate weights (such as

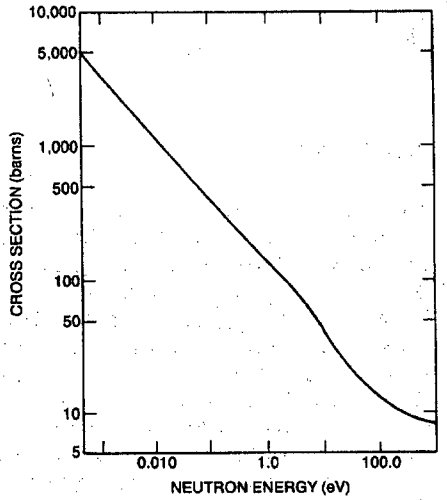

Fig. 12.4 Low-energy total neutron cross section of boron (Ref. 1).

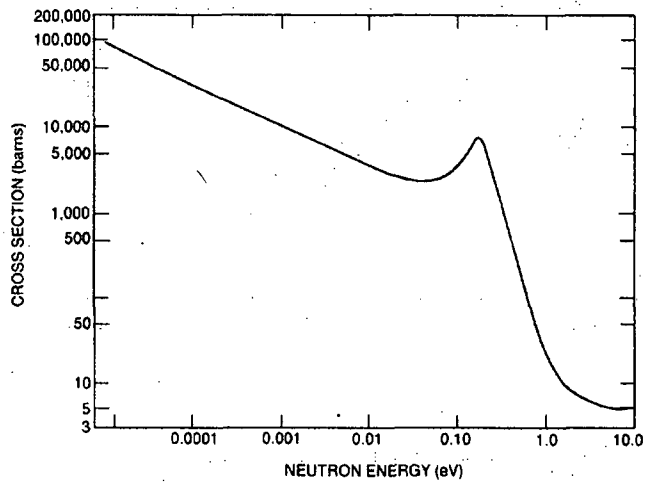

***Fig. 12.5** Low-energy total neutron cross section of cadmium (Ref. 1).*

cadmium, nickel, iron), resonances can be found below 1 keV. These resonances have heights and widths between those of light and heavy nuclei.

Some exceptions to the general trends exist in ^{1}H and ^{2}H where there are no resonances at all and in nuclei with "magic" numbers of protons or neutrons where the behavior may be similar to that of light nuclei despite the actual atomic weight. In practice, it is necessary to rely on tables of cross sections for the nuclei of interest because there is no convenient way to calculate cross sections. Some microscopic cross sections are included in the second table in Section 12.3.

Some neutron-induced fission cross sections important for nondestructive assay are shown in Figure 12.6. The fissile isotopes ^{235}U and ^{239}Pu have large cross sections (about 1000 b) for fission by thermal or near-thermal neutrons. For fission by fast neutrons (10 keV to 10 MeV), these cross sections are reduced to 1 to 2 b. The fertile isotopes ^{238}U and ^{240}Pu have negligible fission cross sections for low-energy neutrons but exhibit a "threshold" near 1-MeV neutron energy. Above 1 MeV the fission cross sections of the fertile isotopes are comparable to those of the fissile isotopes.

12.3 MACROSCOPIC INTERACTIONS

12.3.1 Macroscopic Cross Sections

Although study of the interactions of a neutron with a single nucleus on the microscopic scale provides a basis for understanding the interaction process, measurements are actually performed with thick samples that often contain a mixture of elements. These additional features are described by using the macroscopic cross sections appropriate for bulk materials.

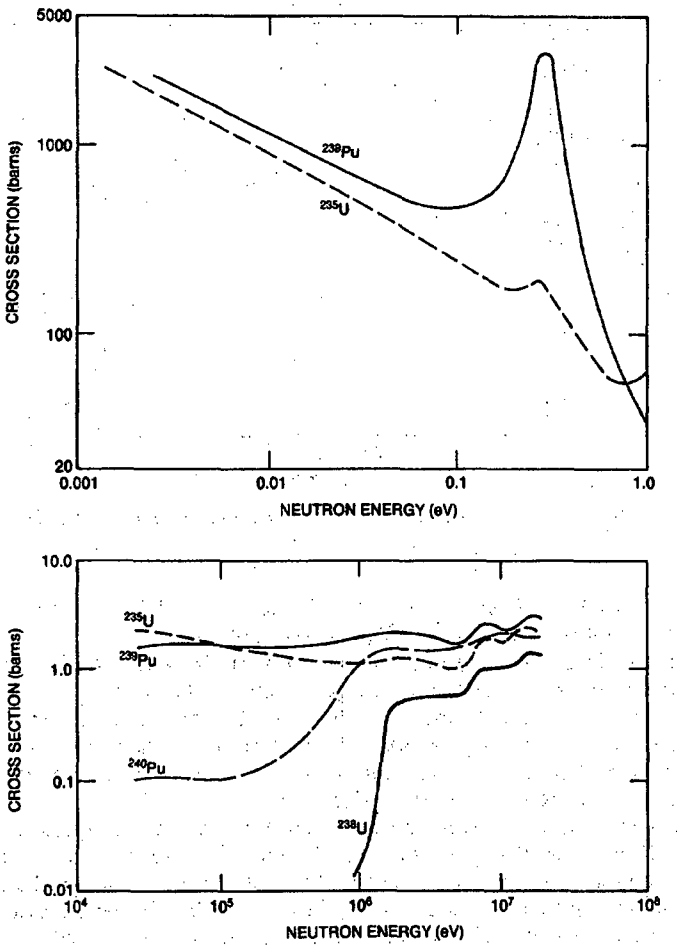

Fig. 12.6 Fission cross sections for some important fissile (^{235}U, ^{239}Pu) and fertile (^{238}U, ^{240}Pu) isotopes (Ref. 1).

The definition of the macroscopic cross section arises from the transmission of a parallel beam of neutrons through a thick sample. The thick sample can be considered to be a series of atomic layers; for each layer we can apply the results found with the microscopic cross-section concept. By integrating through enough atomic layers to reach a depth x in the sample, the intensity I(x) of the uncollided neutron beam is

$$I(x) = I_0 e^{-N\sigma_t x} \tag{12-3}$$

where I_0 is the intensity of the beam before it enters the sample, N is the atom density, and σ_t is the total cross section. Figure 12.7 shows the uncollided intensity remaining in a parallel beam as it passes through a thick layer of matter. Note that the fraction transmitted without collisions, $I(x)/I_0$, depends on the energy of the neutrons through the energy dependence of the microscopic total cross-section σ_t.

An expression similar to Equation 12-3 is used for gamma-ray attenuation. In that case, low-energy gamma rays are very likely to be absorbed and thus removed not only from the parallel beam but from the material entirely. With neutrons at low energies, elastic scattering is the most likely event. Although Equation 12-3 gives the intensity of the neutrons that have had no interaction up to a depth x, the actual number of neutrons present that can be detected may be much larger because of multiple scattering, multiplication, or finite detector acceptance angle.

The total macroscopic cross section is $\Sigma_t = N\sigma_t$. Σ_t has dimensions of cm^{-1} (see Equation 12-3 above) and is analogous to the linear attenuation coefficient for gamma rays. If only a particular type of interaction is of interest, a macroscopic cross section for it alone can be defined using its microscopic cross section in place of the total cross section. For quantitative calculations, the concept of macroscopic cross section is less used than the analogous gamma-ray linear attenuation coefficient because of the complications of multiple scattering and other effects mentioned in the previous paragraph.

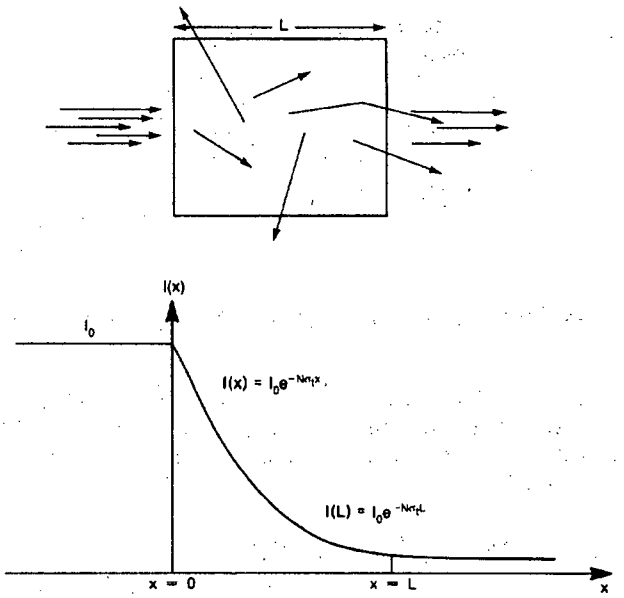

Fig. 12.7 *The intensity of a parallel beam of uncollided neutrons decreases exponentially as it passes through a thick layer of matter.*

If the sample is a compound instead of a simple element, the total macroscopic cross section is the sum of the macroscopic cross sections of the individual elements:

$$\Sigma = \Sigma_1 + \Sigma_2 + \Sigma_3 \ldots \quad . \tag{12-4}$$

The atom density N_i of each element i is given by

$$N_i = \rho N_a n_i / M \tag{12-5}$$

where ρ is the density of the compound; M is the molecular weight of the compound; N_a is Avogadro's number, 6.022×10^{23} atoms/mole; and n_i is the number of atoms of element i in one molecule. From Equations 12-4 and 12-5 the general form of the macroscopic cross section can be written as

$$\Sigma = \frac{\rho N_a}{M}(n_1\sigma_1 + n_2\sigma_2 + n_3\sigma_3 + \ldots) \quad . \tag{12-6}$$

As an illustration of these equations, the total macroscopic cross section for 1-MeV neutrons in $^{nat}UO_2$ (density 10 g/cm^3, molecular weight 270) is calculated from the data in Table 12-2.

Table 12-2. Nuclear data for $^{nat}UO_2$

Isotope	n_i	σ_t at 1 MeV (b)
^{235}U	0.007	6.84
^{238}U	0.993	7.10
^{16}O	2.000	8.22

$$\Sigma_t = \frac{(10)(0.6022)}{270}[(0.007)(6.84) + (0.993)(7.10) + 2(8.22)] = 0.525 \text{ cm}^{-1} \quad . \tag{12-7}$$

Powers of 10^{24} and 10^{-24} have been cancelled in Avogadro's number and in the cross-section values. These cross-section values were taken from Table 12-3 (Ref. 2), which is a compilation of microscopic and macroscopic cross sections at two neutron energies, 0.025 eV (thermal) and 1 MeV.

12.3.2 Mean Free Path and Reaction Rate

A very descriptive feature of the transmission of neutrons through bulk matter is the mean-free-path length, which is the mean distance a neutron travels between interac-

tions. It can be calculated from Equation 12-3 with $N\sigma_t$ replaced by Σ_t. The mean-free-path length λ is

$$\lambda = 1/\Sigma_t \quad , \tag{12-8}$$

the reciprocal of the macroscopic cross section. For the case of 1-MeV neutrons in UO_2 calculated above, a macroscopic cross section of 0.525 cm^{-1} implies a mean-free-path length of 1.91 cm.

The mean-free-path length has many qualitative applications in assay instruments and shielding. (a) If the mean-free-path length of neutrons emitted by a sample in a passive assay instrument is long compared to the dimensions of the sample, it is likely that most of the neutrons will escape from the sample and enter the detection region. (b) If the number of collisions required to thermalize a neutron is known, the necessary moderator thickness of a shield can be estimated. (c) If the thickness of a shield is many times the mean-free-path length of a neutron trying to penetrate the shield, then the shield fulfills its purpose. (Because the mean-free-path length is a function of the neutron's energy, the actual calculation is not so simple.)

A closely related concept is that of the reaction rate. When traveling with a speed v, a neutron has an average time between interactions of λ/v. The reaction rate is the frequency with which interactions occur: v/λ, or $v\Sigma_t$. In uranium oxide, for example, a 1-MeV neutron will have a reaction rate of 7.26×10^8 per second (from Equations 12-2 and 12-7). This does not mean, however, that in one second there will be that many reactions; with each collision the neutron's energy decreases and the cross section changes, thereby altering the instantaneous reaction rate.

The paths of neutrons in matter can be simulated with Monte Carlo calculations. Figure 12.8 shows a few paths for neutrons with 1 MeV of energy entering cylinders of different materials. The mean-free-path length depends on both the type of material and the energy of the neutron. After each collision, the energy is decreased and the mean-free-path length is affected accordingly. Figure 12.8 shows that a cylinder of polyethylene is more effective in preventing the transmission of neutrons than a cylinder of heavy metal. A neutron loses most of its energy by colliding with the light elements in polyethylene and then the mean-free-path length becomes small as the cross sections increase. An important effect of polyethylene is that it seemingly retains a large fraction of the neutrons near a certain depth; these neutrons have had enough collisions to lose nearly all their kinetic energy. If a thermal-neutron detector is placed in this region, the chance of detecting neutrons is optimized.

12.4 EFFECTS OF MODERATION IN BULK MATTER

It is often a design goal to reduce or moderate the speed of neutrons in the sample region or the detector region or both. Recalling the general 1/v trend of interaction cross sections (Figures 12.3 through 12.6), the purpose of the reduction in speeds is to increase the probability of an interaction. In other regions, it may be desirable to hinder interactions by choosing materials that are poor moderators or by adding low-energy neutron absorbers to remove neutrons once they become moderated.

Table 12-3. Neutron cross sections of common materials[a]

Material	Atomic or Molecular Weight	Density (g/cm^3)	Cross Sections[b] E = 0.0253 eV σ_t (b)	σ_a (b)	Σ_t (cm^{-1})	Σ_a (cm^{-1})	E = 1 MeV σ_t (b)	σ_a (b)	Σ_t (cm^{-1})	Σ_a (cm^{-1})
Al	27	2.7	1.61	0.232	0.097	0.014	2.37	0.000	0.143	0.000
B	10	2.3	3845	3843	533	532	2.68	0.189	0.371	0.0262
B	11	2.3	5.28	0.005	0.665	0.0006	2.13	0.000	0.268	0.000
Be	9	9.0	6.35	0.010	3.82	0.0060	3.25	0.003	1.96	0.0018
C	12	1.9	4.95	0.003	0.472	0.0003	2.58	0.000	0.246	0.000
Nat Ca	40.08	1.55	3.46	0.433	0.081	0.101	1.14	0.004	0.027	0.0001
Cd	112	8.7	2470	2462	115.5	115.2	6.50	0.058	0.304	0.0027
Nat Cl	35.45	Gas	50.2	33.4	Gas	Gas	2.30	0.0005	Gas	Gas
Nat Cu	63.55	8.94	12.5	3.80	1.06	0.322	3.40	0.011	0.288	0.0009
F	19	Gas	3.72	0.010	Gas	Gas	3.15	0.000	Gas	Gas
Fe	56	7.9	14.07	2.56	1.19	0.217	5.19	0.003	0.441	0.0003
Nat Gd	157.25	7.95	49 153	48 981	1496	1491	7.33	0.223	0.223	0.0068
H	1	Gas	30.62	0.33	Gas	Gas	4.26	0.000	Gas	Gas
H	2	Gas	4.25	0.000	Gas	Gas	2.87	0.000	Gas	Gas
He	3	Gas	5337	5336	Gas	Gas	2.87	0.879	Gas	Gas
He	4	Gas	0.86	0.000	Gas	Gas	7.08	0.000	Gas	Gas
Li	6	0.534	938	937	50.3	50.2	1.28	0.230	0.069	0.0123
Li	7	0.534	1.16	0.036	0.053	0.0017	1.57	0.000	0.072	0.0000
Nat Mg	24.31	1.74	3.47	0.063	0.150	0.0027	2.66	0.001	0.115	0.0000
Mn	55	7.2	14.5	13.2	1.14	1.04	3.17	0.003	0.250	0.0002
N	14	Gas	12.22	1.9	Gas	Gas	2.39	0.021	Gas	Gas
Na	23	0.971	3.92	0.529	0.100	0.0134	3.17	0.000	0.081	0.0000
Ni	59	8.9	23.08	4.58	2.10	0.416	3.66	0.0008	0.322	0.0001
O	16	Gas	3.87	0.000	Gas	Gas	8.22	0.000	Gas	Gas
Pb	204	11.34	11.40	0.18	0.381	0.0060	4.39	0.0033	0.147	0.0001

[a]Ref. 2.

[b]A zero value means zero to the number of figures shown.

Table 12-3. Neutron cross sections of common materials[a] (continued)

Material	Atomic or Molecular Weight	Density (g/cm^3)	Cross Sections[b] E = 0.0253 eV σ_t (b)	σ_a (b)	Σ_t (cm^{-1})	Σ_a (cm^{-1})	E = 1 MeV σ_t (b)	σ_a (b)	Σ_t (cm^{-1})	Σ_a (cm^{-1})
Pu	238.05	19.6	599.3	562.0	29.72	27.87	6.66	0.190	0.330	0.0094
Pu	239.05	19.6	1021	270	50.4	13.3	7.01	0.026	0.346	0.0013
Pu	240.05	19.6	294	293	14.5	14.4	7.15	0.108	0.352	0.0053
Pu	241.06	19.6	1390	362	68.1	17.7	7.98	0.117	0.391	0.0057
Pu	242.06	19.6	26.7	18.9	1.30	0.922	7.31	0.098	0.357	0.0048
Nat Si	28.09	2.42	2.24	0.161	0.116	0.0084	4.43	0.001	0.230	0.0001
Th	232	11.3	20.4	7.50	0.598	0.220	7.00	0.135	0.205	0.0040
U	233.04	19.1	587	45.8	29.0	2.26	6.78	0.069	0.335	0.0034
U	234.04	19.1	116	103	5.70	5.07	8.02	0.363	0.394	0.0178
U	235.04	19.1	703	96.9	34.3	4.74	6.84	0.117	0.335	0.0057
U	236.05	19.1	13.3	5.16	0.648	0.251	7.73	0.363	0.377	0.0177
U	237.05	19.1	487.5	476.4	23.6	23.1	6.72	0.135	0.326	0.0066
U	238.05	19.1	11.63	2.71	0.562	0.131	7.10	0.123	0.343	0.0059
Nat U	238.03	19.1	16.49	3.39	0.797	0.1637	7.01	0.120	0.343	0.0058
Nat W	183.85	19.3	23.08	18.05	1.459	1.141	6.95	0.057	0.439	0.0036
CH_2	14	0.94			2.68	0.027			0.449	0.0000
H_2O	18	1.0			2.18	0.022			0.560	0.0000
D_2O	20	1.1			0.410	0.000			0.420	0.0000
Average Fission Products of:										
^{235}U	117		4496	4486			7.43	0.00036		
^{239}Pu	119		2087	2086			7.48	0.00093		

[a]Ref. 2.

[b]A zero value means zero to the number of figures shown.

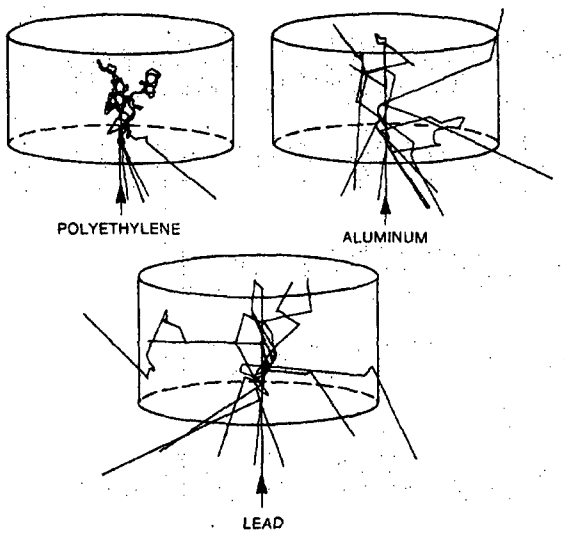

Fig. 12.8 Neutrons with 1 MeV of kinetic energy are shown entering cylinders of material from the bottom and then being scattering or absorbed. The paths were calculated using a Monte Carlo technique.

For example, in the assay of plutonium, moderation is not a desirable effect in the sample region. High-speed neutrons are more able to penetrate the sample and they have lower fission cross sections so that multiplication is less than with low-speed neutrons. On the other hand, in the detector region, moderation increases the detection efficiency for detectors such as ^{3}He proportional counters. By placing hydrogenous material (such as polyethylene) around the detectors, the neutrons can be counted with more efficiency. Also needed is a filter that will let high-speed neutrons enter the detector region where they can become moderated but will not let the moderated neutrons return to the sample region where they could produce additional fissions. A layer of material with a large absorption cross section for slow neutrons (such as cadmium, Figure 12.5) placed between the sample region and the detector region is effective in this regard.

A standard basis for comparing moderating abilities of different materials is the moderating power. If one material has a larger moderating power than another, less of that material is needed to achieve the same degree of moderation. Two factors are important: (1) the probability of a scattering interaction and (2) the average change in kinetic energy of the neutron after such an interaction. To be an effective moderator, both the probability of an interaction and the average energy loss in one scatter should be high. The moderating power is defined as $\xi\Sigma_s$, where Σ_s is the macroscopic scattering cross section and ξ is the average logarithmic energy decrement in a scatter. This decrement is $\ln(E_{before}) - \ln(E_{after})$. When elastic collisions in an element with atomic weight A dominate the scattering process, the decrement becomes

$$\xi = 1 - \frac{(A-1)^2}{2A} \ln \frac{(A+1)}{(A-1)} \quad . \tag{12-9}$$

For $A > 2$, ξ can be approximated by $2/(A+0.67)$ (Ref. 3). The moderating power of a compound is given by

$$\xi\Sigma_s = \frac{\rho N_a}{M}(n_1\sigma_1\xi_1 + n_2\sigma_2\xi_2 + \ldots) \quad , \tag{12-10}$$

where ρ is the density of the compound, M is its molecular weight, N_a is Avogadro's number, n_i is the number of atoms of element i in one molecule, σ_i is the microscopic scattering cross section for element i, and ξ_i is the logarithmic energy decrement for element i.

A material with a large moderating power might nevertheless be useless as a practical moderator if it has a large absorption cross section. Such a moderator would effectively reduce the speeds of those neutrons that are not absorbed, but the fraction of neutrons that survive may be too small to be used in a practical manner. A more comprehensive measure of moderating materials is the moderating ratio, $\xi\Sigma_s/\Sigma_a$. A large moderating ratio is desirable; it implies not only a good moderator but also a poor absorber. For a compound, the moderating ratio is given by Equation 12-10 with each σ_i replaced by σ_s/σ_a for element i.

Table 12-4 gives the moderating powers and ratios for some common moderator materials for neutrons in the 1-eV to 100-keV energy range (Ref. 4). Ordinary water has a higher moderating power than heavy water because the atomic weight of hydrogen is half that of deuterium. But the hydrogen nucleus (a proton) can absorb a neutron and create deuterium much more readily than a deuterium nucleus can absorb a neutron and create tritium. This difference in absorption cross sections gives heavy water a much more favorable moderating ratio. However, because of its availability and low cost, ordinary water is often preferred. The solid materials given in the table have a higher moderating ratio than ordinary water and can have fabrication advantages. Polyethylene is commonly selected as a moderator because of its high moderating power and moderating ratio.

Table 12-4. Moderating powers and ratios of selected materials (Ref. 4)

Moderator	Moderating Power (1 eV to 100 keV)	Moderating Ratio (Approximate)
Water	1.28	58
Heavy Water	0.18	21 000
Helium at STP	0.00001	45
Beryllium	0.16	130
Graphite	0.064	200
Polyethylene (CH_2)	3.26	122

12.5 EFFECTS OF MULTIPLICATION IN BULK MATTER

When a neutron interaction yields more than one neutron as a product, a multiplication event has occurred. More neutrons will be present in the material after the interaction than before. The most widely known multiplication event is fission, but other absorption interactions, such as (n,2n), can be important contributors to multiplication.

Of the neutrons in a given material at a given moment, some will eventually escape and the others will be absorbed. Additional neutrons can originate in the material as products of the absorptions. The definition of the multiplication M is the total number of neutrons that exist in the sample divided by the number of neutrons that were started. If 100 neutrons are started in the sample and an additional 59 are found to be created from multiplication events, the multiplication is 1.59. Only a fraction of the first generation of 100 neutrons produces additional neutrons through multiplication events; the others escape or are absorbed by other types of interactions. The same fraction of the second generation produce a third generation, and so on. The number of neutrons remaining in the sample steadily decreases until it is zero and the total number of neutrons produced by all the multiplication events is 59.

A related concept that is more commonly used is the multiplication factor. It relates the numbers of neutrons in successive generations. There are two categories of multiplication factors that apply to different physical sizes of the material involved.

If the material is infinite in extent, the multiplication factor is written k_∞ and is defined as the ratio of the number of neutrons in one generation to the number in the previous generation. Because of the infinite size of the material, all neutrons of a generation become absorbed. Thus k_∞ is also the ratio of the number of neutrons produced in one generation to the number absorbed in the preceding generation.

If the material is not infinite in size, some neutrons in a generation may escape through the surface and not be absorbed; these are "leakage" neutrons. The multiplication factor for this more practical situation is called k_{eff}. It is defined as the ratio of the number of neutrons produced in one generation to the number either absorbed or leaked in the preceding generation. The multiplication factor k_{eff} is the more practical ratio for safeguards work because instruments are often made small to comply with size and weight constraints.

As an example of k_{eff} and its connection with the multiplication M, consider the case described earlier. The original 100 neutrons would constitute the first generation. If the original neutrons create 37 neutrons through reactions, the 37 neutrons would be the next generation. The multiplication factor in this case is thus 0.37. With k_{eff} less than one, the number of neutrons in succeeding generations decreases, eventually reaching zero. As Table 12-5 indicates, it takes 7 generations to reduce the number of neutrons from 100 to about zero.

The number of neutrons in one generation is found by multiplying the number in the previous generation by the multiplication factor k_{eff}, which in this example is 0.37. This is a statistical process, of course, and the exact number in any generation cannot be exactly known, but for large numbers of neutrons the ratio of populations in successive generations is very nearly constant.

Table 12-5. Example of neutron population decline

Generation	Average No. of Neutrons for $k_{eff} = 0.37$
1	100
2	37
3	14
4	5
5	2
6	1
7	0
	159

The multiplication M is readily connected to the multiplication factor k_{eff} when k_{eff} is less than one. By adding together all the numbers of neutrons in all the generations, the geometric sum can be found:

$$M = 1/(1-k_{eff}), \quad k_{eff} < 1 \quad . \tag{12-11}$$

With the multiplication of 1.59 in Table 12-5, the multiplication factor is 0.37, showing that the number of neutrons is decreasing in successive generations.

As k_{eff} approaches one, the value of M becomes larger and larger, as shown in Figure 12.9. When $k_{eff} = 1$, the formula shows that there is no limit to the number of neutrons that will be produced; in practice, there is a finite number of nuclei that can produce neutrons, so the number of neutrons created is finite but extremely large. Criticality is said to be reached when $k_{eff} = 1$. If k_{eff} is larger than one, the sample is supercritical; with k_{eff} less than one, the sample is subcritical.

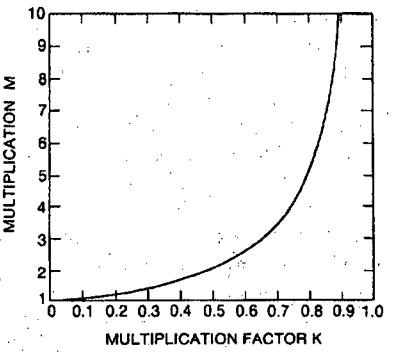

Fig. 12.9 *The multiplication M is shown as a function of the multiplication factor k_{eff}. Only subcritical values (k_{eff} less than one) are included here.*

12.6 NEUTRON SHIELDING

To protect personnel from the biological effects of neutrons and to reduce background counts, neutron shielding is often necessary. The selection and arrangement of shielding materials vary with the circumstances. Some general principles can be derived from the neutron interactions with matter described earlier in this chapter.

Thermal neutrons with energies of 0.025 eV or less are absorbed with great effectiveness by thin layers of boron or cadmium, as suggested by the large cross sections shown in Figures 12.4 and 12.5. Boron is often used in the form of boron carbide (B_4C) or boron-loaded solutions. One commonly used material is Boral, a mixture of boron carbide and aluminum, which is available in sheets of varying thickness. Cadmium has the disadvantage of emitting high-energy gamma rays after neutron capture, which may necessitate additional gamma-ray shielding. A comparison of Figures 12.4 and 12.5 shows that cadmium is more effective than boron for absorbing thermal neutrons, whereas boron is more effective for absorbing epithermal neutrons (energy range 0.1 eV to 10 eV).

High-speed neutrons are more difficult to shield against because absorption cross sections are much lower at higher energies. Thus it is first necessary to moderate high-speed neutrons through elastic or inelastic scattering interactions. Inelastic scattering or absorption may again produce potentially hazardous gamma rays; for example, neutron capture in hydrogen releases a 2.224-MeV gamma ray. An effective radiation shield consists of a combination of materials: hydrogenous or other low-A materials to moderate neutrons; thermal neutron absorbers; and high-Z materials to absorb gamma rays. Examples of hybrid shielding materials are polyethylene and lead, concrete containing scrap iron, and more exotic materials such as lithium hydride.

In safeguards work with small samples of fissionable materials or weak neutron sources, shielding may be restricted to several centimeters of polyethylene. The shielding properties of polyethylene are illustrated in Figure 12.10, which gives dose rates on the surface of a sphere of polyethylene with a ^{252}Cf source in its center. The source emits neutrons with a high-energy fission spectrum comparable to most uranium and plutonium isotopes. Also produced are fission gamma rays and additional 2.224-MeV gamma rays from neutron capture in polyethylene. Neutrons provide most of the dose for spheres less than 22 cm in radius; beyond that, source gamma rays are the major contributors, followed by gamma rays from capture reactions. By increasing the radius from 5 to 12 cm or from 20 to 37 cm, the total dose rate can be reduced by a factor of 10. A rule of thumb for neutron dose reduction is that 10 cm of polyethylene will reduce the neutron dose rate by roughly a factor of 10.

More effective shields can sometimes be obtained by adding boron, lithium, or lead to polyethylene. The addition of boron or lithium results in a lower capture gamma-ray dose than that provided by pure polyethylene; lead effectively attenuates the source and the capture gamma-ray flux because it is a heavy element. However, because neutrons provide most of the dose up to a radius of 22 cm, the addition of these materials has little effect until the shield becomes substantially thicker than 22 cm. Figure 12.11 shows the effects on the total dose of adding other materials to polyethylene; these effects are important only for shields thicker than 30 cm. Since boron- lithium-, or lead-loaded

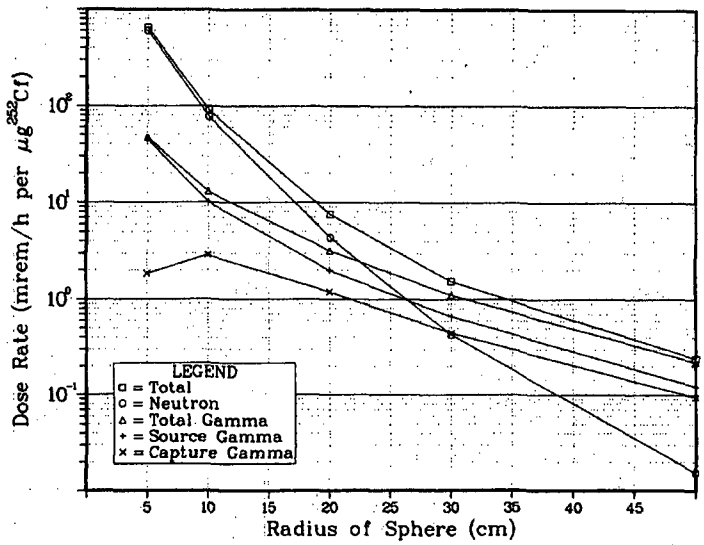

Fig. 12.10 *Various dose rates on a spherical surface from a point ^{252}Cf source in polyethylene. (Data supplied by G. E. Bosler, Los Alamos.)*

polyethylene is substantially more expensive than pure polyethylene, the additional cost is an important consideration.

12.7 TRANSPORT CALCULATIONAL TECHNIQUES

Neutron histories are difficult to determine because of the large number of different interactions possible in materials. This difficulty is further increased when the composition of matter changes frequently along the path of a neutron, as it often does throughout the volume of an assay instrument. Techniques for calculating the behavior or transport of neutrons and gamma rays in such circumstances are important for the design of assay instruments, the interpretation of measurements, and the development of shielding configurations. Two techniques for calculating the transport of neutrons in matter are described briefly in Sections 12.7.1 and 12.7.2.

12.7.1 Monte Carlo Techniques

The probability of a neutron interaction occurring is an important feature in the description of neutrons traveling through matter. Instead of trying to predict what an individual neutron may do, one can use procedures to predict what fraction of a large number of neutrons will behave in some manner of interest. Calculational techniques that, in simplistic terms, predict neutron events with "rolls of dice" (actually the generation of random numbers in a computer) are called Monte Carlo methods. The

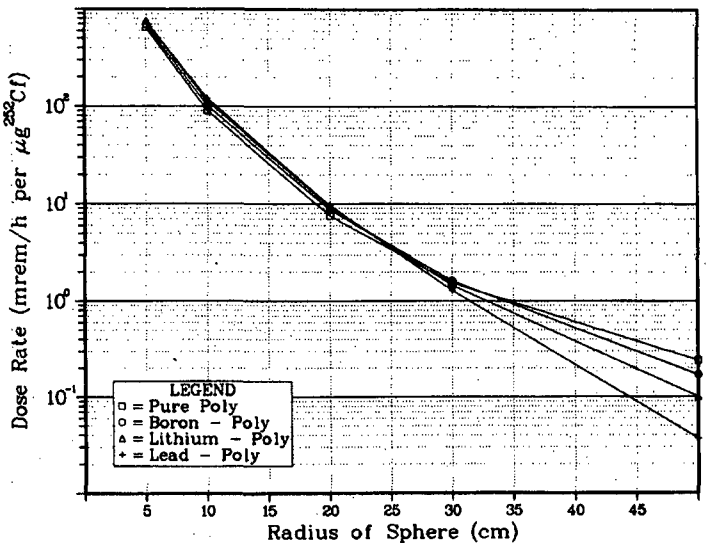

Fig. 12.11 Total dose rate on a spherical surface from a point ^{252}Cf source in various materials. (Data supplied by G. E. Bosler, Los Alamos.)

response of an assay system can often be calculated from the transport of many individual neutrons, despite the inclusion of a few improbable neutron histories that deviate drastically from the average behavior.

The Monte Carlo method can allow a detailed three-dimensional geometrical model to be constructed mathematically to simulate a physical situation. A neutron can be started at a selected location with a certain energy and direction. It travels distances that are consistent with the mean-free-path lengths in the materials, with random variations from the expected mean. At the end of each step in the neutron's path, a decision may be made to simulate a certain interaction, with the decision based on the cross section for the interaction with that material at that neutron energy. If an interaction is selected, the results of the interaction are simulated and its consequences followed. Eventually, a point is reached where no further interest in the neutron exists and its history is terminated. This might occur with the escape of the neutron or its moderation to very low energy. The neutron might be absorbed followed by the emission of a gamma ray of no interest, or it might undergo a multiplication event. If a multiplication event occurs, the histories of the new neutrons are followed. In principle, the history of a simulated neutron is one that might actually occur with a real neutron.

By repeating this procedure for many thousands of neutrons and by keeping tallies of how many enter a detector region, how many cause fissions, how many escape through a shield, or whatever else is of interest, an average behavior and its uncertainty are gradually deduced. Many specialized techniques may be used to get good average values with the fewest number of neutrons, but there are cases where even a fast computer cannot provide enough histories within the constraints of time and budget. Nonetheless,

Monte Carlo techniques provide essential assistance in design work by closely modeling the actual geometry of a problem and by having imaginary neutrons that simulate the motions and interactions of real ones. Examples of the results of Monte Carlo calculations are the shielding calculations in Figures 12.10 and 12.11 and the coincidence counter design calculations described in Chapters 14 and 17.

12.7.2 Discrete Ordinates Techniques

Analytical transport equations exist that describe the exact behavior of neutrons in matter. However, only approximate numerical solutions to these equations can be obtained for complicated systems. Procedures for obtaining these numeral solutions are classified as discrete ordinates techniques.

Some important differences distinguish discrete ordinates techniques from Monte Carlo techniques. Only one- or two-dimensional geometries are generally practical with a discrete ordinates process, and the neutrons are considered to be at discrete locations instead of moving freely through a three-dimensional geometry. In a two-dimensional discrete ordinates case, for example, it is as if the surface material were covered by a wire mesh and the neutrons existed only at the intersections of the wires. Furthermore, the energy of a neutron at any time must be selected from a finite set, in contrast to the continuously varying energy of a neutron in the Monte Carlo method.

Despite these disadvantages, discrete ordinates techniques can produce useful results in many cases. For problems involving large volumes and amounts of materials (such as reactor cores), the Monte Carlo technique can be too cumbersome and slow; a discrete ordinates solution might be feasible.

REFERENCES

1. D. I. Garber and R. R. Kinsey, "Neutron Cross Sections, Vol. II, Curves," Brookhaven National Laboratory report BNL 325 (1976).

2. Evaluated Nuclear Data File ENDF/B-V (available from and maintained by the National Nuclear Data Center of Brookhaven National Laboratory).

3. J. R. Lamarsh, *Introduction to Nuclear Reactor Theory* (Addison-Wesley, Reading, Massachusetts, 1966).

4. S. Glasstone and A. Sesonske, *Nuclear Reactor Engineering* (D. Van Nostrand Co., Inc., Princeton, New Jersey, 1967).

13

Neutron Detectors

T. W. Crane and M. P. Baker

13.1 MECHANISMS FOR NEUTRON DETECTION

Mechanisms for detecting neutrons in matter are based on indirect methods. Neutrons, as their name suggests, are neutral. Also, they do not interact directly with the electrons in matter, as gamma rays do. The process of neutron detection begins when neutrons, interacting with various nuclei, initiate the release of one or more charged particles. The electrical signals produced by the charged particles can then be processed by the detection system.

Two basic types of neutron interactions with matter are available. First, the neutron can be scattered by a nucleus, transferring some of its kinetic energy to the nucleus. If enough energy is transferred, the recoiling nucleus ionizes the material surrounding the point of interaction. This mechanism is only efficient for neutrons interacting with light nuclei. In fact, only hydrogen and helium nuclei are light enough for practical detectors. Second, the neutron can cause a nuclear reaction. The products from these reactions, such as protons, alpha particles, gamma rays, and fission fragments, can initiate the detection process. Some reactions require a minimum neutron energy (threshold), but most take place at thermal energies. Detectors exploiting thermal reactions are usually surrounded by moderating material to take maximum advantage of this feature.

Detectors employing either the recoil or reaction mechanism can use solid, liquid, or gas-filled detection media. Although the choice of reactions is limited, the detecting media can be quite varied, leading to many options. This chapter describes gas-filled proportional counters, scintillators, fission chambers, ^{10}B-lined chambers, and other types of neutron detectors. Gas detectors are discussed in the order of their frequency of use in Sections 13.4.1 through 13.4.4; plastic and liquid scintillators, in Section 13.5; and other types of detectors, in Section 13.6.

The energy information obtained in neutron detection systems is usually poor because of the limitations of the available neutron-induced reactions. Recoil-type counters measure only the first interaction event. The full neutron energy is usually not deposited in the detector, and the only energy information obtained is whether a high- or low-energy neutron initiated the interaction. Reaction-type counters take advantage of the increased reaction probability at low neutron energies by moderating the incoming neutrons. But knowledge of the initial neutron energy before moderation is lost. The energy recorded by the detector is the reaction energy (plus, perhaps, some of the remaining initial neutron energy). Thus, in general, neutron detectors provide information only on the number of neutrons detected and not on their energy. Information on

the range of detected neutron energies can usually be inferred from the detector type and the surrounding materials. If information on the neutron energy spectrum is needed, it can sometimes be obtained indirectly, as discussed in Section 13.7.

13.2 GENERAL PROPERTIES OF GAS-FILLED DETECTORS

Gas-filled detectors were among the first devices used for radiation detection. They may be used to detect either thermal neutrons via nuclear reactions or fast neutrons via recoil interactions. After the initial interaction with the neutron has taken place, the remaining detection equipment is similar, although there may be changes in high-voltage or amplifier gain settings to compensate for changes in the magnitude of the detected signal. Figure 13.1 shows a typical setup for neutron counting with a gas-filled detector. Figure 13.2 shows some commonly used detectors.

The exterior appearance of a gas detector is that of a metal cylinder with an electrical connector at one end (occasionally at both ends for position-sensitive measurements). The choice of connector depends on the intended application; simple wire leads and most other common types are available. Detector walls are about 0.5 mm thick and are manufactured from either stainless steel or aluminum. The performance of either material is quite satisfactory, with only slight differences in neutron transmission or structural strength. Steel walls absorb about 3% of the neutrons; aluminum walls, about 0.5%. Thus, aluminum tubes are usually preferred because of their higher detection

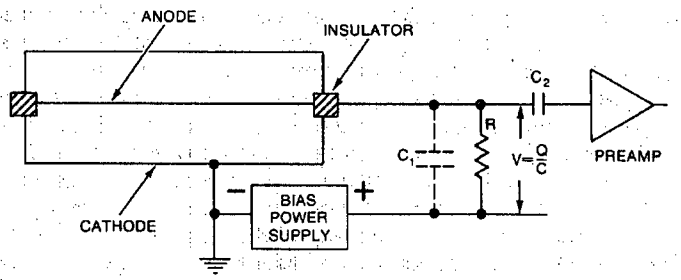

Fig. 13.1 Typical setup for gas-filled neutron detectors.

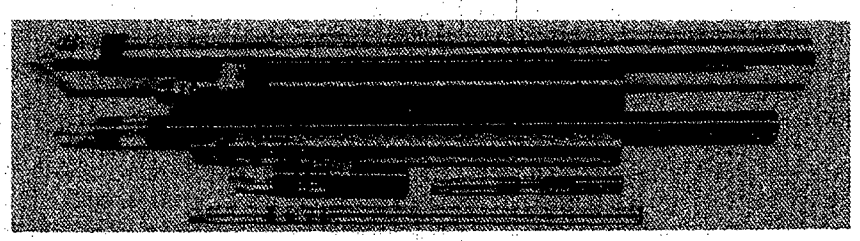

Fig. 13.2 Various sizes of BF_3 and ^3He neutron detectors.

efficiency. However, steel tubes have some small advantages over aluminum tubes for certain applications: they require less careful handling during assembly, the connecting threads are less susceptible to galling, and impurities can be kept lower. In very low count-rate applications, a background of about 1 count/min has been observed and attributed to radium impurity in aluminum (Ref. 1).

The central wire shown in Figure 13.1 is typically 0.03-mm-thick gold-plated tungsten. Tungsten provides tensile strength for the thin wire, and the gold plating offers improved electrical conductivity. The wire is held in place by ceramic insulators.

Sometimes the interior walls are coated with activated charcoal. This coating is used for tubes filled with boron trifluoride (BF_3) gas and also for ^{3}He-filled tubes operated in high neutron fluxes. The activated charcoal serves to absorb electronegative gases that build up during neutron irradiation. For example, in a BF_3-filled detector three fluorine atoms are released with each neutron capture. The fluorine atoms will combine with electrons released in subsequent neutron captures. Initially, this process reduces the electric pulse amplitude and eventually output pulses are eliminated altogether (Ref. 2). Additional details on the design of gas-filled detectors are given in Refs. 3 and 4.

As described in Section 13.1, the detection of neutrons requires the transfer of some or all of the neutrons' energy to charged particles. The charged particle will then ionize and excite the atoms along its path until its energy is exhausted. In a gas-filled detector, approximately 30 eV is required to create an ion pair. The maximum number of ion pairs produced is then E/30 eV, where E is the kinetic energy of the charged particle(s) in eV. For example, an energy transfer of 765 keV will release a total positive and negative charge of about 8×10^{-15} coulombs.

If little or no voltage is applied to the tube, most of the ions will recombine and no electrical output signal is produced. If a positive voltage is applied to the central wire (anode), the electrons will move toward it and the positively charged ions will move toward the tube wall (cathode). An electrical output signal will be produced whose magnitude depends on the applied voltage, the geometry of the counter, and the fill gas. These parameters determine whether the detector operates in the ionization region, the proportional region, or the Geiger-Mueller region. These different operating regions are shown in Figure 13.3.

In the ionization region, enough voltage has been applied to collect nearly all the electrons before they can recombine. At this point, a plateau is reached and further small increases in voltage yield no more electrons. Detectors operated in this region are called ion chambers. The charge collected is proportional to the energy deposited in the gas and independent of the applied voltage.

The region beyond the ionization region is called the proportional region. Here the electric field strength is large enough so that the primary electrons can gain sufficient energy to ionize the gas molecules and create secondary ionization. If the field strength is increased further, the secondary electrons can also ionize gas molecules. This process continues rapidly as the field strength increases, thus producing a large multiplication of the number of ions formed during the primary event. This cumulative amplification process is known as avalanche ionization. When a total of "A" ion pairs result from a single primary pair, the process has a gas amplification factor of A. "A" will be unity in an ionization chamber where no secondary ions are formed and as high as 10^3 to 10^5 in a well-designed proportional counter. Note that in the proportional region the charge collected is also linearly proportional to the energy deposited in the gas.

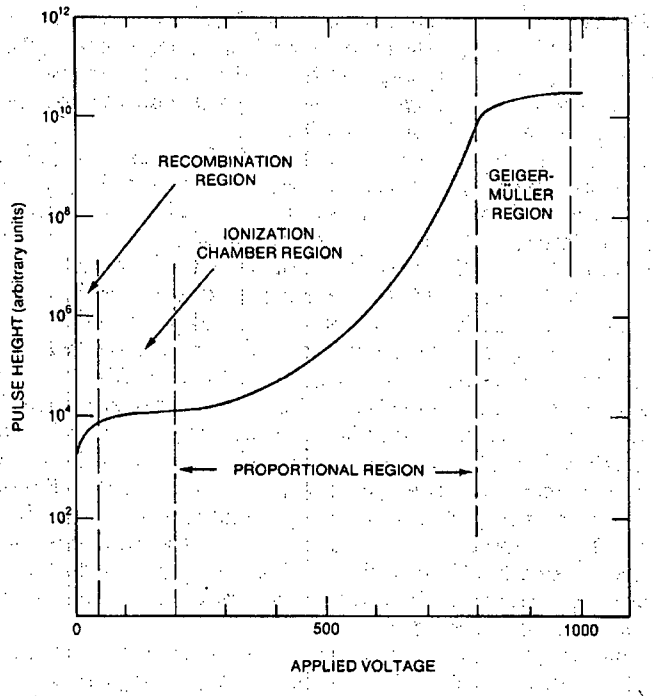

Fig. 13.3 Pulse-height vs applied-voltage curves to illustrate ionization, proportional, and Geiger-Mueller regions of operation.

For the amplification process to proceed, an electron must acquire sufficient energy, in one or more mean free paths, to ionize a neutral molecule. The mean free path is the average distance the electron travels between collisions in proportional-counter gas and equals approximately 1 to 2 μm. For amplifications of 10^6, fewer than 20 mean free paths are necessary, which indicates that only a small region around the wire is involved in the multiplication process. In the rest of the volume, the electrons drift toward the anode. Because the amplification process requires a very high electric field, an advantage of the cylindrical detector design is the high electric field near the inner wire. The total amplification will be proportional to the electric field traversed, not the distance traversed.

At the same time that the electrons are drifting toward the anode, the positive ions are drifting toward the cathode. In a proportional counter, the drift velocity of the electrons is approximately 3 orders of magnitude larger than the drift velocity of the positive ions. Because the avalanche is formed near the anode wire, the electrons with a larger drift velocity are collected in an extremely short time interval (within 10^{-8} s); the slower drifting positive ions are collected on the cathode over a much longer time interval. The pulses observed have an initial fast risetime because of the motion of the electrons and a

subsequent slower risetime because of the motion of the positive ions. In addition, because the positive ions are initially formed close to the anode and must drift across the entire anode-to-cathode gap, the pulse amplitude is largely due to the drifting of the positive ions. The pulse reaches full amplitude only when the positive ions are fully collected. For a typical proportional counter this collection process may take 200 μs. Through differentiation, the pulse can be made much shorter without a substantial loss of pulse height so that rapid counting is possible. It is possible to approach the time dispersion caused by the variation in the drift time of the primary electrons from the interaction site to the anode wire. This time dispersion depends on tube voltage and diameter and has been reported (Ref. 5) as 1.1 μs (CH_4), 2.5 μs (^{3}He), and 17 μs (^{4}He) for some typical gas-filled tubes.

As the applied voltage is increased further, the proportionality between the primary charge deposited and the output signal is gradually lost. This loss is primarily due to saturation effects at the anode wire. As the primary ions reach the high field regions near the anode wire, the avalanche process begins and quickly grows to a maximum value as secondary electrons create additional avalanches axially along the wire. Unlike operation in the proportional region where the avalanche is localized, the avalanche now extends the full length of the anode wire and the multiplication process terminates only when the electrostatic field is sufficiently distorted to prevent further acceleration of secondary electrons. For weakly ionizing primary events, amplification factors of up to 10^{10} are possible. Detectors operated in this region are called Geiger-Mueller counters. Geiger counters require very simple electronics and form the basis for rugged field inspection instruments. Because they are saturated by each event, Geiger counters cannot be used in high-count-rate applications, but this limitation does not interfere with their use as low-level survey meters.

Neutron counters operated in either the ionization or proportional mode can provide an average output current or individual pulses, depending on the associated electronics. Measuring only the average output current is useful for radiation dosimetry and reactor power monitors. For assay of nuclear material it is customary to operate neutron counters in the pulse mode so that individual neutron events can be registered.

Gas-filled detectors typically employ ^{3}He, ^{4}He, BF_3, or CH_4 as the primary constituent, at pressures of less than 1 to about 20 atm depending on the application. Other gases are often added to improve detector performance. For example, a heavy gas such as argon can be used to reduce the range of the reaction products so that more of their kinetic energy is deposited within the gas and, thereby, the output pulse-height resolution is improved. Adding a heavy gas also speeds up the charge collection time, but has the adverse effect of increasing the gamma-ray sensitivity (Ref. 6).

A polyatomic gas may also be added to proportional counters to serve as quench gas. The rotational degrees of freedom available to polyatomic gas molecules serve to limit the energy gained by electrons from the electric potential, thus helping to dampen and shorten the avalanche process and improve the pulse-height resolution. Gases such as BF_3 and CH_4 are already polyatomic gases and require no additional quench gas. Tubes filled with ^{3}He and ^{4}He often have a small quantity of CH_4 or CO_2 added. Because BF_3 and CH_4 gases are polyatomic, detectors filled with these gases require higher operating voltages. Also, the relatively large quantity of polyatomic gas restricts the intercollisional energy gain so that these detectors are usually not operated at fill pressures as high as those used for detectors filled with monoatomic gases.

13.3 GAMMA-RAY SENSITIVITY OF NEUTRON DETECTORS

The neutron detectors described in this chapter are sensitive in some degree to gamma rays as well as neutrons. Because most nuclear material emits 10 or more times as many gamma rays as neutrons, the gamma-ray sensitivity of a neutron detector is an important criterion in its selection. For measurements of spent fuel, where gamma-ray fluxes of 1000 R/h or more are encountered, the gamma-ray sensitivity of the detector may dominate all other considerations.

In any detector, gamma rays can transfer energy to electrons by Compton scattering (see Chapter 2), just as neutrons transfer energy to other nuclei by scattering or nuclear reactions. Compton scattering can take place in the detector walls or the fill gas, yielding a high-energy electron that in turn produces a column of ionization as it traverses the detector. In some detectors, electronic pulses induced by gamma rays are comparable in size to neutron-induced pulses; in other detectors, they are much smaller, but can pile up within the resolving time of the electronics to yield pulses comparable to neutron pulses. Four factors should be considered when evaluating the relative magnitudes of the neutron and gamma-ray signals:

(1) The presence of gamma-ray shielding has a substantial effect on the relative magnitude of the signals. For example, for a detector exposed to 1-MeV fission neutrons in the presence of 1-MeV fission gamma rays, 5 cm of lead shielding absorbs roughly 0.1% of the neutrons and 90% of the gamma rays.

(2) Some detector materials and designs favor the absorption of neutrons. Table 13-1 gives examples for thermal- and fast-neutron detectors. From the table it is clear that thermal neutrons can be absorbed with much higher probability than gamma rays. For fast-neutron detection, the neutron and gamma-ray interaction probabilities are comparable.

Table 13-1. Neutron and gamma-ray interaction probabilities in typical gas proportional counters and scintillators

	Interaction Probability	
Thermal Detectors	Thermal Neutron	1-MeV Gamma Ray
^{3}He (2.5 cm diam, 4 atm)	0.77	0.0001
Ar (2.5 cm diam, 2 atm)	0.0	0.0005
BF_3 (5.0 cm diam, 0.66 atm)	0.29	0.0006
Al tube wall (0.8 mm)	0.0	0.014
	Interaction Probability	
Fast Detectors	1-MeV Neutron	1-MeV Gamma Ray
^{4}He (5.0 cm diam, 18 atm)	0.01	0.001
Al tube wall (0.8 mm)	0.0	0.014
Scintillator (5.0 cm thick)	0.78	0.26

Table 13-2. Neutron and gamma-ray energy deposition in typical gas proportional counters and scintillators

Thermal Detectors	Alpha or Proton Range (cm)	dE/dx for 400-keV Electron (keV/cm)	Average Neutron Reaction Energy Deposited (keV)	Electron Energy Deposited (keV)[a]	Ratio of Neutron to Electron Energy Deposition
^{3}He (2.5 cm diam, 4 atm)	2.1	1.1	~500	4.0	125
^{3}He (2.5 cm diam, 4 atm) + Ar (2 atm)	0.5	6.7	~750	24.0	30
BF_3 (5.0 cm diam, 0.66 atm)	0.7	3.6	~2300	25.7	90
Fast Detectors					
^{4}He (5.0 cm diam, 18 atm)	0.1	6.7	1000	48	20
Scintillator (5.0 cm thick)	0.001	2000	1000	400	2.5

[a]This calculation assumes a path length of $\sqrt{2} \times$ tube diameter.

(3) In some detectors neutrons deposit more energy than gamma rays do. Neutrons may induce a nuclear reaction that releases more energy than the Compton scattering of the gamma ray imparts to the electron. (The average energy imparted by a 1-MeV gamma ray is roughly 400 keV). Also, in gas detectors the range of the electron is typically much longer than the range of the heavy charged particles produced by neutron interactions. When the gas pressure is chosen to just stop the heavy charged particles, the electrons will escape from the tube after depositing only a small fraction of their energy in the gas. Table 13-2 gives some numerical examples of these effects. The table also shows that for fast-neutron detection by plastic scintillators the relative neutron and gamma-ray energy deposition is comparable.

(4) The charge collection speeds for neutron and gamma-ray detection may be different. This effect is very dependent on the choice of fill gas or scintillator material. In gas detectors, the long range of the electron produced by a gamma-ray interaction means that energy will be deposited over a greater distance, and more time will be required to collect it. An amplifier with fast differentiation will then collect relatively less of the charge released by a gamma-ray interaction than a neutron interaction. In scintillators, there is less distinction between the two kinds of events. In some circumstances, however, pulse-shape discrimination between neutrons and gamma rays can be achieved (see Section 13.5.3).

To achieve good gamma-ray discrimination, it is often necessary to use materials or material densities that are not optimum for neutron detection. The result may be a reduced neutron detection efficiency. Table 13-3 lists the neutron detection efficiency and approximate gamma-ray radiation limit for various neutron detector types. The detection efficiency is for a single pass through the detector at the specified energy. The actual efficiency for a complete detector system depends on the geometry, and the obtainable efficiency can be lower than the estimate given in Table 13-3. Additional details on these detectors and their gamma-ray sensitivity are given in the following sections.

Table 13-3. Typical values of efficiency and gamma-ray sensitivity for some common neutron detectors

Detector Type	Size	Neutron Active Material	Incident Neutron Energy	Neutron Detection Efficiency[a] (%)	Gamma-Ray Sensitivity (R/h)[b]
Plastic scintillator	5 cm thick	^{1}H	1 MeV	78	0.01
Liquid scintillator	5 cm thick	^{1}H	1 MeV	78	0.1
Loaded scintillator	1 mm thick	^{6}Li	thermal	50	1
Hornyak button	1 mm thick	^{1}H	1 MeV	1	1
Methane (7 atm)	5 cm diam	^{1}H	1 MeV	1	1
^{4}He (18 atm)	5 cm diam	^{4}He	1 MeV	1	1
^{3}He (4 atm), Ar (2 atm)	2.5 cm diam	^{3}He	thermal	77	1
^{3}He (4 atm), CO_2 (5%)	2.5 cm diam	^{3}He	thermal	77	10
BF_3 (0.66 atm)	5 cm diam	^{10}B	thermal	29	10
BF_3 (1.18 atm)	5 cm diam	^{10}B	thermal	46	10
^{10}B-lined chamber	0.2 mg/cm^2	^{10}B	thermal	10	10^3
Fission chamber	2.0 mg/cm^2	^{235}U	thermal	0.5	$10^6 - 10^7$

[a]Interaction probability for neutrons of the specified energy striking the detector face at right angles.
[b]Approximate upper limit of gamma-ray dose that can be present with detector still providing usable neutron output signals.

13.4 GAS-FILLED DETECTORS

13.4.1 ^{3}He and BF_3 Thermal-Neutron Detectors

Gas-filled thermal-neutron detectors use either BF_3 or ^{3}He. In the case of BF_3, the gas is enriched in ^{10}B. Helium-3 is only about 1 ppm of natural helium, so it is usually obtained by separation from tritium produced in reactors. The nuclear reactions that take place in these gases are

$$^{3}He + n \rightarrow {}^{3}H + {}^{1}H + 765\ keV \qquad (13\text{-}1)$$

$$^{10}B + n \rightarrow {}^{7}Li^* + {}^{4}He + 2310\ keV$$

$$\text{and } {}^{7}Li^* \rightarrow {}^{7}Li + 480\ keV \ . \qquad (13\text{-}2)$$

These reactions are exothermic and release energetic charged particles into the gas. The counters are operated in the proportional mode, and the ionization produced by these particles initiates the multiplication process that leads to detection. The amount of energy deposited in the detector is the energy available from the nuclear reaction.

In the case of ^{3}He, the neutron causes the breakup of the nucleus into a tritium nucleus, ^{3}H, and a proton, ^{1}H. The triton and the proton share the 765-keV reaction energy. In the case of ^{10}B, the boron nucleus breaks up into a helium nucleus (alpha

particle) and a lithium nucleus, with 2310 keV shared between them. Ninety-four percent of the time the lithium nucleus is left in an excited state from which it subsequently decays by emitting a 480-keV gamma ray. This gamma ray is usually lost from the detector, in which case only 2310 keV is deposited. About 6% of the time the lithium nucleus is left in the ground state, so that 2790 keV is deposited in the detector. This double reaction mode yields an additional small full-energy peak in the pulse-height spectrum of BF_3 tubes.

The cross section for the ^3He reaction (Equation 13-1) is 5330 b for thermal neutrons, and the cross section for the ^{10}B reaction (Equation 13-2) is 3840 b. Both reaction cross sections are strongly dependent on the incident neutron energy E and have roughly a $1/\sqrt{E}$ dependence. Figure 13.4 illustrates these cross sections (Ref. 7). As an example, a 2.54-cm-diam tube with 4 atm of ^3He has a 77% efficiency for thermal neutrons (0.025 eV). (This configuration is nearly optimum for thermal neutrons; more ^3He would give relatively little additional efficiency and would usually not be cost-effective.) At 100 eV the efficiency is roughly 2%; at 10 keV, roughly 0.2%; and at 1 MeV, roughly 0.002%. Because of this strong energy dependence, it is customary to embed ^3He or BF_3 detectors in approximately 10 cm of polyethylene or other moderating materials to maximize their counting efficiency (see Chapter 14 for additional details on detector design).

Figure 13.5 is a typical pulse-height spectrum from a ^3He proportional counter (Ref. 8). The shape of this spectrum is due primarily to (1) the kinematics of the reaction process and (2) the choice of amplifier time constants. The full-energy peak in the spectrum represents the collection of the kinetic energy of both the proton and the triton. (It should be emphasized that this peak represents the 765 keV released in the reaction and is not a measure of the incident neutron energy.) If one or the other particle enters the tube wall, less energy is collected in the gas, which results in a low-energy tail. Since the two charged particles are emitted back-to-back, one or the other is almost certain to

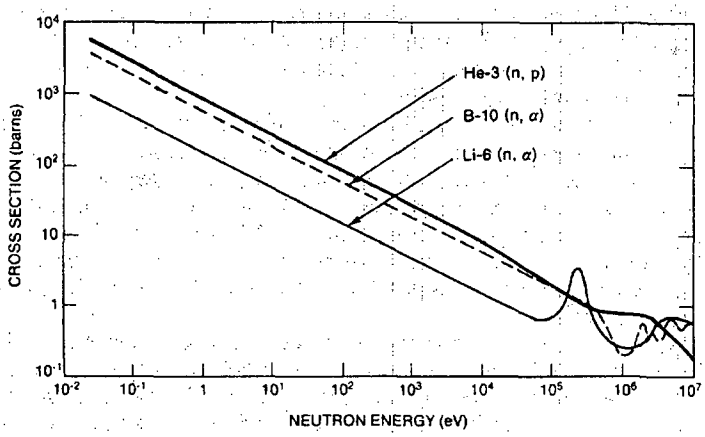

Fig. 13.4 *$^3He(n,p)$, $^{10}B(n,\alpha)$, and $^6Li(n,\alpha)$ cross sections as a function of incident neutron energy (Ref. 7).*

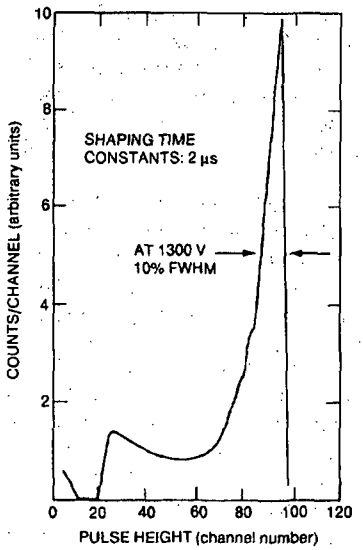

Fig. 13.5 Differential pulse-height spectrum for thermal neutrons detected by a ^{3}He-filled counter.

be detected. Thus, there is a minimum collection energy, with a wide valley below, and then a low-energy increase resulting from noise and piled-up gamma-ray events. If the discriminator is set in the valley, small changes in tube voltage or amplifier gain will not affect the count rate. The result is a very stable (approximately 0.1%) detection system.

The choice of amplifier time constant determines the degree of charge collection from the tube. Time constants of 2 μs or greater result in nearly complete charge collection and yield spectra such as the spectrum shown in Figure 13.5, with 5 to 15% resolution (FWHM) of the full-energy peak. Time constants of 0.1 to 0.5 μs cause complete loss of the peak shape, but allow counting at higher rates with less noise pickup and gamma-ray interference. A 0.5-μs time constant is a commonly used compromise between good resolution and high-count-rate capability.

Helium-3 tubes are usually operated in the range of +1200 to 1800 V. Over this range the increase in counting efficiency with voltage caused by improved primary charge collection is very slight, about 1%/100 V (Ref. 8). (A typical plateau curve is shown in Figure 13.6.) On the other hand, the total charge collected (due to multiplication in the gas) changes rapidly with voltage, about 100%/100 V. When ^{3}He tubes are used in multiple detector arrays, it is important to specify good resolution (on the order of 5% FWHM) and uniform gas mixture so that the position and width of the full-energy peak will be the same for all tubes.

A pulse-height spectrum for a BF_3 proportional counter is shown in Figure 13.7 (Ref. 1). For BF_3 tubes, the resolution is in the range 5 to 30% (FWHM) but is usually not as good as for ^{3}He. Gas pressures are in the range 0.2 to 2 atm. To help compensate for the lower pressure, tube diameters are usually 5 cm. Operating voltages are in the range +1400 to 2800 V, higher than for ^{3}He. Plateau curves are similar to those of ^{3}He. BF_3 gas is less expensive than ^{3}He, so that manufacturing costs are less. However, the larger neutron absorption cross section for ^{3}He and the larger possible fill pressure make its

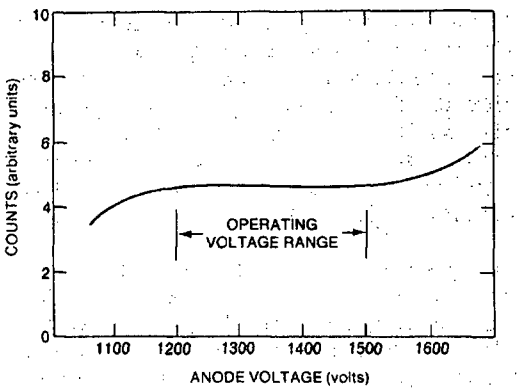

***Fig. 13.6** Typical plateau curve for a gas-filled ^{3}He counter.*

cost per detected neutron lower in the United States. Another advantage of ^{3}He-filled detectors is that helium is an inert gas whereas BF_3 is toxic. However, US Department of Transportation regulations place detectors with more than 2-atm fill pressure in the high-pressure compressed gas category, so that ^{3}He-filled detectors are often more difficult to ship.

Helium-3 and BF_3 detectors find many applications in passive and active neutron assay because they are relatively stable, efficient, and gamma-insensitive. The detection efficiency for thermal neutrons is high, and the interaction probability for gamma rays is low, as indicated in Table 13-1. Also, much more energy is deposited in the gas by neutron interactions than by gamma-ray interactions, as indicated in Table 13-2. However, if the gamma dose is more than that emitted by typical plutonium and uranium samples, the response of ^{3}He and BF_3 detectors will be affected.

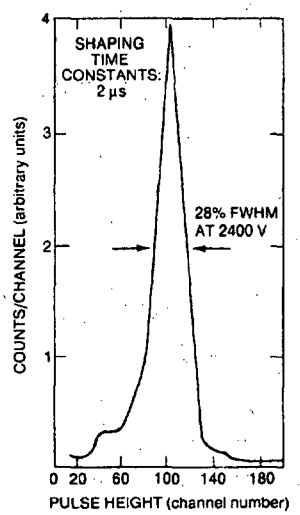

***Fig. 13.7** Differential pulse-height spectrum for thermal neutrons detected by a $^{10}BF_3$-filled counter.*

As an example, Figure 13.8 shows the effect of increasing gamma-radiation fields on a ^{3}He detector (4 atm) containing argon (2 atm) (Ref. 9). The practical operating limit is on the order of 1 R/h. Some improvement can be obtained by replacing argon with about 5% CO_2, as illustrated in Figure 13.9 (Ref. 10). The improvement is due to the removal of the relatively high-Z argon (the electron density is proportional to the Z of the molecule). However, removal of the argon reduces the relative size of the full-energy peak because the reaction products now have longer ranges and deposit less of their energy in the gas. Also, the longer ranges lead to slower charge collection and roughly 35% longer electronic deadtimes.

The gamma-ray sensitivity of BF_3 detectors is comparable to but perhaps slightly better than ^{3}He. The ^{10}B reaction deposits more energy in the gas than the ^{3}He reaction, but gamma-ray interactions also deposit more energy (see Table 13-2). The ^{3}He reaction has a higher cross section than the BF_3 reaction. The cross section for a gamma-ray interaction will depend on the relative amounts of ^{3}He, argon, and BF_3 and on the relative tube wall thicknesses (see Table 13-1). BF_3 detectors can operate in gamma-radiation fields up to 10 R/h, which is better than the performance of ^{3}He + argon counters. However, the performance of ^{3}He + CO_2 counters is comparable to that of BF_3.

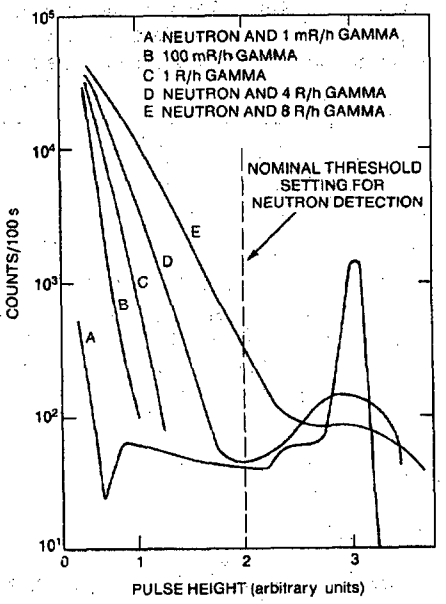

Fig. 13.8 *Gamma-ray pile-up effects for a ^{3}He proportional counter tube 2.54 cm in diameter and 50.8 cm in length.*

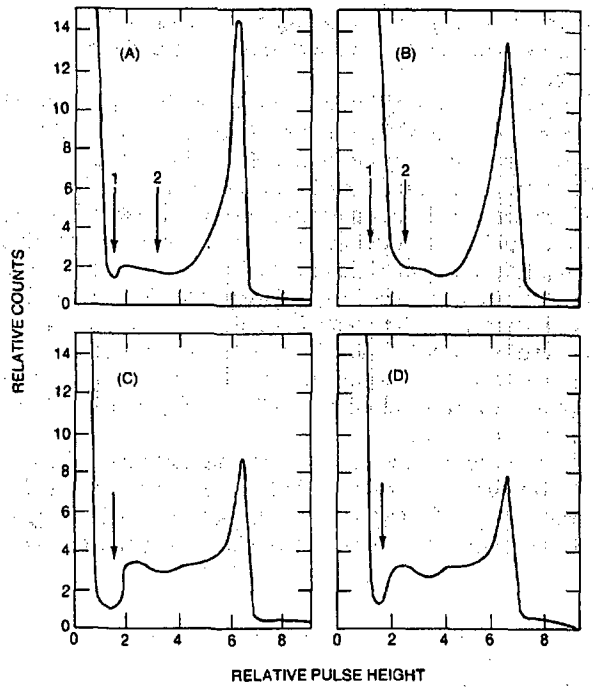

Fig. 13.9 *Differential pulse-height spectra for various ^3He neutron detectors. The amplifier time constant was set at 0.5 μs. (a) $^3He + Ar + CH_4$ mixture with neutron source; (b) $^3He + Ar + CH_4$ mixture with neutron plus 1-R/h gamma-ray source; (c) $^3He + 5\% CO_2$ mixture with neutron source; (d) $^3He + 5\% CO_2$ mixture with neutron plus 1-R/h gamma-ray source.*

13.4.2 ^4He and CH_4 Fast-Neutron Detectors

Helium-4 and CH_4 fast-neutron detectors rely on the recoil of light nuclei to ionize the gas in the tube. The interaction is the elastic scattering of the neutron by a light nucleus. If the recoiling nucleus is only a hydrogen nucleus (proton), the maximum possible energy transfer is the total neutron kinetic energy E. For heavier elements the maximum energy transfer is always less. For a nucleus of atomic weight A, the maximum energy transfer is (Ref. 7):

$$E(max) = \frac{4A\,E}{(A+1)^2} \qquad (13\text{-}3)$$

For a single scattering event, the actual energy transferred to the recoiling nucleus lies between 0 and E(max) depending on the scattering angle and has equal probability for any value in this range.

Equation 13-3 shows that the target nucleus must have low atomic weight to receive a significant amount of energy from the neutron. Hydrogen is the most obvious choice; it can be used in a gaseous form or, more commonly, in liquid or plastic scintillators (see Section 13.5). Popular gas detectors usually employ methane (CH_4), which has a high hydrogen content, or ^{4}He, which has a maximum energy transfer of 0.64 E(n). (Helium-3 gas is also a suitable candidate by these criteria, but it is usually not used because of the stronger thermal reaction described in Section 13.4.1.) Figure 13.10 illustrates the elastic scattering cross sections for ^{1}H and ^{4}He, showing that they match the shape of the fission-neutron energy spectrum fairly well. Note that the cross sections are substantially lower than those given in Figure 13.4 for ^{3}He and ^{10}B. The efficiency for detecting a fast neutron by an elastic scattering interaction is about 2 orders of magnitude lower than the efficiency for capture of a thermal neutron. Thus a single ^{4}He or CH_4 tube has an intrinsic efficiency of about 1%.

These gas counters are operated as proportional counters with voltages in the range of +1200 to 2400 V. Gas fill pressures are typically 10 to 20 atm for ^{4}He. Relative to ^{4}He, the polyatomic gases CH_4 or H_2 again require higher operating voltages, have slightly lower efficiencies, are limited to lower pressures, and exhibit faster signal risetimes. The

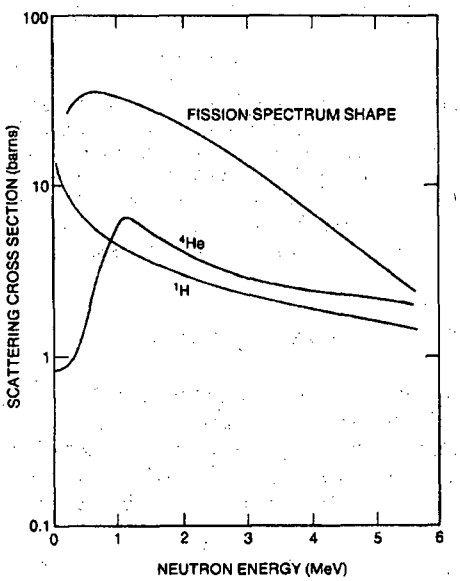

Fig. 13.10 *^{1}H and ^{4}He elastic scattering cross sections, with a fission spectrum shape (not drawn to scale) superimposed.*

gamma-ray sensitivity of the two types of counters is comparable. Neutron counting can be done in gamma-radiation fields of roughly 1 R/h if a moderately high threshold is set (Ref. 11).

Figure 13.11 shows a pulse-height spectrum from a ^{4}He proportional counter collected with a ^{252}Cf neutron source. The observed spectrum shape is the convolution of the following effects:

(1) the ^{252}Cf spontaneous fission neutron spectrum, as illustrated in Figure 11.2,

(2) the probability of transferring an energy between 0 and E(max) to the recoiling nucleus,

(3) the probability of multiple neutron scatterings and the probability of losing recoiling nuclei in the tube walls (see Ref. 12, Figure 8-14 for an example),

(4) the detection of low-energy noise pulses and gamma-ray pile-up events.

Because of these effects the pronounced peak in the initial neutron energy spectrum may be lost, or nearly lost, as indicated in Figure 13.11. Nevertheless, some energy information remains, and more can be obtained by attempting to unfold the above effects. It is customary to set a threshold high enough to reject low-energy noise and gamma-ray events, but low enough to collect many of the medium- and high-energy neutron events. Since the threshold must be set on a sharply falling curve, a recoil detector is not as stable as a thermal detector.

Despite the apparent disadvantages of recoil-type detectors in terms of lower efficiency and stability, the detection process takes place without prior thermalization of the incident neutron. Thus the neutron is detected very rapidly and some information on its initial energy is preserved. Fast-neutron counters can detect neutrons in the energy range of 20 keV to 20 MeV, and some are useful for fast coincidence counting with 10- to 100-ns resolving times. It is also possible to set a threshold that will reject gamma rays and low-energy neutrons, a feature that is particularly suitable for active assay systems.

13.4.3 Fission Chambers

Fission chambers are a variation of the gas-filled counters previously described. They detect neutrons that induce fissions in fissionable material coated on the inner walls of the chamber. Often the exterior appearance of fission chambers is quite similar to that of other gas counters, although they are also available in smaller diameters or in other shapes. The fissionable material is usually uranium highly enriched in ^{235}U. A very thin layer (0.02 to 2 mg/cm^2 surface thickness) is electroplated (sometimes evaporated or painted) on the inner walls. The thin layer is directly exposed to the detector gas. After a

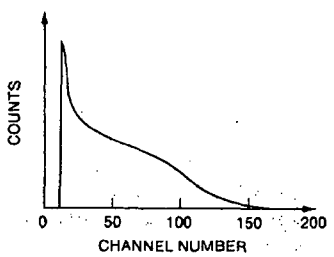

Fig. 13.11 Differential pulse-height spectrum of ^{4}He proportional counter for a ^{252}Cf source.

fission event, the two fission fragments travel in nearly opposite directions. The ionization caused by the fission fragment that entered the gas is sensed by the detector; the fragment traveling in the opposite direction is absorbed in the detector walls (Ref. 13).

The two fragments share about 160 MeV of energy, but their range is quite short. For a typical plating material such as uranium, the average fission fragment range is only about 7 μm, equivalent to about 13 mg/cm^2 of coating thickness. Consequently, fission fragments that are produced at a depth of more than 7 μm in the detector wall cannot reach the gas to cause ionization. Furthermore, most fragments exit at a grazing angle, so that their path length is longer than the minimum needed to escape. Because the coating must be kept thin to allow the fission fragments to enter the gas, the fission chamber uses only a small quantity of fissionable material and has a low detection efficiency. For thermal neutrons, the intrinsic efficiency is typically 0.5 to 1%. Fast neutrons can also be detected, but with even lower efficiency.

Fission chambers are operated in the ion chamber mode because the ionization caused by the fission fragments is sufficient and no further charge multiplication within the detector is necessary. The electronics configuration shown in Figure 13.1 is frequently used, with an applied voltage in the +200 to 600 V range. A mixture of 90% argon and 10% methane is a common fill gas. At this pressure the range of fission fragments is about 2 cm.

Figure 13.12 shows a pulse-height spectrum from a ^{235}U chamber (Ref. 14). If energy losses in the coating or in the walls are not too great, the double hump shape caused by light and heavy fission fragments (near 70 and 100 MeV) is visible. Also, an alpha-particle background is present at low energies because nearly all fissionable material contains alpha-emitting isotopes. The alpha-particle energy is typically 5 MeV, whereas the fission fragment energy is an order of magnitude larger. Thus the threshold setting of the counting electronics can be set above the alpha-induced signal. At this threshold setting, some of the low-energy fission-fragment pulses will be lost. Plutonium has a much higher alpha activity than uranium; as a consequence more alpha pulses pile up and the threshold for plutonium-lined fission chambers must be set higher than for uranium-lined chambers.

Because of the large quantity of energy deposited by the fission fragments, fission chambers have the highest insensitivity to gamma rays (roughly 10^6 R/h) of any of the

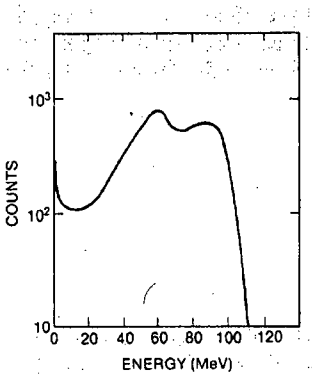

Fig. 13.12 Differential pulse-height spectrum of a ^{235}U fission chamber with a coating thickness of about 0.8 mg/cm^2.

neutron detectors. They are the only detectors capable of direct unshielded neutron measurement of spent reactor fuel. This passive measurement feature applies to both high neutron and gamma-ray fluxes. The inherently low efficiency of fission chambers is compensated for by the large number of neutrons available for counting.

13.4.4 ^{10}B-Lined Detectors

Detectors lined with ^{10}B lie between ^{3}He and $^{10}BF_3$ proportional counters and fission chambers in terms of neutron detection efficiency and gamma-ray insensitivity. Structurally, ^{10}B-lined detectors are similar to fission chambers with the neutron-sensitive material, boron, plated in a very thin layer (about 0.2 mg/cm^2) on the walls of the detector.

The ^{10}B-lined detectors rely on the nuclear reaction given in Equation 13-2 to detect neutrons. Either the alpha particle or the lithium nucleus enters the detection gas (not both, since they are emitted back to back), and the detection process is initiated. Because the range of the alpha particle is about 1 mg/cm^2 in boron, the plating must be thin and the detection efficiency (on the order of 10%) is lower than for BF_3 gas-filled counters. However, since the nuclear reaction does not take place in the fill gas, the gas can be optimized for fast timing. Argon at 0.25 atm pressure, with a small admixture of CO_2, is one common choice. The counter is operated in the proportional mode at a voltage of +600 to 850 V (Ref. 15).

Figure 13.13 shows the pulse-height spectrum of the ^{10}B-lined chamber described above. The stepped structure of the spectrum is caused by the fact that either the alpha particle or the lithium nucleus can enter the gas. Because the lighter alpha particle carries more of the energy, the step resulting from the alpha particle is shown farther to the right. The large number of low-energy pulses is due to the energy loss of the particles in the boron coating of the walls. The detector threshold is usually set above these low-energy

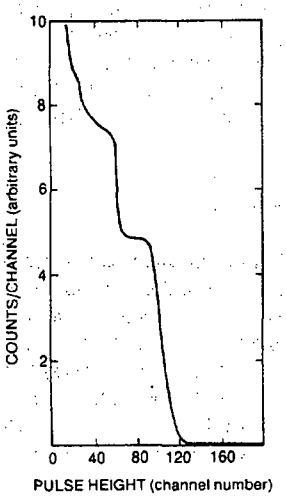

Fig. 13.13 *Differential pulse-height spectrum of a ^{10}B-lined proportional counter.*

pulses. Because there is no well-defined "valley" to set the threshold in, the count-rate plateau curve is roughly 10%/100 V (Ref. 15).

The ^{10}B-lined counter can detect thermal neutrons with moderate efficiency and fast neutrons with low efficiency. It is most useful for applications where it is necessary to detect neutrons in the presence of high gamma-ray fields. With proper electronics, the detector can be operated in a gamma-ray flux as high as 1000 R/h with a 50% loss in neutron detection efficiency resulting from the higher discriminator setting required to reject piled-up gamma events (Ref. 15). The higher gamma-ray insensitivity of the ^{10}B-lined counter relative to the BF_3 gas-filled counter is due to the lower fill pressure and lower operating voltage, which reduce the size of gamma-ray pulses relative to neutron pulses.

13.5 PLASTIC AND LIQUID SCINTILLATORS

13.5.1 Background

Plastic and liquid (organic) scintillators are often used for fast-neutron detection because of their fast response and modest cost. Fast response is particularly beneficial for coincidence counting applications where the ratio of real to accidental coincidence events can have a significant impact on the statistical precision of measurement. Although organic scintillators have response times of a few nanoseconds, the coincidence resolving time for assay applications is usually dictated by the dynamic range of neutron flight times (tens of nanoseconds) from the sample to the detectors. (A 500-keV neutron will traverse a flight path of 1 m in ~100 ns.) The resolving times of coincidence counting systems that moderate fast neutrons prior to detection, on the other hand, are dominated by the dynamic range of times (tens of microseconds) required for thermalization.

The major disadvantage of organic scintillators in nondestructive assay applications is their high gamma-ray sensitivity. Detection probabilities for neutrons and gamma rays are comparable, and the pulse-height spectra resulting from monoenergetic radiation of both types are broad and overlapping. Hence, pulse height alone yields little information about particle type. In certain organic scintillators, however, electronic pulse-shape discrimination techniques can be used to effectively distinguish between neutron and gamma-ray interactions.

13.5.2 Neutron and Gamma-Ray Interaction Mechanisms

Fast neutrons interact in scintillators through elastic scattering with the nuclei present (mostly carbon and hydrogen). For fission spectrum or (α,n) neutrons, most of the useful scintillator light comes from recoiling hydrogen nuclei (protons). This occurs because a neutron can transfer 100% of its energy in an elastic scattering interaction to a recoiling proton but only 28% can be transferred to a recoiling ^{12}C nucleus. The kinetic energy of the recoiling protons is absorbed by the scintillator and is ultimately converted to heat and visible light. The visible light can be collected in a photomultiplier tube optically coupled to the scintillator and converted to an electronic pulse whose magnitude is related to the kinetic energy of the recoiling proton.

A good scintillation material for neutron detection has relatively high efficiency for converting recoil particle energy to fluorescent radiation, good transparency to its own radiation, and good matching of the fluorescent light spectrum to the photomultiplier-tube response. Many commercially available scintillators such as NE102 and NE213 adequately satisfy these criteria. Table 13-4 gives examples of plastic and liquid scintillators that are widely available. The wavelength of maximum scintillation light emission is typically ~400 nm. At that wavelength, light attenuation lengths are in the range 1 to 5 m. Since light can travel relatively long distances in the scintillator material without significant attenuation, organic scintillators with dimensions of the order of 1 m are not uncommon.

Although the mechanism by which fast neutrons transfer their kinetic energy to protons in an organic scintillator is identical to that in a hydrogen or methane recoil proportional counter, a number of features of the overall detection process are markedly different. This distinction is largely due to the differences in physical properties of organic scintillators and gases. The density, for example, of gas in a recoil proportional counter is of order 10^{-3} g/cm^3, whereas that of an organic scintillator is of order unity. This difference in density means that for a given detection path length in the two materials the probability of interaction for both neutrons and gamma rays will be substantially higher in the scintillator than in the proportional counter. Figure 13.14 illustrates the energy dependence of the interaction probability (expressed as attenuation coefficients) for neutron and gamma-ray interactions in NE213. This figure shows, for example, that a 1-MeV neutron has an interaction probability of ~78% in a 5-cm-thick NE213 liquid scintillator, whereas a 1-MeV gamma ray has an interaction probability of ~26%.

In addition, the ranges of the recoiling protons and electrons will be substantially shorter in the scintillator than in the proportional counter. Except for events occurring near the boundaries of the detectors, this fact is of little importance when considering the recoiling protons. However, the shortened range of the recoil electrons in the organic

Table 13-4. Some representative plastic and liquid scintillators for neutron detection

Type	I.D.	Mfg[a]	Light Output (% of anthracene)	Decay Const (ns)	Wavelength of Max. Emission (nm)	H/C Atomic Ratio	Comments
Plastic	NE102A	1	65	2.4	423	1.104	general use
	NE104	1	68	1.9	406	1.100	fast timing
	NE111A	1	55	1.6	370	1.103	ultrafast timing
	Pilot B	1	68	1.8	408	1.100	general use
	Pilot U	1	67	1.4	391	1.100	ultrafast timing
Liquid	NE211	1	78	2.6	425	1.248	general use
	NE213	1	78	3.7	425	1.213	fast n (P.S.D)
	BC501	2	78	3.7	425	1.213	fast n (P.S.D)
	NE228	1	45		385	2.11	high H/C ratio
	NE311	1	65	3.8	425	1.701	boron-loaded
	NE323	1	60	3.8	425	1.377	gadolinium-loaded

[a]Manufacturer code: (1) Nuclear Enterprises, Ltd.; (2) Bicron Corp.

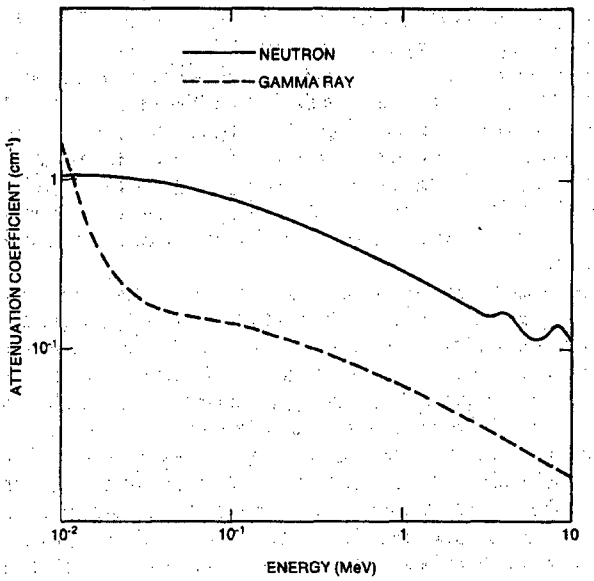

Fig. 13.14 Attenuation coefficients as a function of incident energy for neutron and gamma-ray interactions in NE213.

scintillators has a profound effect in that high-energy electrons can stop inside the detection volume. For example, a 500-keV electron can deposit all of its energy in a scintillator while depositing only a small fraction in a gas proportional counter.

Furthermore, recoiling electrons and protons of the same initial energy produce differing amounts of light in a scintillator. This result is apparently due to the differing ionization densities along the slowing-down paths in the two cases. The light output for protons is always less than that for electrons of the same energy, as shown in Figure 13.15 (Refs. 7 and 16). Also, the light output for the two particle types has a different dependence as a function of energy. (Carbon-12 recoils give even less light than proton recoils of the same energy, further reducing their already small contribution to the detection process.) As a rule of thumb, 60-keV electrons and 500-keV protons give approximately equal amounts of light in a typical organic scintillator.

13.5.3 Pulse-Shape Discrimination

The mechanism by which a fraction of the kinetic energy of the recoiling particles is transformed into visible light in an organic scintillator is very complex. However, a few features can be simply stated. The major components of the scintillator light decay in times of the order of a few nanoseconds. This means that, in principle, organic scintillators can operate at very high counting rates. However, there is a weaker, longer-

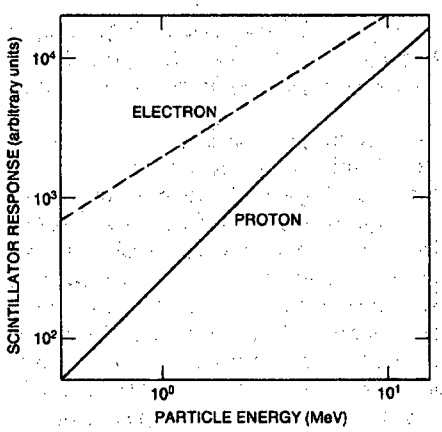

Fig. 13.15 *Scintillation light yield as a function of particle energy for electrons and protons in NE102. The data are taken from Refs. 7 and 16.*

lived component of the radiation from many scintillators that corresponds to delayed fluorescence. Consequently, the total light output can often be represented by the sum of the two exponential decays referred to as the fast and slow components of the scintillation. The slow component has a characteristic decay time in the range of a few hundred nanoseconds. The fraction of the total light observed in this weaker, slower component is a function of the type of particle inducing the radiation. Heavier particles have higher specific ionization and produce more delayed fluorescence light. Figure 13.16 (Ref. 17) illustrates the time dependence of scintillator pulses in stilbene, a solid organic crystal scintillator, when the crystal is excited by different types of radiation.

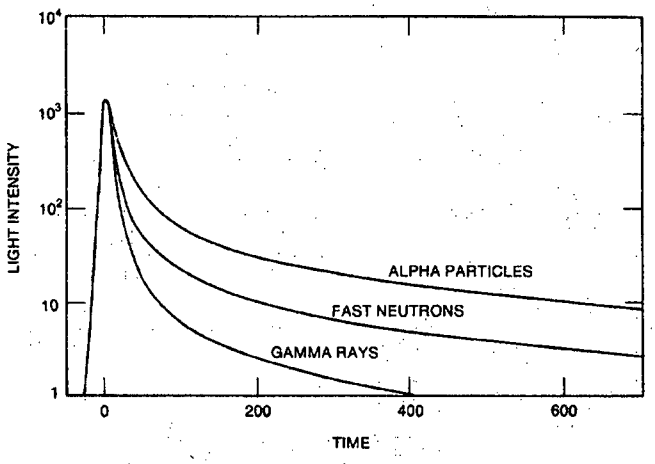

Fig. 13.16 *The time dependence (in nanoseconds) of scintillation pulses in stilbene when excited by different incident particle types (Ref. 17). Note that the light intensity is plotted on a logarithmic scale.*

This time dependence makes it possible to identify particles that have differing rates of energy loss but produce the same amount of light in the scintillator. This procedure is termed pulse-shape discrimination and is used to reject gamma-ray events in neutron detection applications of organic scintillators.

Pulse-shape discrimination is achieved by electronically exploiting the light-emission time-dependence properties of different types of radiation incident on organic scintillators. The most common method used for pulse-shape discrimination in organic scintillators is based on passing the photomultiplier-tube pulse through a bipolar-shaping network, usually a double-delay line. The zero-amplitude crossing of this bipolar pulse depends on the risetime and shape of the initial pulse but is independent of amplitude. Thus, a measure of the pulse shape is given by the time interval between the leading edge of the initial pulse (which is independent of pulse shape) and the zero crossing of the bipolar-shaped pulse. An example of a circuit employing this method is given in Figure 13.17 taken from Ref. 18. Also indicated in the figure are schematic representations of recoil electron and proton pulses at different points in the circuit.

The performance of a pulse-shape discrimination circuit is usually stated in terms of a figure of merit. This measure compares the separation of neutron and gamma-ray-induced events in the time-difference spectrum to the sum of the widths of the individual event distributions as shown in Figure 13.18. The figure of merit is generally reduced by increases in either the dynamic range of processed input pulse heights or the

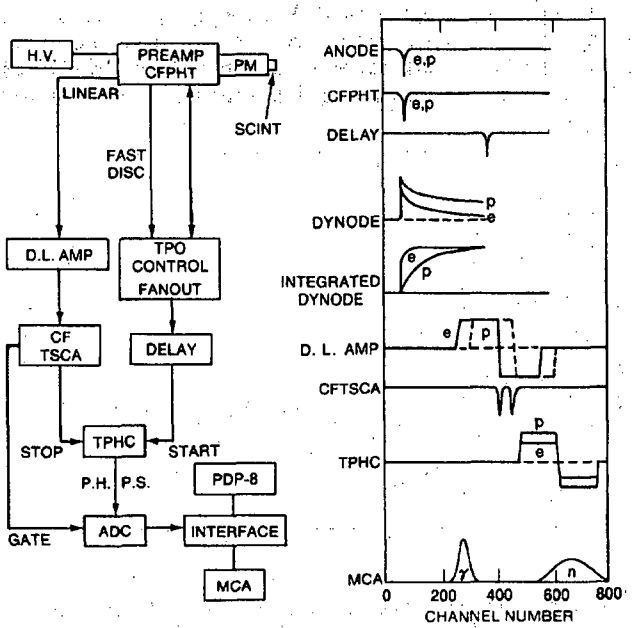

***Fig. 13.17** Pulse-shape discrimination circuit employing the "crossover/leading-edge" time-difference method (Ref. 18).*

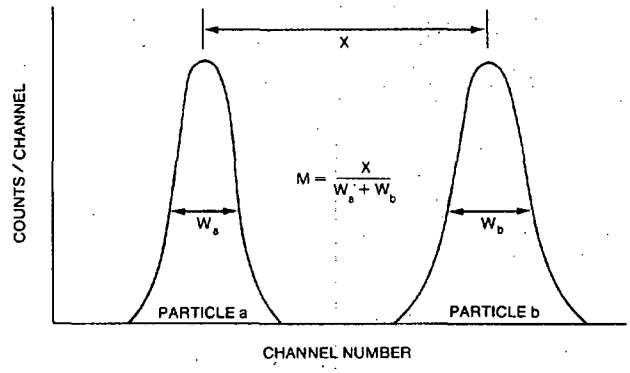

***Fig. 13.18** Illustration of the figure of merit, M, for measuring performance of pulse-shape discrimination systems.*

gross counting rate. Successful operation of pulse-shape discrimination circuits with dynamic ranges of 100 at counting rates of 10^4 s^{-1} have been reported (Ref. 18). Figure 13.19 shows experimental results obtained with an NE218 liquid scintillator and a plutonium-beryllium neutron/gamma-ray source.

Another common approach to pulse-shape discrimination involves integrating the charge contained in the early risetime part of the pulse and comparing it to the integral of the charge in the late part of the pulse. In a recent application (Ref. 19) of this method, the anode pulse from the photomultiplier tube is split and the early and late parts of the pulse are separately gated into integrating analog-to-digital converters. The ratio of the digital results for the late and early parts of the pulse then gives a pulse-shape discrimination spectrum similar to that shown in Figure 13.20.

13.6 OTHER TYPES OF NEUTRON DETECTORS

This section describes several neutron detectors that have not found widespread use for nuclear material assays. Like the other detectors described in this chapter, they rely ultimately on either recoil interactions or direct nuclear reactions to detect neutrons.

Some scintillators are manufactured with neutron-active material added to achieve enhanced neutron detection capability. The purpose is to achieve more localized and more rapid detection of neutrons than is possible with gas counters. Gadolinium, ^{10}B, and ^6Li are typical materials "loaded" into the scintillator. The neutron-active material initiates the light production by releasing energetic charged particles or gamma rays when the neutron is captured. After the initial interaction with the neutron occurs, the detection process is the same as if the light were produced by a gamma ray. Because the scintillator is also a gamma-ray detector, its gamma-ray sensitivity is generally very high. There are, however, several possible configurations with good neutron detection efficiency and low gamma-ray sensitivity.

One useful configuration for thermal-neutron counting consists of lithium-loaded glass scintillators. ZnS(Ag) crystals in a glass medium or cerium-activated silicate glasses

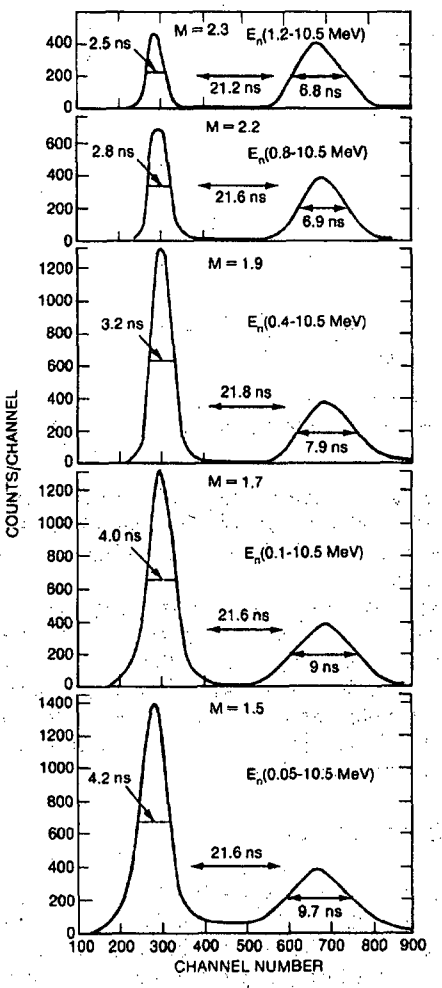

Fig. 13.19 *Risetime distributions for different neutron energy dynamic ranges for an NE218 liquid scintillator and a plutonium-beryllium neutron/gamma-ray source (from Ref. 18).*

are available. Thermal neutrons interact with ^{6}Li via the (n,α) reaction, and the heavy alpha particles excite the scintillator. Detectors of this type are available in sheets with thicknesses of about 1 mm. For thermal neutrons, efficiencies of 25 to 99% are possible in gamma-ray fields on the order of 1 R/h. The low gamma-ray sensitivity is due to the high thermal-neutron capture cross section, the large 4.78-MeV energy release in the reaction, and the thinness of the detector (Ref. 7).

If ZnS(Ag) crystals are dispersed in Lucite, detection of fast neutrons is possible. The interaction mechanism is the elastic scattering of neutrons by hydrogen. The recoiling

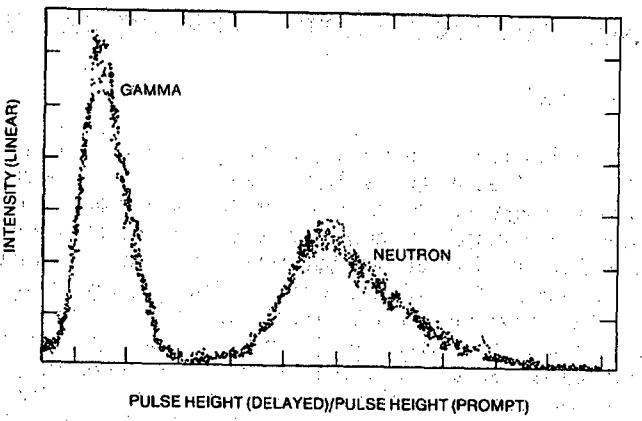

Fig. 13.20 *Ratio of delayed gate ADC conversion to prompt gate ADC conversion for NE213 (Ref. 19).*

proton deposits its energy in the scintillator, and by transfer reactions the ZnS(Ag) crystals are excited. ZnS(Ag) offers good gamma-ray insensitivity because relatively high energies are required to excite the light-emitting property of the zinc sulfide crystals. Detectors that consist of ZnS(Ag) crystals dispersed in Lucite are called Hornyak buttons (Ref. 20); their efficiency is low (on the order of 1%) because the poor light transmission properties of this material limits its use to small sizes. Thin sheets have also been used for measurements of waste crates at the Rocky Flats Plant (Ref. 21). Hornyak buttons can operate in gamma fields up to about 1 R/h because of the properties of ZnS(Ag) and because the thinness of the detector limits the gamma-ray-induced energy deposition.

Most neutron detectors combine neutron-sensitive material and detection electronics into one inseparable unit. However, it is possible to employ a detection system that is more compact and portable by using only the neutron-sensitive material. This material is first placed at the point of interest, then removed for measuring the actual neutron flux by observing isotopic or crystalline structure changes. An example is the use of thermoluminescent dosimeters (TLDs), which consist of crystals that, when heated, emit an amount of light proportional to the dose received. Thermoluminescent dosimeters are primarily used for gamma-ray measurements, but one common crystal, LiF, can be made to be neutron sensitive by increasing the enrichment of ^{6}Li (Ref. 7).

Activation foils, used for criticality safety and low-level detection, provide other examples of the use of neutron-sensitive material. One application has been the use of thin copper sheets to monitor plutonium migration in soil near nuclear waste storage sites (Ref. 22). The technique relies on neutron capture in ^{63}Cu to yield ^{64}Cu, which decays to $^{64}Ni + e^{+}$ with a 12.7-hour half-life. The foils are buried long enough to achieve an equilibrium level of ^{64}Cu and then retrieved to permit measurement of the positron emission rate. Plutonium concentrations as low as 10 nCi/g have been monitored.

13.7 MEASUREMENT OF NEUTRON ENERGY SPECTRA

13.7.1 Background

As noted in Section 13.1, passive neutron assays are usually based on counting neutrons without regard to their energy. This is because (1) radioactive materials emit neutrons with broad energy spectra that are very similar from one isotope to another and (2) neutron detection is an indirect process that preserves little information about the incident neutron energy. This chapter has shown that neutron detection usually produces a broad spectrum of events that are only indirectly related to the neutron energy. A partial exception is found in the case of recoil detectors such as ^{4}He gas-filled counters and plastic scintillators. However, none of the detectors described in this chapter can distinguish nuclear isotopes on the basis of their neutron energy.

As a consequence, passive neutron assay is usually based on the counting of thermal or fast neutrons, with perhaps some tailoring of the detector or its surroundings to favor a particular broad energy interval. Detectors are also chosen on the basis of their ability to produce fast (10 to 100 ns) or slow (10 to 100 μs) output signals for coincidence counting. Some detectors are also designed to have a detection efficiency that is nearly independent of neutron energy.

13.7.2 Techniques

Although measurement of neutron energy spectra is not necessary for passive neutron assay, it is sometimes important for research or instrument development activities. Such a measurement is difficult, but possible by a variety of techniques. These techniques include proton recoil spectrometers, neutron time-of-flight measurements, and ^{3}He spectrometers. An example of the use of ^{3}He spectrometers in measuring neutron energy spectra follows.

The ^{3}He spectrometer developed by Shalev and Cuttler (Refs. 23 and 24) has been used to measure delayed neutron energy spectra. (The AmLi neutron spectrum given in Figure 11.5 was also measured with an instrument of this type.) The spectrometer is a gas-filled proportional counter containing ^{3}He, argon, and some methane. Neutrons are detected via the ^{3}He (n,p) reaction in the energy range of 20 keV to 2 MeV. In this energy range the reaction cross section is smooth and nearly flat, declining from roughly 10 to 1 b. To detect these fast neutrons the tube is not enclosed in moderating material; rather, it is wrapped in cadmium and boron sheets to reduce the contribution of the much stronger thermal ^{3}He (n,p) reaction (5330 b). Also, a lead shield is often added to reduce the effects of gamma-ray pile-up on the neutron energy resolution. The intrinsic efficiency is low, on the order of 0.1%.

The energy spectrum of a ^{3}He spectrometer includes a full energy peak at the neutron energy E_n + 765 keV, a thermal neutron capture peak at 765 keV, and a ^{3}He (n,n′) elastic scattering recoil spectrum with a maximum at 0.75 E_n (from Equation 13-3). To emphasize the full energy peak at E_n + 765 keV, long charge collection time constants of 5 to 8 μs are used. This favors the slower proton signals from the (n,p) reaction over

the faster signals from recoiling ^{3}He nuclei. It is also helpful to collect data in a two-dimensional array of charge collected vs signal risetime in order to obtain more pulse-shape discrimination. In this way a neutron energy spectrum can be obtained, although it must be carefully unfolded from the measured data.

REFERENCES

1. Engineering Data Sheets 1.21 and 1.22 for BF_3 Proportional Counters (Reuter-Stokes, Inc., Cleveland, Ohio, 1979).

2. A. E. Evans, H. O. Menlove, R. B. Walton, and D. B. Smith, "Radiation Damage to ^{3}He Proportional Counter Tubes," *Nuclear Instruments and Methods* 133, (1976).

3. D. H. Wilkinson, *Ionization Chambers and Counters* (Cambridge University Press, Cambridge, Massachusetts, 1950).

4. P. Rice-Evans, *Spark, Streamer, Proportional, and Drift Chambers* (The Richelieu Press, London, 1974).

5. T. L. Atwell and H. O. Menlove, *Measurement of the Time Resolution of Several ^{4}He and CH_4 Proportional Counters* in "Nuclear Safeguards Research Program Status Report, September—December 1973," Los Alamos Scientific Laboratory report LA-5557-PR (February 1974).

6. T. D. Reilly, "The Measurement of Leached Hulls," Los Alamos Scientific Laboratory report LA-7784-MS (July 1979), pp. 57-63.

7. G. F. Knoll, *Radiation Detection and Measurement* (John Wiley & Sons, Inc., New York, 1979).

8. Engineering Data Sheets 1.02 and 1.03 for ^{3}He Proportional Counters (Reuter-Stokes, Inc., Cleveland, Ohio, 1978).

9. T. W. Crane, "Shielding for ^{3}He Detectors" in "Nuclear Safeguards Research Program Status Report, May—August 1976," Los Alamos Scientific Laboratory report LA-6675-PR (January 1977), p. 3.

10. T. W. Crane, "Gas Mixture Evaluation for ^{3}He Neutron Detectors," in "Nuclear Safeguards Research and Development Program Status Report, May—August 1977," Los Alamos Scientific Laboratory report LA-7030-PR (March 1978), p. 39.

11. M. L. Evans, "NDA Technology for Uranium Resource Evaluation, January 1—June 30, 1978," Los Alamos Scientific Laboratory report LA-7617-PR (1979), pp. 36-41.

12. T. Gozani, *Active Nondestructive Assay of Nuclear Materials, Principles and Applications,* NUREG/CR-0602, SA1-MLM-2585 (US Nuclear Regulatory Commission, Washington, DC, 1981).

13. R. W. Lamphere, "Fission Detectors," in *Fast Neutron Physics,* I, J. B. Marion and J. L. Fowler, Eds. (Interscience Publishers, Inc., New York, 1960).

14. S. Kahn, R. Harman, and V. Forgue, *Nuclear Science and Engineering* 23, 8 (1965).

15. Engineering Data Sheet 1.41 for a ^{10}B-Lined Proportional Counter (Reuter-Stokes Inc., Cleveland, Ohio, 1979).

16. R. L. Craun and D. L. Smith, "Analysis of Response Data for Several Organic Scintillators," *Nuclear Instruments and Methods* 80, 239 (1970).

17. L. M. Bollinger and G. E. Thomas, *Review of Scientific Instruments* 32, 1044 (1961).

18. D. W. Glasgow, D. E. Velkley, J. D. Brandenberger, and M. T. McEllistrem, "Pulse-Shape Discrimination for Wide Dynamic Range Neutron Scattering Experiments," *Nuclear Instruments and Methods* 114, 535 (1974).

19. C. L. Morris, J. E. Bolger, G. W. Hoffman, C. F. Moore, L. E. Smith, and H. A. Thiessen, "A Digital Technique for Neutron-Gamma Pulse Shape Discrimination," *Nuclear Instruments and Methods* 137, 397 (1976).

20. W. F. Hornyak, "A Fast Neutron Detector," *Review of Scientific Instruments* 23 (6), 264 (1952).

21. R. A. Harlan, "Uranium and Plutonium Assay of Crated Waste by Gamma-Ray, Single Neutron, and Slow Coincidence Counting," in Proc. American Nuclear Society Topical Conference on Measurement Technology for Safeguards and Materials Control, Kiawah Island, South Carolina, November 26-28, 1979 (National Bureau of Standards Publication 582, 1980), p. 622.

22. L. E. Bruns, "Capability of Field Instrumentation to Measure Radionuclide Limits," Rockwell Hanford report RHO-LD-160 (1981), p. 45.

23. S. Shalev and J. M. Cuttler, *Nuclear Science and Engineering* 51, 52 (1973).

24. H. Franz, W. Rudolph, H. Ohm, K. L. Kratz, G. Herrmann, F. M. Nuh, D. R. Slaughter, and S. G. Prussin, "Delayed-Neutron Spectroscopy with ^{3}He Spectrometers," *Nuclear Instruments and Methods* 144, 253 (1977).

14

Principles of Total Neutron Counting

J. E. Stewart

14.1 INTRODUCTION

Total neutron counting accepts all pulses arising from neutron reactions (events) in the sensitive volume of a detector. No attempt is made to isolate events that occur nearly simultaneously as is done in coincidence counting.

A simple total neutron counting system consists of the components shown schematically in Figure 14.1. All detector events producing an amplifier output pulse with an amplitude greater than a threshold set by the integral discriminator are counted for a set time in a scaler. The usual choice of discriminator setting is high enough to reject low-amplitude pulses produced by gamma rays and electronic noise and low enough to count all neutron-induced pulses. It is important to note that the pulse-height spectra of ^{3}He and BF_3 neutron proportional counters contain no information about the energy of the detected neutrons. However, some information can be obtained through proper design of the moderating and absorbing materials surrounding the counters.

This chapter covers basic principles that are important in using total neutron counting for passive assay of materials containing uranium and plutonium. It does so using the example of polyethylene-moderated ^{3}He proportional counters. Such detectors are routinely used for a wide variety of neutron counting applications in nuclear facilities throughout the world.

14.1.1 Theory of Total Neutron Counting

The total neutron counting rate is given by the simple formula

$$T = \varepsilon M_L S \qquad (14\text{-}1)$$

where T = total neutron count rate (counts/s)
ε = absolute detection efficiency (counts/n)
M_L = sample leakage multiplication (dimensionless)
S = sample neutron source intensity (n/s).

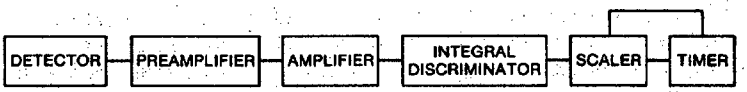

Fig. 14.1 The basic components of a simple total neutron counting system.

The absolute detection efficiency ε is the number of counts produced by the detector per neutron emitted from the sample. The sample leakage multiplication M_L is the number of neutrons emitted from the outer surface of the sample per neutron born inside the sample. The sample neutron source intensity S is the number of neutrons per second born in the sample.

The organization of this chapter is based on Equation 14-1. Factors affecting S, M_L, and ε are presented in relation to their influence on passive assays.

14.1.2 Comparison of Total and Coincidence Counting

Before describing the basic principles of total neutron counting, it is instructive to compare total neutron counting with coincident neutron counting. (Principles of neutron coincidence counting are described in detail in Chapter 16.) Generally, total neutron counting is responsive to *all* neutrons emitted from the sample, whereas coincidence counting responds only to the time-correlated neutrons.

The three important sources of neutrons for passive assays are (α,n) reactions, spontaneous fissions, and induced fissions (see Chapter 11 for a comprehensive description of neutron origins). The (α,n) reaction produces neutrons randomly in time. Fissions produce neutrons in bursts of 0 to 8. Coincidence circuitry can discriminate between neutrons produced from fissions and those produced in (α,n) reactions. This feature allows passive assay of plutonium nuclides with high spontaneous fission rates (most commonly ^{240}Pu) even in the presence of significant (α,n) reaction rates and room background. Also, active neutron coincidence methods use external sources of (α,n) neutrons to induce fissions in the sample, and the fission neutrons are counted using coincidence electronics. Total and coincident neutron counting are responsive in different ways to the three sources of neutrons in both passive and active assay, as shown in Table 14-1. Note that for active assay, the spontaneous fission neutron source can be made relatively small by choosing a strong (α, n) neutron source.

Table 14-1. Sensitivity of neutron counting techniques to the three sources of neutrons

Assay Method	Total Counting	Coincidence Counting
Passive Assay	(α,n), SF[a], IF[b]	SF, IF
Active Assay	(α,n), SF, IF	SF, IF

[a]SF - spontaneous fission neutrons.
[b]IF - induced fission neutrons.

Usually, the fewer neutron sources an assay technique is responsive to, the more specific it is to particular isotopes. The more isotope-specific the method is, the more useful it is for assay. In general, passive total neutron counting is the least isotope-specific of the techniques represented in Table 14-1. However, in those cases where only one of the three sources of neutrons dominates, passive total neutron counting can be used for assay. For example, UF_6 containing highly enriched uranium and PuF_4 are materials where the (α,n) source of neutrons dominates. Both uranium and plutonium

metal samples are examples where spontaneous fission is the dominant neutron source. In each of these examples, induced fission can be a complicating factor for both total and coincidence neutron counting. Because induced fissions increase the average multiplicity of simultaneous neutron emission from the sample and because the response of coincidence electronic circuits (for example, the shift register described in Chapter 16) increases faster than the average multiplicity, total counting is less sensitive to induced fission effects.

The coincidence count rate is proportional to ε^2 whereas the total count rate is proportional to ε. Variations in sample matrix materials (such as moisture) can alter the average energy of neutrons emitted from samples and thereby change the detector efficiency ε. Neutron coincidence counting is therefore more sensitive to changes in ε than is total counting. Also, total counting yields much better precision than coincidence counting in the same count time.

A disadvantage of total counting relative to coincidence counting is its sensitivity to background neutrons. Typically, background neutrons are randomly distributed in time and are easily discriminated by coincidence circuitry. A separate background count or neutron shielding or both are used to eliminate background total counts. In many cases, however, the background totals rate is insignificant compared to the totals rate from the sample and these measures are unnecessary.

In practice, total and coincidence neutron counting are often used together to correct sample/detector induced-fission (self-multiplication) effects. A complete discussion of this topic can be found in Chapter 16, Section 16.8.4.

14.2 PRIMARY NEUTRON PRODUCTION SOURCES

The first of the three important factors affecting total neutron counting is primary neutron production in the sample. Primary neutron production is from (α,n) reactions and spontaneous fission; secondary neutron production is from induced fission. Induced fission and neutron absorption in the sample are commonly considered together and called multiplication. Chapter 11 describes physical processes of primary neutron production and gives spontaneous fission and (α,n) reaction neutron yields from actinide isotopes of interest for passive neutron assays. Yields from (α,n) reactions are given for oxides and fluorides.

This section describes those features of neutron production in compounds of uranium and plutonium that affect assays based on total neutron counting. General calibration principles are discussed assuming no multiplication effects. In other words, neutron production by induced fission and neutron loss by neutron absorption are ignored. These topics are covered in Section 14.3, Neutron Transport in the Sample.

14.2.1 Plutonium Compounds

To apply total neutron counting as a signature for one or more isotopes of uranium or plutonium requires knowledge of the chemical form and isotopic composition of the sample. This point is well illustrated with examples. Consider 100-g samples of plutonium in the form of metal, PuO_2, and PuF_4 with three plutonium isotopic compositions representative of low-, medium-, and high-burnup fuel from light-water

reactors. Table 14-2 gives neutron production rates for each isotope, process, and form. The rates were computed from yields in Tables 11-1 and 11-3 in Chapter 11. Neutron production from spontaneous fission depends on the isotopic composition of the sample, but not on its chemical form. Neutron production from (α,n) reactions depends on both. The conclusions drawn from Table 14-2 are

(1) For plutonium metal, which has no (α,n) component, ^{240}Pu dominates primary neutron production (98, 96, and 65% for the three plutonium isotopic compositions).

Table 14-2. Primary neutron production rate in plutonium metal, PuO_2, and PuF_4 for three plutonium isotopic compositions

		Neutron Production Rate for 100 g of Pu (n/s)		
Isotope	Amount (wt%)	Metal (spontaneous fission)	PuO_2 (α,n)	PuF_4 (α,n)
^{238}Pu	0.024	62	322	52 800
^{239}Pu	89.667	2	3 416	502 135
^{240}Pu	9.645	9 838	1 360	202 545
^{241}Pu	0.556	0	1	95
^{242}Pu	0.109	187	0	29
^{241}Am	0.327[a]	0	880	144 417
	Totals	10 089	5 979	902 021
^{238}Pu	0.059	153	791	129 800
^{239}Pu	82.077	2	3 127	459 631
^{240}Pu	16.297	16 623	2 298	342 237
^{241}Pu	1.231	0	2	209
^{242}Pu	0.336	578	1	91
^{241}Am	0.162[a]	0	436	71 546
	Totals	17 356	6 655	1 003 514
^{238}Pu	1.574	4 077	21 092	3 462 800
^{239}Pu	57.342	1	2 185	321 115
^{240}Pu	24.980	25 480	3 522	524 580
^{241}Pu	10.560	0	14	1 795
^{242}Pu	5.545	9 537	11	1 497
^{241}Am	1.159[a]	1	3 118	511 863
	Totals	39 096	29 942	4 823 650

[a] ^{241}Am wt% relative to plutonium.

Total neutron counting of plutonium metal is a signature for the effective ^{240}Pu ($^{240}Pu_{eff}$) mass, where

$$^{240}Pu_{eff} = 2.43\,(^{238}Pu) + {}^{240}Pu + 1.69\,(^{242}Pu)\ . \tag{14-2}$$

The constants 2.43 and 1.69 account for the greater specific (per gram) spontaneous fission neutron production in ^{238}Pu and ^{242}Pu relative to ^{240}Pu. (Equation 14-2 differs slightly from Equation 16-1 (Chapter 16) for coincidence counting because of different neutron multiplicity distributions for the even plutonium isotopes.) If the plutonium isotopic composition is known, the total plutonium mass can be inferred from the $^{240}Pu_{eff}$ determination obtained from a calibration of the total neutron count rate. In other words (assuming a multiplication of 1),

$$T = \varepsilon\ S = k_0\ {}^{240}Pu_{eff} = k_1\ Pu \tag{14-3}$$

where k_0 and k_1 are empirical constants, and $^{240}Pu_{eff}$ and Pu represent $^{240}Pu_{eff}$ and plutonium masses, respectively.

(2) For PuO_2, the ratio of (α,n) to spontaneous fission neutron production is 0.59, 0.38, and 0.77 for the three plutonium isotopic compositions. Depending on composition, ^{238}Pu, ^{239}Pu, ^{240}Pu, and ^{241}Am are significant contributors to (α,n) neutron production in PuO_2. The total neutron production in PuO_2 is described by a generic equation of the form

$$S = a_1\,(^{238}Pu) + a_2\,(^{239}Pu) + a_3\,(^{240}Pu) + a_4\,(^{242}Pu) + a_5\,(^{241}Am) \tag{14-4}$$

where the multipliers a_1 through a_5 are specific neutron production rates for both spontaneous fission and (α,n) reactions in PuO_2 and the quantities in parentheses are plutonium isotopic masses. The multipliers are determined from plutonium isotopics and specific (α,n) and spontaneous fission yields for each isotope. If these are known, total plutonium mass can be determined from a calibration of the form

$$T = \varepsilon\ S = k_2\ Pu \tag{14-5}$$

where k_2 is an empirical constant and Pu stands for plutonium mass. Recall that Equation 14-5 assumes no multiplication effects ($M_L = 1$).

(3) For PuF_4, (α,n) reactions produce more than 98% of the neutrons for the three isotopic compositions. Generally, neutron production in PuF_4 is described by an equation similar to Equation 14-4,

$$S = a_6\,(^{238}Pu) + a_7\,(^{239}Pu) + a_8\,(^{240}Pu) + a_9\,(^{241}Am)\,. \tag{14-6}$$

The multipliers a_6 through a_9 are specific neutron production rates for (α,n) reactions in PuF_4 with small components from spontaneous fission. As with PuO_2, if plutonium isotopics are known, the total plutonium mass can be determined by total neutron counting of PuF_4 using the simple (multiplication-free) calibration

$$T = \varepsilon S = k_3 Pu. \tag{14-7}$$

Again, the constant k_3 must be determined empirically.

For the examples shown in Table 14-2, ^{241}Am values were taken at the time of analysis. Americium-241 is a daughter of ^{241}Pu. Americium-241 content increases with time because its half-life exceeds that of its parent. To calculate the ^{241}Am concentration at some time t knowing the initial concentrations of ^{241}Pu and ^{241}Am at time zero, use Equation 21-11 of Chapter 21.

14.2.2 Uranium Compounds

Just as for plutonium compounds, total neutron counting of uranium compounds requires prior knowledge of the chemical form and isotopic composition. Examples of uranium forms and compositions frequently found in the nuclear fuel cycle are characterized as to primary neutron production in Tables 14-3 and 14-4. Considered are 10-kg samples of uranium in the form of metal, UO_2, UO_2F_2, and UF_6. Table 14-3 treats ^{235}U enrichments of 0.2, 0.7, 3.0, and 18.2% (low-enriched uranium or LEU); Table 14-4 treats enrichments of 31.7, 57.4, 69.6, and 97.6% (high-enriched uranium or HEU). Spontaneous fission and (α,n) neutron rates are given by isotope and form for each enrichment. The rates were computed from yields in Tables 11-1 and 11-3 in Chapter 11 and from yields shown in Ref. 1 (UO_2F_2). The general conclusions drawn from these tables are

(1) Uranium-238 spontaneous fission dominates neutron production in uranium metal for ^{235}U enrichments below ~70%. This allows ^{238}U assay based on total neutron counting of large uranium metal samples for all but the highest ^{235}U enrichments. Because of the low neutron rates relative to plutonium metal, longer count time and larger samples are required for acceptable precision. Linear calibrations of total neutron count rate versus ^{238}U mass combined with ^{235}U enrichment are used for total uranium-metal determinations with low-enrichment material (see Chapter 15, Section 15.4.1, Box Counter). The calibration takes the form

$$T = \varepsilon S = k_4 {}^{238}U = k_5 U \tag{14-8}$$

where k_4 and k_5 are empirical constants.

(2) For UO_2, total neutron production [spontaneous fission plus (α,n)] is nearly constant for enrichments less than ~60%. With increasing enrichment, the spontaneous fission component decreases as the (α,n) component increases. At enrichments more than 60%, the (α,n) component grows rapidly. Uranium-234 alpha decay is the dominant source of (α,n) reactions in UO_2 for enrichments of 3% or greater. Total neutron production in UO_2 is generally described by

$$S = b_1 (^{234}U) + b_2 (^{235}U) + b_3 (^{238}U) \tag{14-9}$$

where b_1 through b_3 are specific neutron production rates for both spontaneous fission and (α,n) reactions in UO_2 and quantities in parentheses represent uranium isotopic masses. They are calculated from known isotopic compositions and specific neutron yields for each process. If these are known, a linear calibration of the form

Table 14-3. Primary neutron production rates in uranium metal, UO_2, UO_2F_2, and UF_6 for four uranium isotopic compositions (LEU)

		Neutron Production Rate for 10 kg of U (n/s)			
Isotope	Amount (wt%)	Metal (spontaneous fission)	UO_2 (α,n)	UO_2F_2 (α,n)	UF_6 (α,n)
^{234}U	0.0005	0	0	9	29
^{235}U	0.1977	0	0	1	2
^{236}U	0.0036	0	0	0	1
^{238}U	99.8	136	1	175	279
	Totals	136	1	185	311
^{234}U	0.0049	0	1	90	284
^{235}U	0.7108	0	0	3	6
^{236}U	-	-	-	-	-
^{238}U	99.28	135	1	174	278
	Totals	135	2	267	568
^{234}U	0.0244	0	7	449	1 415
^{235}U	3.001	0	0	11	24
^{236}U	0.0184	0	0	2	5
^{238}U	96.96	132	1	170	271
	Totals	132	8	632	1 715
^{234}U	0.0865	0	26	1 592	5 017
^{235}U	18.15	1	1	65	145
^{236}U	0.2313	0	1	28	67
^{238}U	96.96	111	1	143	228
	Totals	112	29	1 828	5 457

$$T = \varepsilon S = k_6 U \tag{14-10}$$

applies, where k_6 is an empirical constant and U stands for uranium mass. UO_2 as usually found in the nuclear fuel cycle (cans, rods, finished assemblies) suggests assay by active neutron techniques rather than passive, because the relatively low passive total neutron rates for standard sample sizes have to compete with room background. Active methods yield signals from ^{235}U-induced fission that are counted with coincidence electronics. Large UO_2 samples, however, may lend themselves to assay by passive total neutron counting depending on sample characteristics and measurement goals.

(3) For UO_2F_2 (a chemical reaction product of UF_6 and water), neutron production is dominated by the (α,n) component. Neutron production rates increase uniformly with ^{235}U enrichment. This is because ^{234}U is enriched along with ^{235}U in enrichment processes based on isotopic mass differences. Equations analogous to Equations 14-9

Table 14-4. Primary neutron rates in uranium metal, UO_2, UO_2F_2, and UF_6 for four uranium isotopic compositions (HEU)

		Neutron Production Rate for 10 kg of U (n/s)			
Isotope	Amount (wt%)	Metal (spontaneous fission)	UO_2 (α,n)	UO_2F_2 (α,n)	UF_6 (α,n)
^{234}U	0.1404	0	42	2 583	8 143
^{235}U	31.71	1	2	114	254
^{236}U	0.3506	0	1	42	102
^{238}U	67.80	92	1	119	190
	Totals	93	46	2 858	8 689
^{234}U	0.2632	0	79	4 843	15 265
^{235}U	57.38	2	4	207	459
^{236}U	0.5010	0	1	60	145
^{238}U	41.86	57	0	73	117
	Totals	59	84	5 184	15 986
^{234}U	0.3338	0	100	6 142	19 360
^{235}U	69.58	2	5	250	557
^{236}U	0.5358	0	1	64	155
^{238}U	29.55	40	0	52	83
	Totals	42	106	6 508	20 155
^{234}U	1.032	1	310	18 989	59 856
^{235}U	97.65	3	7	352	781
^{236}U	0.2523	0	1	30	73
^{238}U	1.07	1	0	2	3
	Totals	5	318	19 373	60 713

and 14-10 describe the passive total-neutron-counting calibration of UO_2F_2 with known isotopic composition. Passive total neutron counting has been used to quantify UO_2F_2 deposits inside process equipment in gaseous diffusion enrichment plants (Ref. 2).

(4) For UF_6 (the standard process material for uranium enrichment), ^{234}U alpha decay and the subsequent $^{19}F(\alpha,n)^{22}Na$ reaction dominate neutron production. The material is similar to UO_2F_2 with the (α,n) component being more dominant because of additional fluorine. For arbitrary enrichment, total UF_6 neutron production is also given by an equation analogous to 14-9. A calibration is then possible with an equation of the form of Equation 14-10.

Passive total neutron counting can be used for verification of UF_6 cylinders of all sizes. It is routinely used for cylinders containing low-enriched UF_6. It is fast, simple, and inexpensive. Small cylinders are counted in nearly 4π geometry ("well" counters). Large cylinders are counted with portable counters such as the "SNAP" (Chapter 15,

Section 15.2). For large, low-enrichment cylinders, simpler calibration expressions than those shown in Equations 14-9 and 14-10 are obtained by assuming a constant ^{238}U weight fraction and a constant ratio of ^{235}U to ^{234}U (see Chapter 15, Section 15.2.2). The data of Tables 14-2, 14-3, and 14-4 are plotted in Figure 14.2. Compared are total spontaneous fission plus (α,n) neutron production rates for plutonium, PuO_2, PuF_4, uranium, UO_2, UO_2F_2, and UF_6. The specific (per gram uranium or plutonium) rates span eight orders of magnitude from uranium metal to PuF_4. Rates are plotted as a function of wt% ^{235}U and ^{239}Pu. The plot is useful for visual comparison and for estimating counting statistics with known detectors and geometries.

14.2.3 Impurities

Rarely are the plutonium and uranium compounds found in the nuclear fuel cycle completely free of impurities. These impurities can significantly alter primary neutron

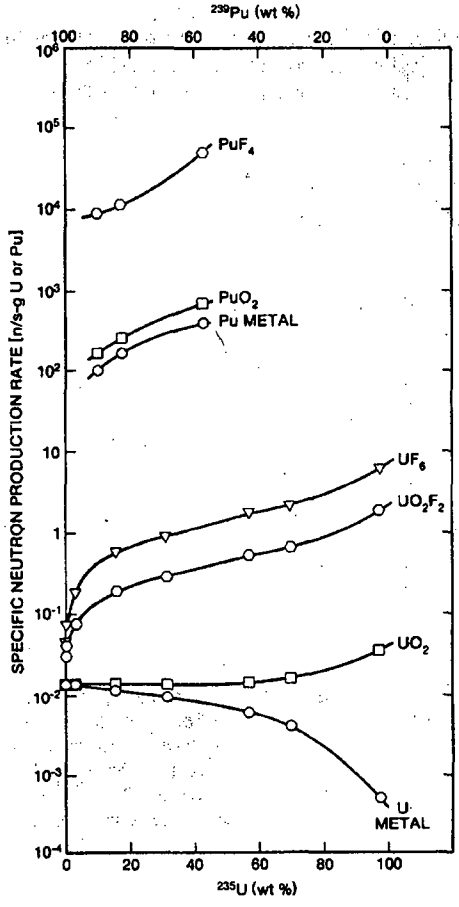

Fig. 14.2 Specific neutron production rates for uranium and plutonium metals, oxides, and fluorides. Data are from Tables 14-2 through 14-4.

production. As an example, consider PuO_2 with H_2O added. Water is commonly found in PuO_2 with a nominal value of 1 wt%. Table 14-2 gives dry PuO_2 (α,n) neutron production values for three plutonium isotopic compositions characteristic of low-, medium-, and high-burnup light-water reactor fuel. The first is approximately 10% ^{240}Pu by weight. The second is approximately 16% ^{240}Pu, and the third is approximately 25% ^{240}Pu. Figure 14.3 shows the dependence of (α,n) neutron production [S(α,n)] on weight percentage water for the three plutonium isotopic compositions. The quantity S(α,n) for the 25% ^{240}Pu material is roughly a factor of 5 higher than for the 16% and 10% materials (because of the high ^{238}Pu fraction) regardless of moisture content. Figure 14.4 displays S(α,n) values for wet relative to dry PuO_2 versus wt% H_2O. It is useful to note that the moisture effect is independent of plutonium isotopic composition. That is, adding 1 wt% moisture yields the same relative change in S(α,n) for 10%, 16%, and 25% ^{240}Pu, namely + 4.4%. This indicates that small changes in initial alpha-particle energies resulting from changes in plutonium isotopics do not significantly affect neutron production in wet PuO_2.

Although many trace contaminants are found in PuO_2, fluorine is usually the most significant for altering S(α,n). Figure 14.5 displays S(α,n) versus F contamination ir PuO_2 (16% ^{240}Pu) with 1 and 9 wt% H_2O. Figure 14.6 shows the S(α,n) values for PuO_2

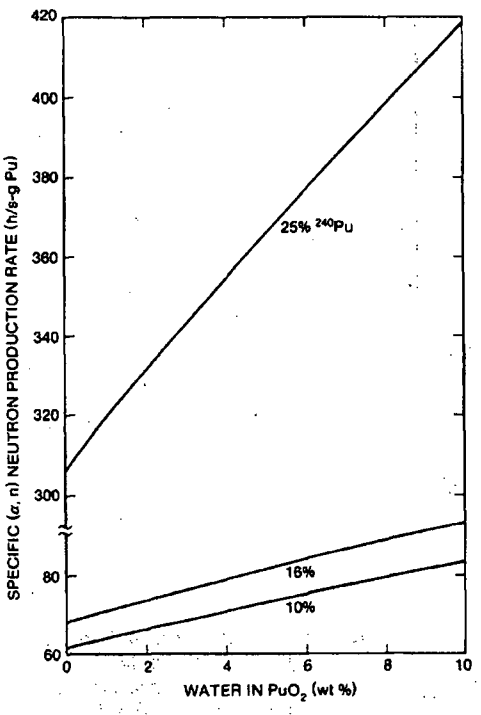

Fig. 14.3 Specific neutron production rates from (α,n) reactions in PuO_2 versus added moisture for ~10% ^{240}Pu, ~16% ^{240}Pu, and ~25% ^{240}Pu plutonium isotopic compositions.

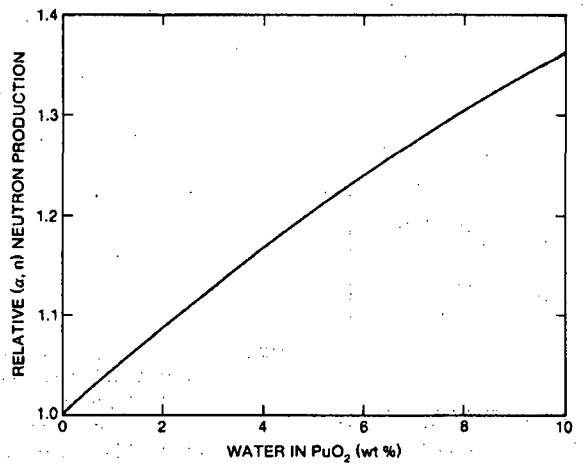

Fig. 14.4 *Neutron production from (α,n) reactions in wet relative to dry PuO_2 versus added moisture. The 10, 16, and 25% ^{240}Pu isotopic compositions fall on a single curve.*

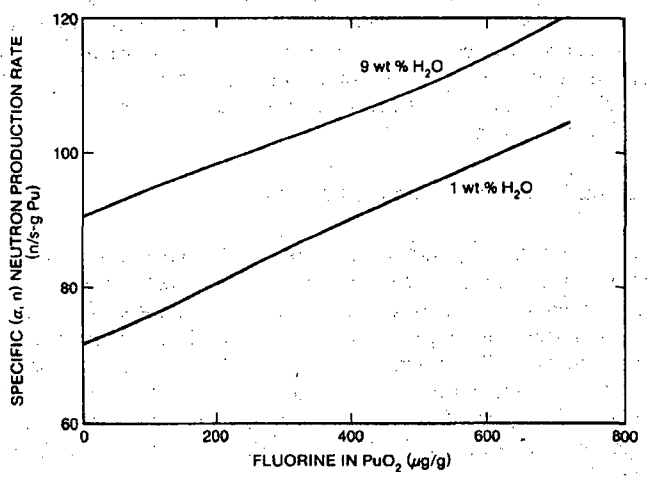

Fig. 14.5 *Specific neutron production rates from (α,n) reactions in PuO_2 versus fluorine contamination for 16% ^{240}Pu plutonium isotopic composition. Both 1 and 9 wt% H_2O cases are shown.*

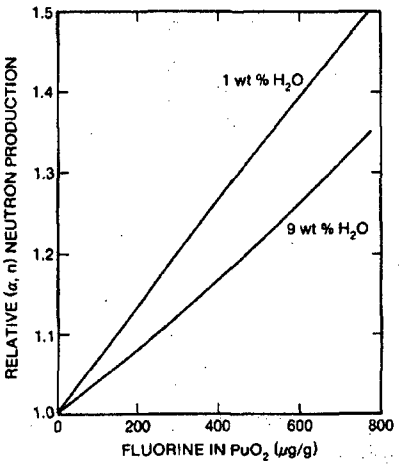

Fig. 14.6 Neutron production from (α,n) reactions in PuO_2 with fluorine impurities relative to pure PuO_2 versus fluorine concentration for 16% ^{240}Pu. Both 1 and 9 wt% H_2O cases are shown.

(16% ^{240}Pu) with fluorine impurities relative to pure PuO_2 versus fluorine concentration. Cases are shown for both 1 and 9 wt% moisture. The *relative* change in S(α,n) from F contamination is greater for dry than for wet PuO_2.

The H_2O and F impurities affect (α,n) neutron production but not spontaneous fission neutron production. If H_2O and F concentrations are known, data such as shown in Figures 14.3 through 14.6 can be used to adjust calibration parameters for total neutron counting assays. These data were calculated using the Los Alamos SOURCES code (Refs. 3, 4). Reference 5 contains results of calculations of the effects of several low-Z trace contaminants on S(α,n) for plutonium metal. Section 11.4 in Chapter 11 gives approximate formulas for calculating contributions to S(α,n) from impurities in uranium and plutonium oxides.

14.2.4 Neutron Energy Spectrum Effects

Neutrons are produced in spontaneous fission and (α,n) reactions with characteristic energy distributions or spectra. These are important in the design of total neutron counters using polyethylene-moderated ^3He detectors. For plutonium compounds, the spontaneous fission spectrum depends slightly on plutonium isotopic composition and not on sample chemistry. The spectrum is dictated by the nuclear kinematics of the spontaneous fission disintegration process, which differ slightly for ^{238}Pu, ^{240}Pu, and ^{242}Pu. Figure 14.7 is a plot of the specific spontaneous fission neutron production spectrum for plutonium with 16% ^{240}Pu. The ^{240}Pu spectrum is described well by the Watt form (Ref. 3)

$$N(E) \propto e^{-E/A} \sinh(\sqrt{BE}) \qquad (14\text{-}11)$$

where E = laboratory neutron energy, A = 0.795, and B = 4.69.

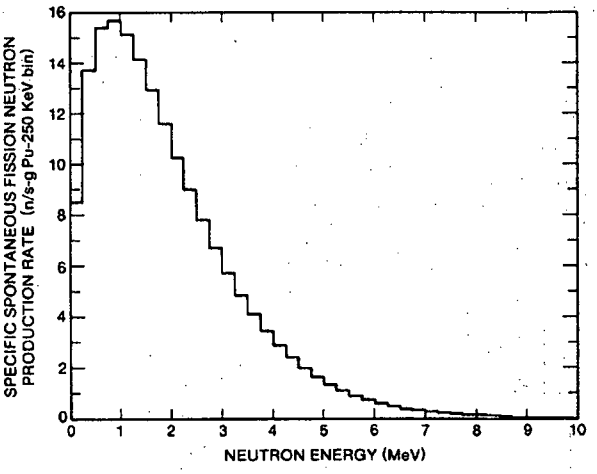

***Fig. 14.7** Specific spontaneous fission neutron production spectrum for Pu with 16% ^{240}Pu.*

The laboratory spectrum of neutron energies from (α,n) reactions in plutonium compounds depends on sample chemistry, impurity levels, and slightly on plutonium isotopic composition. Sample composition determines the slowing down spectrum of alpha-particle energies and the (α,n) reaction cross-section dependence on alpha-particle energy. Figure 14.8 displays four specific (α,n) neutron production spectra for PuO_2 (16% ^{240}Pu) with variable moisture and fluorine contamination. An increase in moisture "hardens" the spectrum slightly and an increase in fluorine "softens" it. Figure 14.9 shows the four total spectra corresponding to the moisture and fluorine concentrations of Figure 14.8. The average energies of these four spectra are not substantially different. This similarity indicates that spectral shape differences are generally not major factors affecting total neutron counting of PuO_2 with moisture and fluorine contamination levels in the ranges used. These ranges are typical of a wide variety of PuO_2 samples.

Figure 14.10 displays normalized neutron production spectra from (α,n) reactions in $^{234}UF_6$. Spectra for two ^{22}Na level branching schemes are shown. The $^{234}UF_6$ (α,n) spectrum is softer than that for PuO_2 with an average neutron energy of approximately 1.2 MeV. For PuO_2, the average is approximately 2.0 MeV.

14.2.5 Thin-Target Effects

In the previous sections, primary neutron production by (α,n) reactions was assumed to take place in samples that qualify as "thick targets." Thick targets are materials where alpha particles lose all their energy in the sample. If the sample density is low enough, neutron production is reduced because alpha particles escape before they undergo (α,n) reactions with target isotopes. Neutron production by ^{234}U alpha particles driving the

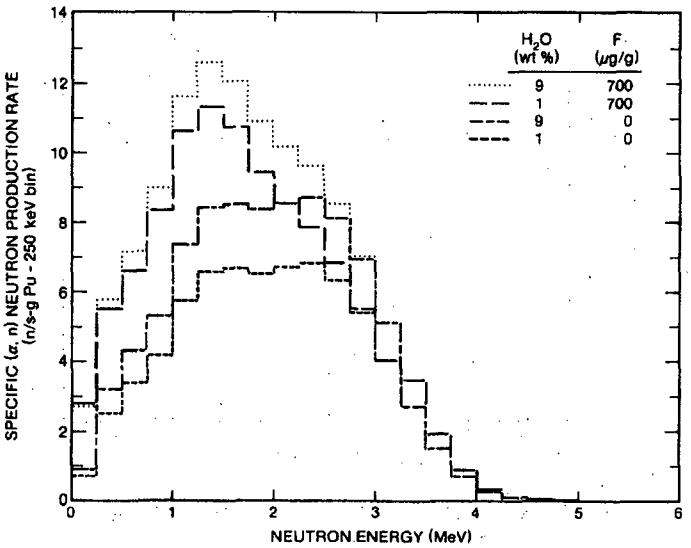

Fig. 14.8 Specific (α,n) neutron production rate spectra of PuO_2 (16% ^{240}Pu) with variable moisture and fluorine content (from SOURCES calculation [Ref. 3]).

$^{19}F(\alpha,n)^{22}Na$ reaction in gaseous UF_6 is a "thin-target" situation. In this case, alpha particles may escape the gas volume at energies above the $^{19}F(\alpha,n)$ cross-section threshold. Reference 6 presents methods for calculating thin-target neutron production in UF_6 gas. Figure 14.11 (from Ref. 6) displays UF_6 neutron production versus projected range. The projected range is the product of atom density and target thickness. Neutron production saturates above approximately 6×10^{19} atoms/cm^2 at the thick-target neutron production value for $^{234}UF_6$. At approximately 1.3×10^{19} atoms/cm^2, the number of neutrons produced per alpha particle is half the thick-target value.

14.3 NEUTRON TRANSPORT IN THE SAMPLE

After specifying the primary neutron production in the sample and relating that to grams of uranium or plutonium, the next logical step in using passive total neutron counting for assay is to consider the number of neutrons that escape the sample per neutron produced. Description of the transport of neutrons in the sample volume (including all the processes of neutron creation and loss) is complex and requires the use of Monte Carlo simulations on large computers for best results. Chapter 12 describes many of the basic principles of neutron transport. Here, we present a simple formula for sample leakage multiplication, discuss numerical results, and describe the use of the formula.

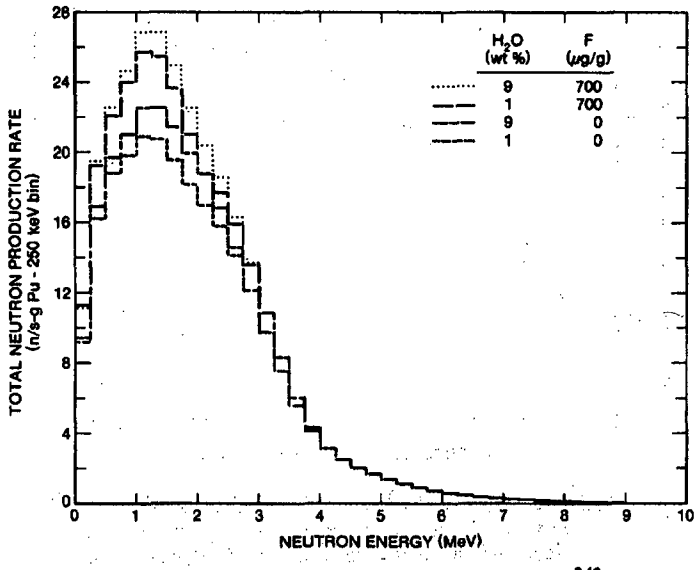

Fig. 14.9 *Total neutron production rate spectra of PuO_2 (16% ^{240}Pu) with variable moisture and fluorine content (from SOURCES calculation [Ref. 3]).*

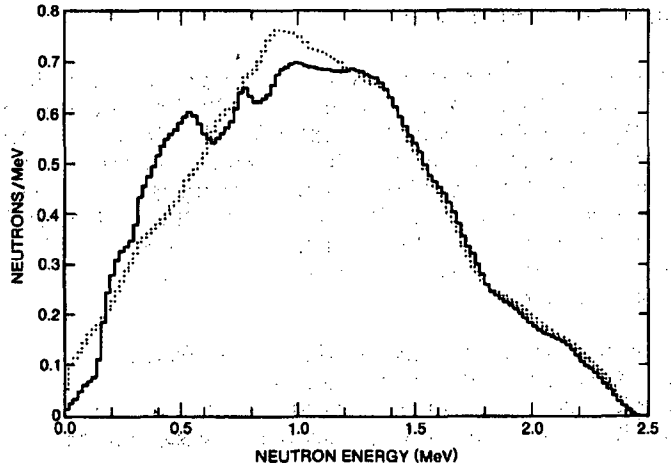

Fig. 14.10 *Normalized (α, n) neutron production spectra of $^{234}UF_6$ (from SOURCES [Ref. 3] calculation) with two ^{22}Na level branching models.*

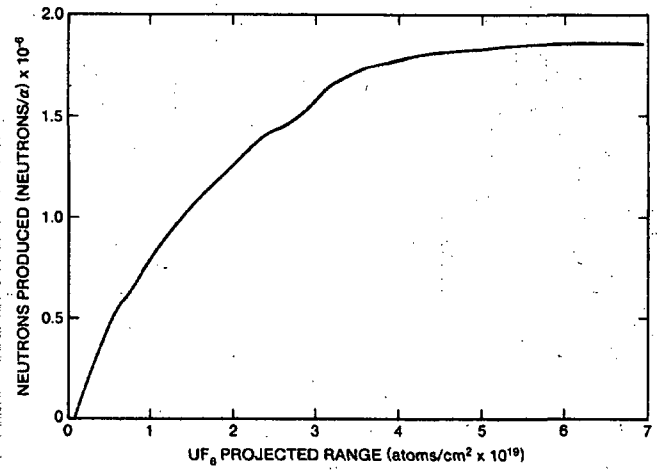

Fig. 14.11 Neutron production by a 4.77-MeV alpha particle from ^{234}U decay versus projected range in UF_6. The range in cm can be obtained by dividing the abscissa by the UF_6 atom density (atoms/cm^3).

14.3.1 Leakage Multiplication

The number of neutrons escaping the sample (and therefore available for counting) per primary neutron produced is called the leakage multiplication of the sample, M_L. The quantity M_L differs from the total multiplication M defined in Chapter 12. The quantity M is the number of neutrons *created* in the sample [from primary source events, induced fissions, (n,2n) reactions, and other events] per primary neutron produced. The quantity M_L accounts for neutron *creation and loss* in the fission and parasitic capture reactions. Therefore, M_L is more pertinent to total neutron counting than is M. The two quantities are closely related, as described below.

The following definitions apply:

ν = the average number of neutrons created by induced fission
p = probability that a neutron will induce a fission
p_c = probability that a neutron will be captured
p_L = probability that a neutron will escape the sample (leakage probability).

A neutron of a given generation can induce a fission with probability p and disappear with probability $1 - p$. In other words,

$$p + p_c + p_L = 1 \quad . \tag{14-12}$$

Also, the number of fissions produced in a given generation per fission in the previous generation is pv. The quantity pv is the multiplication factor k from reactor physics discussed in Chapter 12. In an induced fission a neutron is absorbed. Therefore the net neutron *profit* per fission is $\nu - 1$.

Consider a sample in which induced fission, neutron capture, and escape are the only possible fates of neutrons. In generation zero, one neutron is produced from spontaneous fission or an (α,n) reaction. In the first generation, there are p fissions and pv new neutrons created with a net neutron profit of $p(\nu - 1)$. In the second generation, there are $p^2\nu$ fissions, $(pv)^2$ new neutrons, and a net profit of $p^2\nu(\nu - 1)$. This multiplication process is shown in Table 14-5 for the first few neutron generations. For all generations, the sum of the number of neutrons created from a single source neutron is the total multiplication M.

$$M = \frac{1}{1 - pv} = \frac{1}{1 - k} \; ; \; k < 1 \quad . \tag{14-13}$$

For all generations, the sum of the net neutron profit is the total net neutron profit per source neutron $(1 - p)/(1 - pv)$. Not all the net neutron profit will escape the sample—some will be captured. The leakage multiplication M_L is the total net neutron profit per source neutron times the probability of escape divided by the probability of disappearance, that is,

$$M_L = \left(\frac{1-p}{1-pv}\right)\left(\frac{p_L}{p_L + p_c}\right) = \frac{p_L}{1-pv} = \frac{1-p-p_c}{1-pv} \quad . \tag{14-14}$$

Finally, from Equations 14-13 and 14-14, the relationship between M_L and M is

$$M_L = p_L M \quad . \tag{14-15}$$

If the probability of capture p_c is small,

$$M_L \simeq (1 - p)\, M = \frac{1 - p}{1 - pv} \quad . \tag{14-16}$$

Table 14-5. The neutron multiplication process through the fourth fission generation

Generation	Number of Fissions	Neutrons Created	Net Neutron Profit
0	—	1 (Source)	1
1	p	pv	$p(\nu - 1)$
2	p(pv)	$(pv)^2$	$p(pv)(\nu - 1)$
3	$p(pv)^2$	$(pv)^3$	$p(pv)^2(\nu - 1)$
4	$p(pv)^3$	$(pv)^4$	$p(pv)^3(\nu - 1)$

If both p_c and p are small, M_L and M are approximately the same. The quantity M is always greater than or equal to M_L.

Equation 14-14, the expression for M_L, depends on three parameters: ν, p, and p_c. These quantities depend on the energy of the neutron inducing a fission or being captured. Therefore, they are understood to represent averages over the slowing-down spectrum of neutron energies in the sample. All three parameters depend on sample composition and density. The probabilities p and p_c depend on sample geometry as well. Multiplication effects caused by neutrons reflecting off the counter back into the sample are understood to be included in p and p_c. Reflection lowers the neutron's energy and increases both p and p_c.

Figure 14.12 shows plots of the leakage multiplication M_L versus the fission probability p; Equation 14.16 was used to generate the plots. Two sets of curves are shown. The lower set of three curves is representative of uranium-bearing samples with $\nu = 2.5$. The upper set of three curves with $\nu = 3.0$ is representative of plutonium-bearing samples. In each set of curves, the capture probability p_c is varied from 0 to 0.02, which covers a wide range of samples.

Figure 14.13 shows plots of both total and leakage multiplication versus PuO_2 mass in a cylindrical volume with a diameter of 8.35 cm. The ^{240}Pu (effective) is 10 wt% of plutonium. The PuO_2 has a density of 1.3 g/cm^3 and contains 1 wt% H_2O. The sample fill height increases as PuO_2 mass increases. The leakage multiplication values were

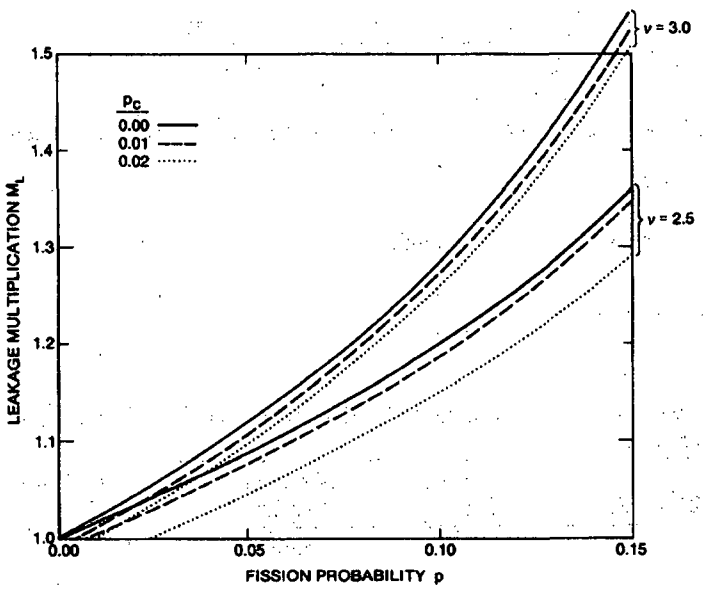

***Fig. 14.12** Leakage multiplication M_L versus fission probability for two values of the average fission neutron multiplicity and three values of the capture probability.*

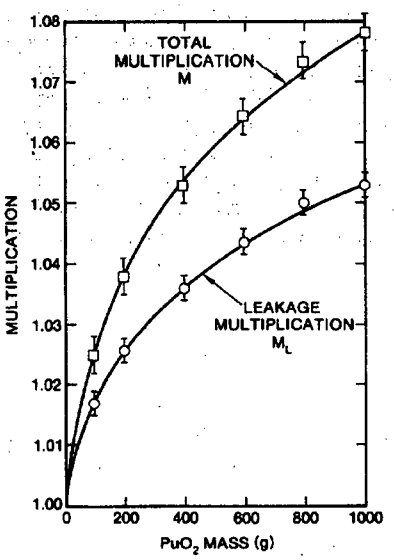

Fig. 14.13 *Leakage multiplication M_L and total multiplication M versus PuO_2 mass in a container with an 8.35-cm inside diameter. The plutonium is 10 wt% ^{240}Pu (effective). The sample PuO_2 has a density of 1.3 g/cm^3 and is 1 wt% H_2O. The fill height increases as mass is added.*

calculated using the Monte Carlo transport code MCNP (Ref. 7). The total multiplication values M were calculated from the leakage multiplication values M_L using the relationship

$$M = \frac{\nu M_L - 1}{\nu - 1} \tag{14-17}$$

with $\nu = 3.13$. This expression can be obtained by combining Equations 14.13 and 14.16. For the samples described by Figure 14.13, the capture probability p_c is negligibly small. The plots clearly show the difference in total multiplication M and leakage multiplication M_L. Reference 8 contains additional information on the MCNP calculations of M_L and information on coincidence multiplication corrections.

14.3.2 Leakage Spectra

Neutrons escaping from a sample have a lower average energy than when first produced in spontaneous fission or (α,n) reactions. Neutrons lose energy in the sample through elastic collisions with light nuclei and inelastic collisions with heavy nuclei. The sample container can also affect the neutron leakage spectrum, but is generally not a major factor. Unless there are intervening materials, the energy spectrum of neutrons escaping the sample container is the spectrum seen by the neutron detector. The shape of this spectrum can be important in determining detection efficiency, as described in Section 14.4.

An example of neutron energy losses in the sample, as calculated with the Monte Carlo Code MCN (Ref. 9), is shown in Figure 14.14. This figure shows the leakage spectrum of neutrons from a 5000-lb (2273-kg) cylinder of UF_6 whose ^{235}U enrichment is 2.5% (Ref. 10). For these calculations, a uniform spatial distribution of 1-MeV neutrons was assumed because the $^{19}F(\alpha,n)^{22}Na$ thick-target energy spectrum (Figure 14.10) was not well known at that time. Figure 14.14 shows the neutron moderation in the large UF_6 sample cylinder to be quite significant. The average energy of the leakage neutrons is 0.44 MeV compared with the average source neutron energy of 1.0 MeV. It should also be noted that about 20% of the source neutrons do not escape from the cylinder because of parasitic capture.

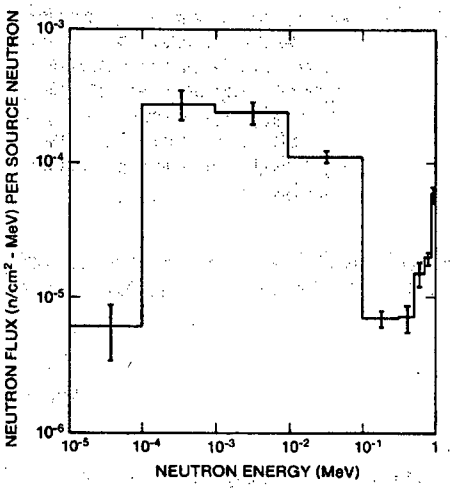

Fig. 14.14 Neutron leakage spectrum from a 5000-lb UF_6 cylinder (2.5% ^{235}U) assuming uniformly distributed 1-MeV source neutrons.

Another leakage spectrum calculation, performed with the MCNP Code (Ref. 7), is shown in Figure 14.15. The sample modeled is 800 g of PuO_2 with a density of 1.3 g oxide/cm^3. The sample contains 706 g of plutonium (10% ^{240}Pu) and 1 wt% water. The cylindrical sample is 8.35 cm in diameter and 11.24 cm in height. The smooth curve in Figure 14.15 is the ^{240}Pu spontaneous fission neutron emission spectrum (Figure 14.7 and Equation 14.11). The calculated sample neutron leakage spectrum is the histogram distribution, with 1σ error bars shown. The average energy of the leakage spectrum is 1.91 MeV compared with 1.93 MeV for the emission spectrum. This implies very little moderation of the source spectrum by this PuO_2 sample. The small buildup in the leakage spectrum between 0.6 and 1.0 MeV is from inelastic scattering by plutonium nuclides and elastic scattering by oxygen. The slight buildup between 10 KeV and 100 KeV is from elastic scattering by hydrogen and oxygen. This buildup would increase with added moisture. For this sample the leakage multiplication is about 1.04.

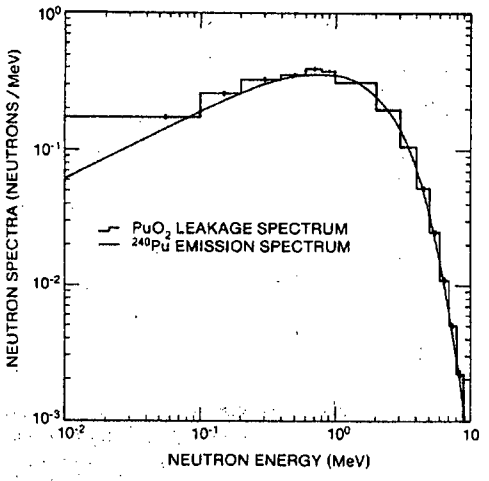

Fig. 14.15 Neutron leakage spectrum from an 800-g PuO_2 sample (10% ^{240}Pu) assuming an energy spectrum characteristic of ^{240}Pu spontaneous fission. Source neutrons were uniformly distributed in the sample volume.

14.4 NEUTRON DETECTION EFFICIENCY

Equation 14.1 defines detector efficiency ε as the number of counts produced by the detector per neutron emitted from the sample. This section describes important factors affecting ε for ^3He proportional counters moderated by polyethylene. These include arrangement of ^3He counters within the polyethylene moderator, moderator design, and the sample leakage spectrum. Also, differences in the energy spectra of signal and background neutrons can be exploited to enhance the signal-to-background counting ratio.

14.4.1 ^3He Counter Arrangement

For a fixed moderator geometry, the location and number of ^3He proportional counters strongly affects counting efficiency. As an example, a series of efficiency calculations was performed using the MCNP Code (Ref. 7) for a variable number of ^3He counters placed within a 1-m-tall annulus of polyethylene. The counting tubes were 1 inch in diameter with 4 atm of ^3He (77% thermal-neutron counting efficiency). The internal and external diameters of the annulus were 7 in. (17.8 cm) and 15 in. (38.1 cm), respectively. The ^3He counters were evenly spaced within the annulus on a circle 11 in. (27.9 cm) in diameter. A 1-MeV monoenergetic source of neutrons was assumed for the calculations. The two curves in Figure 14.16 show the results of the calculations. The curve belonging to the left ordinate is the absolute counting efficiency versus number of ^3He counters. This curve shows a peak counting efficiency of about 29% for 28 ^3He counters. Because ^3He proportional counters are expensive, absolute counting efficiency is sometimes compromised. The curve belonging to the right ordinate is the counting efficiency per ^3He counter (an index of cost effectiveness) versus the number of counters.

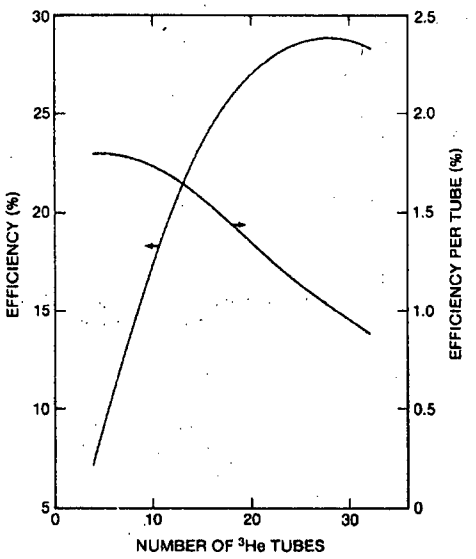

Fig. 14.16 Results of Monte Carlo calculations of total neutron counting efficiency versus number of ^{3}He counting tubes for the configuration described in Section 14.4.1.

A reasonable compromise for this example would be 16 ^{3}He counters. Choice of the number of ^{3}He counters would also depend on sample neutron emission intensity and desired counting precision.

14.4.2 Moderator Design

With a fixed number and arrangement of ^{3}He counters, the amount and location of polyethylene moderator can also strongly influence counting efficiency. As an example, calculations were done for a polyethylene slab 10 in. (25.4 cm) long, 6 in. (15.3 cm) tall, and 1.57 in. (4.0 cm) thick (see Figure 14.17). Two ^{3}He counters are embedded within the slab with their axes parallel to the slab's long axis and separated by 2.1 in. (5.3 cm). The counters have a 10-in. active length, 4-atm fill pressure, and 1-in. diam. A ^{252}Cf neutron source is located 15.75 in. (40 cm) from the slab on a line perpendicular to the plane of the ^{3}He counters. The Monte Carlo Code MCNP (Ref. 7) was used to calculate detection efficiency for various polyethylene thicknesses in front of and behind the ^{3}He counters (relative to the source). The Watt fission spectrum was used for the calculations (Equation 14-11) with A = 1.025 and B = 2.926 for ^{252}Cf. These parameters and this slab geometry represent typical values encountered in actual neutron detectors.

Results of the calculations are shown in Table 14-6 and Figure 14.18. The precisions of the calculated relative efficiencies are approximately ±1%. The total slab thickness can be obtained by adding front and back polyethylene thicknesses because thickness is measured from the ^{3}He tube centers. The moderator configuration for highest detection efficiency is 6 cm of polyethylene in front of the ^{3}He counters and 8 cm behind. Note that for fixed rear polyethylene thickness, efficiency peaks and then decreases with increasing

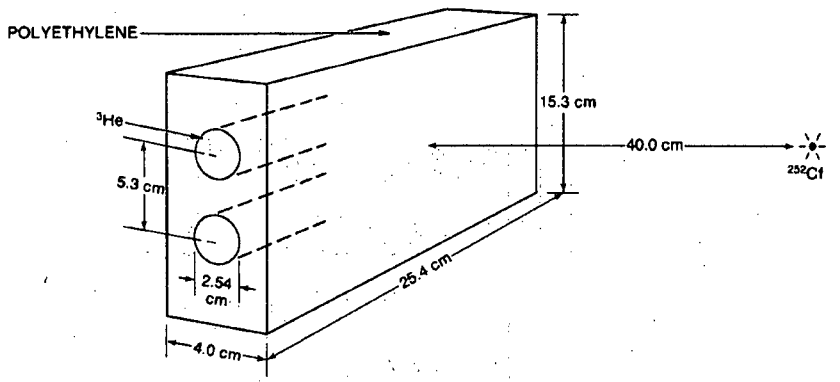

Fig. 14.17 *The geometry used for a series of Monte Carlo calculations of detector efficiency. In the calculations, the thickness of polyethylene in front of and behind the two ^{3}He counters was varied.*

front polyethylene thickness. The decrease is due to neutron capture in hydrogen. For fixed front polyethylene thickness, efficiency approaches an asymptotic value with increasing rear polyethylene thickness. This effect is due to neutron reflection from the rear polyethylene. Often, size and weight constraints limit the total polyethylene moderator thickness to be used. In the U.S., polyethylene is typically purchased in slabs 4 in. (10.2 cm) thick. If, for ease of fabrication, the total slab thickness is constrained to this value, the ^{3}He counters should be placed with 4.6 cm of polyethylene in front and 5.6 cm behind for optimum efficiency.

14.4.3 Effect of Neutron Energy Spectrum

For a particular neutron detector design, the detection efficiency will depend on the incident neutron energy because of the dependence of the ^{3}He(n,p) cross section on neutron energy and the moderating effect of hydrogen in polyethylene. Given a particular neutron leakage spectrum, the detector can be designed to maximize counting efficiency for that spectrum. For applications where the signal-to-background ratio is small, it is desirable to design the detector to discriminate against background neutrons with different energy spectra. Two examples, one for neutrons from UF_6 and one for neutrons from PuO_2, are given in this section.

Collimated neutron slab detectors have been designed to monitor neutron levels in UF_6 gas centrifuge enrichment plants. The detectors are described in Section 15.3.1 and illustrated in Figure 15.4 of Chapter 15. Each detector contains eleven 1-in.-diameter ^{3}He counters embedded in a 10.2-cm by 30.5-cm by 61-cm polyethylene slab. The slab is wrapped in cadmium and covered with thick polyethylene shielding except on the 1860-cm^2 open face, which is covered by 1.3 cm of polyethylene. The polyethylene, along with the cadmium, filters out low-energy background neutrons. Figure 14.19 is a schematic cross section of the detector.

Table 14-6. Relative efficiency of a simple slab detector for variable polyethylene moderator in front of and behind the ^{3}He counters

Back Polyethylene Thickness (cm)	Front Polyethylene Thickness (cm)												
	2	2.5	3	3.5	4	4.5	5	5.5	6	6.5	7	7.5	8
2	0.181	0.271	0.334	0.430	0.489	0.521	0.560	0.608	0.622	0.639	0.659	0.615	0.575
2.5	0.242	0.351	0.419	0.508	0.577	0.625	0.661	0.700	0.706	0.717	0.687	0.690	0.644
3	0.301	0.426	0.494	0.596	0.645	0.665	0.713	0.757	0.782	0.765	0.747	0.733	0.692
3.5	0.374	0.497	0.565	0.668	0.717	0.762	0.779	0.821	0.825	0.839	0.807	0.771	0.742
4	0.425	0.547	0.611	0.719	0.769	0.812	0.830	0.872	0.867	0.866	0.826	0.799	0.773
4.5	0.469	0.597	0.650	0.766	0.797	0.847	0.871	0.886	0.908	0.901	0.862	0.839	0.792
5	0.511	0.628	0.688	0.798	0.844	0.887	0.896	0.919	0.946	0.919	0.889	0.849	0.808
5.5	0.547	0.658	0.723	0.833	0.860	0.911	0.917	0.943	0.963	0.944	0.894	0.848	0.810
6	0.564	0.682	0.745	0.843	0.874	0.921	0.941	0.952	0.973	0.965	0.898	0.858	0.815
6.5	0.580	0.696	0.759	0.858	0.895	0.936	0.940	0.962	0.986	0.955	0.910	0.875	0.820
7	0.604	0.703	0.755	0.874	0.909	0.935	0.961	0.975	0.977	0.963	0.921	0.873	0.832
7.5	0.600	0.703	0.773	0.873	0.908	0.945	0.957	0.978	0.989	0.968	0.920	0.873	0.826
8	0.613	0.722	0.775	0.872	0.913	0.954	0.968	0.983	1.000	0.969	0.929	0.883	0.835

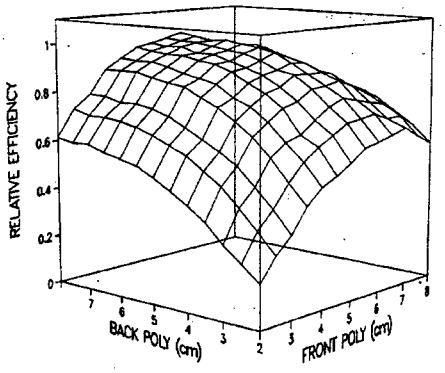

Fig. 14.18 *Relative ^{252}Cf neutron detection efficiency as a function of front and back polyethylene thickness for the small slab detector illustrated in Figure 14.17.*

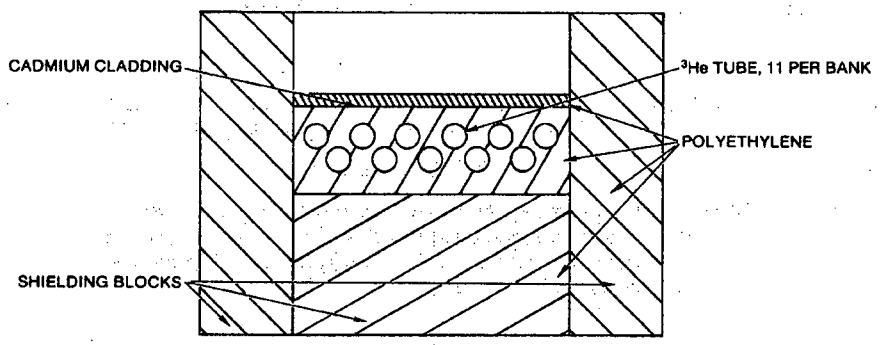

Fig. 14.19 *Cross section of the collimated neutron slab detector.*

The UF_6 monitor was designed to have a neutron energy efficiency profile similar to the $^{19}F(\alpha,n)^{22}Na$ neutron energy spectrum (Figure 14.10). It was also designed to minimize the response to low-energy background neutrons from cosmic rays. This was accomplished by measuring and calculating the effect of three different thicknesses of polyethylene filters on the detector's open face. (Ref. 11). Figure 14.20 is a plot of calculated neutron energy response profiles for three thicknesses of polyethylene: 0, 1.3 cm, and 2.5 cm. The effect of a polyethylene filter is to reduce detection efficiency at all incident neutron energies, but with greater reductions at the lower energies where most of the background neutrons from cosmic rays are found. These calculations indicate that a 1.3-cm filter is a good compromise between high efficiency for 1.0-MeV neutrons and low efficiency for 0.1-MeV neutrons. A more comprehensive study of UF_6 detector optimization for low signal-to-background ratios is reported in Ref. 12.

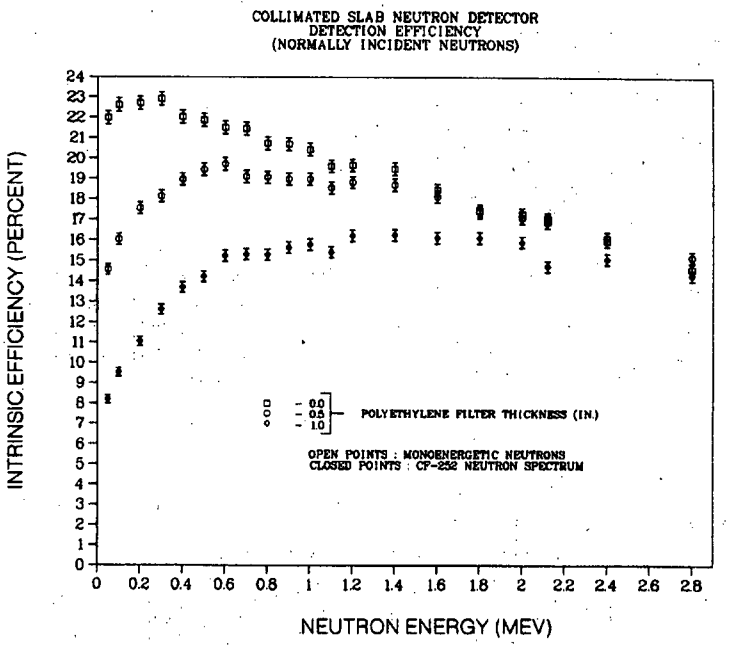

Fig. 14.20 Calculated detection efficiency of the collimated slab detector as a function of the energy of neutrons normally incident on the open face. Results are shown for three thicknesses of polyethylene filter covering the open face: 0, 1.3, and 2.5 cm.

The High-Level Neutron Coincidence Counter (HLNCC) is a detector designed primarily for passive neutron coincidence counting of PuO_2 (Ref. 13 and Section 17.2.2 of Chapter 17). Its neutron energy efficiency profile is given in Figure 14.21. If this efficiency profile is compared with the leakage spectrum from a representative PuO_2 sample (Figure 14.15), it can be seen that the HLNCC efficiency is a maximum for neutron energies lower than those actually emitted. In other words, the HLNCC, which was designed to be small and lightweight, contains too little polyethylene and is "undermoderated."

REFERENCES

1. W. B. Wilson, R. T. Perry, and J. E. Stewart, "Neutron Production in UO_2F_2 from the Spontaneous-Fission and Alpha Decay of Uranium Nuclides and Subsequent $^{17,18}O$ (α,n) and ^{19}F (α,n) Reactions," in "Applied Nuclear Data Research and Development, April 1-June 30, 1981," P. G. Young, Comp., Los Alamos National Laboratory report LA-9060-PR (December 1981), p. 50.

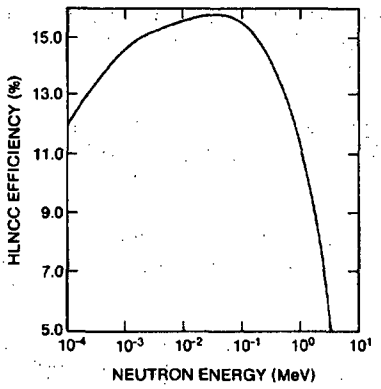

Fig. 14.21 *Calculated detection efficiency of the High-Level Neutron Coincidence Counter (HLNCC) as a function of the energy of neutrons emitted isotropically in the center of the detector well.*

2. R. H. Augustson, R. B. Walton, W. Harbarger, J. Hicks, G. Timmons, D. Shissler, R. Tayloe, S. Jones, R. Harris, and L. Fields, "Measurements of Uranium Holdup in an Operating Gaseous Diffusion Enrichment Plant," in "Proceedings of the ANS/INMM Conference on Safeguards Technology: The Process-Safeguards Interface," Hilton Head Island, South Carolina, November 28-December 2, 1983, US DOE New Brunswick Laboratory, Conf. No. 831106 (August 1984), pp. 77-88.

3. W. B. Wilson, R. T. Perry, J. E. Stewart, T. R. England, D. G. Madlund, and E. D. Arthur, "Development of the SOURCES Code and Data Library for the Calculation of Neutron Sources and Spectra from (α,n) Reactions, Spontaneous Fission, and β^- Delayed Neutrons," in "Applied Nuclear Data Research and Development Semiannual Progress report, October 1, 1982-March 31, 1983," E. D. Arthur, Compiler, Los Alamos National Laboratory report LA-9841-PR (August 1983), p. 65.

4. W. B. Wilson, "Calculations of (α,n) Neutron Production in PuO_2 with Variable Moisture and Fluorine Contamination," Los Alamos National Laboratory memorandum T-2-M-1581, to J. E. Stewart (March 1985).

5. W. B. Wilson, R. T. Perry, and J. E. Stewart, "Neutrons from the Spontaneous Fission of Plutonium Nuclides and from the (α,n) Reactions of Their Decay Alpha Particles with Trace Contaminants of Li, Be, B, C, N, O, F, Na, Mg, Al, Si, Cl, and As in Pu Metal," Los Alamos National Laboratory report (available on request from Group N-1, MS E540).

6. J. E. Stewart, "Neutron Production by Alpha Particles in Thin Uranium Hexafluoride," Los Alamos National Laboratory report LA-9838-MS (July 1983).

7. Los Alamos Monte Carlo Group X-6, "MCNP - A General Monte Carlo Code for Neutron and Photon Transport, Version 2B," Los Alamos Scientific Laboratory report LA-7396-M, Rev. (November 1979).

8. N. Ensslin, J. Stewart, and J. Sapir, "Self-Multiplication Correction Factors for Neutron Coincidence Counting," *Nuclear Materials Management* VIII (2), 60 (1979).

9. E. D. Cashwell, J. R. Neergaard, W. M. Taylor, and G. D. Turner, "MCN: A Neutron Monte Carlo Code," Los Alamos Scientific Laboratory report LA-4751 (1972).

10. R. B. Walton, T. D. Reilly, J. L. Parker, J. H. Menzel, E. D. Marshall, and L. W. Fields, "Measurements of UF_6 Cylinders with Portable Instruments," *Nuclear Technology 21,* 133 (1974).

11. J. E. Stewart and S. M. Simmonds, "Neutron Energy Response of an Area Neutron Monitor," in "Safeguards and Security Progress Report, January-December 1984," Los Alamos National Laboratory report LA-10529-PR (1986), p. 85.

12. J. E. Stewart and H. O. Menlove, "Design Study of an Optimized In-Cascade Neutron Monitor for Centrifuge Plants," in "Safeguards and Security Status Report: February-July 1982," Los Alamos National Laboratory report LA-9595-PR (February 1983), pp. 57-63.

13. M. S. Krick and H. O. Menlove, "The High-Level Neutron Coincidence Counter (HLNCC): User's Manual," Los Alamos Scientific Laboratory report LA-7779-M (ISPO-53) (June 1979).

15

Total Neutron Counting Instruments and Applicatons

J. Sprinkle

15.1 INTRODUCTION

Total neutron counting instruments are usually unsophisticated instruments that do not measure neutron energy directly. They are simpler than neutron coincidence counters, are capable of detecting smaller quantities of neutron producing materials, and are less sensitive to multiplication effects and efficiency variations. However, they are less capable of determining which isotope or chemical compound produced the neutrons. Sometimes these instruments use partial energy discrimination to reduce the signal from undesired components. More typically, they rely on administrative controls to ensure that only the appropriate materials are assayed.

Many assay instruments for total neutron counting use moderated ^{3}He detectors. The ^{3}He detectors are relatively simple to operate and their reliability is excellent. They can tolerate approximately 10^{13} fast n/cm^2 without serious radiation damage and they provide adequate discrimination against gamma rays in fields less than 1 R/h. Reasonable detection efficiencies can be achieved through careful design. Tubes of 2.5-cm diameter containing 4 atm of ^{3}He have an intrinsic detection efficiency of 90% for thermal neutrons. Detector banks with these tubes placed 5 cm apart can be designed to have absolute detection efficiencies of about 20% for spontaneous fission neutrons. Detector banks have also been built with BF_3 tubes, which provide somewhat better discrimination against gamma rays (see Chapter 13).

This chapter describes several total neutron counting instruments and applications in order of increasing size and complexity. It concludes with examples of three instruments used for special applications: two moisture monitors and an energy-independent long counter.

15.2 THE SHIELDED NEUTRON ASSAY PROBE (SNAP)

The Shielded Neutron Assay Probe (SNAP) is the simplest and most portable of the neutron detectors described in this chapter. An upgraded version, the SNAP-II (Ref. 1), is illustrated in Figure 15.1. SNAP-II consists of two ^{3}He counters (2.5-cm diam, 20-cm active length, 4-atm fill pressure) embedded in a 12.7-cm-diam polyethylene cylinder. The 12.7-cm diameter of the cylinder is optimum for the detection of 1- to 2-MeV fission neutrons. The polyethylene cylinder is wrapped in a thin cadmium sheet to preferentially absorb any background of thermal neutrons. Along its axis is a hole for inserting

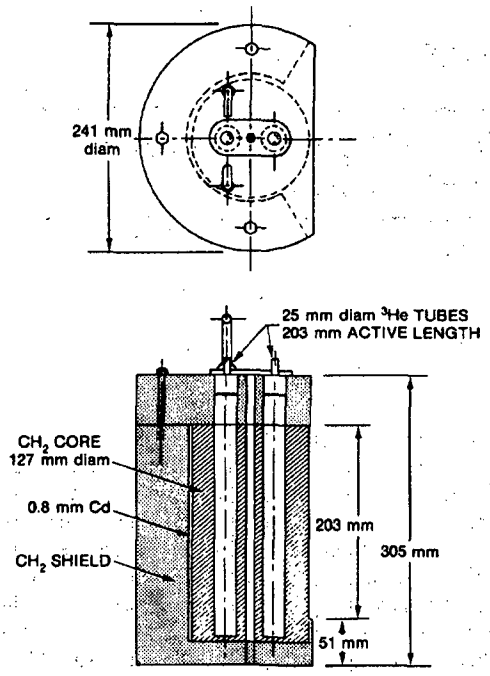

Fig. 15.1 The SNAP-II detector (Ref. 1).

individual reactor fuel rods. This configuration provides an option for high-efficiency assay of plutonium-bearing rods in the hole. Outside the cylinder is a 5.7-cm-thick directional shield whose thickness is limited to ensure portability of the detector. The weight of the SNAP-II is only 10 kg.

With its directional shield, SNAP-II has a viewing angle of 120°. Figure 15.2 shows the relative sensitivity of the detector as a function of angle around the detector axis, as measured with a PuLi source. The front-to-back detection ratio is 4.2 for the PuLi source (average neutron energy of 0.65 MeV) but decreases to 2.2 for a ^{252}Cf spontaneous fission source (average neutron energy of 2.2 MeV).

The intrinsic efficiency of the SNAP-II detector for fission neutrons is approximately 17%, representing a significant improvement over the 10% obtained with the original SNAP detector (Ref. 2). In addition, the active area of the SNAP-II detector is more than twice that of its predecessor; consequently the absolute detection efficiency for a point source at 1 m is improved by a factor of 4.5, to approximately 0.01% (Ref. 1). For other source-to-detector distances, the absolute detection efficiency varies as $(r + a)^{-2}$ where r is measured in centimeters from the detector axis and a is a constant that depends on the diameter of the moderator cylinder. The constant, a, is typically about 3 cm, and r must be greater than 3a for the approximation to be valid. This efficiency function is not valid if the detector is close to surfaces that reflect neutrons (such as a concrete floor). For field exercises that require the use of the SNAP-II in an area surrounded by neutron sources and reflectors, determination of the appropriate background count may be

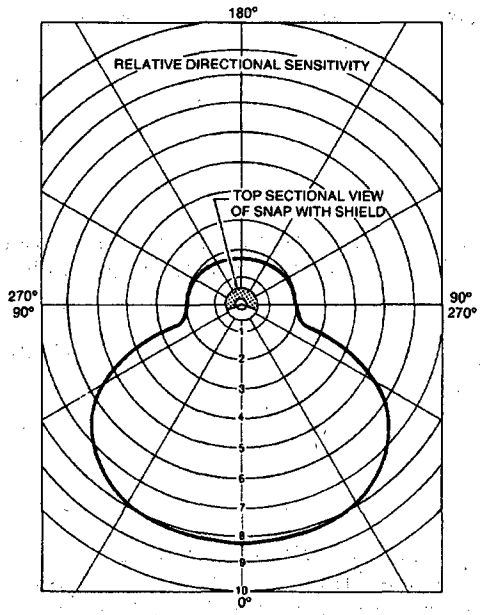

Fig. 15.2 *Directional sensitivity of the SNAP detector, as measured in the midplane with a PuLi source (average energy 0.65 MeV) (Ref. 2).*

difficult. In these instances, it has been helpful to fit a matching wedge of polyethylene into the viewing angle of the detector.

The SNAP-II has been designed for field work and is used in the total neutron counting mode because the signal to be measured is often weak. It is important to use compact, simple electronics. Commercially available packages such as the Eberline SAM I or the Ludlum Model 22 are well suited for this application. These units contain a high-voltage power supply, preamplifier and amplifier boards, discriminators, and scalers in one small portable box.

The SNAP detector provides only limited information about the energy or direction of the neutrons that are detected. It is often used for holdup measurements or verification measurements where good reference standards are not available; examples of such uses follow.

15.2.1 Verification of Plutonium Metal

A SNAP detector has been used to verify the ^{240}Pu content of plutonium metal buttons at the Hanford Works in Richland, Washington (Ref. 3). The major neutron source in metallic plutonium is the spontaneous fission of ^{240}Pu. In addition, buttons containing 2000 g of plutonium exhibit significant multiplication effects. These effects can increase the totals count rate by as much as 90% and are dependent on the button geometry.

At Hanford, the measured SNAP response, T total neutrons/s, was represented as

$$T(n/s) = k\ m\ I\ F \tag{15-1}$$

where k = calibration constant
m = elemental plutonium mass
I = ^{240}Pu mass fraction

and F is a factor that accounts for multiplication within the button. F was determined empirically by fitting a series of Monte Carlo calculations of multiplication within buttons, with the following result:

$$F = 1 + (1 - aI)m/b \tag{15-2}$$

$$a = \frac{619.5\,(d - 2.673)^2 + 1801}{b} \tag{15-3}$$

$$b = 417.8\,(d - 1.333)^2 + 1757 \tag{15-4}$$

where d is the button diameter in inches, and a and b are also given in inches.

Equation 15-1 can be solved for either m or I. At Hanford, one button was chosen as the "standard" and the remaining were assayed as unknowns. A statistical analysis of the assay of 248 buttons yielded 8 outliers. The ^{240}Pu content of the other 240 buttons was verified. The mass range of the buttons was 1453 to 2204 g and the ^{240}Pu mass fraction ranged from 4.6 to 18.1%. The measurement uncertainty was 2% (1σ), and the precision in 30-s counts was better than 1%.

15.2.2 Verification of UF_6 Cylinders

SNAP detectors have been used at enriched uranium production and storage facilities to verify the contents of UF_6 cylinders (Ref. 4). In UF_6, neutrons are produced by spontaneous fission of ^{238}U and by the ^{19}F(α,n)^{22}Na reaction. The dominant alpha-particle emitter is ^{234}U. In natural UF_6, 80% of the neutrons are due to (α,n) reactions and the rest to spontaneous fission. As the enrichment increases, the contribution of the (α,n) reaction increases sharply. In particular, as the enrichment increases from 3 to 90%, the neutron production rate increases by a factor of 30. Consequently the totals neutron count rate is a sensitive measure of the UF_6 mass and enrichment. Neutrons penetrate UF_6 quite well but are subject to absorption and multiplication effects. Table 15-1 lists the calculated neutron leakage fraction from various cylinders. At the higher enrichments, multiplication effects begin to dominate over absorption effects.

To verify the contents of a UF_6 cylinder, the SNAP detector is placed adjacent to the cylinder and parallel to its axis, at a position midway between the cylinder ends. This geometry is less position dependent, less sensitive to the cylinder's fill height, and more convenient for the operator than a geometry that requires the operator to hold the SNAP against the end of the cylinder. Backgrounds caused by neighboring cylinders are often large. Reasonable background estimates (at sea level) are obtained by aiming the

Table 15-1. Neutron leakage fraction from various cylinders

Cylinder Type	UF_6 Mass (kg)	^{235}U Enrichment (wt%)	Leakage Fraction
14 ton	12,700	0.71	0.55
30B	1,500	0.71	0.80
12B	140	3.00	0.97
5A	15	10.00	1.00
5A	15	35.00	1.00
2S	1	65.00	1.01
2S	1	90.00	1.02

detector upward toward the sky rather than downward toward the cylinder. The response from cylinders at the edge of a large cylinder array may be smaller than the response near the center of the array. For cylinders containing UF_6 of different enrichments, the total neutron count rate T is given by

$$T = [cf(234) + df(238)]\ m \tag{15-5}$$

where m is the total uranium mass, c and d are empirical calibration constants, and f(234) and f(238) are the isotopic mass fractions of ^{234}U and ^{238}U, respectively.

For low enrichments, f(238) is nearly constant, and the ratio f(234)/f(235) is very nearly constant. Then Equation 15-5 can be simplified to

$$T = [e + gf(235)]\ m \tag{15-6}$$

where e and g are the calibration constants. Clearly, if the isotopic composition of the UF_6 is the same for all cylinders, Equation 15-6 can be further simplified to $T = hm$, with h being the single calibration constant.

Measurement uncertainties of 5% are typical for 2 1/2-, 10-, and 14-ton cylinders. With 60- to 120-s counting times, statistics do not contribute appreciably to these uncertainties. Experience in the field suggests that each cylinder size requires a different calibration, perhaps because different solid angles are subtended at the detector by the various cylinders. If the cylinder fill heights vary by 50%, the uncertainties will increase to approximately 10%. Measurements made with the SNAP detector can help identify solid residues in emptied cylinders (heels), but the small amount of material involved causes poor precision in the results and may require long count times, on the order of 1000 s.

15.2.3 Holdup Measurements

SNAP detectors have been used in nuclear fuel-cycle facilities to measure the holdup of nuclear material (Refs. 5 through 7). The material to be measured must be a strong neutron source. All forms of plutonium qualify, but uranium must be enriched and in a matrix suitable for (α,n) reactions so that the signal will be large enough to be useful.

The primary advantage of using neutron-based techniques for holdup measurements is the penetrability of the neutrons. They can be detected from pumps, furnaces, and other heavy equipment that is too dense to permit the escape of gamma radiation. The disadvantages of neutron techniques are their lack of spatial resolution, their lack of isotopic specificity, and their sensitivity to matrix effects. The matrix effects include reflection, multiplication, moderation by moisture, and (α,n) reactions in low-Z materials. Most of these effects are present to some degree in all holdup situations and make the interpretation of neutron measurements difficult. Use of a combination of neutron and gamma-ray measurements is usually the most reliable approach.

Calibration of the SNAP detector for holdup measurements requires standards with isotopic and chemical compositions that are similar to those of the material held up in process, for the reasons mentioned above. To calibrate for a particular geometry, it is helpful to use mockups of the actual equipment. As in all process holdup measurements, 25 to 50% uncertainties are typical. Additional information on holdup measurements with neutrons is included in Section 20.6 of Chapter 20.

15.2.4 Other Applications

Simple detectors like the SNAP can be used as neutron monitors in and around storage vaults and reactors (Refs. 8 and 9). The monitors are used to check for a constant neutron flux. They may have hardened electronics, simple mass-produced electronics, or bare ^{3}He tubes, depending on the application.

15.3 SLAB DETECTORS

Slab detectors contain an array of thermal neutron detectors inserted into a slab of moderating material. They are larger and heavier than SNAP detectors but provide higher detection efficiencies and better directionality if heavier shielding and collimators are added. Slab detectors are typically operated with a combination of standard NIM electronics modules (such as high voltage, amplifier, single-channel analyzer, and scaler) and customized preamplifiers. The preamplifiers are small enough to fit inside the junction box that contains the connections to the tubes. Pulse-height analysis with a multichannel analyzer is sometimes used, but scalers and single-channel analyzers are more frequently found in routine operation.

Slab detectors often consist of ^{3}He tubes placed parallel to each other in a moderator block (Ref. 10). The size and number of tubes vary with the application. Figure 15.3 shows a slab detector that contains nine ^{3}He tubes (2.5-cm diam, 4-atm fill pressure) embedded in a 10-cm-thick polyethylene slab. The junction box holds the tubes rigidly and encloses the high-voltage buss wire and preamplifier in an air-tight, electrically shielded space. For some applications the polyethylene slab is covered with a thin cadmium sheet to absorb thermal neutrons.

15.3.1 Monitoring of UF_6 Enrichment

A slab detector can be operated unshielded or it can be placed inside a shield to obtain direction-sensitive response. Figure 15.4 illustrates a shielded, directional slab detector

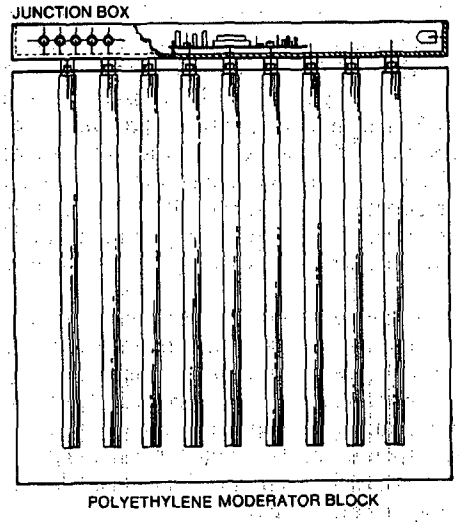

Fig. 15.3 *Side view of slab detector with nine 2.5-cm-diam ^{3}He proportional counters. The junction box contains a preamplifier board.*

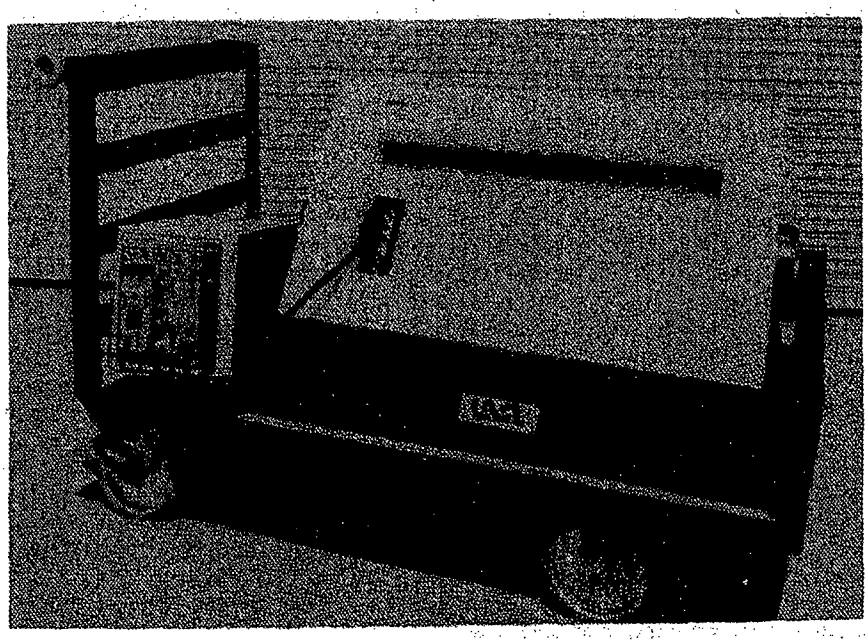

Fig. 15.4 *A slab detector with directional shielding designed for monitoring UF_6 enrichment.*

designed for monitoring UF_6 enrichment. It has a viewing angle of ~90°, smaller than that of the SNAP-II. However, its front-to-back discrimination is nearly five times better. The detector exhibits a front-to-back ratio of 33 for an AmLi source and a ratio of 9 for a ^{252}Cf source. The intrinsic detection efficiency is ~18% for a fission neutron spectrum. The absolute detection efficiency for a point source varies approximately as $1/r$ for r less than the detector dimension and as $1/r^2$ for r more than twice the detector dimension. This relationship is not valid if neutron absorbers or reflectors are present. To determine the neutron background, the detector can be rotated 180° to face away from the source of interest. Or the aperture can be covered with a thick piece of polyethylene. Four-in.-thick polyethylene reduces the neutron signal by approximately a factor of 10.

An array of slab detectors has been proposed for verification of the proper operation of centrifuge facilities (Ref. 11). Detection is possible because highly enriched uranium production is accompanied by elevated neutron levels from (α,n) reactions following ^{234}U decay in gaseous UF_6. Because of its lower mass, $^{234}UF_6$ is enriched even more than $^{235}UF_6$ in the separation process. Since the quantity of highly enriched uranium can be quite small, the increase in slab detector response can also be quite small compared with normal background. Sensitivity can be enhanced with proper design (see Chapter 14) and by using filtering and decision analysis techniques (Ref. 12).

A proposed system would consist of an array of optimized detectors within a process building having centralized data collection and processing. During normal unattended operation a minicomputer would poll the detectors remotely. Based on experimental benchmarks and Monte Carlo simulations, detection sensitivities should be adequate to detect production of highly enriched uranium. Potential sources of false alarms include normal motion of UF_6 cylinders and neutron sources used to verify criticality alarms.

15.3.2 Holdup Measurements

Slab detectors have been used for plutonium holdup measurements after a cleanout operation (Ref. 13). The model used to interpret the results assumed that the geometry of the source material could be approximated by a uniform plane near the floor. This assumption could be investigated by moving the detector and repeating the measurement. The detector was 0.23 m^2 in frontal area and unshielded. The cadmium absorbers were removed to obtain maximum sensitivity to low-energy neutrons. The advantages of using neutron techniques over gamma-ray-based techniques are that shielding of the source material is less of a problem and room return (neutrons scattered off room surfaces) tends to enhance the counter response to material at the edge of the room. These two effects reduced the number of measurement positions required to adequately survey the facility. The room-to-room shielding was good; consequently, cross talk between rooms was not a problem. The chemical and isotopic form of the plutonium was known, so that the response per gram could be determined. The detector response was averaged over several measurement positions to reduce the detector's sensitivity to hot spots (or to determine if they existed). Although this procedure yields 50% results at best, such results are adequate for applications that involve a few hundred grams of plutonium spread thinly over large areas.

15.4 THE 4π COUNTER

The 4π counter is designed to surround the sample, so that the solid angle for neutron detection approaches 4π. This configuration provides the highest possible counting efficiency and the best configuration for shielding. Shielding can be placed on all of the external surfaces of the detector to reduce the effect of nondirectional neutron backgrounds. The sample to be assayed is placed in the central well or sample chamber. Usually the 4π counter is designed to give a reasonably flat response over the volume of this chamber. This feature is very important for heterogeneous samples. Most 4π counter designs are optimized for a particular measurement application, and administrative controls are required to ensure that the samples have the appropriate fill height, composition, and matrix. If the samples are well-characterized and consistent with respect to neutron transport characteristics, assays with a few percent uncertainty are easily obtained.

The 4π counter electronics resembles a collection of slab detector electronics. Typically four to six banks of neutron detectors are used and their outputs are combined to yield the total neutron count rate. With the addition of a coincidence circuit, the same configuration can be used for coincidence counting. For either total or coincidence counting the operation of the counter is usually automated by including a calculator or computer. The computer can be programmed to control the counting electronics, convert the response to a mass measurement using a calibration function, and provide measurement control.

15.4.1 Box Counter

Figure 15.5 shows the design of a 4π counter used at the United Nuclear Corporation (UNC) in Richland, Washington, (Ref. 14) to measure end crops from the fuel extrusion process. The end crops are at least 75 wt% low-enriched uranium, the rest being zircalloy and copper. They are packaged in large shipping crates and loaded onto the counter with a fork lift. Typical net sample weights are 320 kg, however they can be as large as 550 kg. For the UNC application total neutron counting was preferred to coincidence counting for several reasons. Total counting is less sensitive to multiplication effects, such as neutron-induced fissions in ^{235}U. It is less sensitive to position-dependent variations in detection efficiency within the sample chamber. The coincidence count rate from ^{238}U is quite low, only two to five times the rate from cosmic-ray-induced events. Total counting provides a rate about 10 times the coincidence count rate, and administrative controls are readily available to ensure that only valid samples are placed in the counter.

The observed signal from the end crops is due primarily to spontaneous fission of ^{238}U. One kilogram of ^{238}U emits 13.6 n/s. The interior of the sample chamber is cadmium-lined. Under these conditions the absolute efficiency for an AmLi neutron source at the center of the chamber is 20%. The external shield is 10.2-cm-thick polyethylene. Independent measurements with a slab counter indicated that the polyethylene shielding reduces the signal from fuel stored in a neighboring room by a factor of 25. In addition, administrative controls limit the amount of uranium outside the counter: none may be placed within 8 ft of the counter and only one box may be placed within 50 ft. The counter is fully automated and the user interacts with a Hewlett

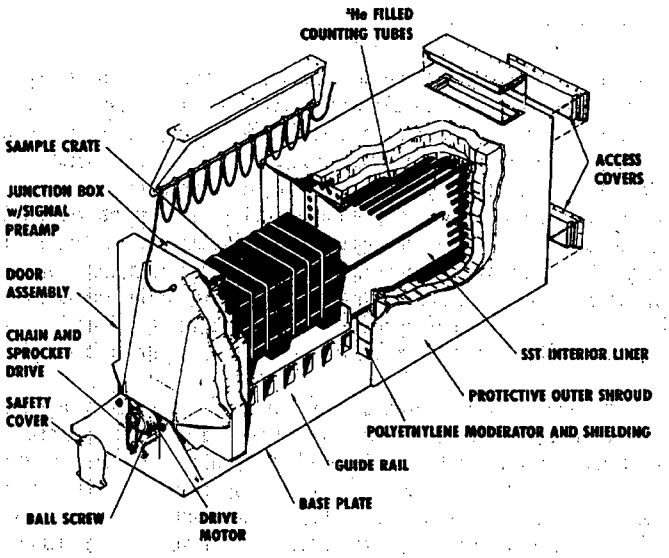

Fig. 15.5 Box counter in use at the United Nuclear Corp (UNC).

Packard HP-85 minicomputer. A daily measurement control procedure verifies that the counter is operating properly. It consists of a background count, which must be below 11 kg effective, and the assay of a standard, which must be within 2% of the known value.

Figure 15.6 is a calibration curve obtained with finished fuel from the extrusion process. Counting times of 1000 s were used; the statistical precision is better than 1%. Three types of fuel were used in the calibration: 0.947%-enriched material in 6-cm-diam cylinders (crosses); 0.947%-enriched material in 3-cm-diam cylinders, so that the packing density is nearly twice as high (circles); and 1.25%-enriched material in 6-cm-diam cylinders (x's). Two different shipping crates were used for the 1.25% material and their weight differed by 20%. The heavier crate provided a 2% lower response than the lighter crate. Assay accuracy is currently limited to 2 to 3% by variations in the shipping boxes. A limited investigation of matrix effects indicates they will be 1% or less. A preliminary comparison with end crops that were dissolved after assay indicates a bias of less than 1%.

15.4.2 Measurement of ^{238}Pu Heat Sources

A small 4π counter has been designed for the assay of ^{238}Pu heat sources at Los Alamos (Ref. 15). The heat sources are 10-g capsules of $^{238}PuO_2$. The plutonium is enriched to 83% in ^{238}Pu and the oxygen is highly enriched in ^{16}O. Heat is produced from the alpha-particle emission associated with the decay of ^{238}Pu. The strong alpha emission rate can also lead to a high neutron production rate via (α,n) reactions in ^{17}O and ^{18}O despite the depletion of ^{17}O and ^{18}O. A quantitative assay of ^{238}Pu is difficult

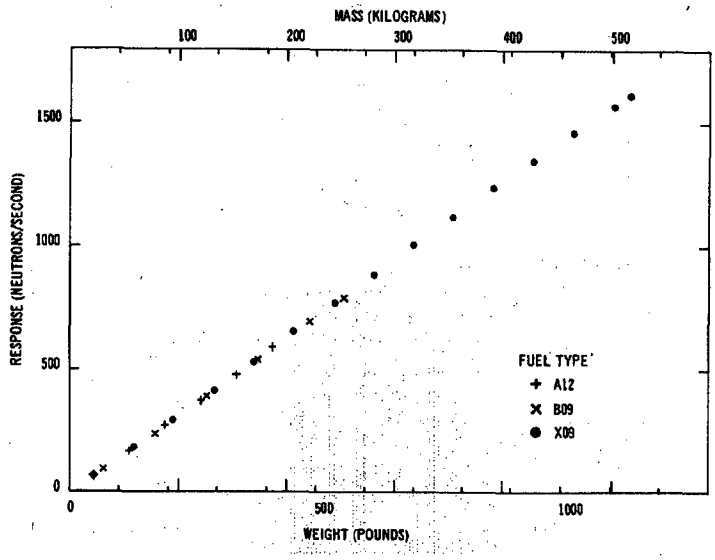

***Fig. 15.6** Calibration data for the UNC box counter showing neutron response as a function of fuel mass.*

because the exact amount of remaining ^{17}O and ^{18}O is unknown. However, the primary objective of the measurement is assurance that the neutron emission from (α,n) reactions has been reduced as low as possible. The $^{238}PuO_2$ material is handled separately from other material in the plutonium facility at Los Alamos. It undergoes different processing and exhibits the rather unique characteristic of producing heat in easily detected amounts. Consequently, administrative controls that ensure that only $^{238}PuO_2$ is being measured are easy to implement.

The heat source counter is illustrated in Figure 15.7. Its design is quite conventional, with high-density polyethylene moderator, cadmium absorber, ^3He counting tubes, aluminum outer skin, and a stainless steel and aluminum sample carrier for placing the heat source into the central counting cavity. A 10-cm-thick polyethylene shield is included to reduce the high background counting rate expected in the plutonium facility. The counter has an efficiency of 18%. Precisions of 0.5% or better are obtained in 100-s count times. The measurement accuracy is 1% within a batch of material and 5% between batches. Most of the batch-to-batch variations are due to different oxygen isotopic distributions.

15.5 MEASUREMENT OF LOW-LEVEL WASTE

Passive neutron counting is often used for measuring nuclear waste material because neutrons can penetrate large waste containers much better than gamma rays can, particularly if the waste contains dense, high-Z materials. Waste containers are typically

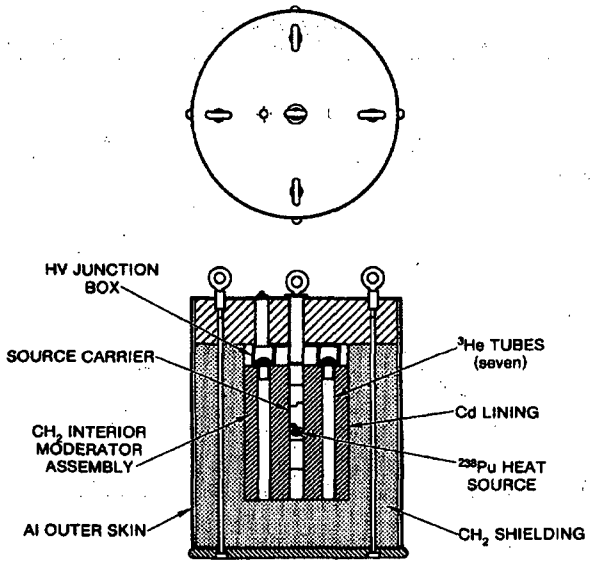

Fig. 15.7 A 4π neutron counter for ^{238}Pu heat sources (Ref. 15).

55 gallons or larger in volume, and passive gamma-ray detectors tend to underestimate the amount of nuclear material because of gamma-ray absorption in the matrix. Neutron measurements, on the other hand, tend to overestimate the amount of nuclear material; (α,n) reactions in the matrix or moderation followed by induced fission create "extra" neutrons. Neutron coincidence counting can substantially reduce this matrix sensitivity by discriminating between source fission neutrons and matrix (α,n) neutrons. However, total neutron counting may be more sensitive to small quantities of nuclear material if (α,n) reactions increase the neutron emission rate. For example, it is several orders of magnitude more sensitive to the fluorides PuF_4 or UF_6. Total neutron counting is often used for discard/save decisions rather than for quantitative assays.

15.5.1 Detection Sensitivity

The neutron emission rates of some common nuclear materials are listed in Tables 14-2, 14-3, and 14-4 (see Chapter 14). From these tables, it is clear that low-Z materials that allow (α,n) reactions can significantly increase the neutron output. Because the neutron output of the plutonium compounds is much higher than the neutron output of the uranium compounds, the sensitivity to plutonium is much better than the sensitivity to uranium. Here the sensitivity of the assay is defined as $\Delta C/C$, where ΔC is the 1-standard-deviation error in the counts C.

An important concept for the measurement of low-level waste is the detectability limit, which is that quantity of material that produces a signal that is larger than

background by the ratio $d = C/\Delta C$. For a background rate b much less than the signal rate, the detectability limit m (in grams) is given by

$$m = d^2/At_1 \quad . \tag{15-7}$$

For a background rate b much larger than the signal rate,

$$m = \frac{d}{A}\sqrt{\frac{b}{t_1} + \frac{b}{t_2}} \quad . \tag{15-8}$$

A is the response rate of the instrument in counts per second per gram, and t_1 and t_2 are the signal and background count times, respectively. Detectability limits at 3σ above background ($d = 3$) are 23 mg for low-burnup plutonium, 0.5 mg for PuF_4, 170 g for natural uranium, and 30 g for natural UF_6 (Ref. 16). These calculations assume 1000-s counting times in a large 4π counter with 15% absolute efficiency. The 4π counter is recommended for assaying low-level waste because of the weak emission rate and heterogeneous nature of the waste.

The calculated detectability limits show that passive neutron counting of low-level waste is usually practical only for plutonium. For 55-gal drums containing 100 kg of nonabsorbing matrix materials, the plutonium limit of 23 mg corresponds to about 23 nCi/g. This detectability limit can easily increase by an order of magnitude for actual drums that contain significant quantities of moderators or neutron poisons. In most cases, however, passive neutron assay overestimates the quantity of nuclear material present because of (α,n) reactions in the matrix. Unless the chemical and isotopic form of the waste is known, no quantitative conclusion can be drawn about the nuclear content of a barrel other than an upper limit.

15.5.2 Assay of 55-Gallon Drums

Total neutron counting of 55-gal drums containing PuO_2-contaminated waste has been investigated at Los Alamos (Ref. 17). Measured were a set of 17 standards constructed at the Rocky Flats Plutonium Processing Facility (Ref. 18). The standards were designed to simulate the contaminated process materials and residues routinely assayed in the Rocky Flats drum counter. Table 15-2 summarizes the characteristics of these drums. A standard deviation of $\pm 16\%$ was obtained for the 17 drums. Since the plutonium isotopics and chemical form were both fixed and well known, the total neutron signal was a reasonable measure of the plutonium content.

15.5.3 Assay of Large Crates

A neutron counter large enough to assay 1.2- by 1.2- by 2.1-m waste crates was developed and used extensively at the Rocky Flats facility (Ref. 19). This 4π counter uses twelve 30-cm-diam ZnS scintillators spaced around the sample chamber. Because these fast-neutron detectors also exhibit some gamma-ray sensitivity, the discriminator thresholds are set above the 1.3-MeV ^{60}Co gamma-ray energy. Most of the neutron

Table 15-2. Physical characteristics of Rocky Flats 55-gallon drum standards

Description	Matrix	Matrix Composition (wt%)	Matrix Av Net Weight (kg)	Matrix Av Density (g/cm^3)	Plutonium (as PuO_2) Loadings (g Pu)
Graphite molds	60-mesh graphite	100	110	0.53	60, 145, 195
Dry combustibles	carbon	90	24	0.12	10, 165, 175
	plastics	5			
	cellulose	5			
Wet combustibles	cellulose	80	51	0.25	28.5, 166
	water	15			
	plastics	5			
Washables	polyvinyl	42	32	0.15	10, 90, 160
	lead gloves	28			
	polyethylene	20			
	cellulose	7			
	surgical gloves	3			
Raschig rings	Pyrex glass with 12% boron as B_2O_3	100	82	0.39	40, 95, 185
Resin	Dowex 1 × 4	100	–	–	25, 110
Benelex-Plexiglas	–	–	–	–	75

signal is also discriminated out, and the measured efficiency of the counter is 0.1%. Although the desired signal is from spontaneous fission neutrons, total counting is preferred to coincidence counting because of the low detection efficiency.

The major sources of inaccuracy for the crate counter are variable matrix effects and the unknown chemical form of the plutonium. Some comparisons with a 55-gal-drum counter show that the crate counter tends to overestimate the plutonium content. Typical crate loadings are less than 100 g; the counting times are 200 s. The results typically agree with tag values within a factor of 4.

The crate counter is used to flag crates that need to be opened and checked more carefully. It periodically locates crates that have been labeled incorrectly. The counter is also used in conjunction with passive gamma-ray counting if more quantitative results are desired.

15.6 SPECIAL APPLICATIONS

The special applications described in this section focus on the neutron energy spectrum observed by some passive assay instruments. In the first two examples, the observed energy spectrum is exploited to determine a specific feature of the sample.

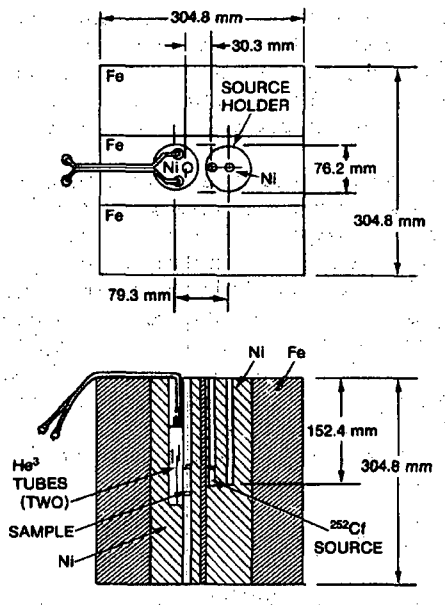

Fig. 15.8 A ^{252}Cf-based hydrogen analyzer.

15.6.1 The ^{252}Cf Hydrogen Analyzer

The ^{252}Cf hydrogen analyzer (Figure 15.8) can determine the hydrogen content of small uranium samples by measuring the softening of the neutron spectrum of a nearby ^{252}Cf source (Ref. 20). The analyzer consists of a steel block with holes bored for two 76-mm-diam nickel cylinders. One cylinder contains the ^{252}Cf source, and the other holds the sample and two ^{3}He neutron detectors, as detailed in Figure 15.9. Because ^{3}He tubes have a higher efficiency for low-energy neutrons, the count rate increases for samples containing hydrogen. This matrix effect is enhanced by using steel reflectors instead of polyethylene moderators around the sample and detectors.

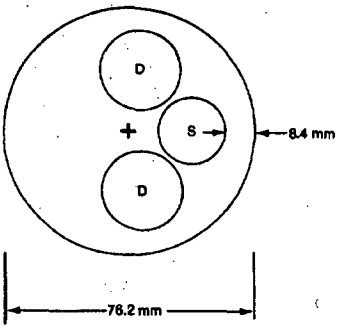

Fig. 15.9 Expanded view of the sample-detector geometry in the ^{252}Cf hydrogen analyzer. The detectors (D) are 25 mm in diameter and the sample chamber (S) is 19 mm in diameter.

The counting electronics requires only a single-channel analyzer. A californium source strong enough to give a count rate of 10 kHz is used so that 0.1% precision can be obtained in reasonable counting times (100 s). Long-term drifts of 0.3% were observed over a 3-day period; however, the actual data consists of a sample measurement preceded or followed by a background measurement. Consequently, long-term drifts are not a problem.

Figure 15.10 demonstrates the response (difference between sample and background counts) as a function of increasing hydrogen. The straight line is a least squares fit to the data. The four samples indicated in the graph had a graphite matrix and were of equal volumes. Figure 15.11 shows the effect of increasing ^{235}U content on the hydrogen analyzer. The hydrogen analyzer was originally designed for use in conjunction with a Small Sample Assay System (SSAS)(Ref. 21) to determine the uranium content of moist uranium fuel rods. The SSAS determines uranium content, but the result is affected by hydrogen content. Consequently an iterative procedure is employed to obtain the best possible assay. First, the SSAS measurement provides a value for uranium content good to about ±10%. Then the hydrogen analyzer results can be used to determine the hydrogen content to ±2 mg, and finally the SSAS result can be iterated to determine ^{235}U to better than 1% accuracy.

15.6.2 Moisture Determination by Detector Ring Ratio

The ratio of total neutron counts in the inner and outer detector rings of a two-ring 4π counter is a measure of the neutron energy spectrum. In a way similar to the ^{252}Cf hydrogen analyzer, the ring ratio can provide information about the moisture content of the sample.

This moisture monitoring technique has been applied to the assay of wet plutonium oxalate (Refs. 22 and 23). The oxalate is precipitated during the conversion of plutonium nitrate to oxide. It is heterogeneous and typically contains 30 to 65 wt% water. The

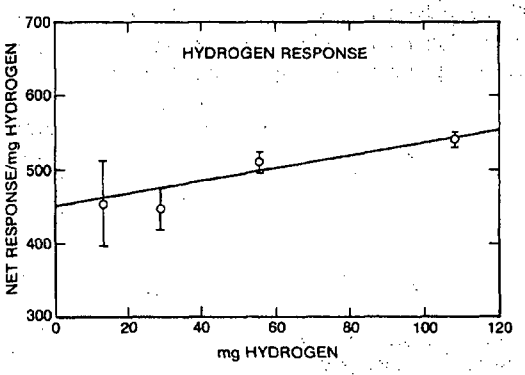

Fig. 15.10 Net signal per milligram of hydrogen as a function of hydrogen content.

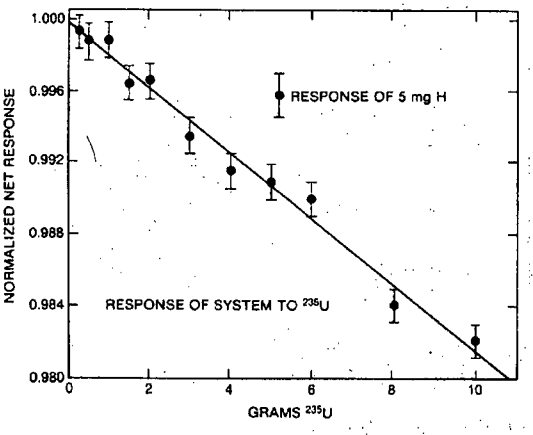

Fig. 15.11 *Effect of ^{235}U on the hydrogen analyzer.*

plutonium assay is done by passive neutron coincidence counting, but a correction for water content is based on the ring ratio. The correction is needed because hydrogen is a better moderator than plutonium oxalate and samples with higher water content decrease the average neutron energy more. The neutron counter contains an inner ring of detectors separated from the sample by 11 mm of polyethylene and an outer ring separated by 33 mm of polyethylene. A change in the neutron energy spectrum affects the two rings differently because of their different depth in the polyethylene.

The counter was calibrated by assaying 19 samples of known plutonium and water content. The mass m of plutonium was expressed as

$$m = aR_o^{(\alpha+\beta T_i/T_o)} \tag{15-9}$$

where R_o = coincidence count rate in the outer ring
T_i = total count rate in the inner ring
T_o = total count rate in the outer ring
and a, α, β are fitted parameters.

An additional 22 samples were assayed nondestructively with a standard deviation of 2.2% (1σ)(Ref. 22) relative to later destructive analyses. Without the ring ratio correction for moisture, the deviation is 50 to 100%.

15.6.3 Energy-Independent Long Counter

There are many uses in fast-neutron studies for a counter whose detection efficiency is independent of the incident neutron energy. One such counter used to calibrate and standardize neutron assay instruments is the long counter (Refs. 10 and 24). The energy response of the long counter is nearly flat, but not entirely energy-independent, as has sometimes been assumed.

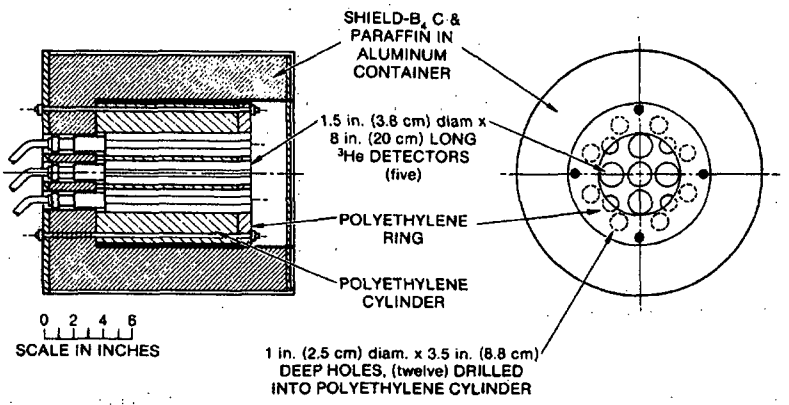

Fig. 15.12 A high-efficiency ^{3}He long counter.

Figure 15.12 shows the design features of a high-efficiency long counter. The neutron source is aligned on the axis of the center ^{3}He detector, at a distance of at least 1 m. The minimum source-to-detector distance, the number and location of the holes in the moderator, and the design of the polyethylene ring in front of the moderator are all essential for achieving the flattest energy response. Figure 15.13 (Ref. 10) shows the response of the counter to broad-spectrum neutron sources; the relative source strengths were known to 3%. Within the accuracy of the source strengths, the counter response appears to be flat from 0.024 MeV to more than 4 MeV. More recent data (Figure 15.14) were obtained with the same counter using a Van de Graaff accelerator to provide relatively monoenergetic neutrons from the ^{7}Li(p,n)^{7}Be reaction (Ref. 25). As the neutron energy was varied from 100 to 1200 keV, a small resonance was observed at 450 keV. Clearly the counter response is not completely energy-independent, but only approximately so.

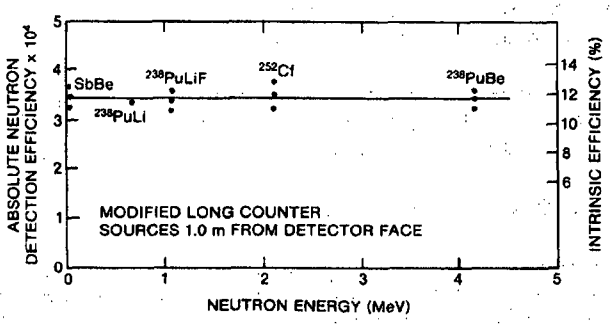

Fig. 15.13 Efficiency of the ^{3}He long counter as a function of neutron energy, as determined with radioactive sources.

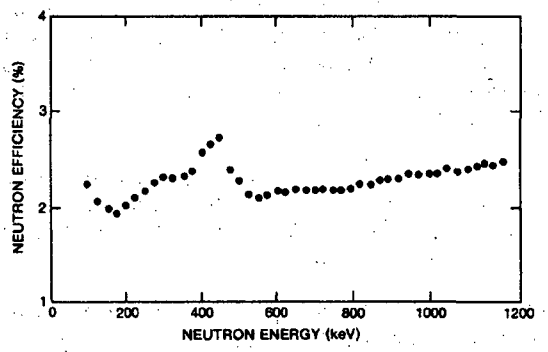

Fig. 15.14 *Efficiency of the ^{3}He long counter as a function of neutron energy, as determined with mono-energetic neutrons.*

REFERENCES

1. H. O. Menlove, T. L. Atwell, and A. Ramalho, "Upgrading of SNAP Neutron Detector, SNAP-II," in "Nuclear Safeguards Research Program Status Report, September—December 1975," Los Alamos Scientific Laboratory report LA-6316-PR (April 1976), pp. 5-6.

2. R. B. Walton and T. L. Atwell, "Portable Neutron Probe, 'SNAP'," in "Nuclear Analysis Research and Development Program Status Report, January—April 1973," Los Alamos Scientific Laboratory report LA-5291-PR (May 1973), p. 14.

3. T. L. Atwell, D. B. Smith, and A. C. Walker "Assay of Plutonium Metal Buttons with a Portable Neutron Counter," in "Nuclear Analysis Research and Development Program Status Report, May—August 1973," Los Alamos Scientific Laboratory report LA-5431-PR (November 1973), pp. 20-23.

4. R. B. Walton, T. D. Reilly, J. L. Parker, J. H. Menzel, E. D. Marshall, L. W. Fields, "Measurement of UF_6 Cylinders With Portable Instruments," *Nuclear Technology* 21, 133 (1974).

5. NRC Guide 5.23, "In-Situ Assay of Plutonium Residual Holdup," Rev. 1 (February 1984).

6. C. Kindle, "In-Situ Measurement of Residual Pu," *Nuclear Materials Management* V, 540 (1976).

7. R. B. Walton, "The Feasibility of Nondestructive Assay Measurements in Uranium Enrichment Plants," Los Alamos Scientific Laboratory report LA-7212-MS (April 1978).

8. J. T. Caldwell, S. W. France, R. D. Hastings, J. C. Pratt, E. R. Shunk, T. H. Kuckertz, and R. Goin, "Neutron Monitoring of Plutonium Storage Vaults," in "Nuclear Safeguards Research and Development Program Status Report, October 1980—January 1981," C. N. Henry, Comp., Los Alamos National Laboratory report LA-8870-PR (November 1981), pp. 21-28.

9. E. J. Dowdy, A. A. Robba, and R. D. Hastings, "Power Reactor Monitor," in "Nuclear Safeguards Research and Development Program Status Report, May—August 1978," S. D. Gardner, Ed., Los Alamos Scientific Laboratory report LA-7616-PR (April 1979), pp. 58-60.

10. L. V. East and R. B. Walton, "Polyethylene Moderated ^{3}He Neutron Detectors," *Nuclear Instruments and Methods* 72, 161 (1969).

11. J. E. Stewart, S. C. Bourret, R. W. Slice, J. T. Markin, C. A. Coulter, and C. A. Spirio, "An Area Neutron-Monitoring Strategy for International Inspections at Centrifuge Enrichment Plants," in "Safeguards and Security Status Report, February—July 1982," Los Alamos National Laboratory report LA-9595-PR (February 1982), pp. 53-56.

12. J. T. Markin, J. E. Stewart, and A. S. Goldman, "Data Analysis for Neutron Monitoring in an Enrichment Facility," European Safeguards Research and Development Association Specialists' Meeting, Petten, The Netherlands, April 27-29, 1982, Los Alamos National Laboratory document LA-UR-81-2304.

13. J. W. Tape, D. A. Close, and R. B. Walton, "Total Room Holdup of Plutonium Measured With a Large-Area Neutron Detector," *Nuclear Materials Management* V (3), 533 (1976).

14. J. K. Sprinkle, Jr., and M. M. Stephens, "End-Crop Box Counter Manual," Los Alamos National Laboratory report LA-9781-M (June 1983).

15. C. O. Shonrock, L. G. Speir, P. R. Collinsworth, and N. Ensslin, "Neutron Counter for ^{238}Pu Heat Source Program," in "Nuclear Safeguards Research and Development Program Status Report, April—June 1980," Los Alamos Scientific Laboratory report LA-8514-PR (February 1981), pp. 5-6.

16. T. Crane, "Measurement of Uranium and Plutonium in Solid Waste by Passive Photon or Neutron Counting and Isotopic Neutron Source Interrogation," Los Alamos Scientific Laboratory report LA-8294-MS (March 1980).

17. T. D. Reilly and M. M. Thorpe, "Neutron Assay of 55-Gallon Barrels," in "Nuclear Safeguards Research and Development Program Status Report, May—August 1970," Los Alamos Scientific Laboratory report LA-4523-MS (September 1970), pp. 26-29.

18. L. Doher, "A Measurement Control Scheme for Plutonium Counting Systems," Proc. Institute of Nuclear Materials Management Annual Meeting, Gatlinburg, Tennessee (May 1970).

19. R. Harlan, "U and Pu Assay of Crated Waste by Gamma-ray, Singles Neutron, and Slow Neutron Coincidence Counting," *Measurement Technology for Safeguards and Materials Control*, T. R. Canada and B. S. Carpenter, Eds. (NBS Special Publication 582, 1980).

20. D. A. Close, R. C. Bearse, and H. O. Menlove, "^{252}CF-Based Hydrogen Analyzer," *Nuclear Instruments and Methods* 136, 131 (1976).

21. A. E. Evans, Jr., *IEEE Transactions on Nuclear Science* 21 (1), 628 (1974).

22. T. W. Crane, "Calibration of a Neutron Coincidence Counter for Measurement of the Plutonium Content of Wet Oxalate Cakes," Los Alamos National Laboratory report LA-9744-MS (April 1983).

23. R. S. Marshall and T. R. Canada, "An NDA Technique for the Assay of Wet Plutonium Oxalate," *Nuclear Materials Management* 107-113 (1980).

24. W. D. Allen, *Fast Neutron Physics*, J.B. Marson and J. L. Fowler, Eds. (Interscience Publications, 1960), Vol. I, p. 361.

25. A. E. Evans, Jr., "Energy Dependance of the Response of a ^{3}He Long Counter," *Nuclear Instruments and Methods* 199, 643 (1982).

16

Principles of Neutron Coincidence Counting

N. Ensslin

16.1 INTRODUCTION

The quantity of uranium or plutonium present in bulk samples of metal, oxide, mixed-oxide, fuel rods, etc., can often be assayed nondestructively by neutron coincidence counting. This powerful technique exploits the fact that neutrons from spontaneous fission or induced fission are emitted essentially simultaneously. In many cases it is possible to obtain a nearly unique signature for a particular nuclear material. The measurement can be made in the presence of neutrons from room background or (α,n) reactions because these neutrons are noncoincident, or random, in their arrival times.

Table 11-1 in Chapter 11 summarizes the spontaneous fission neutron yields and multiplicities of many isotopes important in the nuclear fuel cycle. For plutonium, the table shows that ^{238}Pu, ^{240}Pu, and ^{242}Pu have large spontaneous fission yields. For uranium, there are no large yields; however, ^{238}U in kilogram quantities will have a measurable yield. Spontaneous fission is usually accompanied by the simultaneous emission of more than one neutron. Thus an instrument that is sensitive only to coincident neutrons will be sensitive only to these isotopes. The quantity of these particular isotopes can be determined even if the chemical form of the material yields additional single neutrons from (α,n) reactions. Then, if the isotopic composition of the material is known, the total quantity of plutonium or uranium can be calculated.

For a plutonium sample containing ^{238}Pu, ^{240}Pu, and ^{242}Pu, the observed coincidence response will be due to all three isotopes. However, ^{240}Pu is usually the major even isotope present in both low-burnup plutonium (~6% ^{240}Pu) and high-burnup, reactor-grade plutonium (~15 to 25% ^{240}Pu). For this reason it is convenient to define an effective ^{240}Pu mass for coincidence counting by

$$^{240}Pu_{eff} = 2.52\ ^{238}Pu + {}^{240}Pu + 1.68\ ^{242}Pu \quad . \tag{16-1}$$

Plutonium-240(eff) is the mass of ^{240}Pu that would give the same coincidence response as that obtained from all the even isotopes in the actual sample. Typically, $^{240}Pu_{eff}$ is 2 to 20% larger than the actual ^{240}Pu content. The coefficients 2.52 and 1.68 are determined by (a) the relative spontaneous fission half-lives of each isotope (Table 11-1), (b) the relative neutron multiplicity distributions of each isotope (Table 11-2), and (c) the manner in which these multiplicities are processed by the coincidence circuitry (see for example Ref. 1). The relative spontaneous fission yields are the dominant effect. The coefficients given above are appropriate for the shift register circuitry described later in this chapter, but would change only slightly for other circuits.

Passive counting of spontaneous fission neutrons is the most common application of neutron coincidence counting. However, because fission can be induced, particularly in fissile isotopes such as ^{239}Pu and ^{235}U, a sample containing large quantities of fissile isotopes can be assayed by coincidence counting of induced fissions. The induced coincidence response will be a measure of the quantity of fissile isotopes present. If the fissions are induced by an (α,n) neutron source, the coincidence circuit can discriminate the induced correlated signal from the uncorrelated source.

Passive and active neutron coincidence counters have found many applications in domestic and international safeguards, as described in Chapter 17. Coincidence counters are usually more accurate than total neutron counters because they are not sensitive to single neutrons from (α,n) reactions or room background. However, the total neutron count rate can provide information that complements the coincidence information. For a wide range of material categories, it is generally useful to measure both the coincidence response and the total neutron response.

16.2 CHARACTERISTICS OF NEUTRON PULSE TRAINS

As an aid to understanding coincidence counting it is helpful to consider the train of electronic pulses produced by the neutron detector. These electronic pulses, each representing one detected neutron, constitute the input to the coincidence circuit. This input can be thought of either as a distribution of events in time or as a distribution of time intervals between events, whichever is more convenient. In any case, the observed distribution is produced by some combination of spontaneous fissions, induced fissions, (α,n) reactions, and external background events. As mentioned in Section 16.1, fission events usually yield multiple neutrons that are correlated or coincident in time, whereas (α,n) reactions and background events yield single neutrons that are uncorrelated or random in time.

16.2.1 Ideal and Actual Pulse Trains

An ideal neutron pulse train containing both correlated and uncorrelated events might look like train (a) in Figure 16.1. An actual pulse train detected by a typical

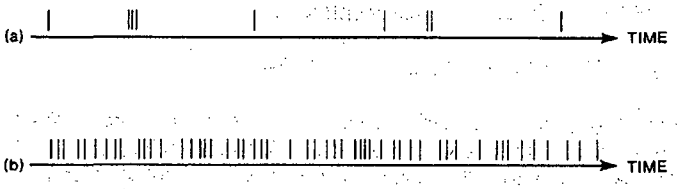

Fig. 16.1 Neutron pulse trains as they might appear on a time axis. (a) An idealized pulse train containing correlated and uncorrelated events. (b) An actual pulse train observed at high counting rates using a detector with typical efficiency and die-away-time characteristics.

neutron coincidence counter will look more complex, as shown by train (b) in Figure 16.1. This is because the neutron coincidence counter design affects the pulse train in several ways.

First, large samples can usually be accommodated in the central well of the coincidence counter. One kilogram of plutonium containing 20% ^{240}Pu will emit about 200 000 n/s. If the coincidence counter has a typical detection efficiency of 20%, the total neutron count rate will be 40 000 n/s, and the mean time interval between detected events will be 25 μs. Second, the typical efficiency $\varepsilon = 20\%$ of a coincidence counter is substantially less than 100%, so that the majority of emitted neutrons are not detected. Most spontaneous fissions are also not detected. If n coincident neutrons are emitted, the probability of detecting k is given by

$$P(n,k) = \frac{n!}{(n-k)!\,k!}\,\varepsilon^k(1-\varepsilon)^{n-k} \quad . \tag{16-2}$$

If in this example two neutrons were emitted (close to the mean spontaneous fission multiplicity of 2.16 for ^{240}Pu), the probability P(2,0) of detecting no neutrons is 0.64. The probability P(2,1) of detecting one neutron is 0.32 and the probability P(2,2) of detecting two neutrons is 0.04. Thus more than half of all fission events are never detected, and most of those that are detected register only one neutron. Actual detected bursts of two or more neutrons are relatively rare, occurring only 4% of the time in the above example. Third, many of the apparent coincidences in the observed pulse train will be due to accidental overlaps of background events, background and fission events, or different fission events.

A fourth important effect is the finite thermalization and detection time of the neutrons in the polyethylene body of the well counter. The process of neutron moderation and scattering within the counter can require many microseconds of time. At any moment the process can be cut short by absorption in the polyethylene, the detector tube, or other materials, or by leakage out of the counter. The process can also be prolonged by neutron-induced fission leading to additional fast neutrons that undergo moderation and scattering before they in turn are absorbed. As a consequence of all of these processes, the neutron population in the counter dies away with time in a complex, gradual fashion after a spontaneous fission occurs. To a good approximation this die-away can be represented by a single exponential:

$$N(t) = N(0)\,e^{-t/\tau} \tag{16-3}$$

where N(t) is the neutron population at time t, and τ is the mean neutron lifetime in the counter, the die-away time. Die-away times are determined primarily by the size, shape, composition, and efficiency of the neutron coincidence counter, but are also slightly affected by scattering, moderation, or neutron-induced fission within the sample being assayed. Typical values for most counter geometries are in the range of 30 to 100 μs. Thus the finite die-away time of the neutron coincidence counter causes the detection of prompt fission neutrons to be spread out over many microseconds. For large samples and typical counters, the mean lifetime may be comparable to, or longer than, the mean time interval between detected events.

As a result of the four effects described above, an actual observed pulse train may contain relatively few "real" coincident events among many "accidental" coincident events. Also, the real events will not stand out in any obvious way from the background of accidental events in the pulse train, as illustrated in train (b) in Figure 16.1. In order to visualize and quantify real and accidental events, it is helpful to use the interval distribution or the Rossi-alpha distribution.

16.2.2 The Interval Distribution

The interval distribution is the distribution of time intervals between detected events. This distribution is given by (Ref. 2):

$$I(t) = \exp\left[-\int_0^t Q(t)d(t)\right] \quad . \tag{16-4}$$

I(t) is the probability of detecting an interval of length t, and Q(t) is the probability of a second event as a function of time following a first event at $t = 0$. For a random neutron source the probability of a second event is constant in time. If the total count rate is T n/s, the normalized interval distribution is $I(t) = Te^{-Tt}$. In this case the interval distribution is exponential, and the most likely time for a following event to occur is immediately after the first event. On a semilogarithmic scale the interval distribution will be a straight line. If real coincidence events are present in addition to random events, the interval distribution is given by a more complex equation (Ref. 3). Figure 16.2 illustrates an interval distribution that contains both coincidence and random events.

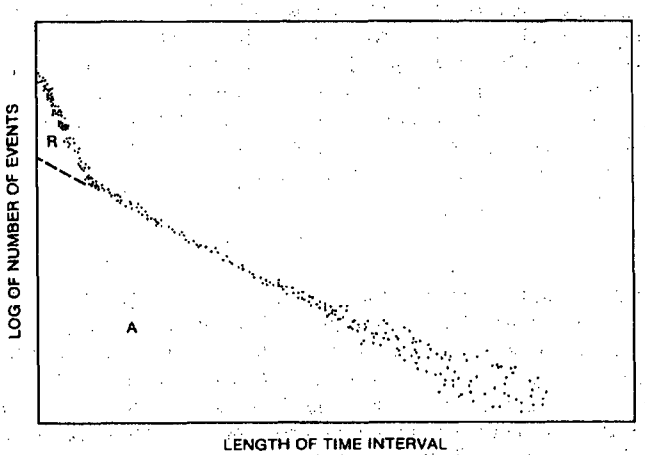

Fig. 16.2 An interval distribution formed by real coincidence events R and accidental events A. The slope of the accidental distribution on this semilogarithmic scale is the total count rate T.

16.2.3 The Rossi-Alpha Distribution

The Rossi-alpha distribution (Ref. 4), developed for reactor noise analysis, is another useful distribution. This distribution is obtained by starting a clock at $t = 0$ with the arrival of an arbitrary pulse. The clock continues to run, and each succeeding pulse is stored by a multiscaling circuit in a bin corresponding to its arrival time. A typical bin width might be 1 μs, and the total number of time bins available might range from 1024 to 4096. When the end of the total time interval is reached, the clock is stopped and the circuit remains idle until another event restarts the process at $t = 0$ again. Thus the Rossi-alpha distribution is the distribution in time of events that follow after an arbitrarily chosen starting event. If only random events are being detected, the distribution is constant with time. If real coincidence events are also present, the Rossi-alpha distribution is given by

$$S(t) = A + Re^{-t/\tau} \quad . \tag{16-5}$$

$S(t)$ is the height of the distribution at time t; A is the accidental, or random, count rate; R is the real coincidence count rate; and τ is the detector die-away time. Figure 16.3 illustrates a Rossi-alpha distribution with R, A, and other variables (defined later) labeled. The exponential die-away of fission events is clearly seen in this distribution.

16.3 BASIC FEATURES OF COINCIDENCE CIRCUITS

16.3.1 Electronic Gates

Coincidence circuits often contain electronic components called "one-shots" or "gate generators" that produce an output pulse of fixed duration whenever an input pulse is received. Gate generators used to convert the input pulses from the neutron detector

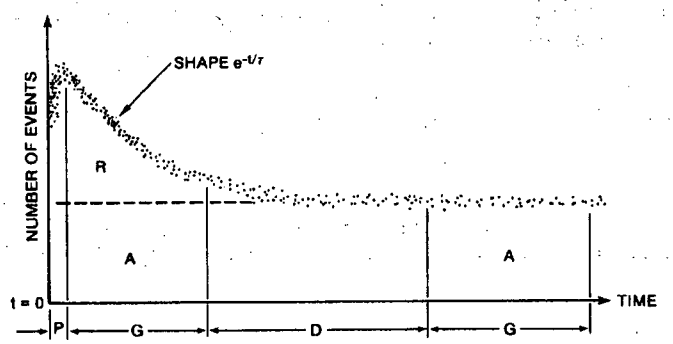

Fig. 16.3 A Rossi-alpha distribution showing detected neutron events as a function of time following an arbitrary starting event. R represents real coincidence events, and A represents accidental coincidence events. P = predelay, G = prompt and delayed gates, D = long delay, and τ = die-away time.

into very short output pulses are called "triggers." Gate generators used to convert the input pulses into long output pulses are called "gates." Such gate generators, as well as amplifiers, detectors, and other circuits, exhibit an electronic deadtime before they can function again. This deadtime is at least the length G of the gate. Depending on the design, this deadtime can be nonupdating or updating.

16.3.2 Updating and Nonupdating Deadtimes

A nonupdating, or nonparalyzable, deadtime is illustrated in pulse train (a) in Figure 16.4. Of the four events, events 1, 2, and 4 initiate gates, but event 3 does not and is lost. Using Equation 16-4, it can be shown that for a true random input rate T, the measured output rate T_m is

$$T_m = \frac{T}{1 + GT} \quad . \tag{16-6}$$

As the input rate becomes very large, the output rate will approach the limiting value 1/G, where G is the gate length.

An updating, or paralyzable, deadtime is illustrated in pulse train (b) in Figure 16.4. The appearance of event 3 causes the gate produced by event 2 to be extended or updated. Consequently, event 4 does not generate a new gate. Only events 1 and 2 initiate gates, and events 3 and 4 are lost. Using Equation 16-4, it can be shown that for random events

$$T_m = T e^{-GT} \quad . \tag{16-7}$$

As the input rate increases, the output rate increases up to a maximum value (which occurs when the input rate is 1/G) and then declines toward 0 (approaches paralysis) as the input rate continues to increase. For input rates that are small, identical deadtime corrections are obtained from Equations 16-6 and 16-7.

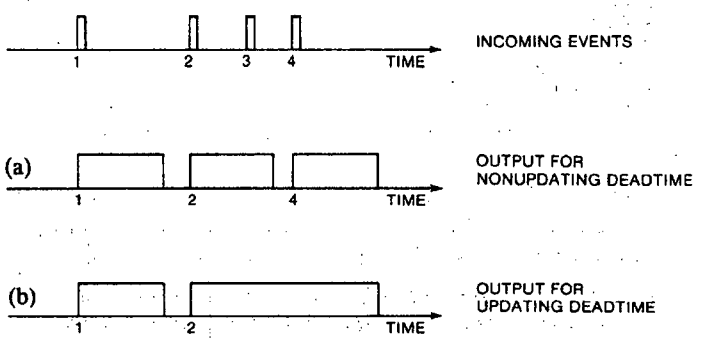

Fig. 16.4 Two gate generators with different electronic deadtime characteristics: (a) nonupdating deadtime; (b) updating deadtime.

16.3.3 Cross-Correlation and Autocorrelation Circuits

Electronic one-shots or gate generators can be combined with scalers in many possible ways to create coincidence circuits. Each combination will be subject to different electronic deadtimes and will require different equations for analysis. For neutron counting, cross-correlation or autocorrelation circuits are the most useful (Ref. 5). A simple cross-correlation measurement is shown in circuit (a) in Figure 16.5. Trigger pulses from detector 1 are compared with gates generated from detector 2. This type of circuit is most useful for very fast detector pulses and short gates because discrimination against detector noise is good and because very few accidental coincidences are produced.

Circuit (b) in Figure 16.5 illustrates an idealized autocorrelation measurement. Both detector inputs are first combined into one pulse train. Then every pulse in the train generates both a short trigger and a long gate, so that every pulse can be compared with every following pulse. Autocorrelation circuits are best suited for thermal-neutron counters because many detector banks can be summed together for high efficiency and because the substantial die-away time of the neutrons causes many overlaps between detector banks. Gate lengths are chosen to be comparable to the die-away time, and a separate, parallel circuit with a delayed trigger or gate is usually used for the subtraction of accidental coincidences (see Sections 16.4 and 16.5).

The autocorrelation circuits described in Section 16.4 and 16.5 are the most important circuits for neutron coincidence counting.

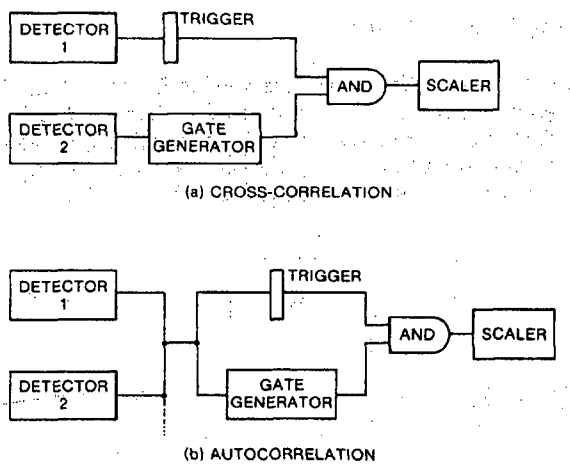

Fig. 16.5 Two types of coincidence circuits: (a) cross-correlation; (b) autocorrelation.

16.4 THREE COMMON COINCIDENCE CIRCUITS

16.4.1 Variable Deadtime Circuit

The variable deadtime circuit, or VDC, was developed in Europe for the assay of plutonium wastes (Refs. 6 through 8). It is a simple circuit (see Figure 16.6), but requires a complex analysis. The variable deadtime circuit consists of one short gate, typically 4 μs, that records most fission and accidental events, and one long gate, typically 32 to 128 μs, that misses most fission events but counts most accidental events. The difference between the two scalers is a measure of the rate of fissions. Both gates are nonupdating, so the net coincidence rate R, using Equation 16-6, is approximately given by

$$R \propto \frac{S_1}{1 - S_1G_1} - \frac{S_2}{1 - S_2G_2} \quad . \tag{16-8}$$

Here S_1 is the count rate in the scaler attached to the short gate, whose length is G_1, and S_2 is the count rate in the scaler attached to the long gate, whose length is G_2.

Equation 16-8 is useful only at count rates of several kilohertz or less because it does not treat the interference between fission and accidental events correctly. (More complex expressions are given in Refs. 9 and 10.) Additional difficulties arise when induced fissions in the sample cause longer fission chains (Refs. 11 and 12). For this reason the variable deadtime circuit is not practical for the assay of large, multiplying samples.

16.4.2 Updating One-Shot Circuit

An updating one-shot circuit (Ref. 10) is illustrated in Figure 16.7. The first half of the circuit generates prompt coincidences between a gate of length G and a short trigger. These coincidences consist of real coincidences (R) and accidental coincidences (A). In order to correct for these accidental events, it is necessary to add a long delay and then measure coincidences between a second, delayed gate of length G and the original short

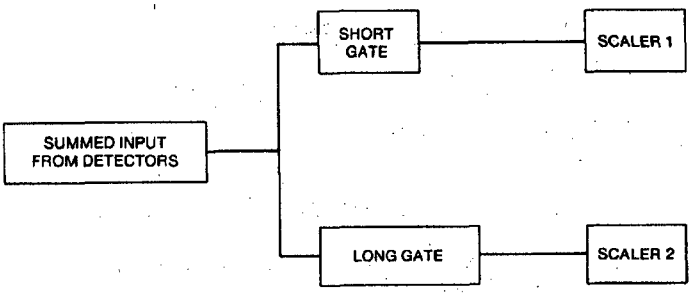

Fig. 16.6 A variable deadtime circuit (VDC).

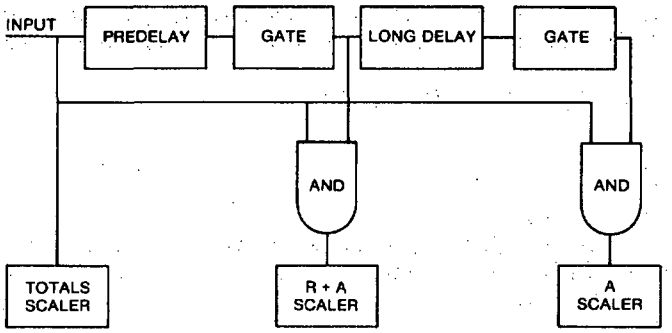

Fig. 16.7 Updating one-shot circuit. The two one-shots are of equal length.

trigger. If the long delay (D) is much longer than the mean neutron lifetime τ in the detector, the second coincidence circuit will measure only accidental events (A). The net coincidence response R is then given by the difference between the two scalers. Figure 16.3 illustrates this process.

Figure 16.3 also shows that an actual measurement of a Rossi-alpha distribution will be subject to several limitations: (a) pulse pileup and electronic deadtimes will perturb the distribution near $t = 0$, so it is customary to begin analysis at time P, the predelay; (b) because the distribution of real events extends beyond the gate interval G, some real coincidences are missed by the prompt gate; (c) in principle, some real events may appear in the delayed gate if D is not long enough. Taking these limitations into account, the true coincidence response of the updating one-shot circuit is given by

$$R = \frac{(R+A)\text{ scaler} - (A)\text{ scaler}}{e^{-P/\tau}(1-e^{-G/\tau})[1-e^{-(D+G)/\tau}]}\, e^{GT} \quad . \tag{16-9}$$

The exponential in the numerator, derived from Equation 16-7, is the correction for the triggers lost during the updating gate G. This large correction limits the usefulness of this circuit to count rates of 20 to 30 kHz or less. Nonupdating one-shot circuits have been built (Refs. 13 and 14), but they are also limited to low count rates.

16.4.3 Reduced Variance Logic

One interesting neutron coincidence circuit has its origins in the field of reactor noise analysis, which is the study of the fluctuations in the count rate of neutron detection systems. From these fluctuations it is possible to calculate the moments of the neutron count distribution (Feynman variance technique) (Ref. 4). The reduced variance logic (RVL) circuit applies this technique to the assay of nuclear material (Refs. 15 and 16).

The RVL circuit collects total neutron counts C over a short time interval of 100 to 2000 μs, depending on the application. This measurement is repeated for a large number of time intervals until a reasonable assay time of 100 to 1000 s is reached. From these measurements the circuit calculates the first moment $\overline{C}$ and the second moment $\overline{C^2}$ of

the count distribution. The variance-to-mean ratio of the count distribution is given by $(\overline{C^2} - \overline{C}^2)/\overline{C}$. For random counts that follow the Poisson distribution, this ratio is unity.

If correlated events are present, the parameter

$$Y = \frac{\overline{C^2} - \overline{C}^2}{\overline{C}} - 1 \tag{16-10}$$

will be nonzero. This parameter is dependent on sample multiplication and independent of the spontaneous fission rate in the sample. Another combination of moments that is proportional to sample mass is

$$Q = \overline{C^2} - \overline{C}^2 - \overline{C} \quad . \tag{16-11}$$

Q is independent of the random, uncorrelated background and is proportional to the coincidence count rate R.

The RVL circuit generates the parameters Q and Y for each sample assayed. For small, nonmultiplying samples, the effective ^{240}Pu mass of the sample is obtained from Q alone. For samples that exhibit significant self-multiplication, the ^{240}Pu mass is obtained indirectly from a nonlinear plot of Y as a function of $(Q/^{240}Pu_{eff})$ obtained with standards of known mass. A correction to Equation 16-11 for electronic deadtime at high count rates is given in Ref. 17.

In field applications, RVL circuits have been used to identify highly multiplying samples (Ref. 18). In fixed plant applications, a computer-based analysis system can be added to obtain higher moments of C and a time interval distribution of the counts. In principle, the RVL circuit uses the same count distribution and provides essentially the same assay information as the shift register circuit described in the following section. In practice, the RVL circuit in its present state of development requires more complex data interpretation algorithms and is limited to lower rates.

16.5 THE SHIFT REGISTER COINCIDENCE CIRCUIT

16.5.1 Principles of Shift Register Operation

In the preceding section it was noted that some common coincidence circuits require large corrections for electronic deadtime. Such corrections are required because coincidence analysis begins with one event at $t = 0$ and continues until $t = G$, the gate length. If n events arrive within a time G, the first event will start the gate and the other $n - 1$ will be detected. A second gate cannot be started until a time of length G has passed, thus creating a deadtime of that length.

An alternative approach is to store the incoming pulse train for a time G, so that every event can be compared with every other event for a time G. In effect, every pulse generates its own gate; it is not necessary for one gate to finish before the next can start. This storage of events eliminates the deadtime effect described above and allows operation at count rates of several hundred kilohertz or more.

It is possible to store incoming pulses for a time G by means of an integrated circuit called a shift register. The circuit consists of a series of clock-driven flip-flops linked together in stages. For example, a 64-stage shift register driven by a 2-MHz clock (0.5 μs/stage) defines a gate G of length 32 μs. Incoming pulses "shift" through the register one stage at a time and the whole process takes 32 μs.

This deadtime-free shift register concept was introduced by Boehnel (Ref. 5). Versions of the circuitry have been developed by Stephens, Swansen, and East (Ref. 19) and improved by Swansen (Refs. 20 and 21) and, most recently, by Lambert (Ref. 22). At present the shift register circuit is the most commonly used circuit for domestic and international coincidence counting applications. Examples are given in Chapter 17.

16.5.2 The R+A Gate

Operation of the shift register coincidence circuit is best visualized by referring to the Rossi-alpha distribution of Figure 16.3. This figure shows a prompt gate G that collects real and accidental coincidences (R+A) and a delayed gate G that collects only accidental coincidences (A). The two gates are separated by a long delay D. Note that coincidence counting does not begin until a short time interval P (the predelay) has passed. During this time, typically 3 to 6 μs, the Rossi-alpha distribution is perturbed by pulse pileup and electronic deadtimes in the amplifiers, and the true coincidence count rate cannot be measured. After the predelay, the prompt R+A gate is defined by a shift register that is typically 32 to 64 μs long.

A simplified diagram of a shift register circuit that measures R+A events is illustrated in Figure 16.8. The input (not illustrated) is the logical OR of all the amplifier-discriminator outputs, thus creating an autocorrelation circuit. Every input event, after the predelay P, passes into and through the shift register. Also, every event entering the shift register increments an up-down counter, and every event leaving the shift register decrements the up-down counter. Thus the up-down counter keeps a continuous record of the number of events in the shift register. Every input pulse, before it enters the

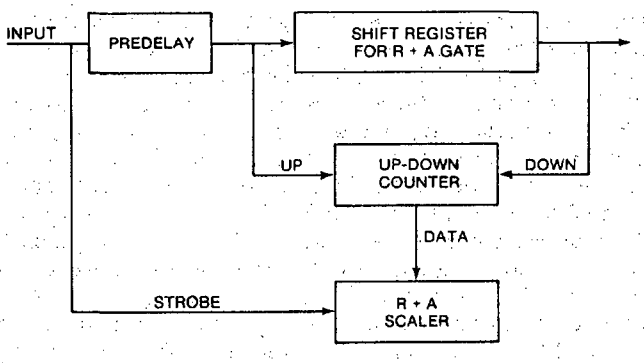

Fig. 16.8 *A simplified block diagram of a shift register coincidence circuit that measures real + accidental (R+A) events.*

predelay and the shift register, also causes the up-down counter to add its contents to the R+A scaler (strobe action).

The above sequence of events ensures that isolated, widely spaced events will never be registered in the R+A scaler. However, if two events appear with a time separation greater than P but less than P + G, then one event will be in the shift register (and the up-down counter will have a count of 1) when the other event strobes the contents of the up-down counter into the R+A scaler. Thus a coincidence will be recorded, as required by Figure 16.3. Note that if three or more events are present within the prescribed time interval, the counting algorithm will record all possible pairs of coincidences between events. For example,

For the following number of closely spaced events...	...the number of recorded coincidences will be	
0	0	
1	0	
2	1	
3	3	
4	6	
n	$n(n-1)/2$	(16-12)

The possible permutations in counting twofold coincidences can exceed the number of events. In practice this counting algorithm is neither beneficial nor harmful, but merely a consequence of treating all events equally.

The coincident events discussed above can represent two or more neutrons from one spontaneous fission (real fission event) or just the random overlap of background neutrons or neutrons from different fissions (accidental events). Thus the counts accumulated by the circuit described above are called R+A counts.

16.5.3 The A Gate

Real fission events R can be determined indirectly by adding a second complete shift register circuit that measures accidental events A. This circuit is identical to the R+A circuit except that a long delay D is introduced between the shift register that defines the A gate and the input event that strobes the contents of the up-down counter into the A scaler. The delay D is usually long compared to the detector die-away time so that no neutrons from fission events near $t = 0$ are still present, as illustrated in Figure 16.3. A common choice for D is approximately 1000 μs, which is very long compared to typical die-away times of 30 to 100 μs. When D is this long, the A scaler will record only accidental coincidences. These include random background events, uncorrelated overlaps between fission and background events, and uncorrelated overlaps between different fission events. The number of accidental events registered in the A scaler will be, within random counting fluctuations, the same as the number of accidental events registered in the R+A scaler if both the A and the R+A shift registers are exactly the same length in time. Then the net difference in counts received by the two scalers is the net real coincidence count R, which is proportional to the fission rate in the sample.

In practice the circuit that measures accidentals can be formed by introducing a second, delayed shift register circuit or by introducing a second, delayed strobe. The latter approach is used in recent circuit designs (Refs. 20 through 22) for simplicity and because it is easy to produce A and R+A gates of the same length. Figure 16.9 (Ref. 23) is a block diagram of a recent shift register coincidence circuit design that includes totals (T), R+A, and A scalers.

The A scaler records accidental coincidences between the total neutron events recorded, and the following relationship is true within random counting fluctuations:

$$A = GT^2 \quad , \tag{16-13}$$

where A and T are expressed as count rates, and G is the coincidence gate length (Ref. 24). This nonlinear relationship shows that A will exceed T when the total count rate is greater than 1/G. By means of Equation 16-13 it is possible to calculate A rather than measure it. However, it is better to measure A with the circuit described above because this corrects continuously and automatically for any change in the total neutron count rate during the assay. Equation 16-13 can then be used later as a diagnostic check for count-rate variations or instrument performance.

16.5.4 Net Coincidence Response R

From Figure 16.3 and the above discussion the true shift register coincidence response is related to the measured scaler outputs by the equation

$$R = \frac{(R+A)\text{ scaler} - (A)\text{ scaler}}{e^{-P/\tau}(1-e^{-G/\tau})[1-e^{-(D+G)/\tau}]} \quad . \tag{16-14}$$

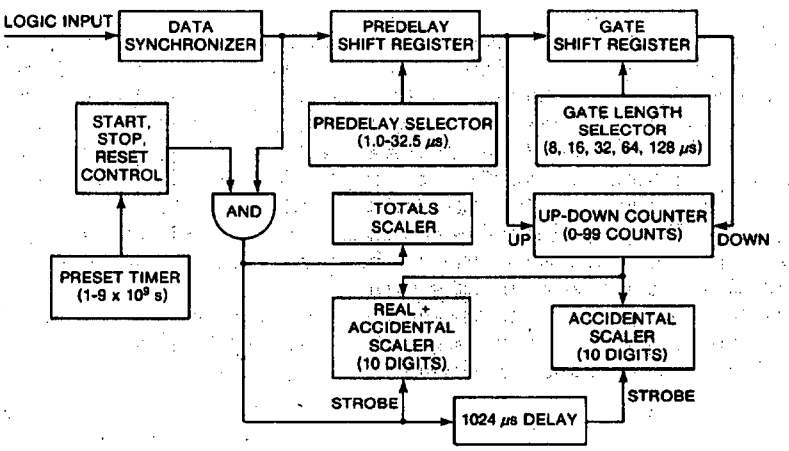

***Fig. 16.9** Block diagram of a complete shift register coincidence circuit including totals, R+A, and A scalers (Ref. 23).*

Equation 16-14 is identical to Equation 16-9 except that the large exponential deadtime correction is not required for the shift register. Smaller corrections for amplifier deadtimes are given in Section 16.6 below. The term $[1 - e^{-(D+G)/\tau}]$ should be very close to unity if the delay D is much longer than the detector die-away time τ. Consequently, this term will be dropped in the following discussions.

In Equation 16-14, R represents the total number of coincidence counts that could be obtained if finite predelays, gate lengths, or delays were not required. In practice it is customary to keep P, G, and D fixed and allow for their effects in the process of calibration with known standards. Then R = (R+A) scaler − (A) scaler is considered to be the true, observed coincidence response. An important equation that relates R to the physical properties of the sample, the detector, and the coincidence circuit can be derived from Equations 16-2, 16-12, and 16-14 (Refs. 5 and 25):

$$R = m_{240}\,(473 \text{ fissions/s-g})\varepsilon^2 e^{-P/\tau}(1 - e^{-G/\tau})\sum_{\nu} P(\nu)\,\frac{\nu(\nu - 1)}{2!} \qquad (16\text{-}15)$$

where

R = true coincidence count rate
m_{240} = ^{240}Pu-effective mass of the sample
ε = absolute detector efficiency
ν = spontaneous fission neutron multiplicity
P(ν) = multiplicity distribution
P = predelay
G = coincidence gate length
τ = detector die-away time.

Equation 16-15 illustrates again that the response of the shift register circuit to ν closely spaced events is proportional to $\nu(\nu - 1)/2$, whereas the response of a conventional circuit would be proportional to $(\nu - 1)$. For practical values of ε and ν, the differences are not great and are automatically accounted for in the calibration process. In Section 16.5.2 it was shown that the expression $\nu(\nu - 1)/2$ represents the sum of all twofold coincidences for ν closely spaced events. Thus the shift register collects all possible valid coincidences. The response of the circuit is still linear with respect to sample mass. However, the sample self-multiplication effects described in Section 16.8 below do affect shift register circuits more than conventional circuits, so that the shift register circuits require larger correction factors.

Equation 16-15 provides a means of determining the detector die-away time τ. If the same sample is assayed in the same way at two different gate settings G_1 and G_2, where G_2 is twice G_1, with the coincidence results R_1 and R_2, respectively, then

$$\tau = -G_1/\ln(R_2/R_1 - 1) \qquad (16\text{-}16)$$

16.6 DEADTIME CORRECTIONS FOR THE SHIFT REGISTER

In the preceding section it was shown that the coincidence gate length G does not introduce deadtimes into the shift register circuit, which permits operation at count rates above 100 kHz. At such high rates, however, a number of smaller deadtimes associated with the analog and digital parts of the circuitry become apparent. These include

- detector charge collection time
- amplifier pulse-shaping time
- amplifier baseline restoration time
- losses in the discriminator OR gate
- shift register input synchronization losses.

These deadtime effects can be studied with time-correlated californium neutron sources, with uncorrelated AmLi neutron sources, and with new digital random pulsers (Ref. 26). Even though the deadtimes can often be studied singly or together, the total effect is difficult to understand exactly because each deadtime perturbs the pulse train and alters the effect of the deadtimes that follow. This section summarizes what is presently known about these deadtimes. Overall empirical correction factors are given, and several electronic improvements that reduce deadtime are described.

16.6.1 Detector and Amplifier Deadtimes

For most shift register systems in use today, the analog electronic components consist of (a) gas-filled proportional counters, (b) charge-sensitive preamplifiers, (c) amplifiers, and (d) discriminators. As described in Section 13.2, a charge signal can be obtained from the gas counter within an average time of 1 to 2 μs after the neutron interaction. This time dispersion is limited by variations in the spatial position of the interaction site, and is not actually a deadtime. However, the ability of the detector to resolve two separate pulses will be comparable to the time dispersion. The preamplifier output pulse has a risetime of about 0.1 μs, and the amplifier time constant is usually 0.15 or 0.5 μs. If all of the electrical components listed above are linked so that one preamplifier and one amplifier with 0.5-μs time constant serve seven gas counters, a total deadtime of about 5 μs is observed (Ref. 27). In practice this deadtime is reduced by using multiple preamplifier-amplifier chains, as described in Section 16.6.4.

The amplifier output enters a discriminator that consists of a level detector and a short one-shot. The one-shot output is 50 to 150 ns long.

16.6.2 Bias Resulting from Pulse Pileup

In addition to actual deadtimes, the electrical components can produce a bias in the shift register output. Bias is defined as the difference between the R+A and A counting rates when a random source such as AmLi is used. For a random source the difference (R+A) − A should be zero; if it is not, the percent bias is 100 R/A. Possible sources of bias include electronic noise; uncompensated amplifier pole zero; shift register input

capacitance; a deadtime longer than the predelay P; or amplifier baseline displacement following a pulse, which is the most important source of bias if the electronic components are properly adjusted to minimize the other sources. Any closely following pulses that fall on the displaced baseline before it is fully restored to zero have a different probability of triggering the discriminator. Bias resulting from pulse pileup is proportional to the square of the count rate and may become noticeable at high count rates. If the baseline is not fully restored in a time less than the predelay time, the effect will extend into the R+A gate and a bias will result.

Figure 16.10 (Ref. 28) illustrates a bias measurement as a function of predelay. The measurement used a coincidence counter with six amplifier channels. The observed bias was reduced to an acceptable value of 0.01% or less for predelay settings of 4.5 μs or more. These results are typical for well-adjusted electronics. For some high-efficiency and long die-away-time counters that operate at rates above 100 kHz, a conservative predelay setting of 6 to 8 μs may be warranted, but in general 4.5 μs is sufficient. At high count rates, R is typically on the order of 1% of A; a pulse pileup bias of 0.01% in R/A implies a relative bias of 1% in R, a bias that is only barely acceptable.

16.6.3 Digital Deadtimes

Because of the deadtime in the amplifier-discriminator chain, it is customary to divide the detector outputs of a coincidence counter among four to six amplifiers. Each amplifier channel may serve three to seven detectors. The discriminator outputs of each channel are then "ORed" together before they enter the shift register (autocorrelation mode). Now the deadtime after the OR gate is much less than before provided the two

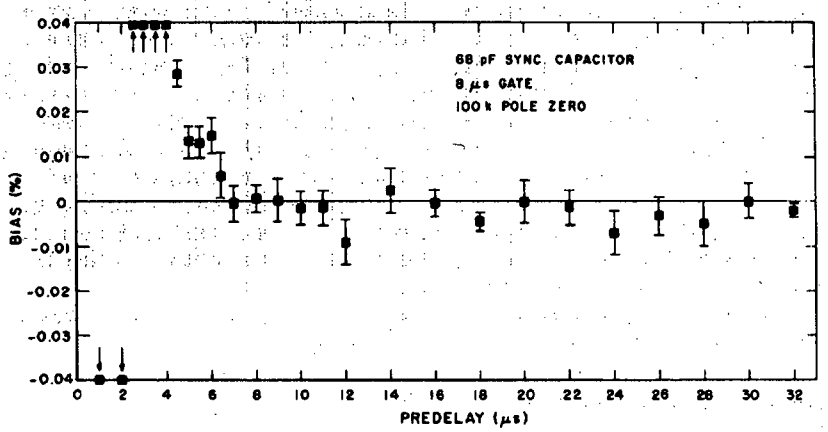

Fig. 16.10 Shift register coincidence bias R/A as a function of predelay P for electronics with 0.5 μs time constant, as measured with a strong random AmLi neutron source. For this measurement, bias was minimized by using optimum values of 100 kΩ for the amplifier pole-zero resistance and 68 pF for the shift register input synchronizer capacitor. Sensitivity to any remaining bias was maximized by using an 8-μs coincidence gate G for the measurements (Ref. 28).

events are from different channels. The deadtime contribution of the OR gate itself can be calculated under the assumptions that (a) no losses occur within a channel because of the longer preceding amplifier deadtime and (b) losses between channels are due to pulse overlap.

$$\text{OR gate overlap rate} = \frac{n(n-1)}{2!}2(\text{disc. output width})(T/n)^2, \tag{16-17}$$

where n is the number of channels and T is the total count rate. The ideal deadtime for an OR gate accepting 50-ns-wide pulses is then

$$\text{OR gate deadtime} = \frac{n-1}{n}(50\text{ ns}) \quad . \tag{16-18}$$

This deadtime is for total events; the coincidence deadtime has not been calculated but would be larger.

The output of the OR gate is a digital pulse stream that enters the shift register. At this point the 50-ns-wide pulses must be synchronized with the 500-ns-wide shift register stages. The limit of one pulse per stage means that some closely following pulses will be lost unless a derandomizing buffer (Section 16.6.5) is used. These losses have been measured with a digital random pulser, as illustrated in Figure 16.11. The shape of this curve is given by

$$\text{measured totals} = (1 - e^{-pT})/p \tag{16-19}$$

where p is the shift register clock period (500 ns in this case) and T is the total input rate (Ref. 29). At low rates, Equation 16-19 yields a nonupdating deadtime of p/2; at high

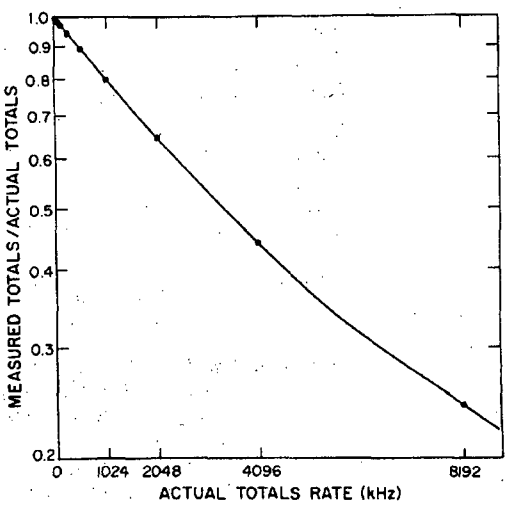

Fig. 16.11 *Shift register synchronizer deadtime as measured with a digital random pulser attached directly to the synchronizer input. The shift register clock period is 500 ns and the digital random pulser has a pulse-pair resolution of 60 ns.*

rates, the deadtime approaches p. The coincidence deadtime is on the order of 2p, as described in Ref. 29. In general, the synchronizer deadtime is small compared to the amplifier deadtime, but it can be appreciable at high count rates. For example, at 256 kHz the totals losses will be 6% and the corresponding coincidence losses will be larger.

16.6.4 Empirical Deadtime Correction Formulas

The total effect of the analog and digital deadtimes described above has not been calculated, but can be determined empirically with californium and AmLi neutron sources. The coincidence deadtime δ_c can be determined by placing a californium source in a fixed location inside a well counter and measuring the coincidence response as stronger and stronger AmLi sources are introduced. During these measurements it is important (1) to center the sources so that all detector channels observe equal count rates and (2) to keep the sources well separated so that scattering effects are minimized. The result of such a measurement is shown in Figure 16.12. Within measurement uncertainties the overall coincidence deadtime is well represented by the updating deadtime equation (Equation 16-7). The totals deadtime δ_t can be measured by the source addition technique, where two californium or AmLi sources are measured in the counter, first separately and then together. An updating deadtime equation also works well for the total count rate correction. Bias can be measured by placing only random AmLi sources in the counter.

Under the assumption that the electronic components have been adjusted so that bias is negligible, as discussed in Section 16.6.2, the overall empirical deadtime correction equations are

$$T(\text{corrected}) = T_m e^{\delta_t T_m} \tag{16-20}$$

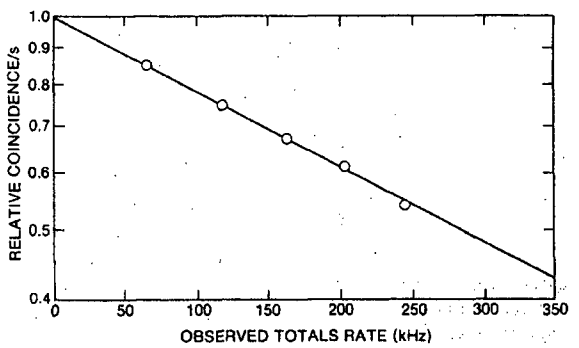

Fig. 16.12 Semilogarithmic plot of relative coincidence response from a californium source as a function of increasing totals count rate resulting from additional AmLi sources. The points are measured values; the line is a least-squares fit to an exponential with deadtime coefficient δ_c = 2.4 μs (Ref. 24).

$$R(\text{corrected}) = R_m e^{\delta_c T_m} \tag{16-21}$$

where T_m is the measured totals rate and R_m is the measured coincidence rate, (R+A) scaler − (A) scaler. Note that in Equations 16-20 and 16-21 the argument of the exponential contains T_m instead of the corrected rate T that appears in Equation 16-7. The use of T_m is a convenient approximation at rates up to about 100 kHz, but at higher rates this approximation forces δ_t and δ_c to become functions of the count rate rather than constants. Values of δ_t and δ_c appropriate for the amplifier chains and 2-MHz-clock shift registers most commonly used today are summarized in Table 16-1 (data compiled from Refs. 27, 30, and 31). For example, six channels of 0.15-μs time-constant amplifiers will have $\delta_c = 0.62$ μs and will exhibit an overall coincidence deadtime of about 6% at 100-kHz counting rates.

From Table 16-1 it is apparent that the deadtime coefficient depends weakly on the detector gas mixture and strongly on the number of amplifier channels available. The number of detector tubes per amplifier channel has no measurable effect on the coefficients, although this situation may change if the detector tubes are subject to count rates in excess of about 20 kHz per tube. Note that all of the coincidence deadtime coefficients in Table 16-1 were measured with a californium source ($\nu = 3.757$) whereas the isotope usually assayed is ^{240}Pu ($\nu = 2.16$). The effect of this difference is not yet known.

16.6.5 AMPTEK Electronics and Derandomizing Buffer

Recent improvements in the analog and digital electronics include faster amplifiers, shorter discriminator outputs, and a derandomizing buffer at the shift register input (Ref. 31). The faster amplifier, which has an effective time constant of about 0.15 μs, consists of a Model A-111 hybrid charge-sensitive preamplifier, discriminator, and pulse shaper manufactured by AMPTEK, Inc., of Bedford, Massachusetts. This unit provides sufficient gain and signal/noise ratio if the ^3He detector tubes are operated at +1700 V.

Table 16-1. Compilation of empirical deadtime coefficients for shift-register-based coincidence counters (Refs. 27, 30, 31)

^3He Detector Gas Additive	Number of Detectors/ Channel	Number of Amplifier Channels	Amplifier Time Constant (μs)	Deadtime (μs)		
				Totals, δ_t	Coincidence, δ_c 0-100 kHz	Coincidence, δ_c 0-500 kHz
Ar + CH_4	7	6	0.5[a]	0.6	2.4	$2.3 + 1.6 \times 10^{-6} T_m$
Ar + CH_4	7	4	0.5	0.87	3.0	$2.8 + 2.7 \times 10^{-6} T_m$
Ar + CH_4	7	2	0.5	2.9	4.7	
Ar + CH_4	7	1	0.5	4.9	12.6	
5% CO_2	7	6	0.5	0.9	3.1	
Ar + CH_4	3	6	0.15[b]	0.16	0.62	$0.62 + 0.20 \times 10^{-6} T_m$

[a] Los Alamos-designed 0.5-μs time-constant amplifier chain (Refs. 22, 23).

[b] AMPTEK A-111 integrated circuit with approximately 0.15-μs time constant in conjunction with a derandomizing buffer on the shift register input (see Section 16.6.5).

The Model A-111 has been incorporated with other electronics on a printed circuit board mounted in a small shielded enclosure. Each enclosure contains an amplifier insensitive to external noise, an LED output monitor, a discriminator output shortened to 50 ns, and connections for "ORing" multiple channels together. Six channels of A-111 units can be operated with a reduced predelay of 3 μs with less than 0.01% bias.

The derandomizing buffer holds pulses that are waiting to enter the shift register, thus eliminating the input synchronization losses described in Section 16.6.3. Input pulses separated by less than 0.5 μs—the shift register clock period—are stored in a 16-count buffer until the shift register can accept them. This circuit eliminates the coincidence deadtime of roughly 1.0 μs associated with the shift register input and permits counting at rates approaching 2 MHz with virtually no synchronizer counting losses. However, as the derandomizing buffer stretches pulse strings out in time, it may create strings longer than the predelay and thereby produce a bias. Because the AMPTEK A-111 amplifier requires a predelay of only 3 μs, the maximum recommended totals rate for less than 0.01% bias is 500 kHz.

With the AMPTEK electronics and the derandomizing buffer, the coincidence deadtime is reduced by a factor of 4 to about 0.6 μs, as noted in Table 16-1. This combination permits passive assays of almost any plutonium samples, with criticality safety of the sample in the well being the only limit.

16.7 UNCERTAINTIES RESULTING FROM COUNTING STATISTICS

In principle the effect of counting statistics on the coincidence response is very complex because the input pulse train contains both random and correlated events and because correlated events can overlap in many ways. Some of the complicating factors are described briefly in this section. For practical coincidence counters these factors are not large, and it is usually possible to calculate measurement uncertainties for coincidence counting with the simple Equation 16-23 given in Section 16.7.1 below.

The major factor that complicates measurement uncertainties is the nonrandom distribution of neutrons from spontaneous fission. Random neutrons from background or (α,n) events follow a Poisson distribution: for n counts, the variance is n and the relative error is $\sigma_n/n = \sqrt{\text{var}(n)}/n = 1/\sqrt{n}$. However, if a spontaneous fission source emits a total of T neutrons in S fissions, with $T = \bar{\nu}S$ where $\bar{\nu}$ is the mean fission multiplicity, the relative error is $1/\sqrt{S}$ rather than $1/\sqrt{T}$. The number of spontaneous fissions follows a Poisson distribution, but the total number of neutrons does not. This is because the emission of more than one neutron per fission does not provide any more information to reduce the measurement uncertainty.

Boehnel (Ref. 5) has shown that counting n spontaneous fission neutrons with an efficiency ε has a variance

$$\frac{\text{var}(n)}{n} = 1 + \varepsilon \frac{\bar{\nu}^2 - \bar{\nu}}{\bar{\nu}} \quad . \tag{16-22}$$

If $\bar{\nu}$ approaches 1 or ε approaches 0, the variance approaches the Poisson distribution value of var(n) = n, but always remains larger. Equation 16-22 implies that the

measurement uncertainty will depend on the multiplicity of the fission source, the fraction of random events ($\nu = 1$) present, and the detector efficiency. Other complicating factors are the detector die-away time and the total count rate, which affect the degree to which events overlap. Coincidence counting will then introduce additional complications.

16.7.1 Simple Error Equation for the Shift Register

For practical values of n and ε, the deviations from the Poisson distribution are not large, as suggested by Equation 16-22 and pulse train (b) in Figure 16.1. If the (R+A) and (A) registers are assumed to be uncorrelated and to follow the Poisson distribution, the relative error is

$$\frac{\sigma R}{R} = \frac{\sqrt{(R+A) + A}}{R} = \frac{\sqrt{R + 2A}}{R} \quad . \tag{16-23}$$

This approximation has been compared with a wide variety of actual measurements and is usually correct to within 15% for plutonium oxide and 25% for californium. Since other uncertainties often limit assay accuracy, it is usually sufficient to know the statistical uncertainty to this level. More exact equations are given in Ref. 5.

Using Equation 16-13, the above uncertainty equation can be rewritten as

$$\frac{\sigma R}{R} = \frac{\sqrt{R + 2GT^2}}{R\sqrt{t}} \tag{16-24}$$

where R and T are deadtime-corrected count rates (Equations 16-20 and 16-21), and t is the count time. In this form, Equation 16-24 is valid for the variable deadtime and updating one-shot circuits as well as for the shift register, as confirmed by measurement (Ref. 10).

Since R is proportional to $(1 - e^{-G/\tau})$, the optimum value of gate length G that minimizes the relative error for a given die-away time τ can be derived by differentiating Equation 16-24. The result is

$$G = \tau(e^{G/\tau} - 1)/2 \approx 1.257\tau \quad . \tag{16-25}$$

16.7.2 Uncertainties for Passive and Active Counting

In passive neutron coincidence counting, the measured total response is proportional to $\varepsilon m_{240} t$, and the measured coincidence response is proportional to $\varepsilon^2 m_{240} t$, where m_{240} is the ^{240}Pu-effective mass and t is the count time. The statistical measurement uncertainty (Equation 16-23 or 16-24) is then proportional to

$$\frac{\sigma R}{R} \propto \frac{\sqrt{k_1 m_{240} + 2k_2 G m_{240}^2}}{\varepsilon m_{240}\sqrt{t}} \tag{16-26}$$

where k_1 and k_2 are two constants of proportionality. For very small samples the relative error is proportional to $1/\sqrt{m_{240}}$; for large samples the relative error is independent of sample mass. In either case the relative error is proportional to $1/\varepsilon$, which implies that the efficiency of the passive well counter should be as high as possible.

Active assay of uranium samples can be carried out with the Active Well Coincidence Counter (AWCC), which uses AmLi sources to induce fissions in ^{235}U (see Section 17.3.1). For the AWCC the statistical measurement uncertainty is again given by Equation 16-23 or 16-24. The coincidence response is proportional to $\varepsilon^2 m_{235} t S$, where m_{235} is the ^{235}U mass, t is the count time, and S is the AmLi source strength. Although the totals response is increased by these induced fissions, the effect is small in practice and for error calculations it is reasonable to assume that the totals response is directly proportional to εSt. Then

$$\frac{\sigma R}{R} \propto \frac{\sqrt{k_1 m_{235} S + 2Gk_2 S^2}}{\varepsilon m_{235} S \sqrt{t}} \tag{16-27}$$

where k_1 and k_2 are two constants of proportionality. For large uranium masses and weak sources, the relative error is proportional to $1/\sqrt{m_{235}S}$, as expected. For strong sources, the relative error is proportional to $1/\varepsilon m_{235}$.

This last relationship has several interesting consequences. First, the relative error is independent of source strength for sources large enough to ensure that R is much less than A. This feature has the advantage that the sources need only be large enough to meet this criterion, which in practice has been measured as 2×10^4 n/s (for two sources, negligible background, and no passive signal from the sample)(Ref. 32). However, this feature has the disadvantage that assay precision cannot be improved by introducing larger sources. Once G, ε, k_1, and k_2 are determined by the design of the well counter, the assay precision can only be varied by varying the counting time. Second, the absolute assay precision is almost independent of sample mass and is determined primarily by the accidental coincidence rate. For the AWCC described in Ref. 32, the absolute assay precision in the "fast configuration" for 1000-s count times is equivalent to 18 g of ^{235}U.

16.8 EFFECTS OF SAMPLE SELF-MULTIPLICATION

Among the effects that may perturb passive coincidence counting, self-multiplication of the coincidence response resulting from induced fissions within the sample is usually dominant. This self-multiplication takes place in all plutonium samples and (to a lesser extent) in all uranium samples. Passive coincidence counters respond to induced fissions as well as to spontaneous fissions. Thus the response from a given amount of spontaneously fissioning material is multiplied and appears to indicate more nuclear material than is actually present. This section describes the magnitude of this effect for plutonium and provides a self-multiplication correction factor that is useful for some assay situations.

16.8.1 Origin of Self-Multiplication Effects

There are two common internal sources of neutrons that induce fissions. One source is the spontaneously fissioning isotopes themselves. For example, neutrons emitted by ^{240}Pu may be captured by ^{239}Pu nuclei and induce these nuclei to fission. The spontaneous fission multiplicity $\nu_s = 2.16$, and the thermal-neutron-induced fission multiplicity $\nu_I = 2.88$ (from Table 11-1). The coincidence circuitry cannot in practice distinguish between these two multiplicities so that both types of fissions may be detected.

The other common source of neutrons is from (α,n) reactions with low-Z elements in the matrix. For example, in plutonium oxide, alpha particles from ^{238}Pu may react with ^{17}O or ^{18}O to create additional neutrons that may induce fissions in ^{239}Pu. The (α,n) neutrons, with multiplicity 1, do not in themselves produce a coincidence response; however, the induced fission neutrons, with multiplicity $\nu_I = 2.88$, do. The magnitude of this coincidence response depends on the alpha emitter source strength, the low-Z element density, the degree of mixing between alpha emitters and low-Z elements, the fissile isotope density, and the geometry of the sample, and in general is not proportional to the quantity of the spontaneously fissioning isotopes that are to be assayed.

The multiplication of internal neutron sources by induced fission is the same process that eventually leads to criticality. What is surprising is the appearance of multiplication effects in the assay of relatively small samples whose mass is far from critical. Even 10-g samples of plutonium metal show 5% enhancements in the coincidence response. At 4000 g of plutonium metal, not too far from criticality, the multiplication of the total neutron output is roughly a factor of 2 and the multiplication of the coincidence response is roughly a factor of 10.

The magnitude of self-multiplication effects on the passive coincidence assay of PuO_2 cans is illustrated in Figure 16.13 (Ref. 33). The data show a definite upward curvature, and the deviation from a straight line determined by the smallest samples amounts to about 38% at the largest sample, 779 g of PuO_2. In the past, self-multiplication effects have often been masked by presenting data without electronic deadtime corrections or by drawing a straight line that seems to pass through most of the data even though the slope does not fit the smallest samples. The latter error is most easily avoided by tabulating coincidence response per gram, as in column 3 of Table 16-2. The following sections discuss other features of Table 16-2 that describe self-multiplication corrections applied to the data.

16.8.2 Calculational Results

Self-multiplication within a sample can be calculated by Monte Carlo techniques. The results of calculations done for the samples listed in Table 16-2 are given in columns 5 to 9. These calculations were carried out with the Monte Carlo code described in Ref. 33; however, the detector itself was not modeled in detail since it was necessary to obtain only the net leakage multiplication across a surface surrounding the sample. The Monte Carlo code selected initial (α,n) or spontaneous fission neutrons according to the ratio

$$\alpha = N_\alpha/\nu_s N_s \tag{16-28}$$

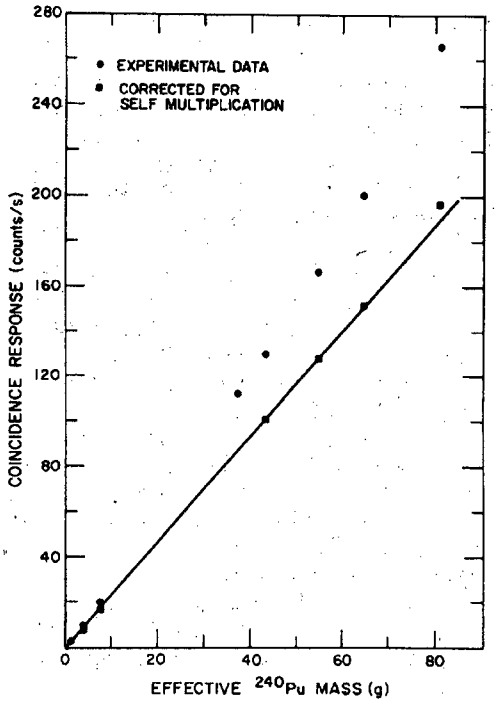

Fig. 16.13 *Coincidence response of PuO_2 standards. The upward curvature in the data is due to self-multiplication in PuO_2. Monte Carlo calculations described in the text were carried out for all but the first and fourth samples in order to correct for self-multiplication, yielding a linear fit to the data.*

where N_α is the number of (α,n) reactions and N_s is the number of spontaneous fissions. The values for α, obtained from Equation 16-32 or 16-35, are given in column 4 of Table 16-2. Each neutron-induced fission chain was followed to its end. The Monte Carlo code calculated the leakage multiplication M_L (defined in Chapter 14), which is related to the probability of fission p by the relation

$$M_L = \frac{1 - p}{1 - p\,\nu_I} \quad . \tag{16-29}$$

The calculated values of M_L are given in column 5 of Table 16-2. These are the ratios by which the total neutron count is enhanced by multiplication, with leakage, absorption, fission, and reflection taken into account. For simplicity, the leakage multiplication is denoted by M in the remaining discussion.

Table 16-2. Self-multiplication correction factors for the plutonium oxide samples in Figure 16.13. Columns 5 through 9 are based on Monte Carlo calculations, and columns 10 and 11 are based on the R/T ratio

1	2	3	4	5	6	7	8	9	10	11
Sample Mass (g)	^{240}Pu-Effective (%)	Coincidence Response/ g-s	α	Leakage Mult., M_L	f_{sf}	f_{an}	Correction Factor, CF	Corrected Response/ g-s	From R/T ratio	
									M_L	CF
20	6.0	2.35(2)	0.66				1.02(1)	2.31(3)		
60	6.4	2.42(2)	1.43	1.005	0.024	0.020	1.04(1)	2.32(3)	1.003	1.03
120	6.4	2.53(2)	1.36	1.010	0.049	0.035	1.08(1)	2.33(3)	1.012	1.08
480	7.8	2.99(3)	0.74				1.28(1)	2.34(4)	1.044	1.26
459	9.5	2.98(3)	0.64	1.046	0.192	0.068	1.26(1)	2.36(4)	1.048	1.28
556	9.9	3.03(3)	0.62	1.049	0.215	0.075	1.29(1)	2.35(4)	1.043	1.25
615	10.6	3.08(3)	0.60	1.056	0.260	0.084	1.34(1)	2.30(4)	1.052	1.30
779	10.4	3.26(3)	0.61	1.061	0.285	0.095	1.38(1)	2.36(4)	1.070	1.41

The Monte Carlo code also calculated a coincidence correction factor

$$CF = 1 + f_{sf} + f_{\alpha n} \tag{16-30}$$

where $1 + f_{sf}$ is the coincidence correction for net multiplication of spontaneous fission neutrons, and $f_{\alpha n}$ is the additional correction for net multiplication of (α,n) neutrons. In Table 16-2, columns 6 and 7 show the relative size of these two induced-fission multiplication effects for the plutonium oxide samples measured. Column 8 shows the overall correction factor CF, and column 9 demonstrates that the corrected coincidence response per gram is now nearly constant.

With the code described above, a series of reference calculations were made to determine the effect of sample mass, density, isotopic composition, and water content on the coincidence correction factor. The results are plotted in Figure 16-14 (Ref. 33). All calculations represent variations about an arbitrary nominal sample of 800-g PuO_2, with a density of 1.3 g oxide/cm^3. This sample contains 706 g of plutonium at 10% $^{240}Pu_{eff}$ and 1 wt% water, in an 8.35-cm-i.d. container. For each calculation, only one parameter was varied from the nominal values. For the mass and density variations, the fill height was adjusted to conserve mass. For the H_2O content variation, the sample density was

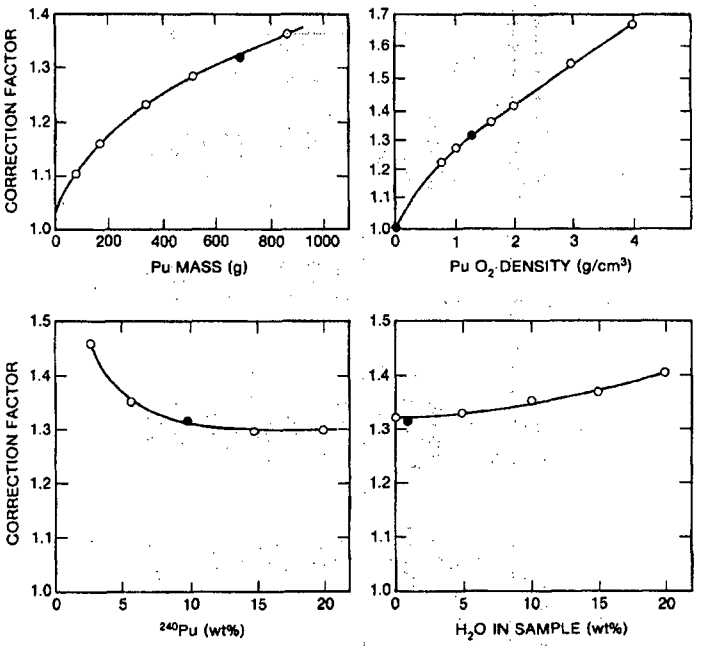

Fig. 16.14 Monte Carlo calculations of self-multiplication effects of various parameters on coincidence counting of PuO_2. The solid data points denote the nominal calculation.

adjusted to conserve volume. Figure 16.14 shows that coincidence correction factors are appreciable even at low mass and low density.

The curves in Figure 16.14 can be used to estimate coincidence correction factors for other similar plutonium oxide samples. The exact range of applicability is not known. For the samples in Table 16-2, the correction factors were calculated directly by the Monte Carlo code, except for the first and fourth samples, which were extrapolated from Figure 16.14, with consistent results.

16.8.3 Effects on Shift Register Response

It is possible to write expressions for the effects of sample self-multiplication on the shift register response. The total neutron count rate T, after subtraction of the background count rate b, is given by

$$T - b = m_{240}(473/s\text{-}g)\,\varepsilon\, M \nu_s (1 + \alpha) \tag{16-31}$$

where m_{240} is the effective ^{240}Pu mass, ε is the detector efficiency, M is the leakage multiplication, ν_s is the spontaneous fission multiplicity, and α is defined by Equation 16-28. If all other quantities are known, α can be determined by inverting Equation 16-31:

$$1 + \alpha = (T - b)/m_{240}(473/s\text{-}g)\varepsilon\, M\, \nu_s \tag{16-32}$$

The coincidence count rate R is given by the following equations (Ref. 34):

$$R = m_{240}(473/s\text{-}g)\,\varepsilon^2 \frac{\overline{\nu(\nu - 1)}}{2} F \quad , \tag{16-33}$$

$$\overline{\nu(\nu - 1)} = M^2\left[\frac{\overline{\nu_s(\nu_s - 1)}}{1 + \alpha\,\nu_s} + \frac{(M - 1)}{\nu_I - 1}\,\frac{(1 + \alpha)}{1 + \alpha\,\nu_s}\,\nu_s\,\overline{\nu_I(\nu_I - 1)}\right] \quad , \tag{16-34}$$

where $\overline{\nu_s(\nu_s - 1)}$ and $\overline{\nu_I(\nu_I - 1)}$ are the reduced second moments of the spontaneous and induced fission multiplicity distributions.

Equation 16-33 is similar to Equation 16-15, with F representing the fraction of coincidences measured, $e^{-P/\tau}(1 - e^{-G/\tau})$. These equations assume that all fission chains produced from the original fission appear to be simultaneous within the resolving time of the coincidence counter. This assumption, called the "superfission concept" (Ref. 5), is valid for thermal-neutron counters because of their long die-away time.

From Equations 16-31 and 16-33 for T and R, and from columns 5 and 8 of Table 16-2, it is apparent that sample self-multiplication affects coincidence counting more than totals counting. As a simple example of this effect, suppose that a spontaneous fission releases two neutrons, one of which is captured by a fissile nucleus which in turn releases three neutrons upon fissioning. The total number of neutrons has increased

from two to four (M = 2). However, the coincidence response has increased from one to six (CF = 6). Thus the ratio R/T has increased with multiplication. Laboratory measurements have shown that R/T can be used as a measure of multiplication. This ratio is the basis of the simple self-multiplication correction described in the following section.

16.8.4 A Simple Correction Factor for Self-Multiplication

Since it is usually not possible to perform a Monte Carlo calculation to determine the self-multiplication of each sample to be assayed, there is a strong need for a self-multiplication correction that can be determined for each sample from the measured parameters R and T. As mentioned earlier, the ratio R/T is sensitive to sample multiplication so that it is possible to use R for the assay and R/T for a multiplication correction. The procedure for calculating this correction for plutonium samples follows.

Step 1: Assay a small 10- or 20-g reference sample that, as an approximation, can be considered as nonmultiplying. Use the same physical configuration and electronic settings as those to be used in Step 2 for assay of larger samples. This measurement yields the values R_0, T_0, and α_0. If the nonmultiplying sample is pure metal, $\alpha_0 = 0$. Otherwise, α_0 can be determined from Equation 16-32 with M = 1. [A multiplying reference sample can also be used if it is sufficient to obtain relative correction factors (Ref. 35).]

Step 2: Now assay an unknown multiplying sample that requires a self-multiplication correction. This measurement yields R and T. If the sample is pure metal, $\alpha = 0$. If the sample is of the same composition as the small reference sample used in Step 1, then $\alpha = \alpha_0$. If the sample is pure plutonium oxide, then from Tables 11-1 and 11-3 it is possible to calculate

$$\alpha = \frac{13\,400\,f_{238} + 38.1\,f_{239} + 141\,f_{240} + 1.3\,f_{241} + 2.0\,f_{242} + 2690\,f_{\text{Am-241}}}{1020\,(2.54\,f_{238} + f_{240} + 1.69\,f_{242})} \qquad (16\text{-}35)$$

if the isotopic fraction f of each plutonium isotope and of ^{241}Am is known. Equation 11-7 can be used to correct the calculated value of α for the presence of major impurities that have high (α,n) cross sections if the concentrations of these impurities are known. For inhomogeneous or poorly characterized plutonium oxide, scrap, or waste where α cannot be determined by one of the above methods, this self-multiplication correction cannot be used.

Step 3: Calculate the ratio

$$r = \frac{R/T}{R_0/T_0}\,\frac{(1+\alpha)}{(1+\alpha_0)} \qquad (16\text{-}36)$$

This ratio will be larger than 1 for multiplying samples with M > 1 because sample self-multiplication increases R more than T. The ratio r is independent of detector efficiency, die-away time, and coincidence gate length. Note that all count rates in Equation 16-36 should be corrected for background and electronic deadtimes.

Step 4: The leakage multiplication M is given by

$$2.062(1 + \alpha)M^2 - [2.062(1 + \alpha) - 1]M - r = 0 \ . \qquad (16\text{-}37)$$

Equation 16-37 can be derived from Equations 16-33 and 16-34 (Refs. 36 and 37).

Step 5: The coincidence counting correction factor for self-multiplication CF is Mr. To summarize,

$$\begin{aligned} &\text{T(corrected for mult.)} = \text{T/M} \\ &\text{R(corrected for mult.)} = \text{R/Mr} \ . \end{aligned} \qquad (16\text{-}38)$$

This self-multiplication correction has no adjustable parameters and is geometry-independent. For example, suppose that two plutonium samples are brought closer and closer together. As this occurs, M will increase, the induced-fission chain lengths will increase, the mean effective multiplicity will increase, and R/T will increase. Equation 16-37 will yield larger values of M, and Equation 16-38 will automatically yield larger correction factors. Examples are given in Ref. 33 and in Figure 17.8.

When Equation 16-38 is used to linearize the calibration curve so that

$$m_{240} = \text{R/kMr} \ , \qquad (16\text{-}39)$$

then Equations 16-31, 16-36, and 16-39 require that the calibration constant k and the detector efficiency ε be related by

$$k = \varepsilon \nu_s (473/\text{s-g}) \frac{R_0}{T_0}(1 + \alpha_0) \ . \qquad (16\text{-}40)$$

This relation is not important in practice because k is usually obtained by calibration, but it may provide a diagnostic to indicate whether the detector efficiency or the small reference sample have been properly measured.

16.8.5 Applications and Limitations of the Simple Correction

Although the self-multiplication correction factors given by Equations 16-37 and 16-38 provide a complete correction with no adjustable parameters, the following assumptions were made in the derivation in order to obtain simple equations:

(1) It was assumed that detector efficiency was uniform over the sample volume. This is not always the case, but is becoming easier to realize with instruments such as the upgraded High Level Neutron Coincidence Counter (HLNCC-II) described in Section 17.2.3.

(2) It was assumed that (α,n) neutrons and spontaneous fission neutrons had the same energy spectra, so that the detection efficiency ε, fission probability p, and induced-fission multiplicity ν_I would be the same for both neutron sources. In general this is not the case, although for plutonium oxide the (α,n) and spontaneous fission neutrons have similar mean energies (2.03 MeV and 1.96 MeV, respectively) but different spectrum shapes.

(3) It was assumed that all fission chains are simultaneous within the die-away time of the detector. This is not true for neutrons that re-enter the sample from the detector (reflected neutrons)(Ref. 5).

These approximations introduce errors into the correction. Values for M given by Equation 16-37 may differ from values obtained from Monte Carlo codes. Values for the coincidence correction factor CF = Mr are usually better, presumably because some errors cancel in the use of ratios. The correction usually gives best fits of 2 to 3% to the data, which is good but is larger than the measurement relative standard deviation (on the order of 0.5%).

Applications of the simple self-multiplication correction are given in Table 16-2, columns 10 and 11, and in Figures 17.8, 17.19, 17.20 and 17.22 for plutonium oxide, metal, and nitrate solutions. Good results have been reported for plutonium oxide in Ref. 22, for plutonium metal in Refs. 33 and 36, and for breeder fuel-rod subassemblies in Ref. 38.

The above applications show that good results, typically 2 to 3%, can be obtained with the self-multiplication correction for well-characterized material despite the assumptions made in the derivation. However, the need to know α, the ratio of (α,n) to spontaneous fission neutrons, for each sample to be assayed poses a severe limitation on the applicability of the technique. For scrap, waste, impure oxide, or metal with an oxidized surface, α cannot be determined. Any error in the choice of α leads to an error of comparable size in the corrected assay value. In such cases the multiplication correction should be used only as a diagnostic for outliers. For many classes of oxide, where α may be somewhat uncertain but sample density and geometry are fixed, Krick (Ref. 39) has found that two-parameter calibration curves without self-multiplication corrections provide the best assay accuracy.

The fundamental limitation of the simple multiplication correction is that only two parameters are measured by each assay, R and T. The number of unknown variables is at least three: the sample mass, the sample self-multiplication, and the (α,n) reaction rate. Further improvements in multiplication corrections can be made if coincidence counters are built that provide a third measured parameter, such as triple coincidences (Refs. 23 and 33).

16.9 OTHER MATRIX EFFECTS

The dominant matrix effect in passive neutron coincidence counting is usually the self-multiplication process described in Section 16.8. If corrections for electronic count-rate losses and self-multiplication can be properly applied, the coincidence response is usually linear with sample mass. However, other matrix effects can affect the assay and may be overlooked at times. These effects are summarized in this section, which is based in part on Ref. 40.

1. (α,n) contaminants

For plutonium samples the most important (α,n) emitters are oxygen and fluorine. Fluorine concentrations of 10 to 400 ppm are typical, and oxygen (in water) may be as

high as several percent. The calculated effect of fluorine and water on the total neutron count rate is given in Section 14.2.3 of Chapter 14. Such (α,n) contaminants may bias the coincidence assay by a few percent. If their concentrations are known, the effects can be accounted for in the self-multiplication correction.

2. Hydrogen content

The hydrogen in water affects the neutron coincidence response by shifting the neutron energy spectrum (see Chapter 14, Section 14.2.4). This increases the detector efficiency and the sample self-multiplication. The former effect can be minimized by careful detector design, and the latter is taken into account by the multiplication correction.

3. Container wall effects

Neutron scattering and reflection by the container wall can increase detection efficiency and sample self-multiplication. An increase in the coincidence count rate up to 7% has been observed. Container effects can be estimated by measuring a californium source with and without an empty sample can.

4. Influence of uranium on plutonium assay

The addition of uranium to plutonium (as in mixed oxide) has the following effects: additional multiplication in ^{235}U; decrease in plutonium multiplication due to a "dilution" of the plutonium; and additional fast multiplication in ^{238}U. Despite different ^{239}Pu, ^{235}U, and ^{238}U fission multiplicities, the multiplication correction works well for mixed plutonium and uranium if there are no additional unknown (α,n) sources.

5. Neutron moderation and absorption (self-shielding)

In plutonium nitrate solutions, moderation leading to increased neutron absorption has been observed (Chapter 17, Section 17.2.7). In active coincidence counting of uranium, neutron absorption and self-multiplication are both strong and opposing effects. The presence of both effects often yields nearly straight calibration curves (Chapter 17, Figures 17.24 and 17.29).

6. Neutron poisons

Boron, cadmium, and some other elements have high thermal-neutron capture cross sections and can absorb significant numbers of neutrons. Problems with neutron poisons have been observed in the active assay of fresh light-water-reactor fuel assemblies.

7. Sample geometry

If the detection efficiency is not uniform over the sample volume, then the coincidence response can vary with sample geometry. Passive counters are now usually designed so that the whole sample will be in the region of uniform efficiency. For active coincidence counters, the source-to-sample distance is very important, and consistent positioning of samples is essential.

8. Sample density

Variations in plutonium oxide density due to settling or shaking during shipping and handling can affect the passive coincidence response by as much as 10%.* The multiplication correction can take these variations into account for samples of similar composition if the samples are within the detector's uniform efficiency region. For active coincidence counting, density variations affect both self-multiplication and self-shielding. No correction is available.

9. Scrap and waste matrices

Here it is helpful to know what the matrix is and to know which of the above-mentioned effects might be present. For plutonium-bearing materials, the coincidence response is usually more reliable than the totals response, but may provide only an upper limit on the quantity of ^{240}Pu. In general, it is useful to measure both the totals and the coincidence response and to use the totals response or the coincidence/totals ratio as a diagnostic to help interpret the coincidence response.

REFERENCES

1. M. S. Krick, "^{240}Pu-effective Mass Formula for Coincidence Counting of Plutonium with Shift Register Electronics," in "Nuclear Safeguards Program Status Report, May—August 1977," J. L. Sapir, Comp., Los Alamos Scientific Laboratory report LA-7030-PR (1977), p. 16.

2. C. H. Westcott, "A Study of Expected Loss Rates in the Counting of Particles from Pulsed Sources," *Royal Society of London,* A194 (1948).

3. C. H. Vincent, "The Pulse Separation Spectrum for the Detection of Neutrons from a Mixture of Fissions and Single-Neutron Events," *Nuclear Instruments and Methods* 138, 261 (1976).

4. N. Pacilio, "Reactor Noise Analysis in the Time Domain," AEC Critical Review Series TID 24512 (1969).

*Private communication from F. J. G. Rogers, Harwell, United Kingdom, 1984.

5. K. Boehnel, "Determination of Plutonium in Nuclear Fuels Using the Neutron Coincidence Method," KFK2203, Karlsruhe, 1975, and AWRE Translation 70 (54/4252), Aldermaston, 1978.

6. J. Jacquesson, *Journal of Physics* 24, Supp. to No. 6, 112A (1963).

7. G. Birkhoff, L. Bondar, and N. Coppo, "Variable Deadtime Neutron Counter for Tamper-Resistant Measurements of Spontaneous Fission Neutrons," Eurochemic Technical Report EUR-4801e (1972).

8. K. Lambert and J. Leake, "A Comparison of the VDC and Shift Register Neutron Coincidence Systems for ^{240}Pu Assay," *Nuclear Materials Management* VII (4), 87 (1979).

9. W. Stanners, "Brief Note on Analysis of VDC Results," Commission of the European Communities, Luxembourg, CEL-DXIII-E (1977).

10. N. Ensslin, M. Evans, H. Menlove, and J. Swansen, "Neutron Coincidence Counters for Plutonium Measurements," *Nuclear Materials Management* VII (2), 43 (1978).

11. A. Prosdocimi and P. Hansen, "Evaluation of the Physical Performances of Neutron Variable Deadtime Counters, Part II—Neutron Physics," Joint Research Centre report FMM/64 (1981).

12. E. W. Lees and B. W. Hooten, "Variable Deadtime Counters, Part III: A Critical Analysis," Atomic Energy Research Establishment report R9701 (1980).

13. C. V. Strain, "Potential and Limitations of Several Neutron Coincidence Equipments," Naval Research Laboratory memorandum 2127 (1970).

14. R. Sher, "Operating Characteristics of Neutron Well Coincidence Counters," Brookhaven National Laboratory report 50332 (1972).

15. E. J. Dowdy, C. N. Henry, A. A. Robba, and J. C. Pratt, "New Neutron Correlation Measurement Techniques for Special Nuclear Material Assay and Accountability," International Atomic Energy Agency report IAEA-SM-231/69 (1978).

16. E. J. Dowdy, G. E. Hansen, A. A. Robba, and J. C. Pratt, "Effects of (α,n) Contaminants and Sample Multiplication on Statistical Neutron Correlation Measurements," Proc. 2nd Annual ESARDA Symp. on Safeguards and Nuclear Material Management, Edinburgh, U.K., March 26-29, 1980.

17. A. Robba, E. Dowdy, and H. Atwater, "Neutron Multiplication Measurements Using Moments of the Neutron Counting Distribution," *Nuclear Instruments and Methods* 215, 473 (1983).

18. K. V. Nixon, E. Dowdy, S. France, D. Millegan, and A. Robba, "Neutron Multiplication Measurement Instrument," *IEEE Transactions on Nuclear Science* NS-30 (1) (1983).

19. M. Stephens, J. Swansen, and L. East, "Shift Register Neutron Coincidence Module," Los Alamos Scientific Laboratory report LA-6121-MS (1975).

20. J. Swansen, N. Ensslin, M. Krick, and H. Menlove, "New Shift Register for High Count Rate Coincidence Applications," in "Nuclear Safeguards Research Program Status Report, September—December 1976," J. L. Sapir, Comp., Los Alamos Scientific Laboratory report LA-6788-PR (June 1977), p. 4.

21. J. Swansen, P. Collinsworth, and M. Krick, "Shift Register Coincidence Electronics System for Thermal Neutron Counters," *Nuclear Instruments and Methods* 176, 555 (1980).

22. K. Lambert, J. Leake, A. Webb, and F. Rogers, "A Passive Neutron Well Counter Using Shift Register Coincidence Electronics," Atomic Energy Research Establishment report 9936 (1982).

23. M. Krick and J. Swansen, "Neutron Multiplicity and Multiplication Measurements," *Nuclear Instruments and Methods* 219, 384 (1984).

24. M. Krick and H. Menlove, "The High-Level Neutron Coincidence Counter User's Manual," Los Alamos Scientific Laboratory report LA-7779-M (1979).

25. M. S. Krick, "Calculations of Coincidence Counting Efficiency for Shift-Register and OSDOS Coincidence Circuits," in "Nuclear Safeguards Research and Development Program Status Report, May—August 1977," Los Alamos Scientific Laboratory report LA-7030-PR (1978), p. 14.

26. J. Swansen and N. Ensslin, "A Digital Random Pulser for Testing Nuclear Instrumentation," *Nuclear Instruments and Methods* 188, 83 (1981).

27. E. Adams, "Deadtime Measurements for the AWCC," Los Alamos National Laboratory memorandum Q-1-82-335 to H. Menlove (April 29, 1982).

28. J. Swansen and N. Ensslin, "HLNCC Shift Register Studies," in "Nuclear Safeguards Research and Development Program Status Report, April—June 1980," G. R. Keepin, Ed., Los Alamos Scientific Laboratory report LA-8514-PR (February 1981), p. 11.

29. C. H. Vincent, "Optimization of the Neutron Coincidence Process for the Assay of Fissile Materials," *Nuclear Instruments and Methods* 171, 311 (1980).

30. H. Menlove, J. Swansen, and E. Adams, "Coincidence Counting Deadtime Study," Los Alamos National Laboratory memorandum Q-1-83-461 (June 27, 1983).

31. J. E. Swansen, "Deadtime Reduction in Thermal Neutron Coincidence Counters," Los Alamos National Laboratory report LA-9936-MS (March 1984).

32. H. O. Menlove, "Description and Operation Manual for the Active Well Coincidence Counter," Los Alamos Scientific Laboratory report LA-7823-M (1979), p. 25.

33. N. Ensslin, J. Stewart, and J. Sapir, "Self-Multiplication Correction Factors for Neutron Coincidence Counting," *Nuclear Materials Management* VIII (2), 60 (1979).

34. K. Boehnel, "The Effect of Multiplication on the Quantitative Determination of Spontaneously Fissioning Isotopes by Neutron Correlation Analysis," *Nuclear Science and Engineering,* 90, 75-82 (1985).

35. M. T. Swinhoe, "Multiplication Effects in Neutron Coincidence Counting: Uncertainties and Multiplying Reference Samples," U.K. Atomic Energy Commission report AERE-R 11678, Harwell, March 1985.

36. N. Ensslin, "A Simple Self-Multiplication Correction for In-Plant Use," Proc. 7th ESARDA Symposium on Safeguards and Nuclear Material Management, Liege, Belgium, 21-23 May 1985.

37. W. Hage and K. Caruso, "An Analysis Method for the Neutron Autocorrelator with Multiplying Samples," Joint Research Centre, Ispra, Italy, report EUR 9792 EN (1985).

38. G. Eccleston, J. Foley, M. Krick, H. Menlove, P. Goris, and A. Ramalho, "Coincidence Measurements of FFTF Breeder Fuel Subassemblies," Los Alamos National Laboratory report LA-9902-MS (1984).

39. M. S. Krick, "Neutron Multiplication Corrections for Passive Thermal Neutron Well Counters," Los Alamos Scientific Laboratory report LA-8460-MS (1980).

40. M. S. Krick, R. Schenkel, and K. Boehnel, in "Progress in Neutron Coincidence Counting Techniques," report of the IAEA Advisory Group Meeting, Vienna, Austria, 7-11 October 1985, IAEA Dept. of Safeguards General Report STR-206.

17

Neutron Coincidence Instruments and Applications

H. O. Menlove

17.1 NEUTRON COINCIDENCE SYSTEM DESIGN PRINCIPLES

Neutron coincidence counting has been used extensively during the past few years for the nondestructive assay of nuclear material. The usefulness of the technique is due primarily to the good penetrability of fast neutrons and the uniqueness of time-correlated neutrons to the fission process and thus the nuclear material content.

In considering the design of a neutron coincidence system, the primary variables that should be considered are: (1) the type of neutron detector, (2) the moderator and shielding materials, and (3) the mass range and sample characteristics. In general, neutron coincidence counters need higher detection efficiency than total neutron counting systems because of the requirement to count at least two neutrons. This requirement makes the coincidence counting rate proportional to the square of the detector efficiency. The high efficiency is usually accomplished by good geometric coupling between the sample and the detector (for example, a 4π or well counter) and by the use of efficient thermal-neutron detectors.

Most of the neutron coincidence counters in current use contain ^{3}He gas tubes because of their high efficiency, reliability, ruggedness, and gamma insensitivity. Tubes containing BF_3 gas are sometimes used to reduce costs or to operate in higher gamma-ray fields; however, their efficiency is about a factor of 2 less than that of ^{3}He tubes. The main disadvantage of ^{3}He and BF_3 gas tubes for coincidence applications is that the neutrons have to slow down to thermal energy via scattering collisions before they are detected in the tubes and this slowing-down process causes a rather large die-away time (τ) in the detector. As a result, the coincidence gate time (G) in the electronics must be set at a relatively large value (10 to 100 μs) to detect the time-correlated coincidence neutrons. Ultimately the large gate length increases the statistical error for high-counting-rate applications.

Computer calculations employing Monte Carlo codes for neutron transport have been used to optimize the design of ^{3}He neutron coincidence detector systems. The following parameters are important in the design: (1) total neutron efficiency for spontaneous fission neutrons, (2) sensitivity to sample matrix materials, (3) neutron die-away time in the detector moderator material, and (4) weight and cost of the system. Neutron coincidence counters have been applied to the assay of a wide range of plutonium masses and container sizes, making it necessary to emphasize different parameters to achieve specified detector characteristics. Examples of the optimization of thermal-neutron counter designs by Monte Carlo calculation are given in Chapter 14.

Several assay systems based on coincidence counting have used fast-neutron recoil detectors to avoid the die-away-time problem associated with thermal counters. Examples of these detectors are liquid and plastic scintillators and ^{4}He gas recoil counters. The scintillators are sensitive to gamma-ray backgrounds and the ^{4}He tubes are relatively inefficient. Examples of coincidence systems based on fast plastic scintillators are the Random Driver, Isotopic Source Assay System, Isotopic Source Assay Fissile, and early models of fuel-pin scanners; all have been documented in previous publications (Refs. 1 through 3).

The remainder of this chapter focuses on thermal-neutron coincidence systems because they dominate the practical applications. Many of these systems have been developed to the stage where commercial equipment is now being used in nuclear fabrication facilities. Recently, inspectors have been using portable equipment to verify operator declaration of nuclear fuel content.

Because of the large range of applications, it has been necessary to develop different assay systems to accommodate difficult types of samples. In contrast to the procedure used in chemical analysis, where the sample is modified to "fit" the instrument, in nondestructive assay the instrument is modified to fit the sample. The following sections describe the instruments, principles of operation, and applications. All of the instruments described are based on the method of neutron coincidence counting using time-correlation electronic circuitry.

17.2 PASSIVE NEUTRON COINCIDENCE SYSTEMS

Neutron assay instrumentation has been standardized by using the neutron coincidence technique as a common basis for a wide range of instruments and applications. The shift-register electronics (Ref. 4) originally developed for the High-Level Neutron Coincidence Counter (HLNCC)(Ref. 5) has been adapted to both passive- and active-assay instrumentation for field verification of bulk plutonium, inventory samples, pellets, powders, nitrates, high-enriched uranium, and materials-testing-reactor, light-water-reactor, and mixed-oxide fuel assemblies. This family of instruments all use the standard shift-register electronics package. The "family tree" in Figure 17.1 shows the relationship between the standard electronics (the trunk), the assay systems (the branches), and the many different applications. The detectors for all of the assay systems are ^{3}He tubes matched to provide the same gain at the same high-voltage settings. Thus, the standard electronics package can be directly substituted between the assay systems with no change in connectors or parameters. Because the electronic components dominate the maintenance work, the total amount of maintenance effort is greatly reduced by this standardization. Operator training is also simplified because an operator trained to use the HLNCC becomes at ease with other systems after only a few minutes of orientation.

Individual instruments that are based on the standard neutron coincidence electronics include

(1) the 55-gal drum counter for scrap barrels;
(2) the HLNCC for bulk plutonium assay;

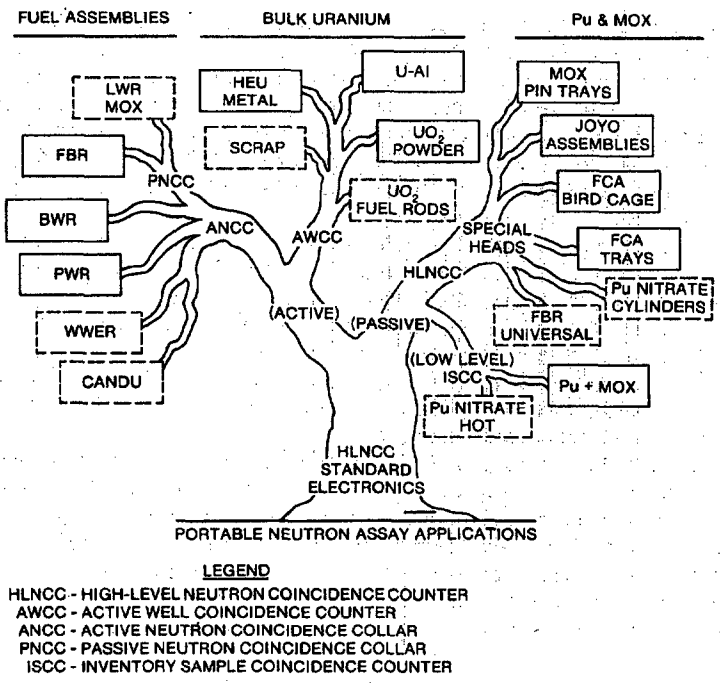

***Fig. 17.1** "Family-tree" diagram of active and passive neutron coincidence systems and applications based on the standard shift-register electronics package developed for the HLNCC.*

(3) special purpose coincidence heads for fast-critical-assembly (FCA) plates and trays, fast-breeder-reactor (FBR) subassemblies, mixed-oxide (MOX) pin trays, and plutonium nitrate bottles;
(4) the Inventory Sample Coincidence Counter (ISCC) for small samples of plutonium nitrate, pellets, and PuO_2 powders;
(5) the plutonium nitrate solution counter for in-line applications; and
(6) the universal FBR subassembly counter.

These and other passive instruments and applications are described in Sections 17.2.1 through 17.2.8.

17.2.1 The 55-Gallon Barrel Counter

An early application of passive neutron coincidence counting to plutonium measurement was the 55-gal barrel counter (Ref. 6). This system was designed to measure compacted scrap and waste in 55-gal barrels or cartons. The material could not be measured by conventional chemical techniques because it was too heterogeneous to sample.

The barrel counter shown in Figure 17.2 contains BF_3 gas tubes imbedded in a polyethylene matrix. The sides of the counter consist of a 10-cm-thick annulus of polyethylene containing thirty-six 5-cm-diam BF_3 detectors; the top and bottom of the counter consist of 10-cm-thick slabs of polyethylene, each containing nine 5-cm-diam BF_3 detectors. The annulus separates into two parts to allow introduction of a 55-gal barrel. The top and sides of the counter are surrounded by a 30-cm-thick water shield. Figure 17.2 shows a general view of the 4π barrel counter in its "open" (separated) configuration, with a 55-gal barrel inserted.

Initially the counter was operated without a cadmium sleeve on the inside of the polyethylene annulus. This configuration kept the neutron counting efficiency as high as possible and resulted in a long neutron lifetime (measured to be 125 μs). The configuration is useful for low-level counting of less than a few grams of plutonium in a barrel. The single-neutron counting efficiency was measured to be 12%, and the coincidence efficiency was measured to be 1.5%. The lifetime of 125 μs decreased to ~50 μs when a cadmium layer was inserted inside the polyethylene annulus and, as expected, the single-neutron and coincidence counting efficiencies also decreased.

It was found that neutrons generated by cosmic rays produce a considerable coincidence background in the counter. At Los Alamos (elevation ~7500 ft), this background amounts to 0.250 ± 0.002 coincidence counts/s—the same rate as from a 0.2-g sample of plutonium (20% ^{240}Pu). This coincidence background limits the sensitivity of the counter to about 0.25 g of plutonium unless a multiplicity measurement is made to correct for cosmic-ray events. Near sea level, where most commercial plutonium processing facilities are located, the cosmic-ray coincidence background will be lower by

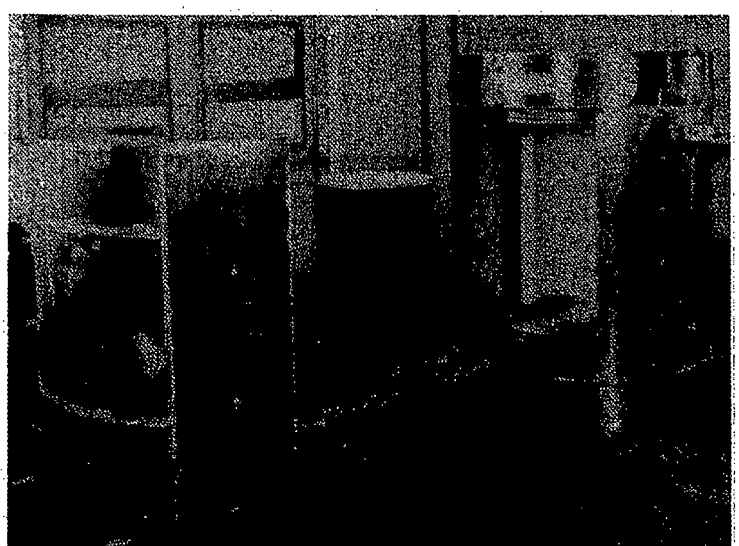

Fig. 17.2 Passive coincidence counter for 55-gal barrels.

roughly a factor of 2. The background rate can also depend somewhat on the mass and composition of the waste container. For example, when six lead bricks (77 kg) were placed in the barrel counter to measure the production of neutrons by cosmic rays in high-Z materials, the observed coincidence counting rate (above background) was 0.91 ± 0.02 counts/s, which is equivalent to about 0.7 g of plutonium (20% ^{240}Pu).

For the assay of plutonium-bearing waste, passive coincidence counting is more accurate than total neutron counting because it is not sensitive to (α,n) reactions in the matrix. However, the detection sensitivity may be less, depending on the chemical form of the material and the background coincidence rate.

17.2.2 The High-Level Neutron Coincidence Counter (HLNCC)

In 1975, work was initiated at Los Alamos to design a portable neutron coincidence counter that could measure cans containing up to 2500 g of PuO_2. The counter was to be modular so that its configuration could be modified to accommodate different geometries such as plates and pins. The design effort led to the hexagonal model shown in Figure 17.3. The intermediate layer of cadmium shown in the figure was added to reduce efficiency, matrix sensitivity, and die-away time for the counter.

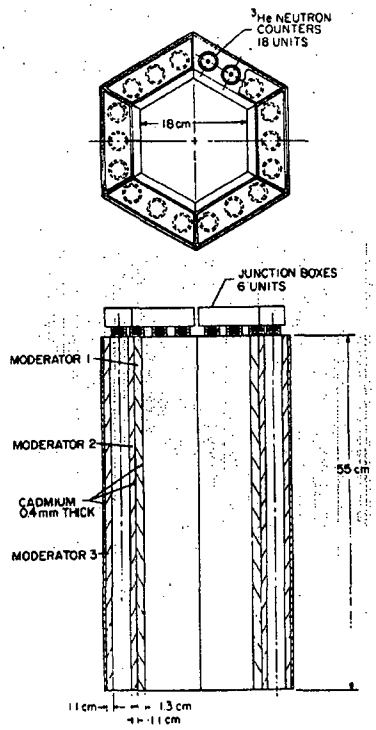

***Fig. 17.3** Portable High-Level Neutron Coincidence Counter (HLNCC) for the assay of high-mass plutonium samples.*

The HLNCC contains six banks of detectors, each bank containing three ^{3}He tubes embedded in a polyethylene matrix. The 25-mm-diam tubes have an active length of 508 mm and are filled to a pressure of 4 atm. The system has an efficiency of ~12% and a neutron die-away time of 32 μs (Ref. 5).

When work was initiated on the HLNCC, the maximum totals count rate that could be processed by coincidence electronics was typically 20 to 30 kHz. For this reason parallel development of a high-speed, portable shift-register electronics package was undertaken. The electronics package (Figure 17.4) contains six channels of electronics, the shift register (see Chapter 16), and a microprocessor to read out the data to a Hewlett Packard HP-97 programmable calculator or other computer. Operation of the system is very simple because of the interface between the shift register and the programmable calculator. The operator needs only to load the sample and press the start button. The data collection, reduction, error analysis, calibration, and readout are performed by the calculator.

During the past 5 years, the HLNCC has been used for a large variety of samples, including bulk PuO_2 powder, mixed-oxide powder, pellets, and pins, and FCA coupons and trays. The maximum design mass of 2.5 kg of plutonium has been extended by over a factor of 2, and the totals counting rate has been pushed up above 300,000 counts/s. At this count rate, there is a large deadtime correction of 3 to 4 for the coincidence rate and the results can only be used relative to a calibration curve with similar counting rates. The standard HLNCC detector and electronics are commercially available and are in use by both plant operators and inspectors.

Recent improvements in the HLNCC detector and electronics are described in the following section.

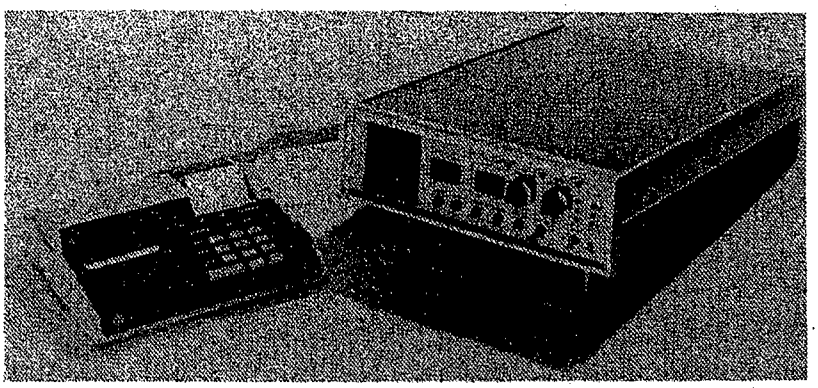

Fig. 17.4 Standard HLNCC shift-register electronics and HP-97 programmable calculator. This unit supplies the requirements for all of the assay systems shown in Figure 17.1.

17.2.3 The Upgraded High-Level Neutron Coincidence Counter (HLNCC-II)

A new upgraded version of the HLNCC has been designed and fabricated. The detector still contains 18 ^{3}He tubes, but in a cylindrical polyethylene body. Faster amplifiers have been incorporated into the electronics, and the detector body has an improved design. The vertical extent of the uniform efficiency counting zone is three times longer than that of the original unit without an increase in size or weight. Figure 17.5 is a cross-section view of the HLNCC-II, and Figure 17.6 is a photograph of the complete system.

A primary design goal for the HLNCC-II was to obtain a uniform or flat counting response profile over the height of the sample cavity while still maintaining a portable system. This was achieved by placing rings of polyethylene as "shims" at the top and bottom of the detector to compensate for leakage of neutrons from the ends. In addition to these outside rings, the interior end plugs were designed to increase the counting efficiency at each end. The end plugs were constructed of polyethylene with aluminum cores to give a better response than plugs made of either material alone would give. Also, the sample cavity has a cadmium liner to prevent thermal neutrons from reflecting back into the sample and inducing additional fissions. Because the cadmium liner does not extend into the region of the end plugs, the polyethylene in the walls of the end plugs becomes an integral part of the moderator material for the ^{3}He tubes.

The totals and coincidence response profiles of the new counter were measured by moving a ^{252}Cf source along the axis of the sample cavity. The normalized response profiles are shown in Figure 17.7, where the dashed curves refer to the original HLNCC. The improvement in response is apparent. Table 17-1 compares some of the key features of the HLNCC and the upgraded HLNCC-II.

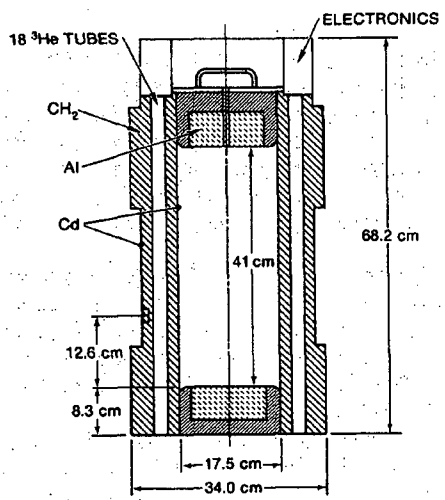

Fig. 17.5 Cross-section view of the upgraded High-Level Neutron Coincidence Counter (HLNCC-II).

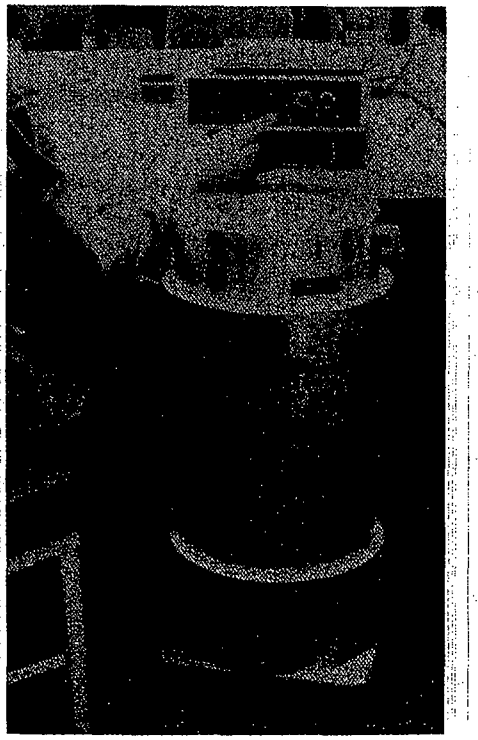

Fig. 17.6 View of the HLNCC-II showing the six indicator lights on the electronics junction box at the top of the unit and the shift-register electronics package on the table top.

The new counting electronics package developed in parallel with the HLNCC-II is based on the AMPTEK A-111 hybrid charge-sensitive preamplifier/discriminator (Ref. 7). Pulses resulting from neutron events are discriminated on the basis of pulse height from noise and gamma-ray events at the output of the preamplifier. This approach eliminates the need for additional pulse-shaping circuitry and allows a maximum counting rate of about 1300 kHz, about four times higher than previously attainable. The electronic deadtime is also a factor of 4 lower than that of the previous system (see Section 16.6.5).

The new electronics package is capable of measuring samples of significantly larger mass, usually limited only by criticality considerations. The small preamplifier/discriminator circuit is placed directly next to the base of the ^{3}He tubes inside a sealed box to enhance the signal-to-noise ratio. Under laboratory conditions, the totals counting stability was measured to be 0.002% over a 2-week counting period. This is the best stability ever observed with nondestructive assay systems.

The HLNCC-II and its new electronics have been used to assay PuO_2, PuF_4, mixed oxide, and other plutonium compounds. An example of the response of the system for PuO_2 both with and without multiplication corrections is shown in Figure 17.8. The

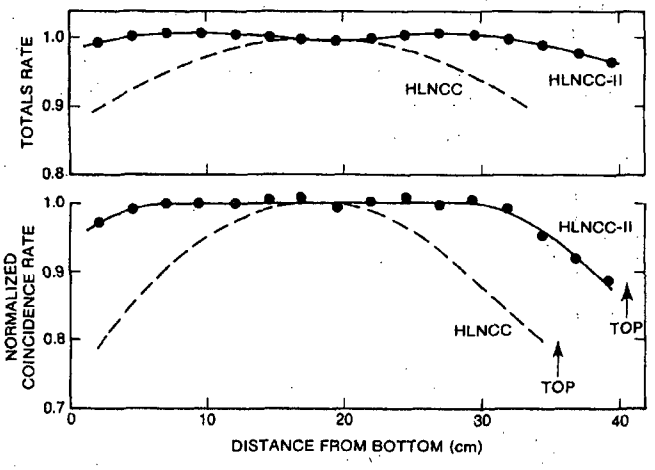

Fig. 17.7 *Normalized response profiles for total and coincident neutron counting for the HLNCC (dashed lines) and the upgraded version HLNCC-II (solid lines), showing a three-times-longer flat response profile for the HLNCC-II.*

Table 17-1. Detector parameter comparison for the HLNCC and the HLNCC-II

Item	HLNCC	HLNCC-II
Cavity diameter	17.5 cm	17.5 cm
Cavity height	35.0 cm	41.0 cm
Outside diameter	32-36 cm	34.0 cm
System weight	48 kg	43 kg
^{3}He tubes:		
(a) Number	18	18
(b) Active length	50.8 cm	50.8 cm
(c) Diameter	2.5 cm	2.5 cm
(d) Gas fill	4 atm	4 atm
(e) Gas quench	Ar + CH_4	Ar + CH_4
Efficiency	12%	17.5%
Die-away time	33 μs	43 μs
Cadmium liner	fixed	removable
Flat counting zone:		
(Coincidence, 2% from max.)	11.0 cm	30.5 cm
(Totals, 1% from max.)	10.5 cm	33.5 cm

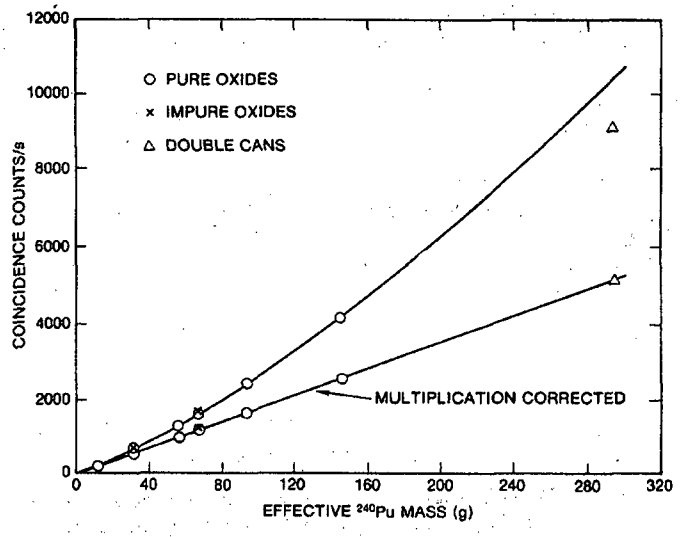

Fig. 17.8 Coincidence response of the HLNCC-II with the new, faster electronics for a variety of large PuO_2 samples, both with and without multiplication correction.

highest mass point, at about 300 g ^{240}Pu-effective, corresponds to two cans of PuO_2 stacked on top of each other. The air gap between the two plutonium masses reduces the geometric coupling compared to that of a single can with the same total mass. This reduction in coupling results in less neutron multiplication and causes the double-can data point to lie below the calibration curve. After the multiplication is corrected for, as described in Section 16.8, the double-can data point lies on the straight line defined by the single-can data.

17.2.4 Special Detector Heads for FCA Coupons

For many applications, it has been desirable to custom design the detector head to the specific application. Even though this specialization proliferates detectors, it reduces assay time, calibration effort, and the number of standards, and decreases the chance of error in the assay. This section and Sections 17.2.5 through 17.2.8 describe some of the special detector heads that have been developed from the HLNCC and that use the same electronics.

At fast critical assemblies, metallic plutonium coupons are typically found in rectangular storage drawers (5 by 5 by 40 cm), and it is desirable to verify the plutonium content without removing the coupons from the trays. The Channel Coincidence Counter (Ref. 8) shown in Figure 17.9 was designed for this purpose.

The principal feature of the detector is the 7- by 7-cm channel, which runs the full length (97 cm) of the detector. This channel is large enough to hold FCA fuel drawers and certain fuel-rod trays, but is small enough to permit high and reasonably uniform

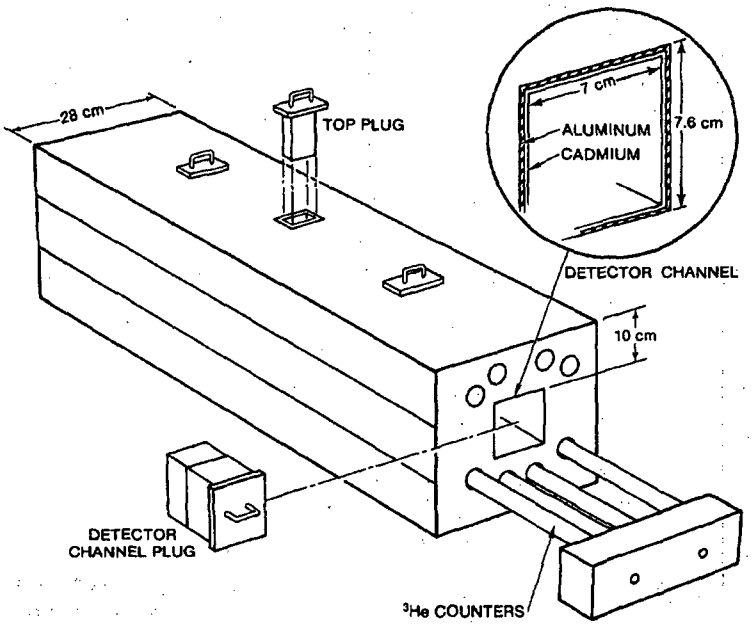

Fig. 17.9 *Isometric diagram of the Channel Coincidence Counter used for the assay of fast-critical-assembly (FCA) fuel trays and mixed-oxide fuel rods.*

coincidence counting efficiency. Three top plugs are also provided with the system. Any one of these can be removed to provide a slot for gamma-ray measurements of the sample. The center top plug is also used as a source holder for detector calibration.

A calibration curve for plutonium plates in FCA drawers is shown in Figure 17.10. The data used for the construction of this curve were acquired with zero-power plutonium-reactor (ZPPR) fuel plates arranged in single, double, and triple rows with matrix materials of iron, aluminum, carbon, and depleted uranium. An increase in the response caused by neutron multiplication is evident for the higher plutonium mass loadings. Also, the data for triple rows of plutonium plates show an increased multiplication compared to single and double rows. The standard self-multiplication correction technique (see Section 16.8) will correct for these differences. The precision for counting FCA drawers is better than 1% in 1000 s. This Channel Coincidence Counter is in routine use at a critical assembly facility (Ref. 9).

A Bird Cage Counter was designed for assaying the same plutonium metal coupons, but it was necessary to make the measurement inside of the "bird cage" used to store and transfer the coupons. The detector consists of ^{3}He tubes in a polyethylene matrix. The detector has a rectangular shape and an open interior region to set over the cylindrical storage canister. The coincidence response shows a neutron multiplication increase for the higher mass loadings. Precision and accuracy of ~1% can be obtained in counting times of 1000 s. This counter is in routine use at FCA facilities.

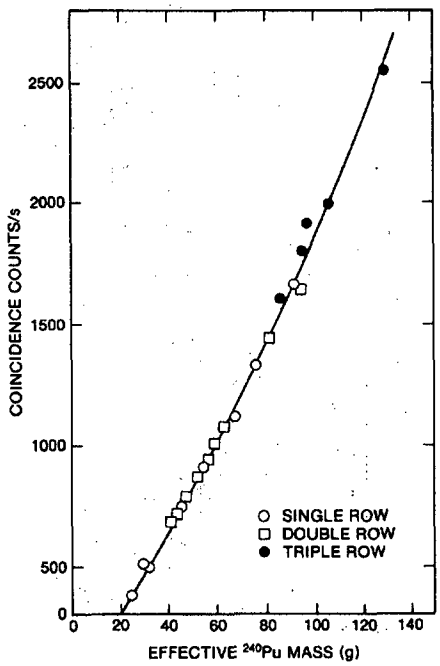

Fig. 17.10 Calibration curve for single, double, and triple rows of plutonium plates in FCA fuel drawers.

17.2.5 Special Detector Heads for FBR Fuel

A special neutron coincidence counter has been designed for verification of FBR fuel pins contained in storage trays (Ref. 10). The tray counter, shown in Figure 17.11, consists of a flat array of ^{3}He tubes in polyethylene slabs. A through slot in the counter provides a cavity for insertion of the stainless steel tray used by the facility operator to handle fuel pins in batches of 24. The tray can be inserted into the front of the counter and removed from the front or back as the user desires. Unlike the more desirable geometry found in cylindrical or hexagonal counters, the tray counter is flat. It is therefore necessary to match the individual detector banks to obtain a uniform spatial response. The uniform response region is ~55 cm long and 30 cm wide, corresponding to the active plutonium region of the fuel pins. The tray requires a clearance height of about 25 mm.

The detector can be used to measure a tray of FBR pins in 2 to 3 min with a sensitivity of much better than one pin. The primary advantage of the counter is that verification of a full tray of pins is possible without unloading or handling individual pins. The FBR fuel-pin tray counter is currently being used at a plutonium fuel fabrication facility.

FBR subassemblies contain large quantities of plutonium (5 to 16 kg), and the verification of this material is of high safeguards importance. Figure 17.12 is a photograph of the cylindrical coincidence counter used for the measurement of FBR fuel subassemblies. The unit consists of 12 ^{3}He tubes placed in a polyethylene annulus for

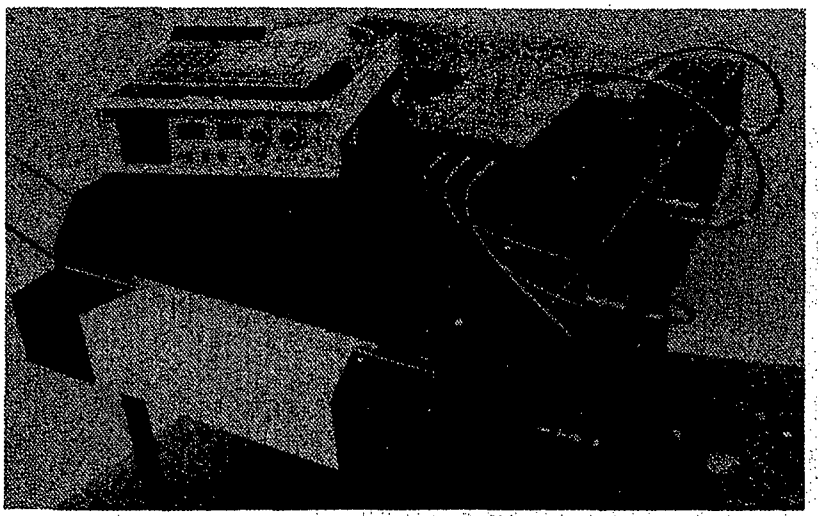

Fig. 17.11 *The fast-breeder-reactor (FBR) fuel-pin tray counter used for the verification of pin storage trays. The standard shift-register electronics package and preamplifier junction box are on top of the counter.*

neutron moderation. The active length of the detector is 1.21 m so that the entire plutonium region is contained inside the counter. The absolute efficiency of the counter is ~7%. The initial design of the counter gave a uniform response over the central 60-cm region, which is adequate for the smaller prototype FBR.

Several FBR reactors have plutonium-active regions as long as 92 cm and use subassemblies with plutonium mass loadings up to 15 kg. The 15-kg mass loading is about a factor of 3 higher than the mass that can be conveniently measured with the conventional electronics designed for the HLNCC. The need to measure entire FBR subassemblies with high mass loadings led to the development of the Universal FBR Counter (UFBR)(Ref. 11). This counter provided the first practical application of the new faster AMPTEK counting electronics (Ref. 7).

Figure 17.13 shows the UFBR detector system with the analog portion of the electronics system located at the top of the cylindrical detector. The detector is long enough to completely contain the active plutonium region of FBR subassemblies. To obtain a flat response over the 92-cm fuel length, each of the 12 ^{3}He tubes is surrounded by a layer of polyethylene and cadmium. The cadmium is removed near the ends of the detector to increase the efficiency at the ends and to compensate for the leakage of neutrons. Figure 17.14 shows the normalized totals and coincidence response as measured along the axis of the detector using a ^{252}Cf source.

In the UFBR counter, the ^{3}He tubes have an active length of 122 cm and a diameter of 2.54 cm and are filled with 4-atm gas pressure. The efficiency of the system is 7.2% and the neutron die-away time is 21.6 μs. These specifications result in a measurement precision of 0.5% (1σ) in a 1000-s counting time for typical FBR fuel subassemblies. Two

Fig. 17.12 Cylindrical coincidence counter for the verification of FBR fuel subassemblies.

of these systems are undergoing field test and evaluation for the future verification of FBR subassemblies. The initial testing and calibration of the system was performed using Fast Flux Test Facility subassemblies at the Washington Hanford Company in Richland, Washington.

17.2.6 Inventory Sample Coincidence Counter (ISCC)

Analysis of plutonium inventory samples by inspectors has been made increasingly difficult by transportation regulations. To reduce shipping requirements and to obtain more timely results, independent on-site verification capability is needed, particularly for reprocessing plants and plutonium facilities. This need has led to the development of the Inventory Sample Coincidence Counter (ISCC)(Ref. 12) for quantitative verification of the amount of plutonium in product inventory samples. The system is portable, and the samples can be assayed in the vials normally used to transfer samples to an analytical

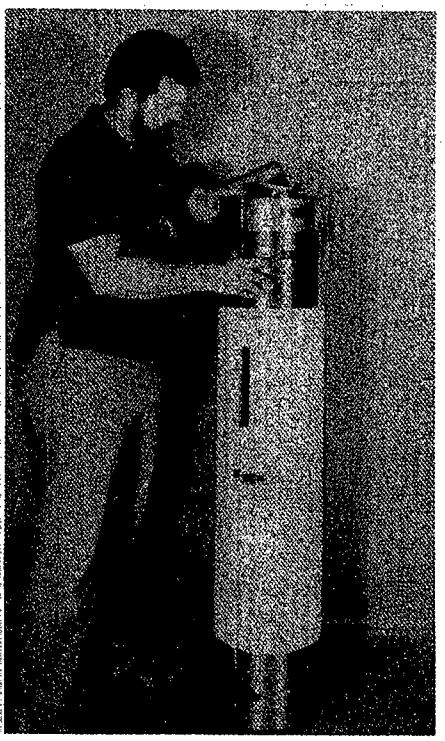

Fig. 17.13 *The Universal FBR (UFBR) Counter with the new AMPTEK electronics used for measuring FBR fuel subassemblies.*

laboratory. Pellets and powders can also be assayed. This unit uses the same electronics as the HLNCC, but it is much more efficient and is designed to operate in a much lower mass range (0.1 to 500 g Pu).

Figure 17.15 shows the ISCC detector body. The sample cavity accommodates samples that fit in the 5-cm-diam by 14-cm-tall cylindrical sample holder. The sample cavity enlarges to a diameter of 8.8 cm by removing the polyethylene cylinder. The high-density polyethylene moderator and the detector tube spacing were designed to make the system relatively insensitive to hydrogenous material in the sample matrix. The 35% efficiency of the ISCC is about three times larger than that of the HLNCC, and thus the required measurement time for small samples is about one-ninth that of the HLNCC.

Because the ISCC is physically limited to small samples, the neutron attenuation and multiplication effects are small and the calibration curves are very nearly a straight line given by the function $m = aR$, where m is the ^{240}Pu-effective mass, R is the coincidence rate, and a is the calibration constant. For solution samples such as plutonium nitrate, there is a slight amount of neutron-induced multiplication. This curvature is approximated by the power function $m = aR^b$, where b is close to unity.

The ISCC can assay individual mixed-oxide pellets or groups of several pellets. Figure 17.16 shows the counting precision (1σ) as a function of measurement time. A sample containing four typical mixed-oxide or fast-breeder-reactor fuel pellets gives a precision

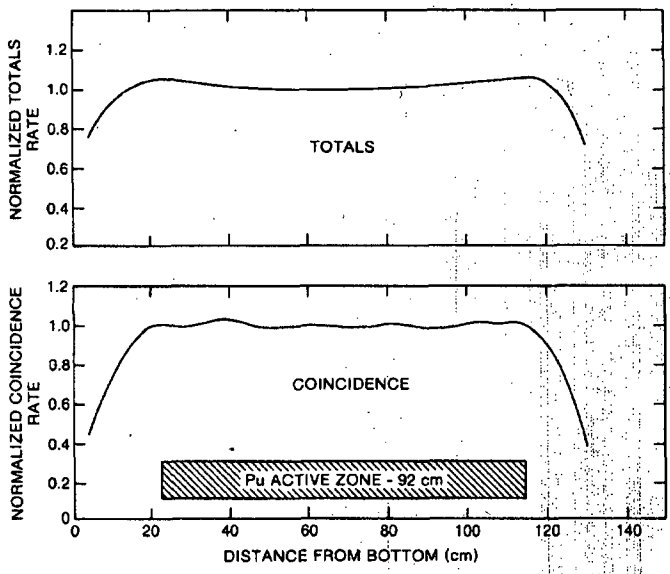

Fig. 17.14 Normalized totals and coincidence response along the axis of the UFBR counter.

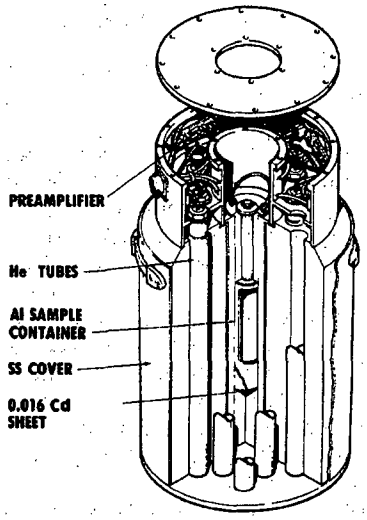

Fig. 17.15 Isometric drawing of the Inventory Sample Coincidence Counter (ISCC).

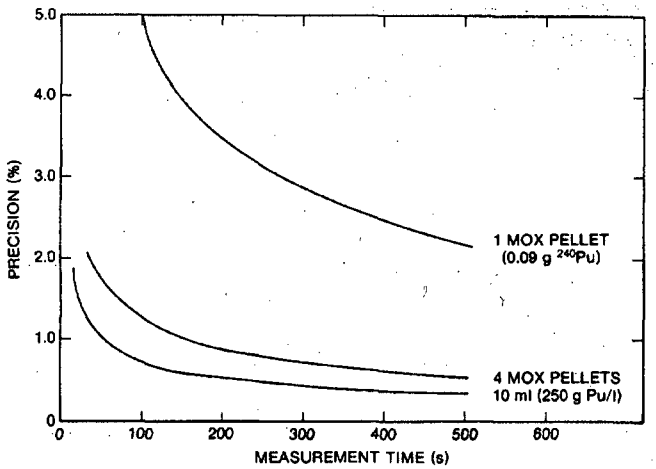

Fig. 17.16 *Assay precision as a function of measurement time for typical mixed-oxide samples in the ISCC.*

of ~1% in 200 s. A set of mixed-oxide fuel pellet standards was used to establish a calibration curve. Figure 17.17 shows the response function for the individual pellets. The percentage of plutonium in the pellets (Pu/PuO_2-UO_2) ranged from 1.4 to 21.6%. A straight line gave an excellent fit to the data. Because of the relatively small amount of material in the sample, the particular shapes or densities do not affect the measurement. Thus, samples of PuO_2 powder fall on the same calibration curve as pellets.

A set of plutonium nitrate solution standards was prepared for use in calibrating the ISCC. The solutions ranged in volume from 3 to 9 mL and the concentration varied from 150 to 350 g/L. The assay results did not depend on the volume over this range, but the solutions with larger plutonium masses gave a slightly larger (~5%) response per gram because of neutron multiplication.

Because the calibration curves are nearly linear, the requirements for physical standards are reduced. A ^{252}Cf calibration source can be used for in-field normalization of the electronics system to a previously measured calibration curve. Another approach is to establish a normalization standard at the nuclear facility. For example, two fuel pellets can be taken from the inventory and carefully measured in the ISCC. Then one pellet can undergo destructive chemical analysis and the other can be sealed and used as a long-term normalization standard. This procedure is essentially the same as that used for the ^{252}Cf source calibration, but the ^{252}Cf source calibration takes less time for the routine normalization measurement and the source can be more easily handled and transported because it contains only ~4 μCi of activity (about 10^6 times less than a plutonium standard).

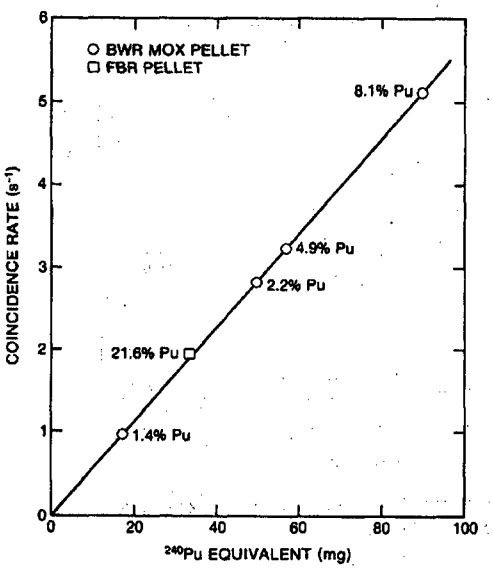

Fig. 17.17 Coincidence response of the ISCC for mixed-oxide fuel pellets (circles).

17.2.7 Counters for Bulk Plutonium Nitrate Solutions

In principle, the spontaneous fission of the even isotopes of plutonium can be detected as readily in solutions as in metals or oxides. The uniform density, distribution, and matrix material of the solution can in fact yield very precise and reproducible assays. In practice, however, neutron moderation and absorption within the solution can bias the assay. This section describes two neutron coincidence counters designed specifically for the assay of solution samples of 1 L or more in which such effects can be observed.

The Solution Neutron Coincidence Counter (SNCC)(Ref. 13) was developed for the assay of flowing solutions that are too bulky or contain too many fission products to assay conveniently by gamma-ray counting. Figure 17.18 illustrates the SNCC with its interior assay chamber of 1-L volume and its inlet and outlet tubes. Twenty-six ^{3}He tubes are tightly spaced in two rings around the chamber to achieve high counting efficiency. The 50-cm active-length tubes confine the sensitive detection volume to the bottle. Partial cadmium liners are used to obtain a nearly flat axial efficiency profile. Because the solution provides ~2.6 cm of moderator thickness, only 1.1 cm of additional polyethylene is used between the solution and the first ring of ^{3}He tubes to provide optimum response for plutonium solutions. With this thickness, the absolute efficiency is 33% and the die-away time is 38 μs. Including its 10-cm-thick polyethylene shield and 1-cm-thick steel shell, the SNCC is 48 cm in diameter by 82 cm long.

The SNCC was installed above an experimental glovebox in the Los Alamos Plutonium Processing Facility. Bottles of solution were transferred to the glovebox by the plant's conveyor system. The solution was then drawn up into the counter by

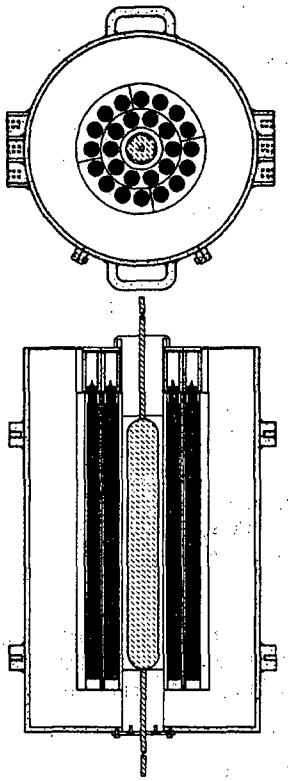

Fig. 17.18 *Top and side views of the Solution Neutron Coincidence Counter (SNCC) showing the 1-L-volume assay chamber and the inlet and outlet tubes.*

vacuum through doubly contained stainless steel tubing. The neutron counter can be assembled or disassembled without disturbing the solution transfer loop. Thus, for an actual in-plant installation, the SNCC can be assembled around an existing pipe without penetration of the plumbing.

Plutonium nitrate solutions ranging from 2 to 100 g/L of plutonium (0.2 to 12 g/L ^{240}Pu) were assayed in the SNCC. Each solution was assayed repeatedly to verify stability and reproducibility. The assay results were compared with chemical analysis of samples by coulometric titration or isotopic dilution mass spectrometry. The results plotted in Figure 17.19 show upward curvature due to self-multiplication in the solution. When corrected for this effect and fitted to a straight line, the nondestructive assay results show a 1.6% scatter relative to chemistry.

A Plutonium Nitrate Bottle Counter (PLBC)(Ref. 14) was designed for the assay of plutonium nitrate in large 10-cm-diam by 105-cm-high bottles. This detector is similar in size and shape to the FBR fuel subassembly counter shown in Figure 17.12. It is intended for use in reprocessing plants or nitrate-to-oxide conversion facilities where

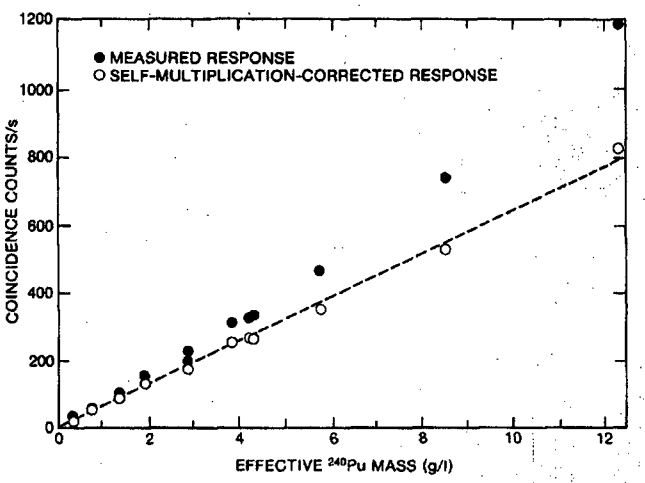

Fig. 17.19 Assay of plutonium nitrate solutions with the SNCC. Neutron coincidence counts per second are plotted as a function of ^{240}Pu concentration, with and without self-multiplication correction.

such large bottles are used. Initial assay results for three of these bottles are shown in Figure 17.20. The middle sample (at about 100 g/L) has more multiplication than the largest sample (about 200 g/L). Above 100 g/L the decrease in hydrogen concentration leads to a decrease in multiplication.

17.2.8 The Dual-Range Coincidence Counter (DRCC)

For many applications of neutron well coincidence counters, it is desirable to assay samples with masses in the range from less than one gram to a few kilograms of PuO_2. To achieve this wide-range capability, the Dual-Range Coincidence Counter (DRCC) (Ref. 15) was designed and fabricated. The dual-range capability is achieved by having two removable cadmium sleeves near the ^3He detectors. These sleeves can be inserted for low-efficiency operation with a short die-away time and removed for high-efficiency counting with a long die-away time.

The geometry of the counter is shown in Figure 17.21. The cadmium sleeves on both sides of the middle polyethylene cylinder (moderator) are removable. The detector consists of 20 ^3He tubes of 2.54-cm diameter filled to a pressure of 4 atm. The inner and outer polyethylene cylinders (moderators) are each 3.0 cm thick. The cadmium sleeve (1.0 mm thick) on the inside of the well stops low-energy neutrons from returning to the sample position, thereby reducing multiplication for high-mass loadings. The outer cadmium sleeve improves the effectiveness of the exterior 10-cm-thick polyethylene shield.

Thus, the counter has two modes of operation: (1) one for the low-mass range, with both removable cadmium sleeves removed for maximum efficiency, and (2) one for the

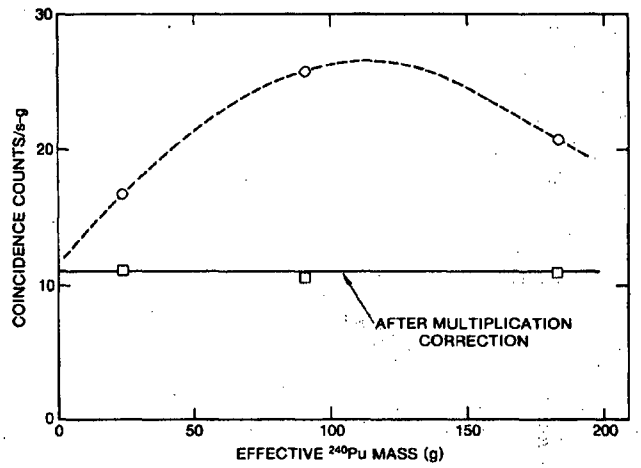

Fig. 17.20 *Assay of large plutonium nitrate cylinders with the Plutonium Nitrate Bottle Counter (PLBC). Coincidence response per gram is plotted as a function of ^{240}Pu mass, with and without self-multiplication correction.*

high-mass range, with all the cadmium sleeves in place to give a short die-away time and correspondingly short electronic gate width in the coincidence circuitry. For operational mode (1), the singles efficiency is 22% and the neutron die-away time is 52 μs. For operational mode (2), the efficiency decreases to 7% and the die-away time decreases to 16 μs.

An in-plant test and evaluation (Ref. 16) of the counter was performed at the Savannah River Plant Separations Area. A variety of incoming plutonium metal and oxide shipments were assayed with the counter. During the test period of 18 months, the dual-range counter operated with good reliability and stability. For large metal and oxide samples, assay precision based on counting statistics and reproducibility was better than 1% (1σ). Assay accuracy was 2% (1σ) for pure metal samples if a self-multiplication correction was used. Assay accuracy was 3% (1σ) for plutonium oxide if separate nonlinear calibration curves, without self-multiplication corrections, were used for each type of oxide. Assay accuracy was on the order of 10% (1σ) for impure metal samples. For a limited number of scrap samples the accuracy varied between 5 and 25% (1σ).

A dual-range counter manufactured by the National Nuclear Corp. is used by the Rockwell Hanford Facility, Richland, Washington, to rapidly verify plutonium-bearing items before shipment or after receipt (Ref. 17). Measurements on roughly 1000 items are reported in Ref. 17. The average scatter (per sample) between the book value and passive neutron assay (see Figure 17.22) is 4% (1σ) for plutonium metal. Other results are 5% (1σ) for plutonium oxide, 3% for polystyrene cubes with mixed plutonium and uranium, 27% for fuel-rod scrap, and 70% for miscellaneous scrap. Summing over each category yields a bias between book value and assay of about 1% for metal, oxide, and the polystyrene cubes, and 10% for the other scrap.

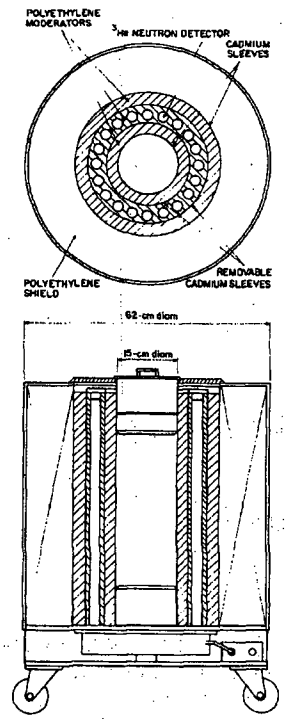

Fig. 17.21 Dual-Range Coincidence Counter (DRCC) for the assay of plutonium samples in the mass range 1 to 4000 g.

The above in-plant experience with the dual-range counter showed that neutron coincidence counting provided assay accuracies of 2 to 4% for well-characterized plutonium metal and oxide. For heterogeneous oxide and impure metal, coincidence counting did not have a clear-cut advantage over total neutron counting. This is because the self-multiplication correction was useful only for pure metal and very well characterized oxides where geometry effects were greater than (α,n)-induced multiplication effects. For other large, multiplying samples the total neutron response often provided a more accurate assay because it was less sensitive to multiplication. On the other hand, for scrap materials with low multiplication where it was necessary to discriminate against neutrons from strong (α,n) reactions or high room backgrounds, the coincidence response was more accurate. For a wide range of material categories, it is generally useful to measure both the coincidence and the total neutron response.

17.3 ACTIVE NEUTRON COINCIDENCE SYSTEMS

The passive HLNCC and the many specialized detector heads that evolved from it have been particularly useful for passive assay of plutonium. However, these instruments cannot be used for passive assay of most uranium samples because of the

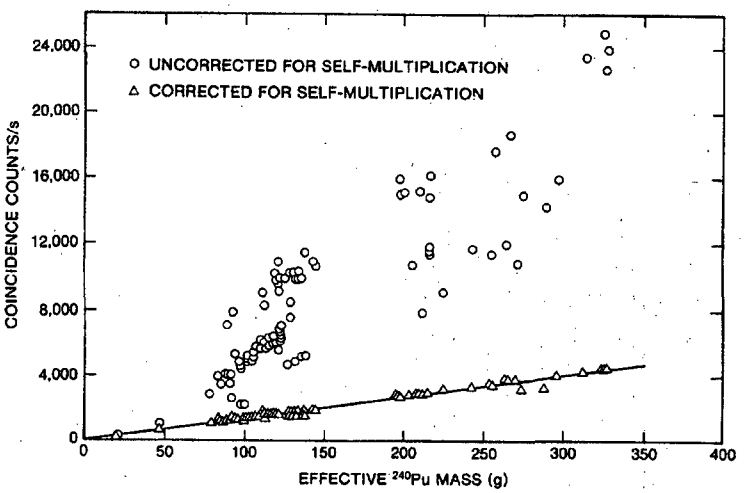

Fig. 17.22 *Assay of plutonium metal with a dual-range counter at the Rockwell Hanford Facility (Ref. 17). When corrected for self-multiplication, the assay data show a 4% (1σ) scatter relative to calorimetry and mass-spectrometry isotopics.*

extremely low spontaneous fission yields. For assay of uranium, active neutron coincidence counters have been developed that use the same electronics package, are equally portable or transportable, and use small AmLi random neutron sources for subthreshold interrogation of ^{235}U or ^{233}U. These active neutron coincidence counters can also be operated in the passive mode by removing the interrogation sources. They are described in this chapter because of their similarity to passive counters. They include

(1) the Active Well Coincidence Counter (AWCC),
(2) the Uranium Neutron Coincidence Collar (UNCC),
(3) the Passive Neutron Coincidence Collar (PNCC), and
(4) the Receipts Assay Monitor (RAM) for UF_6 cylinders.

17.3.1 The Active Well Coincidence Counter (AWCC)

Figure 17.23 illustrates the design of the AWCC (Ref. 18). The appearance is very similar to that of a passive coincidence counter except for the two small ($\sim 5 \times 10^4$ n/s) AmLi neutron sources mounted above and below the assay chamber. Two rings of ^3He tubes give high efficiency for counting coincidence events from induced fissions. The AmLi sources produce no coincident neutrons but do cause many accidental coincidences that dominate the assay error (see Section 16.7.2). Thus the polyethylene moderator and cadmium sleeves are designed for most efficient counting of the induced fission neutrons but inefficient counting of the (α,n) neutrons from the AmLi interrogation source.

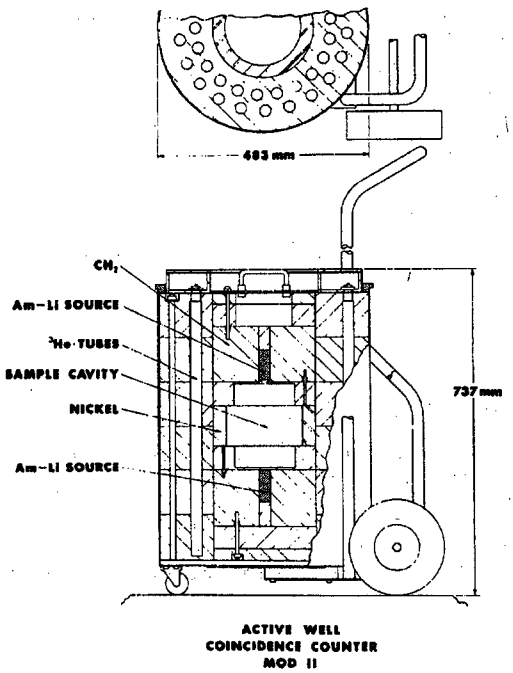

Fig. 17.23 Schematic diagram of the Active Well Coincidence Counter (AWCC) showing the ^{3}He detector locations, the neutron moderators, and the cadmium-lined sample cavity.

The nickel reflector on the interrogation cavity wall gives a more penetrating neutron irradiation and a slightly better statistical precision than would be obtained without it. With the nickel in place, the maximum sample diameter is 17 cm. For larger samples, the nickel can be removed to give a sample cavity diameter of 22 cm. The end plugs have polyethylene disks that serve as spacers; the disks can be removed to increase the sample chamber height. Removing the disks on the top and bottom plugs allows the cavity to accommodate a sample that is 35 cm tall.

A cadmium sleeve on the outside of the detector reduces the background rate from low-energy neutrons in the room. A cadmium sleeve in the detector well removes thermal neutrons from the interrogation flux and improves the shielding between the ^{3}He detectors and the AmLi source; with this cadmium sleeve in place the AWCC is said to be configured in the "fast mode." The neutron spectrum is relatively high energy, and the counter is suitable for assaying large quantities of ^{235}U. With the cadmium sleeve removed, the AWCC is in the "thermal mode." The neutron spectrum is relatively low energy and the sensitivity of the counter is greatly enhanced, but the penetrability of the interrogation neutrons is very low. In the thermal mode the counter is suitable for assaying small or low-enriched uranium samples.

Table 17-2 summarizes the performance characteristics of the AWCC for both the fast and thermal modes of operation. The absolute assay precision is nearly independent of

Table 17-2. Performance characteristics of the AWCC

Characteristic	Thermal Mode	Fast Mode
Detection efficiency		28%
Die-away time		50 μs
Range	0-100 g ^{235}U	100-20 000 g ^{235}U
Low-enrichment U_3O_8	11 counts/s-g ^{235}U	0.18 counts/s-g ^{235}U
High-enrichment metal	NA	0.08 counts/s-g ^{235}U
Absolute precision for large samples (1000 s)	0.3 g ^{235}U	18 g ^{235}U
Sensitivity limit[a] for small samples (1000 s)	1 g ^{235}U	24 g ^{235}U

[a]Defined as net coincidence signal equal to 3σ of background in 1000-s counting times.

the mass being assayed, (see Section 16.7.2). In general, the AWCC is best suited for high-mass, highly enriched uranium samples and should not be used for low-^{235}U-mass samples except for well-defined samples in the thermal mode. The AWCC can also be used for the passive assay of plutonium by removing the AmLi sources.

In comparison with the conventional fast Random Driver (Ref. 1), the AWCC is more portable, lightweight, stable, and less subject to gamma-ray backgrounds. This last feature makes it applicable to ^{233}U-Th fuel-cycle materials, which generally have very high gamma-ray backgrounds from the decay of ^{232}U. The Random Driver has the advantage that the neutron interrogation spectrum has a higher average energy and thus gives better penetration (Ref. 19). Also, the Random Driver has a 1000-times-shorter coincidence gate length, making it possible to use higher interrogation source strengths to improve sensitivities.

The AWCC has been evaluated for several measurement problems that are of interest to inspectors. These include (1) high-enriched-uranium (93% ^{235}U) metal buttons weighing approximately 1 to 4 kg, which are input materials to fabrication facilities; (2) cans of uranium-aluminum scrap generated during manufacture of fuel elements; (3) cans of uranium-oxide powder; (4) mixtures of uranium oxide and graphite; (5) uranium-aluminum ingots and fuel pins; and (6) materials-testing-reactor (MTR) fuel elements.

Typical calibration curves are shown in Figures 17.24 and 17.25 for cases (1), (3), and (4). All the calibration curves show the effects of neutron absorption within the uranium, and Figure 17.24 also shows the opposing effect of self-multiplication within the metal.

Recent field tests (Ref. 20) with MTR fuel elements have shown that it is possible to obtain ~1% accuracy in assay times of 400 s. The advantage of the AWCC over the traditional gamma-ray assay for MTR fuel elements is that the AWCC has no problems with different plate geometries and lower ^{235}U enrichments. For applications to MTR-type fuel elements and plates, the AWCC is reconfigured as shown in Figure 17.26 (Ref. 21). The two AmLi sources are positioned in the interior of the polyethylene insert that holds the MTR elements. Figure 17.27 shows the calibration curve for typical MTR fuel plates and elements.

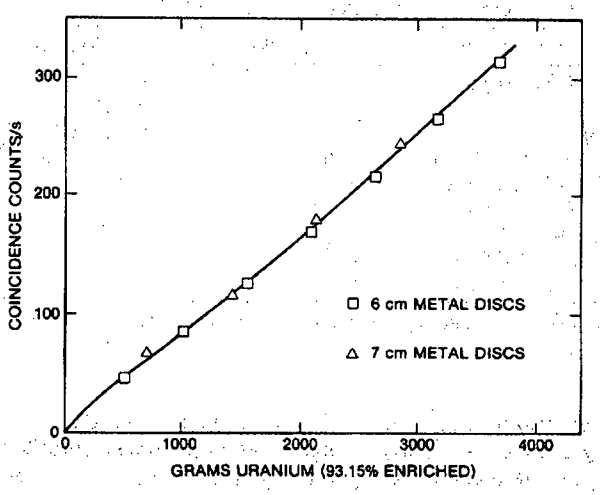

Fig. 17.24 AWCC response as a function of uranium mass for 6- and 7-cm metal discs stacked together to obtain the total masses shown (Ref. 19).

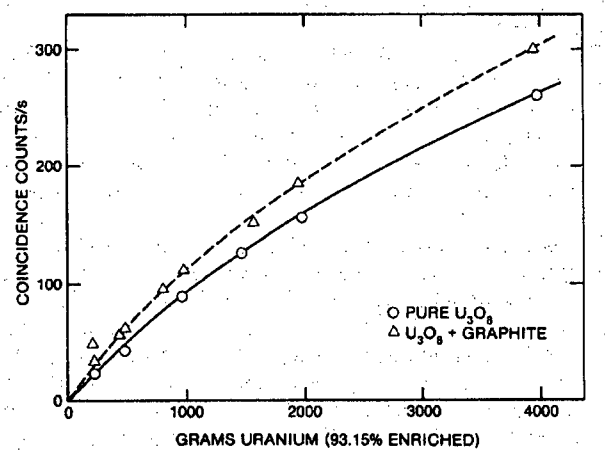

Fig 17.25 AWCC response as a function of uranium mass for highly enriched uranium oxide powder and mixtures of uranium oxide and graphite (Ref. 19).

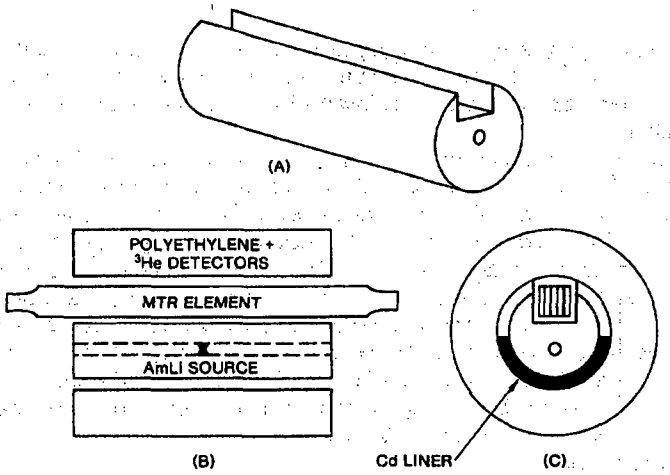

Fig. 17.26 *Horizontal configuration of the AWCC with a polyethylene insert used for the assay of materials-testing-reactor (MTR) fuel plates and elements.*

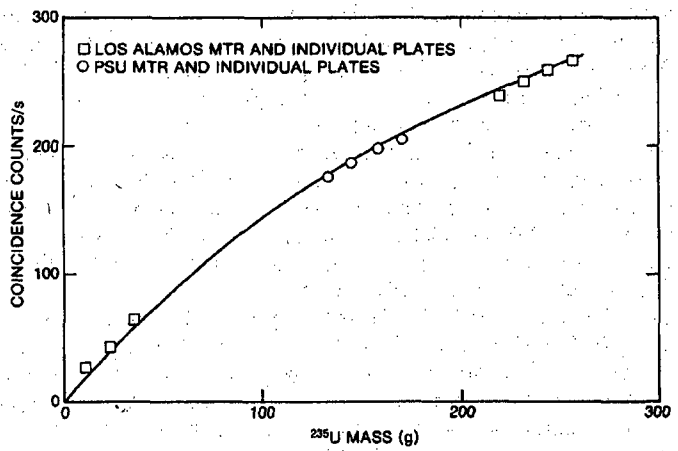

Fig. 17.27 *Calibration curve for MTR fuel plates and elements measured in the AWCC.*

17.3.2 The Uranium Neutron Coincidence Collar (UNCC)

For safeguards purposes, it is of high interest to measure full fuel assemblies because they constitute the output product from the plant and the input to the reactors. Enriched uranium is often transferred from one installation or country to another in the form of fuel assemblies.

An active neutron interrogation technique (Ref. 22) has been developed for measurement of the ^{235}U content in fresh fuel assemblies. The method employs an AmLi neutron source to induce fission reactions in the fuel assembly and coincidence counting of the resulting fission reaction neutrons. Coincidence counting eliminates the undesired neutron counts from the random AmLi interrogation source and room background. When no interrogation source is present, the passive neutron coincidence rate gives a measure of the ^{238}U through the spontaneous fission reactions. When the interrogation source is added, the increase in the coincidence rate gives a measure of ^{235}U. The Uranium Neutron Coincidence Collar (UNCC) system can be applied to the fissile content determination in boiling-water-reactor (BWR), pressurized-water-reactor (PWR), and other type fuel assemblies for accountability, criticality control, and safeguards purposes.

Active neutron systems using thermal neutron interrogation, such as the UNCC, have neutron self-shielding problems that limit the sensitivity in the interior of an assembly, but the present UNCC compensates for this limitation by fast-neutron multiplication, which is higher in the central region. The multiplication effect is enhanced by the coincidence counting because of the increase in the effective number of time-correlated neutrons emitted by the sample when multiplication occurs. In effect, the system works like a reactivity gage for the fuel assembly, and the removal of fissile material from the assembly lowers the neutron reactivity and thus the coincidence response.

The UNCC consists of three banks of ^{3}He tubes and an AmLi source embedded in a high-density polyethylene body with no cadmium liners. The 18 ^{3}He neutron detector tubes are 2.54 cm in diameter and 33 cm long (active length). The polyethylene body performs three basic functions in the system: (1) general mechanical support, (2) interrogation source neutron moderation, and (3) slowing down of induced fission neutrons prior to their detection in the ^{3}He tubes. For inspection applications, it is desirable to make the system portable. The weight of the detector system is $\sim$30 kg.

The complete assay system shown in Figure 17.28 consists of the detector body, the electronics unit, the HP-97 calculator, and a support cart. For applications, the cart is moved next to a fuel assembly. The back detector bank of the unit is hinged to aid in positioning the system around the fuel assembly.

Tests and evaluations of the UNCC have been performed at both PWR (Ref. 23) and BWR (Ref. 24) fuel fabrication facilities. Active-mode interrogation to measure ^{235}U content and passive-mode coincidence counting to determine ^{238}U content were both carried out. The UNCC measures the ^{235}U or ^{238}U content per unit length, which is proportional to the enrichment for a given type of assembly. The sample region is $\sim$400 mm long, centered in the midplane of the detector body.

A series of measurements were performed (Ref. 23) using full-size (17- by 17-rod) PWR assemblies with enrichments ranging from 1.8 to 3.4% ^{235}U. The thermal-neutron interrogation was saturated for all of the fuel assemblies; however, the measured response continued to increase as a function of enrichment because the fast-neutron

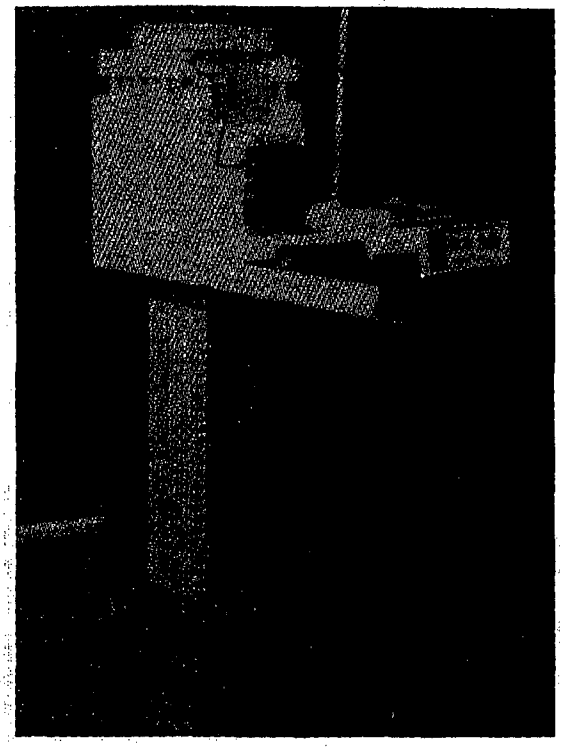

Fig. 17.28 *Uranium Neutron Coincidence Collar (UNCC) with the standard coincidence electronics package in position for the measurement of a mock PWR fuel assembly.*

multiplication increased with increasing enrichment. Similar measurements were performed for BWR fuel, and the calibration curve in Figure 17.29 corresponds to 8- by 8-rod BWR fuel assemblies.

In summary, the statistical precision for a 1000-s run varied from 0.6 to 0.9% (1σ), depending on the type of assembly. For longer counting periods, the ultimate precision was about 0.1% for repeat runs with a fixed geometry. The response curve was not saturated and continued to increase as the enrichment increased through the normal range of LWR fuel. Relative loading variations as small as 1.9% can be detected in a measurement time of 1000 s. Longer measurements can further reduce the statistical uncertainties. The UNCC has recently been put into routine use for inspection applications.

17.3.3 The Passive Neutron Coincidence Collar (PNCC)

The UNCC just described has been modified for verification of mixed-oxide fuel contained in FBR subassemblies or LWR assemblies (Ref. 25). Mixed-oxide fuel assemblies have a strong internal neutron source from the spontaneous fission of ^{240}Pu and from (α,n) reactions, so it is not necessary to use an external AmLi neutron source to

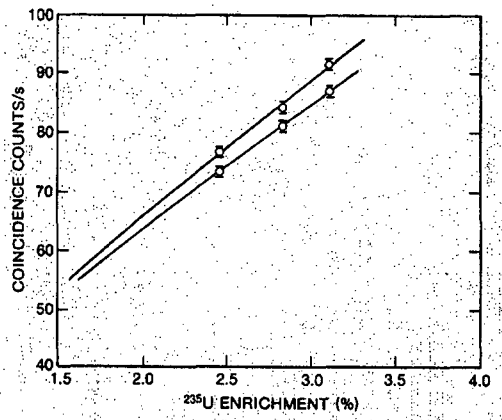

Fig. 17.29 Calibration curves for the UNCC applied to 8- by 8-rod BWR fuel assemblies with different gadolinium loadings.

induce fissions. The Passive Neutron Coincidence Collar (PNCC) (Figure 17.30) is similar to the UNCC except that the side containing the AmLi neutron source has been replaced by a fourth detector bank and removable cadmium liners have been placed between the detector and the fuel assembly. The PNCC has been designed with the same basic dimensions and specifications as the standard UNCC for interchangeability of parts.

In the passive mode, the neutrons originating from spontaneous fission reactions are measured using normal neutron coincidence counting to determine the ^{240}Pu-effective. In the active mode, the passive neutrons are reflected back into the assembly to induce fission reactions in the fissile component of the fuel. To determine the fraction of the neutrons resulting from the reflection process, the albedo of the boundary surrounding the assembly is changed by inserting and removing a cadmium liner.

Both the coincidence rate (R) and totals rate (T) are measured with and without the cadmium absorber. The normal passive-mode calibration curve corresponds to R vs ^{240}Pu-effective, and it is generally necessary to make corrections for the multiplication from the fissile component. Various techniques have been used to make this correction, and the present cadmium ratio determination gives a measure of the fissile component and multiplication.

The induced fission rate from the reflected neutrons is proportional to the quantity R (without cadmium) $-$ R (with cadmium) $=$ ΔR. However, ΔR is also proportional to the neutron source strength, which is different for each subassembly. To remove the source strength from the response function, one divides by T to obtain the quantity ΔR/T, which is related to the fissile content independent of the source strength.

Preliminary measurements with FBR subassemblies have been carried out at the Windscale Works in the United Kingdom (Ref. 26). Both the passive and active modes were evaluated. Figure 17.31 shows the results of the measurements; the lower curve corresponds to the normal ^{240}Pu-effective results with the cadmium liners in place and the upper curve shows the increase in response when the liners are removed. This increase is caused by the additional fissions from the self-interrogation of thermal

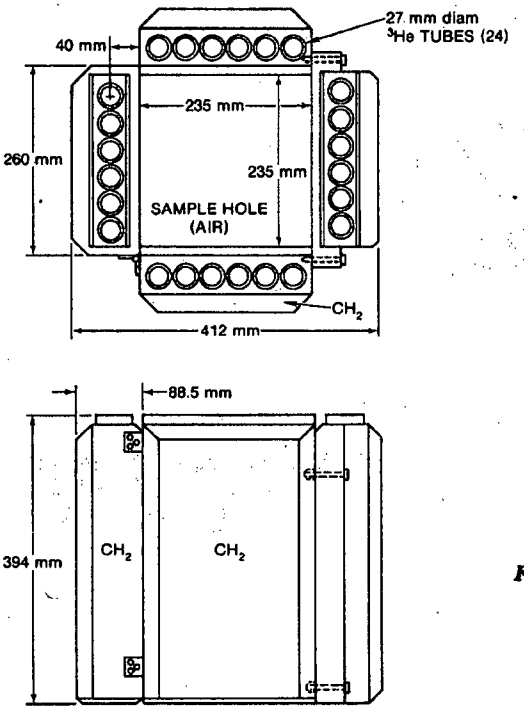

Fig. 17.30 *Schematic diagram of the Passive Neutron Coincidence Collar (PNCC) used for the passive/active assay of mixed-oxide fuel assemblies.*

neutrons. If there were no fissile material present, there would be no separation in the curves. The results of the tests gave a standard deviation of 0.75% for the passive measurement and 3 to 7% for the active measurement for a 1000-s counting time. The unit will be used in the future for verifying the plutonium content of fresh fuel assemblies.

17.3.4 Receipts Assay Monitor (RAM) for UF_6 Cylinders

In order to safeguard and account for the highly enriched uranium produced by enrichment plants, it is necessary to measure the ^{235}U content of UF_6 product storage cylinders. For enrichments above 20% ^{235}U, the UF_6 is stored in Model 5A cylinders that are nominally 127 mm in diameter and 914 mm tall. Current methods of measuring enrichment of this material include counting the 186-keV gamma-ray emissions from ^{235}U near the surface of the cylinder. A new neutron assay technique has been developed (Ref. 27) that directly samples the entire UF_6 volume of Model 5A storage cylinders to determine ^{235}U content. This passive technique, based on self-interrogation and coincidence counting, was identified after evaluating a variety of possible applications of the Neutron Coincidence Collar. The coincidence counter that was developed to implement this technique is the RAM illustrated in Figure 17.32.

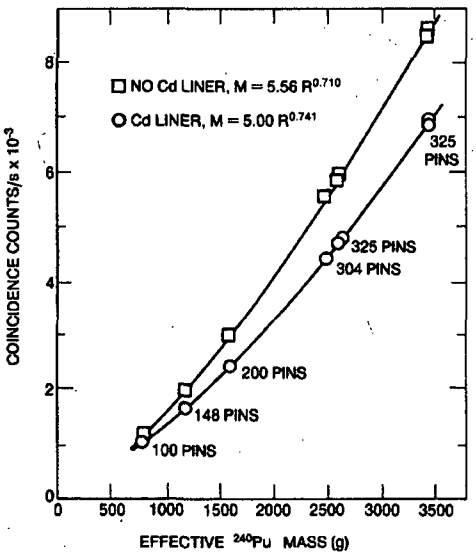

Fig. 17.31 Results of passive assay of FBR fuel subassemblies with different pin loadings using the PNCC.

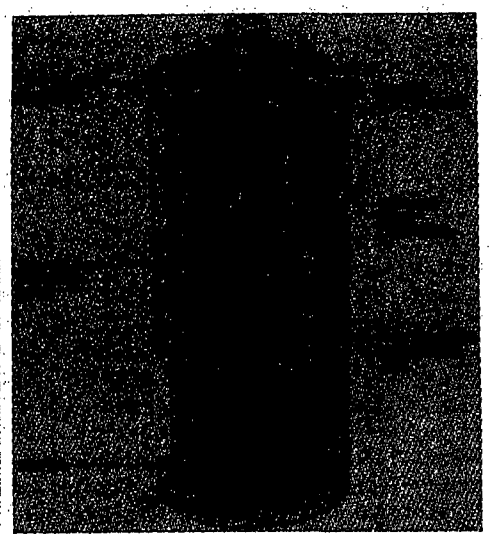

Fig. 17.32 Receipts Assay Monitor (RAM) used to verify the ^{235}U content of Model 5A UF_6 cylinders.

The RAM (Ref. 27) contains 20 ^{3}He tubes of 61-cm active length. Cadmium sleeves on the ^{3}He tubes are used to obtain a flat efficiency profile over the UF_6 fill height, which is typically 30 to 40 cm. Fast AMPTEK electronics are built into the top of the counter, and some shock absorbing materials are provided in this region to minimize possible impacts from UF_6 cylinders as they are lowered into the well. A unique feature of the RAM is the motor-driven cadmium liner, which can be operated manually or by an external microcomputer. A typical assay sequence consists of a 120-s measurement with the liner down and a 360-s measurement with the liner up, yielding a counting precision of about 0.5%.

In this new passive/active coincidence technique, passive neutrons from (α,n) reactions in the UF_6 are utilized to induce fission reactions (active) in the ^{235}U. Because the (α,n) neutrons are emitted randomly in time, the coincidence counting rate R gives a direct measure of the induced fission rate. The (α,n) "interrogation source strength" is measured by the totals counting rate T. The ratio R/T is proportional to M(M − 1), where M is the net leakage multiplication, and is independent of the (α,n) source strength. The quantity M(M − 1) is, in turn, closely related to ^{235}U content.

The primary source of (α,n) neutrons in enriched UF_6 is the alpha decay of ^{234}U reacting with fluorine atoms (see Table 11-3 in Chapter 11). In addition, ^{232}U can contribute a small fraction of the alpha particles. There is also a source of time-correlated neutrons from the spontaneous fission of ^{238}U. This rate is low (1.36×10^{-2} n/s-g ^{238}U) and is negligible for the higher enrichments because of the decrease in ^{238}U and the increase in ^{234}U. The magnitude of the ^{238}U spontaneous fission contribution is about 10% of the induced ^{235}U signal for an enrichment of 20% ^{235}U; it is less than 1% for enrichments greater than 50% ^{235}U (see Tables 14-3 and 14-4 of Chapter 14).

Figure 17.33 shows assay results for 38 Model 5A UF_6 cylinders measured by self-interrogation (Ref. 27). The coincidence-to-totals ratio R/T was corrected by a factor

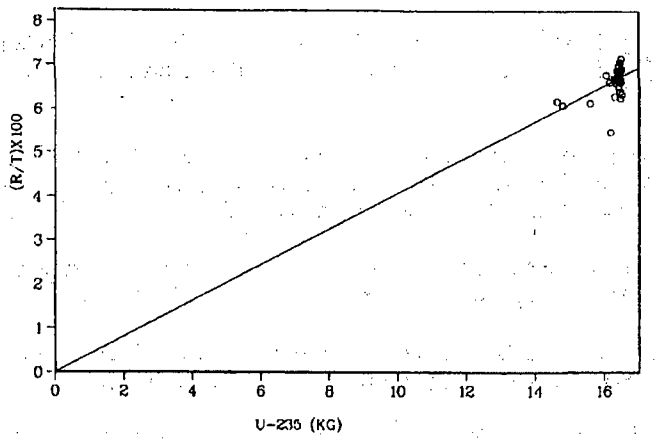

Fig. 17.33 *Assay results for 38 Model 5A UF_6 cylinders measured with the RAM. The passive, corrected R/T ratio is plotted as a function of ^{235}U content.*

based on the increase in the totals rate that occurs when the cadmium liner is removed. This correction factor helps compensate for variations in UF_6 density and self-multiplication from one cylinder to the next. The observed scatter about the fitted curve is about 10% (1σ) without the correction and 2.8% with the correction. This scatter is expected to decrease as the correction based on the movable cadmium liner becomes better understood. Data for many partially-filled cylinders is not shown in Figure 17.33, but the corrected R/T ratio is expected to provide a nearly linear calibration curve, and should be able to verify the ^{235}U content over a wide range of fill heights.

REFERENCES

1. J. E. Foley and L. R. Cowder, "Assay of the Uranium Content of Rover Scrap with the Random Source Interrogation System," Los Alamos Scientific Laboratory report LA-5692-MS (1974).

2. D. Langner, T. Canada, N. Ensslin, T. Atwell, H. Baxman, L. Cowder, L. Speir, T. Van Lyssel, and T. Sampson, "The CMB-8 Material Balance System," Los Alamos Scientific Laboratory report LA-8194-M (August 1980).

3. T. Gozani, *Active Nondestructive Assay of Nuclear Materials, Principles and Applications*, NUREG/CR-0602 and SAI-MLM-2585, (US Nuclear Regulatory Commission, Washington, DC, 1981).

4. J. E. Swansen, P. R. Collinsworth, and M. S. Krick, "Shift-Register Coincidence Electronics System for Thermal Neutron Counters," *Nuclear Instruments and Methods* 176, 555 (1980).

5. M. S. Krick and H. O. Menlove, "The High-Level Neutron Coincidence Counter (HLNCC): Users' Manual," Los Alamos Scientific Laboratory report LA-7779-M (1978).

6. J. E. Foley, "4π Neutron Counter for 55-Gallon Barrels," in "Nuclear Safeguards Research and Development Program Status Report, September—December 1970," Los Alamos Scientific Laboratory report LA-4605-MS (January 1971), pp. 24-26.

7. J. E. Swansen, "Dead-Time Reduction in Thermal Neutron Coincidence Counters," Los Alamos National Laboratory report LA-9936-MS (1984).

8. M. S. Krick and H. O. Menlove, "Channel Coincidence Counter: Version 1," Los Alamos Scientific Laboratory report LA-8404-MS (June 1980).

9. A. J. G. Ramalho, E. Dahn, E. G. Selleck, V. Kupryashkin, and A. Dubreuil, "The High-Level Neutron Coincidence Counter (HLNCC) Family of Detectors and Its Use," International Symposium on Recent Advances in Nuclear Materials Safe-

guards, Vienna, Austria, November 8-12, 1982, International Atomic Energy Agency report IAEA-SM-260.

10. L. Cowder and H. O. Menlove, "Neutron Coincidence Counter for MOX Fuel Pins in Storage Trays: Users' Manual," Los Alamos National Laboratory report LA-9493-M (August 1982).

11. G. W. Eccleston, H. O. Menlove, and O. R. Holbrooks, "Universal Fast Breeder Reactor (FBR) Coincidence Counter Design," in "Safeguards and Security Status Report, February—July 1982," J. Shipley and D. Smith, Comps., Los Alamos National Laboratory report LA-9595-PR (February 1983), pp. 29-31.

12. H. O. Menlove, O. R. Holbrooks, and A. Ramalho, "Inventory Sample Coincidence Counter Manual," Los Alamos National Laboratory report LA-9544-M (November 1982).

13. N. Ensslin, E. Adams, D. Bowersox, and J. Stewart, "Neutron Coincidence Counting of Plutonium Solutions," *Transactions of the American Nuclear Society* 39, 335-336 (1981).

14. H. O. Menlove, E. L. Adams, and O. R. Holbrooks, "Plutonium Nitrate Bottle Counter Manual," Los Alamos National Laboratory report LA-10009-M (1984).

15. N. Ensslin, M. L. Evans, H. O. Menlove, and J. E. Swansen, "Neutron Coincidence Counters for Plutonium Measurements," *Nuclear Materials Management* VII (2), 43-65 (1978).

16. N. Ensslin, A. Gibbs, C. Denard, and P. Deason, "Test and Evaluation of the Dual-Range Coincidence Counter at the Savannah River Plant," Los Alamos National Laboratory report LA-8803-MS (April 1981).

17. G. A. Westsik, "Rockwell Dual Range Coincidence Counter," Rockwell Hanford Operations report RHO-QA-SA-004 (1984).

18. H. O. Menlove, "Description and Operation Manual for the Active Well Coincidence Counter," Los Alamos Scientific Laboratory report LA-7823-M (1979).

19. H. O. Menlove, N. Ensslin, and T. E. Sampson, "Experimental Comparison of the Active Well Coincidence Counter with the Random Driver," Los Alamos Scientific Laboratory report LA-7882-MS (1979).

20. M. S. Krick and P. M. Rinard, "Field Tests and Evaluations of the IAEA Active Well Coincidence Counter," Los Alamos National Laboratory report LA-9608-MS (December 1982).

21. R. Sher, "Active Neutron Coincidence Counting for the Assay of MTR Fuel Elements," Los Alamos National Laboratory report LA-9665-MS (February 1983).

22. H. O. Menlove, "Description and Performance Characteristics for the Neutron Coincidence Collar for the Verification of Reactor Fuel Assemblies," Los Alamos National Laboratory report LA-8939-MS (August 1981).

23. C. Beets, "Optimization of NDA Measurements in Field Conditions for Safeguards Purposes," Centre D'Etude de L'Energie Nucleaire Third Progress Report BLG553—Contract RB/2274 (January 1982).

24. H. O. Menlove and A. Keddar, "Field Test and Evaluation of the IAEA Coincidence Collar for the Measurement of Unirradiated BWR Fuel Assemblies," Los Alamos National Laboratory report LA-9375-MS (December 1982).

25. H. O. Menlove, "Passive/Active Coincidence Collar for Total Plutonium Measurement of MOX Fuel Assemblies," Los Alamos National Laboratory report LA-9288-MS (May 1982).

26. H. O. Menlove and A. Keddar, "Field Test and Evaluation of the Passive Neutron Coincidence Collar for Prototype Fast Reactor Fuel Subassemblies," Los Alamos National Laboratory report LA-9449-MS (August 1982).

27. J. E. Stewart, N. Ensslin, H. O. Menlove, L. R. Cowder, and P. J. Polk, "Confirmatory Measurements of UF_6 Using the Neutron Self-Interrogation Method," Proc. Inst. Nucl. Matl. Manage. Conference, Albuquerque, New Mexico, July 1985, Los Alamos National Laboratory document LA-UR-85-2567.

18

Irradiated Fuel Measurements

J. R. Phillips

18.1 INTRODUCTION

There are over 100 nuclear power plants operating in the US with a total installed generating capacity of more than 85 GW (gigawatts, 1 GW = 10^9 W) (Ref. 1). These reactors discharge 5 000 to 10 000 irradiated fuel assemblies each year. Some of the assemblies are cooled for a year or two and then reinserted into the reactor to optimize the burnup of the residual fissile material; others, having reached their maximum design burnup, are placed in the storage pond at the reactor site until they are sent to a long-term storage facility or to a waste disposal site. These thousands of fuel assemblies are safeguarded by counting the individual assemblies and accepting the operator-declared values for the depletion of the initial fissile material (^{235}U or ^{239}Pu) and for the buildup of the fissile plutonium isotopes (^{239}Pu and ^{241}Pu). To augment this modest method of accountability, a variety of nondestructive measurement techniques have been developed for verifying the operator-declared values.

Before irradiation, power reactor fuels can be characterized using the gamma-ray and neutron measurement techniques discussed in Chapters 7, 8, 15, and 17. However, after a significant exposure of the fuel in the reactor, the uranium and plutonium signatures are completely masked by radiation from fission products, activated structural components, and transuranic elements that build up as a result of the fission process. Thus neither gamma-ray nor neutron measurements of irradiated fuel yield signatures for ^{235}U, ^{239}Pu, or ^{241}Pu. Instead, indirect signatures must be used to estimate these quantities. These indirect signatures are based on radiation from fission products or transuranic elements and are used to determine the burnup and cooling time of the irradiated fuel. From the burnup, the buildup of ^{239}Pu and ^{241}Pu in the fuel can then be estimated by calculational techniques.

It is also possible to use active neutron interrogation techniques to determine the amount of fissile material present in irradiated fuel assemblies. These measurement techniques require the use of a highly active neutron source (for example, ^{252}Cf) or an accelerator and generally require fixed, in-plant equipment.

This chapter describes the physical characteristics of reactor fuel (Section 18.2), indirect signatures for burnup (Section 18.3), and gamma-ray and neutron measurements of irradiated fuel (Sections 18.4 and 18.5). Section 18.6 summarizes passive and active methods for estimating the plutonium content of irradiated fuel.

18.2 CHARACTERISTICS OF REACTOR FUEL

18.2.1 Physical Description

With the exception of one high-temperature gas-cooled reactor (Fort St. Vrain), all power reactors presently operating in the US are either pressurized water reactors (PWRs) or boiling water reactors (BWRs). Research is under way on fast breeder reactors (FBRs). The fuel and core parameters of PWRs, BWRs, and FBRs are compared in Table 18-1 (Refs. 2 and 3). Figure 18.1 illustrates the differences in fuel pin and assembly sizes.

Reactor fuel initially consists of fissionable material (^{235}U or ^{239}Pu) plus fertile material (^{238}U). These materials are usually present in ceramic oxide or carbide forms because of their improved corrosion characteristics, relative ease of fabrication, and better radiation-damage characteristics. In PWRs or BWRs the fuel is in the form of UO_2 ceramic pellets that are about 1 cm in diameter and 2 cm in length. The pellets are stacked in a stainless steel or Zircaloy tubing to an active length of 3.7 m. Zircaloy is a zirconium alloy used in most PWR and BWR fuels because of its low neutron absorption cross section. The fuel is contained in a cladding material to protect it from chemical reaction with air, water, or other material used as coolant.

Table 18-1. Fuel and core parameters for reactors

	PWR	BWR	FBR
Fuel Parameters			
Cladding material	Zircaloy-4	Zircaloy-2	SS 316
Cladding diameter	0.95 cm	1.23 cm	0.74 cm
Cladding thickness	0.06 cm	0.08 cm	0.03 cm
Fuel material	UO_2	UO_2	$(U,Pu)O_2$
^{235}U initial enrichment	2.1/2.6/3.1%	2.8% average	25% Pu
Pellet diameter	0.82 cm	1.04 cm	0.67 cm
Pellet height	1.5 cm	1.04 cm	0.7 cm
Assembly array	15 × 15 or 17 × 17	8 × 8	hexagonal (17/side)
Fuel pins/assembly	201 or 264	63	217
Core Parameters			
Number of fuel assemblies	193	740	394
Total amount of fuel	98 000 kg	150 000 kg	25 000 kg
Core diameter	340 cm	366 cm	222 cm
Core active length	366 cm	376 cm	91 cm
Plant efficiency	33%	34%	39%
Design fuel burnup	33 GWd/tU	28 GWd/tU	100 GWd/tU
Refueling cycle	1/3 fuel/yr	1/4 fuel/yr	1/3 fuel/yr

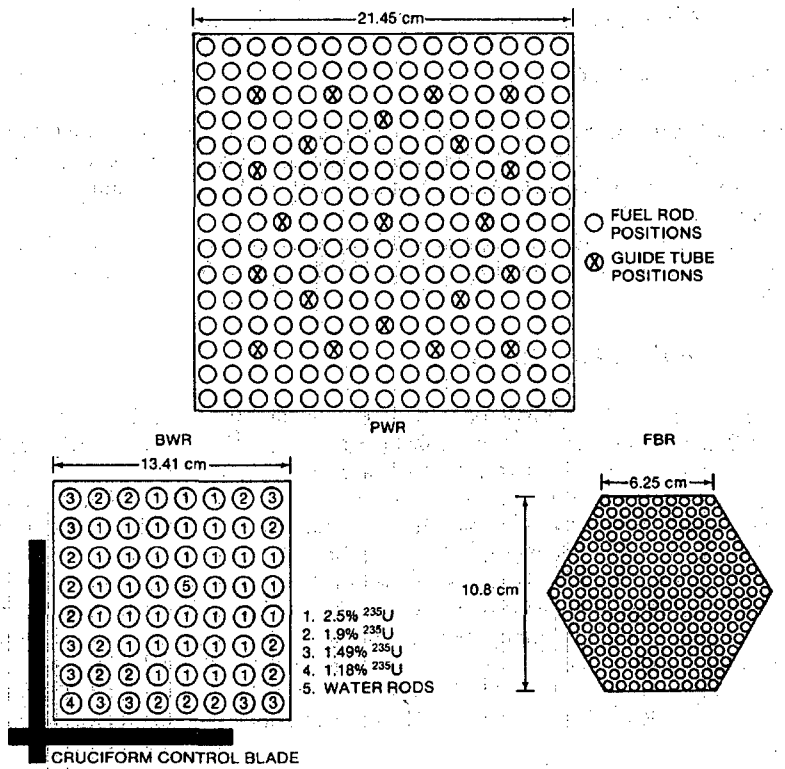

Fig. 18.1 *Cross-sectional views of PWR (top), BWR (bottom left), and FBR (bottom right) fuel assemblies.*

When irradiated fuel rods are chopped and leached during reprocessing, baskets of leached hulls are generated. The remaining fissile material in the leached hulls constitutes a kind of irradiated fuel. Measurement of this material is important for good process accountability (Ref. 4).

18.2.2 Definition of Burnup and Exposure

Two common terms for fuel irradiation, burnup and exposure, are often used interchangeably. Burnup (in atom percent) is defined as the number of fissions per 100 heavy nuclei (uranium or plutonium) initially present in the fuel. Exposure is defined as the integrated energy released by fission of the heavy nuclides initially present in the fuel. Exposure has dimensions of megawatt or gigawatt days (thermal output of the reactor) per metric ton (1000 kg) of initial uranium: MWd/tU or GWd/tU. For nondestructive measurements of irradiated fuel, the latter definition is more useful because the actual content of heavy nuclides is not directly determined.

The two definitions are approximately related by the following equation:

$$1 \text{ at \% burnup} \approx 9.6 \text{ GWd/tU} \tag{18-1}$$

The relationship between burnup and exposure changes as a function of burnup because of the changing ratio of uranium to plutonium fissions. The amount of energy released by the fission of plutonium (212 MeV) is about 5% more than the amount released by ^{235}U (202 MeV).

Table 18-1 includes average design values for reactor fuel burnup. Actual values can range up to 55 to 60 GWd/tU for PWRs, 45 to 50 GWd/tU for BWRs, and 150 GWd/tU for FBRs.

18.2.3 Fission Product Yields

In fission reactions the primary sources of energy are the fissioning of ^{235}U, ^{239}Pu, and ^{241}Pu, with some contribution from the fast fissioning of ^{238}U. Table 18-2 (Ref. 5) lists the relative number of fissions for each of these four isotopes as a function of fuel exposure for one typical case. The table shows that the plutonium isotopes begin to contribute a significant part of the total after only a few GWd/tU exposure, and above 20 GWd/tU exposure they become the dominant source of fissions.

Each fission results in the formation of two medium-mass fission products. Figure 18.2 (Refs. 6 and 7) shows the mass yield curves for the thermal neutron fission of ^{235}U and ^{239}Pu. The primary difference between the two curves is the slight shift to higher atomic mass number of the ^{239}Pu curve with respect to the ^{235}U curve. The shift can be seen in the relative fission yields of ^{106}Ru from ^{235}U and ^{239}Pu. Fissions in ^{239}Pu yield 11 times as much ^{106}Ru as fissions in ^{235}U. Thus a measurement of the gamma-ray output

Table 18-2. Percentage of total fissions as a function of fuel exposure for PWR fuel with an initial enrichment of 2.56% ^{235}U

Fuel Exposure (GWd/tU)	^{235}U	^{238}U	^{239}Pu	^{241}Pu
0	100.0	0.0	0.0	0.0
1.2	88.1	6.7	5.1	0.01
4.7	76.3	6.9	16.4	0.35
9.9	60.6	7.4	29.6	2.4
15.1	49.5	7.8	37.5	5.3
20.0	41.1	8.1	42.8	8.0
25.6	32.9	8.5	47.3	11.3
29.6	27.6	8.8	40.9	13.7
34.7	23.8	9.9	58.2	18.1
40.0	16.7	9.3	55.3	18.7
46.8	11.7	9.6	57.5	21.2

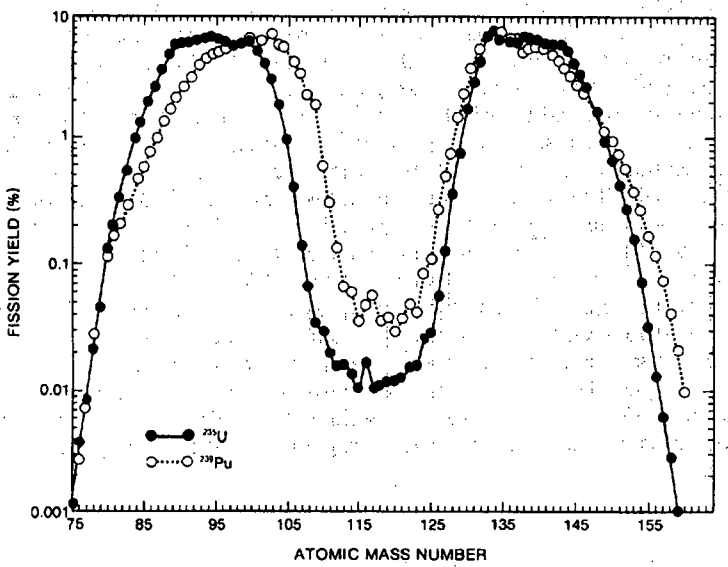

Fig. 18.2 *Mass distribution of fission products for the thermal fission of ^{235}U and ^{239}Pu (Refs. 6 and 7).*

of ^{106}Ru can determine the relative proportion of ^{239}Pu fissions to total fissions. On the other hand, an isotope like ^{137}Cs has nearly identical fission yields from both ^{235}U and ^{239}Pu. The ^{137}Cs gamma-ray output can be used to determine the total number of fissions.

Most of the fission products are initially rich in neutrons and undergo beta decay to approach stability. In addition to emitting beta particles, the fission products also emit gamma rays, which result in measurable signatures. Figure 18.3 shows the gamma-ray spectrum of a PWR fuel assembly having an integral exposure of 32 GWd/tU and a cooling time of 9 months (time since discharge from the reactor). As can be seen from this spectrum, there are only about 10 isotopes that can be measured. Table 18-3 (Ref. 8) lists the most dominant isotopes, along with their gamma rays and half-lives. The fission yields are the number of nuclei of each isotope (in percent) produced on the average per thermal neutron fission in ^{235}U or ^{239}Pu. In addition to the fission product gamma rays, gamma rays from the activation of fuel cladding and structural materials such as ^{54}Mn, ^{58}Co, and ^{60}Co are also present; they are included in Table 18-3.

Uranium present in a neutron flux can also capture neutrons and build up transuranic nuclides as illustrated in Figure 18.4 (Ref. 5). Many of these nuclides produce neutrons through spontaneous fission or (α,n) reactions; the spontaneous fission and (α,n) neutron production rates for the primary neutron sources—^{238}Pu, ^{240}Pu, ^{242}Pu, ^{241}Am, ^{242}Cm, and ^{244}Cm—are included in Tables 11-1 and 11-3 in Chapter 11.

The gamma rays from fission products and the neutrons from transuranic nuclides completely mask the gamma rays and neutrons from the uranium and plutonium isotopes in the fuel. This effect is shown in Table 18-4, which lists the relative atom densities and gamma-ray output per gram of initial uranium for ^{137}Cs, the 186-keV signature of ^{235}U, and the 414-keV signature of ^{239}Pu. These results are based on the actual irradiation history of a PWR fuel assembly. The fuel had an initial ^{235}U enrichment of 2.6% and was irradiated for four reactor cycles to a maximum exposure of 46.8 GWd/tU. The fission-product and transuranic-nuclide densities were calculated using a reactor fuel depletion code (Refs. 6 and 7). Even though the atom densities for ^{137}Cs, ^{235}U, and ^{239}Pu are comparable at the 46.8 GWd/tU exposure level, the number of ^{137}Cs gamma rays being emitted is 4.5×10^7 and 2.7×10^7 times the number of principal ^{235}U and ^{239}Pu gamma rays, respectively. The ^{137}Cs isotope is just 1 of about 10 dominant gamma-emitting fission products.

Similar results are obtained when one examines the neutron output of irradiated fuel materials. Table 18-5 (Ref. 4) lists the neutron output of uranium oxide fuel after an exposure of 33.0 GWd/tU and a cooling time of 1 yr. The passive neutron yield of the plutonium is dominated by 2 orders of magnitude by the neutron yield of the curium isotopes.

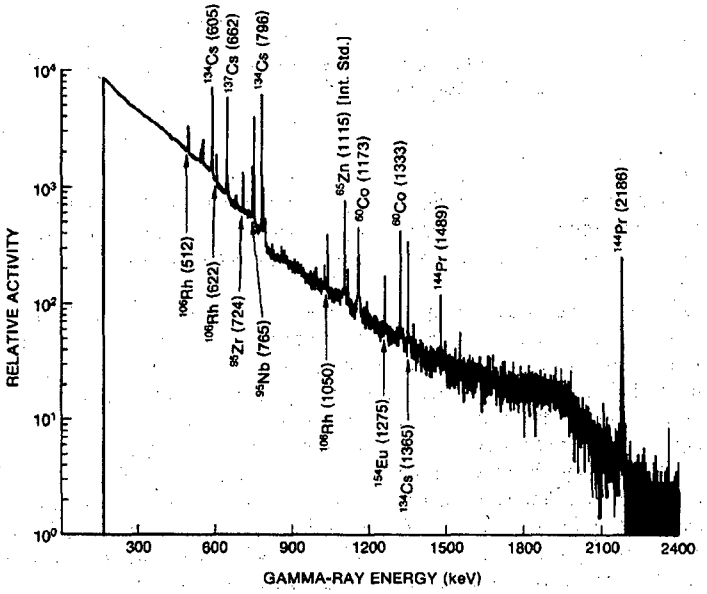

Fig. 18.3 Gamma-ray spectrum of a PWR fuel assembly with an exposure of 32 GWd/tU and a cooling time of 9 months.

Table 18-3. Isotopes measurable by gamma rays in a typical irradiated fuel assembly (Ref. 8)

Fission Product Isotopes	Half-Life	Fission Yield in ^{235}U (%)	Fission Yield in ^{239}Pu (%)	Gamma-Ray Energy (keV)	Branching Ratio (%)
^{95}Zr	64.0 days	6.50	4.89	724.2	43.1
				756.7	54.6
^{95}Nb	35.0 days	6.50	4.89	765.8	99.8
^{103}Ru	39.4 days	3.04	6.95	497.1	86.4
				610.3	5.4
^{106}Ru-Rh	366.4 days	0.40	4.28	622.2	9.8
				1050.5	1.6
^{134}Cs	2.06 yr	1.27×10^{-5} [a]	9.89×10^{-4} [a]	604.7	97.6
				795.8	85.4
				801.8	8.7
				1167.9	1.8
				1365.1	3.0
^{137}Cs	30.17 yr	6.22	6.69	661.6	85.1
^{144}Ce-Pr	284.5 days	5.48	3.74	696.5	1.3
				1489.2	0.3
				2185.6	0.7
^{154}Eu	8.5 yr	2.69×10^{-6} [a]	9.22×10^{-5} [a]	996.3	10.3
				1004.8	17.4
				1274.4	35.5
Activation Products					
^{54}Mn	312.2 days			834.8	100.0
^{58}Co	70.3 days			811.1	99.0
^{60}Co	5.27 yr			1173.2	100.0
				1332.5	100.0

[a] Europium-154 and ^{134}Cs values are given only for direct production of the isotope from fission. Actually, each of these isotopes is produced primarily through neutron absorption. For PWR fuel material irradiated to 25 GWd/tU, the "accumulated fission yields" of ^{154}Eu and ^{134}Cs were calculated as 0.15% and 0.46%, respectively.

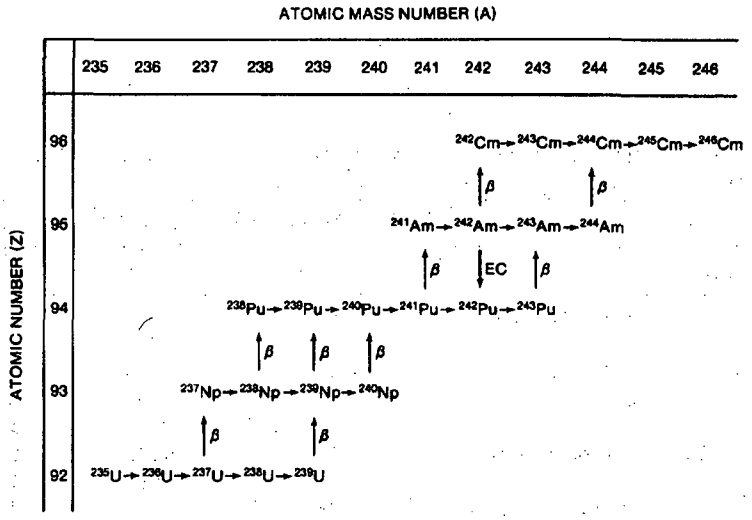

Fig. 18.4 Principal neutron capture reactions (horizontal arrows) and beta decay reactions (vertical arrows) leading to the formation of transuranic nuclides in irradiated fuel. Both stable and metastable states exist for ^{240}Np, ^{242}Am, and ^{244}Am.

Table 18-4. Comparison of atom density and gamma-ray activity of ^{137}Cs with ^{235}U and ^{239}Pu

Fuel	^{137}Cs		^{235}U		^{239}Pu	
Exposure (GWd/tU)	Atom Density[a]	661.6 keV (gammas/g U)	Atom Density[a]	185.72 keV (gammas/g U)	Atom Density[a]	413.69 keV (gammas/g U)
0	0.0	0.0	6.28 E+19	1.06 E+03	0.0	0.0
1.2	1.94 E+17	1.20 E+08	5.94 E+19	1.00 E+03	1.66 E+18	2.28 E+01
4.7	7.63 E+17	4.73 E+08	5.05 E+19	8.51 E+02	5.39 E+18	7.41 E+01
9.9	1.60 E+18	9.94 E+08	3.98 E+19	6.70 E+02	8.74 E+18	1.20 E+02
15.1	2.43 E+18	1.51 E+09	3.12 E+19	5.25 E+02	1.05 E+19	1.44 E+02
20.0	3.17 E+18	1.97 E+09	2.47 E+19	4.16 E+02	1.14 E+19	1.57 E+02
25.6	4.05 E+18	2.51 E+09	1.87 E+19	3.14 E+02	1.19 E+19	1.64 E+02
29.6	4.64 E+18	2.87 E+09	1.52 E+19	2.56 E+02	1.20 E+19	1.65 E+02
34.7	5.40 E+18	3.35 E+09	1.15 E+19	1.94 E+02	1.20 E+19	1.65 E+02
40.0	6.15 E+18	3.81 E+09	8.59 E+18	1.45 E+02	1.20 E+19	1.65 E+02
46.8	7.14 E+18	4.43 E+09	5.80 E+18	9.78 E+01	1.18 E+19	1.62 E+02

[a]Number of atoms per gram of initial heavy metal.

Table 18-5. Typical neutron production from oxide fuel

Nuclide	g/tU	n(SF)/s-tU	n(α,n)/s-tU
^{238}Pu	1.35×10^2	3.67×10^5	2.48×10^6
^{240}Pu	2.32×10^3	2.02×10^6	4.66×10^5
^{242}Pu	4.61×10^2	8.16×10^5	
^{241}Am	8.83×10^1		3.21×10^5
^{242}Cm	2.43	5.44×10^7	1.15×10^7
^{244}Cm	18.3	2.07×10^8	1.88×10^6
		2.65×10^8	1.66×10^7

18.3 INDIRECT SIGNATURES FOR FUEL BURNUP

As described in Section 18.2.3, passive neutron or gamma-ray assay of irradiated fuel cannot directly measure fissile element content or fuel burnup because of the high ambient radiation levels. This section describes a variety of indirect techniques for qualitative or quantitative determination of fuel burnup, most of which exploit these high ambient radiation levels.

18.3.1 Physical Attributes

Before determining burnup, an inspector can identify the irradiated fuel assemblies and verify their mass. The fuel assemblies are discrete units stamped with identification numbers. If the water in the storage pond is clear, the identification numbers can be read using a set of binoculars and a floating Plexiglas window to eliminate water ripples. If the water is not clear enough to permit this easy verification, an underwater periscope or TV camera (available at most reactor storage ponds) can be used. Information about the physical integrity of the fuel assembly can be obtained by using a load cell to verify the mass. Most storage ponds have a crane mechanism for moving the stored fuel assemblies, and a load cell can be mounted on the crane.

Visual inspection of a fuel assembly can usually indicate whether the assembly has been in the core. A fresh fuel assembly has a shiny surface, whereas the surface of an irradiated fuel assembly has undergone slight oxidation resulting in a dull reddish layer. Also, visible encrustation may build up on the irradiated fuel assembly, and the assembly may be slightly bent or twisted.

18.3.2 Cerenkov Radiation

The gamma rays from fission and activation products produce electrons that result in the emission of Cerenkov light. Thus, measurement of Cerenkov light can be used to indicate the presence of gamma-emitting material. This indirect signature has been used to verify spent-fuel assemblies stored underwater (Refs. 9 and 10).

Electromagnetic Cerenkov radiation is emitted whenever a charged particle passes through a medium with a velocity exceeding the phase velocity of light in that medium. In water, the phase velocity of light is about 75% of the value in vacuum. Thus, for example, any electron passing through water and having at least 0.26 MeV of kinetic energy will emit Cerenkov radiation. Irradiated fuel assemblies are a prolific source of beta particles, gamma rays, and neutrons. All three types of emissions can produce Cerenkov light, directly or indirectly.

The most significant production of Cerenkov light is from high-energy fission product gamma rays that interact with the fuel cladding or storage water. This interaction produces electrons and positrons by Compton scattering and other effects. Calculations of the number of Cerenkov photons generated from these beta particles indicate that Cerenkov light production in the visible wavelength range of 4000 to 6000 Å is negligible for gamma rays with energies below 0.5 MeV, but rises steeply with higher energy. A 2-MeV gamma ray produces 500 times more Cerenkov light than a 0.6-MeV gamma ray.

The absolute Cerenkov light level and its decay with time are related to burnup. Hiding a diversion either by substitution of dummy fuel assemblies or by incorrectly stating burnup would be difficult as long as the Cerenkov light intensity can be measured accurately.

18.3.3 Single Fission Product Gamma-Ray Activity

The buildup of specific fission products can be used as a quantitative measure of burnup. The absolute gamma-ray activity of a particular fission product can serve as a burnup monitor if the following conditions are met (Ref. 11):

(1) The fission product should have equal fission yields for the major uranium and plutonium fissioning nuclides. If the yields are substantially different, the effective fission yield will depend somewhat on the reactor's operating history.

(2) The neutron capture cross section of the fission product must be low enough so that the observed fission product concentration is due only to heavy element fission and not to secondary neutron capture reactions.

(3) The fission product half-life should be long compared to the fuel irradiation time, so that the quantity of fission product present is approximately proportional to the number of fissions.

(4) The fission product gamma rays must be relatively high energy (500 keV or more) to escape from the fuel pin. For a 1-cm-diam oxide fuel pin, 39% of the 662-keV ^{137}Cs activity is absorbed within the pin. This strong self-absorption implies that, in practice, passive gamma-ray measurements of fuel assemblies are limited to the outer rows. A further complication is that a nonuniform neutron flux during irradiation can lead to nonuniform burnup within the assembly. This is particularly true for BWR fuel assemblies because two sides of each assembly are adjacent to control blades.

If the above conditions are satisfied, the measured gamma-ray activity I(counts/s) from the fission product is proportional to the number N of fission product nuclei formed during irradiation:

$$I = \varepsilon k S N \lambda e^{-\lambda T} \tag{18-2}$$

where ε = absolute detector efficiency
k = branching ratio
S = attenuation correction
λ = fission product decay rate
T = cooling time.

After solving Equation 18-2 for N, the fuel burnup can be calculated from the equation

$$\text{at \% burnup} = 100 \times (N/Y)/U \tag{18-3}$$

where Y = effective fission product yield
U = number of initial uranium atoms.

Cesium-137 is the most widely accepted indicator of fuel burnup because its neutron absorption cross sections are negligible, its yields from both ^{235}U and ^{239}Pu are approximately the same, and its 30-yr half-life makes a correction for reactor power history unnecessary (Ref. 11). Figure 18.5 shows the calculated buildup of ^{137}Cs for the 46.8 GWd/tU exposure PWR fuel assembly described in Section 18.2.3. The ^{137}Cs buildup is approximately linear over the entire range of burnup. A comparison of measured ^{137}Cs activity with burnup is given in Section 18.4.3. Past experience with the ^{137}Cs burnup monitor shows that the absolute ^{137}Cs activity can determine burnup to an accuracy of 1 to 4% for individual fuel rods.

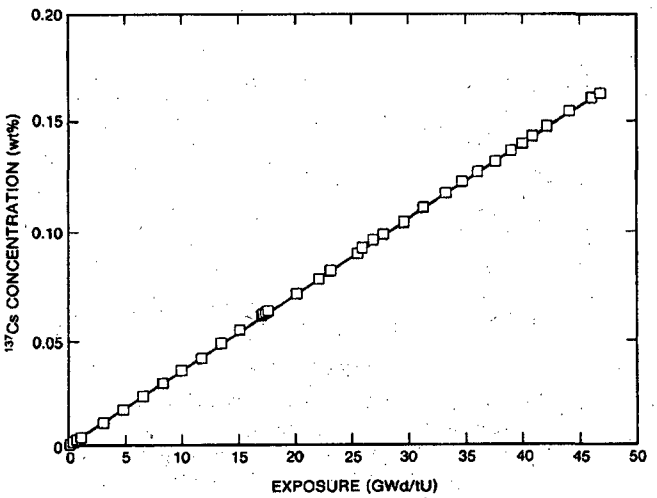

Fig. 18.5 *Calculated dependence of the ^{137}Cs fission product concentration, expressed as a percentage of the initial uranium concentration, on exposure for the 46.8 GWd/tU exposure PWR fuel assembly described in Section 18.2.3.*

For gamma-ray measurements of leached hulls, the 2186-keV line of ^{144}Ce-Pr is preferred to the 662-keV line of ^{137}Cs because of its greater penetrability and because ^{144}Ce-Pr is less susceptible to leaching during fuel dissolution.

18.3.4 Total Gamma-Ray Activity

The total gamma-ray activity of irradiated fuel is the sum of the activities from each fission product and transuranic element, with each activity given by an equation like Equation 18-2. Most of the gamma-ray activity comes from a few important fission products. The contribution of each of these fission products to the total activity varies with cooling time, as illustrated in the example given in Figure 18.6. For cooling times greater than 1 yr, the total gamma-ray activity is roughly proportional to burnup. For shorter cooling times, this relationship does not hold because the total gamma-ray activity is dominated by the buildup and decay of short-lived fission products like ^{95}Nb and ^{95}Zr. The concentrations of these isotopes depend, in part, on the reactor operating history and the proximity of reactor control materials. After longer cooling times, the short-lived isotopes have decayed and the detector response is dominated by long-lived isotopes that are less dependent on operating history and other factors.

A rapid way to determine the consistency of operator-declared values for burnup and cooling time has been developed using total gamma-ray activity (Refs. 12 and 13). The total activity is divided by the declared burnup and is plotted as a function of the declared cooling times. The result is a relationship of the form aT^b, where a and b are scaling parameters and T is the cooling time. An example of this relationship for PWR fuel assemblies is given in Figure 18.7. The shape of the curve is due primarily to the half-lives of ^{134}Cs and ^{137}Cs.

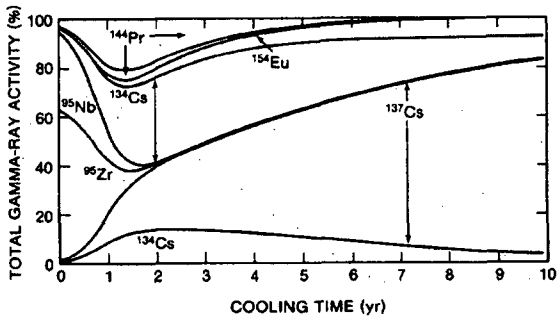

Fig. 18.6 *An example of the variation in fission product gamma-ray activity as a function of cooling time, with each major gamma ray given as a percentage of the total activity. Note that ^{144}Pr and ^{134}Cs each have two major gamma rays shown. The curves are based on measurements of a PWR fuel assembly with an exposure of 12.18 GWd/tU and a cooling time of 2 yr. The extrapolation to longer and shorter cooling times was done by calculation.*

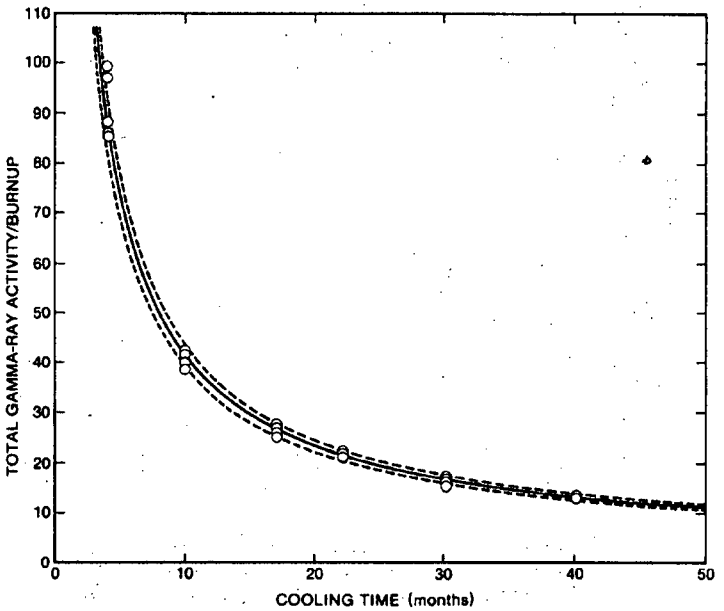

Fig. 18.7 *Measured total gamma-ray activity divided by burnup as a function of cooling time for PWR fuel assemblies. The fitted curve illustrates how the total gamma-ray activity can be used to verify the consistency of operator-declared values for burnup and cooling time.*

18.3.5 Fission Product Activity Ratios

The burnup of irradiated fuel can also be determined from the ratios of some fission product isotopes. The isotopic ratios can be determined from gamma-ray activity ratios using equations like Equation 18-2. The two most commonly used isotopic ratios are $^{134}Cs/^{137}Cs$ and $^{154}Eu/^{137}Cs$.

Cesium-134 is produced by neutron capture on the fission product ^{133}Cs; therefore, its production requires two neutron interactions. The first is the neutron that causes fission of the uranium or plutonium, and the second is the ^{133}Cs (n,γ) reaction. Because these interactions are the primary source of ^{134}Cs, the concentration of ^{134}Cs within the fuel is approximately proportional to the square of the integrated flux. By dividing the concentration of ^{134}Cs by the concentration of ^{137}Cs, which is directly proportional to the integrated flux, the ratio becomes approximately proportional to the burnup (total flux). This is a simplified explanation in that there are other factors such as the spectral dependence of the (n,γ) cross section that must be considered in a more rigorous derivation. However, in practice, the $^{134}Cs/^{137}Cs$ isotopic ratio has worked well for determining the burnup of both light-water-reactor and fast-breeder-reactor fuel materials (Refs. 14 and 15). The $^{154}Eu/^{137}Cs$ isotopic ratio also has a fairly linear dependence on exposure (Refs. 8 and 16).

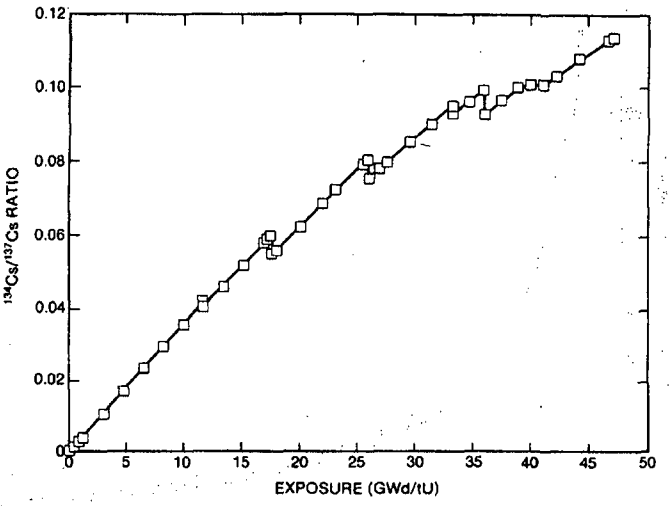

Fig. 18.8 *Calculated dependence of the $^{134}Cs/^{137}Cs$ isotopic ratio on exposure for the PWR fuel assembly described in Section 18.2.3. Discontinuities in the curve are due to discontinuities in the reactor operating history.*

Figure 18.8 shows the calculated $^{134}Cs/^{137}Cs$ isotopic ratio as a function of exposure for the 46.8 GWd/tU PWR fuel assembly described in Section 18.2.3. The discontinuities in the curve of Figure 18.8 are due to discontinuities in the reactor operating history, which emphasizes the fact that the use of isotopic ratios requires correcting for the decay of the isotopes. This correction is important for the $^{134}Cs/^{137}Cs$ ratio because of the 2.06-yr half-life of ^{134}Cs. For the $^{154}Eu/^{137}Cs$ isotopic ratio the 8.5-yr half-life of ^{154}Eu and the 30.2-yr half-life of ^{137}Cs make the correction less important. In general, calibration curves are computed to the time of discharge to eliminate the effects of the different decay rates of the fission products. Several techniques have been suggested to obtain cooling time corrections by examining certain isotopic ratios (Refs. 13 and 16 through 18).

For field measurements, fission product activity ratios are easier to determine than absolute activities because only relative detector efficiencies must be known. However, it is still necessary to correct for changes in detection efficiency with gamma-ray energy. The ^{134}Cs, ^{137}Cs, and ^{154}Eu gamma rays have different energies and therefore different detection efficiencies. A relative efficiency calibration can be performed using multiple gamma rays from ^{134}Cs and ^{154}Eu; the procedure is identical to that described in Section 8.4.1 of Chapter 8 for determining the relative efficiency curve for plutonium isotopic composition measurements. This allows one to obtain the relative detection efficiency of the corresponding gamma rays using only the original gamma-ray spectra.

18.3.6 Total Neutron Output

The total neutron output of irradiated fuel can also serve as an indicator of burnup, and has both advantages and disadvantages relative to the gamma-ray output. The neutron signal comes only from the fuel, not from the cladding materials. Attenuation of the neutron signal within the fuel assembly is less than attenuation of the gamma-ray signal; in fact, induced fissions within the assembly result in nearly equal response from both interior and exterior fuel pins. The neutron measurements can be made soon after the fuel is discharged from the reactor, while the gamma-ray signal is still dominated by the decay of short-lived isotopes that reflect recent reactor power levels. A disadvantage of the neutron signal is that the quantity of primary neutron emitting isotopes is only indirectly correlated to exposure. Also, in principle, neutron detectors are sensitive to gamma rays, although the fission chambers used for measurements today are almost completely insensitive to gamma rays.

The five principal neutron sources in a PWR fuel assembly with a typical exposure of 31.5 GWd/tU are plotted in Figure 18.9 as a function of cooling time. For other fuel assemblies or different burnup levels, ^{241}Am or ^{246}Cm may also be significant neutron sources. However, ^{244}Cm and ^{242}Cm are usually the two dominant neutron-emitting isotopes. Because of the short half-lives of these two isotopes (18.1 and 0.45 yr, respectively), the cooling time of the fuel must be known to interpret correctly the total neutron output. Operator-declared values for the cooling time can be verified by measuring the total gamma-ray activity, as described in Section 18.3.4.

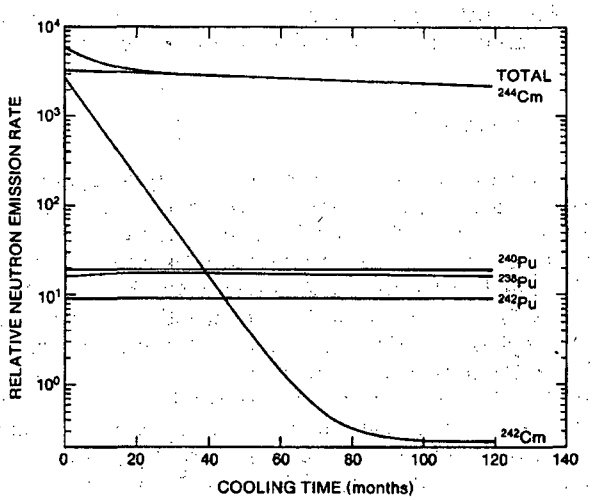

Fig. 18.9 *The five principal neutron sources in a PWR fuel assembly with an exposure of 31.5 GWd/tU. At long cooling times, the decay of ^{242}Cm follows the decay of its parent, ^{242m}Am, a metastable state of ^{242}Am with a half-life of 153 years.*

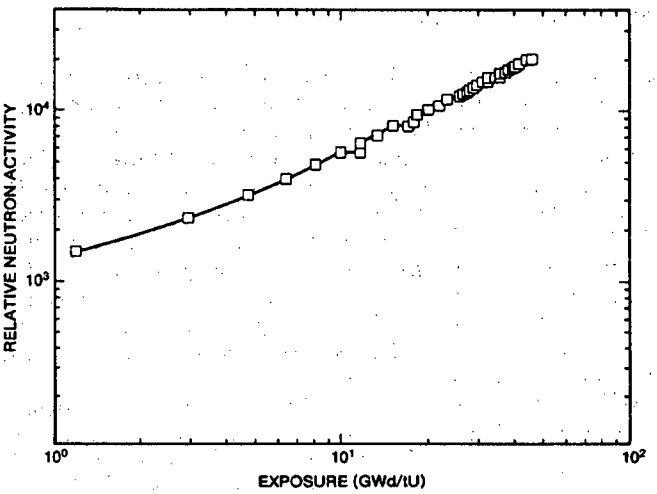

Fig. 18.10 Calculated dependence of total neutron output on exposure for the PWR fuel assembly described in Section 18.2.3.

Figure 18.10 shows the calculated relationship between the total neutron output and exposure for the PWR fuel assembly described in Section 18.2.3. Above 10 GWd/tU exposure, the relationship can be approximated by the following empirical power function:

$$\text{neutron rate} = \alpha\,(\text{exposure})^{\beta} \tag{18-4}$$

Equation 18-4 has been demonstrated for a wide variety of light-water-reactor fuels (Refs. 19 through 22), and makes it possible to determine burnup from the observed total neutron output. The value of β is usually between 3.0 and 4.0.

The rate of buildup of the principal neutron-emitting transuranic isotopes is relatively insensitive to the initial fuel density and power levels; however, the initial ^{235}U enrichment and the fuel irradiation history can significantly influence the rate of buildup. Figure 18.11 shows the effect that initial ^{235}U enrichment has on the neutron emission rate. [The effects of attenuation and multiplication have not been incorporated into these values.] For identical exposures the lower-enriched fuel has a higher neutron emission rate. Lower-enriched fuel has less fissile material per unit volume and therefore requires a higher neutron fluence to achieve the same burnup as a higher-enriched fuel. The higher neutron fluence results in more ^{242}Cm and ^{244}Cm buildup and a correspondingly higher neutron emission rate.

Noncontinuous irradiation histories can also have a significant effect upon the neutron emission rate as is evidenced by the curves presented in Figure 18.12. The effect of noncontinuous irradiation history is short-term, due primarily to the increased buildup of ^{242}Cm following any period of cooling time. During any nonirradiation

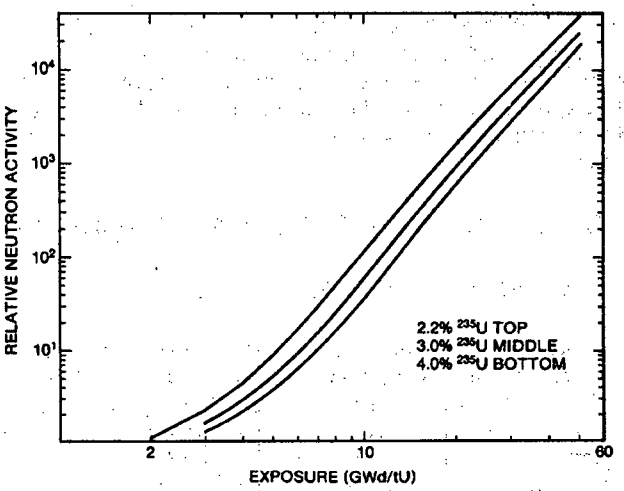

Fig. 18.11 *Calculated dependence of total neutron output on initial fuel enrichment for identical exposure values. The calculations are based on the PWR fuel assembly described in Section 18.2.3.*

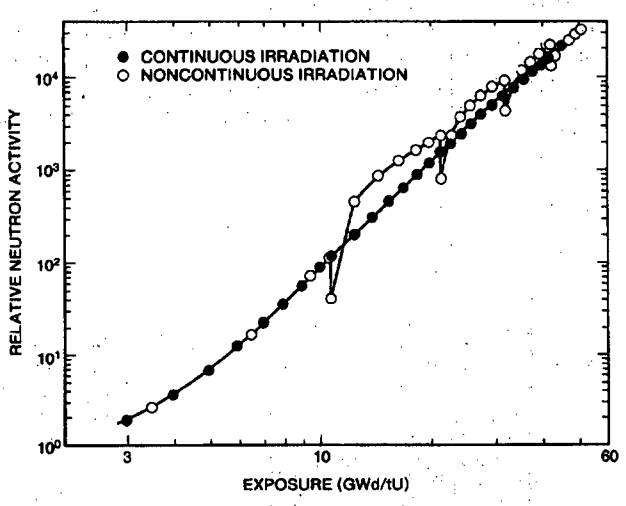

Fig. 18.12 *Calculated dependence of total neutron output on reactor operating history for the PWR fuel assembly described in Section 18.2.3. A continuous 5-yr irradiation history (closed circles) is compared with a discontinuous history of alternating years of operation and cooling (open circles).*

period, ^{241}Pu ($t_{1/2}$ = 14.35 yr) decays to form ^{241}Am ($t_{1/2}$ = 433.6 yr). When this material is reinserted into a high-neutron flux, large amounts of ^{242}Cm form through neutron capture in ^{241}Am. If the fuel were measured after a longer cooling time (~2 yr), most of the ^{242}Cm would have decayed, and the measured neutron emission rates would be more consistent with the rates obtained from fuel material that had undergone continuous irradiation.

18.4 GAMMA-RAY MEASUREMENT OF IRRADIATED FUEL

18.4.1 Total Gamma-Ray Activity Measurements

The total gamma-ray activity of submerged fuel assemblies can be measured with ion chambers, scintillators, or thermoluminescent dosimeters (TLDs). Ion chambers and scintillators provide a direct readout with only 1 to 2 min required for positioning the detectors and collecting the data. Thermoluminescent dosimeters must be removed from the water and read out with special instrumentation. Figure 18.13 illustrates a geometry used for gamma-ray measurements of irradiated fuel assemblies and shows an ion chamber placed adjacent to the top of a fuel assembly.

When the total gamma-ray activity is measured at the top of the fuel assembly, the response is due primarily to ^{60}Co, ^{58}Co, and ^{54}Mn activation products in the structural material. When the fuel assembly is raised above the storage rack, but still submerged, total gamma-ray-activity measurements can be made alongside the assembly. Then the response is due primarily to fission products in the fuel rods. Under these conditions, the consistency of operator-declared values for cooling time and burnup has been verified to an accuracy of about 10%. Fuel assemblies with unusual irradiation histories have been identified easily. An ion chamber designed to be placed against the side of a fuel assembly has been incorporated into the fork detector described in Section 18.5.

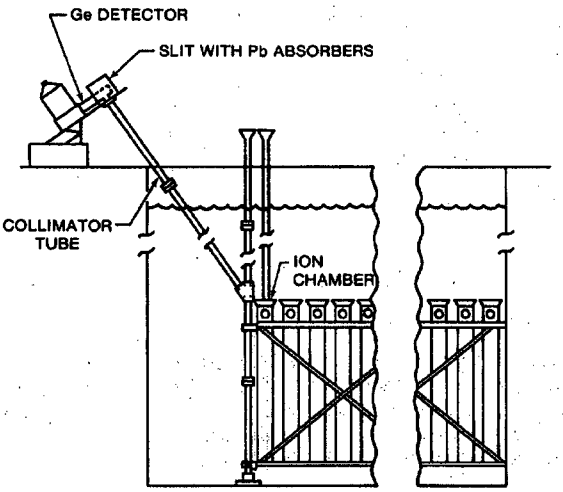

Fig. 18.13 Gamma-ray measurements of irradiated fuel in a storage pond. The figure shows a high-resolution germanium detector with its collimator tube and an ion chamber installed at the top of a storage rack. The fuel assembly is raised vertically for measurement.

18.4.2 High-Energy Gamma-Ray Activity Measurements

A more specific gamma-ray measurement can be made with a Be(γ,n) detector. Such a detector consists of a ^{235}U fission chamber surrounded by polyethylene, which is in turn surrounded by beryllium. Neutrons produced by a photoneutron reaction in the beryllium are thermalized in the polyethylene and detected by the fission chamber. Because the threshold for photoneutron production in beryllium is 1665 keV, the only significant fission product signature observed by this detector is the 2186-keV gamma ray from ^{144}Ce-Pr.

If the Be(γ,n) detector is placed alongside irradiated-fuel materials, it will measure relative ^{144}Ce-Pr fission product activity and will be insensitive to lower-energy activation products. Like other gamma-ray detectors, this detector is not useful at the top of an irradiated fuel assembly because the gamma rays are shielded by structural materials. Neutrons emitted by the fuel or produced by (n,2n) reactions in the beryllium can interfere with the photoneutron measurement if their numbers are significant.

18.4.3 High-Resolution Gamma-Ray Spectroscopy

More detailed information on fuel burnup can be obtained by high-resolution gamma-ray spectroscopy. The concentration of individual fission products can be determined by measuring single fission product gamma-ray activities; these isotopic concentrations can be related to fuel burnup (see Section 18.3.3). Also, some gamma-ray activity ratios can be used to calculate fission product isotopic ratios that can be related to burnup (see Section 18.3.5).

The objective of high-resolution measurements is to obtain gamma-ray spectra that accurately represent the fission- and activation-product inventory of the entire fuel assembly. The instrumentation required to perform these measurements is more complex than that required for total gamma-ray activity measurements or Cerenkov glow measurements. A germanium detector with a standard high-resolution amplifier and a multichannel analyzer is required to collect and analyze the spectra. Some type of magnetic storage medium is highly desirable for recording the data. The germanium detector views the submerged fuel assembly through a long, air-filled collimator (with a minimum length of 3 m for radiation shielding), as illustrated in Figure 18.13. Individual fuel assemblies must be moved to the scanning system by the facility operator for measurement.

The air-filled collimator defines the volume segment of the fuel assembly from which the gamma-ray spectrum is collected. Because of its length, the collimator reduces the dose rate at the detector to an acceptable level. The maximum dose rate obtained with a 5-cm-diam, 6-m-long collimator from 40-GWd/tU exposure fuel with a 2-yr cooling time is only about 10 mR/h. Usually the background radiation level is in approximately the same range. The germanium detector must be shielded from the background radiation; otherwise, the detector will not be sensitive to the gamma rays from the fuel assembly. Also, thin pieces of lead, copper, and cadmium may be placed in front of the detector to reduce the source intensity from the fuel assembly.

The self-attenuation of the fuel material can significantly influence the measured signals. For example, as discussed in Section 18.3.5, the isotopic ratio $^{154}Eu/^{137}Cs$ can be used to determine the burnup of fuel assemblies. Nearly 92% of the measured ^{137}Cs signature (661.6 keV) originates in the three outer rows of fuel pins in a PWR fuel assembly (Ref. 23). However, because only 78% of the ^{154}Eu signature (1275 keV) originates in these three outer rows, the ratio $^{154}Eu/^{137}Cs$ does not sample exactly the same volume segment of the fuel assembly.

The data analysis for high-resolution measurements is not difficult when only relative values are needed. The net areas for ^{137}Cs, ^{134}Cs, and ^{154}Eu can be obtained from the multichannel analyzer; the isotopic concentrations and isotopic ratios can be obtained using Equation 18-2. For isotopic ratios, the relative efficiency corrections can be obtained by using a relative efficiency calibration, as described in Section 18.3.5 (Refs. 24 through 26). This technique corrects for differences in the self-attenuation of the source materials, the detector efficiency, and the scanning geometry. Also, standard analysis techniques generally require correction for isotopic decay to the time of discharge from the reactor or some other specified time. The ^{137}Cs concentration and the $^{134}Cs/^{137}Cs$ and $^{154}Eu/^{137}Cs$ isotopic ratios can then be plotted for a set of fuel assemblies to obtain the relative burnups. If one destructive analysis of the fuel is available, absolute values for the burnups can be calculated.

Many reports (for example, Refs. 16 and 27) describe the use of gamma rays to characterize irradiated fuel materials. Two such applications are given in Figures 18.14 and 18.15, which compare the ^{137}Cs activity and the $^{134}Cs/^{137}Cs$ isotopic ratio with burnup for 14 PWR fuel assemblies with exposures of 16 to 33 GWd/tU. Each data set was analyzed using regression analysis to obtain the linear relationship. The other two lines on each plot represent the 95% confidence limits that a subsequent measurement would fall within these limits. The average differences between the regression line and the measured data points were 4.9% for ^{137}Cs and 4.6% for $^{134}Cs/^{137}Cs$. Similar numbers in the range of 4 to 8% can be obtained under most measurement conditions.

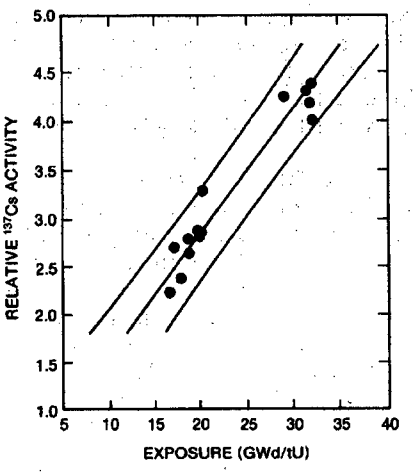

Fig. 18.14 Correlation of the measured ^{137}Cs activity (arbitrary units) with declared exposure for 14 PWR assemblies (Ref. 16).

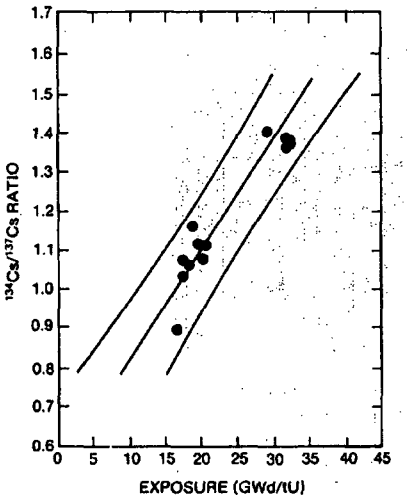

Fig. 18.15 *Correlation of the measured $^{134}Cs/^{137}Cs$ isotopic ratio with declared exposure for 14 PWR assemblies (Ref. 16).*

18.4.4 Cerenkov Radiation Measurements

The Cerenkov glow measurement provides a rapid nondestructive technique for verifying the presence of a gamma-ray source distributed within the fuel assembly. It can also be used to determine the absence of fuel pins in a fuel assembly. The fuel assemblies can be verified without placing any instrumentation into the storage pond water. However, most of the artificial lighting has to be eliminated, which the facility operator may not allow. When the artificial lighting can be eliminated, the inspector must move around in a darkened environment to carry out the measurements. Thus, the Cerenkov instrument should (1) be lightweight and easy to position by hand, (2) give an immediate result, (3) be insensitive to radiation damage, and (4) have an accuracy ensuring a meaningful measurement of the fuel inventory.

Figure 18.16 shows an instrument that is capable of both viewing the Cerenkov glow emitted and also determining the intensity of the glow (Ref. 10). The instrument is composed of two basic components: an image-amplifying portion and an electro-optical package that uses a photomultiplier tube to measure the intensity of the light passing through the aperture and field lens. The photomultiplier tube output current provides a digital readout indication of the intensity of the incoming light. Calibration of the instrument is done using a carbon-14 phosphor light source built into a special lens cap.

The light intensity profile is very sharp as the instrument is scanned horizontally across the top of an assembly because of the highly collimated nature of the emitted Cerenkov light. For fuel stored in standard vertical assemblies, penetrations in the top plates and tie plates and interstices between the fuel pins serve as Cerenkov light channels. These channels allow radiation from the entire length of the fuel assembly to be sampled by viewing from above. A series of measurements have been performed at storage facilities to demonstrate the usefulness of the technique for rapid verification of

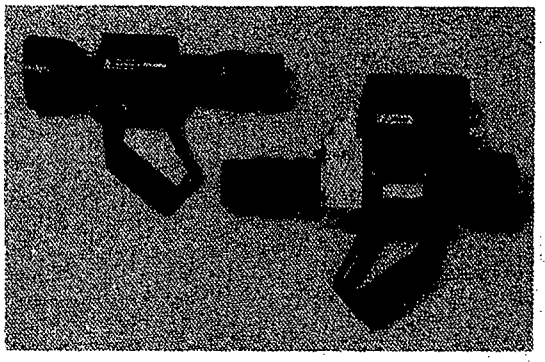

Fig. 18.16 Hand-held instrument for viewing the Cerenkov glow from irradiated fuel and determining its intensity. The instrument (shown on the right) is an adaptation of a commercially available night-vision device (shown on the left).

irradiated fuel assemblies (Ref. 10). Figure 18.17 shows the Cerenkov image of two PWR fuel assemblies in a storage rack at a reactor storage pond. The bright spots correspond to the guide tube positions of a 15 × 15 fuel assembly. Adjacent fuel assemblies do not exhibit similar sets of bright spots because the observer is not aligned with the axes of the assemblies.

The Cerenkov glow measurements are less susceptible to crosstalk among adjacent assemblies than are gamma-ray intensity measurements made at the top of the assemblies (Ref. 28). This is because Cerenkov light is channeled up from the entire length of the assembly, whereas gamma-ray measurements made at the top are mainly due to activation of the structural components. The spatial extent of the Cerenkov glow surrounding an isolated irradiated assembly in water is determined by the gamma radiation from the assembly's outer pins. The thickness of water required to reduce the intensity of 1-MeV gamma rays to one-tenth is ~36 cm, which is a reasonable estimate of the Cerenkov "halo" around an isolated point source. Fission product radiation from an assembly's inner pins, however, must penetrate a much denser composite of fuel cladding and interstitial water, which greatly reduces crosstalk.

18.5 NEUTRON MEASUREMENT OF IRRADIATED FUEL

Neutron measurements of irradiated fuel are relatively easy to make and can provide a rapid indication of burnup. The detection equipment is simple and easy to operate and a preliminary analysis of the data can be performed at the facility. A neutron detector is placed adjacent to the fuel assembly and the signal is analyzed using a single-channel analyzer. A ^{235}U fission chamber is the preferred detector because of its insensitivity to gamma rays. Although neutrons can penetrate the fuel assembly more readily than gamma rays can, their attenuation in water is more severe. The gamma-ray signal

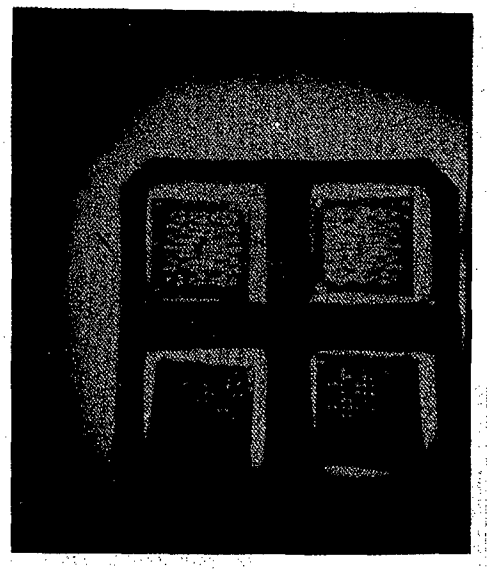

Fig. 18.17 Cerenkov glow image of two PWR fuel assemblies in a reactor storage pond.

decreases by a factor of 10 in roughly 36 cm, whereas the neutron signal decreases by a factor of 10 in about 10 cm. Thus it is important to position the neutron detector close to the fuel assembly.

18.5.1 The Fork Detector and ION-1 Electronics Package

Figure 18.18 illustrates a neutron measuring system developed for use by safeguards inspectors (Refs. 29 and 30). The system is designed to measure the total neutron and total gamma-ray activity of a submerged fuel assembly. The two principal components, a fork detector and an ION-1 electronics package, are shown in Figure 18.19.

The fork detector is a watertight polyethylene detector head containing two sets of ion chambers and fission chambers for measuring opposite sides of the fuel assembly simultaneously. Each arm contains an ionization chamber operating in the current mode to measure the total gamma-ray output and two fission chambers operating in the pulse mode to measure the total neutron output. In each arm, one fission chamber is wrapped in cadmium and one is bare. If it is necessary to determine the boron content of the water (typically 2000 ppm) to correct the neutron count rate, this can be done with the ratio of counts in the bare and cadmium-wrapped fission chambers (Refs. 31 and 32). The fork detector is available with two different apertures, one for PWR and one for BWR assemblies.

The ION-1 electronics package is a battery-powered, microprocessor-based unit that performs internal diagnostics and assists the inspector with data collection and analysis (Ref. 33). If measurements are to be made along the vertical length of the fuel assembly in order to obtain an axial burnup profile, the ION-1 can step the inspector through the scanning procedure.

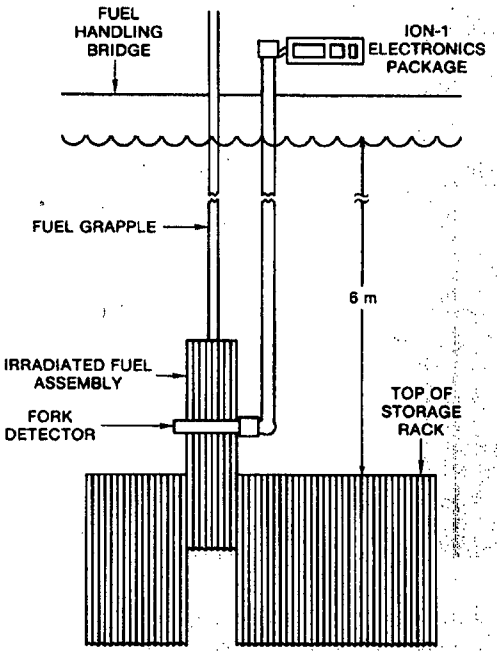

Fig. 18.18 Schematic of an irradiated-fuel measurement system for total neutron and total gamma-ray measurements. The system consists of an ION-1 electronics package, a long cable boom, and a fork detector.

Most measurements with the ION-1 electronics package and fork detector are made only at the axial midpoint of the fuel assembly. An average of 5 to 7 min is required to (1) position the fuel-handling bridge, (2) raise the fuel assembly partially out of the storage rack, (3) perform the measurements, and (4) replace the fuel assembly in the storage rack. Including time for assembly and disassembly of equipment, a measurement campaign at a reactor storage pond typically requires 2 to 3 days. With proper calibration, the fork detector can determine the burnup of individual fuel assemblies to about 5%.

18.5.2 Neutron Measurement of Burnup

Measurement results from a BWR irradiated-fuel storage facility are shown in Figure 18.20. The measured neutron activity of 36 BWR fuel assemblies is plotted as a function of declared exposure, which varied from 8.5 to 29 GWd/tU. One fuel assembly with a noncontinuous irradiation is clearly identified as an outlier. This particular fuel assembly had been irradiated to 18.0 GWd/tU, placed in the storage pond for 3 yr, and then returned to the reactor for an additional 3 GWd/tU exposure. During the 3-yr interim between exposures, the ^{241}Pu decayed to form ^{241}Am, which in turn yielded large quantities of ^{242}Cm when the fuel was returned to the reactor (see Section 18.3.6).

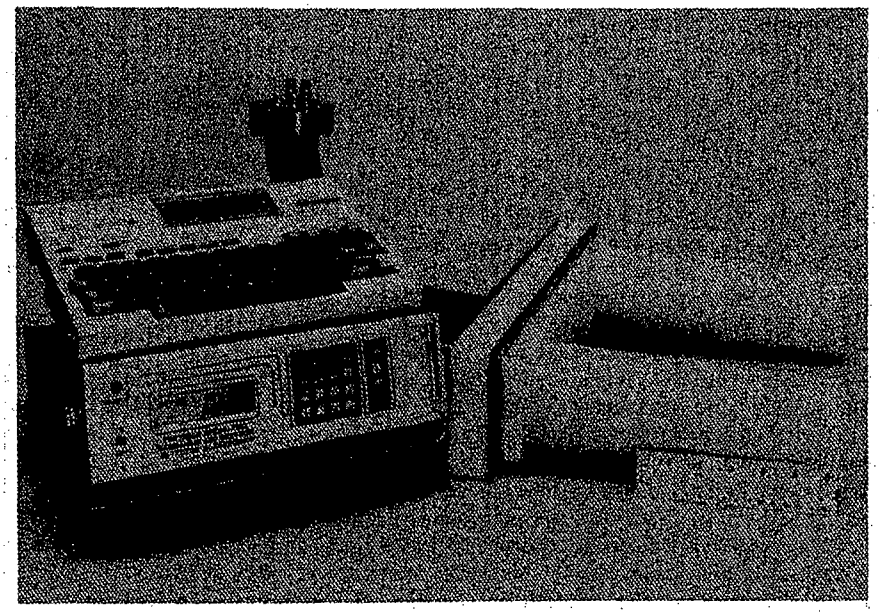

Fig. 18.19 *The ION-1 electronics package and the fork detector.*

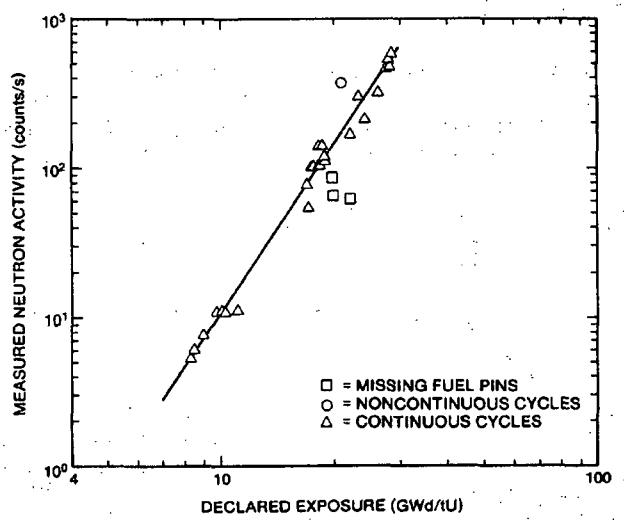

Fig. 18.20 *Measured neutron activity of 36 irradiated BWR fuel assemblies plotted as a function of declared exposure. The solid line is a power function fit to the experimental data.*

Three other data points in Figure 18.20 lie significantly below the fitted line. These assemblies had been reconstituted from other assemblies having various exposures. Also, several fuel pins were missing from each of these fuel assemblies. Both of these factors contributed to the lower measured neutron emission rates. If the reconstituted assemblies and the assembly with the noncontinuous irradiation history are excluded from the data analysis, an average difference of 3.0% exists between the declared exposure values and the values obtained from a power function relationship between count rate and exposure (Equation 18-4). This power function was determined by a least squares fit of the experimental data, and yields $\beta = 3.7$. By applying a correction for cooling time, the data for the assembly with the noncontinuous irradiation history can also be brought into good agreement.

Figure 18.21 shows neutron measurements made at a PWR fuel storage facility. The response of 17 irradiated fuel assemblies is plotted as a function of declared exposure, which varied from 25 to 35 GWd/tU. These data identify an enrichment effect that was predicted by burnup calculations, as described in Section 18.3.6. Four assemblies with initial ^{235}U enrichments of 2.4% have significantly higher neutron count rates compared with assemblies with identical exposures and cooling times but with initial ^{235}U enrichments of 3.6%. Lower-enriched fuel has less fissile material and therefore requires a higher neutron fluence to achieve the same exposure level as higher-enriched fuel. From the figure it is evident that the data for fuel with an initial enrichment of 3.6% form an excellent power law relationship between count rate and exposure, with $\beta = 3.9$. The operator-declared exposures differ from calculated values by an average of 0.9%.

18.6 DETERMINATION OF THE FISSILE CONTENT OF IRRADIATED FUEL

Sections 18.4 and 18.5 have described a variety of passive nondestructive measurement techniques for irradiated fuel materials. Each of these techniques provides an indirect measure of fuel burnup. Neither the unique gamma-ray signatures nor the

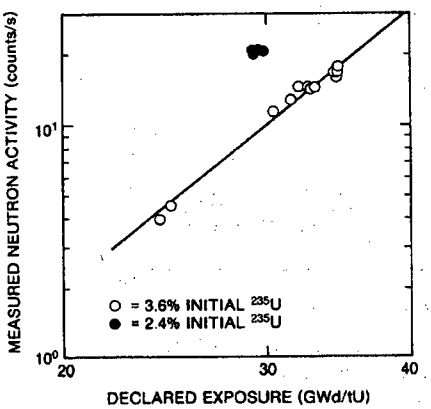

Fig. 18.21 Measured neutron activity of 17 irradiated PWR fuel assemblies plotted as a function of declared exposure. The solid line is a power function fit to the assemblies having an initial enrichment of 3.6%.

neutron signatures of the uranium or plutonium isotopes can be measured directly. To determine the actual concentration of fissile material, there are two possible approaches. One method uses calculated or empirically determined correlations to relate burnup to residual ^{235}U and plutonium content. The other method uses active neutron interrogation to override the passive neutron signal and obtain a net induced response from the fissile isotopes. Both methods are currently being developed by investigators in several countries. The methods are described briefly in the remainder of this section.

18.6.1 Indirect Determination from Passive Burnup Measurements

Most passive nondestructive measurements of irradiated fuel in the field are now limited to verification of the relative burnup levels of the assemblies. Within the constraints of time and manpower, it is customary to measure as many assemblies as possible, but most assemblies are measured at only one position along their length. If the measurements at this position are representative, the relative burnups of the assemblies can be obtained. Previously established correlations between burnup and the passive radiation levels then verify that the measurements are consistent with operator-declared values for burnup and cooling time. (Operator-declared values for burnup are only good to about 5% because of variations in core parameters.) Because it is very difficult to remove fissile material from the assemblies without also removing the fission product radiation sources, this verification implies that the fissile material is intact.

In principle, the fissile content of the fuel can be determined indirectly from the measured gamma-ray and neutron signals. First, it would be necessary to obtain an absolute value for the fuel burnup by destructive analysis of a section of the fuel. Then high-resolution gamma-ray measurements of single fission product activities or fission product activity ratios could be normalized to the destructive analysis to obtain an absolute calibration. Neutron measurements could also be related to the absolute burnup. Both neutron and gamma-ray measurements would have to be integrated along the axial profiles of the fuel assemblies to correct for variations in burnup. If an absolute calibration performed at one facility were used at another facility, the calibration would have to be adjusted for a variety of reactor-specific parameters including fuel enrichment, power history, and moderator and poison concentrations. Some examples of the influence of such parameters are given in Sections 18.3.5 and 18.3.6.

If absolute values for fuel burnup can be established, the concentration of fissile isotopes can be obtained by calculation. These calculations are usually carried out by complex computer codes such as CINDER (Refs. 6 and 7). An example of the result of such a calculation is given in Figure 18.22, which plots the concentration of the plutonium isotopes as a function of burnup. The accuracy of such computer codes for uranium and plutonium is typically 5 to 10%. If the reactor operating history is not known, the error may increase by an additional 5 to 15% (Ref. 11).

This indirect determination of fissile content from passive radiation measurements is very difficult because of the many measurement variables and reactor core parameters involved. Indirect correlation of fissile content with passive measurements is vulnerable to uncertainty, whereas direct correlation of fuel integrity with measurement is now a well-established and reliable technique.

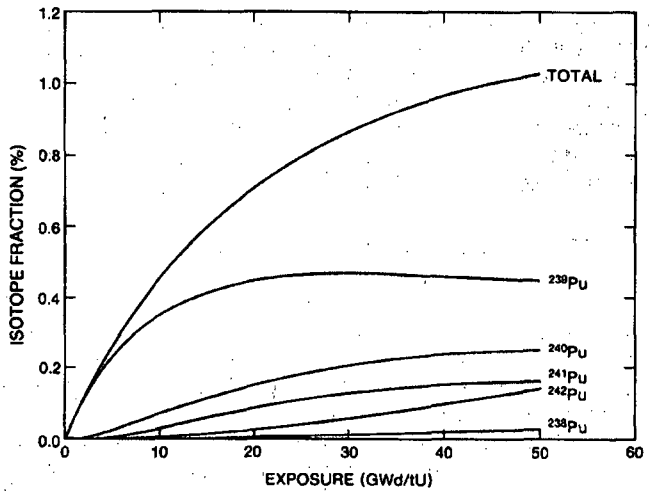

Fig. 18.22 Relative concentrations of the plutonium isotopes (expressed as weight percent of initial uranium) as a function of exposure. The data were obtained by calculation with the EPRI-CINDER Code (Ref. 5).

18.6.2 Determination by Active Neutron Interrogation

A direct measurement of the fissile content of irradiated fuel is possible using a large neutron source to induce fissions. The source can be an accelerator, a 14-MeV neutron generator, or an isotopic source like RaBe, SbBe, or californium. The source is positioned near the irradiated fuel, where it produces an induced fission signal proportional to the amount of fissile material. Typical neutron source strengths must be on the order of 10^8 to 10^9 n/s to induce a fission signal that is comparable in size to the passive neutron yield. In practice, active neutron interrogation systems cannot distinguish between uranium and plutonium. The induced fission response is proportional to the total fissile mass of ^{235}U, ^{239}Pu, and ^{241}Pu.

A combined active and passive neutron assay system has been developed by G. Schulze, H. Wuerz, and others (Ref. 19) using a ^{252}Cf source. The system can determine fuel burnup and initial uranium content. The plutonium content can be obtained indirectly from isotopic correlations.

Several facilities have used the delayed neutron activation technique to measure irradiated fuel. The reprocessing facility at Dounreay, United Kingdom, has used a 14-MeV neutron generator to assay baskets of leached hulls (Ref. 34). Recently this assay system was converted to a californium Shuffler for the neutron interrogation (Ref. 35). A large californium Shuffler system has also been developed for the assay of highly enriched irradiated uranium (Ref. 36). However, at the present time there are no active neutron systems in operation to measure power reactor fuel assemblies. This is because

active neutron systems require an accelerator or neutron generator or a large, heavily shielded isotopic source, which has limited the use of these systems to fixed, in-plant installations in research laboratories or reprocessing facilities. The status of active neutron techniques and measurement results is summarized in Refs. 4 and 11.

18.7 SUMMARY OF NONDESTRUCTIVE TECHNIQUES FOR VERIFICATION OF IRRADIATED FUEL

Table 18-6 summarizes the nondestructive assay techniques available for the verification of irradiated-fuel assemblies. Depending on the level of verification needed, an inspector might use one or more of the gamma-ray or neutron techniques described in this chapter. In general, the most effective verification would be obtained by a combination of gamma-ray and neutron techniques.

REFERENCES

1. *Nucleonics Week,* January 2, 1986.

2. Duderstadt and Hamilton, *Nuclear Reactor Analysis* (John Wiley and Sons, Inc., New York, 1976).

3. A. V. Nero, *A Guidebook to Nuclear Reactors* (University of California Press, Berkeley, California, 1979.

4. T. D. Reilly, "The Measurement of Leached Hulls," Los Alamos Scientific Laboratory report LA-7784-MS (1979).

5. G. E. Bosler, J. R. Phillips, W. B. Wilson, R. J. LaBauve, and T. R. England, "Production of Actinide Isotopes in Simulated PWR Fuel and Their Influence on Inherent Neutron Emission," Los Alamos National Laboratory report LA-9343 (1982).

6. T. R. England, W. B. Wilson, and M. G. Stamatelatos, "Fission Product Data for Thermal Reactors, Part 1: A Data Set for EPRI-CINDER Using ENDF/B-IV," Electric Power Research Institute report EPRI NP/356, Part 1, and Los Alamos Scientific Laboratory report LA-6745-MS (1976).

7. T. R. England, W. B. Wilson, and M. G. Stamatelatos, "Fission Product Data for Thermal Reactors, Part 2: Users Manual for EPRI-CINDER Code and Data," Electric Power Research Institute report EPRI NP/356, Part 2, and Los Alamos Scientific Laboratory report LA-6746-MS (1976).

Table 18-6. Nondestructive assay techniques for verification of irradiated-fuel assemblies

Special Level of Verification	Measurement Technique		Instrumentation
	Gamma Ray	Neutron	
Physical characteristics			Visual inspection
Indication of irradiation exposure	Cerenkov		Cerenkov viewing device
	Presence of gamma radiation		Ion chambers Thermoluminescence detectors Scintillators
		Presence of neutron radiation	Fission chambers ^{10}B detectors
Physical integrity of fuel assembly	Cerenkov		Cerenkov viewing device
	Relative intensities of high-energy gamma rays		Germanium detector Be(γ,n) detector
		Relative values of neutron emission rates	Fission chambers ^{10}B detectors
Presence of fission products and actinides	Qualitative identification of specific gamma-ray lines		Germanium detector Be(γ,n) detector
		Relative values of neutron emission rates	Fission chambers ^{10}B detectors

Table 18-6. (cont.)

Special Level of Verification	Measurement Technique		
	Gamma Ray	Neutron	Instrumentation
Relative concentrations of fission products and actinides	Quantitative measurement of ^{137}Cs, $^{134}Cs/^{137}Cs$, and $^{154}Eu/^{137}Cs$; correlation with operator-declared information		Germanium detectors
		Quantitative measurement of neutron emission rate; correlation with operator-declared information	Fission chambers ^{10}B detectors
Direct measurement of fissile content	Indirectly through correlations between NDA measurements and destructive analyses		Germanium detectors
		Quantitative measurement of induced fissions in special nuclear material	Neutron source Fission chambers ^{10}B detectors

8. D. Cobb, J. Phillips, G. Bosler, G. Eccleston, J. Halbig, C. Hatcher, and S. T. Hsue, "Nondestructive Verification and Assay Systems for Spent Fuels," Los Alamos National Laboratory report LA-9041, Vol. 1 (April 1982).

9. E. J. Dowdy, N. Nicholson, and J. T. Caldwell, "Irradiated Fuel Monitoring by Cerenkov Glow Intensity Measurements," Los Alamos Scientific Laboratory report LA-7838-MS (1979).

10. N. Nicholson and E. J. Dowdy, "Irradiated Fuel Examination Using the Cerenkov Technique," Los Alamos National Laboratory report LA-8767-MS (1981).

11. S. T. Hsue, T. W. Crane, W. L. Talbert, and J. C. Lee, "Nondestructive Assay Methods for Irradiated Nuclear Fuels," Los Alamos Scientific Laboratory report LA-6923 (1978).

12. J. R. Phillips, G. E. Bosler, J. K. Halbig, S. F. Klosterbuer, and H. O. Menlove, "Nondestructive Verification with Minimal Movement of Irradiated Light-Water Reactor Fuel Assemblies," Los Alamos National Laboratory report LA-9438-MS (1982).

13. P. M. Rinard, "A Spent-Fuel Cooling Curve for Safeguard Applications of Gross-Gamma Measurements," Los Alamos National Laboratory report LA-9757-MS (1983).

14. Advisory Group Meeting on the Nondestructive Analysis of Irradiated Power Reactor Fuel, International Atomic Energy Agency report AG-241 (October 29-November 2, 1979).

15. J. R. Phillips, B. K. Barnes, and T. R. Bement, "Correlation of the Cesium-134/Cesium-137 Ratio to Fast Reactor Burnup," *Nuclear Technology* 46, 21 (1979).

16. J. R. Phillips, J. K. Halbig, D. M. Lee, S. E. Beach, T. R. Bement, E. Dermendjiev, C. R. Hatcher, K. Kaieda, and E. G. Medina, "Application of Nondestructive Gamma-Ray and Neutron Techniques for the Safeguarding of Irradiated Fuel Materials," Los Alamos Scientific Laboratory report LA-8212 (1980).

17. S. T. Hsue, C. R. Hatcher, and K. Kaieda, "Cooling Time Determination of Spent Fuel," *Nuclear Materials Management* 8, 356-367 (Fall 1979).

18. A. J. G. Ramalho and W. E. Payne, "Spent Fuel Measurements Using High-Resolution Gamma Systems," *Nuclear Materials Management* 8, 76 (1979).

19. G. Schulze, H. Wuerz, L. Koch, and R. Wellum, "Neutron Assay Plus Isotopic Correlations: A Method for Determining Pu and Burnup in Spent LWR Fuel Assemblies," *Proc. Second Annual Symposium on Safeguards and Nuclear Materials Management*, Edinburgh, Scotland, March 26-28, 1980 (European Safeguards Research and Development Association, Brussels, Belgium, 1980), pp. 396-403.

20. J. R. Phillips, G. E. Bosler, J. K. Halbig, S. F. Klosterbuer, D. M. Lee, and H. O. Menlove, "Neutron Measurement Techniques for the Nondestructive Analysis of Irradiated Fuel Assemblies," Los Alamos National Laboratory report LA-9002-MS (1981).

21. P. Fedotov, N. M. Kazarinov, and A. A. Voronkov, "The Use of Neutron Scanning Method for Analysis of Spent VVER Assemblies in Safeguarding Systems," presented at the IAEA Advisory Group Meeting on Methods and Techniques for NDA Safeguards Measurements of Power Reactor Spent Fuel, Vienna, October 28-November 2, 1979.

22. S. T. Hsue, J. Stewart, K. Kaieda, J. Halbig, J. Phillips, D. Lee, and C. Hatcher, "Passive Neutron Assay of Irradiated Nuclear Fuels," Los Alamos Scientific Laboratory report LA-7645-MS (1979).

23. J. R. Phillips and G. E. Bosler, "Calculated Response Contribution of Gamma Rays Emitted from Fuel Pins in an Irradiated PWR Fuel Assembly," Los Alamos National Laboratory report LA-9837 (1983).

24. R. J. S. Harry, J. K. Aaldijk, and J. P. Braak, "Gamma Spectrometric Determination of Isotopic Composition Without Use of Standards," in Proceedings of the International Symposium on Nuclear Materials Safeguards, Vienna, October 20-24, 1975 (IAEA-SM-201/68).

25. T. N. Dragnev, "Intrinsic Self-Calibration of Nondestructive Gamma Spectrometric Measurements (Determination of U, Pu, and Am-241 Isotopic Ratios)," International Atomic Energy Agency report IAEA/STR-60 (1976).

26. T. R. Bement and J. R. Phillips, "Evaluation of Relative Detection Efficiency on Sets of Irradiated Fuel Elements," Proc. of the 1980 DOE Statistical Symposium, October 29-31, 1980 (CONF-801045).

27. T. Suzaki, H. Tsuruto, and S. Matsura, "Non-Destructive Gamma-Ray Spectrometry and Analysis on Spent Fuel Assemblies of the JPDR-I Core," Japan Atomic Energy Research Institute report JAERI-memo 8164 (1979).

28. C. E. Moss and D. M. Lee, "Gross Gamma-Ray Measurements of Light-Water Reactor Spent-Fuel Assemblies in Underwater Storage Arrays," Los Alamos Scientific Laboratory report LA-8447 (1980).

29. J. R. Phillips, G. E. Bosler, J. K. Halbig, S. F. Klosterbuer, H. O. Menlove, and P. M. Rinard, "Experience Using a Spent-Fuel Measurement System," presented at the 24th Annual Meeting of the Institute of Nuclear Materials Management, Vail, Colorado, July 10-13, 1983.

30. R. N. Olsen, Ed., "Instructions for the Use of the ION-1 and the Fork Detector," International Atomic Energy Agency report IMI No. 42 (November 1984).

31. P. M. Rinard, "Neutron Measurements in Borated Water for PWR Fuel Inspections," Los Alamos National Laboratory report LA-10068-MS (1984).

32. P. M. Rinard and G. E. Bosler, "BWR Spent-Fuel Measurements with the ION-1/Fork Detector and Calorimeter," Los Alamos National Laboratory report LA-10758-MS (1986).

33. S. Klosterbuer and J. Halbig, "Portable Spent-Fuel Gamma-Ray and Neutron Detector Electronics User Manual," Los Alamos National Laboratory report LA-8707-M (1983).

34. B. McDonald, G. Fox, and W. Bremner, "Nondestructive Measurements of Plutonium and Uranium in Process Wastes and Residues," in *Safeguarding Nuclear Materials*, Proc. Symp., Vienna, 1975 (IAEA Pub 408, Vol. II, p. 589, 1976).

35. G. Eccleston, H. Menlove, T. Van Lyssel, G. Walton, D. C. Garcia, and G. Ortiz, "Dounreay Shuffler," in "Safeguards and Security Progress Report, January-December 1983," Los Alamos National Laboratory report LA-10170 (September 1984), p. 59.

36. G. W. Eccleston, H. O. Menlove, and M. W. Echo, "A Measurement Technique for High Enrichment Spent Fuel Assemblies and Waste Solids," *Nuclear Materials Management* 8, 344-355 (1979).

19

Perimeter Radiation Monitors

P. E. Feblau

19.1 INTRODUCTION

Perimeter radiation monitors are located at the periphery of nuclear-material and radioactive-contamination control areas to detect accidental or covert removal of radioactive materials. Two types of perimeter monitors are in use today: contamination monitors and nuclear-material monitors. Contamination monitors detect contamination on the surface of a person or an object where the radiation comes from an extended area viewed without intervening absorbers. Nuclear-material monitors must be able to detect small, possibly shielded quantities of nuclear material that may be hidden, for example, in a briefcase. In this case the small source size and the presence of absorbers reduces the radiation intensity. This chapter discusses the two applications of perimeter monitors but gives primary emphasis to nuclear-material monitors.

The need to detect contamination predated security concerns so that when the need for monitors to detect nuclear material arose, hand-held contamination monitors were available. However, because security personnel had to interpret an analog meter display to use this type of instrument, their attention was distracted from the security search. Automatic portal monitors (Ref. 1) and hand-held monitors (Ref. 2) were developed to eliminate the distraction. These monitors provide audible alarm signals that allow the operator to devote full attention to the security search. More recently, the responsibility of employers to furnish top-grade contamination monitoring equipment to employees has fostered development of automatic, high-sensitivity contamination monitors (Ref. 3). These, as well as modern nuclear-material monitors, are designed for high sensitivity, dependability, and easy maintenance.

Diversion monitors meet Department of Energy (Ref. 4) and Nuclear Regulatory Commission (Ref. 5) requirements to search each person, package, or vehicle leaving a nuclear-material access area. Contamination monitors meet radiation safety standards for monitoring persons leaving a radioactive-contamination area. In both cases, visual or manual searches may be ineffective, but radiation monitors sense radiation emitted by the materials and can conduct unobtrusive, sensitive, and efficient searches. The monitors provide timely notice of contamination or diversion before the controlled material can leave an access area.

Examples of diversion monitors are the automatic portal monitor (shown in Figure 19.1 with its detectors positioned beside a passing pedestrian) and the hand-held monitor (shown being manually scanned over a pedestrian in Figure 19.2). The versatile hand-held monitors have many applications, even to contamination monitoring, but their effectiveness depends on the operator making a thorough scan. In contrast, portal monitors are fully automatic.

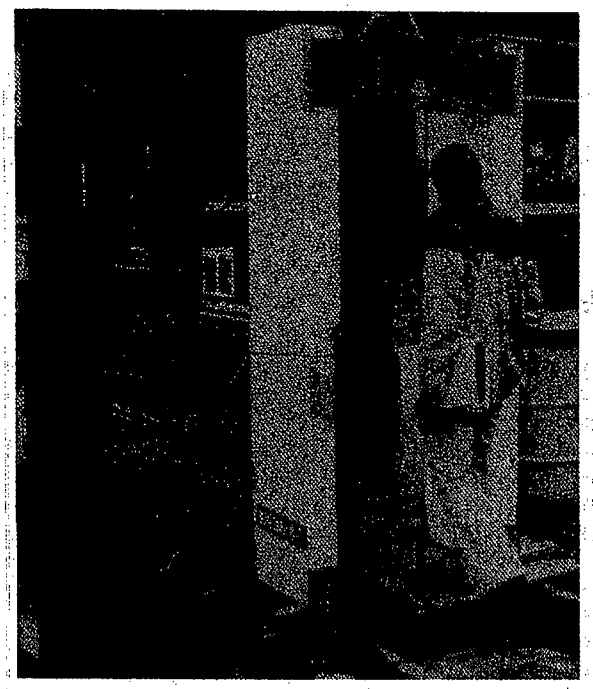

Fig. 19.1 Automatic nuclear-material portal monitor with large plastic scintillators to monitor pedestrians.

New monitor designs locate detectors inside an enclosure (see Figure 19.3) where an individual being monitored must stand near radiation detectors for an extended period. The longer monitoring period and the proximity of the occupant and the detectors improve detection sensitivity; these principles have been applied to both pedestrian and motor-vehicle monitoring.

19.2 BACKGROUND RADIATION EFFECTS

Radiation monitors are influenced by background radiation and the variation of its intensity with time. The intensity of the background radiation influences the effectiveness of monitoring. Alarm thresholds must be set well above background intensity to avoid alarms from counting statistics (one cause of nuisance alarms). The required threshold setting becomes proportionately higher as the background intensity increases, causing the monitoring sensitivity to decrease. In an occupied monitor, rapid variations in background intensity, which can be caused by natural background radiation processes, movement of radioactive materials, or radiation-producing machinery, may be mistaken for nuclear-material signals and cause another type of nuisance alarm. An example of a natural background radiation process leading to rapid intensity variation is

Fig. 19.2 *Monitoring with hand-held instruments is highly effective when the operator is well trained and motivated.*

the decay of ^{226}Ra in soil. Its gaseous daughter, ^{222}Rn, can escape the soil to decay in the atmosphere. These daughter products, which are themselves radioactive, may attach to dust particles that form condensation points for raindrops. When the raindrops fall to the ground they temporarily increase background intensity (see Figure 19.4).

19.3 CHARACTERISTICS OF DIVERSION AND CONTAMINATION SIGNALS

19.3.1 Radiation Sources

As described in Chapter 1, nuclear materials can be detected by their spontaneous radiations. These radiations—alpha, beta, gamma ray, x ray, and neutron—each have a different ability to penetrate materials. Alpha radiation is not very penetrating and is easily stopped by several centimeters of air. Except when contamination detectors almost touch the emitter, alpha radiation contributes little signal to a radiation monitor.

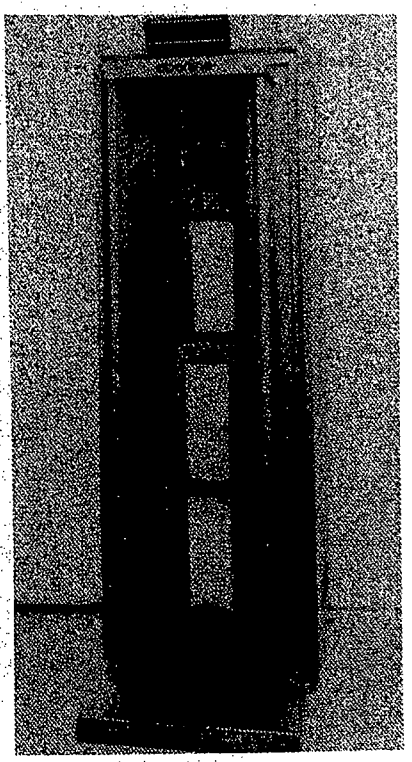

Fig. 19.3 This sensitive contamination monitor measures each side of the occupant's body separately. (Photo courtesy of Eberline Instrument Corp., Santa Fe, New Mexico.)

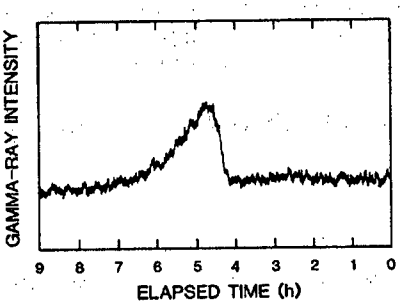

Fig. 19.4 A background intensity record showing a road bed monitor count-rate increase during brief intense precipitation.

More penetrating forms of radiation that easily pass through air can be detected at a distance. However, the shielding provided by detector cabinets and nuclear-material packaging may exclude all but gamma-ray and neutron signals. One important aspect separates the signals available to contamination and diversion monitors: contamination usually lies on a surface where its radiation is readily detected, whereas diversion monitors must sense penetrating radiation from material that is encapsulated. Hence, contamination monitors often detect many forms of radiation but diversion monitors primarily detect gamma rays and neutrons. The nuclear-material diversion monitors discussed in the remainder of this chapter mainly detect gamma rays but do have some neutron sensitivity. Figure 19.5 illustrates absorption of three types of radiation in different materials.

Internal absorption of source radiation also may significantly alter detection signals. For example, nuclear materials shield their own gamma radiation; the extent of self-absorption depends on the physical form of the material. Figure 19.6 illustrates self-absorption in different shapes and sizes of highly enriched uranium. Thin uranium materials such as powders and foils emit most of their radiation, whereas more compact shapes such as spheres and cylinders absorb most of it. The cylinders in Figure 19.6 emit in proportion to their surface area, which increases as the 2/3 power of the mass, giving rise to the straight line in the plot.

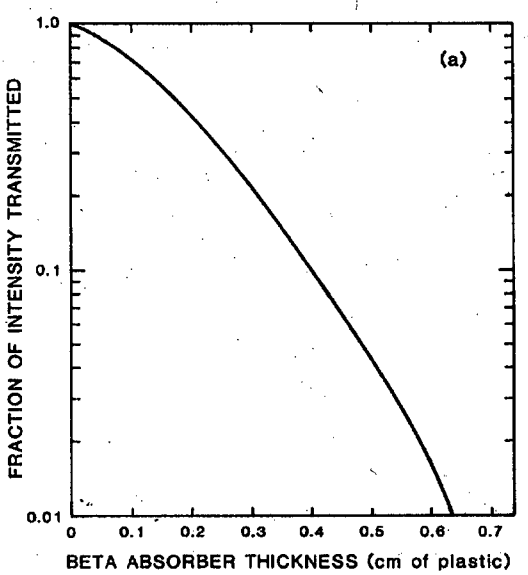

Fig. 19.5 (a) *Continuous spectrum beta rays (end point 1.9 MeV) are easily absorbed in a few centimeters of plastic.*

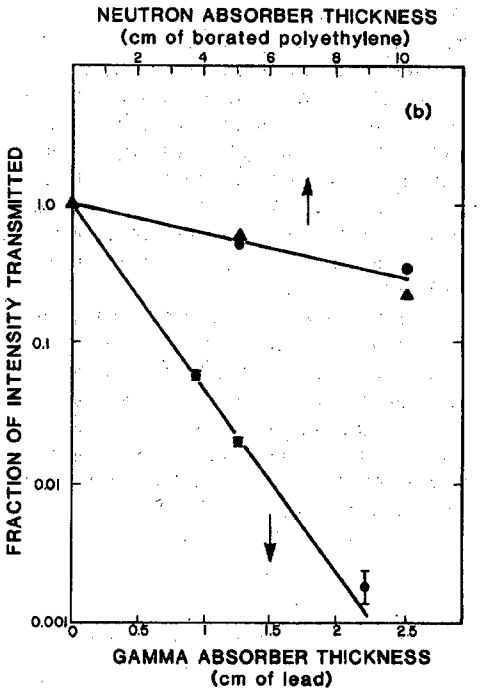

Fig. 19.5 (b) Plutonium gamma rays are absorbed in modest thicknesses of lead, but its neutrons are less affected by large thicknesses of borated polyethylene.

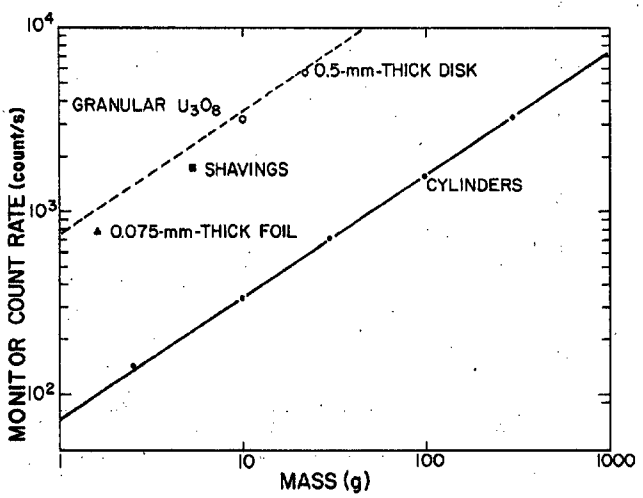

Fig. 19.6 The form of highly enriched uranium influences the self-absorption of gamma rays. The emitted intensity varies with the surface area rather than the mass.

19.3.2 Time-Varying Signals

Diversion or contamination signals are usually present in a monitor for only a short time interval. Unless the occupant is stationary, signals from nuclear material will vary during the monitoring period as the occupant moves toward and away from the detectors. Figure 19.7 illustrates the net signal in a monitor as a pedestrian passes through carrying nuclear material. The time integral of the variable signal is about 60% of that for a stationary occupant. Good monitor design ensures that the monitoring period matches the intense part of the signal as closely as possible. Techniques for obtaining this optimum situation are discussed in Section 19.4.

A complementary effect that diminishes signals in a monitor is the reduction in background intensity caused by an occupant. Ambient background radiation from the monitor's surroundings can be partly absorbed by the person or vehicle occupying the monitor. The reduction in intensity may be only 1.5% for pedestrians but is much greater for motor vehicles. Figure 19.8 illustrates the reduction caused by the presence of a truck in a vehicle monitor. The reduction ranges from 10% to 25% for different-size vehicles. Because the monitor's alarm threshold is constant, a much larger signal is required to alarm an occupied monitor than one that is unoccupied.

19.4 SIGNAL ANALYSIS

19.4.1 Detecting Radiation Signals

Radiation monitors use signal analysis to decide whether a measurement indicates a background signal alone or a background signal plus an additional radiation signal. Unfortunately, statistical variations in background and monitoring measurements preclude a simple comparison. Although the expected background may be determined

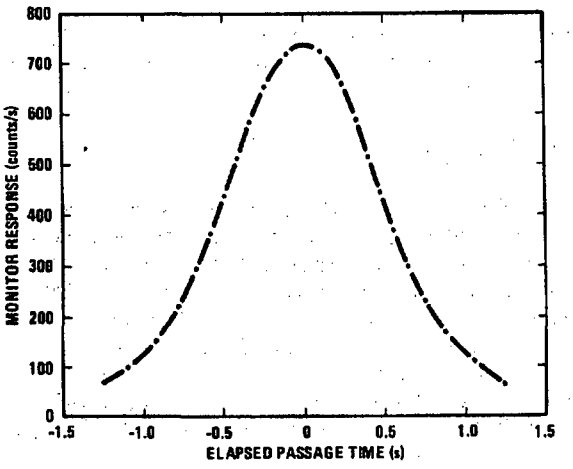

Fig. 19.7 A bell-shaped signal intensity profile results from a pedestrian carrying nuclear material through a portal monitor.

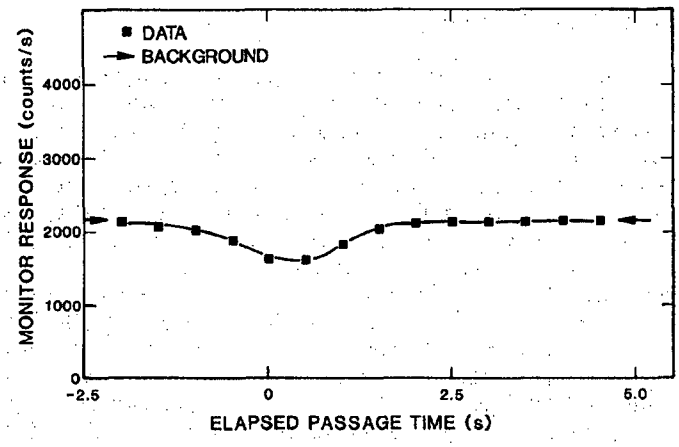

Fig. 19.8 An inverted bell-shaped reduction in the monitor's response to background radiation results from the passage of a vehicle.

from a long, precise measurement, each monitoring measurement is necessarily short and imprecise. If background measurements have an expected count B, individual measurements will range many standard deviations higher and lower than B; one standard deviation in this instance is the square root of the count B. Comparisons of monitoring measurements must allow statistical variations of several times the square root of B to exclude nuisance alarms. Each monitoring measurement is usually compared to an alarm threshold equivalent to that given by Equation 19-1. An alarm is sounded when the measurement equals or exceeds the alarm threshold M.

$$M = B + N\sqrt{B} \tag{19-1}$$

where N = alarm increment (number of standard deviations, usually 3 or 4). Alarms are real when they result from real signals and are nuisance alarms when they result from statistical variation or background changes.

19.4.2 Analog Detection Methods

A simple and dependable method for making monitoring decisions is provided by an analog method (Ref. 6) that compares monitoring intensities to background intensities with two circuits having different time constants (Figure 19.9). The slow circuit remembers background intensity over a period of perhaps 20 s, whereas the monitoring circuit has a fast, 0.4-s time constant. The comparator is calibrated by adjusting the input—an analog signal from a ratemeter—until a chosen sensitivity and nuisance-alarm rate are achieved. Once properly adjusted, the circuit operates continuously and is prepared to monitor signals whenever they appear. A drawback to analog circuits is the manual adjustment procedure; precise adjustment can take a great deal of time. Digital logic methods, on the other hand, are free of most adjustments.

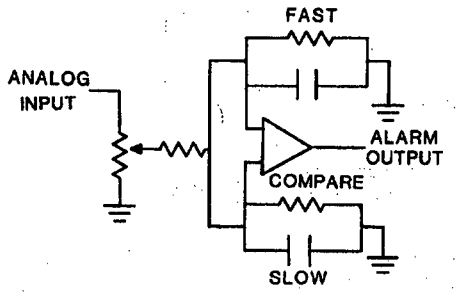

Fig. 19.9 This analog circuit compares monitoring intensity to background intensity.

19.4.3 Digital Detection Methods

Alarm decisions can be made by digital circuits and microprocessors. Equation 19-1 can be implemented, for example, by comparing the result of a 0.4-s monitoring measurement contained in a digital register to a stored alarm threshold derived from an earlier background measurement. The stored alarm threshold might have been derived from an earlier 20-s background measurement, divided by 50 to obtain B, plus an added multiple of the square root of B. In this case, the comparison is a numerical one with no calibration required. This single-interval method does have a shortcoming: it is not continuous so the measurement interval may not match the most intense part of the signal (see Figure 19.7). However, digital logic methods are easily changed to overcome such shortcomings. The improvements described below include the moving-average method, the stepwise method, and the sequential hypothesis test.

A digital method that performs well in free-passage monitors uses a moving average of monitoring measurements. Short measurement periods are used (for example, 0.2 s) and the counts from four or more measurement periods are summed and compared to the alarm threshold. After the first group of four or more periods, each new measurement is added and the oldest measurement is subtracted from the sum. Every new sum is compared to the alarm threshold; measurements then continue unless an alarm occurs or the monitor is no longer occupied. Because monitoring is continuous and many decisions are made, the alarm threshold must be higher than for the single-interval test (described in the preceding paragraph) to achieve the same statistical-alarm probability. However, the moving-average method obtains greater sensitivity because it measures the most intense part of the signal.

A simple stepwise method (Ref. 7) shortens measurement periods in monitors that require the occupant to wait until a measurement is completed. An extended monitoring period achieves higher detection sensitivity without an increased statistical-alarm frequency. The waiting time can be shortened by subdividing the measurement period into steps where intermediate decisions are made. The full period is needed only when all intermediate decisions call for an alarm. Otherwise, monitoring is completed after the first step that does not call for an alarm. Each intermediate alarm threshold has the same source detection sensitivity as the full measurement period but has a higher statistical-alarm probability. Figure 19.10 illustrates the technique; all but about 2.3% of the vehicles not carrying radioactive material will depart after the first interval, which has a

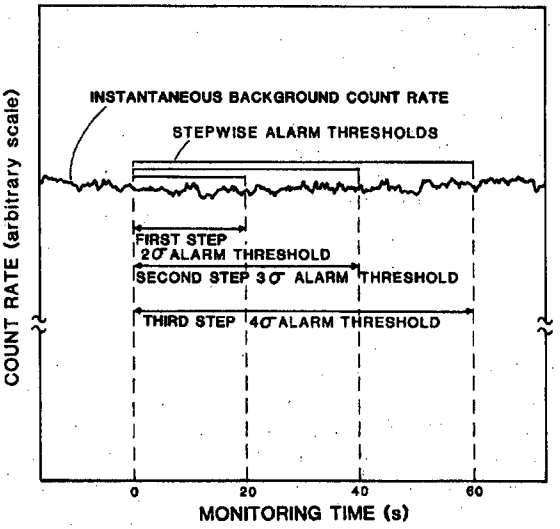

Fig. 19.10 *The stepwise method makes intermediate decisions at lower alarm thresholds that maintain sensitivity at the expense of more frequent false alarms. The penalty for the occasional false alarm is to wait for one more step. For the thresholds shown in this figure, the average waiting time is reduced by two thirds.*

two-standard-deviation alarm threshold. Those that are detained are measured for one or more additional periods and the results are added to the first result and reanalyzed at successively higher alarm thresholds. If alarms persist, the final measurement and final decision are made as if no intermediate decisions had been made.

Work performed by Wald (Ref. 8) during the 1940s developed a sequential hypothesis test to reduce quality control measurement time in manufacturing. The sequential hypothesis test also shortens the measurement time in radiation monitoring (Ref. 9). This method uses a sequence of short measurements, each followed by a hypothesis test. The outcome of each test is one of three possible decisions: the accumulated measurements represent background, the measurements require an alarm, or the measurements must continue before a decision can be made. If one of the first two possible decisions is not reached quickly enough, a final decision is made by some other method.

In discussing applications of this method, Ref. 9 reports an average measurement period that is 22% as long as that required by the single-interval method, with no increase in statistical-alarm frequency. Monitoring is also rapid when a nuclear-material signal is present unless the radiation intensity is very near the alarm threshold. In that case the sequential hypothesis test requires as much time as the single-interval method.

19.4.4 Long-Term Monitoring

Long-term monitoring is a novel technique that achieves high sensitivity through repeated measurements applied in conjunction with, but independent of, other standard techniques (Ref. 10). The method can detect repeated instances of contamination or diversion of nuclear material in quantities too small to detect in normal monitoring. One application of the method sums the net monitoring results for pedestrians entering an area and compares this sum to the sum for pedestrians leaving the area. Any difference between the two may signify contamination or diversion of nuclear material.

The long-term monitoring method calculates the net signal during occupancy by subtracting from each measurement an average background determined before and after the measurement. Although individual measurements are imprecise, the average net signal for hundreds of passages is quite precise. In fact, this method provides the most precise measurement of the average background radiation attenuation by monitor occupants.

In addition to being able to average monitoring results for large populations, the method can require identification of each occupant so that data for each individual can be recorded. Then analysis of long-term averages of the incoming and outgoing measurements for an individual can identify cases of repeated contamination or diversion of small quantities of nuclear material. For cases where each outgoing passage involves contamination or diversion and each incoming passage does not, the long-term monitoring method is ten times more sensitive than other methods.

19.5 RADIATION DETECTORS

Perimeter monitors use a different type of radiation detector depending on whether they are designed to detect contamination or diverted nuclear material. Gas proportional counters are most appropriate for detecting the radiation from contamination, and scintillators are most appropriate for detecting the penetrating radiation from diverted material. The general properties of gas proportional counters and inorganic scintillators are discussed in Chapter 3; organic scintillators, which are widely applied to perimeter diversion monitoring, are discussed in this section along with gas-flow proportional counters for perimeter contamination monitoring. These inexpensive, large-area detectors are well adapted to the requirements of perimeter monitoring.

19.5.1 Plastic Scintillators

Plastic scintillation detectors are solid organic scintillators that contain fluorescent compounds dissolved in a solidified polymer solute (Ref. 11). These materials have low density and low atomic number so they lack strong photoelectric absorption. They detect gamma rays by detecting Compton recoil electrons, and they detect neutrons by detecting recoil protons. These detectors do not display full-energy peaks; they display a continuous spectrum from the Compton edge down to zero energy. Although organic scintillators are poor energy spectrometers and have low intrinsic detection efficiency,

they make excellent large-area, low-cost radiation counters. Their low cost results from the use of inexpensive materials and simple packaging; NaI(Tl) crystals, on the other hand, are expensive to grow and to protect from moisture and thermal shock.

The large size of plastic scintillators gives them good total detection efficiency even though their intrinsic efficiency is low. Total efficiency is the product of a detector's intrinsic efficiency and the fraction of emitted photons that strike the detector. The latter factor depends on the size of the detector. The large detector size also provides more uniform monitoring than would an array of small detectors.

Plastic scintillation detectors do have some shortcomings. They produce only about 10% as much light as NaI(Tl) detectors, and their large size makes uniform light collection difficult. Uniform light collection is important to minimize the spread in pulse heights resulting from detection of radiation in different parts of a detector. Reference 12 describes methods for obtaining total internal reflection of scintillation light and for making a large detector's response homogeneous. Low light production is compensated for by using bialkali cathode photomultipliers that provide good signal amplification with low photocathode dark current and noise.

Low photomultiplier noise is important in organic scintillators because the Compton pulse-height spectrum extends down to zero pulse height. Noise sets a practical limit to the pulse amplitude that can be detected; this bias level limits the intrinsic detection efficiency. The bias level influences detection efficiency over a broad range of incident gamma-ray energy as illustrated in Figure 19.11. Bialkali photocathodes can operate near the 0.045-V bias level at room temperature.

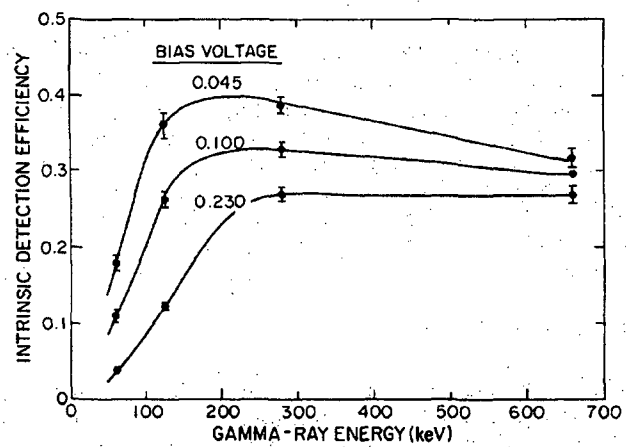

Fig. 19.11 *Low bias voltage is essential to good intrinsic detection efficiency in organic scintillators. The data illustrated here were taken with a detector that yielded 2-V pulse height for incident 662-keV gamma rays.*

19.5.2 Gas-Flow Detectors

An inexpensive form of gas proportional counter is the very large area gas-flow proportional counter. Very thin detector windows (100 $\mu g/cm^2$) transmit the low-energy radiation emitted by surface contamination into the detector interior, which is a thin, large-surface-area cavity. An argon-methane mixture slowly flows through the cavity and then is burned or recirculated with a small quantity of new gas. Argon is the counting gas, and methane lowers the operating voltage and quenches discharges between counter electrodes. Discharges caused by contaminants in the counting gas or by secondary emission from metallic counter parts cause electronic noise. The flat-slab geometry has a nonuniform electric field and gain so the instrument serves as a counter rather than an energy spectrometer. Although the very large gas-flow proportional counter is a noisy detector, its good low-energy response and low cost make it attractive for contamination monitoring where measurements can be repeated freely without significant penalty.

19.6 PERIMETER MONITOR COMPONENTS

The perimeter radiation monitor shown in Figure 19.1 monitors pedestrians, and that shown in Figure 19.12 monitors motor vehicles. Each monitor has similar components (Figure 19.13). The detectors sense radiation and transmit information to the monitor's control unit, which provides power, signal conditioning, and signal analysis. The control unit usually has an occupancy sensor to determine when to measure background and indicator lamps and sounders to announce alarms.

19.6.1 Components and Their Functions

The components and functions of a radiation monitor are described below:

(1) Detector: Detect radiation from a particular region of space, usually the region between two or more detectors.

(2) Signal Conditioning Electronics: Transform the detected radiation charge pulses into voltage pulses that can be transmitted to another device for analysis.

(3) Single-Channel Analyzer (SCA): Select the pulses in a desired energy region. The output is a standard logic pulse.

(4) Control Unit: Count the SCA logic pulses. Use the result to derive alarm levels or monitoring measurements. Test background measurements against high- and low-background thresholds to detect malfunction. Display each new background result. Compare monitoring measurements to the alarm threshold (Section 19.4). Use the occupancy sensor to determine when to measure background and when to monitor. Assist with monitor calibration.

(5) Occupancy Sensor: Sense the presence of a person or vehicle and, if important, the direction of travel.

(6) Output Device: Communicate monitoring results by visual signals (flashing lights) and audible signals (chirps).

(7) Power Supplies: Convert line power to the direct-current voltages needed to operate the detectors and electronics.
Some of these devices and functions are discussed below in more detail.

19.6.2 Signal Electronics

Noise is present in any detection system and some of it can be eliminated by combining two voltage-level discriminators to form an SCA. An SCA acceptance window that is limited to a particular band of energies can optimize the performance of a radiation monitor. For example, because the intense part of the gamma-ray spectrum of highly enriched uranium lies in a narrow energy region, an acceptance window limited to that gamma-ray energy region gives the best detection sensitivity for uranium, even when such poor spectrometers as organic scintillators are used.

Fig. 19.12 *The components of this vehicle monitor carry out the same basic functions as a pedestrian monitor. (Manufactured by Jomar Systems, Inc., Los Alamos, New Mexico.)*

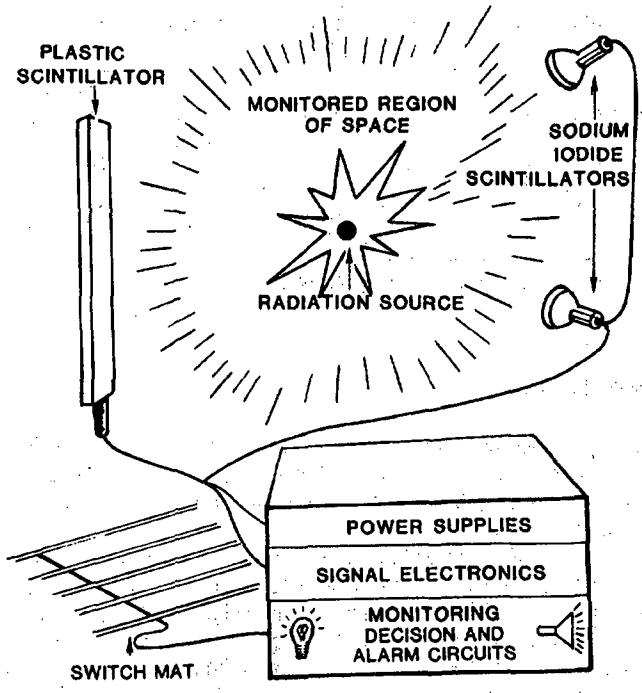

Fig. 19.13 *The basic components of a perimeter radiation monitor. The monitor must detect radiation, sense the presence of an occupant (with the switch mat), make decisions, and announce the result.*

Table 19-1 gives an example of how uranium detection sensitivity varies with the size of the acceptance window. The figure of merit in the table, S divided by the square root of B, relates the net signal S in a particular window to the standard deviation of the background in the same window. The greater the figure of merit, the easier it is to detect a uranium source and the lower is the minimum detectable quantity. For the values shown in the table, source detection was improved by about 50% with an optimum SCA window.

Scalers count the SCA logic pulses during a measurement period. Most scalers have counting intervals that match the average time that signals are present in a monitor. At the end of each counting interval, the scaler transfers its sum to the decision logic. When the monitor is unoccupied, many such sums are averaged to obtain a precise background value. During monitoring, each sum is compared to the alarm threshold.

Table 19-1. Figures of merit and detected mass for three SCA windows[a]

SCA Window (V)	Energy Window (keV)	$S/\sqrt{B}$	^{235}U Mass Detected (g)
0.3-0.85	70-215	7.87	10
0.21-1.5	46-385	6.93	12.2
0.3-7.0	70-1735	6.0	15.2

[a]Source, spherical masses; background, 21 μR/h.

19.6.3 Power Supplies

High voltage for detectors is provided by a regulated electronic circuit that maintains an essentially constant output voltage. To use a single power supply for multiple scintillation detectors, each photomultiplier voltage-divider circuit is provided with a series potentiometer to adjust its gain.

Monitors using NIM electronic modules for amplifier, SCA, and high-voltage power supplies use low-voltage power from the NIM bin. Where microprocessor electronics are used, low-voltage power supplies can operate from trickle-charged batteries. This feature makes the monitor's controller insensitive to short-term power failure. Without back-up power, a monitor must restart after each power loss with some operating delay.

Some kind of back-up line power should be provided for the entire monitor in case of long-term power failure. This requirement is often met by facility back-up power; if not, it can be provided temporarily by commercial power units. In other cases, hand monitoring suffices as a back up during power outage.

19.6.4 Diagnostic Tests

Simple diagnostic tests can identify faults in radiation monitors as soon as they occur. The tests may be performed by separate modules or incorporated in the program of a microprocessor control unit. Background tests simply compare the measured background to high and low thresholds. A malfunctioning monitor may have a high or low background because of an inoperative or noisy detector. Inadvertent shielding of the detector or storage of radioactive material near the monitor will also be detected by a background test. To detect such anomalies as they occur, each new background value is usually checked and, if necessary, flagged by an audible or visual alarm.

More complex diagnostic techniques examine the monitor's counting statistics to determine if the counts originate from radiation detection or noise. Reference 13 describes a long-term analysis method that can diagnose noise even in the presence of sources or varying background intensity.

Variance analysis is suitable for short- or long-term analysis and is also used for detector calibration (Ref. 14). This technique calculates the mean and variance of a group of counts. If these quantities are nearly identical, the variance analysis test quickly

establishes that the detectors are operating properly. Noise can be detected in a single measurement set, and minor noise problems that may influence nuisance-alarm frequency can be detected by averaging the results for many sets.

19.7 MONITOR CALIBRATION

Improper calibration is a common cause of problems such as frequent nuisance alarms and lack of sensitivity. Calibration involves adjusting the detector gains so they all provide the same response to a calibration source and then adjusting the SCA to respond to radiation in the desired energy region. Gas counters require little calibration but scintillation detectors must be calibrated periodically.

19.7.1 Scintillation Detector Calibration

Calibrating a scintillation detector begins by setting the photomultiplier high voltage to a chosen value, typically 1000 V, and continues by adjusting each detector's gain potentiometer to obtain the same pulse-height response for a test source (for example, a 5-μCi ^{137}Cs source). The source is placed in the same way next to each detector and the pulse height is observed at the amplifier output with an oscilloscope. Next, the amplifier gain is adjusted to give the desired pulse amplitude; pulse heights between 2- and 4-V are commonly used for ^{137}Cs.

19.7.2 Single-Channel Analyzer Calibration

Both upper- and lower-level discriminators must be adjusted to form the SCA window. The upper-level discriminator can first be set to a desired value from Table 19-2 by using an oscilloscope. For monitoring plutonium, an upper level of 450 keV is appropriate; for highly enriched uranium, 220 keV.

The lower-level discriminator can be set in the same fashion to 60 keV; however, lower settings that are still above the noise may improve performance. One way to set lower values is to adjust the discriminator while making source-in and source-out intensity measurements until a maximum value of the figure of merit $S/\sqrt{B}$ is achieved

Table 19-2. Gamma-ray pulse heights in NaI(Tl) and plastic scintillators[a]

Gamma-Ray Energy (keV)	NaI(Tl) Detector Pulse Height (V)	Plastic Detector Maximum Pulse Height (V)
662	2	2
450	1.36	1.20
220	0.66	0.42
60	0.18	0.05

[a]Detectors calibrated to 2-V pulse height for 662-keV gamma ray.

(Section 19.6.2). This slow procedure can be replaced by a variance analysis technique for much quicker results. The discriminator is decreased to the point where the variance analyzer just indicates noise, then it is raised slightly to the point where noise is no longer indicated.

19.7.3 Periodic Calibration Checks

A daily test is important to determine whether the monitor is functioning properly. If a low-intensity source (1 μCi of ^{133}Ba) is used for the daily test, both operation and calibration are verified. A more thorough test with nuclear material is performed on a quarterly basis. Additional information on monitor calibration is available in Reference 15.

19.8 MONITOR EVALUATION METHODS

Laboratory evaluation can verify a monitor's ability to detect radioactive material reliably and can reveal shortcomings in design. Summaries of evaluations have been published for pedestrian nuclear-material monitors (Ref. 16), for vehicle nuclear-material monitors (Ref. 7), and for contamination monitors (Ref. 3). These evaluations were carried out with monitors that were operated for long periods without recalibration while their statistical-alarm frequency and detection sensitivity were determined.

Statistical-alarm frequency and sensitivity are interdependent, and determining one has little meaning without determining the other. Statistical-alarm testing requires recording alarms in a constant background environment over a long enough period to observe 10^5 or more decisions. A timing switch is used to operate the monitor periodically, and the background is updated between monitoring periods. The statistical-alarm probability is obtained by dividing the observed number of alarms by the total number of monitoring tests performed. The statistical-alarm probability per passage of an occupant is then the product of statistical alarms per test and the average number of tests per passage. This type of testing ignores background reduction by an occupant, a factor that may overestimate the statistical-alarm frequency in normal operation.

Monitor sensitivity can be determined by observing the probability for a monitor to detect the passage of nuclear material or contamination test sources. The background intensity and the method of passing the test source through the monitor must be regulated, as well as other factors that affect performance. Because there is always some spatial variation in detector efficiency, testing should be done in the least sensitive part of the monitor; for example, at shoe level in a pedestrian monitor. The test source should be carried through the monitor by different individuals using their usual manner of walking. For a general discussion of monitor testing, see Ref. 17.

19.9 EXAMPLES OF PERIMETER MONITORS

19.9.1 Hand-Held Perimeter Monitors

Hand-held contamination monitors usually measure the dose rate for a single type of radiation, although some multipurpose instruments use filters or more than one type of detector to sense different types of radiation. Contamination monitors are simple, inexpensive, analog devices that are operated sporadically and are usually powered by batteries. Three contamination monitors are shown in Figure 19.14. Two of them monitor gamma radiation: the one at the left uses a NaI(Tl) detector and the one at the right uses a large-area Geiger-Mueller counter. The monitor at the center is a prototype, multipurpose instrument having detectors for four types of radiation including neutrons. This instrument (Ref. 18) addresses a need for a versatile monitor having standard field-maintenance and calibration procedures. The sensitivity of hand-held contamination monitors varies a great deal; most sense radiation intensities above 0.1 μR/h, although NaI(Tl) monitors can operate at the natural background intensity of a few μR/h.

The three hand-held nuclear-material monitors shown in Figure 19.15 have scintillation detectors and battery operated electronics; two use NaI(Tl) detectors, and the one at the left uses a plastic scintillator. The instruments usually have rechargeable batteries and are operated continuously to monitor pedestrians and vehicles. Each monitor sounds an audible signal when it senses a significantly increased radiation intensity. Besides their use as perimeter monitors, these highly sensitive gamma-ray detecting instruments can be used as area radiation monitors or as survey monitors for salvaged

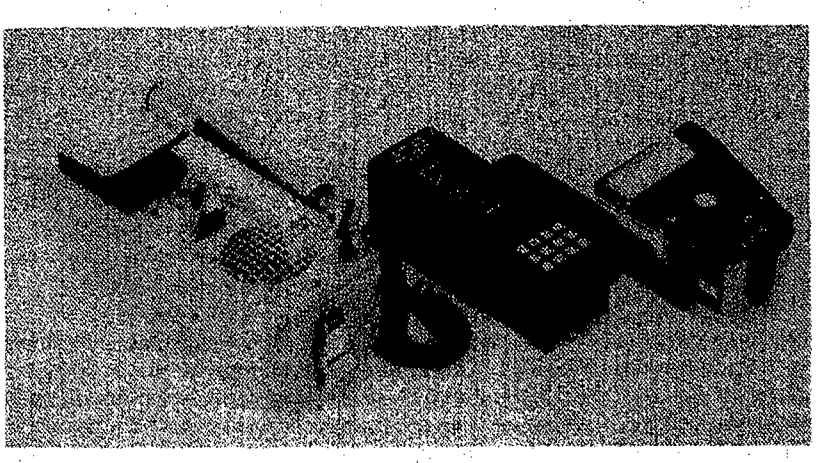

Fig. 19.14 *Three different hand-held contamination monitors. From left: a NaI(Tl) gamma-ray survey meter, a multipurpose monitor with four detector types, and a Geiger-Mueller surface-contamination monitor. (Left- and right-hand units manufactured by Technical Associates, Canoga Park, California.)*

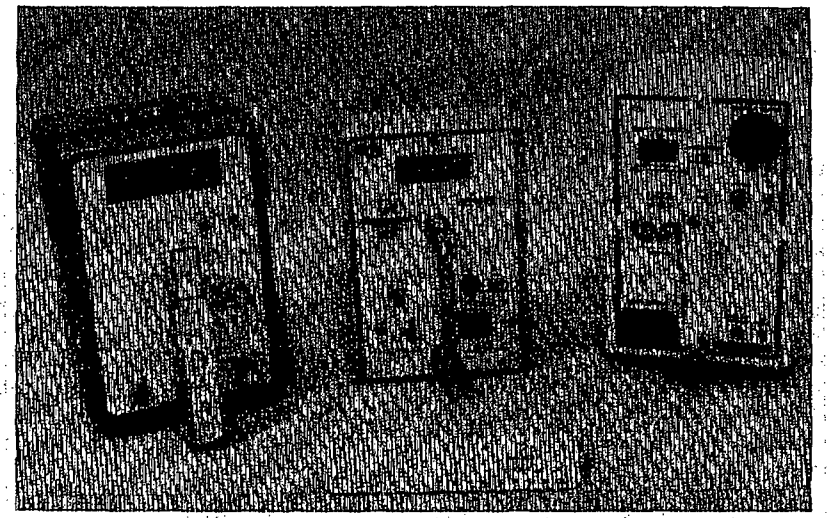

Fig. 19.15 Three hand-held nuclear material monitors that automatically detect significant intensity increases above background. (Left and center units manufactured by TSA Systems, Inc., Boulder, Colorado. Right-hand unit manufactured by CMS, Inc., Goleta, California.)

equipment. They sense radiation intensities of a few μR/h and can detect about 0.5 μCi of ^{137}Cs in a rapid but careful search (Ref. 19). They can detect a few grams of highly enriched uranium or a fraction of a gram of low-burnup plutonium under worst-case conditions. (Worst-case conditions are 25-μR/h background intensity and maximum self-absorption in the nuclear material.) Better performance will always be obtained under routine circumstances. Frequent statistical alarms, one or two per minute, are easily tolerated in these instruments because alarms in a specific area locate the radioactive material. Occasional alarms that are not repeated in the same area do not detract from monitoring effectiveness because they verify that the instrument is operating.

19.9.2 Automatic Pedestrian Monitors

Automatic contamination monitors for use with pedestrians are commercially available as traditional walk-through portals with gas-flow proportional counters that detect quantities below 1 μCi of ^{137}Cs and as high-sensitivity wait-in monitors that detect quantities below 100 nCi of fission or activation products. Figure 19.3 illustrates a portal that achieves high sensitivity by requiring pedestrians to place their body surfaces against the proportional counters. The proximity between body surface and detector and an extended monitoring period both help to achieve high sensitivity.

Nuclear material walk-through monitors (Figure 19.1) can detect less than 10 g of highly enriched uranium and less than 0.3 g of low-burnup plutonium under worst-case operating circumstances. The typical statistical-alarm frequency is 1 per 4000 passages.

19.9.3 Automatic Vehicle Monitors

Automatic contamination monitors for use with vehicles are rare because the interior surfaces of a vehicle usually must be monitored closely. An exception is the roadbed monitor shown in Figure 19.16 that has a detector positioned below the vehicles to sense activated accelerator target material that may be transported from a facility. This Los Alamos monitor alarms at about twice background intensity. It provided the first evidence of contaminated Mexican steel introduced into the United States in 1983.

Automatic vehicle monitors for nuclear material range from simple drive-through portals as shown in Figure 19.17 to the complex station shown in Figure 19.12. Except for detector spacing, vehicle portals are similar to pedestrian portals. Moving-vehicle portals detect intensity increases of about 15% above background; for worst-case conditions, they can detect less than 10 g of low-burnup plutonium with less than 1 statistical alarm per 4000 passages under worst-case conditions.

Vehicles wait in the monitoring station shown in Figure 19.12 for a minute or less. The detectors are located in small groups above and below the vehicle, and each detector group is treated as a separate monitor with its own signal-conditioning and decision-logic electronics. The long monitoring time and the proximity of a detector group to the

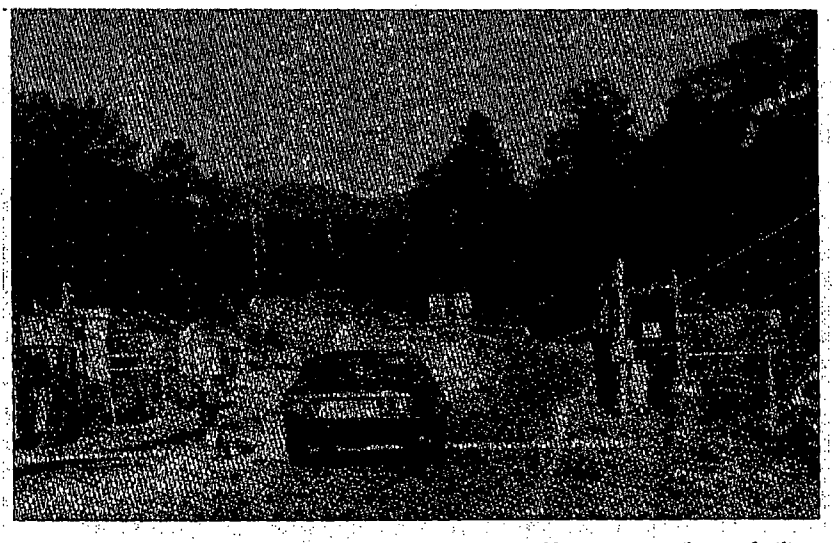

***Fig. 19.16**. This vehicle monitor checks for activated material leaving an accelerator facility. Its underground detector triggers an alarm and photographs the vehicle when it senses a doubling of radiation intensity.*

Fig. 19.17 The nuclear-material portal monitor tests vehicles passing slowly (8 km/h) through the detector columns.

area being monitored lead to high sensitivity; the alarm threshold is about 5% above background to detect nuclear material quantities similar to those detected in pedestrian monitors.

19.9.4 Monitor Performance Summary

Tables 19-3 (Ref. 15) and 19-4 (Ref. 20) summarize the range of performance obtained in different nuclear material monitors. Table 19-3 lists mass detection categories for walk-through pedestrian monitors under worst-case conditions (defined in footnote a and Section 19.9.1) and at a statistical-alarm frequency of 1 per 4000 passages. The masses that can be detected are given for four performance categories, each of which requires particular combinations of detectors, portal spacing, and detection logic complexity.

The four performance categories in Table 19-3 are based on regulatory goals for detecting specified amounts of nuclear material. Category I requires the detection of 1 g of low-burnup plutonium at 25 μR/h background intensity. This goal can be met with small detectors, portal spacings of 80 cm or more, and simple detection methods. Category II requires the detection of 10 g of highly enriched uranium, and Categories III and IV require performance better than present regulatory goals. Categories II through IV all require large detectors, portal spacings of 80 cm or less, and advanced detection algorithms. Note that the detection of smaller masses of nuclear material entails the

Table 19-3. Mass detection categories of walk-through nuclear material monitors (Ref. 15)[a]

Category	Description	Uranium[b](g)	Plutonium[c](g)
I	Standard plutonium	64	1
II	Standard uranium	10	0.29
III	Improved sensitivity	3	0.08
IV	High sensitivity	1	0.03

[a]Test conditions are 25 μR/h background intensity, standard metallic test source attached below an interior ankle of an individual walking at his normal speed, and pace adjusted to swing the source through the monitor. Test results must give 95% confidence that the probability of detection is 50% or greater at a statistical-alarm rate of 1/4000 passages or better.
[b]Highly enriched uranium.
[c]Low-burnup plutonium freshly separated from daughter products, or shielded with 0.4- to 0.8-mm-thick cadmium.

Table 19-4. Worst-case mass detection sensitivity in nuclear material vehicle monitors (Ref. 20)

Vehicle Monitor Type	Minimum Detected Mass[a]		Statistical-Alarm Rate[b]
	Low-Burnup Plutonium (g)	HEU (g)	
Hand-held	3-9	100-300	1/100
Vehicle portal	10	1000	1/4000
Monitoring station	0.3	40	3/1000

[a]Under worse-case conditions in a 1-ton van that is stationary except in the 5-m-wide portal where it travels at 8 km/h. Background intensity is 20 μR/h, and shielding by vehicle structures is highly significant. Detection implies a detection probability of 50% or greater. Better performance is obtained under routine circumstances.
[b]Statistical rates are for an empty monitor.

detection of smaller signals. Hence, the higher categories are more sensitive to process-related background variations. Category III and IV monitors are only appropriate when the background is relatively constant.

Table 19-4 summarizes mass detection sensitivities for different types of vehicle monitors. These performance estimates are also for worst-case conditions (defined in footnote a and Section 19.9.1).

REFERENCES

1. EG&G Inc., Santa Barbara Division (R. W. Hardy, R. B. Knowlen, C. W. Sandifer, and W. C. Plake), US Patent No. 3,670,164, 1972.

2. W. E. Kunz, "Portable Monitor for Special Nuclear Materials," Los Alamos Scientific Laboratory publication LASL-77-18 (1977).

3. M. Littleton, "High Sensitivity Portal Monitors—A Review," Institute of Nuclear Power Operations report 82-001-EPN-01 (1982).

4. US Department of Energy Order 5632.2, "Physical Protection of Special Nuclear Material," 1979.

5. US Atomic Energy Commission Regulatory Guide 5.7, "Control of Personnel Access to Protected Areas, Vital Areas, and Material Access Areas," 1973.

6. P. E. Fehlau, J. C. Pratt, J. T. Markin, and T. Scurry, Jr., "Smarter Radiation Monitors for Safeguards and Security," *Nuclear Materials Management* XII (Proceedings Issue), 294 (1983).

7. P. E. Fehlau, C. Garcia, Jr., R. A. Payne, and E. R. Shunk, "Vehicle Monitors for Domestic Perimeter Safeguards," Los Alamos National Laboratory report LA-9633-MS (1983).

8. A. Wald, *Sequential Analysis* (Dover Publications, Inc., New York, 1973).

9. P. E. Fehlau, K. L. Coop, and J. T. Markin, "Application of Wald's Sequential Probability Ratio Test to Nuclear Materials Control," in Proceedings of Joint Specialists Meeting, ESARDA/INMM, Ispra, Italy, 1984.

10. C. N. Henry and J. C. Pratt, "A New Containment and Surveillance Portal Monitor Data Analysis Method," *ESARDA* 10, 126-131 (1979).

11. C. R. Hurlbut, "Plastic Scintillators—A Survey," presented at American Nuclear Society winter meeting, Nov. 1985 (available from Bicron Corp., Newbury, Ohio).

12. P. E. Fehlau and G. S. Brunson, "Coping with Plastic Scintillators in Nuclear Safeguards," *IEEE Transactions on Nuclear Science* NS-30, 158 (1983).

13. E. Appel, M. Giannini, and A. Serra, "A New Method of Self-Diagnosis for Pulse Measuring Systems," *Nuclear Instruments and Methods* 192, 341 (1981).

14. K. V. Nixon and C. Garcia, "Hand-Held Pulse-Train-Analysis Instrument," *IEEE Transactions on Nuclear Science* NS-30, 331 (1983).

15. P. E. Fehlau, "An Applications Guide to Pedestrian SNM Monitors," Los Alamos National Laboratory report LA-10633-MS (1986).

16. P. E. Fehlau, T. E. Sampson, C. N. Henry, J. M. Bieri, and W. H. Chambers, "On-Site Inspection Procedures for SNM Doorway Monitors," Los Alamos Scientific Laboratory report LA-7646 (NUREG/CR-0598) (1979).

17. P. E. Fehlau, "Standard Evaluation Techniques for Containment and Surveillance Radiation Monitors," *ESARDA* 15, 195 (1982).

18. C. J. Umbarger, G. O. Bjarke, B. H. Erkkila, F. Trujillo, D. A. Waechter, and M. A. Wolf, "New Generation of Radiacs: Small Computerized Multipurpose Radiation Monitors," *IEEE Transactions on Nuclear Science* NS-30, 528 (1983).

19. P. E. Fehlau, "Hand-Held Search Monitor for Special Nuclear Materials, User's Manual," Los Alamos National Laboratory publication LALP-84-15 (1984).

20. P. E. Fehlau, "An Applications Guide to Vehicle SNM Monitors," Los Alamos National Laboratory report LA-10912-MS (1987).

20

Attribute and Semiquantitative Measurements

N. Ensslin and H. A. Smith, Jr.

20.1 INTRODUCTION

Nuclear material measurements are usually quantitative assays where the measurement goal is to fix a numerical value on the amount of nuclear material present. The assays are performed with the highest accuracy and precision possible, and prior knowledge about the samples may be extensive. There are however a number of measurement challenges that can be met with more qualitative information on samples about which prior knowledge may vary widely. Some examples follow:

- characterization of unlabeled or mislabeled samples
- go/no-go determination of nuclear material content for recovery, burial, transport, or criticality safety
- rapid inventory verification to check consistency of declared values
- confirmation of shipper values by the receiver
- location of nuclear material holdup
- process monitoring
- control of material movement.

Most of these tasks can be accomplished with qualitative or semiquantitative measurements that are rapid enough to save time, money, and personnel exposure.

Nondestructive assay techniques are well suited to these types of measurements because they are usually fast, nonintrusive, and capable of measuring the package as a whole. If the nondestructive measurement is careful and accurate, it may be considered a *material assay.* If the measurement is completely qualitative and only determines some signature, fingerprint, quality, or characteristic of the material, it may be considered an *attribute measurement.* Between these extremes are semiquantitative measurements such as waste characterization, monitoring of material movement, rapid inventory verification, and identification and measurement of material holdup . These semiquantitative measurements are often very important to the day-to-day operation of nuclear fuel-cycle facilities.

Section 20.2 summarizes nuclear material attributes and how they can be measured. The remainder of the chapter discusses semiquantitative measurements of waste (Section 20.3), confirmatory measurements for inventory verification and shipping (Section 20.4), and holdup measurements (Sections 20.5 and 20.6). These semiquantitative measurements are more than attribute measurements but less than full quantitative assays. For discussions of two other measurement problems that fall into the

category of semiquantitative measurements, see Chapter 18 on irradiated fuel assay and Chapter 19 on portal monitoring.

20.2 MEASUREMENT OF NUCLEAR MATERIAL ATTRIBUTES

The most fundamental task in measuring nuclear material attributes is simply to identify the presence or absence of nuclear material in a sample. In this regard the term "nuclear material" refers to all forms and combinations of uranium and plutonium, to radioactive sources, and to americium, thorium, and other radioactive elements. The primary radiation attributes (regardless of material type) are listed below:

- alpha radiation
- beta radiation
- gamma radiation
- infrared radiation (heat)
- total neutron radiation
- coincident neutron radiation
- high fission cross section for thermal neutrons (yielding prompt and delayed gamma rays and neutrons).

(Information on the radiation emission rates of these attributes is summarized in Chapters 1, 11, and 21 and in Refs. 1 and 2.)

Nuclear material in elemental form is also very dense and strongly attenuates gamma radiation. A further attribute of uranium and plutonium is the discontinuities in their x-ray absorption cross section at the K- and L_{III}-absorption edges (Chapter 9). Of all the attributes listed above, only the gamma-ray transmissions at the absorption edges provide a unique identification. In practice, however, the fissile character of uranium and plutonium is essentially unique, since fissile isotopes of other elements would not be expected in fuel-cycle facilities. Gamma-ray spectroscopy also provides an unambiguous identification, especially if the spectra are measured with high resolution. Although the other attributes mentioned are necessary features of nuclear material, they are not sufficient for unique identification.

In a full-fledged nuclear material assay, almost all of the attributes cited above are measured at one time or another. A simple way to view attributes measurements is to regard them as incomplete assays. The data are taken in the same way as for complete assays but the measurements are made more quickly, with less precision, and often without any use of the absolute calibration of the instrument. Even semiquantitative confirmatory or verification measurements may involve only a determination of the relative magnitude of the attribute responses from sample to sample. Table 20-1 summarizes the measurement instruments that are commonly available in nuclear facilities and the attributes they can reveal. Some active assay instruments are included for completeness.

Attribute measurements can be a very effective tool for characterizing, verifying, or monitoring nuclear material. Measured one at a time, nuclear material attributes provide simple answers to inventory questions. Measured in combination, they can provide very reliable or even unique information with a minimum of effort.

Table 20-1. Measurement instruments and the attributes they reveal

Instrument	Attribute
Visual inspection	packaging, history, color
Scales	weight, density
Alpha counter	presence of alpha particles; contamination
Geiger counter	gross beta/gamma activity; presence of U, Pu, or Am
Gamma spectrometer	gamma-ray spectrum; U, Pu signature; enrichment; burnup
Radiograph	density, distribution, shape
Densitometer	density; x-ray absorption edges; U, Pu signature
Calorimeter	heat output; presence of high alpha activity; warmth implies Pu, Am
Passive total neutron counter	neutron emission; presence of spontaneous fissions or (α,n) reactions
Passive neutron coincidence counter	spontaneous or induced fissions; presence of Pu or Cf likely
Active neutron coincidence counter	induced fissions; presence of U or Pu likely
Californium shuffler	delayed neutrons from induced fissions; presence of U or Pu likely
Fuel-rod scanner	delayed neutrons or gamma rays; presence of U or Pu likely

20.3 QUANTITATIVE SCREENING OF WASTE

20.3.1 Purpose

Nuclear fuel-cycle facilities often generate large quantities of waste that is only slightly contaminated or that is assumed to be contaminated because of its proximity to other materials. This type of waste is usually packaged in 55-gal. drums or larger containers and sent to retrievable storage in shallow burial sites. To minimize the volume of waste that will ultimately have to be retrieved, it is important to determine the level of radioactivity in the waste at the point of generation. Current regulations permit burial of waste in nonretrievable storage if the level of radioactivity is below 100 nCi/g of waste. (The average level of radioactivity in US soil is about 10 nCi/g. Until recently, the cutoff for permanent burial was set at this limit.) The purpose of nondestructive screening of low-level waste is to supplement or replace administrative controls for waste sorting at the 100-nCi/g level. Present experience suggests that the volume of nonretrievable waste can then be reduced by a factor of 10 or more.

Nondestructive measurement of low-level waste is difficult because the containers used are large [ranging from 2-cu-ft boxes (57 L) to 55-gal. drums (208 L) to 4- by 4- by 7-ft crates (3300 L)] and the quantities of nuclear material involved are small. A radiation level of 100 nCi/g is equivalent to about 160 mg of ^{239}Pu, 1 g of ^{233}U, or 4.4 kg of ^{235}U in 100 kg of waste. Because of the large container sizes and the low level of radioactivity,

nondestructive measurements emphasize sensitivity rather than accuracy. The measurement goal is often 1- to 10-nCi/g sensitivity and ±20% accuracy. This level of accuracy is considered sufficient for waste screening, with the proviso that large systematic underestimations must be avoided so that significant quantities of recoverable nuclear material are not lost and so that the actual quantity of buried nuclear material does not exceed criticality safety guidelines.

20.3.2 Gamma-Ray and Neutron Sensitivities

Table 20-2 summarizes the approximate detectability limits of nondestructive assay techniques for ^{235}U and plutonium (10% ^{240}Pu, 90% ^{239}Pu) (Refs. 3 through 5). The detectability limits are given for 1000-s measurements with the signal being three standard deviations above background (99% confidence level). The detectability limit is a function of the detector response per gram of nuclear material and of the ambient background (as given by Equations 15-7 and 15-8 in Chapter 15). The limits quoted in Table 20-2 are based on reasonable estimates for background contributions. The detectability limit is also a function of the detector size and efficiency. The limits in Table 20-2 are measured or extrapolated values for detectors that can accommodate 55-gal. drums for cases where no lead shielding is required to reduce the gamma-ray background from fission products in the waste.

In general, passive gamma-ray counting by segmented scanning is not quite sensitive enough to screen waste at the 100-nCi/g level. For contamination levels above 1 g, segmented gamma-ray scanning is the most reliable technique for quantitative measurements of ^{235}U and ^{239}Pu up to the limit of penetrability of the 186- and 414-keV gamma rays. For 57-L cardboard boxes containing waste with an average density of 0.1 g/cm^3, passive counting of L x rays has a demonstrated sensitivity of less than 1 nCi/g (Ref. 6).

Although passive gamma-ray measurements of nuclear waste are usually biased low because of gamma-ray self-attenuation, passive neutron measurements are usually

Table 20-2. Nuclear waste detectability limits[a] (Refs. 3 through 5)

Nondestructive Assay Technique	Efficiency (%)	^{235}U	Pu (10% ^{240}Pu)
Passive gamma-ray counting	1	100 mg	100 mg
Passive thermal neutron counting	15	N/A	18 mg
Passive thermal neutron coincidence counting	15	N/A	6 mg
Passive fast neutron coincidence counting	25	N/A	300 mg
Active thermal neutron coincidence counting	15	10 g	35 g
Active fast neutron coincidence counting	25	70 mg	130 mg
Photoneutron interrogation (3×10^8 n/s)	0.25	8 mg	6 mg
Delayed neutron counting (2×10^9 n/s source)	15	6 mg	14 mg
Differential die-away neutron counting	14	1 mg	1 mg

[a]1000-s counting time; signal 3σ above background; no fission-product gamma-ray shielding; nuclear material in oxide form.

biased high because of additional neutrons from (α,n) reactions. Examples of (α,n)-reaction effects are given in Section 15.5.1. Active neutron techniques are not subject to the effects of passive backgrounds if the interrogation source is strong enough. However, active techniques can be strongly biased either high or low depending on the effects of matrix moderation and absorption on the incoming and outgoing neutrons. For a given waste-screening application, the choice of measurement technique should be made on the basis of cost, simplicity, sensitivity, and penetrability.

20.4 CONFIRMATORY MEASUREMENTS

20.4.1 Purpose

The transfer and storage of unirradiated nuclear materials is a frequent and large-scale activity at many NRC and DOE facilities. Many safeguards issues arise during the process of shipping, receiving, and inventory verification. Measurements can help to confirm that (a) material has not been diverted in transit, (b) the item identification is correct, (c) there is no undue radiation hazard to workers, and (d) inventory records are credible. Such confirmatory measurements may be simpler than measurements made for accountability purposes. For example, they require less time and less unpacking or repackaging of material. They also may be more versatile. However, in general, they are less accurate. Confirmatory measurements determine such attributes as weight, gamma-ray spectrum, total neutron radiation, and enrichment that—taken as a whole—are very difficult to imitate.

When nuclear material is transferred from one facility to another, present regulations require that the receiver verify the piece count, identification, and gross weight of the items in the shipment. Normally the receiver should perform accountability measurements on the items within 10 calendar days. In practice, however, this is often difficult to achieve because of (a) limitations in the availability of personnel and nondestructive assay equipment, (b) the length of time required for performing chemical analysis and transferring shipments into and out of storage vaults, and (c) the radiation exposure to personnel during packing and unpacking. Also, difficulty in measuring a relatively small number of scrap materials can delay closing the material balance on the shipment. One safeguards approach to alleviating these problems is to make confirmatory measurements at both the shipping facility and the receiving facility with similar or identical instruments (Ref. 7). Such measurements can confirm that there are no missing, incorrect, or bogus items in the shipment.

When nuclear material is stored at a facility, present regulations require periodic inventory of the entire facility and its storage vault. Confirmatory measurements made during that time on a random sample of the inventory can help identify mislabeled items and increase the credibility of the inventory process (Ref. 8).

20.4.2 Nondestructive Assay Options

Nondestructive assay techniques are well suited for confirmatory measurements because of their speed and their ability to measure an entire item. In some cases, it is also

possible to measure the shipping container itself, although with some loss of precision and accuracy. Options based on nondestructive assay of plutonium or uranium radiation attributes are summarized in this section.

For most plutonium samples, a combination of calorimetry and gamma-ray spectroscopy provides the best available accuracy: 0.5 to 2% for homogeneous materials. However, this instrumentation is usually reserved for accountability measurements because of its relatively high cost, complexity, and low throughput. Passive gamma-ray counting of the 414-keV ^{239}Pu peak in either a far-field geometry or by segmented scanning is a simpler option for materials of low density. However, most plutonium-bearing materials that are attractive for diversion are too dense for gamma-ray counting and are best measured by passive neutron counting. The technique is relatively simple, and can sometimes be applied to 30- or 55-gal. shipping drums without unpacking their contents. The neutron well counter should have uniform efficiency over the volume of the sample. Also, the electronics deadtime should be small and well known so that count ratios can be determined accurately.

Confirmatory neutron measurements of plutonium can be based on total or coincident counting, but coincident counting is a more specific attribute. Counting times are in the range of 100 to 1000 s. Typical accuracies for quick confirmatory measurements are 1 to 10% for well-characterized materials, 25% for impure scrap, and 50% for heterogeneous materials with high (α,n) rates (Ref. 8). However, the repeatability of raw measurement results is approximately 1%. It would be very difficult technically to construct a bogus item with the same weight, total neutron count rate, and coincident neutron count rate as a real item. This is also true for heterogeneous materials with high alpha decay rates where the assay accuracy is poor but the neutron attribute measurement is quite precise.

For passive neutron measurements of plutonium, the following guidelines show how the observed count rates are related to specific material attributes:

(1) The total neutron count rate is proportional to fertile content but also depends on the (α,n) reaction rate. If the fertile content can be determined from the coincident count rate, then any "excess" total count rate can be attributed to chemical compounds or impurities.

(2) The neutron coincidence rate is proportional to fertile content, but may be enhanced by induced fissions.

(3) The coincidence/totals ratio is a function of sample self-multiplication and, indirectly, fissile content. For heterogeneous plutonium scrap with very strong (α,n) reactions, the coincidence/totals ratio may provide the best possible measure of ^{239}Pu content, perhaps within 10%, if an iterative correction for ^{240}Pu content is made (Ref. 9).

(4) The difference in coincident neutron response with and without a cadmium liner in the well counter, divided by total neutron response, is a measure of fissile content (Section 17.3.3 and Ref. 10).

Confirmatory measurements of uranium are more difficult than those of plutonium. The alpha-particle emission rates are not high enough to permit heat production measurements. Enrichment measurements are possible with the 186-keV gamma ray, but they sample only the surface of the material and require a well-collimated geometry outside of the shipping drum. Far-field gamma-ray measurements can be used for low-density materials. They have also been used to confirm high-density materials to within a factor of 2 (Ref. 8).

The measurement of bulk uranium samples requires the use of active neutron systems, with the simplest being the Active Well Coincidence Counter (AWCC) (Section 17.3.1). In the thermal mode the AWCC is appropriate for samples containing from 5 to 100 g of ^{235}U. In the fast mode the instrument is limited to samples containing 50 g of ^{235}U or more, even for 1000-s counting times, because of the high accidental coincidence background of the interrogation sources. Good coupling must be maintained between the sources and the uranium, which usually requires the use of small containers. Thus, active coincidence counting of uranium is not as versatile or as easy to apply as passive coincidence counting of plutonium.

Two specific applications of active neutron counting of uranium are summarized below:

(1) Mixed uranium/plutonium samples: The passive coincidence response is proportional to ^{240}Pu but may be enhanced by induced fission in ^{235}U. Correction for self-multiplication can compensate for induced fission but will not provide a direct measure of ^{235}U content. Determination of ^{235}U or ^{239}Pu fissile content is not practical by active coincidence counting and requires more complex active neutron systems.

(2) Highly enriched uranium in UF_6 cylinders: The coincidence/totals ratio is proportional to ^{235}U content to within 2 to 10% (Section 17.3.4).

20.4.3 Recent Experience

Several examples follow of recent confirmatory measurements at Hanford, Rocky Flats, Los Alamos, and Savannah River. The examples illustrate different approaches and different levels of accuracy; they are arranged roughly in order of increasing degrees of confirmation.

Verification of a wide variety of stored nuclear material has been obtained by performing confirmatory measurements on a random sample of the inventory (Ref. 8). Passive neutron coincidence counting of plutonium and passive gamma-ray counting of uranium in a far-field geometry were the preferred techniques. Roughly 5% of the measurements were invalidated because of poor counting statistics, unsuitable material matrices or geometries, or lack of appropriate standards. Another 5% were judged as not confirmed because of results inconsistent with those obtained earlier on similar items. For the latter 5%, a superior instrument or technique was used to perform an accountability measurement. In about half of these cases the more accurate accountability measurement verified that the original item label was indeed incorrect.

Confirmation of incoming plutonium scrap metal has been accomplished by passive neutron coincidence counting of "bird cage" shipping containers (Ref. 11). Measurement of the shipping container itself rather than the individual interior items resulted in an eightfold reduction in work hours and a thirtyfold reduction in radiation exposure. Measurement accuracy was roughly 5% (1σ) for the shipping container as a whole compared to 2.5% (1σ) for the individual items. The receiver was able to verify the incoming shipment within three working days.

Confirmatory measurements of plutonium oxide have been performed by both the shipper and the receiver, each using a neutron coincidence counter of different design (Ref. 8). The counters measured the individual cans outside of their shipping drums. No attempt was made to normalize the response of one counter to the other. Instead, the

confirmation was based on the ratio of the responses. The total neutron count ratios were consistent to 0.5% (1σ), and the coincidence count ratios were consistent to 1.5% (1σ) before and after shipment. The receiver also compared his measurement of the actual plutonium mass as obtained by coincidence counting with that obtained by calorimetry for eight batches of cans. This comparison was not as accurate, having a 4.1% (1σ) scatter. The reduced accuracy of the mass determination is attributed to differences in settling, oxide density, moisture, or isotopics between batches. For example, the coincidence response of a 1-kg plutonium oxide can will change by about 1% for a 5% change in density (see Figure 16.14 in Chapter 16).

Shipper and receiver confirmatory measurements of plutonium-bearing ash, sand, slag, crucible, and oxide have been carried out by segmented gamma scanners of different design (Ref. 8). Standards were fabricated by the shipper, calibrated on the shipper's calorimeter, and sent to the receiver. The receiver's measurements of ^{239}Pu content agreed with the shipper's measurements to within 1 to 4% (1σ).

Confirmatory measurements of impure plutonium metal and oxide have been made with two identical neutron coincidence counters that measure 30-gal.-drum shipping containers. Figure 20.1 shows cutaway views of one of the counters. The counters are the first instruments designed specifically for confirmatory measurements (Ref. 12). The design features two doors, drum rollers, a drum positioner, and void spaces in the polyethylene wall to flatten the vertical efficiency profile. Normalization of response between shipper and receiver is accomplished by exchange of ^{252}Cf sources, source measurement data, and background measurement data. The confirmatory measurements consist of three 100-s total neutron counts. Initial results provided a shipper/receiver verification within 2 to 3% for oxide and within 1% for metal (Ref. 11). There is some evidence of a small bias that may be due to settling of the contents during shipment.

20.5 NUCLEAR MATERIAL HOLDUP

The term "holdup" refers to the accumulation of nuclear material inside the processing equipment of nuclear facilities. Other common terms for such material are "hidden inventory," "normal operating loss," and "in-process inventory." The choice of terminology depends in part on the application or point of view. For example, the nuclear material that remains in the facility after the runout of all bulk product may be called "in-process inventory." The material that remains after thorough brushing, wiping, acid leaching, and rinsing may be called "fixed holdup."

Because of the high economic value of nuclear material and the need to ensure radiation safety and criticality safety and to safeguard against theft or diversion, it is important to minimize holdup, to measure or model its magnitudes, and to remove it. Holdup causes and mechanisms, holdup magnitudes, and holdup modeling and measurement techniques are discussed in the remaining sections of this chapter.

20.5.1 Causes and Mechanisms

Nuclear material tends to accumulate in cracks, pores, and regions of poor circulation within process equipment. In addition, the internal surfaces of pipes, tanks, ducts,

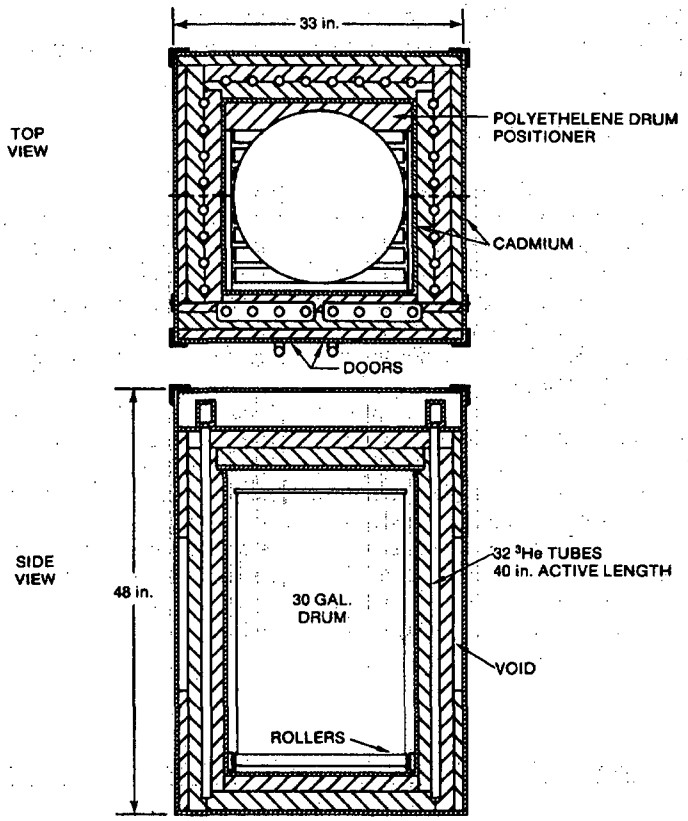

Fig. 20.1 *Cutaway view of one of the Confirmatory Measurement Counters built specifically for shipper and receiver confirmatory measurements of plutonium in 30-gal. shipping drums (Refs. 11 and 12).*

furnaces, gloveboxes, and other equipment can acquire appreciable deposits. When the internal surface areas are large, the total holdup can be enough to affect the plant inventory difference (Ref. 13). The amount of holdup depends on the nature of the process and on the physical form of intermediate solutions, precipitates, and powders. Also, process upsets can lead to large, rapid, and unexpected depositions of material.

Some of the mechanisms for material accumulation (Ref. 14) are summarized below:

(1) gradual sedimentation and settling of fine particles in regions of poor circulation or low flow rate

(2) chemical reaction of nuclear materials with interior walls or migration of the materials into the walls

(3) solid or liquid product formation or precipitation resulting from inadvertent chemical reactions

(4) electrostatic deposition and buildup of charged particulates
(5) splashing, bubbling, or caking of materials resulting from unregulated chemical reactions.

20.5.2 Magnitude of Holdup

From the holdup mechanisms outlined in the preceding section it is possible to identify regions where holdup may be high. These include elbows, junctions, and seams in pipes and ducts; regions of stagnant flow or regions with turbulent flow; equipment with large interior surfaces such as Raschig-ring tanks, filters, gloveboxes, and furnaces; and wet operations with corrosive acids or high concentrations of nuclear material. The magnitude of the holdup in these regions is difficult to estimate because it depends on such factors as plant layout, frequency of process upsets, maintenance and cleanout procedures, and throughput.

Some typical holdup magnitudes observed in equipment at several uranium and plutonium processing facilities are given in Table 20-3. The numbers shown are typical of regions of high holdup only, but they suggest that extrapolation over all of the major process areas in a facility can yield tens or hundreds of kilograms of total holdup. As a fraction of total throughput, the holdup can be in the range of 0.1 to 0.2% even after thorough destructive cleaning. When nuclear material is first introduced into a new facility, the initial holdup can be 1 to 10% of the initial throughput. Because facility design can affect the amount of holdup, the Nuclear Regulatory Commission has proposed design considerations to minimize holdup (Refs. 15 through 17).

Table 20-3. Typical magnitudes of holdup in facility equipment

Gloveboxes	0 - 50 g
Gloveboxes (after destructive cleaning)	2 g/m^2
Grinders	1 - 100 g
V-blenders	1 - 50 g
Glovebox prefilters	2 - 100 g
Final filters	10 - 100 g
Equipment interiors (after routine cleaning)	10 - 50 g/m^2
Pipes (after destructive cleaning)	0.3 g/m
Ducts (no cleaning)	1 - 100 g/m
Glass columns	1 g
Annular tanks	1 - 10 g
Raschig-ring filled tanks (after rinsing)	1 - 500 g
Dissolver trays	10 - 500 g
Small calciners	5 - 50 g
Furnaces	50 - 500 g
Furnace trays	1 - 10 g
Incinerators	1000's g
Concrete spill basins	1000's g

20.5.3 Statistical Modeling

Determining the location of material held up in process equipment and recovering it is very difficult. Even measuring the quantity of holdup is difficult and subject to many uncertainties (see Section 20.6). A possible alternative method for obtaining some of the holdup data required for periodic inventory is to estimate the holdup through statistical modeling (Ref. 14). This approach would begin with careful, controlled holdup measurements (either nondestructive or cleanout) of a process operation under known conditions of temperature, flow rate, throughput, and so forth. The measured holdup would be modeled as a function of the important variables. Then future holdup in this process operation could be estimated and predicted on the basis of the model.

A series of controlled holdup deposition and measurement experiments have been conducted to test the validity of this approach (Ref. 14). Figure 20.2 shows the layout of the equipment used during one such experiment designed to determine the holdup of uranium dust as a function of material characteristics, airflow rate, and dusting material. A mechanical dust-generating apparatus located inside the glovebox provided a source of airborne dust. Radioactive tracers were incorporated into the uranium oxide at a concentration of about one part per billion in order to increase the accuracy of the gamma-ray holdup measurements. Comparison with cleanout showed that the holdup measurements were accurate to about 20%.

Some of the data from the experiment are illustrated in Figure 20.3 (Ref. 14). This figure shows filter holdup increasing as a function of airflow and throughput. The holdup can be modeled as a quadratic function of throughput, as illustrated by the smooth curves in the figure. These data provide a good example of holdup that increases

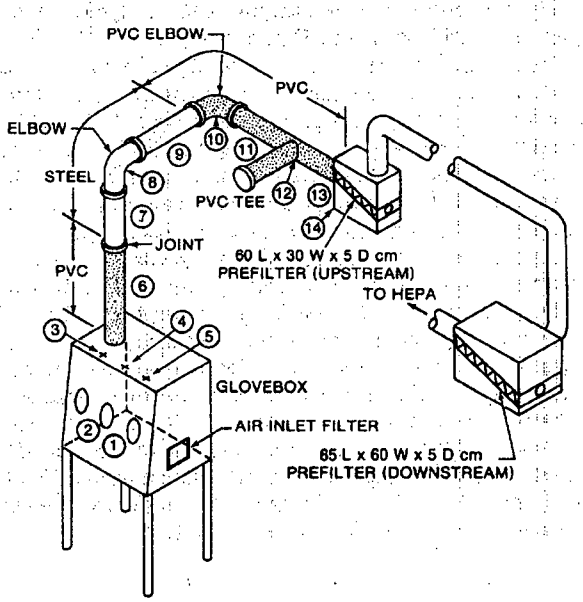

Fig. 20.2 Layout of equipment used during a controlled holdup deposition and measurement study, showing the glovebox where dust is generated, ducts, filters, and the location of 14 measurement points (Ref. 14).

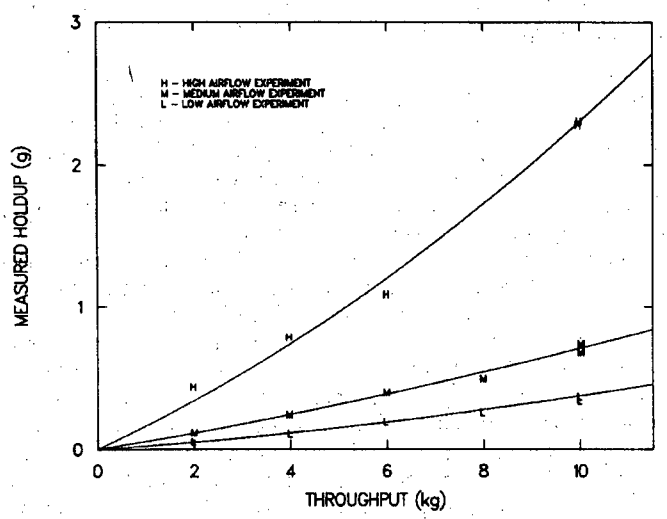

Fig. 20.3 Holdup of fine U_3O_8 powder as a function of airflow rate and total throughput as measured at the exhaust air filter (location 14 in Figure 20.2) during a controlled dust-generation experiment (Ref. 14).

steadily with increasing throughput. Another typical pattern observed in controlled experiments is illustrated in Figure 20.4 (Ref. 14). Holdup inside a calciner increased rapidly as a linear function of throughput until a coating was built up. Then the holdup fluctuated about a steady-state value until operating conditions changed. In this case, an increase in calciner operating temperature from 700°C to 900°C caused another increase in holdup. During the period of steady-state operation the data were fitted to a Kalman filter model, as indicated by the smoothed curve in the middle of the figure.

The behavior illustrated in Figure 20.4 is somewhat representative of a process facility as a whole. When nuclear material is first introduced into a new facility, holdup may build up rapidly as equipment becomes coated and cracks become filled. During subsequent years of steady operation and routine cleanout, holdup increases more slowly and may tend to approach some asymptotic value.

The controlled holdup deposition and measurement experiments described above suggest that holdup estimation models can be useful if they are based on good initial measurements, if process operation is stable, and if the data base is updated periodically. Under these conditions the frequency and number of measurements can be reduced. Controlled-holdup experiments also provide an example of the best accuracy obtainable in holdup measurements made under ideal conditions. The accuracies reported for these experiments (Ref. 14) are included in the summary of published holdup measurement accuracies given in the table in Section 20.6.7.

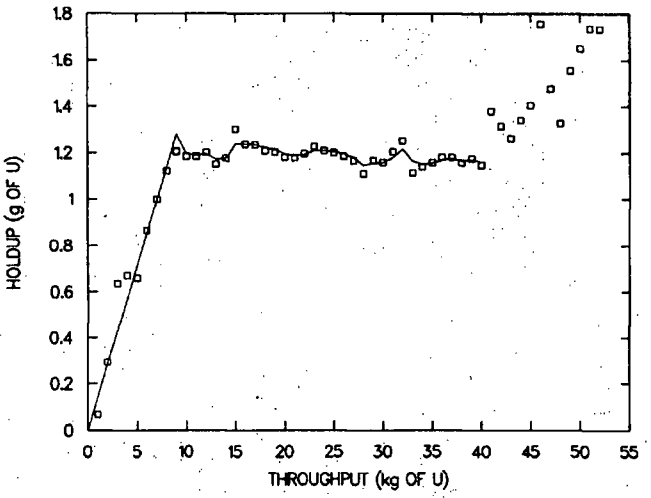

Fig. 20.4 *Holdup of uranium oxide in a calciner as a function of throughput, as determined during a controlled holdup experiment. This figure is an example of the leveling out of holdup at a steady-state value after an initial buildup. At a throughput of 40 kg, an increase in furnace temperature resulted in another buildup (Ref. 14).*

20.6 THE ART AND SCIENCE OF HOLDUP MEASUREMENTS

The measurement of nuclear material held up in processing plants is both an art and a science. It is subject to the constraints of politics, economics, and health and safety requirements, as well as to the laws of physics. For the practitioner, the measurement process is often long and tedious and is performed under difficult circumstances, as suggested by Figure 20.5. The work combines the features of a detective investigation and a treasure hunt, as aptly described by Zucker and Degen (Ref. 18). In fact, the cost of a thorough holdup measurement campaign is in the range of $10 per gram of detected material—comparable to the price of gold.

Nuclear material held up in pipes, ducts, gloveboxes, heavy equipment, floors, walls, and so forth, is usually distributed in a diffuse and irregular manner. It is difficult for the assayist to define the measurement geometry, identify the form of the material, and measure it without interference from adjacent sources of radiation. For these reasons holdup measurement is an art that requires experience, imagination, a sense of proportion, and luck.

Holdup measurement also requires a scientific knowledge of radiation sources and detectors, calibration procedures, geometry, and error analysis. These topics are discussed in the remainder of this chapter.

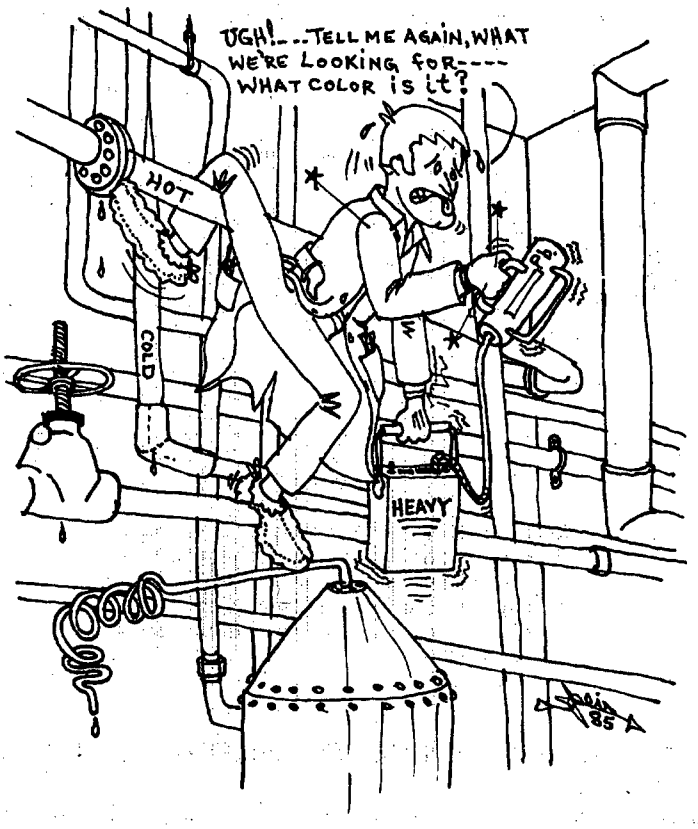

Fig. 20.5 Holdup measurements are both an art and a science and, as this cartoon illustrates, are usually conducted under difficult circumstances.

20.6.1 Useful Radiation Signatures

Table 20-4 lists gamma-ray and neutron radiation sources that are penetrating enough to measure holdup of uranium and plutonium. The tabulated neutron energies are approximate averages for the actual spontaneous fission, induced fission, or (α,n) reaction neutron spectra. The neutron intensities are approximate values (calculated from Tables 11-1 and 11-3 in Chapter 11) that indicate the relative ease or difficulty of assaying various isotopes or compounds.

Most holdup measurements of uranium and plutonium are based on passive detection of the 186-keV ^{235}U gamma-ray peak and the 375- to 414-keV ^{239}Pu complex. Both portable sodium iodide detectors and thermoluminescent dosimeters (TLDs) are usually set up to respond to these gamma rays because they are the highest energy (and therefore the most penetrating) gamma rays available at useful intensities. These

Table 20-4. Useful radiation signatures for holdup measurements

Isotope	Technique	Signature	Intensity
^{235}U	passive gamma	186-keV gammas	43 000 γ/g-s
	active neutron	1-MeV neutrons	
UO_2	passive neutron	2-MeV neutrons	0.03 n/g-s[a]
UO_2F_2	passive neutron	1-MeV neutrons	2.0 n/g-s[a]
UF_6	passive neutron	1-MeV neutrons	5.8 n/g-s[a]
^{238}U	passive gamma	1001-keV gammas	100 γ/g-s
Pu	passive heat	infrared	
^{239}Pu	passive gamma	414-keV gammas	34 000 γ/g-s
		375-keV gammas	36 000 γ/g-s
		129-keV gammas	140 000 γ/g-s
^{240}Pu	passive neutron	2-MeV neutrons	1000 n/g-s
PuO_2	passive neutron	2-MeV neutrons	120 n/g-s[b]
PuF_6	passive neutron	1-MeV neutrons	7300 n/g-s[b]

[a]High-enriched uranium with 1% ^{234}U.
[b]Low-burnup plutonium with 0.03% ^{238}Pu, 6.5% ^{240}Pu, 92.5% ^{239}Pu.

intensities are sufficient to measure holdup with a sensitivity of 1 g. When uranium is mixed with thorium, measurement of the 186-keV ^{235}U peak may be difficult because of interferences from 200- to 300-keV radiation from thorium daughters (Ref. 19). When plutonium is measured with sodium iodide detectors, it is customary to set a window from 375 to 450 keV. This window will collect most 414-keV gamma rays and many 375-keV gamma rays but will exclude 332-keV gamma rays from ^{241}Pu or ^{241}Am (Ref. 13).

Large quantities of ^{238}U can be assayed with the low-intensity but very penetrating 1001-keV gamma rays from ^{234m}Pa, a daughter of ^{238}U. After chemical separation of uranium, about a hundred days are required for the activity to come into equilibrium at the intensity given in Table 20-4.

Passive neutron counting may be helpful when it is necessary to measure holdup in pumps, valves, or other heavy equipment that is too dense to permit the escape of gamma rays. Neutrons penetrate metal and large holdup deposits better than gamma rays do, but they require more nuclear material to produce a strong signal. Neutron measurements are more difficult to interpret because neutrons do not have a unique energy, are difficult to collimate, are subject to multiplication and moderation effects, and can be increased in number by (α,n) reactions in chemical compounds. These effects cause neutron measurements to overestimate the amount of holdup, whereas self-attenuation effects cause gamma-ray measurements to underestimate the amount of holdup.

As indicated in Table 20-4, passive neutron counting of uranium in oxide or fluoride form is possible for reasonably large quantities. The neutron signal is due to (α,n) reactions in oxide or fluoride compounds. Active assay of ^{235}U is also possible but is very sensitive to nearby reflectors, moderators, and absorbers, and the response is

roughly proportional to the inverse fourth power of the uranium-to-instrument distance (Ref. 20). Passive neutron measurements of plutonium are quite practical, with spontaneous fission in ^{240}Pu being the primary neutron source unless large quantities of fluoride compounds are present.

The possible use of infrared scanning devices to locate plutonium holdup is being studied at several facilities. The primary source of infrared radiation is the heat generated in the alpha decay of ^{238}Pu. Infrared scanning of equipment to locate "hot spots" is probably feasible, but it is not known if quantitative measurements can be made.

20.6.2 Detectors and Readout Instrumentation

Because of the difficult circumstances under which holdup measurements must be carried out, the instrumentation should be portable, rugged, and easy to use. Simple push-button operation and low power consumption is also desirable in case battery-powered operation or operation inside plastic bags is necessary. All these requirements are satisfied by most of the equipment used today, which consists primarily of survey meters, portable multichannel analyzers, and collimated sodium iodide detectors.

Survey meters are geiger counters or small collimated or uncollimated sodium iodide detectors that respond to beta or gamma radiation. They are used for rapid surveys of large areas to locate holdup concentrations, and are usually equipped with audible rate meters. Quantitative holdup measurements are then performed with sodium iodide detectors (see Figure 20.6). The resolution and efficiency of these detectors, about 7 to 10%, is usually adequate for holdup measurements. Typical crystal sizes are 5-cm diam by 5-cm depth for plutonium measurements and 5-cm diam by 1-cm depth for uranium measurements. The detectors are collimated to limit their field of view. The collimators should consist of about 1.5 cm of lead for plutonium measurements and 0.5 cm of lead for uranium measurements in order to absorb at least 98% of the incident radiation (Refs. 13 and 21). An equivalent thickness of lead should cover the back of the detector to reduce background radiation. Also, the front face of the detector should be covered with 1.5 mm of lead (for plutonium measurements) and 0.8 mm of cadmium (for uranium and plutonium measurements, placed inside the lead) to reduce the count rate from x rays.

Commercially available electronics packages for sodium iodide detectors include the Eberline Stabilized Assay Meter (Chapter 4), the Brookhaven Stabilized Assay Meter (Ref. 18), and the Rocky Flats Assay Meter (Ref. 22), which uses Ludlum electronics. These packages are all portable, stabilized dual-channel analyzers. Portable multichannel analyzers are useful for identifying holdup of unknown composition and are now becoming available in packages small enough to serve as replacements for the stabilized assay meters. Commercial instruments include the Nuclear Data ND-6, the Canberra Series 10, and the Davidson Model 2056-4K.

The shielded neutron assay probe detector described in Chapter 15 can be used for neutron measurements of holdup (Ref. 23). The low front-to-back detection ratio, which ranges from 2 to 4, requires careful attention to background and the use of a collimator plug shield (Ref. 13). In general, 10 to 15 cm of polyethylene will reduce the intensity of

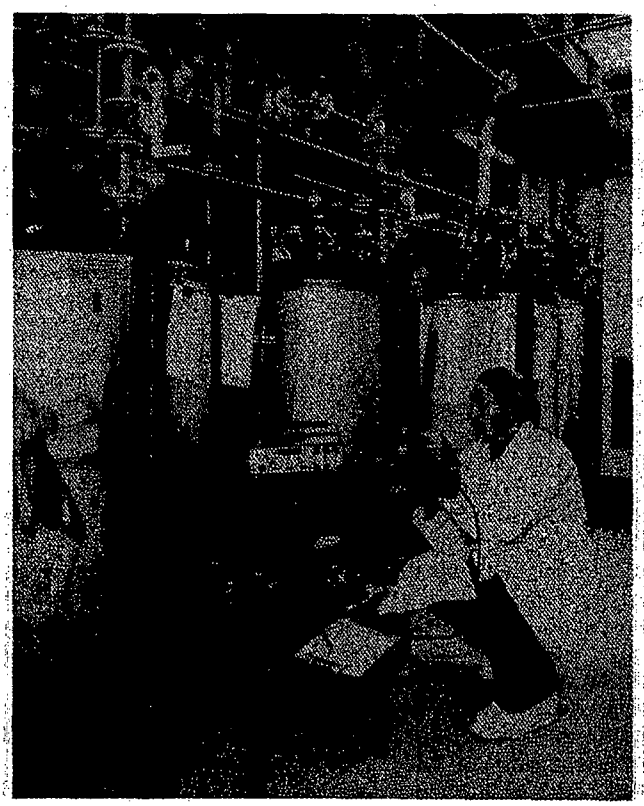

Fig. 20.6 *An example of the use of a collimated sodium iodide detector and a portable electronics package to measure holdup in Raschig-ring filled tanks.*

fission neutrons by a factor of 10. Large slab detectors can be employed for holdup measurements where portability is not a concern. Slab detectors have been used to estimate total room holdup (Ref. 24) and holdup in large calciners (Ref. 25).

Thermoluminescent dosimeters (TLDs) have been placed around the outside of gloveboxes (Ref. 26) and in the otherwise inaccessible interiors of calciners (Ref. 27). Lithium fluoride and calcium fluoride are common TLD crystals. Lithium fluoride has the advantage of greater availability, whereas calcium fluoride has a higher sensitivity and does not require a complex annealing cycle. For either material a graded shield is required to discriminate against low-energy x rays.

20.6.3 Holdup Measurement Procedures

Planning holdup measurements begins with several technical and nontechnical considerations. One important factor is whether or not measurements are to be periodic, routine, and can be started before hot operation of the facility commences. Where possible, measurements in advance of hot operation are very helpful in defining holdup collection zones, measuring backgrounds, measuring attenuation through equipment walls, and calibrating for difficult geometries. Brackets, fixtures, and special shields can be manufactured and installed for later use. Another important consideration is whether the holdup measurements are to be absolute or relative. Absolute measurements are more desirable because they yield values for the total grams held up in the facility. However, a change in holdup is easier to measure than the actual holdup because systematic errors tend to cancel. Periodic relative measurements may be sufficient for monitoring routine cleanout operations or for ensuring that holdup is not affecting the plant's monthly inventory balance.

The holdup measurement campaign itself consists of the following steps:

(1) The measurement team studies the plant process and consults with plant operators to identify areas of potentially high holdup.

(2) A quick radiation survey with collimated or uncollimated survey meters indicates those areas where most material is held up.

(3) Most of the remaining measurement time is allocated to those areas with the majority of material. Other areas are measured more lightly or estimated by extrapolation. Note however that large areas with low holdup per unit area may contain large amounts of material. Conversely, localized hot spots may contain relatively small absolute quantities.

(4) The holdup detectors are collimated and calibrated using known standards. Small check sources are used to monitor instrument stability. Each detector is calibrated for point, line, and area collection zones.

(5) Quantitative measurement of holdup in the facility begins at this point. Each item of equipment to be measured is characterized as a point, line, or area holdup collection zone. The field of view of the detector is limited so that each collection zone can be resolved from its neighbors and from the background. The measurement team records the date, time, counting interval, collection zone identification, assumed collection geometry, source-to-detector distance, type and thickness of intervening material, and count rate. Each holdup measurement should be long enough to yield several hundred or several thousand counts. Then a background measurement is made by using a collimator plug or a movable shield or by moving the detector sideways so it misses the zone but views the same background.

(6) To obtain an estimate of uncertainty, the collection zone should be measured from a different direction, from a different distance, by assuming a different geometry (for example, point vs area), or by using a different measurement technique. In this matter the judgment and experience of the team members are paramount. They must guess at the distribution of material and choose measurement distances and calibration geometries accordingly in order to average holdup fluctuations and use their time to best advantage.

(7) Although attenuation corrections, gram values of holdup, and error estimation can be calculated later, the team members should do some rough calculations on the spot. This is very important to ensure that they are spending their time where it is most needed and are not making large measurement errors.

20.6.4 Point, Line, and Area Calibrations

During a measurement campaign each holdup collection zone is characterized as a point, line, or area source so that the observed count rate can be easily converted to grams of nuclear material. For example; a pump, filter, or valve may be considered a point source if the holdup is distributed over distances that are small compared to the source-to-detector distance and if the holdup is entirely within the detector field of view; a long pipe or duct may be considered a line source; a wall, floor, or broad rectangular duct that extends well beyond the detector field of view may be considered an area source. Sometimes the choice of point, line, or area calibration is not obvious and is a matter of judgment or experience. Sometimes the measurement team may try two or even all three possibilities and compare the final results for the holdup. Or the team may measure the count rate as a function of distance from the collection zone to help establish the proper calibration choice. For a point source, the measured response falls off as the inverse square of the distance ($1/r^2$). For a line source, the response falls off as the inverse of the distance ($1/r$). For a uniform area source, the response is independent of distance. This last case is not as obvious as it seems; it is predicated on the finite viewing angle of the collimated detector, which views an area that increases as r^2, thereby canceling the $1/r^2$ falloff in response with distance.

Point, line, and area calibrations can of course be obtained from point sources, line sources, and area sheet standards, as described in Section 20.6.5. However, it is also possible, and usually easier, to obtain all three calibrations from a single point source. The procedure for doing this with a gamma-ray detector is described below.

(1) Collimate the detector by recessing it in its lead shield by one or two crystal diameters to obtain a viewing half-angle $\theta/2$ of 15 to 30 degrees (see Figure 20.7). This collimation must now remain fixed because the line and area calibration constants are strongly dependent on the field of view.

(2) Place the point calibration source at a fixed distance r_0 (typically 1 to 2 m). Determine the count rate C_0. Now move the source sideways in fixed steps of width s (typically 10 to 20 cm), as illustrated in Figure 20.7. Determine the count rate C_i at each step i, with each count rate corrected for background. The result is a response curve similar to the example in Figure 20.8.

(3) The curve of detector response as a function of sideways displacement falls off because of the finite viewing angle of the collimated detector. If the collimation were perfect, with viewing half-angle $\theta/2$, the detector could view a length $L \approx r_0\theta$ of a line source or an area $A \approx \pi r_0^2\theta^2/4$ of an area source. Actually, the equivalent length L of a uniform line source that gives the same count rate as the integrated response curve is

$$L = 2s \sum C_i/C_0 - s \quad . \tag{20-1}$$

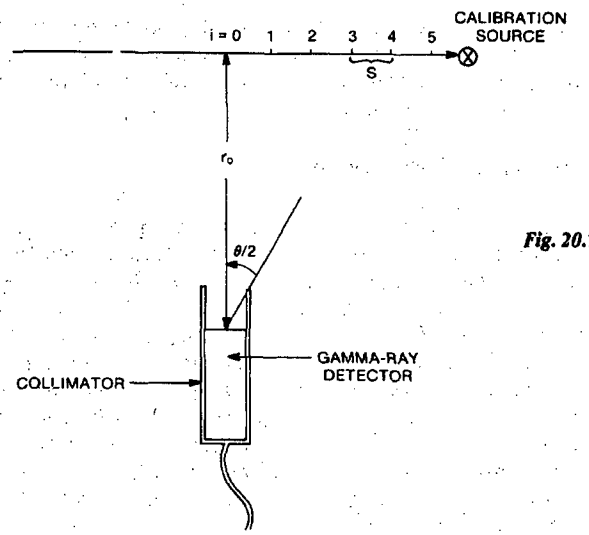

Fig. 20.7 The geometry required for calculating line and area calibrations. At a fixed distance r_0 the point calibration source is moved sideways in fixed steps s.

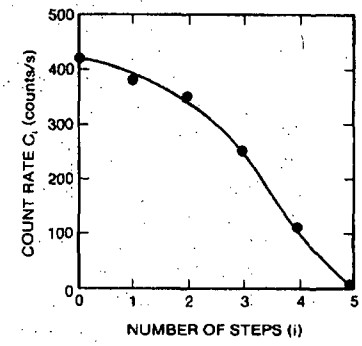

Fig. 20.8 Collimated gamma-ray detector response as a function of sideways displacement in number of steps. The response falls off because of the finite viewing angle of the collimated detector. The equivalent length L and equivalent area A viewed by the detector can be calculated from this curve.

(4) The equivalent area A of a uniform area source that gives the same count rate as the integrated response curve is

$$A = \sum a_i C_i / C_0 \quad . \tag{20-2}$$

To obtain this equation we have imagined that at each sideways position i of the point source, the measured response is representative of that which would be obtained over an annular ring of inner radius $(i - 1/2)s$ and outer radius $(i + 1/2)s$. The area a_i of each annulus is $2i\pi s^2$, except that $a_0 = \pi s^2/4$.

(5) If the point source standard contains m_0 grams of nuclear material, the point calibration for holdup is

$$m(\text{holdup}) = m_0 \frac{C}{C_0} \frac{r^2}{r_0^2} \text{ (grams)} \quad (20\text{-}3)$$

where C is the observed count rate corrected for background, r is the detector-to-holdup distance, and m is the mass of holdup in grams.

(6) The line calibration is

$$m(\text{holdup/m}) = \frac{m_0}{L} \frac{C}{C_0} \frac{r}{r_0} \text{ (g/m)} \quad . \quad (20\text{-}4)$$

C_0 must be measured at the distance r_0 used to determine L.

(7) The area calibration is

$$m(\text{holdup/m}^2) = \frac{m_0}{A} \frac{C}{C_0} \text{ (g/m}^2\text{)} \quad . \quad (20\text{-}5)$$

C_0 must be measured at the distance r_0 used to determine A.

(8) Note that the preceding equations assume that the same standard, of mass m_0, is used to determine L, A, and C_0. This is convenient in practice but not essential. One standard could be used for the measurements required to calculate L and A with Equations 20-1 and 20-2, and another could be used to provide m_0 and C_0 for Equations 20-3 through 20-5.

20.6.5 Calibration Standards and Check Sources

In principle, the geometry of a calibration standard should be the same as the geometry of the unknown being measured. For holdup measurements this is usually not possible. Therefore, in practice, point, line, and area standards are used to approximate equipment geometries. Also, as described in the preceding section, a single small calibration standard can be used to obtain point, line, and area calibrations. For gamma-ray measurements, 1 to 5 g of ^{235}U or ^{239}Pu is sufficient. Even for these small gamma-ray standards, self-absorption is significant and must be corrected for (see, for example, Table 20-5). For neutron measurements, 10 to 20 g of plutonium (6 to 20% ^{240}Pu) gives an adequate count rate. In the neutron standard, self-absorption and self-multiplication are negligible, but it is important to establish by calculation or measurement that the neutron production rate in the standard is representative of actual plant material.

To ensure the stability and reliability of portable radiation detectors in a plant environment, it is necessary to carry along small check sources. The performance of the detectors should be checked against these sources every 1 to 4 h. The point calibration standards described in the preceding paragraph (or even somewhat smaller sources) are suitable for this application.

Some holdup measurement teams have fabricated sheet standards to supplement their point calibration standards. One common technique involves sprinkling oxide powder on transparent plastic sheets coated with adhesive (Ref. 18). Uranium oxide has also been mixed with silicon rubber and deposited on sheets (Ref. 19). The sheet standards can be used for area calibrations or rolled up in pipes and ducts for line calibrations. The sheet standards may be difficult to fabricate or use, however, because the oxide may be deposited nonuniformly and may become stiff, causing it to crack or flake.

In any facility there may be special material holdup geometries that cannot be approximated by point, line, or area sources. Sometimes it is possible to mock up these geometries with combinations of sheet standards and point standards. Another alternative is to put known standards inside the actual process equipment, although this can usually be done only before the equipment is placed into operation.

20.6.6 Self-Absorption and Attenuation Corrections

A chronic problem in passive gamma-ray holdup measurements is the tendency to underestimate holdup because of self-absorption in the material itself or attenuation in intervening materials. Self-absorption of the gamma rays in uranium or plutonium can be very severe, as indicated by the two examples in Table 20-5. Although the assayist cannot correct for self-absorption because the density and distribution of the material are unknown, he may be able to make some allowance for self-absorption in estimating errors.

Table 20-5. Estimated self-absorption and attenuation corrections for common materials encountered in holdup measurements

Intervening Material	Correction for 186-keV Gamma Rays	Correction for 414-keV Gamma Rays
1-g-cube UO_2	2.95	
10-g-cube UO_2	5.97	
1-g-cube PuO_2		1.28
10-g-cube PuO_2		1.66
Rubber glove	1.05	1.04
0.25-in. Plexiglas	1.11	1.08
1.0-in. water	1.42	1.30
0.25-in. aluminum	1.24	1.18
8-in. × 8-in. HEPA filter	1.43	1.31
0.063-in. steel	1.20	1.12
0.125-in. steel	1.44	1.25
0.250-in. steel	2.08	1.55
0.063-in. lead	6.83	1.44

Attenuation of the gamma rays by intervening pipe walls, gloveboxes, or other materials can be determined by calculation or by transmission measurements. A transmission measurement is illustrated in Figure 20.9, where a source (typically ^{137}Cs) is positioned behind a duct. The measurement procedure, calculation of transmission, and conversion to a self-attenuation correction factor is the same as that given in Chapter 6. The procedure is rarely used during a holdup measurement campaign because it is time-consuming, physically awkward, and requires different electronic settings to measure the 662-keV cesium peak. Instead, it is usually sufficient to calculate the attenuation by estimating the thickness and composition of the intervening materials.

Table 20-5 provides examples of gamma-ray transmission through common materials and the associated attenuation correction. Although in practice the attenuation correction is only an estimate, it is very important to make this estimate for *every* holdup measurement until it is known by experience where the correction can be neglected. Otherwise the holdup measurement is merely a lower limit on the amount of material actually present.

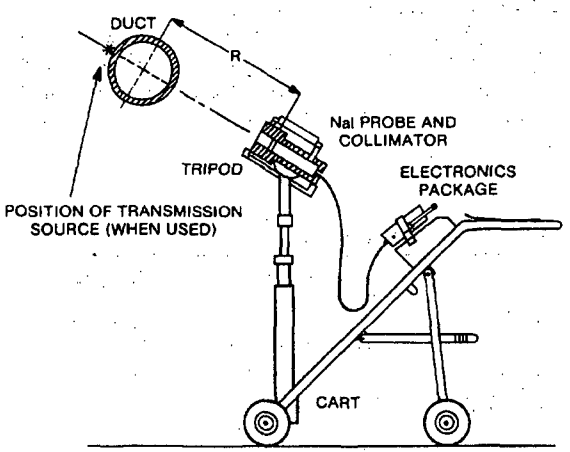

Fig. 20.9 Holdup measurement of a duct showing placement of transmission source for attenuation correction measurement.

20.6.7 Error Estimation

Both the art and science of holdup measurements are involved in the process of estimating measurement errors. These errors are large and numerous; their causes are summarized below in a somewhat subjective ordering of decreasing importance:

(1) Unknown material distribution, which affects the source-to-detector distance and the validity of the chosen point, line, or area calibration.

(2) Self-absorption in the material or its matrix.

(3) Gamma-ray attenuation by intervening materials.

(4) Background interference from distant line-of-sight objects or from adjacent, unresolved material.
(5) Detector instability or improper calibration.
(6) Unrepresentative standards.
(7) Statistical imprecision.
(8) Uncertainty in material isotopic composition.

Statistical imprecision is the only source of error that can be treated in a rigorous fashion; it is usually negligible compared with other errors.

The most important technique for error estimation available to the measurement team is that of measuring each collection zone in several different ways. After each measurement is properly corrected for distance, background, attenuation, and so forth, and a gram value for holdup is obtained, the different values should be averaged together. The measurement standard deviation can be estimated or calculated from the range of values.

To estimate the accuracy of a series of holdup measurements, the holdup must be measured both before and after a cleanout campaign. If the actual amount of material removed can be determined by sampling and chemical analysis or by other nondestructive assay techniques, then the measurement accuracy can be calculated. Previous calibrations can be updated, and error estimates can be reassessed.

Table 20-6 gives a brief summary of published comparisons of holdup measurements and cleanout campaigns in existing facilities; the overall accuracy of holdup measurements can be estimated from the data. In general, the accuracy of holdup measurements is ±50%, although better results can be obtained for favorable geometries or carefully controlled measurement campaigns.

Table 20-6. Typical accuracy of holdup measurements

Reference	Material	Location	Measurement Technique	Accuracy (±) (%)
19	HEU oxide	ducts	passive gamma	10-20
		filters	passive gamma	50-100
23	PuO_2	gloveboxes	passive gamma	10
			passive neutron	15
24	PuO_2	gloveboxes	passive gamma	50
		total rooms	passive neutron	50
26	PuO_2	gloveboxes	TLDs	20
14	HEU oxide	ducts	passive gamma	20
		precipitator	passive gamma	15
		calciners	passive gamma	20
		pipes	passive gamma	10
		pumps	passive gamma	25
28	UF_6	enrichment cascade	passive gamma	50

REFERENCES

1. D. Rogers, Ed., *Handbook of Nuclear Safeguards Measurement Methods,* NUREG/CR-2078 (US Nuclear Regulatory Commission, Washington, DC, 1983).

2. M. Anderson and J. Lemming, "Selected Measurement Data for Plutonium and Uranium," Mound Laboratory report MLM-3009 (1982).

3. T. Crane, "Measurement of Uranium and Plutonium in Solid Waste by Passive Photon or Neutron Counting and Isotopic Neutron Source Interrogation," Los Alamos Scientific Laboratory report LA-8294-MS (1980).

4. T. Crane, "Versatile System for Measuring Nuclear Waste in 55-Gal. Drums," in "Safeguards and Security Status Report, February—July 1983," J. Shipley and D. Smith, Eds., Los Alamos National Laboratory report LA-9595-PR (1983), pp. 24-29.

5. J. Caldwell, D. Close, T. Kuckertz, W. Kunz, J. Pratt, K. Haff, and F. Schultz, "Test and Evaluation of a High-Sensitivity Assay System for Bulk Transuranic Waste," *Nuclear Materials Management* XII, 75 (1984).

6. D. Close, T. Crane, J. Caldwell, W. Kunz, E. Shunk, J. Pratt, L. Franks, and S. Kocimski, "Advances in Measurement of Alpha-Contaminated Wastes," *Proc. American Nuclear Society Topical Meeting on the Treatment and Handling of Radioactive Waste,* Richland, Washington, April 19-22, 1982, p. 292.

7. C. A. Coulter, "Safeguards Uses of Confirmatory Measurements," Proceedings of the Inst. of Nuclear Mat. Manage., Albuquerque, New Mexico (July 1985).

8. R. S. Marshall, R. P. Wagner, and F. Hsue, "Experience with Confirmation Measurement at Los Alamos," LA-UR-85-2667, Proceedings of the Inst. of Nuclear Mat. Manage., Albuquerque, New Mexico (July 1985).

9. H. Menlove, "Passive/Active Assay of PuF_4 and (α,n) Salts," Los Alamos National Laboratory memorandum Q-1-84-161 to N. Ensslin (February 1984).

10. H. Menlove and A. Keddar, "Field Test and Evaluation of the Passive Neutron Coincidence Collar for Prototype Fast Reactor Fuel Subassemblies," Los Alamos National Laboratory report LA-9449-MS (1982).

11. J. Cadieux, C. Denard, and P. Deason, "Confirmatory Measurement Experiences at the Savannah River Plant," Proceedings of the Inst. of Nuclear Mat. Manage., Albuquerque, New Mexico (July 1985).

12. J. Gilmer, "Confirmatory Measurements Counter for Shipper-Receiver Verification," Proceedings of the Inst. of Nuclear Mat. Manage., Albuquerque, New Mexico (July 1985).

13. NRC Regulatory Guide 5.23, "In-Situ Assay of Plutonium Residual Holdup," Rev. 1 (February 1984).

14. K. K. S. Pillay, R. Picard, and R. Marshall, "Estimation Methods for Process Holdup of Special Nuclear Materials," NUREG/CR-3678, LA-10038 (June 1984).

15. NRC Regulatory Guide 5.8, "Design Considerations for Minimizing Residual Holdup of Special Nuclear Material in Drying and Fluidized Bed Operations" (May 1974).

16. NRC Regulatory Guide 5.25, "Design Considerations for Minimizing Residual Holdup of Special Nuclear Material in Equipment for Wet Process Operations" (June 1974).

17. NRC Regulatory Guide 5.42, "Design Considerations for Minimizing Residual Holdup of Special Nuclear Material in Equipment for Dry Process Operations" (January 1975).

18. M. Zucker and M. Degen, "Holdup Measurement for Nuclear Fuel Manufacturing Plants," *Nuclear Materials Management* X, 239 (1981).

19. B. Disselhorst, J. Glancy, and D. Brush, "Survey Techniques for Measuring ^{235}U," General Atomic Company report GA-A14426 (1977).

20. N. Ensslin and E. Sanford, "An Active Neutron Holdup Measurement Technique," in "Program Status Report, Safeguards and Security Research and Development, February—July 1981," Los Alamos National Laboratory report LA-9110-PR (1982), pp. 13-15.

21. NRC Regulatory Guide 5.37, "In-Situ Assay of Enriched Uranium Residual Holdup," Rev. 1 (October 1983).

22. J. Lawless, "The Rocky Flats Assay Meter," Rockwell International, Rocky Flats Plant report SSS-81-1 (1981).

23. C. Kindle, "In-Situ Measurement of Residual Plutonium," *Nuclear Materials Management* V (3), 540 (1976).

24. J. Tape, D. Close, and R. Walton, "Total Room Holdup of Plutonium Measured with a Large-Area Neutron Detector," *Nuclear Materials Management,* V (3), 533 (1976).

25. T. Crane, "Richland/Hanford PUREX: Screw Calciner Holdup Monitor," in "Safeguards and Security Progress Report, January—December 1983," Los Alamos National Laboratory report LA-10170 (1984), p. 16.

26. H. Preston and W. Symons, "The Determination of Residual Plutonium Masses in Gloveboxes by Remote Measurements Using Solid Thermoluminescent Dosimeters," United Kingdom AEA report AEEW-R1359, Winfrith, England (1980).

27. R. Marshall, N. Ensslin, R. Picard, and R. Siebelist, "Summary Report on Uranium Holdup Estimation," Los Alamos National Laboratory document Q-4/82-489, p. 66, April 1982.

28. R. Walton, "The Feasibility of NDA Measurements in Uranium Enrichment Plants," Los Alamos Scientific Laboratory report LA-7212-MS (1978).

21

Principles of Calorimetric Assay

R. Likes

21.1 INTRODUCTION

Calorimetry is the quantitative measurement of heat. It measures the transfer of energy from one system to another caused by temperature differences. Applications of calorimetry include measurements of the specific heats of solids and liquids, the heats of vaporization and combustion, and the rate of heat generation (power) from radionuclides. For the last mentioned application, radiometric calorimeters are used. They are specifically designed to measure the power associated with alpha, beta, or gamma decay of radioactive materials. The technique was first used in 1903 to determine the heat produced from radium.

Methods of calorimetry are now being applied with precision and accuracy to the passive nondestructive assay of nuclear materials, especially plutonium and tritium. This chapter discusses the calorimetric assay of plutonium. The important features and advantages of calorimetric assay are listed below (Refs. 1 and 2):

(a) The entire sample can be measured.

(b) The assay is independent of sample geometry (only equilibrium time is affected).

(c) The assay is independent of matrix material composition and distribution, including nominal moisture concentrations.

(d) The assay is independent of nuclear material distribution within the sample, including the effects of sample self-attenuation.

(e) Electric current and potential measurements are directly traceable to National Bureau of Standards (NBS) reference materials.

(f) Calorimetric assay discriminates between uranium and plutonium isotopes in most cases (only plutonium is assayed).

(g) Calorimetric assay is applicable to a wide range of material forms (including metals, alloys, oxides, fluorides, mixed oxides, waste, and scrap). Representative plutonium standards are not needed.

(h) Calorimetric assay is comparable to chemical assay in precision and accuracy if the isotopic composition is well characterized.

(i) Calorimetric assay is a completely nondestructive assay procedure when coupled with high-resolution gamma-ray spectroscopy isotopic analysis.

Calorimetric assay is based on accurate temperature measurements and requires good temperature stability and control. In general the technique is more accurate but less rapid or less portable than other nondestructive assay techniques described in this book. It can often provide accurate reference measurements for improving the calibration of other assay techniques such as neutron coincidence counting (Ref. 3).

Calorimetric assay is most precise for materials with high plutonium concentrations such as powders, fuel pellets, and metals. Calorimeters are being used extensively for nuclear materials accountability and for shipper-receiver confirmatory measurements of plutonium. When applied to concentrated, homogeneous plutonium-bearing materials, calorimetry is comparable in accuracy to weight plus chemical analysis with precisions approaching 0.1%. For high-density scrap, calorimetry plus gamma-ray spectroscopy can approach a precision and accuracy of 1% if the scrap has homogeneous isotopic composition.

This chapter discusses the principles of heat production, specific power determination, calorimeter types, methods of operation, and basic sources of assay error. Chapter 22, Calorimetric Assay Instruments, describes existing calorimeters of various types, including small calorimeters for laboratory use and bulk assay calorimeters for in-plant applications.

21.2 HEAT PRODUCTION IN RADIONUCLIDES

The energy associated with the spontaneous decay of radioactive isotopes consists of the kinetic energy of the alpha and beta particles emitted, the electromagnetic energy of the gamma rays, and the recoil energy of the daughter product, which collectively is termed the disintegration energy of a particular isotope. If the daughter product is not in the ground state as a result of the decay, additional gamma-ray and internal conversion electron energy will be released when the daughter decays to the ground state. Each radioactive isotope has a specific disintegration energy associated with its particular decay scheme; for example, ^{239}Pu decays to ^{235}U + alpha + 5.15 MeV.

Radiometric calorimeters operate on the principle that almost all of the energy associated with the decay of radioactive materials placed in the sample chamber is absorbed in the form of heat within the calorimeter. The radioactive decay of all uranium and plutonium isotopes generates heat, but only the plutonium isotopes, because of their shorter half-lives and thus higher specific activities, generate heat at a high enough rate (power) to be measured accurately. Most of the plutonium decay energy is released as alpha or beta particles and converted to heat energy through absorption. A small portion is carried away by neutrons and gamma rays, however this portion is generally less than 0.01% of the total decay energy (Ref.1).

Calorimetric assay of plutonium is the process of measuring with a calorimeter the rate of heat released by the radioactive decay of the plutonium and determining the proper analytical factor for converting the calorimetric power measurement to mass. This section describes in detail the production of heat in plutonium. Section 21.3 describes the calculations required to determine the specific power—the factor that relates the power measurement to plutonium mass.

21.2.1 Alpha Particles

The dominant radioactive decay mode of the plutonium isotopes is alpha decay. The mechanism by which heavy particles such as alpha particles transmit their kinetic energy to surrounding material is usually ionization. In its penetration of material until the loss of all of its initial energy, the alpha particle undergoes a large number of "collisions,"

with smaller and smaller amounts of energy loss per collision. These small energy losses are of the order of magnitude characteristic of infrared radiation, that is, heat energy.

The range of alpha particles in various materials relative to their range in air is given by the Bragg-Kleeman rule, Equation 11-2 in Chapter 11. The range of 5- to 6-MeV alpha particles is on the order of 5 μm in common materials. Thus virtually all of the energy released by alpha decay will remain within the sample as heat.

21.2.2 Beta Particles

The determination of energy losses in matter is much more complicated with beta decay or electron capture than with alpha decay. With beta decay, a variety of competing mechanisms are involved: ionization, bremsstrahlung radiation, neutrino production, and conversion electron emission. The energy deposited locally in an absorber in the form of heat is, on the average, one-third of the maximum disintegration energy accompanying the beta decay of a particular radionuclide. The remaining energy is lost from the heat measurement.

The primary mechanism through which low- and intermediate-energy beta particles lose their energy in matter is ionization. Bremsstrahlung is predominant with respect to high-energy beta particles if their kinetic energy is greater than their rest mass (511 KeV). The energy loss resulting from ionization is proportional to the atomic number Z of the absorbing material and increases logarithmically with energy. The energy loss that is due to bremsstrahlung radiation is proportional to Z^2 and increases linearly with energy. The conclusion is that at high energy the energy loss resulting from radiation is predominant. The radiation length is defined as the path length of the absorber in which the electron emerges with 1/e of its initial energy. For a 2-MeV electron, a typical radiation length in plutonium oxide is several millimeters.

Accompanying each beta particle is an antineutrino, which carries with it part of the disintegration energy. Neutrinos are extremely penetrating with respect to matter, so that a portion of the beta emission disintegration energy is not locally deposited.

The emission of conversion electrons is an alternative mechanism to de-exitation of a nucleus by gamma-ray emission. The energy of conversion electrons can also be transferred to surrounding material by ionization or bremsstrahlung.

21.2.3 Gamma Rays

The decay of a radioisotope by the emission of a particle, such as an alpha or beta particle, usually leaves the daughter nucleus in an excited state. A daughter nucleus making a transition gives up excess energy by means of gamma-ray emission, internal conversion, or internal pair production. Of these, gamma-ray emission is the dominant process. Gamma rays emitted from nuclear materials usually have energies ranging from a fraction of an MeV to a few MeV. In this range, gamma rays usually interact with matter by photoelectric effect, Compton scattering, or pair production. If these interactions do not occur within the sample, the energy associated with high-energy gamma-ray emission is not captured by the calorimeter. As indicated earlier, this lost energy is a small percentage of the total disintegration energy of the plutonium isotopes.

21.2.4 Other Emissions

In addition to the primary alpha, beta, and gamma emissions, radionuclides also emit neutrons through the spontaneous fission process. The energy lost through neutron emission is many orders of magnitude less than the total disintegration energy.

Chemical reactions, such as oxidation, and radiochemical processes, such as those associated with fission products in reprocessing plant solutions, are other possible sources of heat. Possible errors from such sources may be estimated by using gamma-ray spectroscopy to detect fission products, by observing any time-dependent power emission, or by comparing calorimetry with other techniques (Ref. 4).

21.3 SPECIFIC POWER DETERMINATION

21.3.1 Definition of Specific Power

Each radioisotope decays at a constant mean rate, λ disintegrations/s, with an energy release of Q MeV. The rate of energy release W for a specific isotope is then given by

$$W(\text{in MeV}) = QN\lambda \tag{21-1}$$

where N is the number of radioactive atoms present. $N = N_0 m/A$, where N_0 is Avogadro's number, m is the mass of the radioisotope in grams, and A is the atomic weight of the isotope in grams. With $\lambda = 0.6931/T_{1/2}$, where $T_{1/2}$ is the isotope's half-life in years, the power in watts as measured in the calorimeter is given by (Ref. 2)

$$W(\text{in watts}) = 2119.3Qm/T_{1/2}A. \tag{21-2}$$

If the total energy released per unit time by a radioactive isotope can be collected in a calorimeter and accurately measured, and if the disintegration energy, half-life, and atomic weight of the isotope are known, the mass of the sample can be determined. Equation 21-2 also shows that the power developed in a calorimeter by radioactive decay is directly proportional to the mass of the isotope present:

$$W = Pm. \tag{21-3}$$

The proportionality constant P is the specific power for the given isotope, measured in watts of power per gram of isotope present. The specific power of a single isotope can be calculated directly from Equation 21-2 if the appropriate parameters are known (computational method) or it can be determined experimentally with Equation 21-3 (empirical method). The procedures for both the computational and empirical methods are detailed in Ref. 4.

Specific power values and other nuclear constants for the isotopes of plutonium are summarized in Table 21-1 (Ref. 4). Note that the specific power of ^{238}Pu is much greater (~250 times) than that of ^{239}Pu because of the shorter alpha half-life of ^{238}Pu. The specific power of ^{241}Am is also considerably larger than that of ^{239}Pu, so the ^{241}Am content at the time of calorimetric assay is very important. Americium-241 content

Table 21-1. Specific power values for the plutonium isotopes (Ref. 4)

Radio-nuclide	Disintegration Energy Release Q(MeV)	Principal Decay Mode	Total Half-Life $T_{1/2}$ (yr)	Specific Power P (mW/g)	Specific Power Std. Deviation (mW/g)
^{238}Pu	5.592	alpha	87.74	567.57	0.26
^{239}Pu	5.243	alpha	24 119	1.9288	0.0003
^{240}Pu	5.255	alpha	6 564	7.0824	0.002
^{241}Pu	0.0055	beta	14.348	3.412	0.002
^{242}Pu	4.985	alpha	376 300	0.1159	0.0003
^{241}Am	5.640	alpha	433.6	114.2	0.42

increases with time because ^{241}Am is produced by the decay of ^{241}Pu, and thus the power from a plutonium sample also increases as a function of time. For the decay of ^{241}Pu to ^{241}Am within the sample, both the parent nucleus and the daughter nucleus contribute to the total power. The contribution of ^{241}Am to the total power is described by Equation 21-11 at the end of Section 21.3.2.

21.3.2 Effective Specific Power

Because actual plutonium samples contain differing amounts of the various isotopes listed in Table 21-1, the total power is the sum of the power from each isotope:

$$W = \sum_{i=1}^{n} m_i P_i \qquad (21\text{-}4)$$

where m_i is the mass of the ith isotope, P_i is the specific power of the ith isotope, and the sum n is taken over the plutonium isotopes and ^{241}Am. If R_i is defined as the mass fraction m_i/M of the ith isotope, where M is the total mass of all the plutonium isotopes, then

$$W = M \sum_{i=1}^{n} P_i R_i \quad . \qquad (21\text{-}5)$$

For calorimetric assay, the important factor is the effective specific power P_{eff}, which is expressed in watts per gram of plutonium and is defined by

$$P_{eff} = \sum_{i=1}^{n} P_i R_i \quad . \qquad (21\text{-}6)$$

In terms of effective specific power, the total mass of all the plutonium isotopes is given by

$$M = W/P_{eff} \quad . \qquad (21\text{-}7)$$

The mass of each particular isotope is given by

$$m_i = R_i W/P_{eff} \quad . \tag{21-8}$$

To obtain accurate calorimetric assays, very good values for the effective specific power of the sample must be known. The effective specific power can be determined by either the empirical method or the computational method (Ref. 4):

(a) *The Empirical Method.* The empirical method of determining effective specific power is well suited to discrete batches of process materials or to cases where the computational method is difficult to apply because the abundances of ^{238}Pu and ^{241}Am are not well known. This method requires both a chemical and a calorimetric analysis of the sample; the calorimetric analysis determines the total power produced by the sample, and the chemical analysis determines the total amount of nuclear material in the sample. Equation 21-7 can then be used to calculate the effective specific power.

(b) *The Computational Method.* The computational method for determining effective specific power is appropriate when very accurate isotopic determinations can be made. If radionuclide abundances R_i can be measured and the specific power values P_i are known for each radionuclide, then the effective specific power for a given isotope mix can be calculated from Equation 21-6.

The relative abundances of the radionuclides can be determined nondestructively by gamma-ray spectroscopy (See Chapter 8) or destructively by mass spectroscopy (Refs. 5 and 6). Destructive methods must include a technique for the determination of ^{241}Am. Plutonium-238 abundance is preferably measured by alpha-particle spectrometry (Ref. 4).

The isotopic mass fractions must be accurately known and corrected for decay to the date of the calorimeter power measurement because the effective specific power is a time-dependent quantity. The corrections for radionuclide decay can be made either by establishing a power growth curve for the sample over a period of at least 30 days or by calculating a correction for growth and decay from the previously determined isotopic abundances. According to Ref. 4, if the power curve method is used, "a minimum of three points should be made to establish a straight line showing power as a function of time. The curve should be checked after an additional 30 days."

The correction for radionuclide decay based on calculation from previously measured radionuclide abundances is usually the easiest approach, as in Equation 21-9.

$$W = M \sum_{i=1}^{n} P_i R_i(t) \quad . \tag{21-9}$$

Equation 21-9 is the same as Equation 21-5 except that $R_i(t)$ expresses the time dependence of the mass fractions. For the plutonium isotopes,

$$R_i(t) = R_i(t_1)\exp[-\lambda_i(t-t_1)]/F(t) \tag{21-10}$$

where $R_i(t)$ = mass fraction of the ith plutonium isotope at time t
t_1 = time of plutonium isotopic analysis
λ_i = decay constant of the ith plutonium isotope

$$F(t) = \sum_{i=1}^{n-1} R_i(t_I)\exp[-\lambda_i(t-t_I)] \quad ,$$

summed over the plutonium isotopes only.

For the daughter nucleus ^{241}Am, the mass fraction is due to both the decay of ^{241}Am and the ingrowth from beta decay of ^{241}Pu:

$$R_A(t) = \frac{F(t_A)}{F(t)} R_A(t_A)\exp[-\lambda_A(t-t_A)] \qquad (21\text{-}11)$$

$$+ K_1K_2 \frac{R_1(t_I)}{F(t)} \frac{\lambda_1\exp[-\lambda_1(t_A-t_I)]}{\lambda_1-\lambda_A} \left\{ \exp[-\lambda_A(t-t_A)] - \exp[-\lambda_1(t-t_A)] \right\}$$

where $R_1(t_I)$ = mass fraction of ^{241}Pu determined at time t_I
$R_A(t)$ = mass fraction of ^{241}Am relative to total plutonium at time t
t_A = time of americium analysis
λ_A = decay constant of ^{241}Am
λ_1 = decay constant of ^{241}Pu
K_1 = 0.9999754, ^{241}Pu branching ratio to ^{241}Am
K_2 = 0.999999905, $^{241}Am/^{241}Pu$ atomic mass ratio.

Lastly, if the total mass of plutonium is known at some time t_m, the mass at any future date is

$$m(t) = m(t_m)\, F(t)/F(t_m) \quad . \qquad (21\text{-}12)$$

21.4 HEAT MEASUREMENT BY CALORIMETRY

A calorimeter consists of a container with a temperature sensor in which the thermal phenomenon under investigation is carried out. In general the container is coupled to its environment by walls that have some thermal resistance. These basic features are illustrated in Figure 21.1 (Ref. 7). Heat liberated in the internal cavity raises its temperature and causes heat to flow across the thermal resistance into the environment according to Equation 21-13:

$$\frac{dQ}{dt} = k(T_{cal} - T_{env}) \qquad (21\text{-}13)$$

where Q = heat energy
k = thermal conductivity
T_{cal} = internal calorimeter temperature
T_{env} = external environment temperature.

Depending on the magnitude of this heat exchange, the calorimeter can be classified as adiabatic or isothermal.

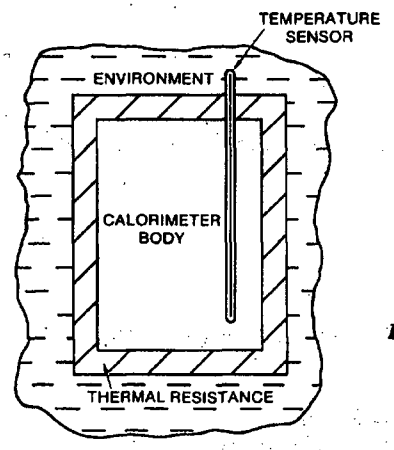

Fig. 21.1 The basic features of a calorimeter are its body or internal cavity, a temperature sensor, a thermal resistance gap, and the external environment. (Figure courtesy of Mound Laboratory.)

21.4.1 Adiabatic Calorimeters

In general, calorimeters are designed with a large thermal resistance between the cavity and its environment. As a result, almost all of the heat produced in the calorimeter body is retained, causing its temperature to increase. By measuring the temperature increase ΔT, one can determine the amount of heat energy released from the formula $Q = C\,\Delta T$, where C is the heat capacity. If the source of heat gives rise to a constant rate of heat production, the internal temperature T_{cal} will rise at a constant rate. If the source of heat is finite, the internal temperature will level off.

An efficient type of adiabatic calorimeter is one designed such that T_{env} is continuously adjusted to match T_{cal} so that the rate of heat transfer $dQ/dt = 0$. This adjustment is accomplished with a regulator that responds to any difference between the two temperatures. Adiabatic calorimeters are best suited to the study of processes such as chemical reactions where it is important to measure the total integrated heat production. Adiabatic calorimeters are not used for the assay of radionuclides because the internal temperature would continue to rise indefinitely.

21.4.2 Isothermal Calorimeters

If the thermal resistance between the sample cavity and the environment is small, the heat produced in the calorimeter is transferred to the surrounding environment. For a sample that produces heat at a constant rate, the entire system will reach an equilibrium condition in which the rate of heat transfer to the environment is equal to the rate of heat production in the sample. The rate of heat transfer is directly proportional to the

temperature difference between the sample chamber and the environment, as described by Equation 21-13, where the thermal conductivity k depends on heat path length, material, and surface shape. It is important that the value of k remain constant because the measurement of the rate of heat transfer is essentially a precision temperature measurement. The value of k is determined for a given calorimeter by calibration.

The calorimeter is classified as isothermal if the sample chamber is held at a constant temperature. If the calorimeter is also designed so that the thermal resistance between the sample chamber and the heat sink is moderate, it is classified as a heat flow calorimeter.

Radiometric calorimeters—those designed for the calorimetric assay of radioactive isotopes—are usually heat flow calorimeters because plutonium samples emit heat at an almost constant power level as a result of the spontaneous decay of their radioactive isotopes. The different types of calorimeters used for plutonium assay that are described in the following section are all heat flow calorimeters.

21.5 TYPES OF HEAT FLOW CALORIMETERS

Although calorimetric assay of plutonium is usually performed by a heat flow calorimeter, no universal calorimeter design is suitable for all applications. Each system is custom designed with many specifications in mind, as described in Section 22.1.2 of Chapter 22. Depending on the specific requirements, the final design may employ features of one or more of the calorimeter types described in this section: twin bridge, over/under bridge, and gradient bridge.

21.5.1 Common Electrical Features

One common feature of modern calorimeters is the precise measurement of temperature by electrical means. The determination of total sample power is then basically an electrical measurement of the temperature difference between the sample chamber and the environmental heat sink or reference chamber.

In twin-bridge calorimeters, both the sample chamber and the reference chamber have two nickel wire windings whose resistance is a function of temperature. The four windings are connected as a transposed-arm wheatstone bridge and are supplied with a constant current, as illustrated in Figure 21.2 (Ref. 7). With this arrangement, the temperature difference between the sample and reference chambers is directly proportional to the bridge potential BP.

With no sample in the calorimeter, a small bridge potential BP_0 (in microvolts, μV) may be observed because of variations in the resistances of the nickel windings. When a reference electrical heat source or radioisotope standard that emits a power level of W_R watts is placed in the sample chamber, the bridge potential will reach an equilibrium value BP_R (μV). The sensitivity S of the calorimeter in microvolts per watt is

$$S(\mu V/W) = (BP_R - BP_0)/W_R \quad . \tag{21-14}$$

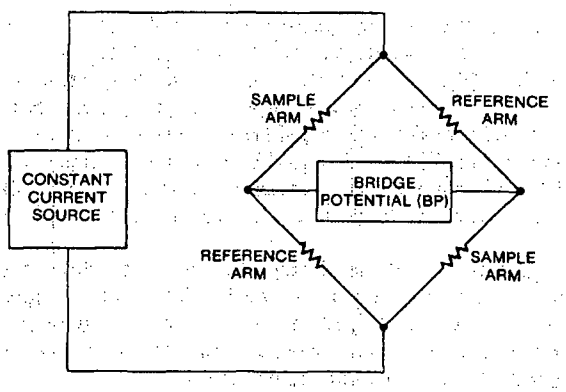

Fig. 21.2 A wheatstone bridge circuit is used to accurately measure the temperature difference between the sample and reference parts of a calorimeter. (Figure courtesy of Mound Laboratory.)

21.5.2 Full Twin-Bridge Calorimeters

To increase calorimetric accuracy, nearly all calorimeters can be arranged as twin calorimeters. The most common example is the isothermal twin-bridge calorimeter developed at Mound Laboratory and used extensively for in-plant assays (Ref. 8). Figure 21.3 shows a cross section of this calorimeter type, and Figure 21.4 is a photograph of a full twin-bridge calorimeter without its surrounding water bath.

The full twin-bridge design consists of two identical thermal elements, sample side and reference side, each separated from the outer wall by an air gap or solid gap that serves as the thermal resistance. Each thermal element has heater wires wrapped around its sample chamber for calibration purposes. Axial heat loss from the sample chamber is minimized by the use of plastic end caps with Styrofoam baffles and metal plates to provide a thermal short from the sample to the calorimeter walls. Two resistance thermometers consisting of thin nickel wire are wound over the entire length of each thermal element to provide an accurate temperature measurement independent of variations in heat flow (Ref. 8).

For operation, the twin calorimeter is immersed in a water bath whose temperature is held constant to about one millidegree. In addition, the use of two identical thermal elements yields a difference signal that is 10 to 100 times more stable than the environmental bath. When a sample is placed in the chamber, the temperature rises until heat losses through the nickel windings, thermal gap, and outer jacket to the water bath equal the heat generated by the sample. When this equilibrium is attained, the temperature difference measured by the bridge potential is proportional to the amount of heat being generated. Precise heat flow calorimeters of this type are designed and

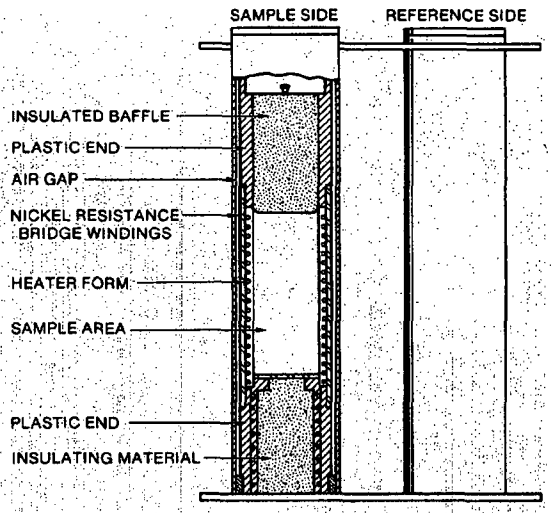

Fig. 21.3 *Cross section of a typical isothermal twin calorimeter with two identical thermal cells, one for the sample and one for reference. (Figure courtesy of Mound Laboratory.)*

constructed so that the thermal paths between the sample chamber and the environment remain constant. Additional care is taken to keep the temperature of the environment constant and to minimize the heat distribution error associated with the location of the sample in the chamber.

The twin-bridge calorimeter provides the best precision, accuracy, sensitivity, and long-term stability for power measurements because of the internal cancellation of many thermal effects. However, the two thermal elements and the environmental bath result in an instrument that is larger and requires more floor space than other designs. Twin-bridge calorimeters have been designed for sample sizes ranging from 1 to 30.5 cm in diameter with an upper limit dictated only by nuclear criticality safety considerations and a lower limit in the range of 0.1- to 0.2-g ^{239}Pu/L (Ref. 8). An application of a twin-bridge calorimeter is described in Section 22.4.1 of Chapter 22.

21.5.3 Over/Under Bridge Calorimeters

In the over/under design, the sample cell is mounted above a somewhat shortened reference cell (Ref. 7), as illustrated in Figure 21.5. Both cells share a single isothermal water jacket that is smaller than the environmental bath used by the twin-bridge calorimeter. The over/under bridge design requires less floor space, but is taller. Also, the over/under design can be used to build a transportable calorimeter. The calorimeter shown in Figure 21.5 can be mounted on a mobile cart along with its circulation bath.

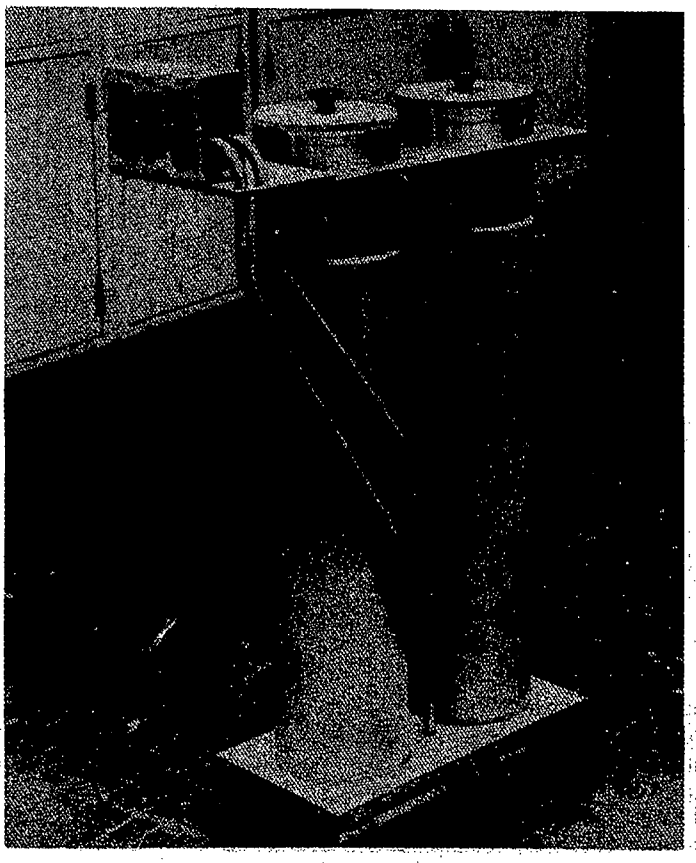

Fig. 21.4 View of an actual twin-bridge calorimeter without its surrounding water bath. (Photograph courtesy of Mound Laboratory.)

The over/under bridge calorimeter has size and cost advantages over the twin-bridge design and provides cancellation of some thermal effects. However, the accuracy is not as good as the full twin-bridge calorimeter. Examples of over/under bridge calorimeters are given in Sections 22.3.1 and 22.4.2 of Chapter 22.

21.5.4 Gradient Bridge Calorimeter

The gradient bridge calorimeter (Figure 21.6) consists of a series of concentric cylinders, with the sample cell cylinder inside the reference cell cylinder (Ref. 7). The gap between the reference cell cylinder and the sample cell cylinder determines the sensitivity of the calorimeter. Outside the reference cylinder is a jacket that provides a uniform

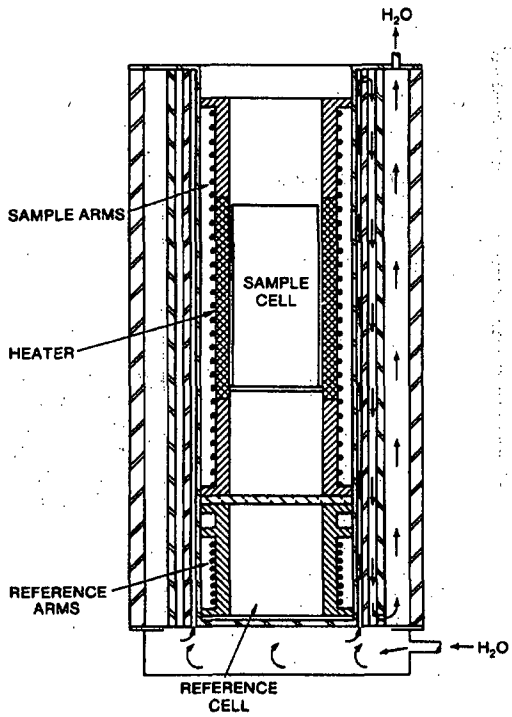

Fig. 21.5 *A transportable calorimeter of the over/under bridge design with the sample cell above the reference cell and a thin water jacket. (Figure courtesy of Mound Laboratory.)*

thermal heat sink. The jacket is in contact with a thin circulating water bath. This design leads to small size and low material and fabrication costs. The gradient design is well suited for transportable versions or glovebox installations, or for large samples where overall bulk should be minimized. The gradient calorimeter is usually operated in the constant temperature servo-control mode described in Section 21.6.3 below. A Mound gradient bridge calorimeter design is described in Section 22.4.4 of Chapter 22.

The isothermal air chamber calorimeter developed by Argonne National Laboratory is a version of the gradient design that does not require a water bath (Refs. 9 and 10). This calorimeter (Figure 21.7) is described in Ref. 10 as "...a constant temperature oven composed of a series of concentric chambers. Each of these chambers is constructed from an aluminum cylinder upon which resistive heating coils and heat sensors are mounted. The cylinders are separated from one another by high thermal-resistance material. The ends of the cylinders are similarly protected by nonconducting plugs and by pancake-type heater coils. Alternating zones of high and low thermal conductivity in

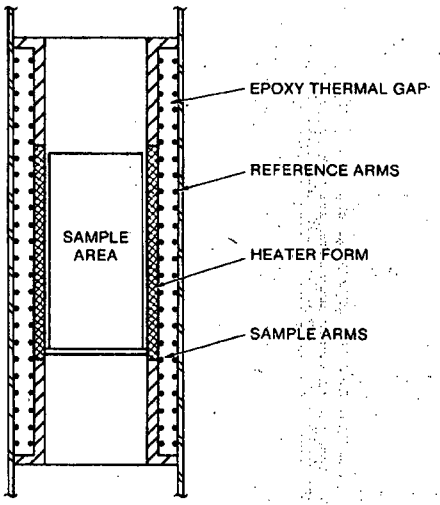

Fig. 21.6 Cross section of a gradient bridge calorimeter design. The environmental heat sink, which would be small or just an air chamber, is not shown. (Figure courtesy of Mound Laboratory.)

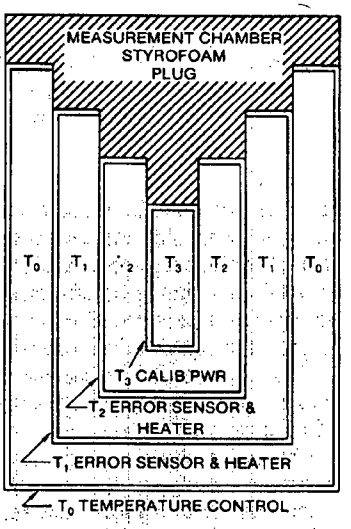

Fig. 21.7 Cross section of an air chamber calorimeter, a version of the gradient bridge calorimeter. (Figure courtesy of Argonne National Laboratory.)

this manner tends to minimize the effects of localized external temperature changes. A temperature profile is established within the calorimeter to eliminate axial heat flow and to ensure that a negative radial temperature gradient is maintained. In the schematic drawing (Figure 21.7), the electronic feedback control circuits will maintain the relation $T_3 > T_2 > T_1 > T_0 > T_{ambient}$. The inner two cylinders (T_3, T_2) act as the measurement chamber. The calorimeter-supplied electrical power is adjusted to maintain the temperature difference between these cylinders to ±20 microdegrees." Calorimeters of this type have been used to measure sealed containers of bulk materials with up to 3 kg of plutonium, mixed-oxide fuel pellets, and fuel rods up to 4 m in length. Examples are given in Sections 22.2.2, 22.3.2, and 22.5.1 of Chapter 22.

21.6 METHODS OF OPERATION FOR HEAT FLOW CALORIMETERS

21.6.1 Replacement Method

In this mode of operation the sample to be measured is placed in the calorimeter and allowed to come to thermal equilibrium. The temperature difference between the calorimeter and the heat sink is determined from the bridge potential. Then the sample is removed and the calorimeter is heated electrically until the same equilibrium temperature difference is obtained. The sample power can be determined from the known power supplied by the heater that replaced the sample. The same chamber of the calorimeter is used for both the sample run and the heater run.

The replacement method consists of the following steps (Refs. 7 and 8):

(1) A bridge potential BP_0 is measured with the sample chamber empty, zero heater power, and the environmental tank under temperature control. BP_0 is normally measured periodically, not for each sample.

(2) The sample to be assayed is placed in the calorimeter and its equilibrium bridge potential BP_S is determined.

(3) The sample is then removed and the heater current required to replace the sample power is calculated. The heater power required is approximately

$$W_H(\text{approx}) = (BP_S - BP_0)/S \tag{21-15}$$

where S is the sensitivity of the calorimeter as determined earlier with Equation 21-14. The required heater current is then calculated. The problem of power dissipation in the wires leading to the heater can be minimized in the twin design calorimeter by running the wires through both the sample and reference chambers so that the effects cancel.

(4) The heater current is applied to the sample chamber until the equilibrium bridge potential BP_H can be determined. Also, the actual exact heater power W_H is calculated from the measured heater current and voltage.

(5) The power of the unknown sample is then

$$W_S(\text{watts}) = W_H + (BP_S - BP_H)/S \quad . \tag{21-16}$$

The above procedure is illustrated in Figure 21.8, which also shows the additional complexity introduced by slow drifts in the instrument.

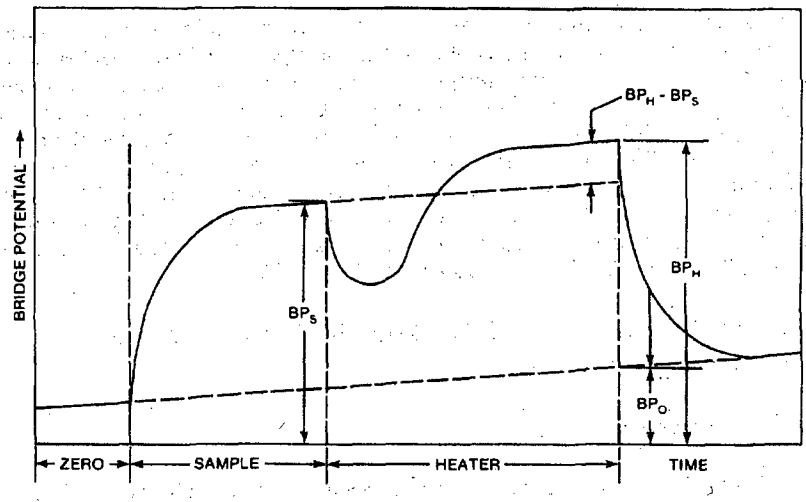

Fig. 21.8 Calorimeter bridge potential as a function of time as observed during the replacement method of operation. The upward slopes illustrate the additional complexity introduced by gradual instrument drifts. (Figure courtesy of Mound Laboratory.)

21.6.2 Differential Method

A twin-bridge or over/under bridge calorimeter can be operated in the differential mode in which electrical heat in the reference side is compared directly to sample heat from the sample side. Because the sample run and the heater run are simultaneous, assays can be made in about half the time required for the replacement method. In practice this time savings is realized only when the sample power is known in advance to about 1%. Thus the differential method is most useful when many samples of approximately the same size are to be assayed. For samples of unknown size this method is only slightly faster than the replacement method (Ref. 8).

When the differential method is used, the sample power at equilibrium is given by

$$W_S(\text{watts}) = W_H + (BP_S - BP_M)/S \quad . \tag{21-17}$$

BP_M is a bridge potential calculated from mW_H, where m is a constant slope. The quantity $(BP_S - BP_M)$ is zero if the heater power exactly matches the sample power; if not, this quantity compensates for small differences between the two sides. The slope m is determined during calibration by running current through the sample and reference heaters in series (Ref. 8).

21.6.3 Constant Temperature Servo-Control Method

In this mode of operation both the sample chamber and the environmental bath are held at constant temperature by a servo-control mechanism. Heater power is used to maintain the sample chamber at a higher temperature than the bath. When a sample is placed in the calorimeter, the servo-controller reduces the heater power by the amount of the sample's power to hold the chamber at constant temperature. This method, also called the isothermal method, may be used with any calorimeter bridge design. Use of the constant temperature method typically reduces assay time by one-third to one-half because the time required to reach equilibrium depends principally on the thermal resistance and heat capacity of the sample and less on the calorimeter body.

Before samples are assayed by the constant temperature method, the baseline power level is set 10 to 20% above the estimated wattage of any calibration standards or actual samples. A baseline power run is made to establish the empty chamber equilibrium power level W_0. This run takes less time than a sample assay because no mass is in the chamber.

When a radioactive sample is placed in the calorimeter, the heater power drops as the servo-controller tries to maintain a constant temperature in the chamber. The new equilibrium power level is W_C, and the sample power is

$$W_S(\text{watts}) = W_0 - W_C \quad . \tag{21-18}$$

Constant temperature control of the calorimeter can be maintained by analog or digital circuits. Digital circuits have the advantage of requiring no adjustments to Equation 21-18 to correct for systematic errors that occur in analog systems.

The constant temperature servo-control method is one of the fastest methods of calorimeter operation, especially when used with "pre-equilibration" of the sample in a separate temperature-controlled environment.

21.7 ASSAY TIME CONSIDERATIONS

The time necessary to complete a calorimetric assay of a radioactive sample is dependent on a variety of factors that influence the time necessary for the system to attain steady-state conditions. These factors include the following:

(a) The type of heat flow calorimeter—twin-bridge, over/under bridge, or gradient bridge.

(b) The thermal resistance and heat capacity of the material used for calorimeter construction and the material the sample is composed of.

(c) The quality of calorimeter construction—tightness of fit, uniformity of air gaps, and so forth.

(d) Physical size of the calorimeter sample chamber and the diameter of the sample.

(e) Sample packaging—location of heat sources inside the package, presence of void spaces, and so forth.

(f) Method of calorimeter operation—replacement, differential, or constant temperature servo-control.
(g) Use of sample preconditioning.
(h) Use of end-point prediction techniques.
(i) Required assay accuracy.

Calorimetric assay of well-characterized small samples may be completed in less than one hour. On the other hand, bulk samples of product or scrap materials require calorimetric assay times of 4 to 16 h to reach thermal equilibrium. Table 21-2 (from Ref. 8) gives a few examples of assay times for a twin-cell, water bath calorimeter. Poor sample packaging consisted of plastic bags and lead shot; good packaging consisted of copper shot. A more complete summary of typical assay times is given in Ref. 1. Some of the factors and techniques that affect assay time are discussed below.

Table 21-2. Some assay times for a twin-bridge calorimeter (Ref. 8)

Assay Conditions	1.0% Equilibrium Time (h)	0.1% Equilibrium Time (h)	0.01% Equilibrium Time (h)
Heater only, no sample, no temperature servo-control	2.8	3.6	4.8
Poorly packaged sample, no temperature servo-control	8.1	10.2	13.1
Well-packaged sample, no temperature servo-control	5.2	6.3	8.0
Poorly packaged sample, constant temperature servo-control	4.7	6.1	8.0
Poorly packaged sample, constant temperature servo-control, sample preconditioned	0.8	1.6	3.0

21.7.1 Calorimeter Design and Operating Method

The physical dimensions and thermal properties of a given calorimeter affect both the equilibrium time and the sensitivity. Decreasing the thermal resistance of a calorimeter will reduce the time required to come to equilibrium, but it will also reduce the observed bridge potential and (from Equation 21-14) the sensitivity. Because reduced sensitivity will lead to reduced accuracy, the choice of calorimeter design must reflect a trade-off between assay time and assay accuracy for the particular sample range. The composition and dimensions of the gap between the sample and the calorimeter wall are important factors.

The replacement method of calorimeter operation is generally the slowest mode of operation because three distinct calorimeter runs are required to complete an assay: a sample run, a heater run, and a periodic baseline (BP_0) run. The differential method,

which can be used with twin-bridge calorimeters, requires only two calorimeter runs because the electrical heat in the reference chamber is constantly compared to the heat developed by the sample. This mode of operation reduces the time necessary for assay completion.

The constant temperature servo-control mode of operation, or isothermal mode, is well suited for reducing assay time; when the calorimeter body is maintained in an equilibrium state, the effect of its time constant is minimized and the assay time is principally dependent on the thermal time constant of the sample. Assay time can be reduced further if the sample temperature is pre-equilibrated to the temperature of the calorimeter, as described in the next section.

21.7.2 Sample Preconditioning

Preconditioning of the sample to about the internal temperature of the calorimeter can be used with the constant temperature servo-control method to reduce assay time, as indicated in Table 21-2. Preconditioning can be used alone or in conjunction with the end-point prediction technique described in the next section. When the sample is first placed in a separate preconditioning water bath and then placed in the calorimeter, the time required to reach equilibrium is reduced because only the sample itself needs to equilibrate to a steady-state heat flow. The gradient gap is already at a steady-state heat flow with respect to the heat sink, and the heater power will reach the equilibrium power level more rapidly.

Several advantages and disadvantages are associated with preconditioning (Ref. 7). The primary advantage is increased throughput. The preconditioning bath can be designed to accommodate more than one sample, and it can be used overnight to prepare samples for assay the next day. The disadvantages are that additional floor space, electronics, and operator action are required. Also, the preconditioning bath temperature must be carefully maintained near the internal temperature of the calorimeter. Any change in the calorimeter's baseline power level will require adjustment of the preconditioning bath temperature.

21.7.3 End-Point Prediction

Prediction of equilibrium is a mathematical technique for reducing calorimeter assay time without affecting calorimeter sensitivity or sample packaging. The technique is applicable to a variety of calorimeter types. Equilibrium values can be predicted reliably with a time savings of about 50% (Refs. 11 and 12).

End-point prediction is based on the principle that the calorimeter's response function is dominated by a single exponential of the form

$$Y = A + Be^{-\lambda t} \tag{21-19}$$

where Y is the time-dependent calorimeter output, A is the equilibrium output signal, B is a scaling constant, and λ is the final thermal decay constant of the calorimeter and its sample (Ref. 11). A calorimeter actually consists of different thermal regions, each having different values for thermal resistance R_i and heat capacity C_i, as illustrated in

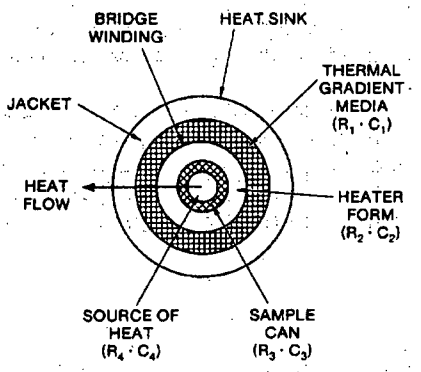

Fig. 21.9 Radial cross section of an idealized calorimeter showing four regions, each having different values for thermal resistance R_i and heat capacity C_i. (Figure courtesy of Mound Laboratory.)

Figure 21.9. The differing thermal properties of each region determine the time required for each region to come to equilibrium with its surroundings. The time required for the entire calorimeter to reach equilibrium is a sum of several exponential response functions. Because the end-point prediction technique is based on the use of Equation 21-19 with a single exponential, the amount of time saved depends on the validity of this approximation. Samples that are poorly packaged, with high thermal resistance or high heat capacity, will be assayed with less time savings.

The procedure for calculating the equilibrium output signal A requires determination of the output signal Y at regular time intervals during the assay (Ref. 7). The values for Y are smoothed and fitted to Equation 21-19 and a value for A is calculated. This procedure is repeated at regular intervals as the assay progresses and as more determinations of Y become available. Figure 21.10 illustrates this process. When the predicted values for A show zero slope within the expected standard deviation, the run is complete. The assay is terminated before the calorimeter actually reaches equilibrium.

21.8 CALORIMETER CALIBRATION

Accurate calibration is needed to relate the observed calorimeter output power to known power values. Two types of standards are commonly used for calibration purposes: electrical and radiometric heat sources. Regardless of the calibration method used, traceability to NBS-certified electrical or radiometric standards is essential (Ref. 4).

21.8.1 Electrical Calibration

Electrical calibration techniques are applicable to calorimetric methods in which heater power either duplicates or replaces sample power (Ref. 4). The power generated in an electrical heater is given by the product of the voltage across the heater and the current through the heater. To calibrate the heater, the current can be determined by measuring the voltage across a standard resistor. This calibration yields the relationship

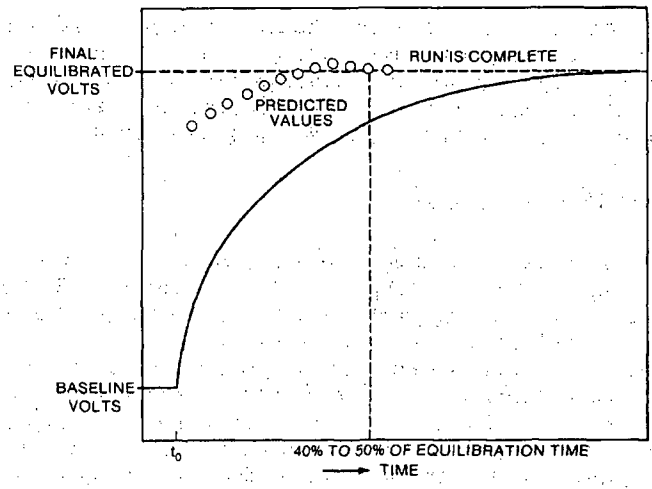

Fig. 21.10 *Graphical representation of the end-point prediction technique. The run is complete when the predicted values show zero slope within the expected standard deviation. (Figure courtesy of Mound Laboratory.)*

between bridge potential and sample power: the calorimeter sensitivity (Equation 21-14). The result is a sensitivity curve as a function of sample power.

Accurate electrical calibration requires that the electrical heater produce the identical change in calorimeter output as an equivalent amount of power from a sample (Ref. 4). This implies that the location of the heater relative to the temperature-measuring device should be the same as that of the radioactive sample. The error associated with this factor is referred to as the heat distribution error. To determine the extent of this error, it is recommended that a small sample be placed at various locations within the chamber and its output measured with respect to location. (One of the radiometric heat standards discussed in the next section would be ideal for this purpose.) Another source of error in electrical calibration is power loss in the heater leads of single-cell calorimeters. The technique for correcting for heater-lead errors is described in Ref. 4.

21.8.2 Calibration with Radioactive Heat Sources

Calibration with radioactive heat sources is a simpler technique and usually preferable because it covers all aspects of calorimeter operation. Standard $^{238}PuO_2$ heat sources that are traceable to NBS reference materials are available from Mound Laboratory in the range 0.04 mW to 100 W (Ref. 7). The sources are compact, and the power output as a function of time can be calculated. The heat sources should span the range of actual sample powers.

In the calibration procedure, the radioactive heat sources are placed in the calorimeter sample chamber in the same manner as the unknown samples. The calorimeter output signal is measured using the known power of each standard heat source. These data are used to generate a calibration curve and an associated sensitivity curve just as in the electrical case. Additional details on this procedure are given in Ref. 4.

21.9 SOURCES OF ERROR

As described in Section 21.3, determination of plutonium content is a two-step process: determination of calorimetric power and determination of effective specific power either by empirical or computational methods. The sources of error in this process are summarized in Table 21-3 (Refs. 4, 7, and 13).

Sources of error in the power determination include (1) imprecision of the calorimeter system—the variance of the system response as a result of variations in room temperature, bath temperature, humidity, sample weight, sample loading and unloading stresses, and so forth; (2) heat distribution error—the variance of the system response resulting from spatial distribution of the sample in the sample chamber; (3) calibration error—the variance of the system response to calibration method and standards; and (4) interference error—heat production from interfering processes such as fission product reactions or chemical reactions.

Sources of error in the determination of effective specific power depend on the method used for this determination: empirical or computational. If the empirical method is used, the possible sources of error are (1) errors in determination of sample power and (2) errors in determination of the content of the plutonium sample. When the computational method is used for determination of effective specific power, the error sources are (1) errors in determination of the sample's isotopic composition and (2) uncertainty in the specific power values (see the last column of Table 21-1). The total assay uncertainty may be estimated by combining the error in the calorimeter power determination with the uncertainty in the effective specific power:

$$\sigma(\mathrm{Pu}) = \sqrt{\sigma^2(\mathrm{W}) + \sigma^2(\mathrm{P_{eff}})} \tag{21-20}$$

The error magnitudes given in Table 21-3 are typical values; in practice, actual values may be quite different. In particular, the errors associated with the determination of isotopic composition depend on the technique used. For concentrations below 0.1%, the errors quoted are typical of radiometric results for ^{238}Pu and ^{241}Am. For concentrations of 0.1 to 1%, the minimum error for mass spectrometric determination is 1%; for concentrations greater than 20%, the minimum error is 0.3%. If the isotopic composition is determined by high-resolution gamma-ray spectroscopy, errors for the major plutonium isotopes are in the range of 0.1 to 10%. Errors in the determination of effective specific power are in the range of 0.3 to 1.0% in 1- to 4-h counting times (Ref. 14 and Chapter 8). Generally, the precision of the calorimeter power measurement is better than the uncertainty associated with the determination of effective specific power.

Table 21-3. Sources of error in calorimetric assay (Refs. 4, 7, and 13)

Error Source	Approximate Magnitude (%)
Power Measurement	
Calorimeter imprecision	<0.1
Heat distribution error	<0.1
Calibration error	<0.1
Interference error	<0.1
Effective Specific Power Determination	
Empirical method	
Sample power	<0.2
Sample plutonium content	<0.2
Computational method	
Isotopic composition	
Concentration <0.1%	2-5
Concentration >0.1%	1.5
Concentration >1%	0.5
Concentration >20%	0.3
Specific power uncertainty	<0.1

REFERENCES

1. W. Rodenburg, "Calorimetric Assay," in "Handbook of Nuclear Safeguards Measurement Methods," D. R. Rogers, Ed., Mound Laboratory report MLM-2855, NUREG/CR-2078 (1983), pp. 533-550.

2. W. Rodenburg, "An Evaluation of the Use of Calorimetry for Shipper-Receiver Measurements of Plutonium," Mound Laboratory report MLM-2518, NUREG/CR-0014 (1978).

3. W. Strohm, S. Fiarman, and R. Perry, "A Demonstration of the In-Field Use of Calorimetric Assay for IAEA Inspection Purposes," *Nuclear Materials Management* XIV (3), 182 (1985).

4. "Calibration Techniques for the Calorimetric Assay of Plutonium-Bearing Solids Applied to Nuclear Materials Control," ANSI N15.22-1975 (American National Standards Institute, Inc., New York, 1975) and 1986 revision.

5. "Methods for Chemical, Mass Spectrometric, and Spectrochemical Analysis of Nuclear-Grade Plutonium Dioxide Powders and Pellets, ANSI N104-1973 (American National Standards Institute, Inc., New York, 1973).

6. "Methods for Chemical, Mass Spectrometric, Spectrochemical, Nuclear, and Radiochemical Analysis of Nuclear-Grade Plutonium Metal," ANSI N572-1974 (American National Standards Institute, Inc., New York, 1974).

7. Mound Calorimetric Assay Training School Manual, Mound Laboratory, Miamisburg, Ohio, October 22-25, 1985.

8. F. O'Hara, J. Nutter, W. Rodenburg, and M. Dinsmore, "Calorimetry for Safeguards Purposes," Mound Laboratory report MLM-1798 (1972).

9. C. Roche, R. Perry, R. Lewis, E. Jung, and J. Haumann, "A Portable Calorimeter System for Nondestructive Assay of Mixed-Oxide Fuels," American Chemical Society Symposium Series, No. 79 (1978).

10. C. Roche, R. Perry, R. Lewis, E. Jung, and J. Haumann, "Calorimetric Systems Designed for In-Field Nondestructive Assay of Plutonium-Bearing Materials," International Atomic Energy Agency/Argonne National Laboratory report IAEA-SM-231/78 (1978).

11. C. L. Fellers and P. W. Seabaugh, "Real-Time Prediction of Calorimetric Equilibrium," *Nuclear Instruments and Methods* 163, 499 (1979).

12. R. A. Hamilton, "Evaluation of the Mound Facility Calorimeter Equilibrium Prediction Program," Rockwell Hanford report RHO-SA-114 (1979).

13. W. Rodenburg, "Some Examples of the Estimation of Error for Calorimetric Assay of Plutonium-Bearing Solids," Mound Laboratory report MLM-2407, NUREG-0229 (1977).

14. T. Sampson, S. T. Hsue, J. Parker, S. Johnson, and D. Bowersox, "The Determination of Plutonium Isotopic Composition by Gamma-Ray Spectroscopy," *Nuclear Instruments and Methods* 193, 177 (1982).

22

Calorimetric Assay Instruments

R. Likes

22.1 INTRODUCTION

This chapter describes some modern calorimeter systems currently in use throughout the nuclear fuel cycle for the nondestructive assay of plutonium. Since 1950, Mound Laboratory (Monsanto Research Corporation, Miamisburg, Ohio) has built over 200 calorimeters of various designs for nuclear material control and accountability, primarily for US Department of Energy (DOE) facilities. Occasionally a few DOE and commercial nuclear facilities have built their own calorimeters. Argonne National Laboratory (University of Chicago, Argonne, Illinois) has built several for use by the International Atomic Energy Agency (IAEA). The calorimeters described in this chapter represent the types of instruments in use today; they include those built by Mound, Argonne, Rocky Flats, and General Electric (GE).

The Mound calorimeters described in this chapter are the analytical calorimeter, the transportable calorimeter, the twin-bridge production calorimeter, and the gradient bridge calorimeter; the Argonne calorimeters are the small-sample calorimeter, the bulk assay calorimeter, and the one-meter fuel rod calorimeter. Also described are Rocky Flats production calorimeters and the GE irradiated fuel assembly calorimeter. The examples given in this chapter are preceded by a summary of typical calorimeter system components and design considerations.

22.1.1 Calorimetric Assay System Components

A typical modern system designed for the calorimetric assay of plutonium-bearing materials consists of the following components:

(a) A precisely machined heat flow calorimeter body of the twin-bridge, over/under bridge, or gradient bridge type. Each cell includes an electric heater circuit for accurate duplication of sample power.

(b) A bridge circuit for the precise measurement of temperature differences between the sample chamber and the environmental heat sink. The electric circuitry includes high-quality potentiometers and digital voltmeters.

(c) A digital or analog readout device, which is usually a minicomputer. The computer controls calorimeter operation, data collection and storage, and data analysis.

(d) Electrical or radioactive heat source calibration standards. Electrical measurements are used to determine temperature differences and to control electrical heater circuits for sample power duplication. Alternatively, radioactive heat source standards may be available to the system for calibration and power determination.

22.1.2 Calorimeter Design Considerations

In the design of a calorimetric assay instrument, many important factors dictate the appearance of the final product. It is not possible to design a single, universal calorimeter that is applicable to all measurement situations. This section lists some of the factors that influence calorimeter design.

(a) *Sample size.* The physical size of the sample dictates the dimensions of the sample chamber; tight thermal coupling of the sample to the calorimeter is essential to minimize assay time. The diameters of sample chambers on existing calorimeters range from 1 to 30 cm.

(b) *Sample power.* In general, high-power samples require low-sensitivity calorimeters with low thermal resistance, and low-power samples require sensitive microcalorimeters with high thermal resistance.

(c) *Calibration.* Calorimeter design is a function of the calibration method to be used—radioactive heat standards or electrical standards.

(d) *Construction materials.* The heat capacities and thermal conductivities of the materials used in construction influence performance.

(e) *Throughput.* The available time per assay influences the choice of calorimeter type and method of operation and the number of calorimeters needed.

(f) *Accuracy.* The desired assay accuracy must be weighed against the needed throughput and available space in choosing the type of calorimeter and the method of operation.

(g) *Plant environment.* Calorimeter design is affected by the working environment and the available floor space. An in-line production plant environment requires different design considerations than a laboratory setting.

22.2 SMALL CALORIMETERS FOR LABORATORY SAMPLES

Small calorimeters can be used in analytical chemistry laboratories to provide nondestructive assays of small plutonium samples. They can be used to determine effective specific power by the empirical method, in which a small sample of plutonium is assayed nondestructively by calorimetry and then destructively by chemistry. Also, small calorimeters provide a means for evaluating sampling errors.

22.2.1 Mound Analytical Calorimeter

The Mound analytical calorimeter was developed specifically for use in an analytical chemistry laboratory (Ref. 1). It is a compact instrument (Figure 22.1) designed for sample sizes up to 5 cm^3 (about 10 g of plutonium). The calorimeter includes an automatic sample loader with a pre-equilibrium position and is designed to fit inside a standard 3-ft glovebox. For samples producing 10 mW of power, the precision and accuracy are better than 0.1%. Performance data for the analytical calorimeter are summarized in Table 22-1 (Refs. 1 and 2). The gram values for accuracy, precision, and range are for low-burnup plutonium with an effective specific power of 2.3 mW/g and with well-known isotopic composition.

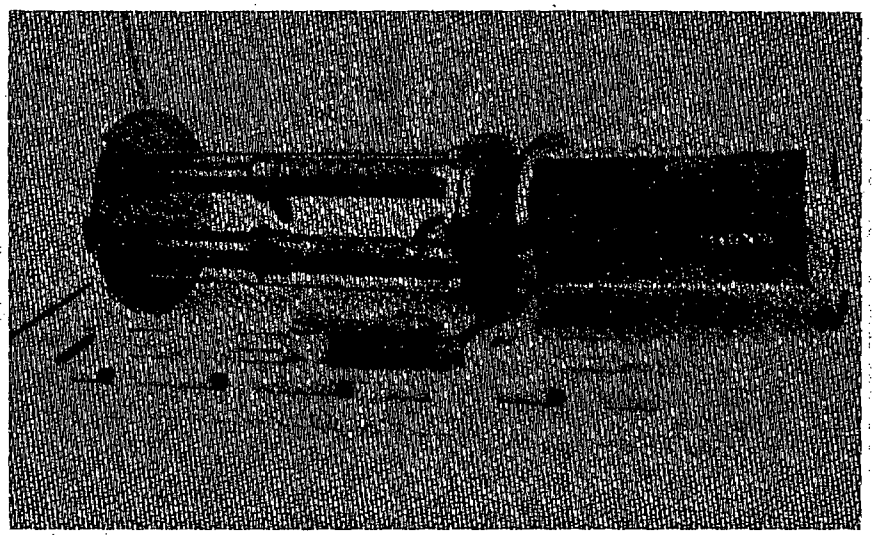

Fig. 22.1. *View of a disassembled Mound analytical calorimeter for the assay of small plutonium samples in 2-dram glass vials. (Photograph courtesy of Mound Laboratory.)*

Table 22-1. Performance data for the Mound analytical calorimeter, assuming 2.3 mW/g and known isotopics (Refs. 1 and 2)

Accuracy	0.008 g
Precision	0.008 g
Range	0.4 to 10 g (1 to 23 mW)
Measurement Sensitivity	0.4 g or 1 mW in a 5-cm^3 container
Assay Time	30-100 min

A wide variety of plutonium-bearing materials, including metal, oxide, and mixed-oxide, have been measured in the analytical calorimeter and then dissolved and analyzed for plutonium content. Comparisons of the results demonstrated that calorimetric assay is both accurate and precise.

22.2.2 Argonne Small-Sample Calorimeter

The Argonne small-sample calorimeter is designed for the assay of up to 6 cm^3 of mixed-oxide fuel in the form of pellets, powders, and solutions (Refs. 3 and 4). Its maximum power range is 45 mW, which is equivalent to 20 g of low-burnup plutonium. The unique feature of this system is its portability, which makes it useful for on-site inspections in the field. Figure 22.2 shows the two modules that make up the system: the isothermal calorimeter and the data acquisition module. The total weight is 18 kg.

The small-sample calorimeter is an isothermal gradient bridge calorimeter. It is a "dry" or "air chamber" calorimeter because of the absence of a water bath heat sink, as described in Section 21.5.4 and shown in Figure 21.7 of Chapter 21. This design requires operation in the constant temperature servo-control mode to obtain good accuracy. Performance data for the small-sample calorimeter are given in Table 22-2 (Refs. 4 through 6). The calorimeter has a precision of about 0.1% in 20 min (Ref. 4). The short assay time and good precision are partly due to double encapsulation of the samples in metal containers to maximize heat transfer.

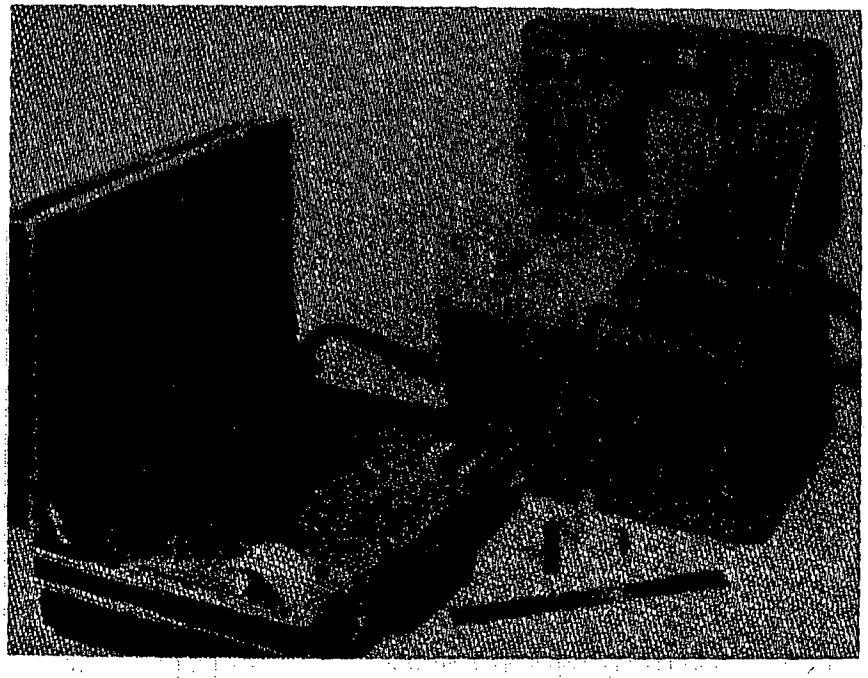

Fig. 22.2 Argonne small-sample calorimeter (right) and its data acquisition system (left). (Photograph courtesy of Argonne National Laboratory.)

Table 22-2. Performance data for the Argonne small-sample calorimeter, assuming 2.3 mW/g and known isotopics (Refs. 4 through 6)

Accuracy	0.01 g
Precision	0.01 g
Range	1 to 20 g (2 to 45 mW)
Measurement Sensitivity	1 g
Assay Time	20 min

The data acquisition module automatically performs electrical calibrations over a selected input range. The calibrations are performed with the aid of a microprocessor calculating the reference voltage to be applied across the calibration resistor coil. This electrical calibration simulates a set of plutonium standards over the measurement range of the instrument (Ref. 4).

An independent test and evaluation of the calorimeter (Ref. 5) found insensitivity to operator and environmental effects. However, the study recommended preheating the sample capsules to avoid a shift in the reference-power baseline. The calorimeter was calibrated with plutonium heat standards, and use of an electrically heated capsule was recommended to check the calibration.

22.3 TRANSPORTABLE CALORIMETERS

Some calorimeters have been designed to be transportable for use at different nuclear fuel-cycle facilities during periodic inventory verification exercises. This portability provides the nuclear material inspector with the ability to verify inventory items independently. In addition, a gamma-ray spectrometer is used to determine plutonium isotopic concentrations so that the calorimeter power measurement can be converted to plutonium mass.

22.3.1 Mound Transportable Calorimeter

The Mound transportable calorimeter was developed for use by DOE inspectors (Refs. 1 and 7). It is similar in design to the larger in-plant instrument described in Section 22.4.1 below, except that the constant temperature bath is replaced by a heat exchanger, a pump, and a small temperature-controlled reservoir. Water from the small bath is pumped through the heat exchanger to maintain the calorimeter at constant temperature. This change significantly reduces the size and weight of the system. The calorimeter is an over/under bridge type (Ref. 1).

Figure 22.3 shows the small water reservoir, the electronics, and the calorimeter body mounted on an aluminum cart. Because the total weight of the system is only 200 kg, it can be moved by one person. The sample chamber can accommodate samples up to 13 cm in diameter and 20 cm high, with a power range of 0.5 to 10 W. The data acquisition system reads the bridge potential, monitors the water reservoir to within 0.001°C, and uses the end-point prediction technique to reduce assay time (Ref. 7).

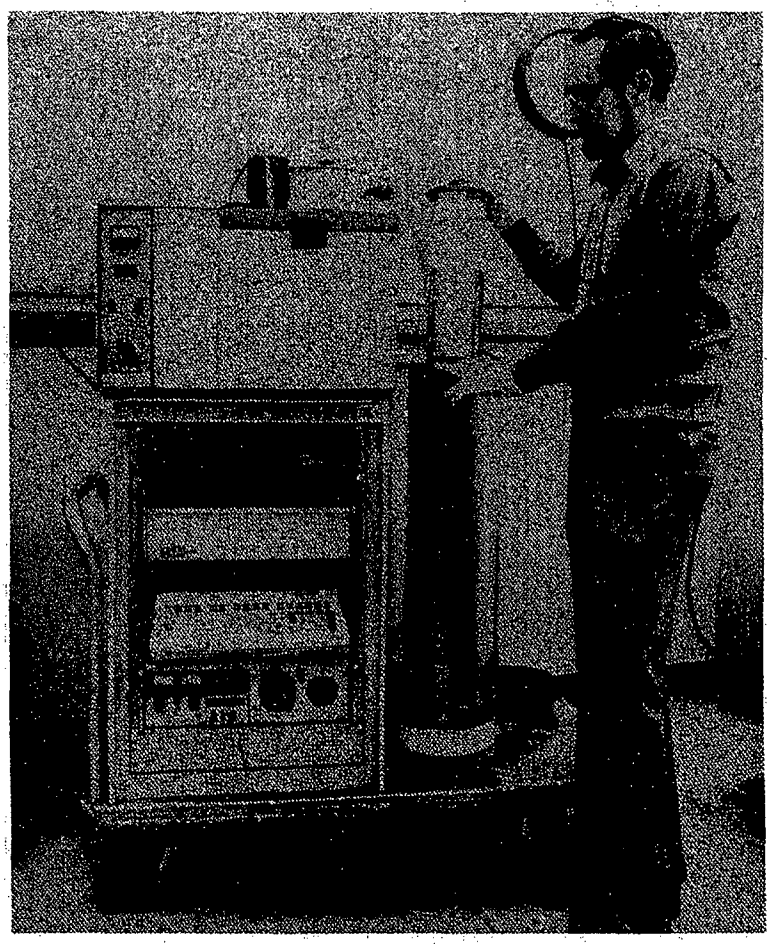

Fig. 22.3 *Mound transportable calorimeter system showing water bath temperature controller (upper left), electronics and data acquisition system (lower left), and over/under bridge calorimeter (right). (Photograph courtesy of Mound Laboratory.)*

In the field, about 4 h are required after unpacking for the water reservoir to come under temperature control and for the intrinsic germanium gamma-ray detector to cool down. During operation, about 4 h are required for each calorimeter power measurement and each gamma-ray spectrum measurement. An on-line computer is used to obtain the isotopic composition from the gamma-ray spectra and to calculate the effective specific power. Reported measurement uncertainties are about 0.3% for the power determination, including precision error, calibration error, and heater lead error, and 1 to 2% for the gamma-ray specific power determination (Ref. 6). Performance data for the transportable calorimeter are summarized in Table 22-3 (Ref. 7).

Table 22-3. Performance data for the Mound transportable calorimeter, assuming 2.3 mW/g and known isotopics (Ref. 7)

Accuracy	0.3%
Precision	0.1%
Range	200 g to 4.4 kg (0.5 to 10 W)
Assay Time	4 h

22.3.2 Argonne Bulk Assay Calorimeter

The Argonne bulk assay calorimeter (Figure 22.4) was developed for use by IAEA inspectors (Refs. 6 and 8). It is designed to measure sealed canisters holding up to 3 kg of high-burnup recycle plutonium in the form of metal, powder, or scrap. This isothermal gradient air calorimeter (see Section 21.5.4 of Chapter 21) operates in the servo-control mode (see Section 21.6.3 of Chapter 21). It consists of five nested servo-controlled cylinders separated from each other by heat-conducting epoxy. The system includes sample preheaters and is completely microprocessor controlled. The sample chamber can accept cans 11 cm in diameter and 33 cm high.

Performance data (Refs. 6, 8, 9, and 10) for the bulk assay calorimeter are summarized in Table 22-4. In one experiment, 18-cm-long mixed-oxide fuel rods were assayed in different numbers and different arrangements (Ref. 6). The assays were unaffected by the geometrical arrangement, and the response per gram was constant to within 0.1% as the number of rods was varied. This behavior differs from that of other assay techniques, where gamma-ray self-attenuation or neutron multiplication may result in nonlinear effects.

A field test of the bulk assay calorimeter was conducted at a mixed-oxide fuel fabrication plant in Belgium (Ref. 9). Five plutonium oxide cans were assayed to an average accuracy of 0.2% (1σ). Most plutonium cans at the facility had a diameter of more than 11 cm and could not be assayed during this test. A recent evaluation of the bulk assay calorimeter at three United Kingdom Atomic Energy Agency facilities involved the measurement of more than 70 standards consisting of plutonium oxide, metal, fuel pellets, or mixed oxide (Ref. 10). Using calorimeter power values and gamma-ray isotopic values, the ratio of measured to declared plutonium mass typically differed from 1 by 0.3%. The absence of a water jacket was considered helpful for such field measurements.

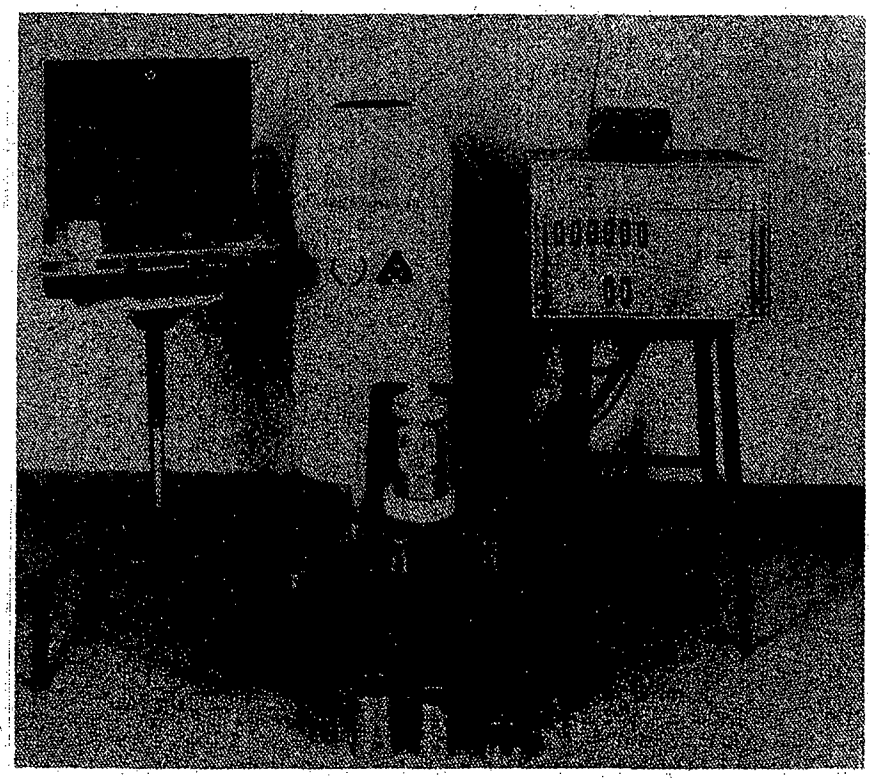

Fig. 22.4 Argonne bulk assay calorimeter (center), with data acquisition system (left), control circuit power bin (right), and sample preheating chambers and calorimeter canisters (front). (Photograph courtesy of Argonne National Laboratory.)

Table 22-4. Performance data for the Argonne bulk assay calorimeter (Refs. 6, 8, 9, and 10)

Accuracy	0.1 to 0.9%
Precision	0.1 to 0.7%
Range	up to 10 kg Pu (1.4 to 26 W)
Assay Time	4 h with end-point prediction

22.4 IN-PLANT CALORIMETERS

22.4.1 Mound Twin-Bridge Production Calorimeter

The twin-bridge production calorimeter (Figure 22.5) is designed for the assay of plutonium metal, oxide, and high-density scrap and waste (Ref. 11). The calorimeter is constructed for use in plant environments. Sample and reference cells are contained in a controlled constant temperature environmental water bath and are about 12 cm in diameter to accept standard cans in which plutonium materials are packaged. Calorimeters that can accommodate gallon-size cans of scrap and waste are also produced in this design. The instrument shown in Figure 22.5 has two twin-bridge calorimeters inside the water bath.

Each twin-bridge calorimeter may include a servo-controller for constant temperature operation, a sample pre-equilibrium chamber, or provisions for the use of end-point prediction techniques. These features can reduce assay time and increase throughput. All electrical measurements are made with bridge circuits or digital voltmeters and are fed directly into the computer data acquisition system. Standard resistors and voltage sources traceable to the National Bureau of Standards are used to ensure accurate measurements. Plutonium-238 heat standards are used for calibration.

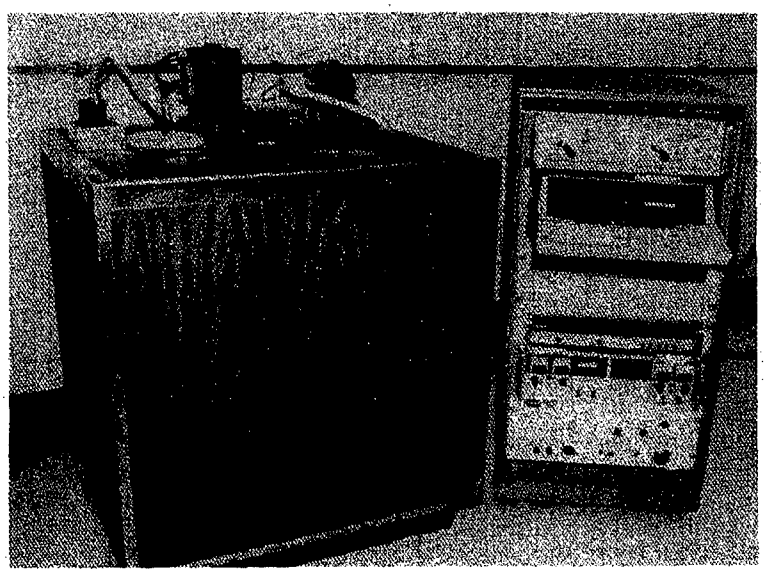

Fig. 22.5 *Mound twin-bridge production calorimeter. The water bath (left) contains two twin-bridge calorimeters. (Photograph courtesy of Mound Laboratory.)*

At the Los Alamos Plutonium Processing Facility, two Model 102 twin-bridge calorimeters sharing a common water bath (Ref. 12) similar to that shown in Figure 22.5 are used to assay plutonium feed and product. To save space, sample pre-equilibrium chambers are not used. All assays are done for 8 h without end-point prediction. A measurement control program requires the weekly measurement of either a 400- or 870-g standard. Measurement control results for 1 yr show that the power determination has a precision of about 0.1% and a drift of about 0.1%. For large samples the effective specific power is determined with a precision of about 0.4 to 0.5% (1σ) by gamma-ray spectroscopy in count times of 1.5 to 2 h. The overall precision in plutonium mass determination is then about 0.5 to 0.7% (1σ) for large, homogeneous samples.* Performance data for the twin-bridge calorimeter are summarized in Table 22-5 (Refs. 11 and 12). Similar performance data has been reported for high-burnup plutonium with an effective specific power of about 14.5 mW/g (Ref. 13).

Table 22-5. Performance data for the Mound twin-bridge production calorimeter, assuming 2.3 mW/g and known isotopics (Refs. 11, 12, and private communication*)

Accuracy	0.1 to 0.2%
Precision	0.1 to 0.2%
Range	100 g to 2.5 kg (.23 to 5.8 W)
Assay Time	8 h

*Private communication from R. Blankenship and F. Hsue, Los Alamos National Laboratory.

By way of comparison, the Los Alamos facility also uses four over/under bridge calorimeters to provide increased throughput capability. These calorimeters are similar in appearance to the calorimeters described in Section 22.4.4 below. Two have 12.4-cm-diam sample chambers; the other two have 17.8-cm-diam sample chambers. The calorimeters are operated with end-point prediction techniques to reduce assay time. For samples containing 2 to 3 kg of plutonium, assay times are typically a little more than 3 h. Small or poorly packaged samples may require up to 8 h, and 100 g is the administrative lower limit on plutonium size to avoid longer assay times. Measurement control results for 1 yr show that these faster calorimeters have a measurement precision of about 0.2% compared to about 0.1% for the twin-bridge calorimeter.*

22.4.2 Mound Calorimeter for Simultaneous Isotopics Measurements

In-plant calorimetric assay requires both sample power measurement with a calorimeter and (for the computational method) determination of sample effective specific power from mass spectroscopy or gamma-ray isotopics measurements. For a series of samples, the most common approach uses sequential measurements of the plutonium isotopics

*Private communication from R. Blankenship and F. Hsue, Los Alamos National Laboratory.

by high-resolution gamma-ray spectroscopy followed by calorimetry. The isotopics measurement and the calorimetric measurement may also be performed simultaneously.

Figure 22.6 is an example of a simultaneous measurement system (Ref. 14). The calorimeter is a Mound transportable over/under bridge type (see Figure 21.5 of Chapter 21) with three layers of water (3.1 cm total), three layers of Plexiglas (2.1 cm total), 1.0 cm of epoxy, 0.6 cm of aluminum, and 0.1 cm of stainless steel between the sample and the gamma-ray detector. The transmission of 100- to 400-keV gamma rays through the calorimeter wall is about 20 to 40%. Because this calorimeter design uses Plexiglas, with a minimum of steel and aluminum, the transmission through the calorimeter is actually higher than the transmission through the x-ray filter on the face of the gamma-ray detector.

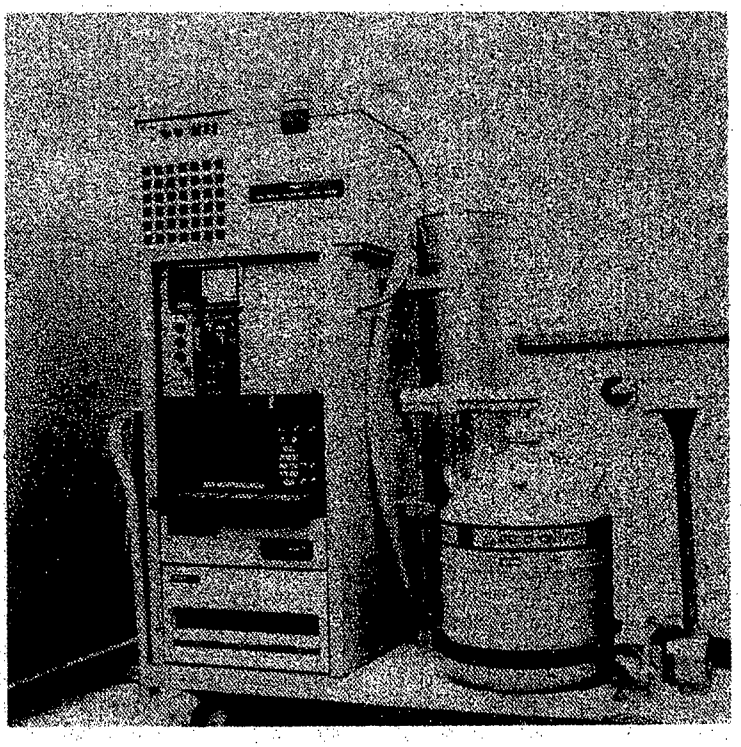

Fig. 22.6 *Mound simultaneous calorimeter power measurement and gamma-ray isotopic composition measurement system. The side-looking germanium detector is placed against the calorimeter body during the measurement. (Photograph courtesy of Mound Laboratory.)*

A typical assay time is 5 h, using end-point prediction techniques, with 0.3% uncertainty in the calorimeter power measurement (Ref. 14). Gamma-ray isotopic data were accumulated for the same time period as the power measurement. The overall assay uncertainty was 1% or less. The performance data are summarized in Table 22-6.

Both the calorimeter and the gamma-ray detector's multichannel analyzer are microprocessor controlled, and data analysis is coordinated by a minicomputer. This system is configured such that data from one sample can be analyzed while another sample is being measured. However, some loss of measurement precision is incurred in making simultaneous measurements because the sample cannot be placed directly against the gamma-ray detector. Sequential measurements are usually preferred to simultaneous measurements unless there are other overriding requirements.

Table 22-6. Performance data for the Mound simultaneous calorimetric assay system, assuming 2.3 mW/g (Ref. 14)

Overall accuracy	1.0%
Power determination accuracy	0.3%
Range	200 g to 4.4 kg (0.5 to 10 W)
Assay time	5 h with end-point prediction

22.4.3 Rocky Flats Production Calorimeters

Multiple-cell calorimeters have been developed at the Rocky Flats Plant for the assay of low-burnup plutonium oxide and scrap (Ref. 15). The calorimeters are of the twin-bridge type, with an air gap between the inner sample cell and the environmental water bath to help maintain a thermal resistance between them. Plutonium oxide cans containing approximately 1400 g are loaded into brass sample holders, which are placed into the measurement cells. Styrofoam plugs are used above and below the sample for insulation. The power output of each can is roughly 3 W. Shortly after the separation of americium from plutonium, 78% of the power output is from ^{239}Pu, 18% from ^{240}Pu, and the rest from ^{238}Pu and ^{241}Pu. The calorimetric assay of sample power is accurate to about 0.2%.

To handle the production load of samples requiring assay, three 8-unit calorimeters are available (Ref. 16). Each unit contains eight cells placed in a circle in a common water bath. Seven cells are available for sample assays, and one is used as a common reference cell.

For the new plutonium processing facility at Rocky Flats, a series of in-line calorimeters have been built by Mound Laboratory and installed under gloveboxes in the shipping and receiving area (Ref. 17). Twenty cells are connected in four banks of five cells each, with each bank having its own water bath. In each bank, one cell serves as the common reference cell for the other four sample cells. Each sample cell can equilibrate a 4-W sample in about 10 h. Overall measurement reproducibility is about 0.7% in all cells.

Calorimetric assay of plutonium scrap and waste encountered in the production process may be adversely affected by large container sizes, longer equilibrium times, or poorly known sample isotopic composition. An extreme example is found in the assay of impure salt residues that contain plutonium and up to 10% americium. In such residues

the americium may contribute 50 to 80% of the total sample power. A determination of plutonium content then requires a careful gamma-ray measurement of the americium to plutonium ratio in material that is very inhomogeneous and contains self-attenuating lumps of plutonium. This measurement has been performed by rotating and scanning the sample in a helical fashion during the isotopics measurement and by determining separate gamma-ray self-absorption correction factors for americium and plutonium (Ref. 18). The specific power is determined with a precision of about 1% and the sample power with a precision of about 0.2% (1σ). Although not yet established, the overall assay accuracy is better than that obtainable from passive gamma-ray or neutron assay, and has resulted in lower inventory difference biases (Ref. 18).

22.4.4 Mound Gradient Bridge Calorimeters

Mound Laboratory has provided four compact gradient bridge calorimeters for the plutonium scrap recovery facility at the Savannah River Plant (Ref. 19). The calorimeters are located in the sample assay room and are used to provide information on the mass of incoming plutonium metal and oxide shipments to the accountability computer. The four calorimeters (Figure 22.7) are connected by insulated water hoses to four separate temperature-controlled water reservoirs. Two of the calorimeters have outer dimensions of 31 cm diameter by 97 cm high, and accommodate standard recovery cans up to 12.4 cm in diameter. The other two calorimeters are 29 cm in diameter and 93 cm high, and only accommodate cans up to 11.0 cm in diameter, so that smaller samples can be assayed with shorter equilibration time.

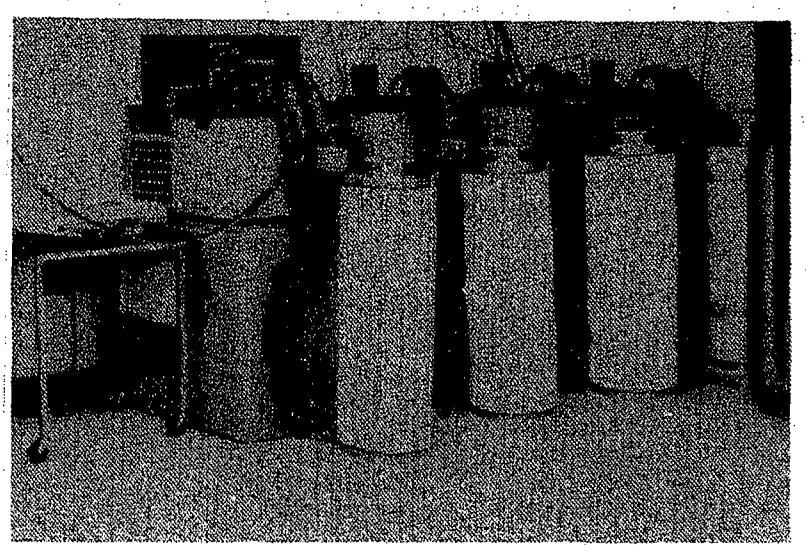

Fig. 22.7 *Array of four Mound gradient bridge calorimeters, two with 11-cm-diam sample chambers and two with 12.4-cm-diam sample chambers.*

The design of each calorimeter body (Ref. 20) is similar to the gradient bridge design shown in Figure 21.6 and described in Section 21.5.4 of Chapter 21. The thermal baffles above and below the sample chamber are made of Styrofoam. Sample weight is transmitted to the floor by a central post so that the accuracy of the bridge potential readings is not affected by strain in the windings. The sample is placed in a special stainless steel can with an O-ring seal that fits tightly into the sample chamber. If possible, air gaps between the sample and the inner wall of this "cal can" are filled with aluminum shot to reduce assay time, and air gaps above the sample are filled with crumpled aluminum foil to prevent air circulation. The time required to reach equilibrium depends on sample diameter, packaging, and the width of any air gap.

The four calorimeters are operated in the constant temperature servo-control mode (Ref. 20). The water bath temperatures are controlled to within 0.001°C, and the temperatures are checked every 2 min. The water temperature is selected such that the ratio of heating to cooling required from the controller is about 1.1. Each reservoir uses about one cup of distilled water per week. The electronics include five computer-controlled digital voltmeters, one for each bridge circuit output and one to monitor room temperature. Each heater winding is connected as a four-terminal resistor so that the voltage across the winding can be determined without errors resulting from power losses in the leads.

Operation of each calorimeter requires periodic baseline power runs to establish the empty chamber power level (Ref. 20). Baseline power runs typically require 2 to 2.5 h, less than actual sample assays, because there is no mass in the sample chamber. The baseline power level (near 15 W) is set at least 3 W greater than the estimated wattage for actual samples or calibration standards. The calorimeters have been provided with small $^{238}PuO_2$ heat source standards mounted in special cans. These standards are measured periodically to monitor instrument performance. Calorimeter performance can be affected if the calorimeter is bumped, if the lid is removed during an assay, or if fluctuations occur in room temperature and humidity, bath temperature, or power supply voltage. For plutonium scrap, assay time can vary widely depending on sample composition, packaging, size, and power. For a typical wattage range of 2 to 12 W, the accuracy of the calorimeter measurement is 0.2% (Ref. 21). Performance specifications for the gradient bridge calorimeters are summarized in Table 22-7.

Table 22-7. Performance specifications for the Mound gradient bridge calorimeters (Ref. 20 and 21)

Accuracy	0.5% at 2 W
Precision	0.1%
Range	500 g to 5 kg (2 to 12 W)
Assay time	4 h for product 8 to 16 h for scrap

22.5 FUEL ROD CALORIMETERS

22.5.1 Argonne One-Meter Fuel Rod Calorimeter

The Argonne one-meter fuel rod calorimeter is intended for the nondestructive assay of the plutonium content of unirradiated mixed-oxide fuel rods (Ref. 22). The prototype for this instrument is an earlier Argonne instrument used for the calorimetric assay of 6-in.-long fuel rods (Ref. 23). A four-meter fuel rod calorimeter has also been built (Ref. 24). Measurements with these instruments are relatively fast because of the small diameter of the sample chamber and the calorimeters are called "fast response" calorimeters.

This calorimetric assay system contains the following components (see Figure 22.8) (Refs. 25 and 26):

1. *Calorimeter box.* The one-meter fuel rod calorimeter is an isothermal gradient air calorimeter (See Section 21.5.4 of Chapter 21) that is operated in the servo-control mode (Section 21.6.3). It has three regions of controlled temperature: the 1-cm-diam sample chamber, the surrounding thermal shield and heating circuits, and the remaining volume of the box. These three regions are controlled to be at 33, 32, and 30°C, respectively.
2. *Preheater.* A preheater for heating rods prior to their injection into the measuring chamber is connected to the calorimeter measurement box. The preheater reduces assay time and provides additional space for holding rods larger than 1 m.
3. *Control console.* The control console contains the servo-control circuits, the temperature sensor controls, and other electrical measurement controls.
4. *Computer.* Data acquisition and analysis and hard-copy printout of results are controlled by a small portable computer.

The effective fuel rod length that can be accommodated by this instrument is 98 cm. Longer fuel rods must be assayed in 1-m segments. Along the axis, the response of the calorimeter to heat sources is nonlinear. A correction must be made for the length of the fuel column and its position (Ref. 22). Also, when the baseline power level is being determined, a dummy fuel rod must be inserted to simulate heat losses through the ends. Calorimeter operation can be checked by an internal electrical calibration or by calibration with electrically heated resistance rods.

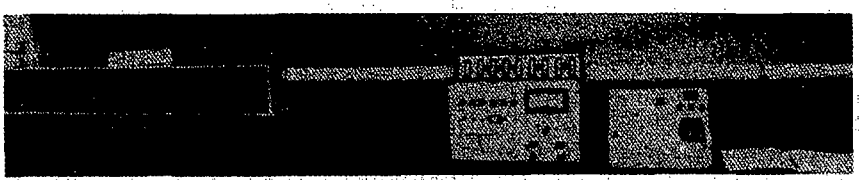

Fig. 22.8 *Argonne Model IV fuel rod calorimetric system for one-meter fuel rods, showing the calorimeter (left), preheater (long white cylinder), and electronics packages. (Photograph courtesy of Argonne National Laboratory.)*

Field test and evaluation exercises of the fuel rod calorimeter were conducted at several Belgian facilities in cooperation with the IAEA (Refs. 27 and 28). At one facility, four different geometries of fuel rods containing from 3.6 to 28.5 g of plutonium and having three different isotopic compositions were measured. All 12 fuel rods were preheated and then measured for 1 h, with each fuel rod measurement preceded by a 1-h baseline power measurement. The precision was 1 mW over the range of 10 to 135 mW. For rods with more than 50 mW of power, the observed accuracy was on the order of 3% (1σ) or less, which was within the errors of measurement and uncertainty in actual plutonium mass (Ref. 27).

Two more batches of 6 and 11 mixed-oxide fuel rods were measured at two other Belgian facilities. Some of the fuel rods were as long as 2.5 m; the inactive portion was kept within the preheater. For fuel rods of the type for which the instrument was designed, the calorimeter performed well, with a measurement precision of about 0.4%. For rods with low power output, the measurement data were inconclusive. Use of the one-meter fuel rod calorimeter for rods with power outputs less than 40 mW is not recommended because the power output would be less than 5% of the baseline power (Ref. 28). Performance data for the Argonne one-meter fuel rod calorimeter are summarized in Table 22-8.

Table 22-8. Performance data for the Argonne one-meter fuel rod calorimeter, assuming 5 mW/g and known isotopics (Refs. 27 and 28)

Accuracy	1 to 3%
Precision	0.4% or 0.2 g (1 mW)
Range	8 to 160 g Pu (40 to 800 mW)
Assay time	15 min to 2 h

22.5.2 General Electric Irradiated Fuel Assembly Calorimeter

The General Electric irradiated fuel storage facility near Morris, Illinois, has developed an in-basin calorimeter for underwater measurements of the heat generated by irradiated fuel assemblies (Ref. 29). The calorimeter is similar in size and shape to a water boil-off calorimeter developed earlier by Pacific Northwest Laboratory for above-water, hot cell measurements (Ref. 30). The General Electric calorimeter is operated in the unloading pit of the fuel storage basin at a depth of about 40 ft. Although the calorimeter was developed to provide heat generation information for planning future irradiated fuel storage needs, it was also possible to correlate the measured heat with fuel burnup.

The in-basin calorimeter (Figure 22.9) is 4.6 m long and consists of two concentric steel pipes (Ref. 29). The 41-cm-diam inner pipe forms the sample chamber, which can be fitted with inserts to support either boiling or pressurized water reactor fuel assemblies. The annular space between the two pipes contains 6 cm of urethane insulation to reduce heat transfer from the calorimeter to the basin water. Temperature measurements inside the sample chamber and outside the calorimeter are made with

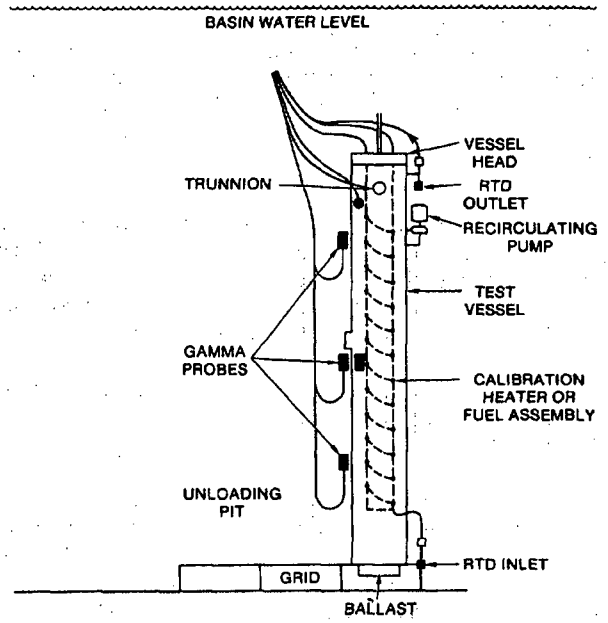

Fig. 22.9 *General Electric-Morris Operations in-basin calorimeter for measurement of irradiated fuel assemblies in the unloading pit of the fuel storage basin—RTD = platinum resistance temperature detector. (Figure courtesy of General Electric-Morris Operations.)*

platinum resistance temperature detectors. A recirculation pump maintains a homogeneous water temperature inside the sample chamber. Gamma radiation monitors are installed on the calorimeter to measure radiation heat losses and axial fuel assembly burnup profiles.

The calorimeter is usually operated with a constant temperature environment. After a fuel assembly is loaded into the calorimeter, a water-tight head is bolted on to seal the sample chamber (Ref. 29). The rise in internal water temperature is monitored over a 5-h period. Water temperature outside the calorimeter is usually stable to 0.1°F if water circulation is provided in the basin. The rate of change of internal water temperature (typically 2°F/h) is proportional to the thermal output of the fuel assembly. The calorimeter is calibrated with a 4-m-long pipe wrapped with electrical heater tape. All measurements are corrected for heater lead power losses, heat capacity variations between calibration and actual fuel, and gamma radiation heat losses.

Reference 29 reports a series of 24 measurements of 14 PWR fuel assemblies with operator-declared burnups of 26 to 40 GWd/tU and cooling times of 4 to 8 yr. The in-basin calorimeter measured thermal powers of 360 to 940 W with a precision of 1%. The

measured power was compared to that calculated from reactor fuel burnup codes. The agreement varied from 15% (if the codes assumed constant irradiation histories) to 1% (if the codes used the actual irradiation histories). For assemblies with the same cooling times, measured power was proportional to burnup to within about 3%.

REFERENCES

1. C. Fellers, W. Rodenburg, J. Birden, M. Duff, and J. Wetzel, "Instrumentation Development for the Enhanced Utilization of Calorimetry for Nuclear Material Assay," in Proc. American Nuclear Society Topical Conference on Measurement Technology for Safeguards and Materials Control, Kiawah Island, South Carolina, November 26-28, 1979, NBS Special Publication 582 (1980), p. 192.

2. W. Rodenburg, "An Evaluation of the Use of Calorimetry for Shipper-Receiver Measurements of Plutonium," Mound Laboratory report MLM-2518, NUREG/CR-0014 (1978).

3. C. Roche, R. Perry, R. Lewis, E. Jung, and J. Haumann, "ANL Small-Sample Calorimeter System Design and Operation," Argonne National Laboratory report ANL-NDA-1 (1978).

4. C. Roche, R. Perry, R. Lewis, E. Jung, and J. Haumann, "A Portable Calorimeter System for Nondestructive Assay of Mixed-Oxide Fuels," American Chemical Society Symposium Series, No. 79 (1978).

5. W. Rodenburg, "Test and Evaluation of an ANL Small-Sample Calorimeter," Mound Laboratory report MLM-2813 (1981).

6. C. Roche, R. Perry, R. Lewis, E. Jung, and J. Haumann, "Calorimetric Systems Designed for In-Field Nondestructive Assay of Plutonium-Bearing Materials," IAEA/Argonne National Laboratory report IAEA-SM-231/78 (1978).

7. J. Lemming, W. Rodenburg, D. Rakel, M. Duff, and J. Jarvis, "A Field Test of a Transportable Calorimetric Assay System," *Nuclear Materials Management* IX (2), 109 (1980).

8. R. Perry, C. Roche, A. Harkness, G. Winslow, G. Youngdahl, R. Lewis, and E. Jung, "The Bulk Assay Calorimeter: Part 1. System Design and Operation, Part 2. Calibration and Testing," Argonne National Laboratory report ANL-NDA-9 (1982).

9. R. Perry and A. Keddar, "Field Test of the Bulk-Assay Calorimeter," Argonne National Laboratory report ANL-NDA-11 (1982).

10. G. M. Wells and F. J. G. Rogers, "Measurements of Plutonium Mass Using an Argonne Bulk Calorimeter," United Kingdom Atomic Energy Agency report NMACT (86) (1986), p. 8.

11. F. O'Hara, J. Nutter, W. Rodenburg, and M. Dinsmore, "Calorimetry for Safeguards Purposes," Mound Laboratory report MLM-1798 (1972).

12. W. Rodenburg, "Some Examples of the Estimation of Error for Calorimetric Assay of Plutonium-Bearing Solids," Mound Laboratory report MLM-2407, NUREG-0229 (1977).

13. W. Strohm, W. Rodenburg, and R. Carchon, "Demonstration of the Calorimetric Assay of Large Mass, High Burn-Up PuO_2 Samples," *Nuclear Materials Management* XIII (Proceedings Issue), 269 (1984).

14. D. Rakel, J. Wetzel, and T. Elmont, "A Field Test and Evaluation of the Simultaneous Calorimetric Assay System," in Proc. Twenty-Fifth Annual Meeting of the Institute of Nuclear Materials Management, Columbus, Ohio, July 1984.

15. F. L. Oetting, "Calorimetry at Dow Rocky Flats," in "Proceedings of the Symposium on Calorimetric Assay of Plutonium, October 1973," Mound Laboratory report MLM-2177 (1974), p. 66.

16. R. B. White and F. L. Oetting, "An Eight-Unit Isothermal Calorimeter," USAEC RFP-1401, Rocky Flats (1969).

17. F. Haas, J. Gilmer, G. Goebel, J. Lawless, J. Pigg, D. Scott, and A. Tindall, "Implementation of NDA Instrumentation in the Rocky Flats Processing Facility," in *Proc. ANS/INMM Conference on Safeguards Technology: The Process Safeguards Interface,* Hilton Head Island, South Carolina, November 28-December 2, 1983 (1984), p. 106.

18. J. G. Fleissner, "NDA of Plutonium in Isotopically Heterogeneous Salt Residues," in *Proc. ANS/INMM Conference on Safeguards Technology: The Process Safeguards Interface,* Hilton Head Island, South Carolina, November 28-December 2, 1983 (1984), p. 275.

19. M. P. Baker, "An Integrated Nondestructive Assay System for a New Plutonium Scrap Recovery Facility," in *Proc. of the 7th Annual Symposium on Safeguards and Nuclear Material Management, ESARDA,* Liege, Belgium, May 21-23, 1985 (1985), pp. 109-112.

20. J. Wetzel, "Calorimeter System Users Manual for the SRP/NSR Facility," Mound Laboratory informal report, May 1986.

21. M. F. Duff, J. R. Wetzel, and J. F. Lemming, "Calorimetry Design Considerations for Scrap Assay," *American Nuclear Society Transaction* 50, 170 (1985).

22. R. B. Perry et al., "One-Meter Fuel Rod Calorimeter Design and Operating Manual," Argonne National Laboratory report ANL-NDA-4 (1981).

23. N. S. Beyer, R. N. Lewis, and R. B. Perry, "Small Fast-Response Calorimeters Developed at Argonne National Laboratory for the NDA of Plutonium Fuel Rods," in "Proceedings of the Symposium on Calorimetric Assay of Plutonium, October 1973," Mound Laboratory report MLM-2177 (1974).

24. S. Brumbach, A. Finkbeiner, R. Lewis, and R. Perry, "Design and Construction Effort for the Four-Meter Fuel Rod Calorimeter", in "Plutonium Calorimetry and SNM Holdup Measurements Progress Report," Argonne National Laboratory report ANL-77-8 (1977).

25. N. S. Beyer, R. B. Perry, and R. N. Lewis, "Advances in Fuel Rod Calorimetry with the ANL FFTF Calorimeter," *Nuclear Materials Management* IV (3), 577 (1975).

26. N. S. Beyer, R. N. Lewis, and R. B. Perry, "Fast-Response Fuel Rod Calorimeter for 36 inch Fuel Columns," *Nuclear Materials Management* III, 118 (1974).

27. W. Rodenburg and A. Keddar, "Test and Evaluation of the One-Meter Fuel Rod Calorimeter at Mol, Belgium, June 1981." Mound Laboratory report MLM-3003 (1982).

28. R. B. Perry and A. Keddar, "Field Test of the One-Meter Fuel Rod Calorimeter," Argonne National Laboratory report ANL-NDA-10 (1982).

29. B. Judson, J. Doman, K. Eger, and Y. Lee, "In-Plant Test Measurements for Spent-Fuel Storage at Morris Operation," General Electric Company report NEDG-24922-3 (1982).

30. J. Creer and J. Shupe, Jr., "Development of a Water Boil-Off Spent-Fuel Calorimeter System," Pacific Northwest Laboratory report PNL-3434 (1981).

23

Application Guide

N. Ensslin, D. Reilly, and H. Smith, Jr.

23.1 INTRODUCTION

This chapter is an applications guide to nondestructive assay (NDA) techniques to aid the user in matching instruments with measurement problems. The figures and tables of this chapter refer to many of the measurement techniques described earlier in the book; several important active techniques are also included. Additional information on active NDA techniques is provided in the Nuclear Regulatory Commission (NRC) manual *Active Nondestructive Assay of Nuclear Materials*, by T. Gozani (Ref. 1). Detailed summaries of NDA measurement methods and results are provided in the NRC *Handbook of Nuclear Safeguards Measurement Methods*, edited by D. R. Rogers (Ref. 2).

Figure 23.1 is an overview of NDA techniques including examples of some common instruments associated with each technique. The figure illustrates the variety of techniques available to the assayist. In the various nuclear fuel cycles, plutonium and uranium appear in many forms, and this can often make it difficult for the user to select the appropriate technique for his measurement needs. This guide attempts to address this problem by summarizing the capabilities of the principal gamma-ray and neutron assay techniques (Section 23.2) and by providing a detailed table that matches nuclear materials with appropriate NDA instruments (Section 23.3).

This guide does not address irradiated fuel measurements, perimeter monitors, or attribute and holdup measurements; these subjects are covered in Chapters 18, 19, and 20.

23.2 CAPABILITIES OF SELECTED PASSIVE AND ACTIVE NDA TECHNIQUES

Gamma rays follow radioactive decay and carry energy information that uniquely identifies the nuclides present in the sample. This information is usually preserved by the detection process. The principal difficulty for gamma-ray assay is to accurately correct for sample attenuation. Gamma-ray attenuation increases with atomic number

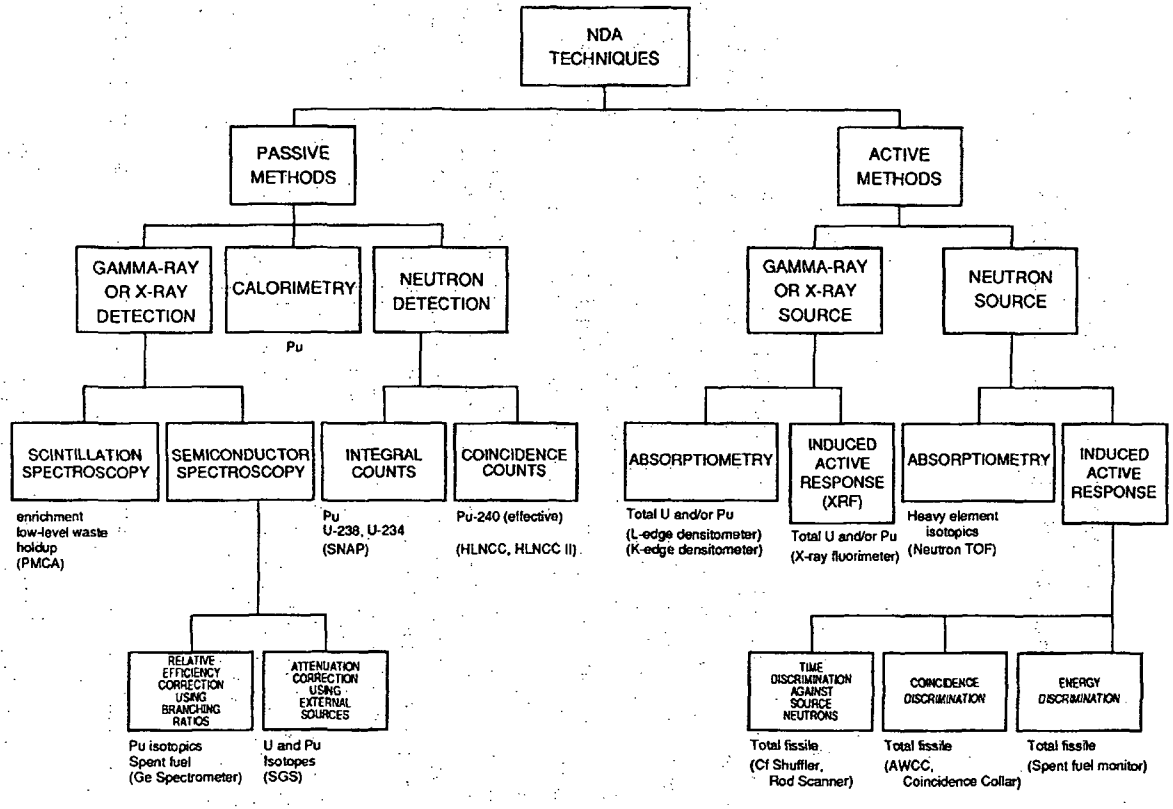

Fig. 23.1 An overview of passive and active NDA techniques, including the names of some common instruments.

and material density, so gamma-ray assay techniques work best for materials with low atomic number (<25) and low density (<1 g/cm^3). Neutrons carry less specific energy information, and even this is lost in the typical detection process. Neutron radiation does not provide information to identify the nuclear species present in the sample. On the other hand, neutrons penetrate dense, high-atomic-number materials (for example lead and uranium) with ease. They have more difficulty with very low atomic number materials, especially anything containing hydrogen, such as water or polyethylene. Gamma-ray and neutron assay techniques are, therefore, complementary because of their different sensitivities to density and material type. In general, passive assay techniques work well on plutonium samples because plutonium decay reactions (alpha decay and spontaneous fission) have high specific activities. The very low specific activities of the uranium decay modes often dictate the use of active measurement techniques.

The figures in this section summarize the accuracy that may be expected for the assay of a single sample using the principal NDA techniques. Figure 23.2 illustrates the "assayability" of various material forms using gamma-ray spectroscopy techniques. Homogeneous, low-density materials such as gases, solutions, and powders can be assayed most accurately. For these materials, gamma-ray assay is the technique of choice because the observed spectral peaks provide unique signatures that identify the nuclear material isotopes present and also yield a quantitative assay of the isotopic mass. It is important to note that gamma-ray spectroscopy provides a clear identification of the nuclear species in a sample, even in cases where the sample is too dense or too heterogenous to permit an accurate determination of mass.

For heterogeneous or dense materials where the gamma-ray attenuation is too high to permit accurate corrections, neutron assay techniques may be preferable. Figure 23.3 illustrates the "assayability" of different nuclear materials using neutron counting techniques. Most large samples of metal, oxide, and high-density scrap and waste require neutron-based techniques. Neutron assay accuracy is degraded if there is a high background from (α,n) reactions or if moderating materials such as moisture or combustible waste are present.

For the assay of plutonium, calorimetry provides a slower but more accurate assay alternative, which is insensitive to the presence of matrix materials (except that matrix materials may increase the assay time by increasing the time required to reach thermal equilibrium). Both calorimetry and neutron assays usually require knowledge of the isotopic composition of the plutonium being measured; gamma-ray spectroscopy provides one way to measure isotopic composition.

Figures 23.4 and 23.5 illustrate the range of performance for the most common gamma-ray and neutron assay techniques. In general, the gamma-ray techniques, where applicable, are more accurate than neutron techniques. Also, passive assay techniques are often more accurate than active assay techniques because the sample matrix can affect both the induced and the interrogating radiation, and the interrogating radiation can interfere with the assay radiation, thereby reducing sensitivity and precision.

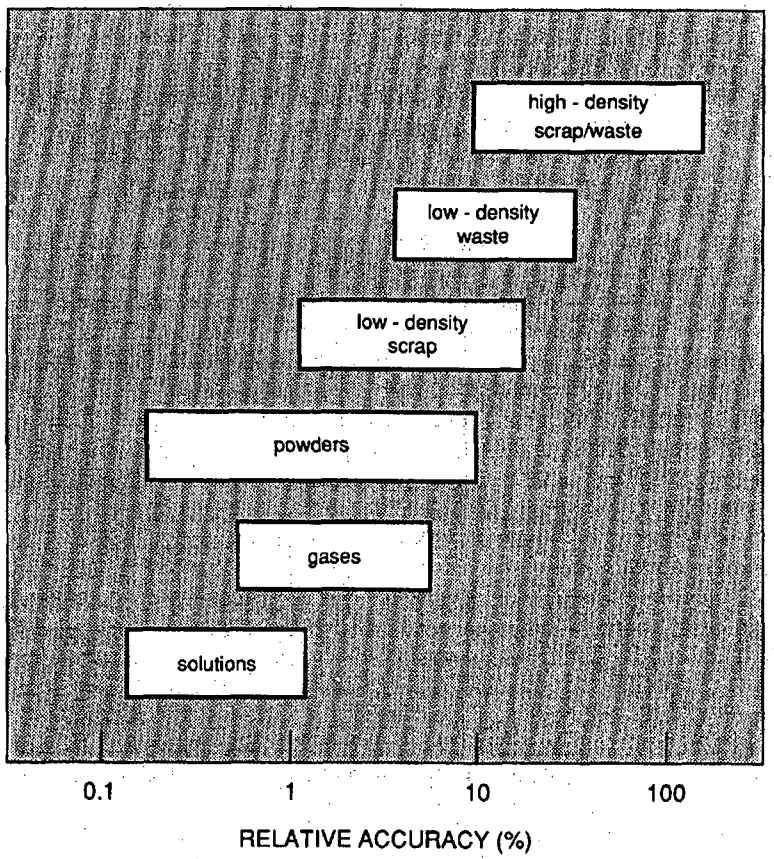

Fig. 23.2 Sample "assayability" using gamma-ray spectroscopy techniques. By way of comparison, destructive analytical chemistry techniques routinely achieve accuracies in the range 0.05% to 0.5%.

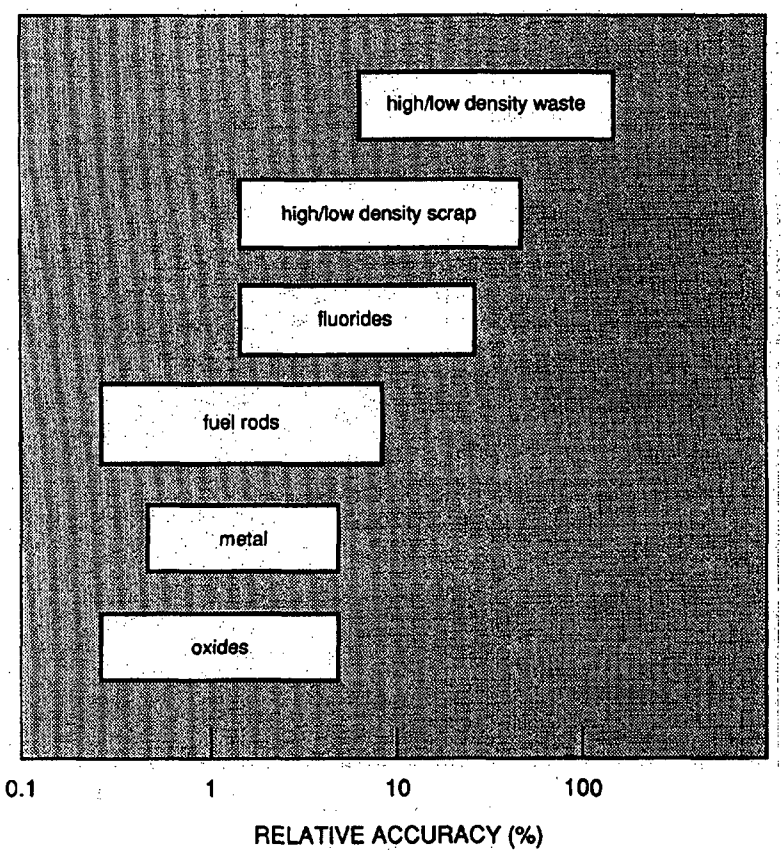

***Fig. 23.3** Sample "assayability" using neutron-based NDA techniques.*

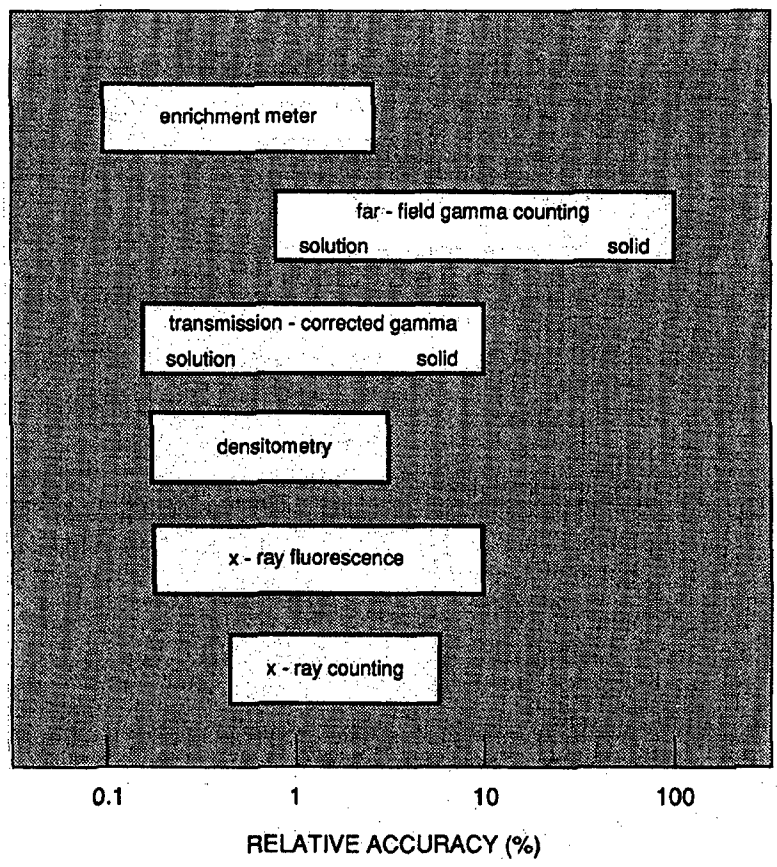

Fig. 23.4 The range of performance for gamma-ray NDA techniques.

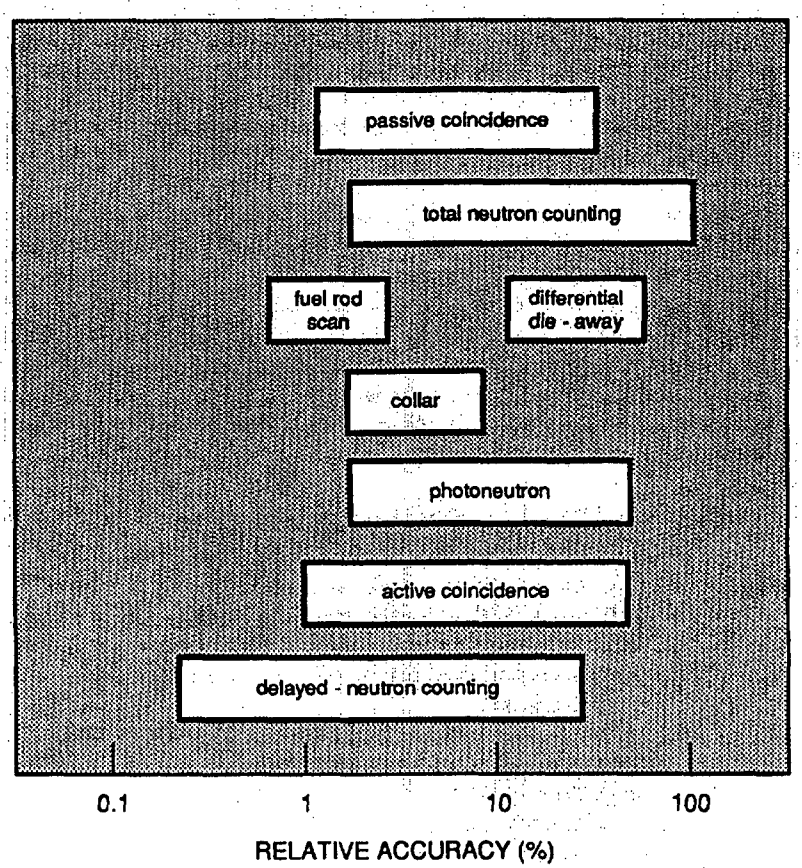

Fig. 23.5 The range of performance for neutron-based NDA techniques.

23.3 NUCLEAR MATERIAL TYPES AND APPLICABLE NDA TECHNIQUES

Table 23-1 provides a list of NDA techniques that may be applicable to a given measurement problem. In spite of its large size, Table 23-1 is not all-inclusive, and every entry is actually a generalization of many possible techniques. The table should serve as a starting point to guide the user toward a suitable technique. More detailed application tables are given in the *Handbook of Nuclear Safeguards Measurement Methods* (Ref. 2). An explanation of the table headings is given below.

Nuclear Material: Table 23-1 covers the following material types: plutonium, high-enriched uranium (HEU), low-enriched uranium (LEU), and mixed uranium and plutonium.

Material Form or Matrix: Table 23-1 covers metal, oxide, fluoride, solutions, fuel pellets and rods, and high- and low-density scrap and waste. In most cases, the assay approach for carbides is the same as for oxides. For fluorides, some assay techniques are suitable for PuF_6 or UF_6 gas and others are suitable for PuF_6, PuF_4, UF_6, or UO_2F_2 in either liquid, powder, or solid form. For neutron-based assay techniques, oxides have low (α,n) yields and fluorides have high (α,n) yields.

Scrap is relatively rich in nuclear material and is usually recycled, whereas the nuclear material content of waste is relatively low and can usually be discarded. Scrap and waste may be suitable for gamma-ray assay, if they have sufficiently low density.

NDA Technique: Table 23-1 covers the following NDA techniques or instruments:

gamma-ray:	Far-field assay without transmission correction (MEGAS: MultiEnergy Gamma Assay System)
	Transmission-corrected assay viewing entire sample.
	Transmission-corrected segmented scan (SGS: Segmented Gamma Scanner)
	Enrichment meter (^{235}U concentration).
	Isotopic composition determination (Pu).
	K-edge densitometry.
	L_{III}-edge densitometry.
	X-ray fluorescence (K or L).
neutron:	Neutron totals counting (SNAP: Shielded Neutron Assay Probe)
	Passive neutron coincidence counting (HLNCC: High-Level Neutron Coincidence Counter)
	Active neutron coincidence counting (AWCC: Active Well Coincidence Counter)
	Active neutron coincidence collar.
	Random driver (fast-neutron coincidence counting).

neutron:	Neutron coincidence self-interrogation. Californium shuffler (delayed neutron counting). Photoneutron interrogation (PHONID: PHOtoNeutron Interrogation Device) Differential die-away technique.
calorimetry:	Plus isotopic measurement.

There are other NDA techniques that are not included in this list, such as the accelerator-based measurements described in Ref. 1.

For each nuclear material and matrix, only the most commonly used techniques are included in the table. The techniques are listed in the order of decreasing accuracy or frequency of use. The choice of technique may depend on the specific measurement problem and on factors such as cost, sample throughput, available space, etc.

Measured Isotopes: The NDA techniques listed in Table 23-1 may determine element or isotope mass or concentration. The user often requires supplemental information, usually isotopic composition, which may be available from the facility or from other destructive or nondestructive measurements. For calorimetric assay, *the accuracy stated in Table 23-1 includes the estimated accuracy of the isotopic measurement.*

Passive or Active: This column indicates whether the technique uses an external neutron or gamma-ray source to irradiate the sample. The neutron coincidence self-interrogation technique, which measures the fissions induced by (α,n) neutrons from internal reactions, is classified as passive.

Range: This column provides a very rough estimate of the applicable mass or concentration range of the NDA technique. The quoted lower limit is the measurability limit rather than the detectability limit, which may be considerably less than the mass given in the table. The range is stated in terms of the *element mass* even if only one isotope is measured.

Time: This is the approximate measurement time required to produce the stated precision.

Precision: This is the reproducibility of a single measurement stated, in percent, as one relative standard deviation. The precision is estimated for mid-range samples and, for active techniques, an optimum interrogation source strength is assumed.

Accuracy: The accuracy is stated, in percent, as one relative standard deviation, and includes the errors due to measurement precision, sample position, calibration, and instrument bias. For calorimetry, the estimated accuracy includes, and is often dominated by, the accuracy of the isotopic determination. The numbers quoted for scrap/waste assume some sorting and segregation into material categories and also assume the presence of few or no self-attenuating lumps of nuclear material.

Reference: References shown as numbers only refer to the section in this book where more detailed information can be found on a given measurement technique. Reference "x.y" refers to Section y in Chapter x. Other sources include Refs. 1 through 9.

Table 23-1. Guide to NDA techniques

Material Form or Matrix	NDA Technique	Measured Isotopes	Passive or Active	Range	Time	Precision (%)	Accuracy (%)	Reference
Pu								
metal	calorimetry/mass spec. isot.	total Pu	P	10 - 6000 g	4 h	0.3	0.3	21.9
	calorimetry/gamma isotopics	total Pu	P	10 - 6000 g	4 h	0.5	1 - 2	21.9
	neutron coincidence (HLNCC)	fertile	P	10 - 6000 g	300 s	0.5	1 - 4	17.2
	neutron totals (SNAP)	fertile	P	10 - 6000 g	30 s	1	2	15.2
	neutron coincidence (AWCC)	fissile	A	10 - 10000 g	1 h	5	5 - 10	17.3
	gamma isotopic	all but ^{242}Pu	P	0.1 - 10000 g	30 - 60 min	0.1 - (3 - 5)	0.1 - 1	8.7.5
oxide	calorimetry/mass spec. isot.	total Pu	P	10 - 6000 g	4 - 6 h	0.3	0.3	21.9
	calorimetry/gamma isotopics	total Pu	P	10 - 6000 g	4 - 6 h	0.5	1 - 2	21.9
	neutron coincidence (HLNCC)	fertile	P	10 - 6000 g	300 s	0.5	1 - 3	17.2
	neutron coincidence (AWCC)	fissile	A	10 - 10000 g	1 h	5	10	17.3
	gamma isotopic	all but ^{242}Pu	P	0.1 - 10000 g	30 - 60 min	0.1 - (3 - 5)	0.1 - 1	8.7.5
PuF_4 powder	neutron totals	fertile	P	1 - 500 g	30 s	1	2 - 5	15.2
	neutron coincidence self-interrogation	fissile	P	50 - 1000 g	600 s	1	5-10	20.4
solutions	transmission-corrected gamma	^{239}Pu conc.	P	0.001 - 400 g/L	1000 s	0.2 - 1	0.2-1	6.9.4
	K-edge densitometry	Pu conc.	A	40 - 500 g/L	1500 s	0.5	0.2 - 1	9.4
	L_{III}-edge densitometry	Pu conc.	A	5 - 100 g/L	1500 s	0.5	0.2 - 1	9.4
	x-ray fluorescence	Pu conc.	A	0.1 - 400 g/L	300 s	0.5	0.3 - 1	10.5
	neutron coincidence (HLNCC)	fertile	P	1 - 500 g	300 s	0.5	1 - 5	17.2

Table 23-1. (Continued)

Material Form or Matrix	NDA Technique	Measured Isotopes	Passive or Active	Range	Time	Precision (%)	Accuracy (%)	Reference
Pu								
fuel rods	neutron coincidence (pin-tray counter)	fertile	P	10 - 1000 g	600 s	1	0.5 - 2	Ref. 8
fuel assembly	neutron coincidence (breeder counter)	fertile/fissile	P	1 - 9 kg	300 s	0.2	0.5 - 2	Ref. 9
scrap/waste	neutron coincidence (HLNCC)	fertile	P	10 - 6000 g	300 s	1 - 5	2 - 30	17.2
(high density)	calorimetry/mass spec. isot.	total Pu	P	10 - 6000 g	8 - 16 h	0.3	0.5	22.4
	calorimetry/gamma isot.	total Pu	P	10 - 6000 g	8 - 16 h	0.5	1 - 2	22.4
	neutron coincidence self-interrogation	fissile	P	50 - 3000 g	1000 s	1	10	20.4
scrap/waste	segmented gamma scan (SGS)	^{239}Pu	P	1 - 1400 g	1000 s	1	1 - 5	6.9.5
(low density)	far-field gamma count	^{239}Pu	P	1 - 1400 g	300 s	1 - 2	1 - 5	6.9
	neutron coincidence (HLNCC)	fertile	P	10 - 6000 g	1000 s	5	5 - 30	17.2
	x-ray count (MEGAS)	^{239}Pu	P	10 μg - 10 g	200 s	10	10 - 50	Ref. 2
	differential die-away	fissile	A	5 mg - 10 g	1000 s	1	30	Ref. 3
HEU								
metal	californium shuffler	fissile	A	1 g - 10 kg	1000 s	0.1	0.5 - 5	Ref. 4
	neutron coincidence (AWCC)	fissile	A	10 g - 10 kg	1000 s	0.5 - 5	1 - 5	17.3
	random driver	fissile	A	50 g - 10 kg	1000 s	1 - 5	1 - 5	Ref. 5
	photoneutron interrogation (PHONID)	fissile	A	1 g - 1 kg	200 s	0.1 - 3	1 - 5	Refs. 6, 7
	enrichment meter	^{235}U (%)	P	200 g - 20 kg	300 s	0.1 - 1	0.1 - 0.5	7.3

Table 23-1. (Continued)

Material Form or Matrix	NDA Technique	Measured Isotopes	Passive or Active	Range	Time	Precision (%)	Accuracy (%)	Reference
HEU								
oxide	transmission-corrected gamma	^{235}U	P	0.1 - 200 g	300 s	1	1 - 2	6.9.3
	enrichment meter	^{235}U (%)	P	200 g - 20 kg	100 s	0.1 - 1	0.1 - 0.5	7.3
	californium shuffler	fissile	A	1 g - 20 kg	1000 s	0.1	0.3 - 3	Ref. 4
	neutron coincidence (AWCC)	fissile	A	10 g - 20 kg	1000 s	1 - 5	1 - 5	17.3
	random driver	fissile	A	50 g - 10 kg	1000 s	1 - 5	1 - 5	Ref. 5
	photoneutron interrogation (PHONID)	fissile	A	1 g - 3 kg	200 s	0.1 - 3	1 - 5	Refs. 6, 7
	neutron totals (SNAP)	^{234}U	P	100 g - 10 kg	500 s	2 - 5	5 - 10	15.2
UF_6 gas	transmission-corrected gamma	^{235}U	P	0.1 - 100 g	1000 s	0.7	1	7.5
UF_6 liquid	enrichment meter	^{235}U (%)	P	200 g - 20 kg	300 s	0.1 - 1	0.25	7.3
UF_6 solid	neutron coincidence (AWCC)	fissile	A	100 - 1000 g	1000 s	1 - 5	1 - 5	Ref. 6
	neutron coincidence self-interrogation	fissile	P	1 - 20 kg	600 s	0.5	3	17.3
	neutron totals	^{234}U	P	10 g - 10 kg	200 s	2	2 - 5	15.2
	enrichment meter	^{235}U (%)	P	200 g - 20 kg	300 s	0.2 - 1	0.5 - 5	7.7
solutions	transmission-corrected gamma	^{235}U conc.	P	0.001 - 400 g/L	1000 s	0.1 - 0.2	0.2 - 1	6.9
	K-edge densitometry	U conc.	A	40 - 500 g/L	1500 s	0.5	0.2 - 1	9.4
	L_{III}-edge densitometry	U conc.	A	5 - 100 g/L	1500 s	0.5	0.2 - 1	9.4
	x-ray fluorescence	U conc.	A	0.1 - 400 g/L	300 s	0.5	0.3 - 1	10.5

Table 23-1. (Continued)

Material Form or Matrix	NDA Technique	Measured Isotopes	Passive or Active	Range	Time	Precision (%)	Accuracy (%)	Reference
HEU								
fuel pellets	random driver	fissile	A	50 g - 10 kg	1000 s	1 - 5	1 - 5	Ref. 5
	neutron coincidence (AWCC)	fissile	A	10 g - 10 kg	1000 s	1 - 5	1 - 5	17.3
	californium shuffler	fissile	A	1 g - 10 kg	1000 s	0.1 - 2	0.3 - 3	Ref. 4
	photoneutron interrogation (PHONID)	fissile	A	1 g - 3 kg	200 s	0.1 - 3	1 - 5	Refs. 6, 7
	gamma-ray well counter	^{235}U	P	0.1 - 10 g	300 s	0.2	0.1 - 0.5	7.3
	enrichment meter	^{235}U (%)	P	200 g - 20 kg	300 s	0.5	0.25 - 1	Ref. 2
fuel rods	neutron coincidence collar	fissile	A	100 g - 10 kg	1000 s	0.5	2 - 4	17.3
	fuel rod scanner	fissile	A	1 - 100 g	30 s	0.1	1	Ref. 1
scrap/waste (high density)	californium shuffler	fissile	A	1 g - 10 kg	1000 s	0.1 - 2	2 - 25	Ref. 4
	neutron coincidence (AWCC)	fissile	A	10 - 1000 g	1000 s	1 - 5	5 - 25	17.3
	random driver	fissile	A	50 - 1000 g	1000 s	1 - 5	5 - 25	Ref. 5
scrap/waste (low density)	segmented gamma scanner (SGS)	^{235}U	P	1 - 200 g	1000 s	1	2 - 10	6.9.5
	transmission-corrected gamma	^{235}U	P	1 - 200 g	300 s	1	2 - 20	6.9.3
	differential die-away	fissile	A	5 mg - 10 g	1000 s	1	30	Ref. 3
	californium shuffler	fissile	A	1 - 1000 g	1000 s	0.5	2 - 25	Ref. 4
	neutron coincidence (AWCC)	fissile	A	10 - 1000 g	1000 s	1 - 5	5 - 25	17.3

Table 23-1. (Continued)

Material Form or Matrix	NDA Technique	Measured Isotopes	Passive or Active	Range	Time	Precision (%)	Accuracy (%)	Reference
LEU								
metal	neutron totals (well counter)	^{238}U	P	1 - 500 kg	1000 s	1	2 - 3	15.4
	neutron coincidence (well counter)	^{238}U	P	2 - 500 kg	1000 s	2 - 5	2 - 5	15.4
	neutron coincidence (AWCC)	fissile	A	1 - 10 kg	1000 s	5	5 - 10	17.3
	californium shuffler	fissile	A	10 g - 10 kg	1000 s	1	1 - 2	Ref. 4
	photoneutron interrogation (PHONID)	fissile	A	10 - 1000 g	200 s	0.1 - 3	1 - 5	Refs. 6, 7
	enrichment meter	^{235}U (%)	P	200 g - 200 kg	300 s	0.2 - 1	0.2 - 0.5	7.3
oxide	enrichment meter	^{235}U (%)	P	200 g - 200 kg	300 s	0.2 - 1	0.2 - 0.5	7.3
	neutron coincidence (AWCC)	fissile	A	1 - 10 kg	1000 s	5	5 - 10	17.3
	californium shuffler	fissile	A	10 g - 10 kg	1000 s	1	1 - 2	Ref. 4
	photoneutron interrogation (PHONID)	fissile	A	10 - 1000 g	200 s	0.1 - 3	1 - 5	Refs. 6, 7
UF_6 gas	transmission-corrected gamma	^{235}U	P	5 - 100 g	1000 s	0.7	1 - 3	7.5
UF_6 liquid	enrichment meter	^{235}U (%)	P	200 g - 20 kg	300 s	0.25 - 1	0.25 - 0.5	7.3
UF_6 solid	neutron coincidence (AWCC)	fissile	A	1 - 10 kg	1000 s	1	2 - 5	Ref. 6
	enrichment meter	^{235}U (%)	P	200 g - 500 kg	300 s	1	1 - 5	7.7
solutions	transmission-corrected gamma	^{235}U conc.	P	1 - 400 g/L	1000 s	0.5	0.5	6.9
	K-edge densitometry	U conc.	A	40 - 500 g/L	1500 s	0.5	0.2 - 1	9.4
	L_{III}-edge densitometry	U conc.	A	5 - 100 g/L	1500 s	0.5	0.2 - 1	9.4
	x-ray fluorescence	U conc.	A	0.1 - 400 g/L	300 s	0.5	0.3 - 1	10.5

Table 23-1. (Continued)

Material Form or Matrix	NDA Technique	Measured Isotopes	Passive or Active	Range	Time	Precision (%)	Accuracy (%)	Reference
LEU								
fuel pellets	neutron coincidence (AWCC)	fissile	A	1 - 10 kg	1000 s	5	5 - 10	17.3
	californium shuffler	fissile	A	1 g - 10 kg	1000 s	1	1 - 2	Ref. 4
	photoneutron interrogation (PHONID)	fissile	A	10 - 1000 g	200 s	0.1 - 3	1 - 5	Refs. 6, 7
	gamma-ray well counter	^{235}U	P	1 - 10 g	300 s	0.1 - 3	0.1 - 0.5	7.3
	enrichment meter	^{235}U (%)	P	200 g - 20 kg	300 s	0.5 - 1	0.25 - 1	Ref. 2
fuel rods	neutron coincidence collar	^{235}U	A	100 g - 10 kg	1000 s	1	2 - 4	17.3
	neutron coincidence collar	^{238}U	P	1 - 10 kg	1000 s	2	5	17.3
	fuel rod scanner	fissile	A	1 - 100 g	30 s	0.1	1	Ref. 1
scrap/waste	californium shuffler	fissile	A	1 g - 10 kg	1000 s	1	5 - 20	Ref. 4
(high density)	neutron coincidence (AWCC)	fissile	A	1 - 10 kg	1000 s	5	10 - 50	17.3
	transmission-corrected gamma	^{238}U	P	100 - 5000 g	1000 s	1	2 - 20	6.9.3
	neutron totals (well counter)	^{238}U	P	10 - 500 kg	1000 s	1	2 - 5	15.4
scrap/waste	segmented gamma scanner (SGS)	^{235}U	P	1 - 200 g	1000 s	1	2 - 10	6.9.5
(low density)	transmission-corrected gamma	^{235}U	P	5 - 200 g	1000 s	1	2 - 20	6.9.3
	differential die-away	fissile	A	5 mg - 10 g	1000 s	1	30	Ref. 3

Table 23-1. (Continued)

Material Form or Matrix	NDA Technique	Measured Isotopes	Passive or Active	Range	Time	Precision (%)	Accuracy (%)	Reference
U & Pu								
oxide	neutron coincidence (HLNCC)	fertile Pu	P	10 - 6000 g	300 s	0.5	1 - 2	17.2
	calorimetry/mass spec. isot.	total Pu	P	10 - 6000 g	4 - 8 h	0.3	0.5	21.9
	calorimetry/gamma isotopics	total Pu	P	10 - 6000 g	4 - 8 h	0.5	1 - 2	21.9
	neutron coincidence (AWCC)	fissile Pu, U	A	50 - 2000 g	1000 s	3	5	17.3
	gamma-ray spectroscopy	all but ^{242}Pu	P	0.1 - 6000 g	1 h	0.1 - (3 - 5)	0.2 - 1	8.7
	gamma-ray spectroscopy	Pu/U mix ratio	P	0.1 - 6000 g	300 s	1	2	7.8
solutions	transmission-corrected gamma	$^{239}Pu/^{235}U$	P	1 - 400 g/L	1000 s	0.5	0.2 - 1	6.9
	K-edge densitometry	Pu & U conc.	A	40 - 500 g/L	1500 s	0.5	0.2 - 1	9.4
	L_{III}-edge densitometry	Pu & U conc.	A	5 - 100 g/L	1500 s	0.5	0.2 - 1	9.4
	x-ray fluorescence	Pu & U conc.	A	0.1 - 400 g/L	300 s	0.5	U:0.3/Pu:2	10.5
fuel pellets	neutron coincidence (HLNCC)	fertile Pu	P	1 - 2000 g	300 s	0.5	1 - 2	17.3
	calorimetry/mass spec. isot.	total Pu	P	10 - 6000 g	8 - 16 h	0.3	0.5	21.9
	calorimetry/gamma isotopics	total Pu	P	10 - 6000 g	8 - 16 h	0.5	1 - 2	21.9
	neutron coincidence (AWCC)	fissile Pu, U	A	50 - 2000 g	1000 s	3	5	17.3
	gamma-ray spectroscopy	all but ^{242}Pu	P	0.1 - 6000 g	1 h	0.1 - (3 - 5)	0.2 - 1	8.7
	gamma-ray spectroscopy	Pu/U mix ratio	P	0.1 - 6000 g	300 s	1	2	7.8

Table 23-1. (Continued)

Material Form or Matrix	NDA Technique	Measured Isotopes	Passive or Active	Range	Time	Precision (%)	Accuracy (%)	Reference
U & Pu								
fuel rods	neutron coincidence collar	fissile Pu, U	A	100 g - 10 kg	1000 s	1	2 - 4	17.3
	neutron coincidence collar	fertile Pu	P	100 - 6000 g	1000 s	1	1 - 2	17.3
	calorimetry/isotopes	total Pu	P	10 - 200 g	1 h	0.4	1 - 3	22.5
	fuel rod scanner	fissile	A	1 - 100 g	30 s	0.1	1	Ref. 1
scrap/waste (high density)	neutron coincidence (HLNCC)	fertile Pu	P	10 - 6000 g	300 s	1 - 5	5 - 30	17.2
	calorimetry/mass spec. isot.	total Pu	P	10 - 6000 g	8 - 16 h	0.3	0.5	22.4
	calorimetry/gamma isotopics	total Pu	P	10 - 6000 g	8 - 16h	0.5	1 - 2	22.4
	neutron coincidence (AWCC)	fissile Pu, U	A	50 - 2000 g	1000 s	5	10 - 50	17.3
scrap/waste (low density)	segmented gamma scanner (SGS)	^{239}Pu	P	1 - 1400 g	1000 s	0.5 - 2	2 - 20	6.9.5
	transmission-corrected gamma	^{239}Pu	P	1 - 1400 g	300 s	1	2 - 25	6.9.3
	neutron coincidence (HLNCC)	fertile Pu	P	10 - 6000 g	1000 s	5	5 - 30	17.2
	differential die-away	fissile Pu, U	A	5 mg - 10 g	1000 s	1	30	Ref. 3

REFERENCE

1. T. Gozani, *Active Nondestructive Assay of Nuclear Materials, Principles and Applications,* NUREG/CR-0602 (US Nuclear Regulatory Commission, Washington, DC, 1981).

2. *Handbook of Nuclear Safeguards Measurement Methods,* D. R. Rogers, Ed., Mound Laboratory report MLM-2855, NUREG/CR-2078 (US Nuclear Regulatory Commission, Washington, DC, 1983).

3. J. Caldwell et al., "Test and Evaluation of a High-Sensitivity Assay System for Bulk Transuranic Waste," *Nuclear Materials Management* XII, 75 (1984).

4. T. W. Crane, "Test and Evaluation Results of the ^{252}Cf Shuffler at the Savannah River Plant," Los Alamos National Laboratory report LA-8755-MS (March 1981).

5. H. O. Menlove, N. Ensslin, and T. E. Sampson, "Experimental Comparison of the Active Well Coincidence Counter with the Random Driver," Los Alamos Scientific Laboratory report LA-7882-MS (June 1979).

6. R. Schenkel et al., "Calibration and Experimental Comparison of the Active Well Coincidence Counter and PHONID-II," Commission of the European Communities report EUR 10377 EN (1986).

7. R. Carchon et al., "Active Interrogation of Pu and U Bulk Samples with PHONID Devices," Proc. 7th ESARDA Symposium on Safeguards and Nuclear Material Management, Liege, Belgium, May 1985, p.153.

8. L. Cowder and H. Menlove, "Neutron Coincidence Counter for MOX Fuel Pins in Storage Trays: Users' Manual," Los Alamos National Laboratory report LA-9493-M (August 1982).

9. H. O. Menlove, G. W. Eccleston, J. E. Swansen, P. Goris, R. Abedin-Zadeh, and A. Ramalho, "Universal Fast Breeder Reactor Subassembly Counter Manual," Los Alamos National Laboratory report LA-10226-M (August 1984).

Appendix A

Statistical Treatment of Assay Data

This appendix provides a brief discussion of the statistical treatment of nondestructive assay data. It contains several useful statistical formulas and procedures for estimating assay errors. The discussion considers random errors (assay precision) only. There is no consideration of the often serious problem of systematic errors (assay bias). For a more thorough discussion of assay precision and bias, please refer to textbooks on statistics.

A.1 GENERAL DEFINITIONS

Assume that some physical quantity x is measured N times, with the results x_1, x_2, x_3, ..., x_N. For example, x could be the plutonium mass of a sample measured with a neutron well counter. The best estimate of the true value of x is the average, or mean value,

$$\bar{x} = \sum_{i=1}^{N} x_i / N \tag{A-1}$$

In general, each individual measurement x_i deviates from the mean. A common indicator of the magnitude of this deviation is the standard deviation

$$\sigma = \sqrt{\frac{\sum_{i=1}^{N} (x_i - \bar{x})^2}{N - 1}} \quad (N > 1) \tag{A-2}$$

The estimated standard deviation is often quoted as the relative standard deviation (RSD), which is given by

$$\sigma_r(\%) = (\sigma/\bar{x})100 \tag{A-3}$$

It is usually assumed that the measurements are distributed about the mean according to a Gaussian (or normal) distribution. An example of the Gaussian distribution is shown in Figure A.1, which is a histogram of 500 measurements with a Gaussian shape superimposed. The mean value of the measurements is 107.3, and the standard deviation σ is 2.43. The abscissa is in units of σ. For a Gaussian distribution, the full width at half maximum height (FWHM) is 2.354σ. One can also estimate the percentage of the measurements that should lie within a specified interval about the mean. Table A-1 summarizes the estimated percentages in units of σ. The distribution of measurements shown in Figure A.1 is very close to these estimates.

Table A-1. Percentage of measurements expected to lie within $\pm w\sigma$ of the mean of a Gaussian distribution

Width of Region, $\bar{x} \pm w\sigma$	Estimated Percentage of Measurements in Region
$\pm 0.6745\sigma$	50.00%
$\pm 1.0000\sigma$	68.27%
$\pm 2.0000\sigma$	95.45%
$\pm 3.0000\sigma$	99.73%

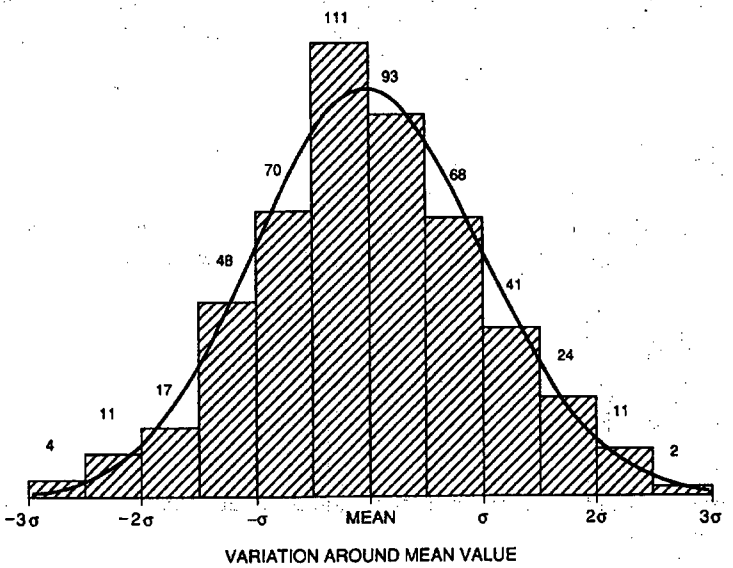

Fig. A-1. *A histogram of 500 measurements distributed about a mean. The solid line is a superimposed Gaussian shape.*

The mean value $\bar{x}$ calculated from Equation A-1 is subject to some measurement uncertainty. The estimated standard deviation of the mean that is determined from N measurements is

$$\sigma_{\bar{x}} = \sigma/\sqrt{N} \quad . \tag{A-4}$$

This equation indicates that the mean is determined more precisely as the number of measurements N increases. From Table A-1, there is a 68% probability that the true mean lies within the range $\bar{x} \pm \sigma/\sqrt{N}$ and a 95% probability that the true mean lies within the range $\bar{x} \pm 2\sigma/\sqrt{N}$.

The standard deviation σ calculated from Equation A-2 is also subject to measurement uncertainty. The standard deviation of the standard deviation follows a chi-square distribution. An approximate equation for the RSD of σ that is correct to about 10% for N greater than 3 is

$$\text{RSD of } \sigma \approx 1/\sqrt{2(N-1)} \, . \tag{A-5}$$

Table A-2 provides a more accurate compilation of the probability that the standard deviation lies within a given interval. (From Table A-1 it can be seen that the interval in Table A-2, 90% probability, has a width of almost 2σ.) Equation A-5 and Table A-2 show that the standard deviation, like the mean, will be determined more precisely as the number of measurements increases, but that there is a large variation in the computed standard deviation even for 20 or 30 repeated measurements.

Table A-2. Standard deviation of the standard deviation for a series of repeated measurements. For example, for 10 measurements, there is a 90% probability that the true standard deviation lies in the interval 0.74σ to 1.59σ, where σ is the standard deviation estimated from Equation A-2

Number of Measurements	Lower Limit of Interval 5% Probability	Upper Limit of Interval 95% Probability
2	0.58	4.41
3	0.62	2.92
4	0.65	2.37
5	0.67	2.09
7	0.71	1.80
10	0.74	1.59
15	0.77	1.44
20	0.80	1.36
25	0.81	1.31
30	0.83	1.27

A.2 PROPAGATION OF ERRORS

Often the final answer, such as grams plutonium, involves several different measurements with different uncertainties. For example, suppose that plutonium mass m = C(P – kB), where C = calibration constant, P = counts in peak window, k = a constant, and B = counts in background window. The variables C, P, and B may all have different uncertainties, which must be combined, or propagated, to arrive at the final error in the mass.

There are several common formulas that can handle most simple combinations of errors. Let $x \pm \sigma_x$ and $y \pm \sigma_y$ be two independent variables, and let k be a constant with no uncertainty.

$$\text{If } z = x + y \text{ or } x - y, \quad \sigma_z = \sqrt{\sigma_x^2 + \sigma_y^2} \,. \tag{A-6}$$

$$\text{If } z = x/y \text{ or } xy, \quad \frac{\sigma_z}{z} = \sqrt{\left(\frac{\sigma_x}{x}\right)^2 + \left(\frac{\sigma_y}{y}\right)^2} \,. \tag{A-7}$$

$$\text{If } z = kx, \quad \sigma_z = k\sigma_x \,. \tag{A-8}$$

For example, for m = C(P – kB),

$$\frac{\sigma_m}{m} = \sqrt{\left(\frac{\sigma_C}{C}\right)^2 + \frac{\sigma_P^2 + k^2\sigma_B^2}{(P - kB)^2}} \,. \tag{A-9}$$

Other formulas for error propagation can be derived by differentiating the equation z = f(x,y) and squaring the result:

$$(dz)^2 = \left(\frac{\partial z}{\partial x}\right)^2 (dx)^2 + \left(\frac{\partial z}{\partial y}\right)^2 (dy)^2 + 2\left(\frac{\partial z}{\partial x}\frac{\partial z}{\partial y}\right)(dx\ dy) \,. \tag{A-10}$$

The cross term contains the product (dx dy). If x and y are independent variables, then dx and dy are uncorrelated. If a series of measurements are made to determine z, then the measurement uncertainties dx and dy fluctuate randomly between positive and negative values, and the cross term (dx dy) has an average value close to 0. Also, the average of squared differentials like $(dx)^2$ is the square of the standard deviation, σ_x^2. Then the square root of Equation A-10 becomes

$$\sigma_z = \left[\left(\frac{\partial z}{\partial x}\right)^2 (\sigma_x)^2 + \left(\frac{\partial z}{\partial y}\right)^2 (\sigma_y)^2\right]^{1/2} \,. \tag{A-11}$$

Equations A-6, A-7, and A-9 can be derived from Equation A-11, as can any other equation needed for more complex error propagation.

A.3 Nuclear Counting Statistics

For measurements involving nuclear particle counting, all of the above information can be applied. In addition, in a nuclear counting measurement, the radioactive decays or other randomly-spaced events usually follow a Poisson distribution, for which the standard deviation σ_x of a single measurement can be estimated by

$$\sigma_x \approx \sqrt{x} \tag{A-12}$$

where x is the actual number of counts. Note that Equation A-12 applies to counts and not to count rate. If a count rate is measured for a time t, yielding a single measurement of x, there is a 68% probability that the actual rate is included in the interval $(x \pm \sqrt{x})/t$.

Consider the example of $m = C(P - kB)$. Assume that k=1 and that σ_C=0.

$\sigma_P \approx \sqrt{P}$, $\sigma_B \approx \sqrt{B}$, and $\sigma_m \approx C\sqrt{P+B}$.

The RSD (in percent) is

$$\sigma_r(\%) = \frac{\sigma_m}{m} \approx 100\frac{\sqrt{P+B}}{P-B}. \tag{A-13}$$

If N measurements are made on the same sample, the RSD of the distribution σ_r can be calculated from Equation A-2 (with m_i replacing x_i) and Equation A-3, or it can be estimated from

$$\sigma_r(\%) \approx 100\frac{\sqrt{\bar{P}+\bar{B}}}{\bar{P}-\bar{B}} \quad . \tag{A-14}$$

The two ways of computing σ_r should yield similar results if the number of repeat measurements, N, is large. If the results are not similar, the counting equipment may be malfunctioning.

Note that all of the discussion in this appendix pertains to the precision or repeatability of measurements. This analysis gives no information regarding the accuracy of a measurement (how well the measurement determines the correct amount of material).

Appendix B

Radiation Safety

The passive nondestructive assay (NDA) techniques described in this book rely on the natural radiation emitted by nuclear material. The assayist should be aware of the amount and type of radiation being emitted by the sample to ensure that the measurement does not pose a safety hazard. This appendix provides some background information on radiation safety and gives some examples of typical sample dose rates.

The radiation emitted by plutonium, uranium, thorium, and reactor fission products consists of alpha particles, beta particles, x rays, gamma rays, and neutrons. Because the alpha particles have a very short range (3-4 cm in air), they do not present a health hazard unless the active material is inhaled or ingested. When monitoring for alpha-particle contamination, the radiation meter must be held very close to the surface. Alpha-particle radiation is usually measured with an ionization chamber that has a very thin metal foil window. Beta particles have a range of several millimeters in most materials, and x rays and gamma rays have ranges of several centimeters or more. A typical beta-gamma meter has a Geiger tube or thin scintillator and a sliding metal window that is opened for measuring beta particles and closed for measuring x rays or gamma rays. Neutron radiation is more penetrating and more hazardous than any of the other radiations and is usually detected with a ^3He or BF_3 detector surrounded with a 20-cm-diameter sphere of polyethylene (a Bonner sphere or "cow").

Radioactive material is usually characterized by its activity or disintegration rate, as measured in curies. One *curie* (Ci) is 3.7×10^{10} disintegrations per second. The amount of energy deposited, the absorbed dose, is given in units of rads. One *rad* is a quantity of radiation that leads to the absorption of 100 ergs (624 200 MeV) per gram of irradiated material. The biological damage produced by a dose of 1 rad varies with the rate of energy loss in tissue. To determine the equivalent dose from different kinds of radiation, one uses the unit *rem* defined as

$$\text{rem(equivalent dose)} = \text{QF} \times \text{rad(absorbed dose)}.$$

Values for the quality factor QF are given in Table B-1. The International Commission on Radiation Protection has recommended that the quality factor for fast neutrons be increased to 20, but as of January 1989 the U.S. Department of Energy recommends that, based on the available data, the quality factor remain at 10. A new international unit of equivalent dose, the *sievert*, is equal to 100 rem.

Table B-1. Quality factor QF for the equivalent dose of different types of radiation

QF =	1	beta, x, gamma radiation
	2.3	thermal neutrons
	5	protons
	10	alpha particles
	10	fast neutrons
	20	massive charged particles like fission fragments

There are several approximate relationships that can be used to convert the strength of gamma-ray and neutron sources into dose rates. For a gamma-ray source of energy E (in MeV) and strength C (in curies),

rem/h at 30 cm $\approx$ 6CE.

For a fast-neutron source, the exposure rate is

$\sim$1 millirem per hour (mrem/h) at 1 m per 10^6 n/s

For a thermal-neutron source, the exposure rate is

$\sim$0.1 mrem/h at 1 m per 10^6 n/s .

Examples of typical dose rates encountered in passive NDA assay are given in Table B-2. The plutonium dose rate may be much higher if the americium content is more than 0.1%.

Table B-2. Some typical dose rates encountered in passive NDA

Radiation Source	Source Strength	Dose Rate at 10 cm (mrem/h)		Dose Rate at 1 m (mrem/h)	
		Neutron	Gamma	Neutron	Gamma
1 μ g ^{252}Cf	2.3 $\times$ 10^6 n/s	230	14	2.3	0.14
100 μCi ^{137}Cs	3.1 $\times$ 10^6 γ/s	0	3.0	0	0.03
PuO_2(6% ^{240}Pu)	1 kg	$\sim$10	$\sim$100	$\sim$0.1	$\sim$1
UO_2 (93% ^{235}U)	1 kg	$\sim$0	1.2	$\sim$0	0.01
Natural bkg	environment	0.01-0.02 (100-200 memr/yr)			

The biological effects of radiation are summarized in Table B-3 for acute (2 hours or less) and chronic (long term) exposures to the whole body. Based on these effects, maximum allowable radiation doses have been established by the International Commission on Radiation Protection. These recommendations are summarized in Table B-4 and may be compared to the natural background radiation level of 0.1 to 0.2 rem/yr. The maximum allowed doses are far below those that would show acute biological effects. Furthermore, in most facilities, worker exposure is held well below the allowed maximum.

The International Commission on Radiation Protection also recommends that the radiation dose should be kept as low as practical or "as low as reasonably achievable (ALARA)." The NDA operator can limit radiation dose from a source in three ways: minimize the exposure time, maximize the distance to the source, and shield the

Table B-3. Biological effects of radiation on the whole body

Dose	Probable Effect
Acute dose below 25 rem	No noticeable effect
Acute dose of 25-75 rem	Blood changes detectable in lab tests
Acute dose above 100 rem	Physical symptoms such as nausea, hair loss
Acute dose of 350 rem	50% fatality rate in 1 month
Acute dose of 600 rem	95% fatality rate
Chronic low-level dose	1 death per 7000 man-rem/yr
Chronic low-level dose	Less than 1% increase in genetic disorders per million man-rem/yr

Table B-4. Maximum allowable radiation doses above natural background

Person	Maximum Dose
Radiation worker	3 rem in 3 months (6 mrem/h continuous in 40-h week) 5 rem in 12 months (2.5 mrem/h continuous in 40-h week)
Pregnant worker	0.5 rem to fetus during pregnancy
General population	0.5 rem in 12 months

source. The operator can measure the dose rate of the source with a health physics instrument or estimate the dose rate by calculation. Unless the dose rate is completely negligible, the operator should minimize the amount of time spent near the source. Because the radiation dose from most sources decreases as the square of the distance, the source should be kept as far away as practical and handled as little as possible. If large sources must be used, then radiation shielding is necessary. Information on gamma-ray attenuation by dense materials is given in Chapter 2, and information on neutron shielding is given in Chapter 12, Section 12.6.

Appendix C

Criticality Safety

The nondestructive assay (NDA) of fissile material often involves placing the sample into a highly reflecting geometry or placing it close to other samples to be assayed. Both of these actions can potentially lead to a criticality accident and fatal radiation exposure. If the proper combination of fissile material, moderators, and reflectors is present, a self-sustaining chain reaction can occur. The NDA user is responsible for the safety of himself and others and should have an awareness of criticality safety. This appendix provides a brief introduction to this subject. Additional information is available in the references listed below. In all situations, the NDA user must consult the Criticality Safety Officer in the facility where the user is working and must follow facility guidelines for handling and storing fissionable material.

Criticality results when the neutron fission process achieves a self-sustaining chain reaction. If the production of neutrons exceeds the loss of neutrons by capture or leakage, the system is said to be supercritical. Criticality depends not only on the quantity of fissile material present (such as ^{235}U or ^{239}Pu), but also on the size and shape of the container, on the nature of any neutron-moderating material present in the container, and on the presence of any adjacent material (including human bodies) that might reflect neutrons back into the container.

The minimum critical masses of some fissionable materials are given in Table C-1. The minimum critical masses occur for spherical geometries, and these masses are lower if the sphere is surrounded by materials that reflect and moderate neutrons. For example, a critical sphere of uranium metal at normal density with an enrichment of 93% ^{235}U has a diameter of about 17.5 cm and a mass of about 49 kg. If the sphere is immersed in water, some of the neutrons are reflected back into the sphere, and the critical diameter drops to about 13 cm, with a corresponding uranium mass of about 22 kg. If sufficient water is also mixed homogeneously with the uranium, the critical diameter increases to 31 cm, but the critical mass of ^{235}U is only 800 g. This last case represents the minimum critical mass of ^{235}U that could be encountered in normal facility processing operations. Table C-1 lists minimum critical masses for three systems: pure metal, pure oxide, and a homogeneous metal-water solution, with the critical mass of each system given bare (no reflectors or moderators) and fully water-reflected (the system is surrounded by an unlimited quantity of water).

Table C-1. Minimum critical masses of some fissionable materials in spherical geometry, bare and fully water-reflected (FWR)

Fissionable Material	Metal (kg)		Oxide (kg)		Solution (g)	
	Bare	FWR	Bare	FWR	Bare	FWR
^{239}Pu(19.7 g/cm^3)[a]	10	5			1000	510
^{239}Pu(14.9 g/cm^3)[a]	16	8	21	14		
^{238}Pu			~30			
^{242}Pu	~80					
^{235}U[b]	49	22	90	43	1600	760
^{233}U	15	7	34	15	1000	500

[a] ^{239}Pu is assumed to be in the form of low-burnup plutonium with approximately 6% ^{240}Pu and 94% ^{239}Pu.
[b] ^{235}U is assumed to be in the form of highly-enriched uranium with approximately 93% ^{235}U and 7% ^{238}U.

Nondestructive assay often places a sample into a highly reflecting geometry for measurement. In particular, passive neutron assay often places the sample into a well surrounded by a thick polyethylene moderator. Some detector wells are lined with cadmium, a neutron poison, but this is not always the case. Although the moderator is not as well coupled to the sample as the fully water-reflected geometry used in Table C-1, it does lead to a measurable increase in neutron reflection and multiplication. The sample itself will usually contain much less than the minimum critical mass of fissionable material, but the NDA operator must be certain that the sample cannot inadvertently contain sufficient material to become critical when placed in the well counter. This can be a difficult problem, particularly for large containers of scrap and waste for which there is no reliable information on the amount of fissionable material, its enrichment, and the matrix in which it is embedded. For small containers of dense material, the operator must also consider the possibility of accidentally placing two containers in the counter.

Another area of concern for the NDA operator is sample storage and transport. It is customary to store many samples in a single vault or safe and to transport them to the NDA instrument in containers that may hold several samples at once. The operator must consider the possibility that, although each individual sample may be critically safe, the storage area or transport container may constitute a stacked array that is not critically safe. Flooding of the array is particularly dangerous, because a flooded array can approach the geometry of a metal-water mixture and, like a reactor fuel assembly, can be much more critical when it is flooded than when it is dry.

The most conservative approach is to rely only on the known gross weight and volume of the sample and assume that the sample-instrument combination constitutes a fully water-reflected geometry. The operator can establish a weight limit for the sample, its transport container, and its storage area that is so low that the given volume could not contain a critical combination of fissionable material and optimum moderator.

If the sample containers are too heavy to meet this conservative limit, there are several other possible ways to arrive at critically safe operating limits. Multiplication measurements may be made inside the assay system (Ref. 1) or neutron transport calculations (such as those described in Chapter 12, Section 12.7) may be carried out using properly validated computational methods (Ref. 2). Many calculations already exist in Refs. 1–7, and some may be applicable to the problem at hand. Another option is administrative control of sample geometry, matrix, or other parameters. If all else fails, it may be necessary to repackage the samples into smaller containers for which critically safe limits can be established.

Regardless of how critically safe limits and operating procedures are established, they must be determined in cooperation with the facility Criticality Safety Officer. This person is an expert because of his experience and training, and the criticality safety of all operations that involve the handling, storage, and measurement of fissionable material are his responsibility as well as the responsibility of the NDA operator.

Considerable information is available on the subject of criticality safety and critical limits. Some of this literature is listed in Refs. 1–8. Reference 3 is an excellent and very readable report that covers the factors influencing critical parameters, critical limit data, computational techniques, and general criticality control practices. References 4 and 5 specify safety limits for a variety of conditions. References 6, 7, and 8 are three of the available compilations of experimental or calculated critical data.

REFERENCES

1. *Safety in Conducting Subcritical Neutron Multiplication Measurements* In Situ, ANSI/ANS-8.6-1983 (American National Standards Institute, New York, 1983).

2. Hugh K. Clark, "Establishing Subcritical Limits," Savannah River Laboratory report DP-MS-73-27 (1973).
   This paper was presented at the Nuclear Criticality Safety Short Course at Taos, New Mexico, May 6–11 (1973). It presents and discusses the draft of a standard prepared by Work Group ANS 8.11 of the ANS Standards Committee for validating calculational methods of establishing subcritical limits for operations with fissionable materials.

3. H. C. Paxton, "Criticality Control in Operations with Fissile Material," Los Alamos Scientific Laboratory report LA-3366 (Rev.)(1972).

4. J. T. Thomas, Ed., "Nuclear Safety Guide TID-7016," US Nuclear Regulatory Commission report NUREG/CR-0095 (ORNL/NUREG/CSD-6)(June 1978).

5. *Nuclear Criticality Safety in Operations with Fissionable Materials Outside Reactors*, ANSI/ANS-8.1-1983 (Revision of ANSI/N16.1-1975)(American National Standards Institute, Inc., New York, 1983).

6. H. C. Paxton and N. L. Provost, "Critical Dimensions of Systems Containing ^{235}U, ^{235}Pu, and ^{233}U, 1986 Revision," Los Alamos National Laboratory report LA-10860-MS (1987).

7. W. R. Stratton, "Criticality Data and Factors Affecting Criticality of Single Homogeneous Units," Los Alamos Scientific Laboratory report LA-3612 (1967).

8. W. E. Converse and S. R. Bierman, "Calculated Critical Parameters," Pacific Northwest Laboratory report PNL-2080-16 (1979).

☆U.S. GOVERNMENT PRINTING OFFICE : 1993 O - 350-602